Department of Human Biology
Division of Biomedical Engineering

Thesis submitted in fulfilment of the requirements for the degree of PhD in Biomedical Engineering

ASTM Assessment of a Novel Shoulder Prosthetic Design: Measurement of Glenoid Edge Motion in Three Degrees of Freedom

Author: Leanne Haworth (HWRLEA001)

Supervisor: Professor Sudesh Sivarasu
Co-Supervisors: Professor Stephen Roche
Associate Professor Bhushan Borotikar

University of Cape Town
August 2024

Acknowledgements

I would like to express my deepest gratitude to my supervisors, Professor Sudesh Sivarasu, Professor Stephen Roche, and Associate Professor Bhushan Borotikar, for their invaluable guidance, encouragement, and unwavering support throughout the entire process of this thesis. Their expertise, patience, and constructive feedback have been instrumental in shaping the direction and quality of this work.

I am also thankful to the members of the MedTech Lab, for their insightful comments and suggestions during the development of this thesis. I am indebted to the members of the Engineering and Electronics Workshop, especially Charles Harris, Tyrone de Wet, and Iekraam Fakier who helped me manufacture the test rig. I would like to thank Sam Voight, Tim Peach, and Chi-Ho Mok for contributing to various concepts and designs related to the test rig realisation during their internships at UCT.

My heartfelt appreciation goes to my family for their support, understanding, and encouragement during this journey. I extend my gratitude to my friends and colleagues, particularly Dr Roopam Dey, for their encouragement, helpful discussions, moral support and the messages from Japan.

Lastly, I would like to acknowledge the financial support provided by the National Research Foundation and the UCT Innovation Builder Fund, which made this research possible.

Declaration

I, Leanne Haworth, hereby declare that the work on which this thesis is based is my original work (except where acknowledgements indicate otherwise) and that neither the whole work nor any part of it has been, is being, or is to be submitted for another degree in this or any other university.

I empower the university to reproduce for the purpose of research either the whole or any portion of the contents in any manner whatsoever.

Abstract

The most common cause for failure of an anatomical shoulder joint prosthesis is loosening of the glenoid component, widely attributed to 'rocking' of the component under eccentric edge loading. The American Society for Testing and Materials (ASTM) set out a standardised test to evaluate glenoid loosening, in which the glenoid is cyclically loaded (for 100,000 cycles) and the vertical displacement of the edges is measured. However, under load the glenoid edges will also deflect horizontally and with a tilting motion. Therefore, the standardised test provides limited information regarding the glenoid behaviour. To measure the complex motions of the glenoid edges, an ASTM conforming test rig was designed and then augmented with a novel edge motion measurement system.

The edge motion measurement system uses LVDT sensors to track the motion of rigid blocks on the end of lever arms connected to the glenoid edges. The block's motion is converted to complex glenoid edge motion using a MATLAB algorithm based on the system geometry. The test rig and edge motion measurement system were functionally validated in preliminary tests. The augmented test rig was then used to evaluate a novel glenoid design compared to an established (5-peg cemented) control glenoid. Six samples of each design were tested, and the resultant motion vectors were statistically compared using 1-dimensional statistical parametric mapping. The design intention of the novel glenoid was to decrease the edge motion by centralising the stresses experienced using gaps in the component surface. However, the experimental results showed increased edge motion on the novel glenoid, which was statistically significant ($P<0.05$) in the vertical and tilting directions.

Observation of overall trends in the glenoid edge motion showed that rather than rocking, a downward and outward deformation of the edges occurs (usually within 5000 cycles). This deformation was further noted to not be a permanent effect, resulting in a time-dependent relaxation of the edges out of their deformed state, which contributes to the edge motion in tension. This contribution is believed to be non-trivial with respect to the overall motion and is likely why the novel glenoid results were counter to what was expected from the FEM.

Overall, the key finding from this thesis was that the deformation and strain recovery of the glenoid components played a larger role in edge motion than the expected 'rocking' and this observation should be accounted for when developing new glenoid designs.

Contents

List of Figures

List of Tables

Abbreviations

ADL	: Activities of daily life/living
ASTM	: American Society for Testing and Materials
CE	: Conformité Européenne
CNC	: Computer numeric control
CT	: Computed tomography
DAQ	: Data acquisition
DGL	: Dynamic glenoid loosening
DOF	: Degrees of freedom
FDA	: Food and Drug Administration
FE	: Finite Element
FEM	: Finite Element Model(ling)
GH	: Glenohumeral
HA	: Hemiarthroplasty
HH	: Humeral Head
ISO	: International Organisation for Standardization
I/O	: Input/Output
IVDS	: *In-vitro* diagnostic medical devices
LHS	: Left hand side
LVDT	: Linear variable displacement transducer
ND	: Neutral deflection, the difference between the glenoid edge position when loaded (in compression or tension) and the edge position when the humeral head is at the glenoid centroid, for a given load cycle.
OBL	: Orthopaedic Biomechanics Laboratory
PC	: Personal computer
PMMA	: Polymethyl methacrylate (bone cement)
PMX	: Precision Measurement eXpandable
PROM	: Patient reported outcome measure
RHS	: Right hand side
RoC	: Radius of curvature
RTSA	: Reverse total shoulder arthroplasty
TSA	: anatomical total shoulder arthroplasty

UCT	: University of Cape Town
SAHPRA	: South African Health Products Regulatory Authority
SDK	: Software Development Kit
SPM1D	: Statistical parametric mapping in one dimension
UHMWPE	: Ultra-high molecular weight polyethylene
UPS	: Uninterrupted power source
1D	: One dimension(al)
2D	: Two dimension(al)
3D	: Three dimension(al)

List of Symbols

α	:	Tilting/rotational motion direction of the glenoid edge (from the vertical axis)
Δx	:	Change in horizontal position
$\Delta x_{glenoid}$	:	Change in horizontal position of glenoid edge
$\Delta x_{centroid}$	:	Change in horizontal position of the centre of the measuring block
Δy	:	Change in vertical position
$\Delta y_{glenoid}$	:	Change in vertical position of glenoid edge
$\Delta y_{centroid}$	:	Change in vertical position of the centre of the measuring block
σ	:	Strength of the Sawbones polyurethan bone substitute material
Ø	:	Diameter
σ_{Bone}	:	Strength of the polyurethane bone substitute
C1-8	:	Control glenoid samples 1 to 8
C_{1-4}	:	Constant values of straight lines 1 to 4 used in the glenoid edge motion calculation
C_{Bx}	:	Centroid of a measuring block
C_{By}	:	Centroid of a measuring block
C_{BL}	:	Centroid of the left-hand side measuring block
C_{BLx}	:	Horizontal (x) co-ordinate of the centroid of the left-hand side measuring block
C_{BLy}	:	Vertical (y) co-ordinate of the centroid of the left-hand side measuring block
C_{BR}	:	Centroid of the right-hand side measuring block
C_{BRx}	:	Horizontal (x) co-ordinate of the centroid of the right-hand side measuring block
C_{BRy}	:	Vertical (y) co-ordinate of the centroid of the right-hand side measuring block
C	:	Indicates compressive load condition
d_{edge}	:	Distance from the glenoid centroid to the glenoid edge
$d_{subluxation}$	:	Subluxation distance, the distance the humeral head has moved from the glenoid centroid when subluxation occurs.
D_{HHT}	:	Total translational distance of the HH in one cycle during cyclic testing
E	:	Compressive modulus
E_{Bone}	:	Compressive modulus of polyurethane bone substitute

f	:	Frequency of HH in cyclic testing
F_{Motor}	:	Force applied by the motor driver linear actuator to the outer weight housing
$F_{f\_Roller\ Block}$	:	Frictional force applied to one roller block (vertical bushing) by the vertical bearing rail
F_{f_seal}	:	Frictional force applied to one roller block (vertical bushing) by the seal on the roller block against the bearing rail
$F_{TotalRoller\ Blocks}$	:	The combined frictional force applied to all four roller blocks (vertical bushing) by the two vertical bearing rails.
$F_{Shear\ Reaction}$	:	The shear force between the surface of the glenoid and the humeral head, resisting horizontal motion of the humeral head.
$F_{Normal\ Load}$	:	The normal (vertical) contact force between the glenoid surface and the humeral head.
$F_{Normal\ Load\ MAX}$	:	The maximum normal (vertical) contact force between the glenoid surface and the humeral head.
$F_{Inertia}$	:	The inertial force required to accelerate (or decelerate) the inner weight housing assembly
F_{W_Inner}	:	The weight of the inner weight housing assembly (including added dead-weights).
F_{W_Outer}	:	The weight of the outer weight housing assembly.
F_{Weight}	:	The static weight applied by the loading system.
F_{f_Rails}	:	The combined frictional force applied to the two vertical bearing rails by all four roller blocks (vertical bushing).
$F_{f\_Horizontal\ Bearing}$	:	The combined frictional force applied to all four horizontal bearings by the two horizontal bearing shafts.
$F_{Reaction\_Shaft}$	:	The combined normal (vertical) force applied by the horizontal bearing shafts to the four horizontal bearings, to support the weight of the outer weight housing assembly.
G_L	:	Left hand side glenoid edge in DGL test rig frame of reference (inferior glenoid edge for the implantation orientation chosen in this research)
G_R	:	Right hand side glenoid edge DGL test rig frame of reference (superior glenoid edge for the implantation orientation used in this research)
H_b	:	Height of the measuring block
L_A	:	Lever arm length
L_b	:	Length of the measuring block
L_P	:	Distance from the glenoid edge to the pivot point on the lever arm
$m_{1,2,3,4}$	:	Gradients of straight lines 1,2, 3, and 4 used in the glenoid edge motion calculation

N1-8	:	Novel glenoid samples 1 to 8
P_{HH}	:	Position of the humeral head along the horizontal motion axis
P90	:	90% of subluxation distance, amplitude of HH motion during cyclic loading
R1-4	:	Resistors 1 to 4 in a strain gauge Wheatstone bridge
$r_{glenoid}$	:	Glenoid internal (surface) radius
r_{HH}	:	Humeral head radius
S_{1L}	:	Sensor 1, Left hand side measuring block (vertical sensor)
S_{1Lx}	:	Horizontal (x) co-ordinate of S_{1L} (fixed)
S_{1Ly}	:	Vertical (y) co-ordinate of S_{1L} (variable)
$S_{1Ly}\_measured$	:	Measured sensor output value of S_{1L} (variable)
$S_{1Ly}\_measured_0$	:	First measured sensor output value of S_{1L}
S_{2L}	:	Sensor 2, Left hand side measuring block (vertical sensor)
S_{2Lx}	:	Horizontal (x) co-ordinate of S_{2L} (fixed)
S_{2Ly}	:	Vertical (y) co-ordinate of S_{2L} (variable)
$S_{2Ly}\_measured$	:	Measured sensor output value of S_{2L} (variable)
$S_{2Ly}\_measured_0$	:	First measured sensor output value of S_{2L}
S_{3L}	:	Sensor 3, Left hand side measuring block (horizontal sensor)
S_{3Lx}	:	Horizontal (x) co-ordinate of S_{3L} (variable)
S_{1Ly}	:	Vertical (y) co-ordinate of S_{3L} (fixed)
$S_{3Lx}\_measured$	:	Measured sensor output value of S_{3L} (variable)
$S_{3Lx}\_measured_0$	:	First measured sensor output value of S_{3L}
S_{1R}	:	Sensor 1, right hand side measuring block (vertical sensor)
S_{1Rx}	:	Horizontal (x) co-ordinate of S_{1R} (fixed)
S_{1Ry}	:	Vertical (y) co-ordinate of S_{1R} (variable)
$S_{1Ry}\_measured$	:	Measured sensor output value of S_{1R} (variable)
$S_{1Ry}\_measured_0$	:	First measured sensor output value of S_{1R}
S_{2R}	:	Sensor 2, right hand side measuring block (vertical sensor)
S_{2Rx}	:	Horizontal (x) co-ordinate of S_{2R} (fixed)
S_{2Ry}	:	Vertical (y) co-ordinate of S_{2R} (variable)
$S_{2Ry}\_measured$	:	Measured sensor output value of S_{2R} (variable)
$S_{2Ry}\_measured_0$	:	First measured sensor output value of S_{2R}
S_{3R}	:	Sensor 3, right hand side measuring block (horizontal sensor)

S_{3Rx}	:	Horizontal (x) co-ordinate of S_{3R} (variable)
S_{1Ry}	:	Vertical (y) co-ordinate of S_{3R} (fixed)
$S_{3Rx\_}measured$:		Measured sensor output value of S_{3R} (variable)
$S_{3Rx\_}measured_0$:		First measured sensor output value of S_{3R}
T	:	Indicates tensile load condition
V_{AV}	:	Average HH velocity during cyclic testing
V_s	:	Supply voltage in a strain gauge Wheatstone bridge
x	:	Horizontal motion direction of the glenoid edge (axis parallel to bone substitute surface)
$x_{corner1,2}$	:	Horizontal co-ordinate of 'Corner 1' or 'Corner 2' in the measuring block motion calculation
y	:	Vertical motion direction of glenoid edge (axis perpendicular to bone substitute surface)
$y_{corner1,2}$	:	Vertical co-ordinate of 'Corner 1' or 'Corner 2' in the measuring block motion calculation

Chapter 1

Introduction

Shoulder arthroplasty is the partial or total replacement of the glenohumeral portion of the shoulder joint. The most common indications for shoulder arthroplasty are osteoarthritis, rotator cuff arthropathy, or glenohumeral joint fracture (Kim et al., 2011)(Australian Orthopaedic Association, 2022). For patients with debilitating pain or loss of range of motion, a shoulder arthroplasty can be an effective means of restoring function, allowing the patient to perform basic actions of daily living and, in so doing, improve their quality of life (Wiater & Fabing, 2009).

In the United Kingdom, 7,203 shoulder arthroplasty surgeries were performed in 2022 (National Joint Registry, 2023). In Australia, 9,003 shoulder arthroplasties were performed in 2021, an increase of 228% since 2008 (Australian Orthopaedic Association, 2022). These numbers are lower than total knee replacement or total hip replacements, but the shoulder arthroplasty is gaining in popularity. In the United States, over 110,000 shoulder arthroplasties were performed in 2017, and it has been predicted that this number will more than double by 2025 (Wagner et al., 2020). While no national database of surgeries performed within South Africa exists to indicate the number performed, these surgeries are offered at many government and private hospitals, including Groote Schuur Hospital, Cape Town.

This introductory chapter provides background on the variations within shoulder arthroplasty surgery, the weaknesses of existing shoulder prosthesis designs, and how new designs are evaluated. Further detail is then provided in a literature review related to the design, clinical outcomes, and methods of evaluating new anatomical Total Shoulder Replacement (TSA) prostheses, as the TSA is the focus of this thesis. The chapter concludes with the research gap identified in the current pre-clinical TSA prosthesis design evaluation methods.

1.1. Background

Shoulder arthroplasty can be performed as a TSA, a Reverse Total Shoulder Replacement (RTSA), or a hemiarthroplasty (HA). In TSA, the glenoid fossa is replaced by a shallow glenoid cup component, and the humeral head is replaced by a hemispherical humeral component (**Figure 1-1 (a)**). An RTSA 'inverts' the anatomical joint configuration, where the glenoid is fitted with a hemispherical 'glenosphere' component, and the humeral head is replaced by a humeral cup component (**Figure 1-1(b**)). A hemispherical humeral component (like that for TSA) replaces only the humeral head in HA, which articulates against the native glenoid fossa.

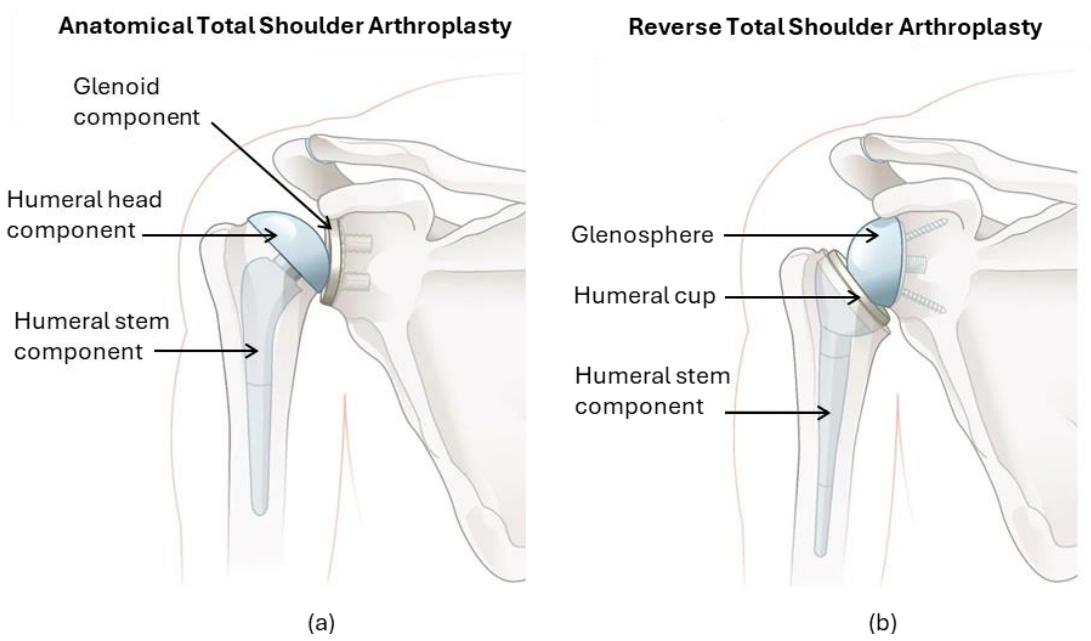

Figure 1-1 *Illustration of a typical TSA (a), where the glenoid fossa is replaced by a shallow glenoid cup component and the humeral head is replaced by a stemmed, hemispherical humeral component, vs an RTSA (b), where the glenoid fossa is instead fitted with a hemispherical 'glenosphere' and a stemmed humeral cup component replaces the humeral head. (Adapted from www.artisanorthopaedics.sg , accessed 2024/01/05)*

The first recorded shoulder arthroplasty was a TSA, performed by Jules-Emile Péan in approximately 1892, but due to infection, the prosthetic was removed after two years (Lugli, 1978). Shoulder arthroplasty saw limited use as a treatment until the 1950s, when Charles Neer successfully used proximal humeral hemiarthroplasty as a treatment for a fracture (Neer, 1955). In 1974, the development of the Neer II prosthesis for TSA saw this procedure begin to be used to treat arthrosis (Flatow & Harrison, 2011).

In 1985, Paul Grammont developed an RTSA prosthesis, which was shown to be a viable treatment for arthritic shoulders with deficient rotator cuff muscles (Grammont & Baulot, 1993). The second generation of the Grammont design in 1997, the Delta reverse prosthesis (DePuy Inc, Warsaw, IN), popularised RTSA in Europe. The Food and Drug Administration (FDA) approval of the Delta III in 2003 opened the use of RTSA in the United States (Boileau, 2011).

The RTSA has been shown to improve the range of abduction and flexion in the shoulder but, in turn, compromises the external rotation achieved compared to an anatomical TSA in which the rotator cuff muscles are functional (Ackland et al., 2015). TSA remains popular for patients with a healthy rotator cuff, as it retains the native joint biomechanics (Gorica et al., 2023). However, the high mobility and low stability of native glenohumeral joint results in TSA prostheses suffering complications such as glenohumeral instability (subluxation), rotator cuff insufficiency, infection, and component loosening (Australian Orthopaedic Association, 2022).

One of the most common failure modes for TSA prostheses is glenoid loosening (Williams & Abboud, 2005). The loosening is attributed to the 'rocking horse effect' (Franklin et al., 1988; Gregory et al., 2009), characterised by repetitive edge loading on the glenoid component by the motion of the humeral head. This creates an eccentric load that tends to lift the opposing edge of the glenoid, eventually causing the fixation to fail.

Methods of evaluating the *in-vivo* failure of the glenoid component include studies evaluating radiolucency around the components, as well as patient-reported outcome measures (PROMs), such as pain, strength, and range of motion (Grob et al., 2021; Ferguson et al., 2013). High degrees of radiolucency around the glenoid fixation, associated with failed fixation or 'unsupported' regions of the glenoid, is associated with poorer functional outcomes in patients and indications for revision (Lazarus et al., 2002). Difficulties with the repeatability of imaging during follow-up limit the use of radiographic studies over multiple years to evaluate ongoing changes to the component fixation. The method provides only 'snapshot' images at set points in time during the life of the prosthesis, so it offers little insight into the progression of glenoid loosening.

To evaluate existing designs before clinical use, both Finite Element Modelling (FEM) and mechanical testing are used. For example, Gupta et al. (2004) and Wahab et al.(2017) developed Finite Element Models (FEM) in which the glenoid component stresses were statically simulated in the *in-silico* environment.

A standardised method for validating novel glenoid designs *in-vitro* is set out by the American Society for Testing and Materials (ASTM) F2028-17 *Standard Test Methods for Dynamic Evaluation of Glenoid Loosening or Dissociation* (American Society for Testing and Materials, 2017). This 'Dynamic Glenoid Loosening' (DGL) test provides a repeatable measure of the loosening rate of the anatomical glenoid component by cyclic loading of the component in a controlled manner. The ASTM DGL test was based on the work of Anglin et al. (2000b), who developed a highly repeatable test method to simulate a 'worst case scenario' of eccentric edge loading using a cyclic linear motion of the humeral head over the glenoid component, with a controlled contact force. The defined measure of glenoid loosening in the test is the vertical edge displacement of the glenoid component before and after loading. The ASTM DGL test is useful when comparing the performance of different glenoid designs and has been widely used, with or without adjustments (Junaid et al., 2010; Gregory et al., 2009; Sabesan et al., 2015).

While the ASTM DGL test provides a strong foundation for *in-vitro* testing of glenoid designs, the information it provides is limited to vertical glenoid edge deflections. Quantifying only the vertical

edge deflection provides limited information regarding the glenoid component's overall motion and material deformations. This limits designers' ability to account for complex motions, which may influence the component survivability.

This research aims to develop a method measuring the motion of the glenoid edges in three degrees of freedom (DOF), i.e. the simultaneous vertical, horizontal, and rotational edge motions, during the cyclic loading of the DGL test. This method will then be used to evaluate a novel glenoid design developed by Dey (2018) at the UCT Orthopaedic Biomechanics Laboratory, by comparison to an existing glenoid design. The overall dynamic motions for both glenoid designs will be investigated to provide better insight into the behaviour of the components and factors that may be influencing their long-term survivability.

1.2. Literature Review

It is useful to understand the current design and failure modes of TSA prostheses, investigate the methods used for *in-vivo* clinical outcomes assessment, and be aware of the regulatory guidance set out by government agencies and industry for developing new TSA prosthesis designs. Guidance on methods of completing *in-vitro* testing can be taken from current academic and industry test equipment, a study of which will also indicate where improvements to existing test methods can be made.

1.2.1. Current TSA Prosthesis Designs

Modern TSA implant systems tend to be modular, with options for selecting humeral and glenoid component sizes. Cemented TSA components are fixed using polymethyl methacrylate (PMMA) bone cement. The PMMA is usually a two-part system comprising bead PMMA powder and an activating liquid mixed in the operating room.

Methods for fixation of the humeral stem components into the humeral medullary cavity include cementation, press-fitting, use of osseointegration, or a combination of the aforementioned (Li et al., 2023). Recently, short stem and stemless TSA humeral component designs (**Figure 1-2**) have been shown to be viable (Kleim et al., 2021; Marigi et al., 2022). The shorter humeral stem allows more freedom in positioning the humeral head component, independent of the humeral bone morphology (Karssiens et al., 2021; Raniga et al., 2022).

Figure 1-2 *Variations of TSA implant humeral stem designs, including (a) the long-stemmed Global Advantage (DePuy -Synthes), (b) the short-stemmed AltiVate (Enovis), and (c) the 'stemless' Affinis® Short (Mathys)*

Glenoid components are typically fixed by a cemented peg or keel (**Figure 1-3**). Glenoid components are typically all-polyethylene, with recent advances in the use of bone ingrowth coatings (Wiater & Fabing, 2009; Noyes et al., 2015). Glenoid components comprising a polyethylene insert attached to a metal back have also been used but were found to have higher rates of revision than all-polyethylene components (Papadonikolakis & Matsen, 2014), and there remains caution regarding their continued use (Malahias et al., 2021).

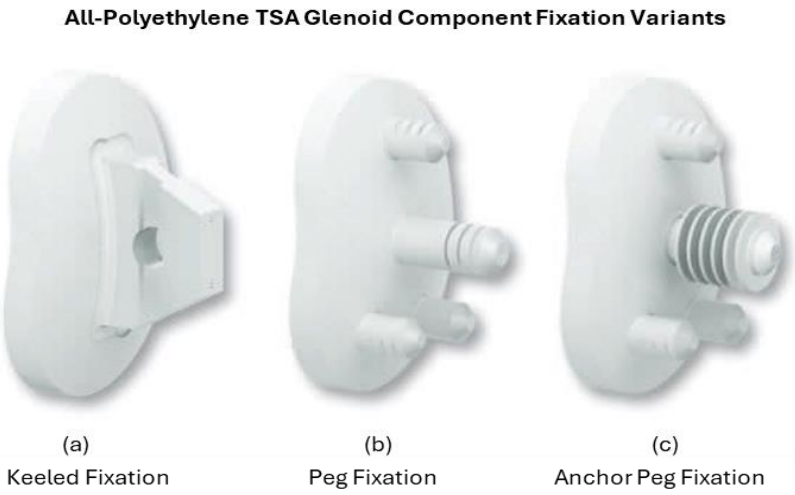

Figure 1-3 *Variations of fixation types for all-polyethylene glenoid components (Aequalis® PerFORM, Tornier), including (a) keeled fixation, (b) pegged fixation and (c) anchor peg fixation.*

The material used in all-polyethylene glenoids varies for different designs, with manufacturers often producing proprietary materials. While standard requirements for medical grade UHMWPE

are set by the International Organisation for Standardization (ISO) and the FDA, differences within the standard limits occur between designs. These differences are induced by using different base resins, production methods (e.g. ram extrusion or cold forging), and cross-linking of the polymer. Various techniques, including gamma radiation, electron beam radiation, or chemical means can be used to induce cross-linking of the polymer (Lewis, 2001).

Cross-linking the material results in improved wear resistance (Fung et al., 2018), which is desirable for reducing the production of polyethylene wear particles associated with osteolytic bone loss (Hopkins et al., 2007). The use of cross-linked material has become standard in hip and knee prostheses and is increasingly being used in TSA prostheses, where it has also been shown to improve the wear performance of the glenoid (Wirth et al., 1996).

Cross-linking UHMWPE has, however, been noted to cause a reduction in other material properties, including ultimate strength, elastic modulus, and fatigue strength (Ansari et al., 2016). The overall effect of these material properties on the long-term survival of TSA components has not been well defined (Lewis, 2001).

1.2.2. Common TSA Modes of Failure

The design of TSA prostheses is continuously evolving for both the glenoid and humeral components. However, survival rates for the TSA remain a concern, particularly for younger patients who need the implant to survive for a longer time or patients with reduced bone stock at the glenoid, for whom revision surgeries may not be feasible (Wiater & Fabing, 2009).

Reported complication rates for TSA prostheses vary. Chin et al. (2006) report a cumulative complication rate of 12% after five years in TSA surgeries with all-polyethylene glenoids. Of these, 4% required revision. Sharplin et al. (2020) reported a surgical revision rate of 5% (based on the revision of 134 out of 2613 surgeries in the New Zealand Joint Registry between 2000 and 2017). In a comparison of data from patients under 65 years of age, Roberson et al. (2017) reported a revision rate of 17.4% after an average of 9.4 years post-surgery. Causes for TSA revision include chronic dislocation of the joint, humeral fractures, infection, and failures or loosening of the TSA prosthesis (Williams & Abboud, 2005). The main failure modes for TSA prosthesis components are glenoid loosening, glenoid wear, and humeral component loosening (Australian Orthopaedic Association, 2022).

A review of complications reported after TSA for a total of 2450 shoulders from 1999 to 2005, performed by Bohsali et al. (2006), showed a glenoid loosening incidence of 6.3%. Sharplin et al. (2020) reported that 44% of failures of cemented polyethylene components reviewed were due

to glenoid loosening. Roberson et al. (2017) attributed 50% of the failures of TSA components to glenoid loosening. Glenoid loosening is widely attributed to uneven loading on the polyethylene glenoid component as the humeral head component moves towards the edge of the glenoid. This eccentric edge loading, known as the 'rocking horse effect' (Franklin et al., 1988; Matsen et al., 2008), causes an unbalanced force which tends to lift the opposite edge of the glenoid component, causing deterioration of the fixation between the prosthetic and the bone, as shown in **Figure 1-4**.

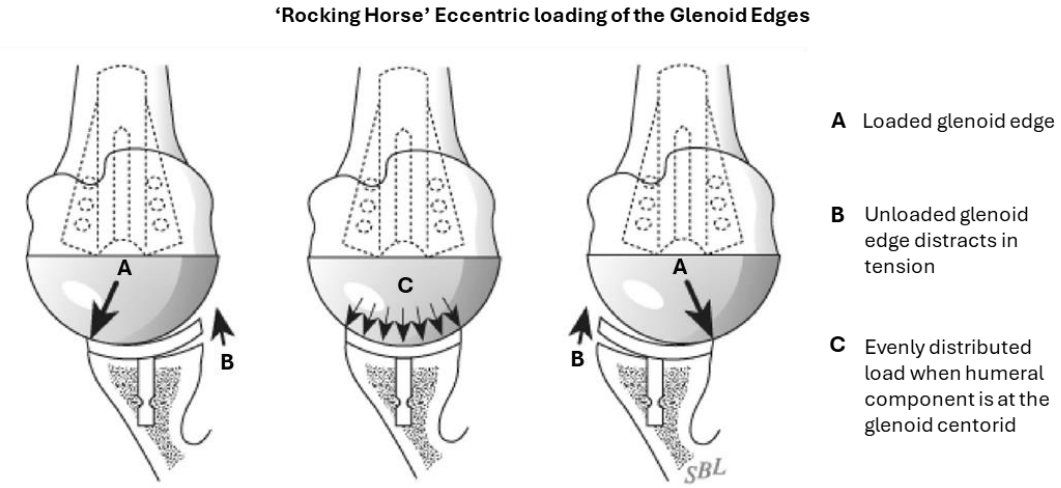

Figure 1-4 *Illustration of the 'Rocking horse effect', in which eccentric loading of the glenoid edge by the humeral component causes a tensile distraction motion at the opposite edge, promoting failure of the glenoid fixation (image adapted from (Matsen et al., 2008)).*

Eccentric loading can result from mispositioning of the glenoid component during surgery (by inferior placement (Iannotti et al., 2005) or abnormal retroversion (Farron et al., 2006), glenohumeral instability due to, for example, subscapularis deficiency or rotator cuff deficiency (Norris & Iannotti, 2002; Hopkins et al., 2006), or the tendency of the patient to bear weight on their shoulder (for example, by use of crutches) (Garreau De Loubresse et al., 2004). It has also been shown that highly conforming prostheses produce higher eccentric loads and associated tensile distractions (Anglin et al., 2001; Walch et al., 2002; Terrier et al., 2006).

Matsen et al. (2008) performed a systematic review of glenoid component failure, in which further modes of glenoid component failure were categorised to develop a more detailed understanding of the cause and possible strategies for preventing the failure. Failure modes associated with failure of the component seating, failure of the initial fixation, and failure of the underlying bone were identified. Improved component seating can be achieved by carefully preparing the underlying bone to match the glenoid components. Curved-back pegged components have better seating performance than flat-backed or keeled components (Klepps et al., 2005). Failure of the initial fixation is attributed to poor adherence of the cement to the pegs and surrounding

bone due to, for instance, fluid or clots interfering with the bonding (Matsen et al., 2008). This allows motion between the component and the bone, increasing the component's susceptibility to loosening by eccentric loading.

Finally, material failure of the glenoid component itself is also observed. In all-polyethylene components, this failure can be in the form of surface deformation), wear, or complete fracture of the component (Braman et al., 2006). Fracture of the component is a risk when the component is poorly supported by the underlying bone/cement and subjected to fatigue loading (Gunther et al., 2002). Fracture is also noted to be a risk when oxidation has degraded the material surface. Polymer cross-linking by Gamma sterilisation in air has been documented to promote oxidation of the material surface (Rockwood & Wirth, 2002). While cross-linked materials have better wear resistance, the relatively poorly documented reduction in other material properties, particularly fatigue strength, remains a concern for using this material in components such as the glenoid, which are subjected to eccentric loading (Lewis, 2001; Gunther et al., 2002).

In summary, of the currently available designs, the best-performing glenoid components are all-polyethylene components with cemented peg fixation. Round-backed components, with matching curved reaming of the bone, outperform those with flat backs. Further, non-conforming components provide better resistance to eccentric loading than conforming ones. However, it is not only the component's design that will decide the success of the TSA surgery but the surgical technique as well.

1.2.3. Surgical Technique and Clinical Evaluations of Outcomes

While the recommendations of the prosthesis manufacturer will drive the exact surgical procedure for a given design, the general procedure for a TSA remains consistent across design types. In the TSA surgery, the anatomical humeral head is resected at the surgical plane, the humeral canal is reamed, and the humeral prosthesis stem is inserted into the humeral medullary cavity. The appropriately sized humeral head component is selected and is usually press-fit onto the stem component. The glenoid is prepared by reaming the glenoid fossa until morselised cancellous bone is exposed. Fixation holes are then drilled into the glenoid surface to match the design's fixation pegs.

The PMMA cement is placed into the peg fixation holes to ensure a strong connection between the peg and the underlying bone. The movement of cement from inside the peg holes to the back of the glenoid surface has been found to be helpful in some cases (Nyffeler, Meyer, et al., 2006) and, in others, not recommended. Matsen et al. (2008) suggest that a thin layer of evenly distributed cement has the effect of filling uneven areas in the underlying bone, allowing better

seating of the back surface of the glenoid and increasing stability. Terrier et al. (2012) recommend a cement thickness of 1mm to 1.5mm to minimise the stress at the bone cement interface. A thicker cement layer, particularly when poorly distributed or damaged over time, increases the possibility of unsupported sections of the glenoid surface, increasing the likelihood of instability during eccentric loading or fatigue damage to the prosthesis. The presence of cement of any thickness behind the glenoid surface also increases the chance of cement particles being generated due to fatigue (Matsen et al., 2008), which in turn may increase the wear of the polyethylene component, promoting osteolytic bone loss (Wirth et al., 1999).

Due to the negative impact on glenoid survival of both poor fixation and glenoid bone loss, care must be taken to minimise these factors during surgery. Methods include careful surface preparation to match the glenoid to the reamed surface, ensuring the fixation holes are cleaned of clots and dried before cementation, and avoiding the use of excessive cement to reduce the heating damage to the bone during setting (Churchill et al., 2004). Further, surgeons should identify if a patient is at particular risk of prosthesis failure due to, for example, poor bone quality, the likelihood of eccentric loading by the use of crutches, or rotator cuff deficiency.

The success of a TSA is not a clearly defined or quantified measure. Rather, patients are evaluated after surgery using scoring methods, which combine several objective outcomes, such as range of motion and strength, with subjective outcomes, such as level of pain and patient satisfaction. Examples of the scoring methods are the Neer, Constant (Constant et al., 2008) and Standard Shoulder Tests.

In addition to patient scoring, the condition of the implant *in-vivo* can be evaluated by monitoring the formation of radiolucent lines in the surrounding bone (Ferguson et al., 2013). A scale for classifying the radiolucency of pegged and keeled glenoid components was published by Lazarus et al. (2002), who investigated the effect of cement support on keeled components and found that unsupported sections of glenoid back result in poorer outcomes. The reported incidence of radiolucency, even immediately after surgery, varies from 0% to 96% (Lazarus et al., 2002; Edwards et al., 2010). A high occurrence of radiolucent lines has been observed below the inferior edge of the glenoid, particularly in patients with a deficient rotator cuff, which tends to increase superior loading of the glenoid (Gregory et al., 2009). This supports the theory that superior edge loading results in crack initiation at the inferior edge of the glenoid by the rocking horse effect. However, the link between observed radiolucency and expected clinical outcomes is still not fully defined (Grob et al., 2021). Further, monitoring the progression of radiolucency in

a single shoulder is hindered by the difficulty in replicating the precise original position of the shoulder in follow-up studies (Nagels et al., 2002).

While optimal surgical technique to promote good component seating and bone-implant integration after surgery will improve the prosthesis survival, improving prosthesis designs remains an ongoing topic of research.

1.2.4. Preclinical Prothesis Design Evaluation

Implantable joint prostheses are classified as Class III Medical Devices by the FDA and the EU and as such new shoulder prosthesis designs must meet a range of statutory requirements in each region to be considered for clinical evaluation. New designs must be reasonably proven to outperform existing designs by in-silico and in-vitro pre-clinical evaluation to justify the clinical risk of bringing a new prosthesis to market.

1.2.4.1. Statutory Requirements

Implantable shoulder prostheses are strictly regulated throughout their development, manufacture, and distribution to ensure the safety of patients. Regulations include general statutory requirements for all medical devices, set out by local government agencies and international institutions such as the ISO and the ASTM. Further regulations related to implantable medical devices, including specifically shoulder implants, are also available. An overview of these regulations and standards is provided in **Figure 1-5**.

In South Africa, the manufacture and distribution of medical devices are overseen by the South African Health Products Regulatory Authority (SAHPRA), by Government Gazette 40480 (2016): *Medicines and Related Substances Act (101/1965): Regulations relating to medical Devices and In-Vitro Diagnostic Medical Devices (IVDS) (*SAHPRA, 2017). This document further requires medical device manufacturers to operate within a certified Quality Management System (QMS) as per *ISO13485 Medical devices — Quality management systems — Requirements for regulatory purposes*. (ISO, 2016)

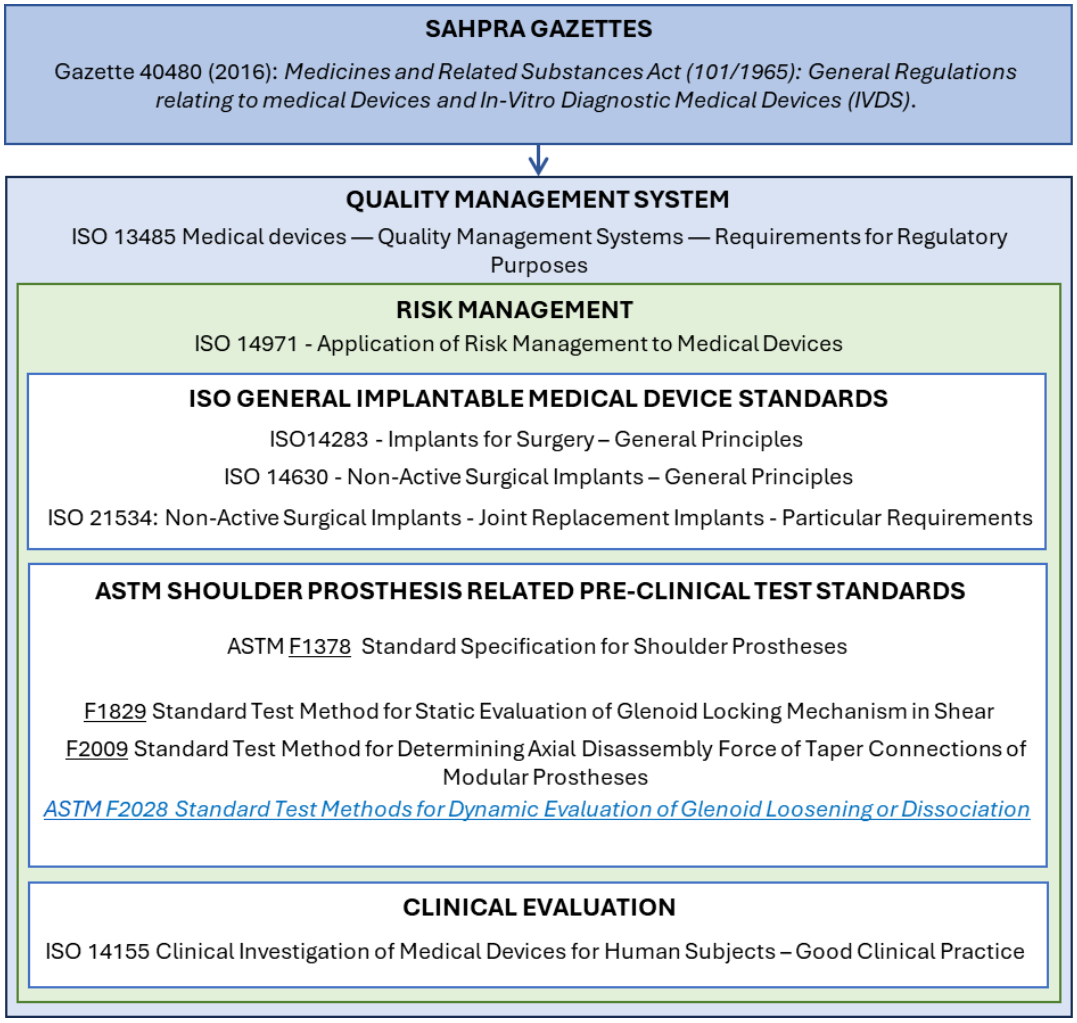

Figure 1-5 *Overview of the standards and regulations applicable to the development and distribution of an implantable shoulder prosthesis in South Africa*

The ISO 13485 standard provides a framework for quality management and assurance throughout the lifetime of the product, from design to manufacture, distribution, and use. Within ISO13485, there is a further requirement for implementing a risk management system as set out in *ISO 14971 - Application of Risk Management to Medical Devices* (ISO, 2019), which details the process of risk assessment and mitigation during all stages of the medical device life. The clinical evaluation of new medical devices is regulated by *ISO 14155 - Clinical Investigation of Medical Devices for Human Subjects – Good Clinical Practice* (ISO, 2020), which sets guidelines for clinical trial procedures and documentation control. The preceding standards provide requirements covering all phases of the design, development, and commercialisation of any new medical device. Further standards are available that are specific to implantable medical devices.

The primary ISO standards for non-active implantable devices are *ISO14283 - Implants for Surgery – Essential Principles of Safety and Performance* (ISO, 2018) and *ISO 14630 -Non-Active Surgical Implants – General Principles* (ISO, 2012). These standards cover the subjects of safety

and performance goals, design attributes and evaluation, acceptable materials (with reference made to biocompatibility testing in further standards), and processes for manufacturing, sterilisation, and packaging for all implantable devices. A further standard governing joint replacements is *ISO 21534 Non-Active Surgical Implants – Joint Replacements - Particular Requirements* (ISO, 2007). While ISO standards relating directly to some types of joint replacements (for example, knee and spine prosthetics) have been created, there is no ISO standard specifically for shoulder prostheses.

For a standard specific to implantable shoulder prostheses, we refer to *ASTM F1378 Standard Specification for shoulder prostheses* (ASTM, 2018). This standard summarises the required features and functionality of TSA and RTSA prostheses. Within ASTM F1378, reference is made to three further standards relating to the testing of failure modes of shoulder prosthetic components. These are *F1829 Standard test method for static evaluation of glenoid locking mechanism in shear* (ASTM, 2009), *F2009 Standard test method for determining axial disassembly force of taper connections of modular prostheses* (ASTM, 2020) and *F2028 Standard test methods for dynamic evaluation of glenoid loosening or dissociation* (ASTM, 2017).

The last of these, ASTM F2028, has been widely used in both *in-vitro* research (Junaid et al., 2010; Gregory et al., 2009; Sabesan et al., 2015), and as the basis for *in-silico* studies (Dey, 2018; Gunther et al., 2011), and is the standard followed in this thesis.

1.2.4.2. In-Vitro Design Evaluation

In the literature, shoulder prosthesis design research has been conducted using different types of test rigs, the primary outcome of which varies. Three common types of test rigs are those that mimic the biomechanics of the shoulder, those that investigate implant component wear, and those that investigate implant component loosening or dissociation. An overview of these test rigs is provided in **Figure 1-6**

TSA Prosthesis Design In-Vitro Test Rig Types
(by primary function)

Biomechanical Simulation	Implant Loosening or Dissociation	Implant Friction and Wear
• Simulate complex motions within the GH joint • Mimic the musculature of the joint using pulleys, wires and cadaveric GH joint samples • Low repetition of motions	• Simulate/induce prosthesis surgical fixation failure • Simple, repetitive "worst case' motion for fixation survival is applied • Moderate repetition of motions (e.g. 100,000 cycles for DGL test)	• Simulate/induce prosthesis sliding contact surface wear • Repetitive representative motion for joint motion (in up to 6 DoF) applied • High repetition of motions (1,000,000+ cycles)

Figure 1-6 *Summary of the primary characteristics of test rigs used for in-vitro evaluation of TSA prostheses, based on whether the rig is used for biomechanical joint simulation, implant fixation survival testing, or implant wear testing.*

Rigs designed to validate biomechanical models aim to mimic the motion of the upper limb by simulating muscle forces using wires controlled by musculoskeletal simulation programming. These rigs allow the contribution of individual muscle components to be evaluated. Changes to joint contact forces during a motion within anatomical or prosthetic devices are also measured. An example of such a rig, developed by Gulotta et al. (2012), is shown in **Figure 1-7**. Similar type rigs were used by Nyffeler, Sheikh et al. (2006) to investigate the effects of glenoid implant retroversion on the joint reaction forces.

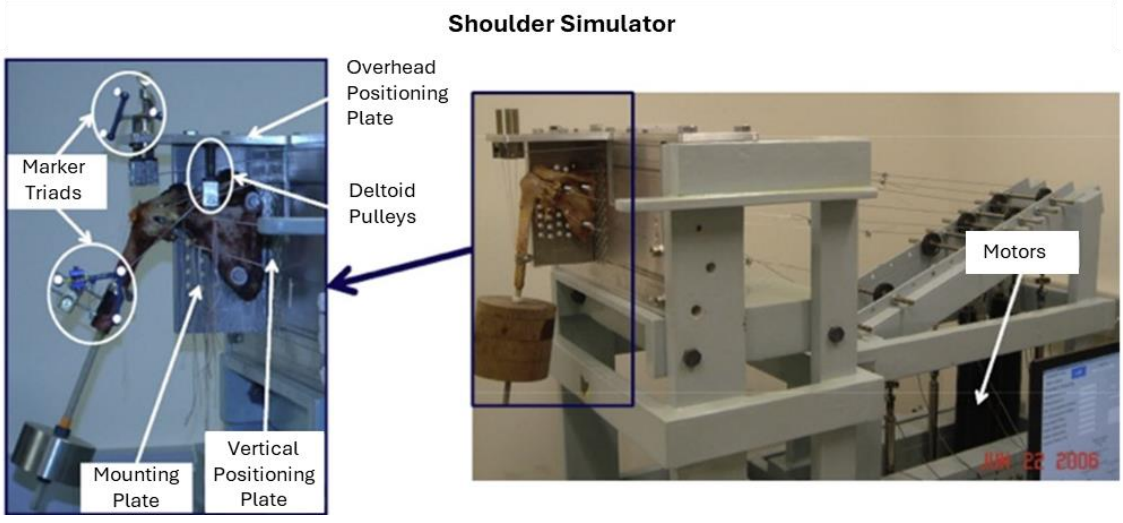

Figure 1-7 *Biomechanical shoulder simulator in which Teflon-coated steel wires are attached to the tendinous insertions of a cadaveric shoulder specimen. The wires, with lines of action that simulate the muscles, are activated by stepper motors controlled by custom software, which mimics the natural joint action (image adapted from (Gulotta et al., 2012)).*

While the muscle wire test rigs allow a very sophisticated method of simulating the true motion of the upper limb and can be used to validate biomechanical models, they are not appropriate for regulatory testing in which high rates of motion repetition and standardisation of the applied motion are required for cross research comparability.

A further type of test apparatus is that designed to perform long-term wear testing. Examples are the Newcastle Test Rig, developed by Smith et al. (2015), and commercially available equipment such as the AMTI ViVo (AMTI, Watertown, MA, USA). This type of rig is characterised by being able to simulate a predefined motion in 6 Degrees of Freedom (DoF), cycled to allow the wear of the components to be evaluated. The duration of wear tests is long, with tests usually performed in the order of millions of cycles.

Implant fixation failure type test rigs, specifically the ASTM F2028 (2017) DGL type test rig), are most relevant to current research. The DGL test provides a repeatable method of evaluating glenoid loosening due to eccentric edge loading, allowing the comparison of different glenoid prosthesis designs. The glenoid component to be evaluated is implanted in a bed of polyurethane bone substitute (with material properties specified by the ASTM (ASTM, 2021)) in the same manner as would be done during a surgical procedure. The humeral component of the prosthesis is held perpendicular to the glenoid component, with a constant controlled contact force (the standard recommends 750 ± 7.5N), as illustrated schematically in **Figure 1-8**.

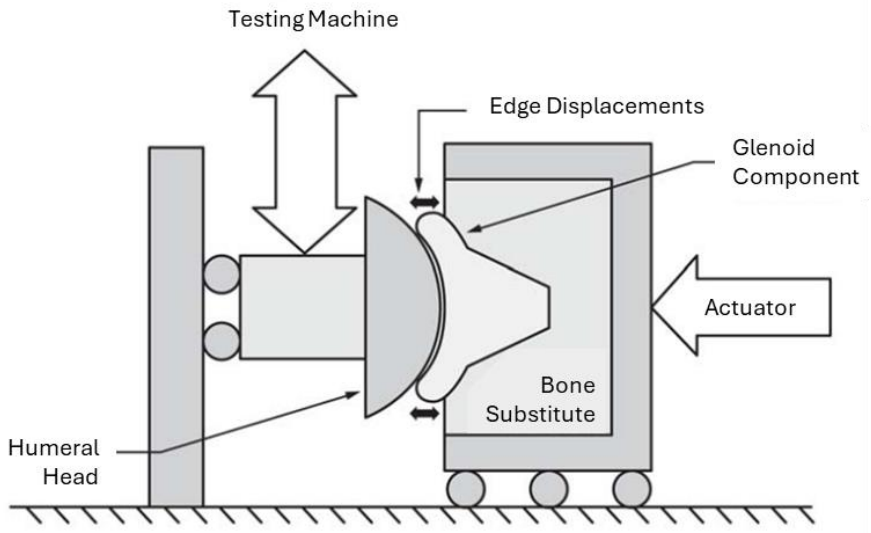

Figure 1-8 *Schematic illustration of the ASTM F2028 DGL test rig, wherein the glenoid component is implanted into a bone substitute. The glenoid is then normally loaded by the humeral head, which then moves with a cyclic shear translation from edge to edge of the glenoid to simulate eccentric edge loading. (Image adapted from ASTM F2028,2014)*

The subluxation distance for a given prosthesis design is first determined. To do this, the humeral component is moved parallel to the glenoid plane at a controlled speed (50mm/min) along either

the major or minor axis of the glenoid while the force resisting the movement is measured. The maximum force measured before the humeral head subluxes is recorded as the subluxation force, and the location along the axis is defined as the subluxation distance.

Cyclic testing is then performed with a position-controlled motion on samples of each design being compared. The humeral head is cycled through the same motion (parallel to the glenoid plane, to 90% of subluxation distance on both sides of the glenoid origin) at a recommended frequency of 2Hz to 6Hz for 100,000 cycles or until the component dissociates from the bone substitute. During this test, it is necessary to provide surface lubrication that maintains the surface temperature at 37°C. The glenoid edge displacements under load are measured before and after the cyclic testing and compared. This test provides a highly repeatable method of comparing the performance of a new glenoid design to an existing one, as the only variable that differs between tests is the design of the glenoid component.

The test apparatus upon which the ASTM F2028 standard was based was developed by Anglin et al. (2000b) and is shown in **Figure 1-9**. The rig consisted of two separate apparatuses, one for determining the glenoid edge displacements before and after the cyclic testing and another for performing the cyclic 'rocking testing'.

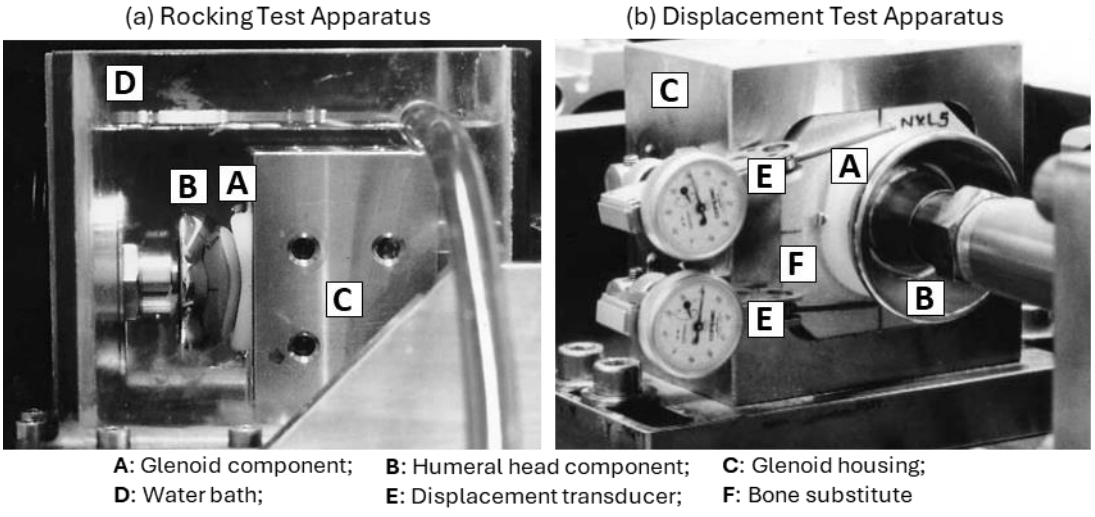

Figure 1-9 *Glenoid loosening test apparatus developed by Anglin et al. (2000). In the rocking test apparatus (a), the glenoid component (A) is cyclically loaded by the humeral component (B) in a temperature-controlled water bath (D). The displacement test apparatus employs a pair of displacement transducers resting on pins in the glenoid edges to measure the displacement of the glenoid edges at different loading conditions before and after the cyclic testing. (Images adapted from* (Anglin et al., 2000b)*)*

The DGL test has been widely used in research reported in the literature, in its standard form and with modifications. Anglin et al. (2001) performed the test on a series of glenoid design pairs to evaluate the comparative vertical tensile distraction caused by the edge loading. They reported

maximum tensile edge displacements after the 100,000 cycle tests ranging from 0.06mm (pegged component) to 0.21mm for a highly constrained component pair.

Stautberg et al. (2017) used the standard DGL test method, followed by a torsional test to failure, to evaluate the effect of removing one of the pegs on a four-peg, 'medium-sized' glenoid component. Six samples of each design were tested, and the edge motions were measured before and after cyclic loading, by dial indicators on pins attached to the glenoid side face, as per the standard DGL test method. No statistical difference was found between edge motions, or rotational failure results for the three and four-peg glenoids.

Sabesan et al. (2015) compared the edge motions induced when the glenohumeral radial mismatch was increased by testing a selection of glenoids with increasing radius of curvature (RoC) using the same sized (Ø44) humeral head. In their study, the ASTM F2028 recommendation of 2Hz was initially used for all their glenoid samples. This resulted in increasing speed of motion on the larger RoC glenoids. They found that the larger RoC glenoids were damaged by shearing deformation of the fixation pegs, accompanied by horizontal motion of the glenoid component over the bone substitute surface. They repeated the tests at a constant velocity for all glenoid sizes to avoid glenoid damage, and added a horizontal motion sensor at the midline of the glenoids in the test. Their test rig appears to have continuously measured the edge deflection during the tests, but their results report only the deflection at the start and after 50,000 cycles. After 50,000 cycles, tensile distractions of 0.1mm to 0.69mm were reported from their testing. Horizontal shift of the centreline of the glenoid was also reported, ranging from 0.18mm to 0.68mm after 50,000 cycles.

An *in-vitro* (cadaver) study performed by Gregory et al. (2009), used a DGL-type test rig in combination with Computed Tomography (CT) imaging to determine the mechanism of crack formation for a keeled glenoid component, which confirmed the crack initiation at the inferior edge of the glenoid. They highlighted the lack of understanding of how the crack formation in loosened components initiates and the lack of clarity in the literature regarding whether the cement-implant interface or the bone-cement interface fails. They found in their research that a mixture of failure types was observed, with cement remaining attached to pegs but not to the back surface of the glenoid.

A further study characterising the progression of fixation failure was performed by Junaid et al. (2010), in which modified '2D extrusion' flat-backed glenoid samples of both pegged and keeled designs were produced. The 2D component had a flat side face, allowing a 'cross-section' of the implant to be visible on the side face of the sawbones. This allowed the authors to observe the

cement condition around the pegs directly. They reported that the fixation failure stared at the inferior edge, where the cement-polyethylene interface de-bonded. The crack between cement and polyethylene grew until it reached a fixation feature such as the peg or keel, then propagated around that feature. In the images published in their research, it is clear that the component rotates as a whole when the edges are loaded (**Figure 1-10**). This adds a horizontal and rotational motion component to the deflection of the edges when eccentrically loaded.

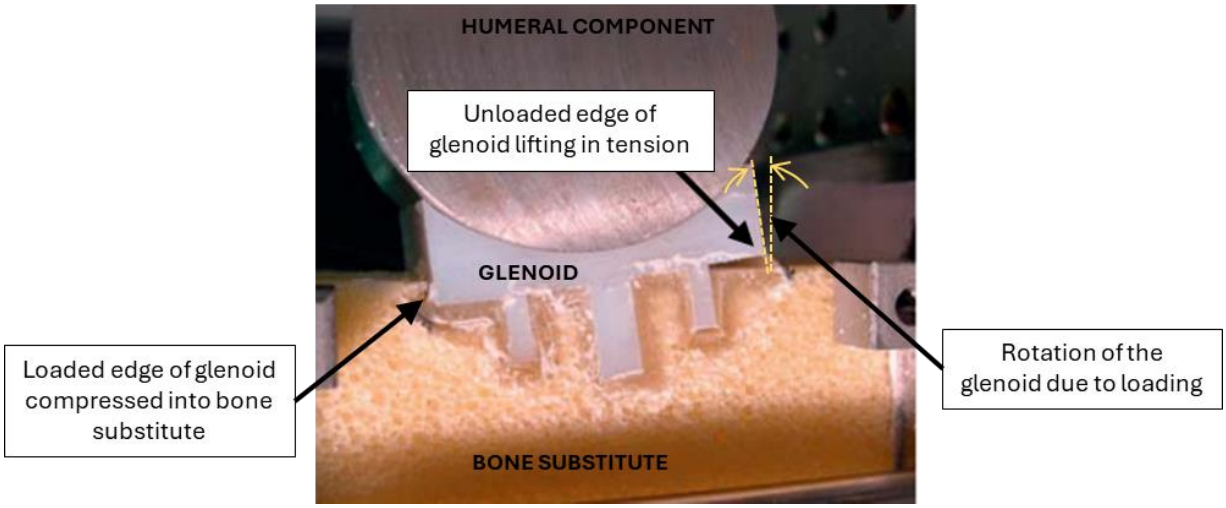

Figure 1-10 *Edge loading of a '2D glenoid' component, showing the tensile distraction that occurs at the unloaded edge, which promotes the formation of cracks at the glenoid/cement interface. The loading further causes the edge under load to compress down into the surface of the bone substitute and results in an overall rotation of the whole glenoid component. (Image adapted from (Junaid et al., 2010))*

From the preceding examples of the application of the DGL test it is apparent that despite the test being designed to be a highly repeatable experiment, there remains a large amount of variation in the way it is used. While the samples tested are expected to vary between researchers, other parameters that are suggested but not mandated by the ASTM standard, such as the applied load, the rate of loading, and number of cycles at which the vertical edge deflections are reported, also vary between studies. This hinders the comparison of results reported in the literature.

Further, the rotational motion apparent on the samples of Junaid et al. (2010), which can reasonably be expected to occur on any deformable component that is experiencing the 'Rocking Horse Effect', is not acknowledged or accounted for in the vertical edge motion measurement strategies reported in literature. The use of pins protruding from the side of the glenoid as a point of measurement, as developed by Anglin et al. (2000b) and recommended by the ASTM, is susceptible to disruption if the pin rotates instead of translating due to vertical glenoid edge motion. The degree of rotation at the point of measurement on the pin should be addressed if the vertical motions reported are to be considered valid.

Another major limitation of *in-vitro* testing is the inability of this type of test to capture the biological responses of living bone (and other tissue) to the test conditions. Bone in particular is strongly influenced by the stresses applied to it, resorbing in the case of stress shielding, and strengthening in response to load and micro-motion stresses (Sukjamsri et al., 2015). Implant designs that rely on osseointegration coatings for fixation will be particularly hindered by the lack of this response *in-vitro*.

To develop better understanding of the stresses that would occur in the bone, to predict how the living bone might respond, the *in-vitro* testing can be accompanied by in-silico modelling such as FEM. FEM and other *in-silico* methods have been widely used as a tool for glenoid design evaluation.

1.2.4.3. In-Silico Design Evaluation

Two popular methods used to simulate the shoulder joint and shoulder joint prostheses are FEM and musculoskeletal modelling. Musculoskeletal models simulate the muscle moment arms and movement of the joint. Established musculoskeletal shoulder models include the Delft shoulder and elbow model (Asadi Nikooyan et al., 2011) and the Newcastle shoulder model (Charlton & Johnson, 2006). These models are run on software such as OpenSim (Delp et al., 2007) or AnyBody (Damsgaard et al., 2006). Musculoskeletal models can be used, for example, to investigate the joint forces during ADLs, to help understand the forces during specific activities for rehabilitation guidance, or to optimise prosthesis placement (Prinold et al., 2013; Glenday et al., 2019).

Finite element models are routinely used in the pre-clinical design and development of glenoids. Terrier et al. (2005) used FEM to investigate the effect of bone cement layer thickness on micromotions and stresses occurring at the cement-bone interface. A keeled, flat back prosthesis was modelled, with a cement layer thickness varying from 0.5 to 2mm at 0.5mm increments. The FEM prosthesis was loaded at 400N and 100N, both centrally and eccentrically. Their results suggest that a cement thickness of 1mm to 1.5mm is optimal to limit cement fatigue and cement-bone interface failure.

Zhang et al. (2013) investigated the effect of articular conformity on the stress distributions within the glenoid. Three glenoids were virtually implanted with conforming, non-conforming, and hybrid surfaces. The glenoids were loaded by superior translation of the humeral head, similar to the subluxation portion of the DGL test. It was found that when centrally loaded, the conformity did not significantly affect the maximum stresses in the components. When eccentrically

loaded, the less conforming component had lower stresses than the conforming one. The hybrid implant design was found to have better glenohumeral contact at the centre and lower eccentric stresses. This suggests that the hybrid design could have superior biomechanical characteristics compared to the conforming and non-conforming designs.

Wahab et al. (2017) used FEM to evaluate the micromotions and stress distributions on glenoids in which the number of fixation pegs was varied. Curved back glenoids with 1, 2, 3, and 4 pegs were modelled and loaded with 750N centrally, in superior-anterior and superior-posterior positions. The stress distributions and micromotion around the pegs were analysed. It was found that the 4-peg glenoid produced the most favourable combination of peg stress, bone retention, and minimisation of cement quantity used.

Finally, Dey (2018) used FEM in the design of the novel glenoid that will be evaluated in this research. The FEM compared a control and the novel design using a similar method as Zhang et al. (2013) by mimicking the DGL subluxation test. The maximum and the minimum stresses were found to be within concentric regions present in the novel design, while they were observed to be on the edges of the control glenoid design. The shift of the location of the peak material stress predicted a reduction in the vertical deflection of the novel glenoid edge under tension. A further observation that can be made from the FEM of Dey (2018) is that the motion at the glenoid edges in tension and compression occurs in not only the vertical direction but also horizontally and with a rotational aspect, as shown in **Figure 1-11**. This phenomenon will be further investigated in the current thesis as part of the DGL testing.

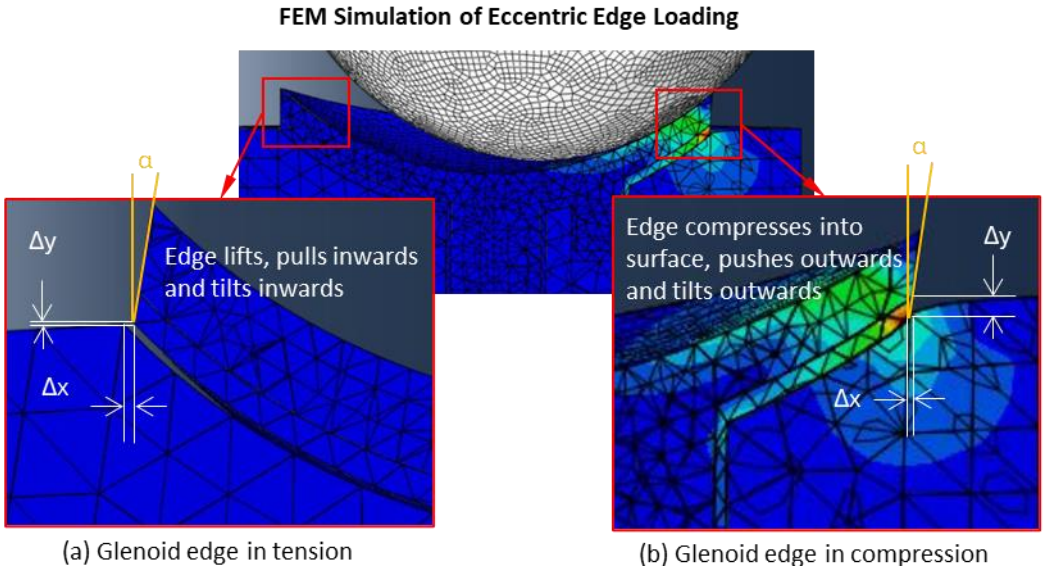

Figure 1-11 *FEM analysis by Dey (2018) of a pegged all-polyethylene glenoid loaded by 750N at the glenoid edge in the manner of the subluxation test portion of the DGL test described by ASTM F2028. At the loaded edge (b), the glenoid material is compressed down into the bone substitute surface (y direction), and the outer edge of the glenoid is pushed*

outwards (in the x direction, away from the centroid) and tilts (α) outwards. At the unloaded edge (a), the tensile distraction causes the edge to lift vertically, pull inwards (towards the centroid) and tilt inwards.

While FE modelling can provide useful predictions of the stresses and material deformations that will occur for a given loading condition, limitations remain in their use in preclinical design evaluations. Firstly, many FE models are not accompanied by an experimental validation of their findings (including Wahab et al. (2017) Zhang et al. (2013) and Dey (2018) listed above). Even where FEM is accompanied by mechanical testing for validation, such as was done by Junaid et al. (2010) who performed a FE analysis to evaluate stresses within their system as the cracks propagated around the glenoid, the FE models usually simulate static or quasi-static loading conditions. Despite the fact that the UHMWPE commonly used in glenoid designs is known to experience viscoelastic and strain-recovery material behaviours, and FE models including these effects have been developed for knee protheses (Quinci et al. , 2014). At the time of writing, no FE models of the glenoid that included these dynamic material properties were found. The true comparison of a dynamic *in-vitro* experiment to a representative dynamic FE model remains a challenge at this time.

1.3. Research Gap

The standard DGL test, used in the literature described for both mechanical and FEM testing, uses only vertical edge deflection as a measure of glenoid edge motion. The tensile vertical edge displacement is used as an indicator of potential fixation failure of a glenoid design. However, measuring only this variable, and particularly measuring it only before and after the cyclic test, limits the understanding of the overall glenoid component motions.

Adding edge motion measurement for the duration of the cyclic testing, as suggested as optional in ASTM F2028, is a good step towards understanding the progressive changes induced in the test sample as cyclic loading proceeds. However, in the standard test, continuous measurement will still provide information on only one dimension of motion.

Collins et al. (1992) noted in a study using cadaveric bone that both tilting and deformation of the glenoid component were occurring (warp and wobble). It is clear from physical testing (Junaid et al., 2010; Sabesan et al., 2015) and observed in the FE model of Dey (2018) that the edges of the component do not only move in the vertical (y) direction. Both horizontal (x) and tilting (α) motions also occur, either due to the 'rocking' of the component as a whole under eccentric loading or due to local deformation of the surface under load, as illustrated in **Figure 1-12**. A lack of information on these additional motions limits our understanding of the overall response of the

glenoid to the cyclic loading, which potentially reduces our ability to evaluate the longevity of the design.

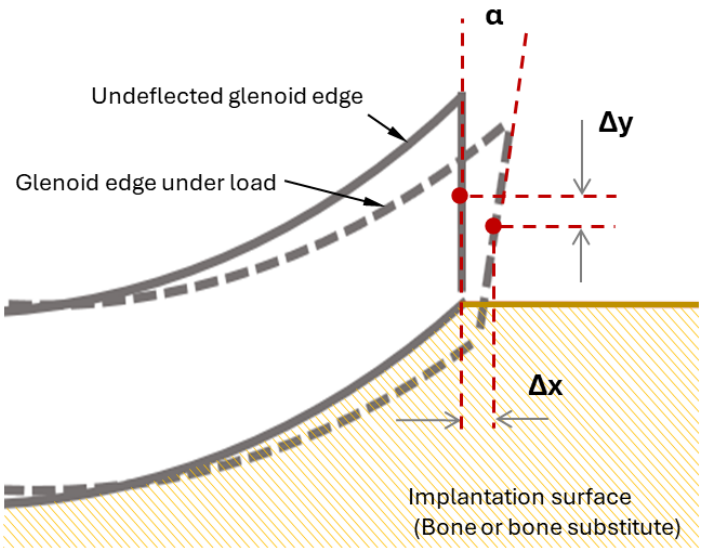

Figure 1-12 *Definition of the vertical (y), horizontal (x), and tilting(α) motions that may occur at the glenoid edge when it is loaded.*

It is further noted that horizontal and tilting motions can confound attempts to measure the vertical motion if the former motions are not adequately considered. Tilting motion, in particular, would induce an 'apparent' vertical motion if the displacement sensor rests anywhere but directly against the side face of the glenoid.

A method of measuring all three of these motions, both to better understand the glenoid response to eccentric loading and to ensure the complex edge motion does not cloud the measured values, would be a valuable addition to the standardised test.

1.4. Research Aims and Objectives

Considering that loosening of the glenoid component is a primary cause of shoulder prosthesis failure in TSA and that existing standardised mechanical test methods for new glenoid designs provide limited understanding of the loosening behaviour of the component, it is proposed that advancement of the test methods would provide a better opportunity for evaluation of new glenoid designs. The following research question, aims, and objectives are set out to investigate this.

1.4.1. Research Question

The test apparatus described by the ASTM F2028 standard measures the motion of the glenoid edge under load but only in the vertical direction.

This research aims to answer the following question:

Firstly, can an ASTM F2028 standard test apparatus be augmented such that the *measurement of the vertical, horizontal, and tilt motion of the glenoid edges during loading is feasible and valid?*

Further, are the *horizontal and tilt motions also significantly influencing the loosening of the glenoid component, and will quantifying the tilt and horizontal motion provide a more comprehensive understanding of the loosening mechanisms of the component?*

This understanding will help to refine the design parameters for future novel shoulder prostheses.

1.4.2. Aims

To answer the research questions, two broad aims are set out:

AIM 1: Develop a standardised ASTM F2028 DGL test rig augmented to continuously measure the vertical, horizontal, and tilting motion of the glenoid edges.

To achieve this aim, a test rig that can perform the ASTM F2028 DGL test must be designed and built. Further, a method for continuously measuring the vertical, horizontal, and tilt motion of the edges of a prosthetic glenoid component must be developed and integrated into the standardised test rig. The function of the augmented test rig must then be validated.

AIM 2: Investigate trends in the measured edge motions and evaluate a novel glenoid component design.

The second aim is to use the augmented test rig to perform a design evaluation of a novel glenoid design (developed by Dey (2018)). The design evaluation will compare the edge motion and loosening behaviour of the novel glenoid to that of a clinically established control and an existing FE model of the novel component under load. The complex edge motions of both designs will be analysed to identify the overall response to the cyclic edge loading as the tests proceed.

1.4.3. Objectives

As the objectives of the study will be centred on both the validation of the measurement method for glenoid edge motion and the validation of a novel glenoid component, a note should be made regarding the types of validation methods. In this research, two types of validation will be referred to: functional and concurrent validation. Functional validation refers to the process of ensuring that the item/apparatus in question performs its required functions correctly for the given application. Concurrent validation is the assessment of the success or failure of a novel design by comparison to an existing 'gold standard' for the same type of product.

To achieve the stated aims, four objectives are defined:

OBJECTIVE 1: To Design and functionally validate an ASTM F2028 DGL test rig.

The test rig on which the cyclic loading of the glenoid components can be performed will be developed in 3 stages, which are the sub-objectives for Objective 1:

1.1: Formulate test rig design requirements based on the recommendations of the ASTM F2028 standard

1.2: Design the ASTM F2028 DGL test rig (excluding the edge motion measurement system)

1.3: Build and functionally validate the test rig (excluding the edge motion measurement system)

OBJECTIVE 2: Design a method for continuous measurement of vertical, horizontal and tilt motion of the glenoid edge.

A measurement system will be designed which is able to continuously measure the vertical (Δy), horizontal (Δx), and tilt motions (α) of both edges of a prosthetic glenoid component while it is being cyclically loaded as recommended in the ASTM DGL test.

Objective 2 is broken into the following sub-objectives:

2.1: Formulate the measurement system design requirements based on the ASTM F2028 standard recommendations and constraints set by the test conditions and physical design of the test rig.

2.2: Design the edge motion measurement system

2.3: Perform preliminary validation of the measurement system *in-silico,* using appropriate motion simulation software.

OBJECTIVE 3: Augment the ASTM F2028 DGL test rig by integrating the edge motion measurement method.

Once the edge motion measurement system has been validated *in-silico,* it will be:

3.1: Physically manufactured/procured.

3.2: Mechanically and electronically integrated into the test rig to create an augmented ASTM F2028 DGL test rig.

3.3: Functionally validated by a Rig Validation Study comprising a series of tests using dummy or expired glenoid samples.

OBJECTIVE 4: Use the Augmented ASTM Test Method to investigate motion trends and concurrently validate a novel glenoid design.

Finally, the augmented test method will be used to concurrently validate a novel glenoid design, developed as part of a previous doctoral thesis by Dey (2018), by comparison of the novel design to an established design. This will require two stages of testing, followed by results analysis, for which the following sub-objectives are defined:

4.1: Perform the augmented ASTM F2028 DGL test on a control glenoid with clinically established features. The full DGL test will be repeated on six samples of the control glenoid.

4.2: Perform the augmented ASTM F2028 DGL test on the novel glenoid design, which has custom surface shape features. The full DGL test will be repeated on six novel glenoid prototype samples.

4.3: Analyse the results of both glenoids to identify overall motion trends and how these may influence fixation survival.

4.4: Evaluate the success of the novel glenoid design based on a comparison of the novel results to the control results and the existing FEM.

1.4.4. Scope

The scope of the research required to achieve the stated objectives includes the design, construction, and validation of the test rig and augmentation method, as well as performing the ASTM F2028 DGL test according to the methods set out in that standard on a set of each the novel and control glenoids. The novel design will be evaluated based on the degree of edge motion and how this may influence the loosening behaviour and fixation survival of the novel component.

The mechanical DGL test methods, as set out by ASTM F2028, focus on a simplified motion with an emphasis on the repeatability of the test. The DGL test and this research do not attempt to mimic the physiologically complex motions possible in the anatomical glenohumeral joint, nor the physiological response of living bone to joint loading. The glenoid components are implanted in a standardised bone substitute material, which is the recommendation of the standard, provides repeatability between the tests and is the material that was implemented in the FEM of the novel glenoid by Dey (2018). No biological tissues are used in the testing.

The design of the novel glenoid component, as well as the FEM used in the results comparison, are the product of work by Dey (2018) and are used in this research as part of the collaboration within the UCT Orthopaedic Biomechanics Research Laboratory.

1.5. Structure of Remaining Thesis

A summary of the thesis structure is provided in **Figure 1-13**. The remainder of this thesis comprises two design chapters, a novel glenoid evaluation chapter, a results discussion, and concluding remarks. The appendices provide additional details relating to design work, MATLAB code, and experimental data.

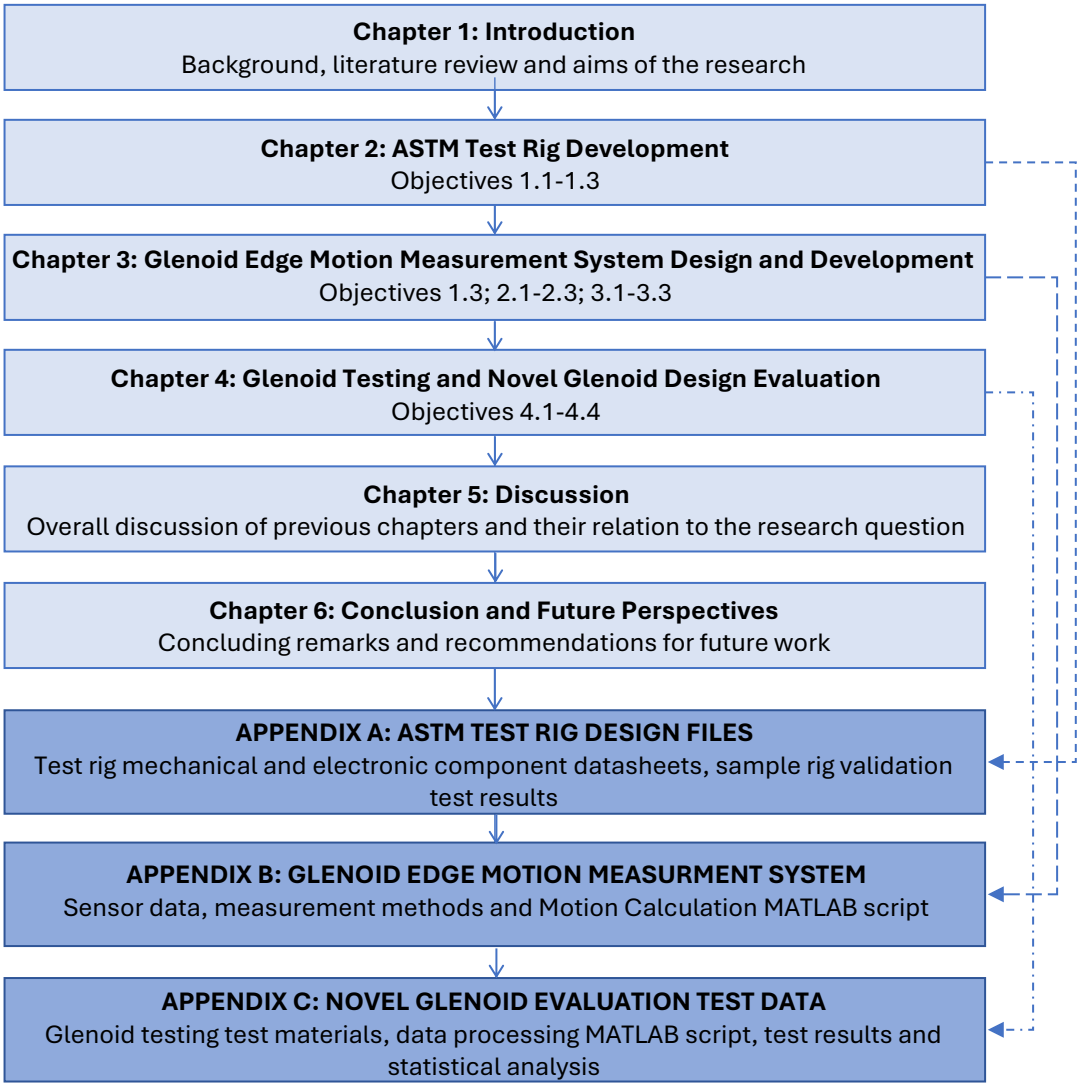

Figure 1-13 *Summary of the thesis structure*

CHAPTER 2: ASTM Test Rig Development

The first design chapter details the design and development of the standardised ASTM F2028 DGL test rig, excluding any glenoid edge motion measurement method. This chapter will cover the work required to meet Objectives 1.1 – 1.2 and the preliminary work towards Objective 1.3.

CHAPTER 3: Glenoid Edge Motion Measurement System Design and Development

The second design chapter focuses on the development of the edge motion measurement method, its integration into the test rig, and the functional validation of the resulting augmented test rig using the augmented rig validation study. This chapter covers the work required to meet Objectives 2.1 – 2.3, Objectives 3.1 to 3.3 and concludes Objective 1.3.

Further, this chapter will address the first part of the research question: *Can an ASTM F2028 standard test apparatus be augmented such that the measurement of the vertical, horizontal, and tilt motion of the glenoid edges during loading is feasible and valid?*

CHAPTER 4: Glenoid Testing and Novel Glenoid Design Evaluation

The novel glenoid evaluation chapter details the DGL testing of both the control and novel glenoids, the results of this testing, a discussion of overall motion trends observed, and the novel design evaluation. This chapter will cover the work required to meet Objectives 4.1 – 4.4.

CHAPTER 5: Discussion

The results of the preceding chapters are discussed, focusing on the implications these may have for the standardised mechanical testing methods, new glenoid designs, and clinical evaluation methods. This chapter speaks to the second part of the research question: *Are the horizontal and tilt motions also significantly influencing the loosening of the glenoid component, and will quantifying the tilt and horizontal motion provide a more comprehensive understanding of the loosening mechanisms of the component?*

CHAPTER 6: Conclusion and Future Perspectives

The final chapter provides concluding remarks and recommendations for future work.

Chapter 2

ASTM Test Rig Development

The design of the Dynamic Glenoid Loosening (DGL) test rig was guided by the ASTM F2028-17 *Standard Test Methods for Dynamic Evaluation Glenoid Loosening* standard (ASTM, 2017) referred to as 'the standard' in this thesis). This chapter gives an overview of the DGL test method and the design requirements it sets. The test rig design concept selection is briefly described, followed by a detailed description of the final designs (excluding the measurement of the edge motions, covered in Chapter 3). Finally, the implementation of the design and preliminary testing of the rig function are described.

This chapter aims to understand the standardised test method, interpret the test rig design requirements from the standard, describe the implementation of the design, and confirm that the final test rig is suitable for use in a novel glenoid design evaluation. This chapter covers the work required to meet Objective 1 (including all sub-objectives 1.1 -1.3).

2.1. Background

As discussed in the literature review, the DGL test is a standardised method for assessing the loosening characteristics of any novel glenoid design compared to those of an established design. The DGL test utilises the motion that simulates the 'rocking horse effect', assumed by the standard to be the cause of glenoid loosening, i.e. the translation of the humeral head (HH) to the eccentric regions of the glenoid. It repeats this motion for 100,000 cycles or until fixation failure. The repetition of the simple linear motion allows for repeatability between tests, which allows comparison of the results between glenoid designs.

The standard DGL test is implemented in 3 stages. First, the translation distance of the HH during the cyclic motion is determined based on the geometry of the components being tested. The translation distance is related to the point on the glenoid surface at which subluxation of the HH would occur. Once the subluxation distance is determined, the glenoid component is lightly worn in or 'conditioned' by subjecting it to a small set of load cycles (e.g. 10) at slow HH speeds. In the minimum standard requirement of the test, the first measurement of vertical edge deflections would occur immediately after the conditioning to record the value of the edge deflections before the cyclic loading. Next, the main cyclic loading is performed (recommended 100,000 cycles). After the cyclic testing, the final vertical edge deflections are measured and compared to the initial values. Optionally, the edge deflections can be continuously measured throughout the test. The standard also sets an optional requirement of measuring the normal translation of the humeral head during the test.

This chapter provides an overview of the DGL test method, from which test rig design requirements were compiled. These requirements form the basis for the final test rig design. The

method of measuring the glenoid edge motions as part of the standard test is excluded from this design stage. Chapter 3 provides a detailed description of the measurement system design.

2.2. Design Requirements

The standard sets out general requirements for the test rig relevant to all stages, as well as specific requirements set by each test stage relating to HH motion and measured variables. Further, additional requirements not explicitly stated in the standard are defined for the test rig design.

2.2.1. General ASTM F2028 Rig and Sample Requirements

The fundamental functional requirement of the DGL test is to hold the humeral and glenoid components of the prosthesis in contact with each other under load while allowing them to be cyclically moved relative to each other. The test rig must maintain a chosen normal load while holding one component fixed and moving the other in the shear direction, as illustrated in **Figure 2-1**.

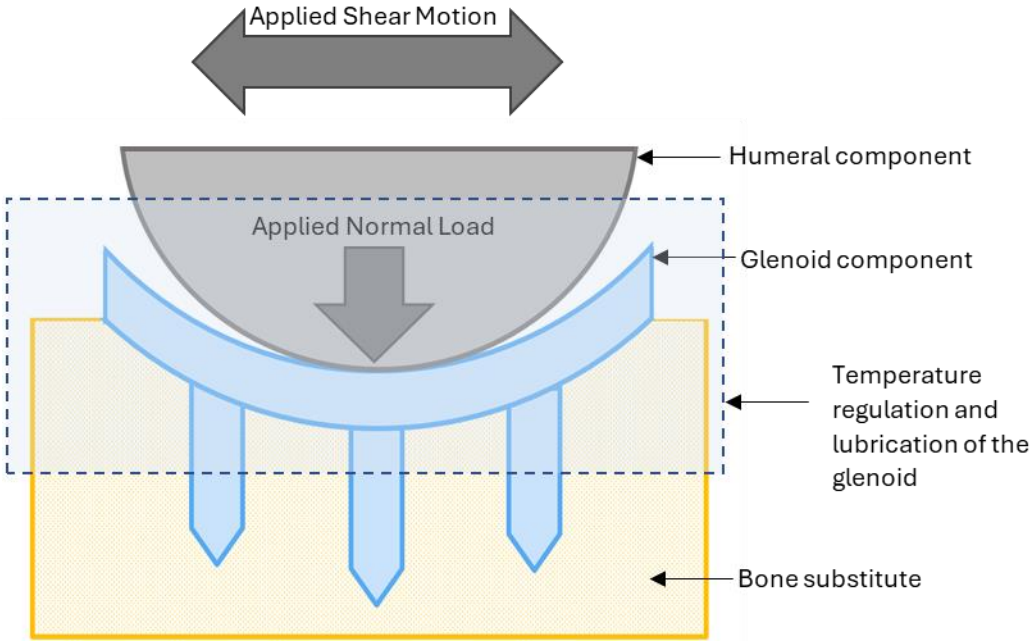

Figure 2-1 *Schematic representation of the DGL test setup requirements for applied normal load, shear translation of the HH on the glenoid, glenoid implantation into a bone substitute substrate, and temperature regulation and lubrication of the glenoid component surface.*

The magnitude of the normal load is not a set requirement, but 750N±7.5N is suggested, as this is likely to produce overall loads on the glenoid in the order of 800N-1000N, representative of moderately strenuous daily tasks, such as lifting a 4kg-8kg weight to the side (ASTM, 2017). The standard suggests higher loads could be justified when testing component strength, although this may exceed typical physiological performance. The rig should be able to set the load based

on operator choice. For equipment selection, a limit of a maximum 1000N normal load was defined.

It is not specified which component should be fixed and which should move; this is decided by individual test rig designs. The velocity of the HH shear motion varies according to which part of the test is being performed, from a minimum of 50mm/min in the subluxation test to a maximum of 2Hz cyclic speed in the cyclic loading test. To prevent damage to the glenoid component or bone substitute substrate during the shear motion, and because polyethylene material properties are temperature dependent, the component surfaces must be lubricated, and temperature regulated. The standard recommends using a temperature-controlled water bath, but other methods are allowed if suitable motivation is provided.

The glenoid components used in the DGL test should be manufactured to be as close to the 'final product' condition as possible. This includes performing any sterilisation processes that may influence material properties. Using suitable surgical bone cement, the samples must be implanted into a bone substitute material of reliably consistent properties (compressive modulus E = 193MPa, strength σ = 7.6MPa), representative of healthy glenoid cancellous bone as per the *ASTM Standard Specification for Rigid Polyurethane Foam for Use as a Standard Material for Testing Orthopaedic Devices and Instruments* (ASTM 2021). A qualified surgeon must perform the implantation in imitation of an actual TSA surgery. Only the HH component of the humeral prosthesis is required, and the same HH can be used for multiple tests, provided there is no degradation of the surface quality.

The general functional requirements of the test rig are summarised below. Each test stage adds more specific requirements to these general requirements.

- Apply a normal load between humeral and glenoid components at a chosen level (750N ±7.5N suggested by the standard).
- Apply shear motion between the humeral and glenoid components (The velocity and amplitude of the shear motion are decided by the individual test stages).
- The contact surface at which motion occurs must be temperature regulated and lubricated by a 37°C±2°C water bath (or another suitably motivated method of temperature regulation).
- The glenoid sample must be implanted in a bone substitute material of E_{Bone} = 193MPa, σ_{Bone} = 7.6MPa.

2.2.2. Test Stage 1: Determination of the Subluxation Distance

The DGL test aims to repeat the motion most likely to cause the loosening of the glenoid component, which has been identified as the motion of the humeral head to the eccentric edges of the component (Franklin et al., 1988). Therefore, it is necessary to determine the farthest point the humeral head would reach on the glenoid before subluxation would occur.

As shown in **Figure 2-2**, as the HH moves across and up the glenoid surface (distance x), the location of the point of contact changes (distance y). Subluxation occurs when the point of contact reaches the glenoid edge, and the resultant contract force is directed out of the glenoid surface (Anglin et al., 2000c). When HH moves further, it slides over the edge of the glenoid and causes material deformation.

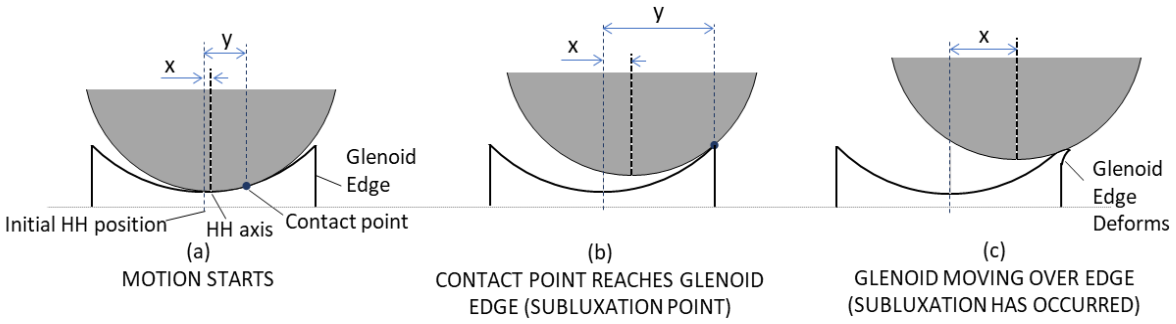

Figure 2-2 *Progression of the HH shear motion from the glenoid centroid, where the point of contact between the HH and glenoid is at the centroid, to the subluxation point, where the point of contact reaches the glenoid edge. Further motion of the HH past the subluxation point causes deformation of the glenoid edge.*

For a rigid body, the subluxation distance can be analytically predicted using the combined component geometry. However, in practice, the flexibility of the polyethylene material means that the glenoid does not behave as a rigid body, and the analytical calculation tends to underestimate the distance, particularly for values of less than 3mm (Anglin et al., 2000c). The subluxation distance must be experimentally determined to account for this flexible material behaviour.

The standard defines the subluxation distance as the distance at which the force resisting the shear motion of the humeral head reaches a peak. The amplitude of the cyclic motion used in the test is prescribed to be 90% of the subluxation distance (referred to as the P90 distance in this research). These distances are illustrated in **Figure 2-3** for a concentric glenoid on which the motion is along the major axis. The DGL test is usually performed along the major axis, as this presents the worst case for eccentric loading, but can be performed on the minor or a diagonal axis if required.

To determine the subluxation distance, the humeral head is positioned at the centroid of the glenoid and the normal load is applied as it would be for the cyclic loading. The humeral head is moved at a speed of 50mm/min along the chosen axis, past the edge of the glenoid, while the shear resistance to motion is measured (from which the position of peak shear is determined). The test is performed in both directions on a single glenoid sample and repeated for two samples of each glenoid type, from which the mean P90 value is calculated.

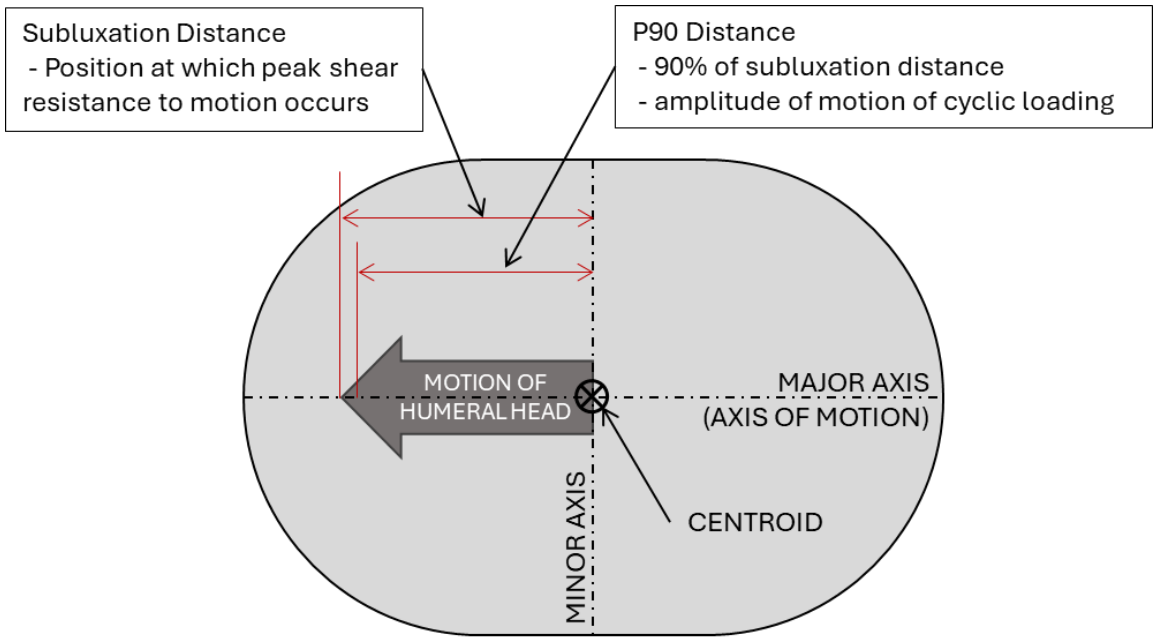

Figure 2-3 *Definition of glenoid geometry and an indication of the P90 distance, used as the amplitude of cyclic shear translation of the HH during the DGL test, for a symmetrical glenoid and motion along the major axis.*

While the maximum shear translation will vary for different glenoid sizes, the motion in the P90 test will set the maximum translation requirement for the rig, as the HH must be moved over the edge of the glenoid. To accommodate large glenoid sizes, a design requirement that the HH be able to move at least ±25mm from the centroid was set. The P90 distance measured will set the minimum translation requirement for the rig. The standard does not specify a motion resolution. Based on the resolution of reported experimental values (Anglin et al., 2001), a resolution of <0.1mm was chosen as a test rig requirement.

The magnitude of the shear resistance to motion depends on the geometry of the glenoid and humeral components (particularly the glenohumeral mismatch) and the glenoid surface frictional properties (Anglin et al., 2000c). The standard suggests that for a 750N normal load, the resultant total loads on the glenoid will be in the order of 800N-1000N (as discussed in Section 2.2.1). Anglin et al. (2000b) report experimentally measured values for the ratio of subluxation to compressive loads of between 0.2 and 1.25. Based on these force ratios and the selected

maximum applied normal load of 1000N, for the rig design equipment selection, it is assumed that the shear load will not exceed 1250N.

The speed of the P90 tests (50mm/min) sets the lower speed requirement for the test rig design. At lower HH translation speeds, there may be a risk of inducing polyethylene creep in the glenoid component (ASTM, 2017). Material yielding at the glenoid edges is expected in the P90 test, and the samples, therefore, cannot be reused for the cyclic testing. Because the motion is slow and not cyclic, temperature regulation is not required at this stage, but the glenoid surface should be lubricated with water (as specified by the standard).

The test rig requirements set by the subluxation distance test are summarised as follows:

- Perform the test on each sample in both directions along the chosen motion axis. (Samples cannot be reused for cyclic testing.)
- Control and continuously log the position of the humeral head.
- Possible shear translation of HH to be at least 25mm±0.5mm in both directions along the chosen axis of motion (the actual required translation will be dependent on the glenoid size).
- Move the HH in shear translation at a rate of 50mm/min relative to the glenoid (sets low-speed motion requirement).
- Measure and continuously log (at LabVIEW sampling rate of ~13Hz) the shear resistance to motion (estimated to be up to 1000N) vs HH position.

2.2.3. Test Stage 2: Sample Conditioning

Once the P90 distance is known, a new glenoid sample is mounted into the rig. Before the initial edge motion measurements are taken, the sample must be briefly 'worn in' by the conditioning test. The conditioning is performed for a low number of cycles at slower speeds than the main cyclic testing, with full normal load applied. The standard does not specify the speed and cycles for conditioning but gives an example of 10 cycles at 0.25Hz. The amplitude of motion for the conditioning is the same as for the main cyclic testing, i.e. P90 distance in both directions from the centroid of the glenoid.

It is further specified that the starting position of the humeral head must be within ±0.5mm of the centroid, determined either by ink marking (for non-concentric glenoids) or by using a known motion path (for concentric glenoids). This starting position should ensure that the total resultant peak loading at each of the glenoid edges (of a concentric glenoid) does not differ by more than

10%. From this, an interpreted requirement is added that at least the normal component of the load should remain within the 10% edge variation range.

The test rig requirements set by the conditioning test are summarised below. After conditioning, the measurement of the edge motions (described in Chapter 3) during cyclic loading can begin.

- Control the position of the humeral head in cyclic motion (approximately 10 cycles).
- The amplitude of motion to be the P90 distance in both directions from the glenoid centroid.
- Humeral head start position should be within ±0.5mm of the glenoid centroid and should result in the total peak loads at the edges of the glenoid being within 10% of each other.
- Speed of motion is intermediate (0.25Hz recommended by the standard).

2.2.4. Test Stage 3: Cyclic Loading

The cyclic loading test takes the same form as the conditioning, with the motion P90 distance towards each edge while under full normal load, for more cycles, and at higher speeds. The standard requires that at least three samples be tested. The standard recommends 100,000 cycles or until the glenoid fixation fails. The test does not aim to extend into the number of cycles at which surface wear becomes pronounced (~10^6 cycles). The speed of the cyclic loading aims to be as fast as possible to reduce the test duration for the high cycle counts while still slow enough to prevent damage to the glenoid surfaces. The standard recommends 2Hz (but allows up to 6Hz) cyclic speeds.

For equipment selection, the frequency values need to be converted to HH motion speed. As the size of the glenoid sample will influence the speeds associated with the specified frequency, an estimate of subluxation distance must be made. For any given glenoid, the total HH translation distance (D_{HHT}) for one full cycle would be [Centroid → +P90 → Centroid→ -P90 → Centroid], or four times the P90 distance. For a selection of glenoids ranging from 25mm to 56mm, Anglin et al. (2000b) reported subluxation distances of 1.2mm to 13.5mm. For a subluxation distance of 13.5mm, the P90 distance will be:

$$P90 = (0.9)(13.5) = 12.15mm \quad [2.1]$$

The total humeral head translation per cycle will therefore be:

$$D_{HHT} = (4)(P90) = (4)(12.15) = 48.6mm \quad [2.2]$$

To cycle the larger glenoid at the standard recommended frequency of (f) 2Hz, the average translation speed (V_{AV}) would be:

$$V_{AV} = fD_{HHT} = 2(48.6) = 97.2\ {}^{mm}/_{S} = 5832\,{}^{mm}/_{min} \quad [2.3]$$

As this is the high end of expected translation distances, this value is rounded down, and the upper limit to allowable humeral head speed during testing is set as 5000mm/min. At this maximum speed, smaller glenoids would be cycled at a higher frequency, in which case the 6Hz limit should be noted and the speed reduced if necessary. It is noted that the speed calculated here is the average speed for the full cycle of HH translation. In practice, the translational velocity of the HH will vary as the humeral head accelerates and decelerates towards and away from the glenoid edges. The speed listed here is used as a limit on the maximum value allowed.

The standard specifies that the vertical displacement of the glenoid edges is to be measured at the cyclic testing stage. The minimum requirement is for edge displacement measurements to be taken before and after cyclic testing, with continuous measurement as optional. For this research, continuous measurement will be implemented during the cyclic testing. However, while the phrase 'continuous' here refers to taking measurements during each cycle of the test, the number of logged points within each cycle will be limited to prevent excessive data set sizes. In this regard, a requirement is set that the test rig must be able to measure and log the edge displacements whenever the humeral head is at the centroid, halfway between the centroid and the P90 distance, and at the P90 distance, in both directions. While the method of measuring edge displacement will be discussed in detail in Chapter 3, the measurement and logging are noted here as rig requirements.

The optional measurement of the HH normal (vertical) translation will not be implemented in the test rig for this research. Monitoring the HH normal translation allows any sudden changes in motion during the test to be observed when edge motion is not continuously monitored, thereby indicating if loosening has occurred. As this rig will continuously monitor the edge motions, the humeral head translation measurement was deemed redundant.

The test rig requirements set by the cyclic load test are summarised as follows:

- Control and log the position of the HH in cyclic motion (100,000 cycles)
- Amplitude of motion to be P90 distance in both directions from the glenoid centroid
- The HH start position should be within ±0.5mm of the glenoid centroid, resulting in the total peak loads at the edges of the glenoid being within 10% of each other during loading (as for conditioning).

- Speed of motion not exceeding 5000mm/min (sets the high-speed motion limit)
- Measure the glenoid edge displacement throughout the cyclic loading (see Chapter 3), with measurement sampling based on HH position.
- Humeral head vertical translation will not be measured.

2.2.5. Other Requirements

Other general design requirements for the test rig, not specified by the standard, are also noted:

Firstly, the test rig is to be permanently installed in a dedicated laboratory space protected from extreme ambient temperatures to ensure minimal temperature fluctuations in the samples, as well as protect the test setup from any other environmental interference. The rig should be provided with a sturdy base with anti-vibration measures, to ensure that the motion of the test rig components during cyclic loading does not induce vibrational interference with any sensor readings taken.

Secondly, the rig should be provided with uninterrupted electrical power through an emergency generator connection and a suitable UPS, to ensure that no data is lost due to power interruptions during the lengthy cyclic tests.

Finally, the rig should be operated from a single user interface based on a laboratory PC, from which all relevant test cycles can be run and data saved. The rig should be able to run offline from internet connectivity, to ensure that the data collection is not compromised by internet service interruptions, but all data must be backed up to cloud storage as soon as a test is completed.

2.3. Design Considerations and Concept Selection

The DGL test rig has four broad design features that required design concept evaluations:

- Control of the cyclic motion of the humeral head across the glenoid surface (shear motion)
- Determination of the P90 distance (measurement of peak shear resistance to motion while logging humeral head position)
- Application of the normal load during the cyclic motion
- Measurement of the edge deflections of the glenoid under load (to be discussed in Chapter 3).

The thermal regulation of the glenoid during the test using a temperature-controlled water bath and the physical setup of the rig in a controlled laboratory space were directly implemented without detailed concept evaluations.

2.3.1. Concept Selection

The concepts considered for applying cyclic motion included electronic actuators and pneumatic and hydraulic systems, as illustrated in **Figure 2-4**. Both pneumatics and hydraulics were eliminated as options due to the infrastructure required to run the systems. An electronic linear actuator with a motor controller was chosen. The motor controller chosen can also monitor motor torque during the cyclic motion, from which the position of peak shear resistance to motion (and hence P90 distance) can be determined.

A second linear actuator (with feedback control to maintain surface force) or a freely moving deadweight was considered for applying the normal load. The deadweight load was chosen for low cost and simplicity.

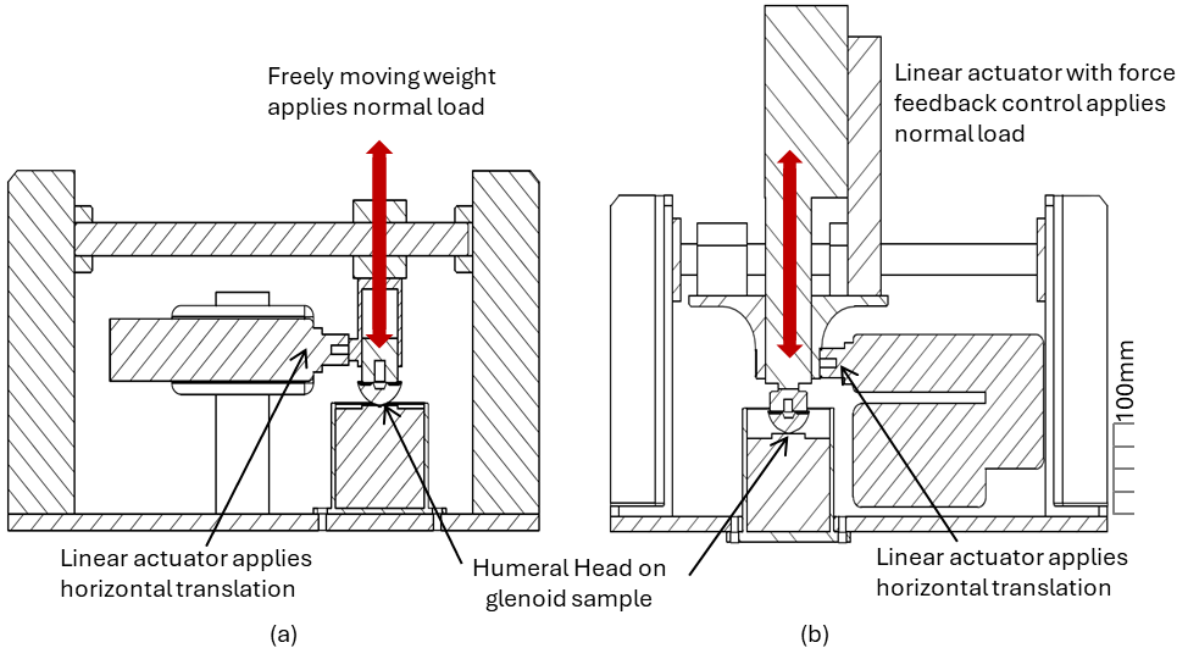

Figure 2-4 *Concepts considered for the normal load application of the DGL test rig where (a) a passive, freely moving weight is used to apply the normal load, or (b) a linear actuator with force feedback control is used to apply the normal load. In both concepts, the glenoid sample is implanted in a fixed housing, and the humeral head (with a normal load applicator) is translated by a shear direction linear actuator.*

Another consideration in the design was whether to move the humeral component (and deadweight load) during the cyclic motion or to move the glenoid sample. Moving the glenoid would be physically easier as it is much lighter, but during continuous edge displacement measurement, moving the glenoid has the potential to disturb the sensors taking the displacement readings. It was, therefore, decided that the glenoid sample should be rigidly fixed to the base of the test rig and the HH, along with the weight, moved.

2.3.2. Final Design

The concepts chosen were developed into a final design. This section provides a brief overview of the DGL rig. Section 2.4 discusses the implementation of each subsystem in detail. Details of components (model numbers and specification sheets, where relevant) are provided in Appendix A1. The final test rig design is illustrated in **Figure 2-5**.

The rig utilises a motor (1) driven linear actuator (2) to move a set of weight housings (3,4), which move the humeral head component (10). The actuator (2) directly moves the outer weight housing (3), which moves horizontally on a pair of bearing shafts (7), allowing the motion and position of the humeral head to be controlled. Inside the outer weight housing (3), the inner weight housing (4) is supported on a pair of vertical bearing rails (5), allowing it to move freely in the vertical direction. The inner weight housing is filled with lead weights (6) to the chosen load level, which applies the normal load to the glenoid component (11) via the humeral head component.

The glenoid is implanted in a Sawbones (PCF20, Sawbones, Vashon Island, Washington, USA) polyurethane foam block (11), which is clamped into a sample assembly housing (12). The sample assembly is bolted to the rig's steel base plate (14), which is, in turn, bolted to a steel frame workbench (with an anti-vibration rubber mat underlay).

The motor controller, temperature control unit, and data acquisition system are mounted adjacent to the test rig, and the operator is provided with a work desk with the laboratory PC. The test rig is installed in an access-controlled, air-conditioned laboratory space and supplied by the building emergency power connection with a generator changeover UPS.

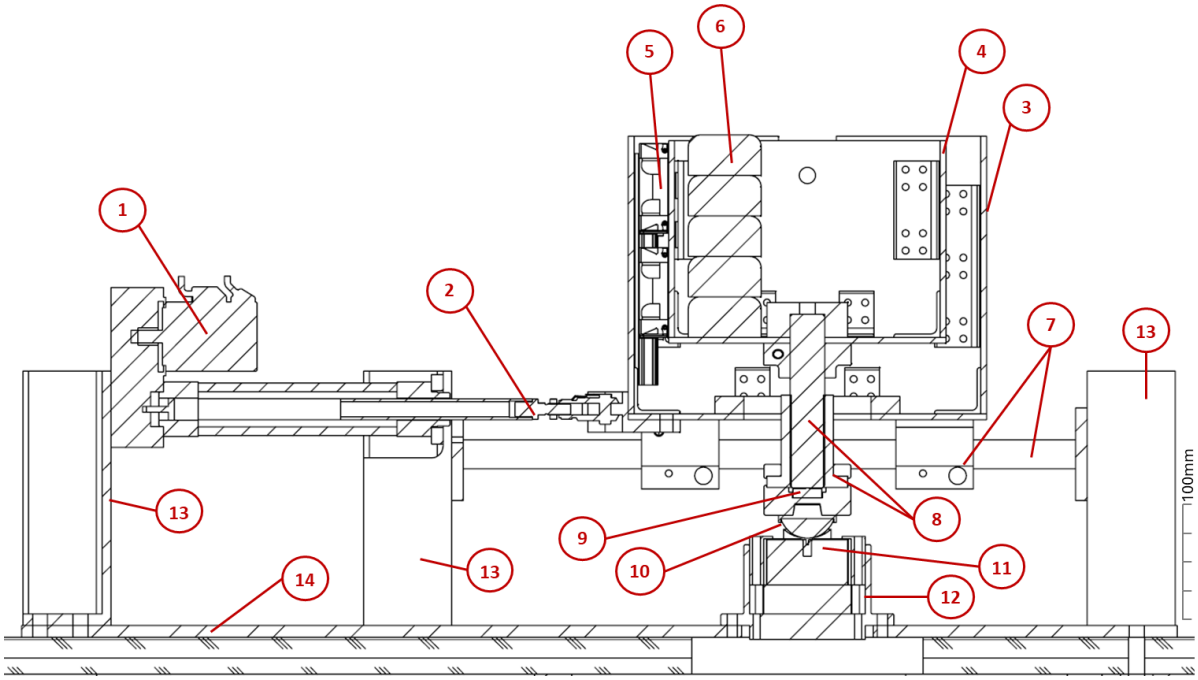

1	Motor
2	Linear actuator
3	Outer weight housing (moved horizontally by linear actuator)
4	Inner weight housing (free to move vertically on bearing rails)
5	Vertical bearing rails and runner blocks
6	Lead ingots (normal load)
7	Horizontal bushings and shafts
8	Anti-torque bearing and shaft
9	Load cell (normal load check measurement)
10	Humeral head with taper attachment
11	Sawbones bone substitute with glenoid sample implanted (clamped into sample housing)
12	Sample housing (bolted to base plate)
13	Steel upright supports
14	Base plate with rubber sheet (bolted to workbench)

Figure 2-5 *Schematic of the final design of the DGL test rig, in which a horizontal linear actuator applies the shear motion by moving a bearing shaft (7) mounted outer weight housing (3). Within the outer weight housing, a vertical rail (5) mounted inner weight housing (4) is free to move in the normal direction. The HH (10) is mounted to the base of the inner weight housing, which transfers the normal load to the glenoid (11). The normal load is applied by placing lead weights (6) inside the inner weight housing until the selected load at the glenoid is achieved. The load is monitored by a load cell (9) mounted at the HH.*

2.4. Design Implementation

The implementation of each subsystem design and rig function is described in detail here, specifically, the motion control system, the force application method, the subluxation distance measurement system, and the temperature-controlled lubrication system. Later sections discuss the validation testing of the rig's subsystems/functions.

2.4.1. Motion Control and Monitoring System

The horizontal cyclic motion is performed by the linear actuator that moves the outer weight housing, shown in **Figure 2-6**. The outer weight housing is a bolted steel plate box, which runs on four linear bushings (Rexroth Linear sets) on a pair of horizontal bearing shafts. The linear actuator and bearing shafts are mounted to steel profile supports, bolted to the test rig base plate.

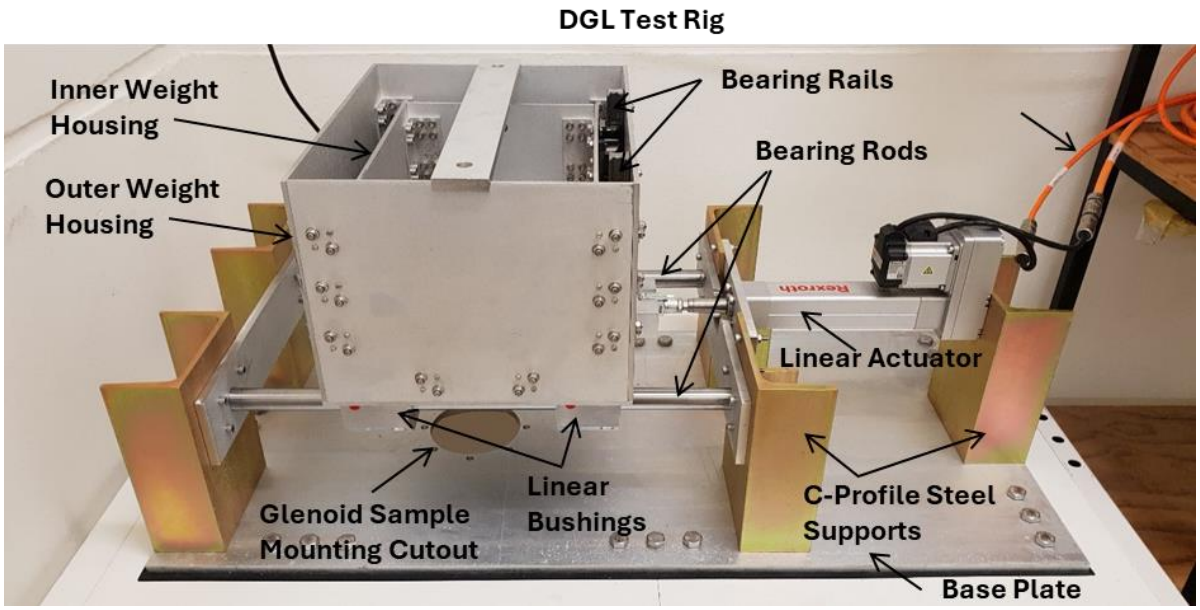

Figure 2-6 *Assembled DGL test rig showing the horizontal linear actuator, which applies the shear motion to the outer weight housing, inside which the inner weight housing can move in the vertical (normal) direction.*

The linear actuator is driven by a motor controlled by a Bosch Rexroth IndraDrive motor controller (Rexroth IndraDrive CS, Bosch Rexroth, Kempton Park, South Africa, (specifications provided in Appendix A1). The IndraDrive setup and control are performed by ethernet connection to the laboratory PC and using IndraWorks (Version 13.14.614.0, Bosch Rexroth) software suite or by LabVIEW (Student Edition 2018, National Instruments, Austin, Texas, USA) using the IndraWorks SDK Add-On (the overall rig user interface is discussed further in Section 2.4.5).

The cyclic motion is defined by setting the absolute position of the centroid as the start position and then moving ±P90 about the centroid (in the horizontal, shear direction, parallel to the

Sawbones surface). The linear actuator has a stroke of 100mm, and the controller uses an absolute position within this stroke. In the final design, the centroid of the glenoid stands at 66.5mm in the actuator frame of reference, used as the start of the motion. To ensure the glenoid is mounted in the correct position, the Sawbones block is lightly press-fit into the circular steel sample housing and clamped into place. The centre of the block is marked with a guide hole and cross-guide lines during manufacture, **Figure 2-7**, to ensure the glenoid is implanted in the correct position. The glenoid sample assembly is bolted rigidly to the base plate of the test rig by eight fixation bolts.

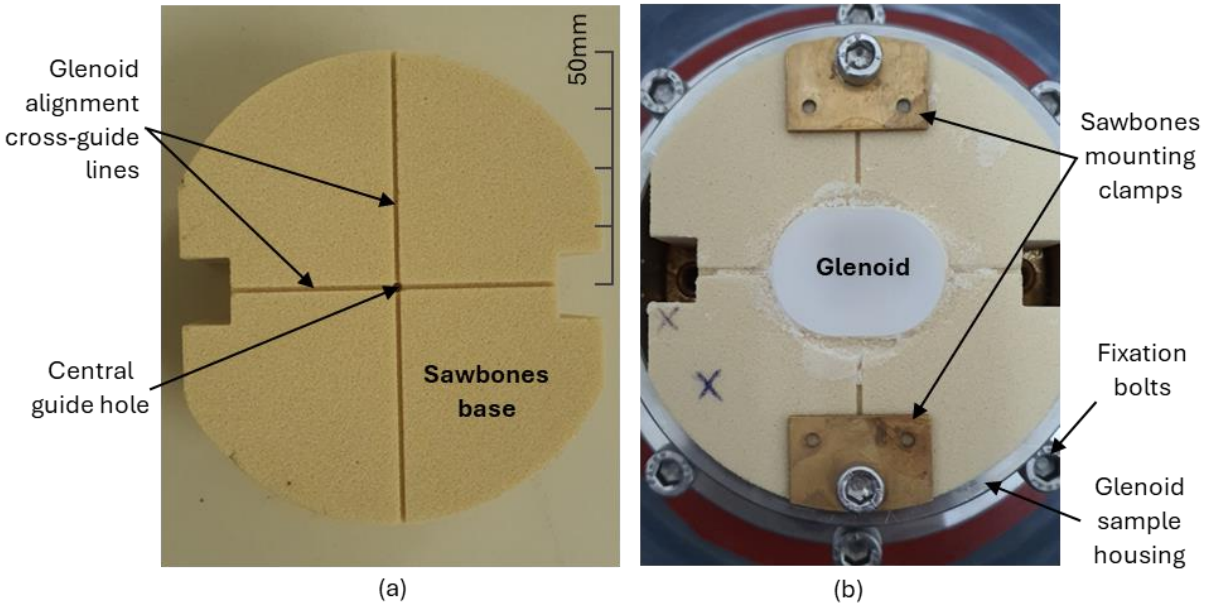

Figure 2-7 *Sawbones bone substitute block (a) before assembly, showing the central guide hole and cross-guides used for glenoid implantation alignment, and (b) clamped into the sample housing after glenoid implantation.*

The user also sets the velocity, acceleration, and jerk values for the motion. The controller monitors the position, velocity, and motor torque, which can be logged to the laboratory PC during testing.

2.4.2. Normal Load Application

The normal force is applied using a deadweight within the inner weight housing. Four rail bushings (Rexroth Runner Blocks, R1651813020, Bosch Rexroth) are attached to the side of the inner weight housing, which mount onto the pair of bearing rails (Rexroth Guide Rail, R16505803, Bosch Rexroth) on the inside face of the outer weight housing (illustrated in **Figure 2-8** (a) and (b) respectively), allowing the inner weight housing to move freely in the vertical direction.

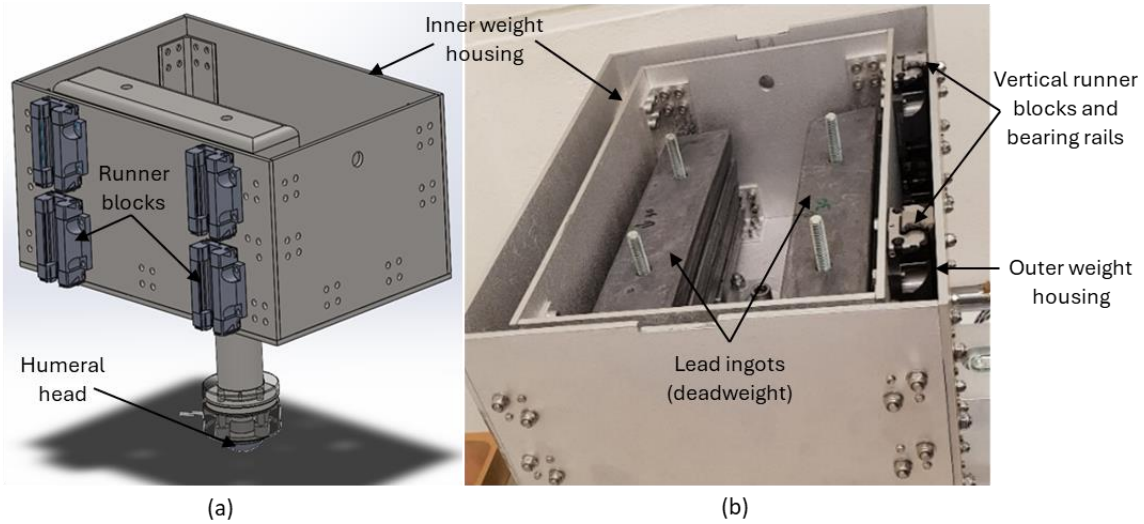

Figure 2-8 *Inner weight housing assembly (a) detail, showing the mounting of the runner blocks and the attachment of the HH assembly, and (b) assembled into the outer weight housing, with lead deadweight added.*

The deadweight load is transferred to the glenoid sample through the HH component, which rests on the glenoid, allowing the glenoid to support the dead weight in the vertical direction, as shown in **Figure 2-9**. As the HH is moved horizontally, it can move upward (vertically, away from the Sawbones surface), following the curve of the glenoid surface, as the inner weight housing moves up the vertical bearing rails.

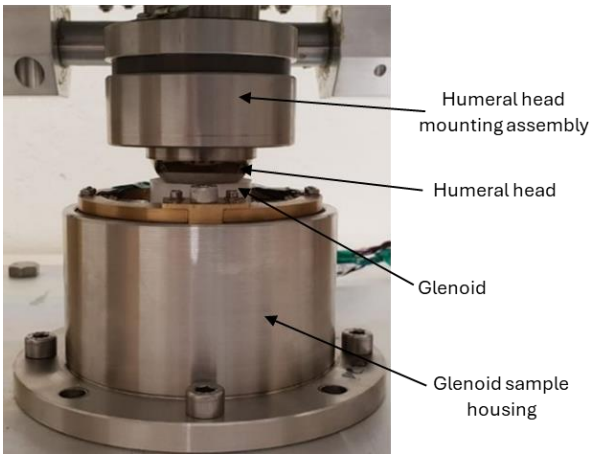

Figure 2-9 *Humeral head mounting assembly, where the humeral head rests on the glenoid component, supporting the weight of the inner weight housing and deadweight. The glenoid is implanted in the Sawbones base and mounted in the sample assembly.*

The humeral head component is mounted to a torque-resistant linear bushing (R072523000, Bosch Rexroth) and shaft (R072403089, Bosch Rexroth) pair. The shaft is rigidly attached to the base of the inner weight housing, as shown in **Figure 2-10**. The humeral head is attached to the bottom of the torque-resistant bushing by a taper attachment block. The bushing is free to move vertically on its shaft. A button load cell is inserted between the bottom face of the shaft and the back of the humeral attachment block.

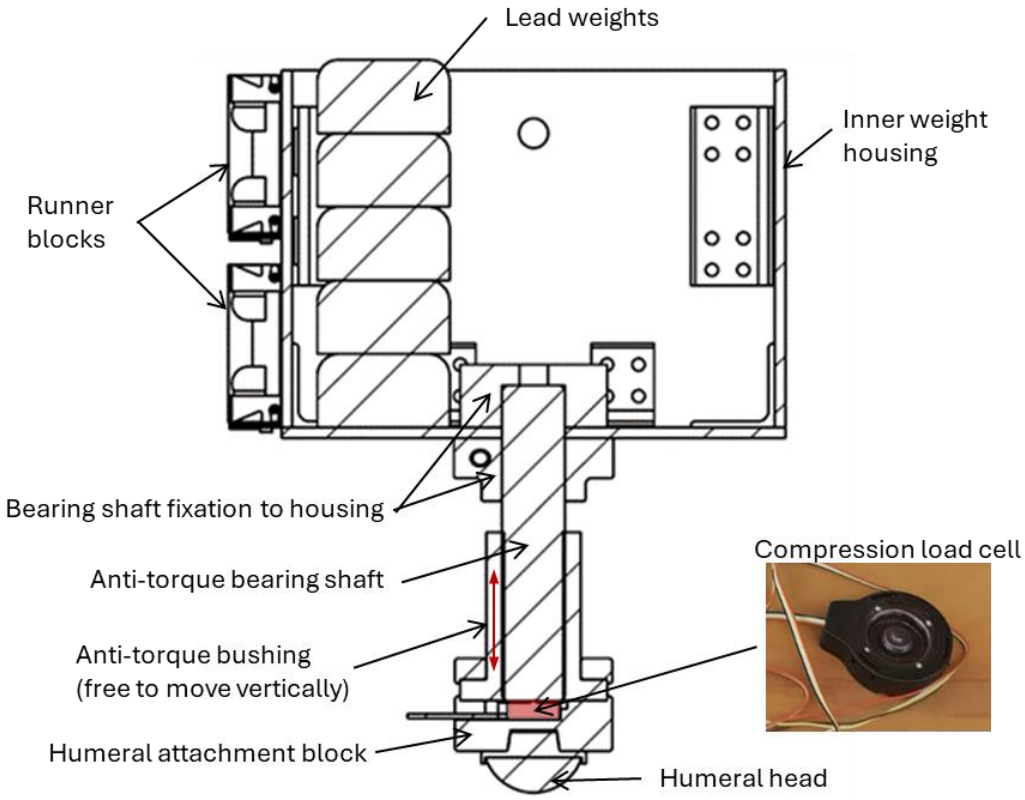

Figure 2-10 *Cross section of the inner weight housing and HH assembly. The HH assembly is attached to a torque-resistant bushing and bearing shaft pair. The HH assembly is free to move in the vertical direction as the bushing slides on the bearing shaft. A compression load cell is inserted between the base of the bearing shaft and the HH. This configuration allows the weight of the inner weight housing to be supported by the load cell, allowing measurement of the applied normal load.*

This arrangement allows the horizontal motion of the outer weight housing to be transferred to the humeral head via the torque-resistant bushing, while also allowing the load cell to support the full weight of the deadload. The force read by the load cell is, therefore, the force transferred to the glenoid component (less the weight of the bushing, humeral head, and taper attachment).

The button load cell is connected to the data acquisition system and is used to monitor and log the normal load applied to the glenoid. A FX1901 (TE Connectivity, Schaffhausen, Switzerland) compression load cell is used, with a nominal range of 200lbf (890N) and a maximum range of 1000N (specification sheet provided in Appendix A2). While the nominal output voltage of the sensor is given in the data sheet, no sensor-specific calibration was provided. Because of this,

and because the sensor will be operating near (or even over its maximum nominal range at high loads), a calibration exercise was performed to determine the sensor output specifically over the range it is expected to be used. Using a Testometric Universal Testing Machine (Testometric X350-5, The Testometric Co Ltd, Rochdale, UK) force application rig, the load cell was excited at the recommended 5V, and the output voltage was measured for the force range of 650 to 850N. The calibration data were used to set up the sensor in the PMX signal amplifier (to be discussed in Section 2.4.5) and are provided in Appendix A2.

The full normal load will comprise three parts; (1) the weight of the inner housing assembly (which is constant) and the added deadweight load (chosen by the operator), (2) the friction on the vertical rail bearing system and (3) any inertial load variations caused by motion of the system. The forces acting on the inner weight housing during a motion from the centroid to the right glenoid edge are shown in **Figure 2-11**. The shear motor force is applied to the inner weight housing via the bearing rails on the runner blocks and is resisted by the shear reaction at the humeral head contact with the surface.

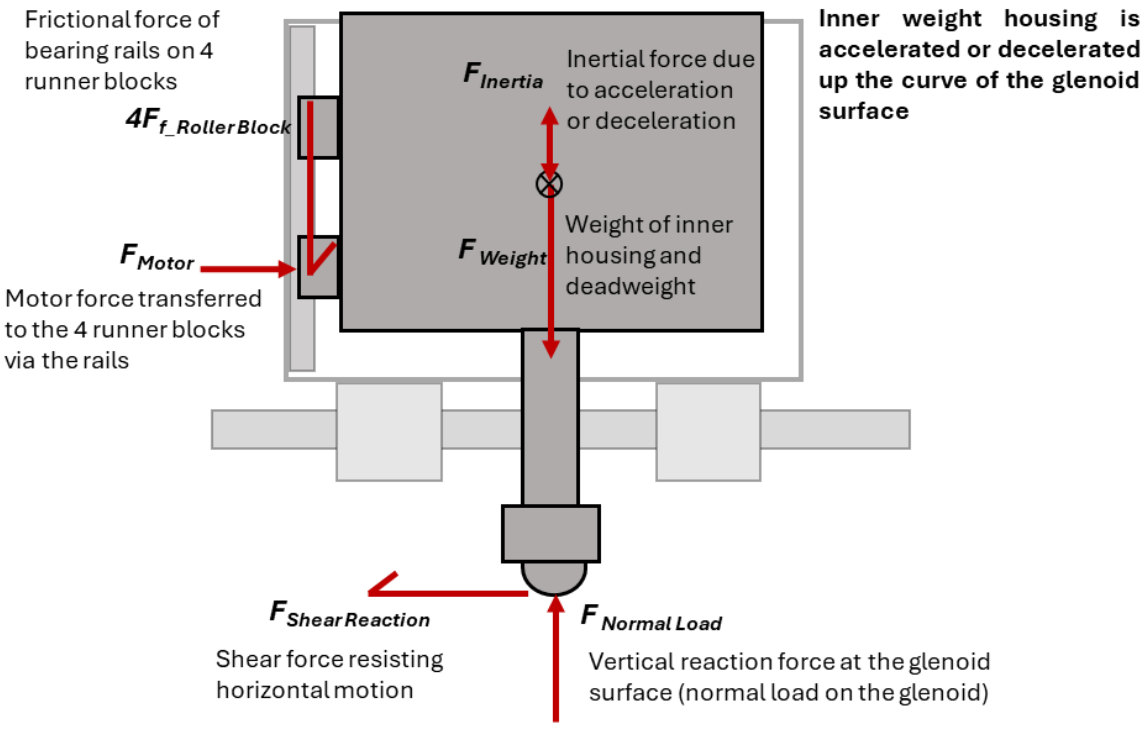

Figure 2-11 *Forces acting on the inner weight housing during a HH motion towards the glenoid edge, moving up the curve of the glenoid surface. In the horizontal direction, the motor force is transferred to the inner weight housing at the runner blocks and is resisted by the shear reaction force at the glenoid surface. In the vertical direction, the weight of the inner weight housing assembly (with deadweight), the frictional force at the runner blocks resisting upward motion, and the inertial force resisting upward acceleration of the weight are counteracted by the normal reaction force at the glenoid surface.*

The rail bearing system was selected to maintain low vertical friction in the vertical motion while ensuring the rigidity of the inner weight housing in the horizontal direction (i.e., the housing must

not tilt during the shear motion). The Rexroth Runner Blocks selected have a light pre-load (Type C1 in the Rexroth classification), which increases system rigidity, and a standard seal. The seal ensures the bushings remain debris-free but adds a nominal frictional resistance to motion. The overall friction in the ball rail system is the friction of the seals (which does not change with load) combined with load-induced friction.

The load-induced friction on the vertical bushings will change with increasing shear load as this load is transferred through these bushings to the outer weight housing. However, these bearings were specifically chosen to have low friction even under high loads, with a coefficient of friction of 0.002-0.003 (Appendix A). As a preliminary 'worst case' estimate, with a shear load of 1000N (as discussed in Section 2.2.2) distributed over the four roller blocks, and a coefficient of 0.003, the load-induced frictional force on each of the vertical bearings will be:

$$F_{f\_Roller\ Block} = \mu \frac{F_{Shear\ Reaction}}{4} \quad [2.4]$$

$$F_{f\_Roller\ Block} = 0.003 \frac{1000}{4} = 0.75\text{N}$$

In equation 2.4, $F_{f\_Roller\ Block}$ is the frictional force per bearing, μ is the roller block co-efficient of friction excluding seal friction, and $F_{Shear\ Reaction}$ is the applied rig shear force, which loads the vertical roller blocks. The nominal kinetic frictional force associated with the bearing seals (F_{f_seal}) is expected to be in the order of 2N per roller block (see Appendix A.1). The total load contribution of the roller blocks ($F_{TotalRollerBlocks}$) is therefore expected to be:

$$F_{TotalRollerBlocks} = 4\left(F_{f\ RollerBlock} + F_{f\ seal}\right) \quad [2.5]$$

$$F_{TotalRollerBlocks} = 4(0.75 + 2)$$

$$F_{TotalRollerBlocks} = 11\text{N}$$

As the humeral head moves up the glenoid surface, this force will resist motion and be added to the deadweight load. Conversely, when the humeral head moves down the curve of the glenoid surface, the frictional force acts upwards to resist downward motion, and the frictional load will be subtracted from the dead load.

In addition to the frictional force, the effective weight of the dead load will vary due to inertial effects as the load is accelerated and decelerated during the motion. Without knowing the motion speed and geometry of the glenoid surface, the inertial effect cannot be calculated precisely. However, a rough estimate is made as an order of magnitude check of this force, using the same motion parameters as for the maximum allowable speed calculation (a subluxation

distance of 13.5mm, 2Hz cyclic speed). Further, assuming an overall vertical motion of 3mm (based on available sample height change from centroid to edge), a static load weight of 750N, and by making assumptions regarding the velocity profiles of the vertical and horizontal motions, the inertial force variation is estimated to be:

$$F_{Inertia} = 59\text{N} \quad [2.6]$$

The details of the calculation and the assumptions made are listed in Appendix A. As for the frictional force, the inertial force will either contribute to or subtract from the total load, in this case, based on whether the load is being effectively accelerated or decelerated within the motion profile.

Overall, the normal load will therefore be:

$$F_{\text{Normal Load}} = F_{\text{Weight}} \pm F_{Inertia} \pm F_{Total\_Roller\ Blocks} \quad [2.7]$$

The maximum variation in normal load would be expected to occur when the inner weight housing accelerates upwards, as the HH moves up the glenoid surface toward the glenoid edge, such that both friction and inertia add to the overall load. In this case, the total normal load for a 750N static weight would be:

$$F_{Normal\ Load\ MAX} = F_{\text{Weight}} + F_{Inertia} + F_{Total\_Roller\ Blocks} \quad [2.8]$$

$$F_{Normal\ Load\ MAX} = 750 + 59 + 11 = 820\text{N}$$

While the inertial contribution calculated here is expected to be a high estimate, it is clear from these calculations that the standard suggested load variation of 750±7.5N will not be achieved. However, the variation induced by these effects is deemed acceptable as long as the peak normal load at the edges does not vary by more than 10% from edge to edge and does not exceed 1000N (as per the requirements in Section 2.2).

Further, to compare the results of multiple tests, the load must be applied consistently. To ensure consistency, a deadweight set must be selected that produces a given static load reading on the load cell (750N recommended), and the same physical set is then used for all tests. The additional forces induced should remain consistent between tests for a given glenoid geometry and cyclic motion. However, as the actual magnitudes of frictional and inertial forces are unknown, it must be confirmed during the rig validation testing that the normal load will remain within the bounds set above.

2.4.3. System to Determine Subluxation Distance

The standard requires the shear resistance to motion to be measured to determine the distance from the glenoid centroid at which this resistance peaks. During the concept evaluation, it was decided instead to use the capability of the IndraDrive motor controller to monitor motor torque, to determine the location of peak shear load.

When the motor moves the weight housing, it must overcome:

- Inertia of the system (during acceleration)
- Internal motor friction forces
- The frictional force of the horizontal linear bushings
- The shear force resisting humeral head motion

For a given dead load and the same mechanical bearing system, the motor torque required to move the HH over a flat surface at a constant speed (as prescribed by the P90 test) should remain constant. When the curved surface of the glenoid is added, the HH is still moved at a constant speed, so no additional inertial forces are expected.

However, the HH (and inner weight housing) now move upwards to follow the surface curve. This causes motion of the runner blocks on the vertical rails, with resultant friction. In this case, we are looking at the friction acting on the bearing rails attached to the outer weight housing. As the inner housing moves upward, the friction force will have an upward action on the rails, as shown in **Figure 2-12**. This upward force will tend to reduce the load on the horizontal bearing system by 'lifting' the outer weight housing. It must, therefore, be determined if this force change will result in a change in the frictional force of the horizontal bushings and, hence, the motor torque.

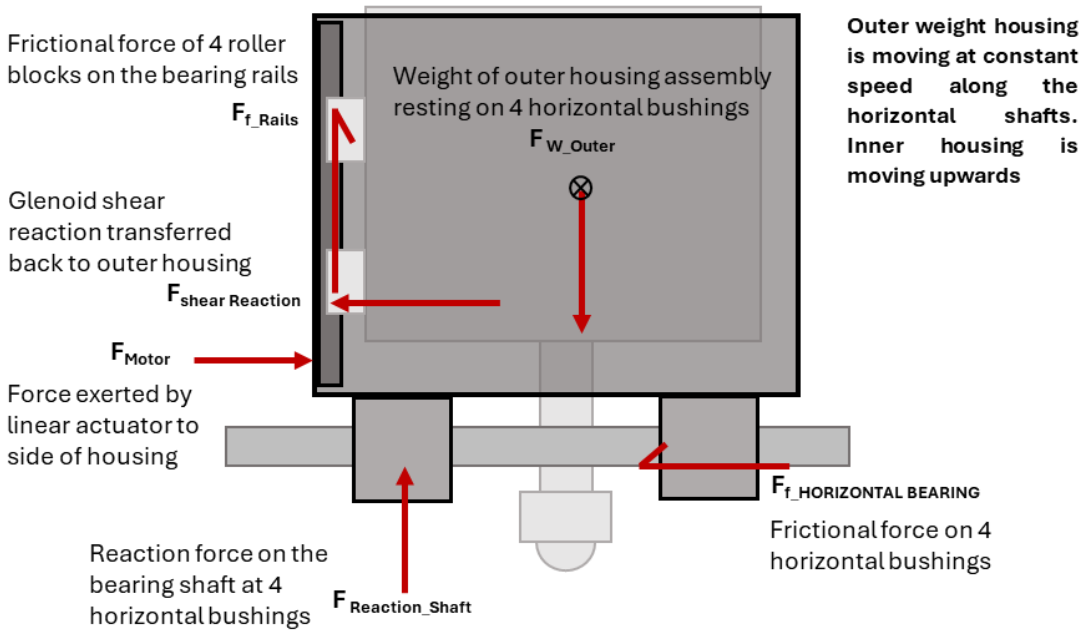

Figure 2-12 *Forces acting on the outer weight housing system during the constant velocity motion of the P90 test. In the horizontal direction, the force applied by the linear actuator will balance the combined force of the friction in the horizontal bearings and the glenoid shear reaction force which is transferred back to the outer weight housing by the roller blocks.*

The seal-induced friction of the rail is constant (as discussed in the previous section). It will, therefore, change the load on the horizontal bearing system compared to motion on a flat surface with no vertical motion but will not vary with the shear force. The seal friction should, therefore, not affect the location of peak shear force. Only the load-induced friction on the vertical bearing system will affect the horizontal bearing load. As per Equation 2.4, this frictional load is expected to be in the order of:

$$4F_{f_{RollerBlock}} = 4(\,0.75\text{N}) = 3N \qquad [2.8]$$

Since the horizontal bearing system has a low load-induced frictional co-efficient (μ = 0.001 - 0.004 (see Appendix A1), the contribution of the change in horizontal bearing friction to the motor torque is estimated to be less than 1N and is taken to be negligible. The internal friction in the horizontal motion system will, therefore, not be meaningfully changed by the addition of the curved glenoid surface.

It is, therefore, reasoned that the only parameter changing the torque requirements of the motor during the P90 test is the force transferred by the curved glenoid surface resisting the shear motion (i.e. the force resisting subluxation). The motor torque will peak at the same location on the glenoid surface as the force resisting the motion does and is used to determine the subluxation location. This expected torque behaviour will be confirmed in the preliminary rig validation testing.

2.4.4. Temperature Regulation and Lubrication System

The temperature control and lubrication system is made up of a water reservoir, a temperature controller that maintains the water at 37°C, and a circulation system that runs the water over the glenoid sample, as shown in **Figure 2-13**. The temperature control system is independent and is always on when the test rig mains power is on.

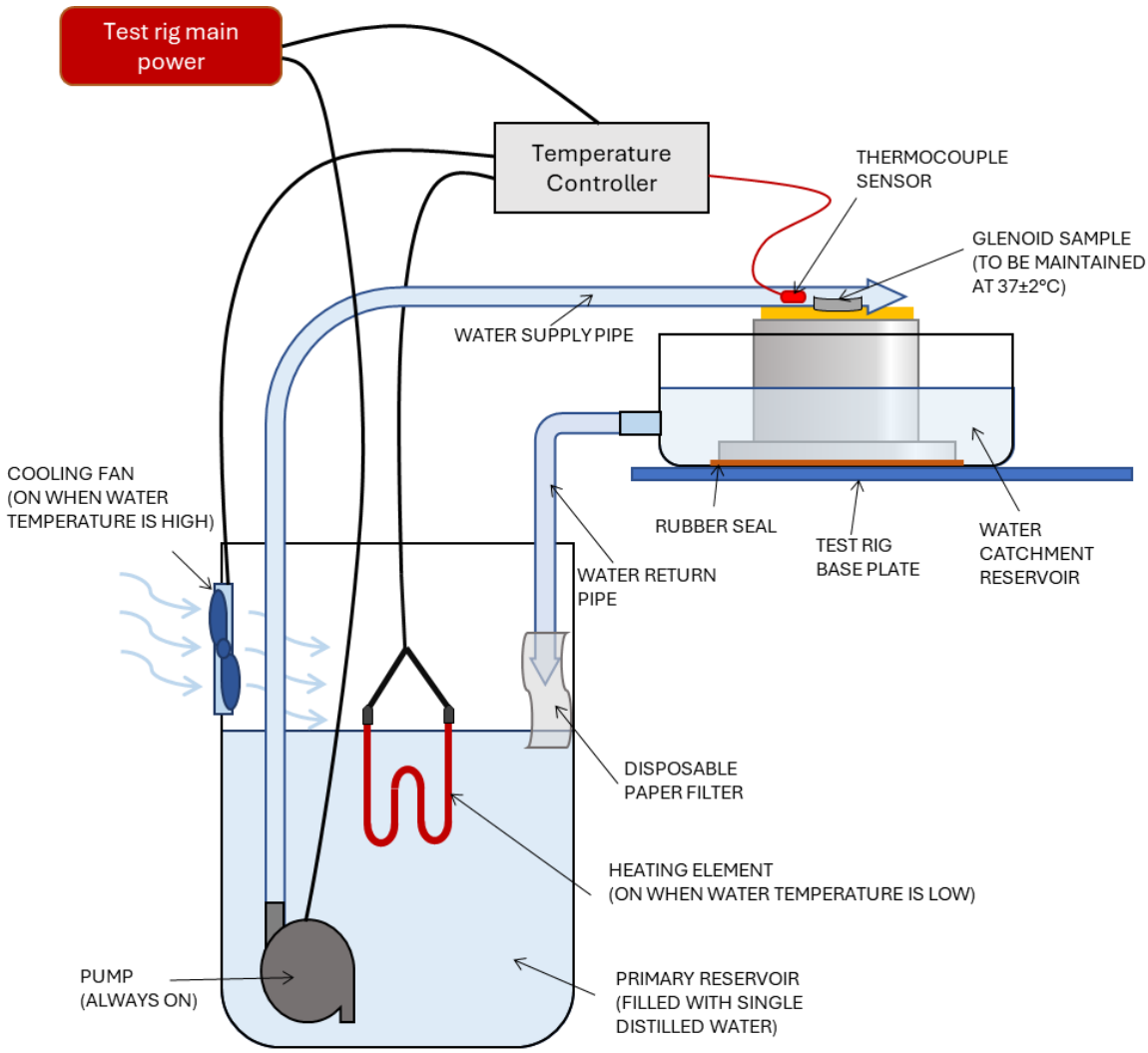

Figure 2-13 *Schematic of the temperature regulation and lubrication system, where 37°C is circulated over the glenoid sample. The temperature is maintained by either heating or cooling, based on a thermocouple reading at the glenoid.*

The primary reservoir is a simple container filled with single distilled water. A constant flow rate pump (260*l*/h) circulates water over the surface of the glenoid sample. The water is collected in a catchment reservoir attached to the sample mounting housing. This housing and the catchment reservoir are attached to the sample housing and are removed from the rig when the glenoid sample is changed. The catchment reservoir is bolted to the test rig base plate by the sample housing fixation bolts. A rubber seal is added between the sample housing and catchment reservoir to prevent leaking from the bolt holes. The outlet of the catchment reservoir

connects to a water return pipe, which gravity feeds the water back to the primary reservoir. The outlet of the water return pipe is fitted with a paper filter, which is replaced as required.

The water circulation was designed to be simple, with no feedback control and an always-on pump. To achieve this, the system was adjusted using different-sized pipework and fixed flow rate pumps until a stable circulation rate was achieved. Using a pump with a 1m head, a 12mm supply pipe, and an oversized (25mm) return pipe ensured that a stable flow was achieved and that the supply never exceeded the gravity-fed return flow.

The cooling fan is mounted into the upper portion of one side of the primary reservoir, and the remaining three sides are perforated to allow airflow. The heating element is suspended below the water surface. The thermocouple sensor of the STC-1000 microcomputer temperature controller is placed inside the outlet of the water supply pipe, at the glenoid sample. The controller maintains the set temperature of 37°C by alternating power to either the heating element or the cooling fan. The controller has a sensitivity of 0.1°C and will engage the heating or cooling systems if a temperature variation of ±0.2°C from the setpoint is sensed. This maintains the setpoint well within the ASTM standard requirement of 37±2°C.

The temperature control system is not connected to the lab PC, so the temperature is not automatically logged. To ensure the reliability of the circulation and consistent water temperature, the temperature is periodically manually logged by observation of the temperature controller output display. The system reliability was checked during the preliminary rig validation testing.

2.4.5. System Control, Data Acquisition and User Interface

The test rig electronics comprise of four main systems, namely the laboratory PC from which the operator controls the tests, the motor controller (Rexroth IndraDrive CS, Bosch Rexroth, Kempton Park, South Africa), the data acquisition system (PMX Modular measuring amplifier system, Hottinger Brüel & Kjær GmbH (HBK, formerly known as HBM), Darmstadt, Germany), and the temperature controller (STC-1000, Xiamen Sino-Cool Refrigeration Parts Industry Co., Ltd, Fujian, China). The interaction of these systems is illustrated in **Figure 2-14** below.

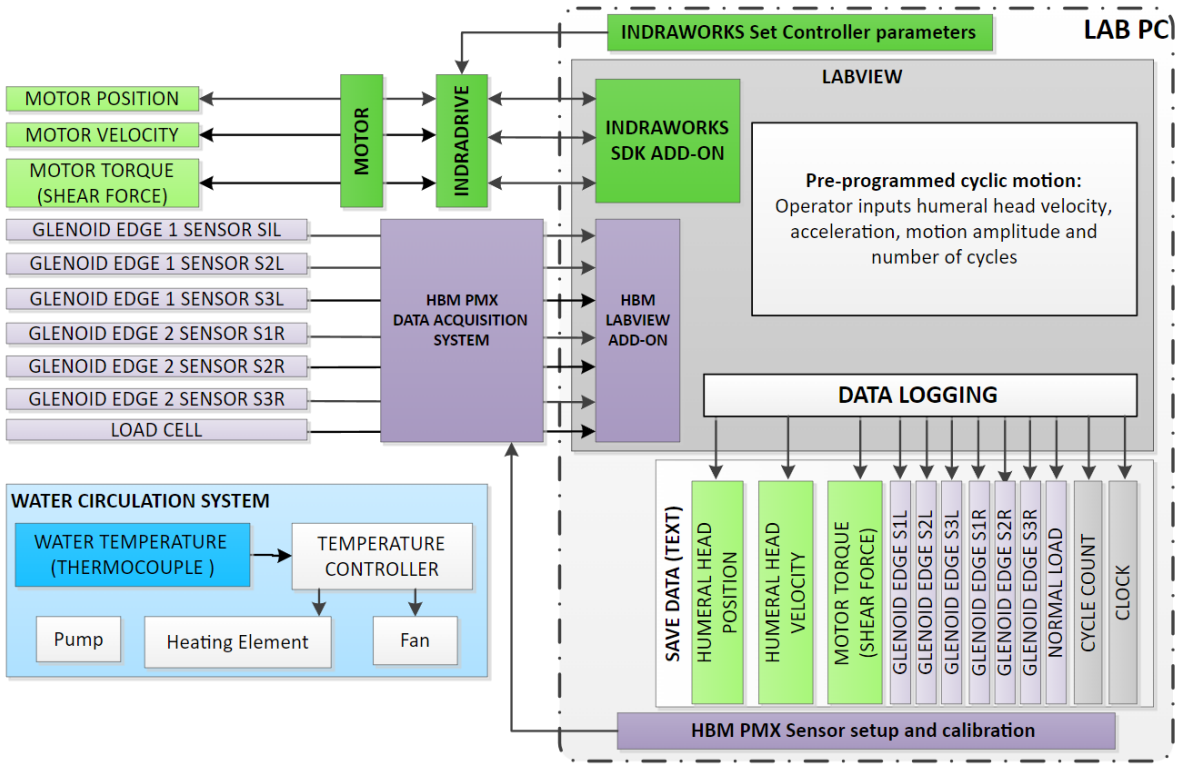

Figure 2-14 *Overview of the DGL test rig electronic systems, including the IndraDrive motor controller and HBK PMX DAQ, which are controlled by the Labview rig control script on the laboratory PC. Independent of the PC is the always-on temperature control system.*

The laboratory PC is used to set up the Rexroth and PMX systems using their respective software. All testing is then performed using LabVIEW, which communicates with the Rexroth and PMX systems via code add-ons. The temperature controller is independent of the PC and automatically seeks the set temperature when the test rig is turned on. The temperature is not logged but is displayed on the temperature controller face and visually checked twice daily.

2.4.5.1. Bosch Rexroth IndraDrive Motor Controller

As mentioned in Section 2.4, the IndraDrive controller is initially set up using the IndraWorks software. The setup includes choosing appropriate units/parameters (for example, rotational speed of the motor vs linear motion of the actuator) and the type of control (motion or force-controlled). For this project, metric units and linear motion were chosen, with motion control. Once the IndraDrive is set up, IndraWorks software is not required for the testing. The IndraDrive is managed by LabVIEW using the IndraWorks SDK add-on.

2.4.5.2. HBM PMX Data Acquisition System

The choice of data acquisition system was informed by the prototyping stage of the glenoid edge measurement system (to be discussed in Section 3.3.2), which was performed concurrently with

the rig design. Initial prototypes used an Arduino (Arduino, Somerville, MA, USA), but this was found to be insufficient. The final choice was an HBK PMX, which is a modular system with four slots into which signal processing cards can be added, as shown in **Figure 2-15**.

The system is fitted with three cards: two PX455 measurement modules for use with multiple sensor types (including strain gauge bridges, load cells, and linear variable displacement transducers (LVDTs)) and a PX878 multi-I/O module with digital and analogue inputs and outputs. The choice of these cards was informed by the use of the force-check load cell, the use of LVDT sensors in the edge motion monitoring system (to be discussed in Chapter 3), and to provide flexibility for the future use of the equipment.

Figure 2-15 *Modular HBK PMX data acquisition system, with two PX455 measurement module cards for use with LVDT and load cell sensors and a PX 878 digital I/O card.*

The user interfaces directly with the PMX on the laboratory PC via ethernet. The PMX interface (**Figure 2-16**) is used to set up sensors initially, based on sensor type, and to input calibration data. At the start of each test, the PMX interface is also used to monitor sensor initial values (specifically the load cell reading) and to position the LVDT sensors used in the glenoid edge motion measurement system. Once testing begins, the PMX measurements are logged by LabVIEW using the HBK LabVIEW add-on.

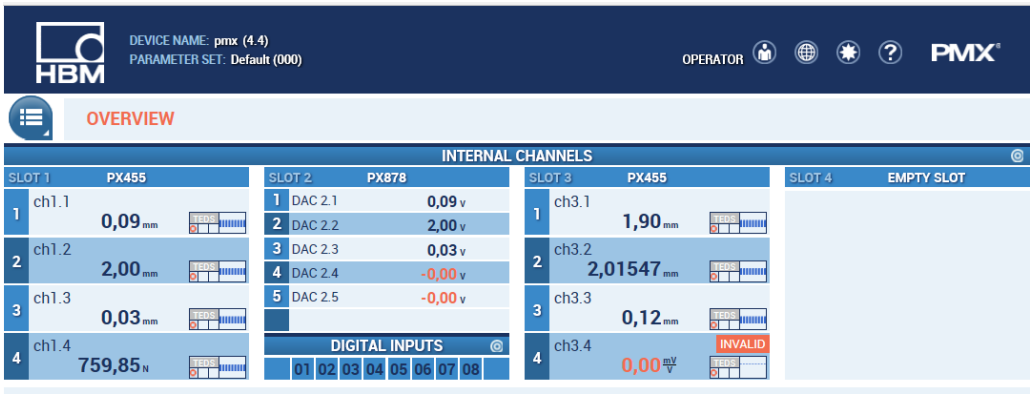

Figure 2-16 *Sample of the HBK PMX user interface, in which 6 LVDT sensors (ch1.1 – ch1.3 and ch3.1 – 3.3) and the compression load cell (ch1.4) have been set up in the PX455 measurement cards*

2.4.5.3. Labview Test Protocols

The main user interface for the testing uses two LabVIEW protocols: the P90 Test protocol and the Glenoid Edge Motion protocol. A description and schematic overview of the protocols is given here.

The P90 Test protocol implements a single motion from the glenoid centroid to a user-set end position, which should be beyond the edge of the glenoid. The user inputs the velocity of the motion, but the standard recommended 50mm/min should be used. The protocol logs the humeral head position, motor torque, and PC clock continuously (i.e. at the automatic LabVIEW data sampling rate of 13Hz) during the motion to a user-specified save file (.txt) on the PC local drive. The P90 Test protocol user interface and schematic principles of operation are shown in **Figure 2-17** and **Figure 2-18**, respectively.

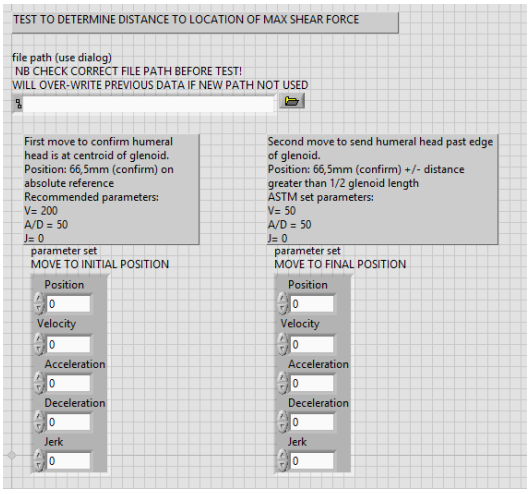

Figure 2-17 *LabVIEW user interface for the P90 Test, where the user inputs the start and end positions and defines the motion for a single move of the humeral head from the centroid of the glenoid to past the edge of the glenoid.*

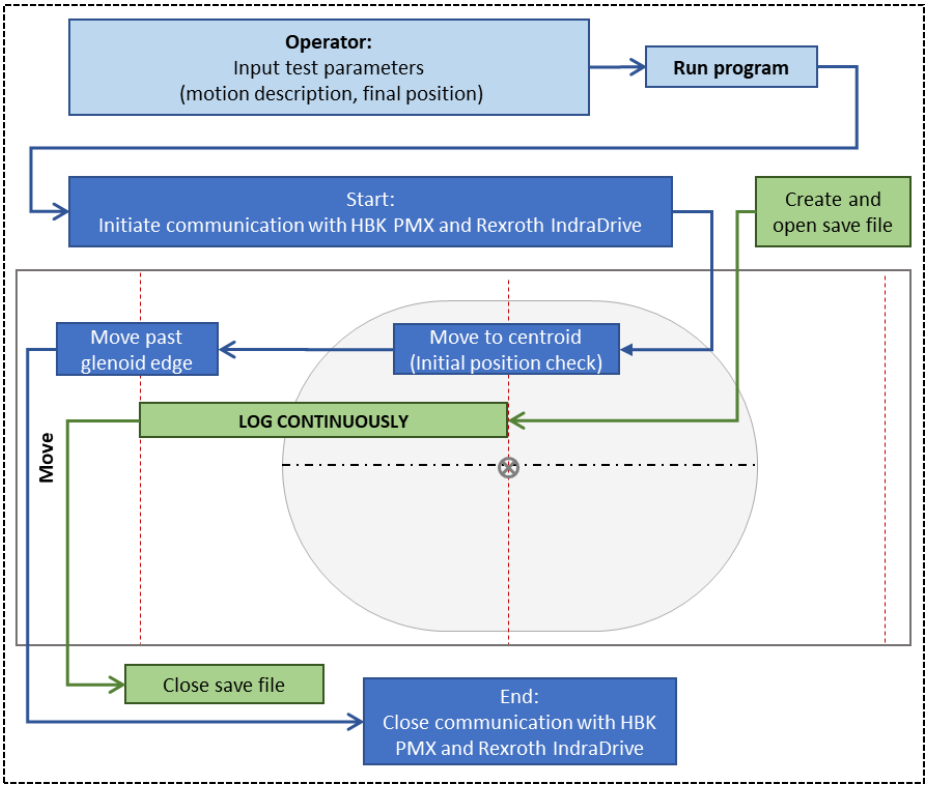

Figure 2-18 *Schematic overview of the P90 Test Protocol, where the HH moves from the centroid of the glenoid to the user-specified end position. The HH position and motor torque are logged throughout the motion at the continuous LabVIEW logging rate (~13Hz). At the end of the move, the HH stops, and the data is saved to the laboratory PC.*

The continuous logging at slow (50mm/min) humeral head velocity gives a high measurement resolution, with at least one measurement every 0.1mm, which allows the comparison of position to motor torque. The P90 Test protocol is repeated twice for each glenoid sample, with the input final position of the humeral head used to change the direction of the motion (i.e. [centroid + P90] mm and [centroid – P90] mm).

The Glenoid Edge Motion protocol implements a cyclic motion of user-set amplitude, velocity, and cycle count. The IndraWorks-SDK add-on also requires the user to set the motor controller's acceleration, deceleration, and jerk values. Once the program is started, the HBK LabVIEW add-on requires the user to select the PMX and appropriate channels that will be monitored. The Glenoid Edge Motion protocol is used for both the conditioning phase and the full cyclic loading tests, with only the testing velocity and number of cycles differing. The user interface for the Glenoid Edge Motion protocol is shown in **Figure 2-19**.

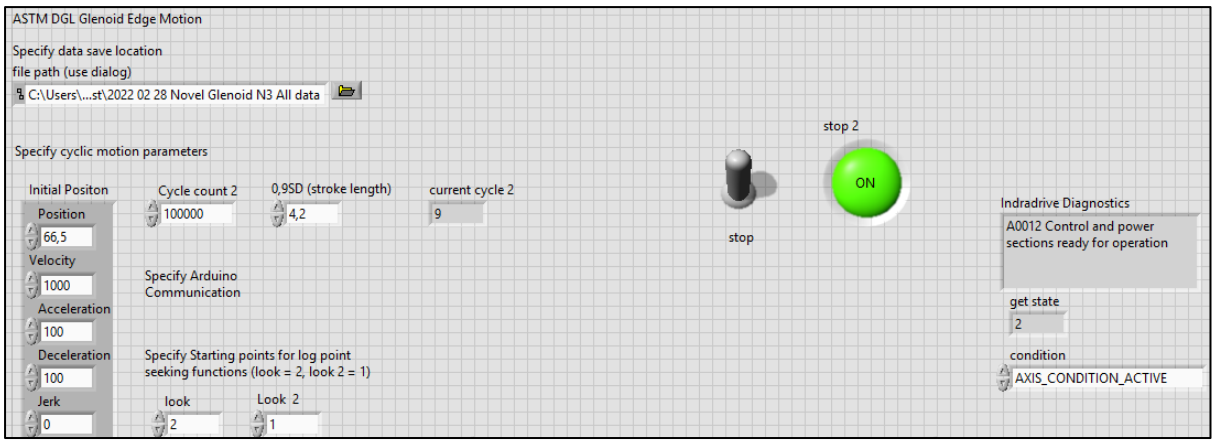

Figure 2-19 *LabVIEW user interface of the Glenoid Edge Motion Test protocol, where the user sets the starting point of the HH motion at the glenoid centroid (66.5mm in the motor frame of reference), sets the motion parameters, the stroke length (P90 for the glenoid), and the number of cycles to be performed.*

During the cyclic motion, the protocol logs data from the PMX, IndraDrive, and PC to a text save file. The values logged (and their source) are:

- Humeral head position (IndraDrive)
- Normal load (PMX)
- Signals from 6 edge displacement measurement LVDTs (PMX)
- Cycle number (LabVIEW)
- Clock (PC)

As decided in the testing requirements section, the protocol does not continuously log all these values at the automatic 13Hz sampling rate, as this would produce excessively large data sets over a 100,000 cycle test. Instead, the values are logged at five humeral head positions; centroid, centroid ±P90/2, and cenroid±P90, for each cycle, as illustrated in **Figure 2-20**.

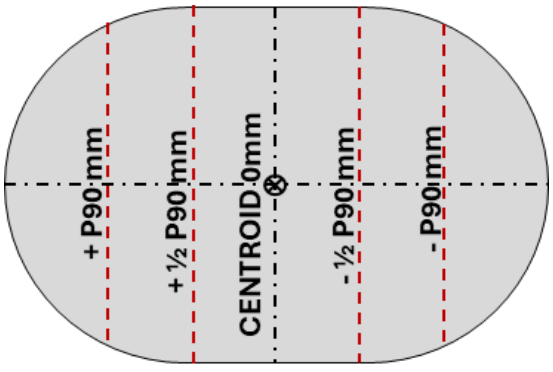

Figure 2-20 *Positions of the HH on the glenoid at which the Glenoid Edge Motion protocol logs data*

The Glenoid Edge Motion LabVIEW protocol uses a flat sequence structure and is schematically illustrated in **Figure 2-21**. After the user has input the required values and selected the PMX

channels, the protocol initiates communication with the IndraDrive and PMX, creates the save file, and begins to move through the sequences.

In the first sequence, valid for Cycle 1 only, the protocol moves the humeral head to the centroid of the glenoid (0mm in the glenoid reference, 66.5mm in the linear actuator absolute frame of reference). This should be the start position of the humeral head when the test is set up, so the first 'move to centroid' should be a position check only. The first set of data is logged.

The humeral head is then moved to [Centroid + P90] mm. Data is logged during the move using a seeking function rather than an exact position, as it would be necessary to stop the humeral head at each location if the exact position was used, which slows down the test considerably. Instead, the data is logged when the humeral head crosses the data log point. The program then seeks the next data log point.

At this point, the program enters the cyclic *for*-loop, where two sequences are repeated for the specified number of cycles. These two sequences move the humeral head from [Centroid + P90] mm to [Centroid – P90] mm and back. During this move, the data is again logged as the humeral head crosses each log location in the respective direction of motion.

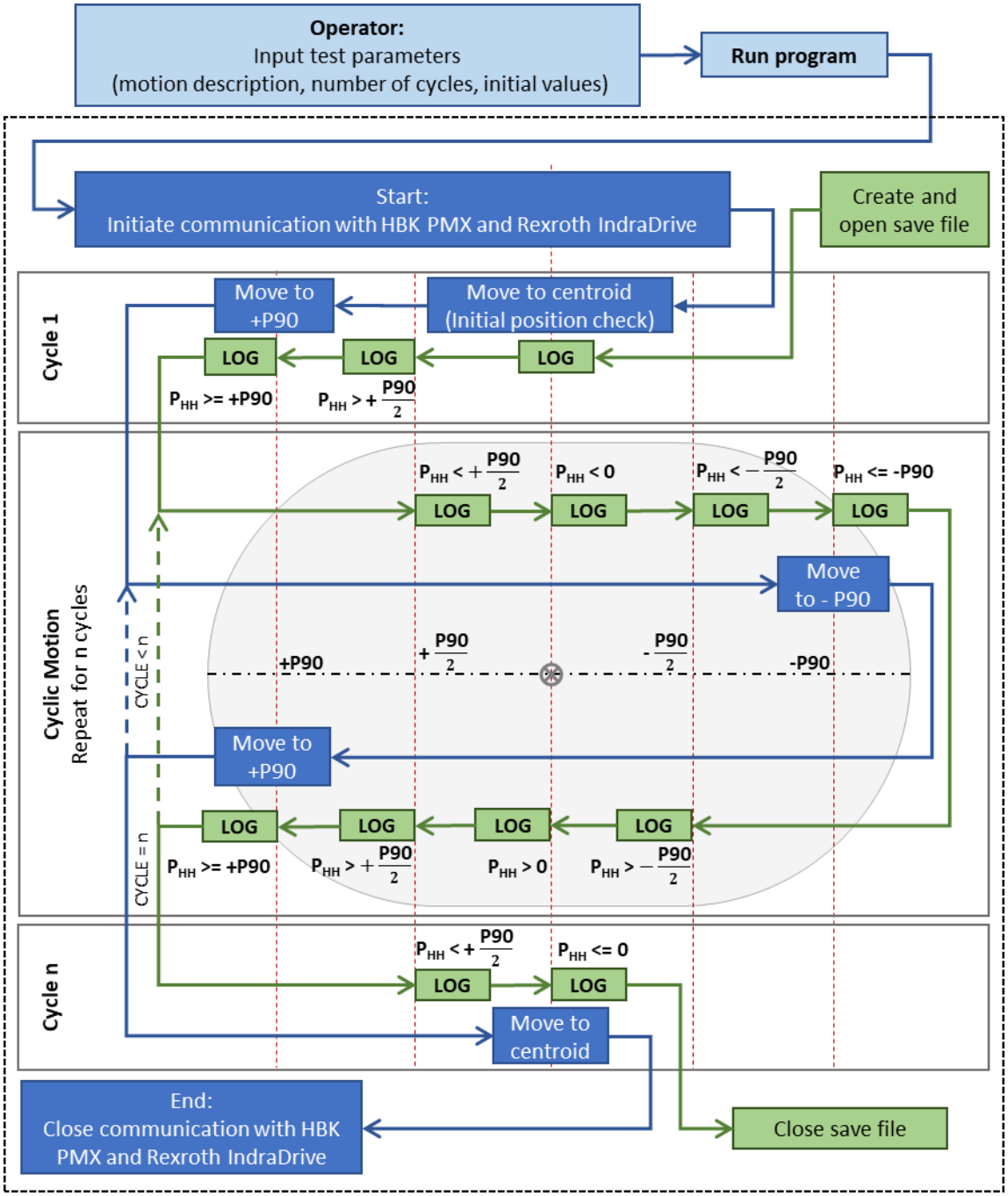

Figure 2-21 *Schematic overview of the Glenoid Edge Motion protocol. The user inputs the required motion parameters, after which the HH motion begins. The program moves through a for-loop for the cyclic loading, logging data at the predefined HH position on the glenoid.*

When the final cycle count is reached, a final sequence moves the humeral head back to the centroid, after which the system closes all communication, closes the save file, and shuts the program down. The data is saved at each log point so that in the event of an interrupted test, the data logged until that point is preserved. Data is saved locally to the PC during testing and backed up to the cloud immediately after each test.

2.5. Manufacturing and Assembly

The final test rig comprises parts manufactured 'in-house' at UCT, purchased mechanical and electronic components, and purchased as well as self-written software. The design and assembly of the test rig were performed with assistance from various others from within UCT and from the industry.

In-house parts were designed with advice from the technical staff at the UCT Department of Human Biology mechanical workshop. These parts were then manufactured by the mechanical workshop or outsourced where specialised equipment was required (e.g. laser cutting, CNC machining, and galvanisation.

The Bosch Rexroth components and software (including the motor controller, linear actuator, and horizontal and vertical bearing systems) were selected with the assistance of the local Bosch Rexroth distributor, Tektra Automation (Pty) (Ltd) (Eikenbosch, Cape Town, South Africa). The installation of the IndraWorks software and the initial setup of the motor controller were performed by a Tektra technical representative, and training in the use of the system was provided. Likewise, the HBK PMX selection and initial setup were performed with the assistance of the local distributor, TANDM Technologies (Pty) (Ltd) (Paardevlei, Cape Town, South Africa), and training in the system use was provided. Once assembly was complete, initial functional validation of the rig, excluding the edge motion measurement system, was performed.

2.6. Preliminary Functional Validation Testing

The full-length validation testing of the system was performed as part of the augmented rig validation study (discussed in Chapter 3) after the edge motion measurement system was added. However, before the full testing could proceed, preliminary testing of the functionality of the rig was performed in order to confirm that:

- The rig can perform the subluxation distance test using the P90 Test Protocol.
- The rig can perform the cyclic loading test using the Glenoid Edge Motion Protocol (and appropriate input parameters for the motion must be chosen).
- The normal load is applied within the limits specified in the design requirements (based on the load cell reading).
- The temperature control and lubrication system functions as required.

The preliminary testing comprised initial tests using either a flat polyethylene surface or expired commercial glenoid samples of various sizes, implanted in a Sawbones substrate. All testing was performed using a Ø44 humeral head, as this was the only size of expired HH component

available. It is noted that the use of 'non-viable' expired glenoid samples and mismatch of humeral head and glenoid size means the data reported here is for rig functional validation purposes only and will not be used in the novel glenoid analysis (described in Chapter 4).

It is further noted that the testing performed here assumes the calibration of pre-calibrated equipment (specifically the motor controller and the temperature controller), as well as the self-performed calibration of the load cell, remain valid and that the values logged/displayed by the system are accurate within the system capability.

The validation testing methodology and results are provided in this section. Discussion of the results and an overall evaluation of the test rig functionality follow in Section 2.7.

2.6.1. P90 Protocol Program Validation Test

The P90 Protocol is used to determine the subluxation distance by comparison of motor torque to the position of the humeral head. The test comprises a single motion, from the centroid to beyond the edge of the glenoid, per test and is repeated once in each direction for each glenoid sample.

2.6.1.1. Aims

The P90 functional validation must confirm that the test executes as specified and that using motor torque to measure the subluxation distance is valid. To achieve this, three aims are defined:

- Verify that the P90 Test Protocol executes the required motion based on operator input, and the motor torque and position values are continuously logged and saved.
- Confirm the motor torque peaks during the motion and that this peak is not caused by factors other than the shear force variation.
- Use the motor torque peak data to calculate the P90 distance of an expired glenoid sample.

The testing was performed first on a flat surface, after which one of the available expired glenoid components, a size 52mm sample, was used.

2.6.1.2. Methodology

The P90 test was run on a flat surface to check protocol execution and to determine the torque behaviour of the system when the glenoid surface shape was absent. Successful protocol execution was checked by performing a move from 66.5mm (in the motor frame of reference), the location at which the glenoid centroid would be when not using a flat plate, to 90mm (in the motor frame of reference), at 50mm/min, and confirming:

- Torque, clock, and position values were saved to the specified file.
- Data was logged at the LabVIEW automatic logging frequency of ~13Hz.
- Start and final logged values for position correspond to the input motion.
- Velocity remained at 50mm/min based on the logged clock and distance variation at each save point.

After the successful execution was confirmed, the protocol was used to measure the motor torque on the flat surface at three load levels, to assess the torque variations in the system when the curved glenoid surface is absent. The three load levels were:

- Full load (750N±10N, all weights added)
- Intermediate load (only the empty inner weight housing, 180N±5N)
- No load (humeral head not in contact with the surface)

Each load was moved at 50mm/min, once in each direction around the motion starting point (66.5mm), for a distance exceeding 20mm (i.e., greater than the distance to the size 52mm glenoid edge). The P90 test was then performed on the expired size 52mm glenoid sample, implanted in a Sawbones base, using the available Ø44mm humeral head. A results analysis was performed to confirm that a torque peak occurs and to compare the flat surface torque variations to those on the curved surface to evaluate the relative influence of the respective variations.

The P90 distance for the test was calculated by:

- Selecting relevant data for each direction by removing the portion of the movement after the humeral head had moved over the glenoid edge.
- Converting the directional torque and distance measurements to absolute torque and distance from the centroid.
- Determining the location of the peak of each run and, from this, the average subluxation distance.
- Calculate the P90 distance = 0.9 x Subluxation distance.

2.6.1.3. Results

A sample test data save file from the protocol execution of the motion from 66.5mm to 90mm on the flat surface at 50mm/min is provided in Appendix A3, showing all data logged as expected. The velocity calculated based on logged clock and position data is plotted against motor displacement in **Figure 2-22**. The figure indicates that the motion start and end values are as specified, and the velocity is maintained at 50±2.5mm/min.

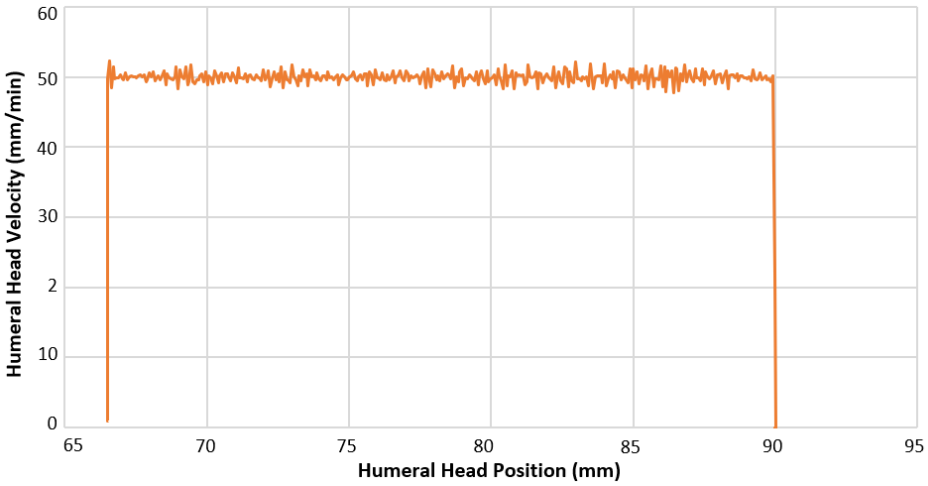

Figure 2-22 *Velocity and position of the HH during the P90 Protocol execution for a move from the expected location of the glenoid centroid (66.5mm) to a location that would be past the glenoid edge, confirming that the motor maintains the desired constant velocity.*

The motor torque values for the three load conditions on the flat surface, in each motion direction, are shown in **Figure 2-23**. The torque is positive or negative, dependant on the direction of motion.

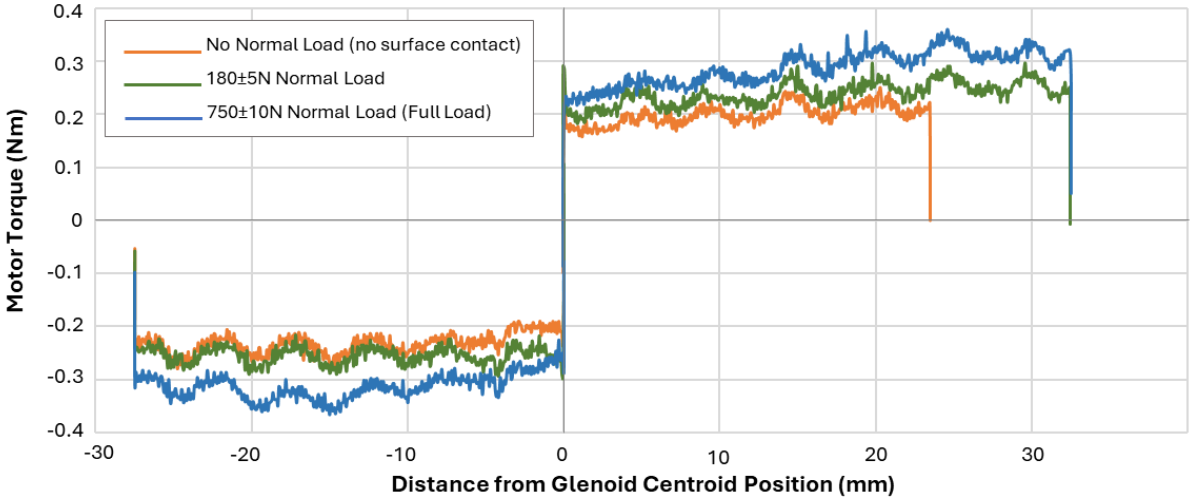

Figure 2-23 *Measured motor torque for motion at a constant speed (50mm/min) on a flat surface, for three load conditions, in both directions away from the position the glenoid centroid would be mounted.*

The measurements show that the motor torque under these conditions does not remain perfectly constant. Each of the curves exhibits a sinusoidal-like pattern and local noise variations. The high load condition varies between ± (0.23 - 0.35) Nm, and the lower two loads between ± (0.175 – 0.2) Nm.

The results of the test performed on the size 52mm glenoid are shown in **Figure 2-24**, with the position expressed as distance from the centroid, but without any conversions for directionality. The torque measured at 750N±10N on a flat surface is also plotted for comparison.

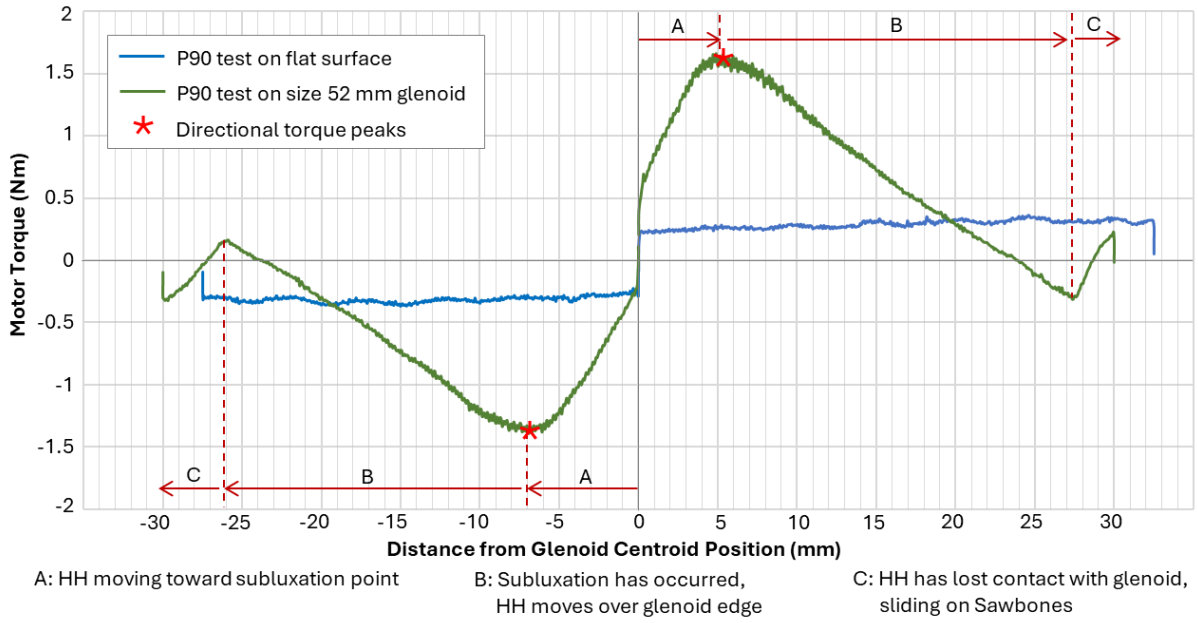

Figure 2-24 *P90 Test motor torque for expired size 52mm glenoid sample (green), in which torque magnitude peaks in the positive and negative motion directions are seen at ~ 5mm and -7mm from the glenoid centroid, respectively, indicating HH subluxation (A). After this peak, the humeral head moves over the glenoid edge, and the torque magnitude decreases (B). After ~25mm in each direction, the HH loses contact with the glenoid and the torque rises as the HH slides on the Sawbones surface (C). The torque for the same load on a flat surface (blue) is plotted for comparison.*

For the glenoid sample, a maximum peak torque in the positive motion direction and a minimum peak torque (i.e., a maximum negative torque) in the negative motion direction occur at approximately 5mm and -7mm from the centroid, respectively. The magnitudes of these torque peaks are approximately 1.6Nm and -1.4Nm, respectively. These peaks are associated with the humeral head contact point reaching the glenoid edge, where subluxation occurs. As the motion continues, the HH moves over and deforms the upper edge of the glenoid, and the torque begins to drop. As the HH moves completely off the glenoid edge, the torque reaches a minimum. After this, the torque begins to rise again, as the HH is driven across the Sawbones surface.

The physical sample used for this test is shown in **Figure 2-25**. As expected, the motion of the humeral head over the edge of the glenoid caused an area of material deformation, located approximately 16.5mm from the centroid. The undeformed edge of this glenoid is 19.5mm from the centroid.

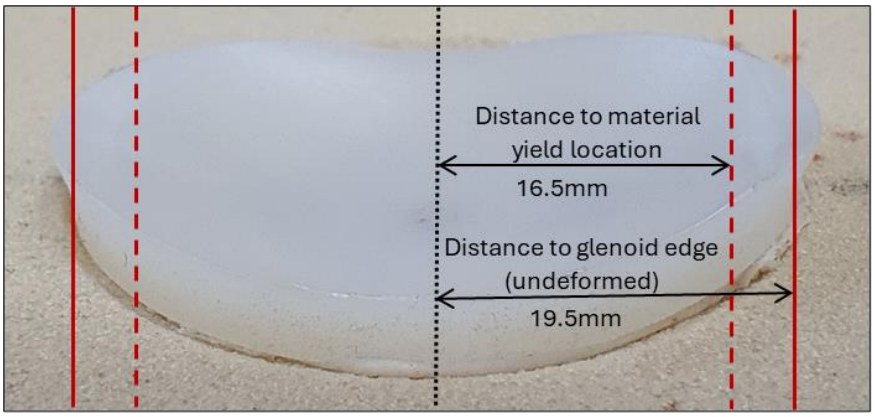

Figure 2-25 *Expired size 52mm glenoid sample after the P90 validation test, in which material deformation at the glenoid edges (at approximately 16.5mm from the centroid) is observed. This deformation is expected due to cold flow of the UHMWPE during the HH subluxation.*

To determine the subluxation distance, the data for the size 52mm glenoid sample were truncated to contain only the relevant HH positions (i.e. when the HH is still in contact with the glenoid surface) and converted to absolute torque and position values. This is shown in **Figure 2-26**, with the locations of the glenoid edge and position of material deformation indicated for reference.

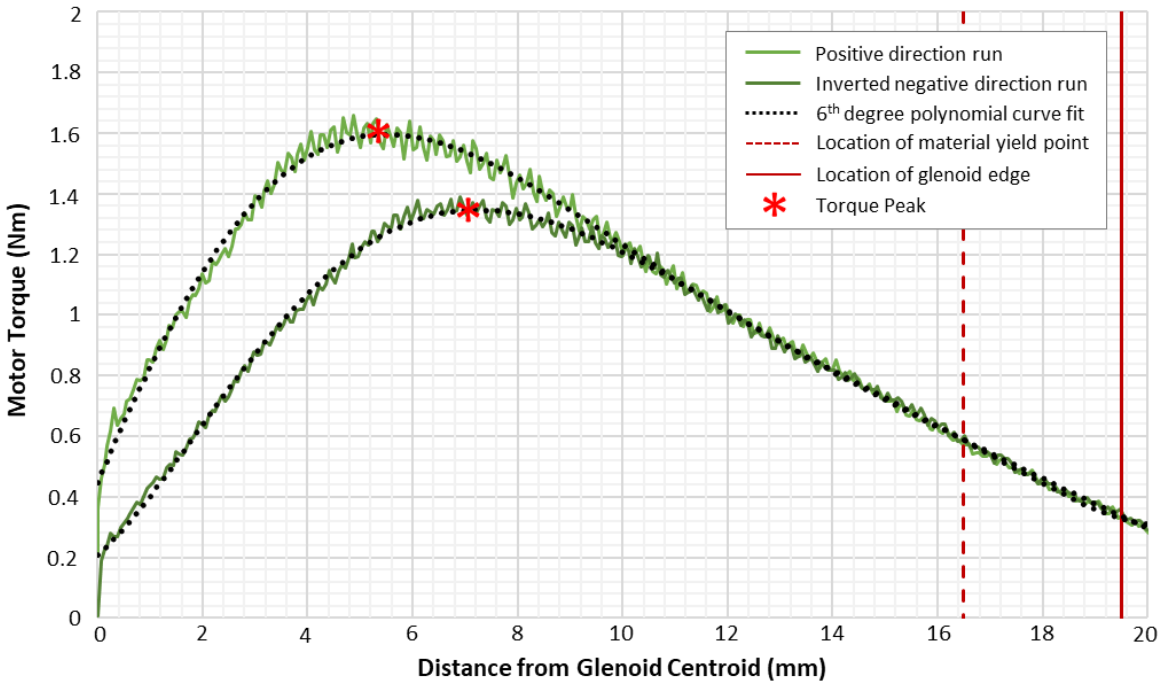

Figure 2-26 *Truncated, absolute motor torque for the P90 test on the size 52 glenoid sample, with 6th-degree polynomial curve fits applied. The two torque peaks are located at 5.3mm and 7.0mm away from the glenoid centroid. From these locations, an average subluxation distance of 6.2mm is calculated, and hence, a P90 distance of 5.6mm is determined.*

To reduce the influence of local noise peaks in the data, each dataset's peak location is determined by employing a curve fit of the experimental data. The curve fit is chosen by

performing a least squares difference evaluation using the MATLAB (MATLAB R202b, MathWorks, Natick, MA, USA) curve fitting toolbox, from which 6th-degree polynomial curve fits are applied to the truncated data sets. Peak values of 5.3mm and 7.0mm are observed, from which an average subluxation distance of 6.2mm is calculated. From this, a P90 distance of 5.6mm is calculated.

2.6.2. Cyclic Motion Validation Test

The main cyclic loading test and the sample conditioning are both executed using the Glenoid Edge Motion Protocol, which controls the HH speed and position while logging desired parameters, as discussed in Section 2.4.5. The validation of this protocol included confirming the protocol executed correctly, as well as developing guidelines for recommended input parameters to be used in the glenoid evaluation testing.

2.6.2.1. Aims

The input parameters required by the IndraDrive controller are target position, actuator speed, acceleration, deceleration, and jerk values. To reduce the overall test duration, these parameters should be chosen to minimise cycle time while ensuring that the surface sliding speeds do not exceed the maximum set out in the design requirements stage (5000mm/min).

Two aims are set for the cyclic motion validation tests:

- Verify that the Glenoid Edge Motion protocol executes the required motion based on user inputs and that the required variables are logged at the appropriate humeral head locations.
- Perform an analysis of the influence of input parameters (velocity, acceleration, and jerk) on overall test duration and choose appropriate parameters to minimise test duration while remaining within the limits set by the design requirements and by the physical response of the mechanical framework.

2.6.2.2. Methodology

As for the P90 test, the confirmation of protocol execution was done by comparing the saved data to the input motion. This was done over several iterations of the protocol. Concurrently with the protocol development, testing was done to optimise the test cycle duration. A series of short cyclic tests (3.5mm translation for 10 cycles) were performed at a range of input parameter combinations, and the overall time to completion of the cycles was measured. These tests identified the fastest feasible test parameter combination for use in the glenoid edge motion testing described in Chapter 4.

2.6.2.3. Results

An example of the saved data for the final protocol, used in a 10-cycle conditioning test of an expired size 44mm glenoid sample is provided in Appendix A3, indicating correct motion execution and all data saved as expected.

Initial investigations of the effects of changing motion parameters showed that increasing the jerk value above zero caused the linear actuator to noticeably overshoot the position setpoint and then oscillate around it before finally reaching the goal. High acceleration values (>±200mm/s^2) had a similar effect. The jerk value was, therefore, left at zero for all timed testing. The other parameters were varied between ±500-2000mm/min for velocity and ±10-200mm/s^2 for acceleration. The parameter combinations with the lowest resultant times over the 10 cycles are provided in **Table 2-1**.

Table 2-1*Effect of changes in HH translation speed and acceleration on the time taken to complete 10 cycles of 3.5mm translation, used to determine the recommended motion input parameters for future cyclic testing.*

Velocity (mm/min)	**Acceleration (mm/s^2)**	**Time (s)**	**Comments**
±500	±50	49.4	Starting parameters for high-speed tests
±500	±100	45.8	Increased acceleration reduces time
±1000	±100	34.6	Increased velocity reduces time. *Optimal motion parameters*
±1000	±200	42.8	Further increase in acceleration increases time
±2000	±100	34.3	Velocity increase reduces time but induces noticeable vibration in rig supports.

As noted in the table, increasing acceleration up to ±100mm/s^2 reduced the test duration, but higher values had the opposite effect. Increasing the velocity always caused a reduction in time, but at ±2000mm/min, the support frame started to exhibit noticeable instability in the reciprocal motion. The velocity was limited to ±1000mm/min to protect the system.

Therefore, the final motion parameters chosen are ±1000mm/min velocity, ±100mm/s^2 acceleration, and 0mm/s^3 jerk. For the conditioning tests, which should be performed at lower speeds, a velocity of ±500mm/min (half the cyclic test velocity) was chosen, with other parameters kept the same. Based on the short tests performed, a full 100,000 cycle test would have a test duration of approximately 97 hours (~4 days).

2.6.3. Normal Load Application Validation Test

As discussed in the design section, the normal load is applied by a deadweight set that produces a static load reading of 750N on the load cell, to which inertial and bearing frictional forces will be added/subtracted during the motion.

2.6.3.1. Aims

The validation of this system should evaluate the combined inertial and frictional forces occurring, must confirm that the peak load at the edges does not vary by more than 10% from edge to edge (as set out in the design requirements), and must confirm the normal load does not exceed 1000N.

Three aims are identified:

- Evaluate the normal load variation at a range of velocity, acceleration, and static load values to determine the influence of inertial force effects on the roller block friction and, hence, on loading.
- Confirm that the normal load does not exceed 1000N during these tests by assessment of overall cyclic test data.
- Confirm edge load peaks do not vary by more than 10% from each other by assessment of force variations within individual cycles.

2.6.3.2. Methodology

An analysis of the loading was performed using an intermediate test protocol, which cyclically moves the humeral head as the Glenoid Edge Motion protocol would, but which logs the force and position continuously along the motion (i.e. at the LabVIEW sampling rate) and is therefore performed for a limited number of cycles (20 to 200).

The test sample used in the load analysis was an expired size 40 glenoid implanted on a Sawbones base. The Ø44mm humeral head was again used. The glenoid sample had been previously subjected to a 5000-cycle full load test, as part of the main protocol development. The sample was, therefore, already conditioned before the force testing was performed. No loosening of the sample due to these prior tests was observed.

The normal load analysis was performed at two loads, with different combinations of velocity and acceleration, to determine if inertial effects influenced the load application. These are summarised in **Table 2-2**.

Table 2-2 *Static load and motion parameters used to investigate the variation in measured normal load during cyclic testing.*

Load (N)	Velocity (mm/min)	Acceleration (mm/s^2)
Empty Housing (180N)	±100	±100
Empty Housing (180N)	±1000	±100
Empty Housing (180N)	±1000	±100
Full Load (750N)	±1000	±100

The measured load variations for each test were compared by normalising the values to the starting static load over the full test. The edge-to-edge load variation was investigated by noting which cycles within the test had high overall load variations and evaluating their in-cycle variation relative to humeral head position.

2.6.3.3. Results

The measured normal loads are shown in **Figure 2-27** for all tests for 60s (approximately 15 cycles at ±1000mm/min, normalised to the individual test starting static load. The variations in normal load due to frictional and inertial force variations are apparent. Over the full range of HH motion for the 750N load condition, there is up to 70N variation in the measured load. The highest peak is at +29N, and the lowest at -40N from the static load. At the lower load of 180N, the overall variation is reduced to approximately 50N. The positive peaks for all three lower load runs fall between 0N and 15N above static. The negative peaks fall between -18N and -28N for the tests with reduced velocity or acceleration and between -25N and -32N for the full velocity test. These overall variations are discussed further in Section 2.7.2.3.

To determine if the test rig's normal load control requirement is being met, the normal load when the HH is at the two edges of the glenoid must be compared by looking more closely at individual cycles. The first two cycles for the 180N and 750N tests (both at 1000mm/min and 100mm/s^2) are shown in **Figure 2-28** and **Figure 2-29**, respectively. These first two cycles are chosen because their peak normal load variations are pronounced compared to later cycles. We see maximum peak loads occur at the glenoid edges in both directions (i.e. at ±P90), while the minimum loads occur as the HH crosses the centroid. Overall, the peak loading at the edges varies in the 180N test by 20N and in the 750N test by 35N, or approximately 5% of the full load.

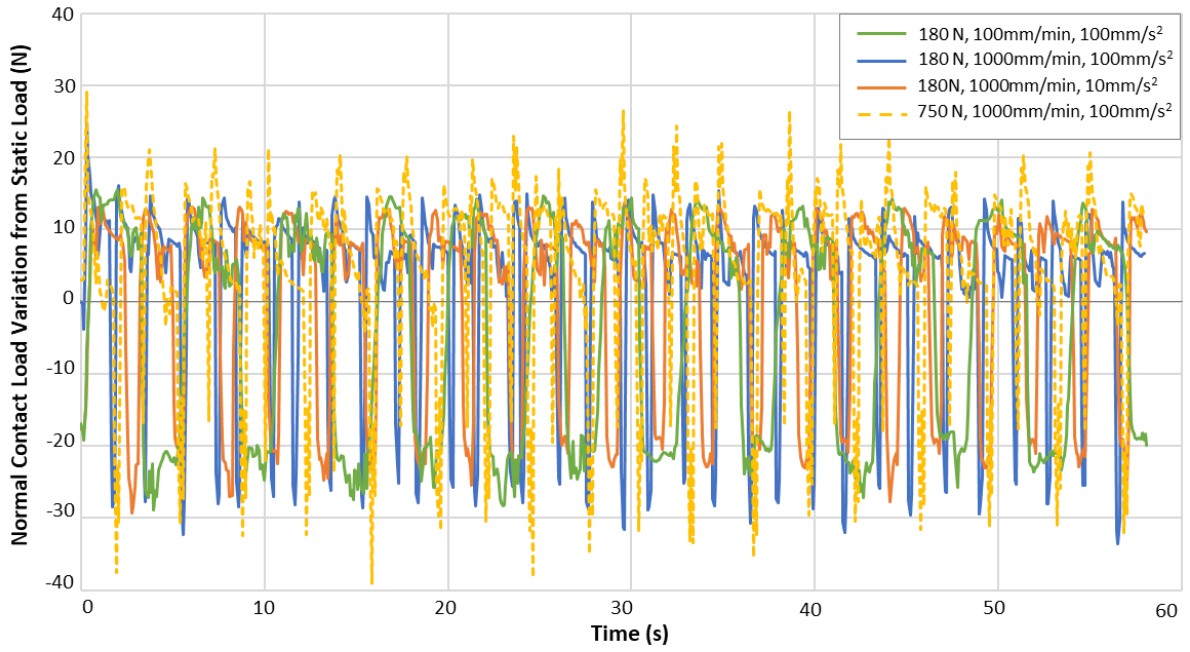

Figure 2-27 *Measured normal contact load between the HH and glenoid (size 40mm expired sample) for four combinations of static load and motion parameters, normalised to the starting static load of each. The variation in measured normal load, caused by changes in the frictional and inertial forces in the mechanical system over the full cyclic motion, is up to ~70N for the 750N load condition and ~50N for the three 180N motion conditions.*

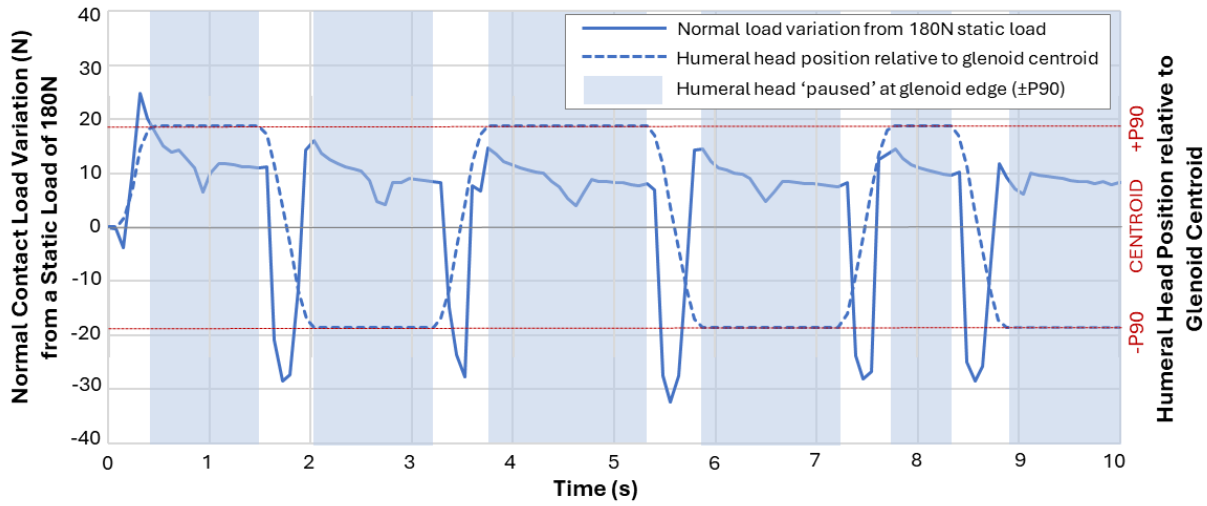

Figure 2-28 *Measured variation of normal load between the HH and glenoid (size 40mm expired sample), relative to a static load of 180N, for two cycles of motion. The highest load is measured at the glenoid edge in both directions (±P90), and the lowest load is measured when the HH is at the glenoid centroid. The load at ±P90 varies by a maximum of ~20N. During the motion, the HH 'pauses' at ±P90 for 0.5 - 2s (indicated by shaded areas), during which the normal load decreases from ~15-25N above static load to ~10N above static load.*

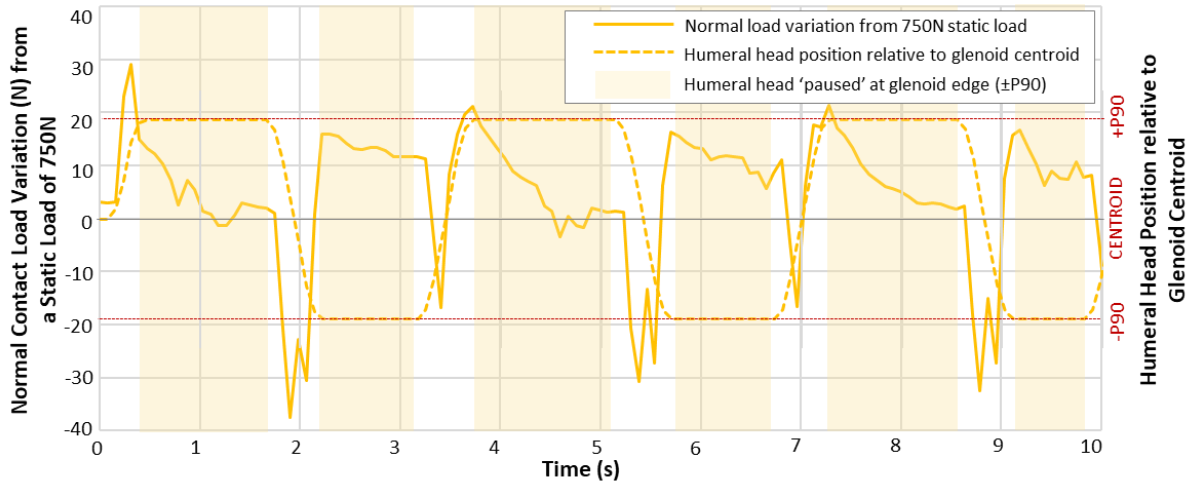

Figure 2-29 *Measured variation of normal load between the HH and glenoid (size 40mm expired sample), relative to a static load of 750N, for two cycles of motion. The highest load is measured at the glenoid edge in both directions (±P90), and the lowest load is measured when the HH is at the glenoid centroid. The load at ±P90 varies by a maximum of ~35N. During the motion, the HH 'pauses' at ±P90 for 0.5 – 1.5s (indicated by shaded areas), during which the normal load decreases from ~25-30N above static load to ~0-5N above static load.*

It is further noted in the individual cycle data that the humeral head exhibits a 'pause' at the motion endpoints (indicated by shaded areas in the figures) of approximately 1.5s in the +P90 position and 1s in the -P90 position. During this pause, the measured force at full load drops by ~30N in the first cycle and 5N to 25N in the remaining cycles. The possible causes of this pause and the reaction of the measured force will be discussed in more detail in Section 2.7.2.3.

2.6.4. Temperature Control and Lubrication Validation Test

The temperature control and lubrication system must ensure that for the full length of the test, the sample and substrate remain wetted and that the sample is maintained at 37±2°C.

2.6.4.1. Aims

The temperature control system validation testing has three aims:

- Verify that the temperature controller switches between cooling/heating functions if the water temperature deviates from the controller setpoint of 37±0.2°C and that the water circulates.
- Verify that the temperature control system reliably maintains the water temperature within the standard required 37±2°C whenever the rig operates.
- Verify that the water circulates continuously and that both sample and substrate remain wet whenever the rig is in operation.

In these tests, it is assumed that the sample will be at the same temperature as the water at the outlet of the supply pipe, which is positioned at the glenoid and is where the thermocouple sensor for the temperature control system is located.

2.6.4.2. Methodology

The testing comprised an initial investigation to confirm basic functionality, followed by longer tests to confirm reliability.

The initial test tested the functionality of the heating, cooling, and circulation/lubrication systems. The heating circuit was checked by filling the reservoir with water at room temperature and observing via the controller display that the heating element turned on, the temperature was raised to 37.0°C, and the element turned off. Similarly, hot water was added to test the cooling circuit, and it was observed that the fan turned on, the water temperature dropped to 37.0°C, and the fan then turned off. The circulation system was checked by confirmation that the in- and out-flow rates did not cause the catchment reservoir to overflow, there were no leaks, and the glenoid was well covered by water at the supply pipe outlet.

The reliability testing was performed concurrently with other rig validation testing by observing the temperature display and lubrication consistency whenever a test was being performed. For early test stages, this monitoring was performed by an operator in the lab for the full duration of the test. After establishing the rig functionality, long-duration tests were monitored twice daily.

2.6.4.3. Results

The initial tests showed that all control components functioned as expected. Fixation of the supply pipe so that the outlet rested against the Sawbones surface approximately 20mm from the glenoid edge ensured good water flow over and around the component.

During the reliability tests, the temperature was noted to be within 0.2°C of the setpoint at all inspections, and circulation of the water over the sample was consistently maintained. It was found that the catchment reservoir attached to the sample housing, which must be bolted to the test rig base plate, did not always have a perfect seal, resulting in a low-volume leak. Further, the warm water temperatures promote evaporation. This slow loss of water, combined with the long test times, meant that the reservoir had to be refilled periodically during the tests. It was found that refilling the reservoir twice a day was sufficient to prevent the added cool water from shifting the reservoir temperature out of the 37±2°C range. A sample of observed data over five days of testing is provided in Appendix A3.

2.7. Discussion

This section discusses the implementation of the DGL test rig requirements and the preliminary functional validation testing results. The conformance and deviations from the standard are noted to confirm that once the edge measurement system has been added, the rig can reliably be used to perform a glenoid design evaluation.

2.7.1. Discussion of Test Rig Design Implementation

The three phases of the DGL test, subluxation distance measurement, conditioning, and cyclic loading, all define different requirements for the test rig. Additionally, requirements relating to the general operation of the equipment were identified. The combined design requirements are summarised in **Table 2-3** below.

***Table 2-3**: Summary of DGL Test rig design requirements*

Variable	Value	Comments
Normal Contact Load	Suggested 750N±7.5N Maintain edge loads within 10% of each other. Must not exceed 1000N	Recommendation in Standard Requirement in standard Self-set limit
Humeral Shear Translation	Will vary with glenoid type/size, Must exceed distance to the glenoid edge Expected max amplitude ±25mm Motion must start at the glenoid centroid	Max values set based on available commercial glenoid designs. Glenoid must be implanted consistently to fall at a known position on the test rig (66.5mm)
Humeral Shear Velocity	Min 50mm/min Max allowable 5000mm/min	Lower values specified by the standard. Upper values based on the ASTM F2028 recommended cyclic frequency.
Shear force	Assumed to be <1250N	Estimate based on load ratios reported by Anglin et al. (2000a)
Sample Temperature	37°C±2°C	Requirement of standard Lubrication of surfaces with water to be maintained
Bone substitute	E_{Bone} = 193MPa σ_{Bone} = 7.6MPa	Requirement of Standard Use certified material
Other Physical/Operational Requirements		
Operation of the test rig to be integrated into a user interface on a laboratory PC		
Rig to be in a fixed location with sturdy mounting and anti-vibration measures		
Rig to be provided with generator power and changeover UPS		

To implement the rig design, concepts were evaluated for control of the cyclic motion, the application of the normal load, and the determination of the location of peak shear resistance to motion. The complete assembled test rig is illustrated in **Figure 2-30**.

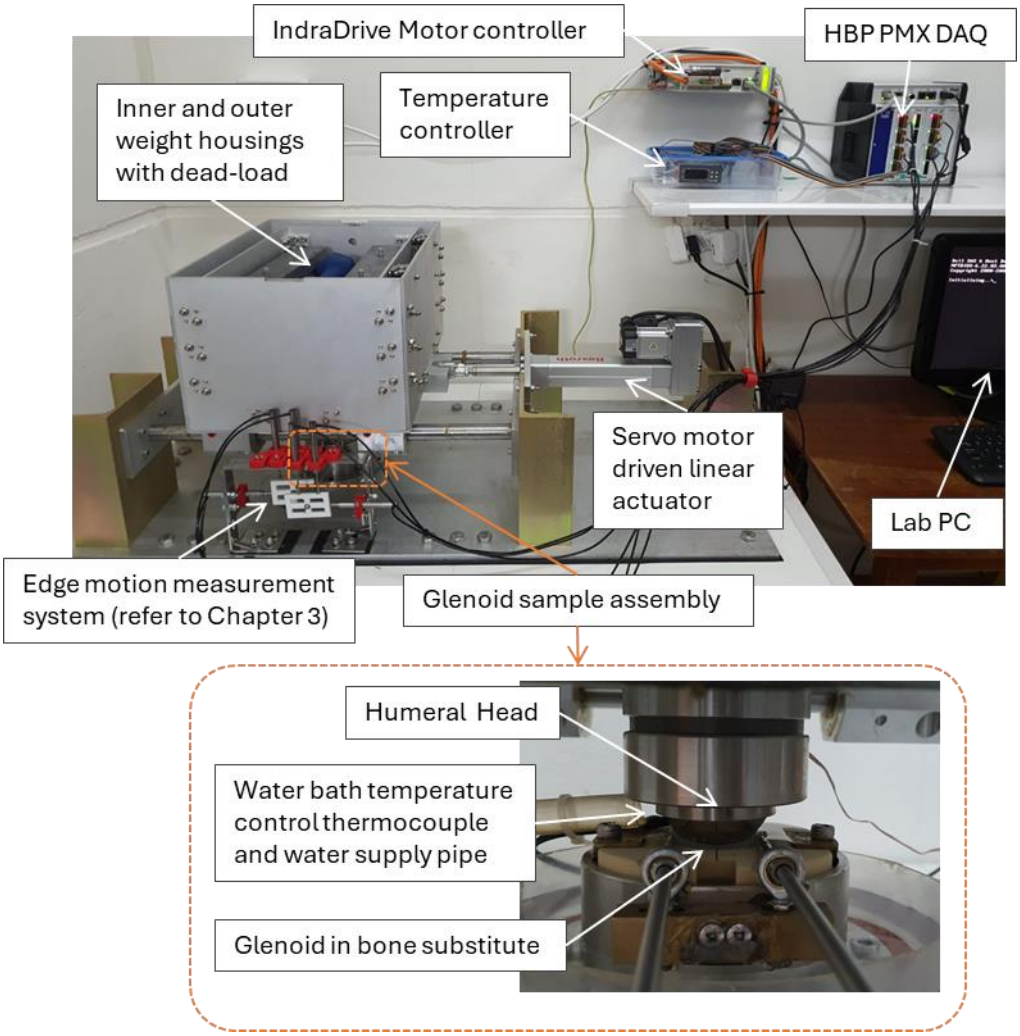

Figure 2-30 *Completed DGL Test Rig*

For the motion actuation and control, an electromechanical solution was chosen, as one of the options suggested by the standard. The normal load application by weights was not suggested in the standard, but the standard does allow for different methods. In literature, the use of weights to apply the load in ASTM F2028-type test rigs was done by Karduna et al. (1998), setting a precedent for the method in principle. In their research, Karduna et al. (1998) used a weight-loaded pulley system attached to the glenoid sample housing to create the contact force. The humeral head was moved in the shear direction but was fixed in the normal direction. Their method avoids the problem of shear acceleration and deceleration of the weights. However, it causes a motion at the glenoid sample that could disrupt attempts to measure edge deflection during the test. As accurate continuous edge deflection measurement was identified as a goal for this study, it was deemed necessary to move the weight in the shear direction while holding the sample mounting rigid.

Using the total motor torque variation to determine the subluxation distance deviates from the standard method of directly measuring the shear force. However, the motor torque variation is expected to follow the same trend as the shear force variation since the shear force is the only changing variable in the P90 test, and the actual value of the shear force is not needed to calculate the subluxation distance. The use of the inherent capability of the motor controller to measure the torque removes the need for additional sensors and calibration. The disadvantage of not directly measuring the shear force is that the resultant total edge loading cannot be calculated to check the starting position of the humeral head. The position must, therefore, be controlled by consistent implantation and fixation of the sample housing at a location with a known centroid position and by confirmation that the variation of the normal load at the glenoid edges is maintained within the 10% variation limit.

While no formal concept evaluation was performed for the temperature control and lubrication system, some iterations were made as other elements of the rig varied. Specifically, in initial prototypes, the glenoid was fully submerged in the catchment reservoir. However, during the glenoid edge motion measurement system design, it became necessary to lower the wall height to prevent clashes with the lever components of the measurement system (to be discussed in Section 3.4.1). This changed the system's configuration from a water bath to a circulating water flow. Water flow over the surface has the additional benefit of preventing debris build-up at the articulating surface, as any grit in the system will be washed off and caught in the return pipe filter. The primary concern with the final design is the slow leaks at the seal between the removable catchment reservoir and the base plate, which must be managed by regular water level checks. However, the surface of the glenoid and the bone substitute substrate remain constantly wetted by temperature-controlled water, ensuring the required lubrication and material temperature are maintained.

2.7.2. Discussion of Preliminary Functional Validation Results

The results of the preliminary functional validation testing are discussed to assess the conformance of the rig design to the design requirements for the three stages of testing and to general functional requirements.

2.7.2.1. P90 Test Validation Discussion

The P90 Test Validation aimed to confirm that the test protocol executes as expected and that using motor torque to determine the subluxation distance is valid. When executing the P90 Test Protocol, the motor velocity and displacement were controlled as desired, and all required values were logged at ~13Hz. The functionality of the protocol is, therefore, suitably validated.

To determine the validity of using motor torque to predict subluxation distance, the relative influence of torque variations on the flat surface to those on the curved glenoid surface must be investigated. Firstly, by understanding the internal torque characteristics of the motor and mechanical system in the given motion, then by adding a 'constant' surface shear force, and finally comparing this to the curved surface shear force.

In the 'no load' condition of the flat surface testing, the weight housings were moved with the humeral head not in contact with the surface. The torque measured in this case is, therefore, a measure of the 'base' torque of the system required to overcome the internal motor friction and the friction in the four horizontal linear bushing sets. Referring back to **Figure 2-23**, the no-load torque starts at approximately ±0.175Nm and varies along the motion with sinusoidal-like variations on a scale of 5mm and noise variations on a scale of <1mm. These variations are likely a combination of the motor speed feedback control adjusting power to maintain the constant horizontal speed and the internal variation in the rolling friction of the linear bushing sets.

The addition of surface contact shear force at 180N adds approximately ±0.02Nm of torque, while the overall shape of the torque curve remains consistent, even to the scale of the 'noise' variations. The torque curve at full load again shows a similar shape but with a larger increase in overall torque (approximately ±0.06Nm more than the base torque). This reinforces the assessment that the flat surface torque trend is determined by the mechanical system rather than the surface shear and that the trend remains consistent for this motion speed and starting point. To determine if these variations influence the P90 distance calculation, the results are compared to those of the P90 test on a curved glenoid surface.

The peak (absolute) torque values during the glenoid surface tests are in the order of ±1.5Nm and occur within 7mm of the centroid. While the full load flat surface torque is approximately ±0.28Nm when the curved surface torque peaks, the observed variation in the flat surface torque at this point is only 0.03Nm. As this is less than 5% of the peak values, the flat surface torque will not skew the location of the main peak unless a larger than normal 'noise' peak creates an artificial local maximum close to the curved surface peak. This is a concern as it is noted that the amplitude of this 'noise' increases (to up to 0.15Nm) near both measured peak values.

For this reason, a trend of the curved surface data, rather than an absolute peak, was used to determine where the measured torque curve gradient switches from positive to negative. This is then taken as the subluxation point. In the data shown in **Figure 2-26**, a 6^{th}-degree polynomial was fit to the data from the centroid to the distance to the glenoid edge. This figure shows that the peak location in the positive direction occurs earlier and has a higher value than the negative

run. This is likely because the sample was implanted with an excess of cement under one edge, causing a raised edge on that side, as shown in **Figure 2-31** below.

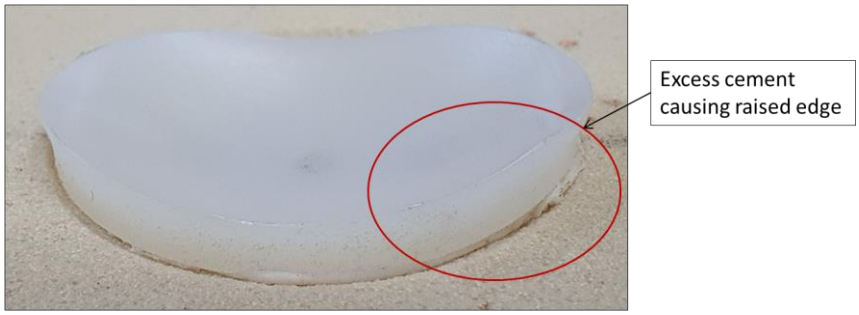

Figure 2-31 *Expired size 52mm glenoid sample used in the P90 test validation, which has unevenly distributed cement, causing the subluxation distance to not be symmetrical around the glenoid centroid.*

Using the described method, the average subluxation distance for the two test runs was calculated as 6.2mm. As a check, the rigid body subluxation distance for the test can be calculated. The rigid body subluxation distance is given (Cofield, 1994) as:

$$d_{subluxation} = d_{Edge}\left(1 - \frac{r_{HH}}{r_{glenoid}}\right) \quad 2.1$$

Where $r_{glenoid}$ is the glenoid radius, r_{HH} is the humeral head radius, d_{edge} is the distance from the centroid to the glenoid edge, and $d_{subluxation}$ is the distance the humeral head has travelled when subluxation occurs. For the 52mm glenoid, a surface radius of $r_{glenoid}$ = 29mm (i.e. 3mm radial mismatch) and distance from centroid to edge of d_{edge} = 19.5mm were measured from the sample. For these values and the size 44 humeral head used (r_{HH} =22mm), the expected rigid body subluxation distance is $d_{subluxation}$ = 4.7mm.

This is lower than the measured value, which is expected since the flexible glenoid does not behave as a rigid body. In their comparison of experimentally measured to rigid body subluxation distances, for a rigid body value of 5mm Anglin et al. (2000c) reported experimental values ranging from approximately 4.9 to 6.2mm. The experimental value of 6.2mm is comparable to the high end of the reported values and is considered reasonable.

It is therefore concluded that using the motor torque variation is a valid method to determine the P90 distance of the glenoids in the novel glenoid evaluation testing.

2.7.2.2. Cyclic Motion Test Validation Discussion

The cyclic motion validation aimed to confirm that the Glenoid Edge Motion protocol could be used to perform the conditioning and main cyclic loading tests, and to select appropriate input motion parameters for these two tests. The protocol validation was again performed by checking that the correct input motion was executed and that all desired data were logged at the correct

intervals along the motion. The logged data file for the tests showed that everything was in order. During the development of the protocol, it was found that two factors played a role in the choice of the input parameters.

The first was the inertial limitation set by the deadweight. While the structure of the rig was designed to resist deflections or instability in the load-bearing framework, there remains a limit to how fast the deadweight can be accelerated and decelerated before inducing instability in the system. The system stability guided the choice of maximum velocity.

The second factor was an observed 'pause' at the target position during the motion (i.e. at the ±P90 mm from the centroid), ranging from approximately 1s to 2.5s. This pause is attributed to the time taken for the controller to 'find' the target position, with the apparent motionlessness actually being a setpoint-seeking oscillation around the goal. As mentioned in the description of the results, any increase in the jerk value caused a visibly wider oscillation around the setpoint, so the jerk was held at zero. The choice of acceleration values also influenced this setpoint-seeking time.

The timed test results show that while higher acceleration values decreased the overall cycle speed initially, after 100mm/s^2 the endpoint pauses started to slow the test. At this point, only increasing the velocity would decrease the cycle time, which was eventually limited by the inertial shock on the system supports. The final motion description values of 1000mm/min, 100mm/s^2, and 0mm/s^3 were chosen from these two limiting factors. The maximum chosen cyclic speed of 1000mm/min remains below the rig design requirement allowable maximum of 5000mm/min.

To observe the velocity profile for all locations during the cycle, a short cyclic test using an intermediate protocol that continuously logged the position and velocity was run at the chosen parameters. The velocity profile, plotted against time and relative to humeral head position, is shown in **Figure 2-32**.

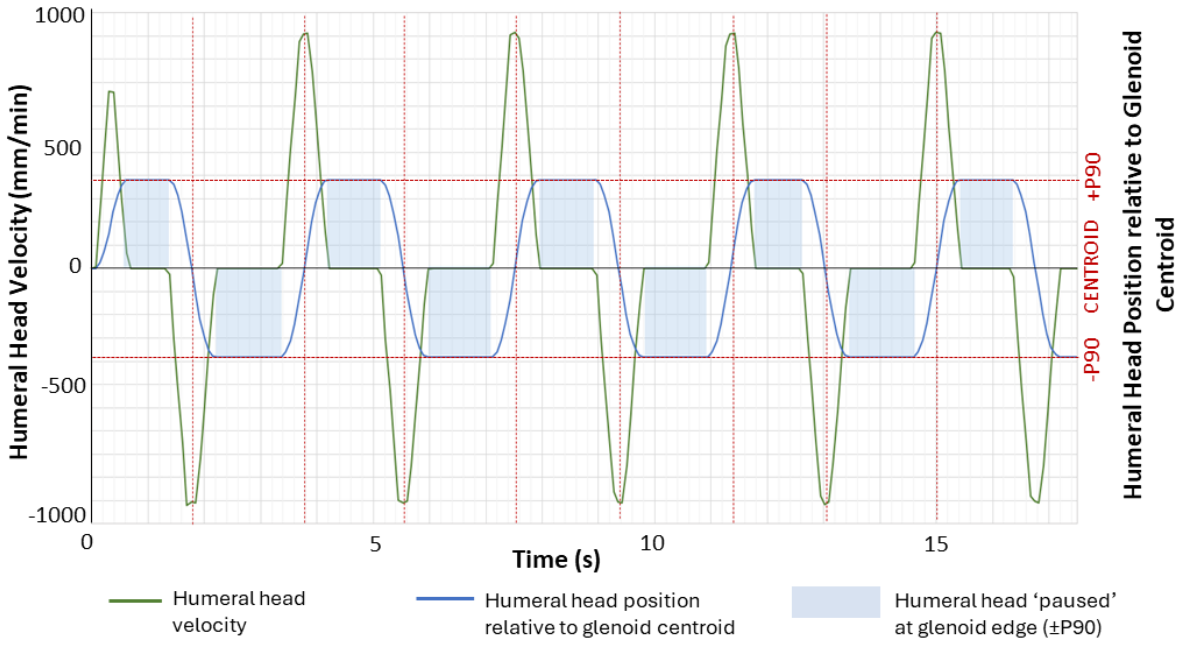

Figure 2-32 *Humeral head velocity profile for the cyclic motion, relative to the position of the HH on the glenoid, for the recommended motion input parameters of 1000mm/min and 100mm/s^2. The absolute HH velocity rises sharply as the HH approaches the glenoid centroid and then decreases as the HH decelerates to a stop at the glenoid edges. The HH 'pauses' at the glenoid edges (indicated by the blue shaded areas) before accelerating back towards the centroid.*

In this figure, the blue shaded areas indicate the endpoint delay 'pause' of approximately 1.2s, also observed during the load variation investigation. This delay is believed to be influenced by the communication between the LabVIEW code and the IndraDrive controller, as simple, early versions of the motion control code showed less susceptibility to the delay than later, more elaborate code versions. The final protocol code had endpoint delays of up to 2.5s.

While no lower limit to cyclic speed is stipulated in the standard, we consider it reasonable to use any speed exceeding the 50mm/min used in the P90 test, which the standard considers high enough to prevent material creep. In literature reported test frequencies below the 2Hz recommendation are common, with reported values of 0.25Hz (Chamseddine et al., 2019), 0.5Hz (Gregory et al., 2009), 1Hz (Wirth et al., 2001), and 1.5Hz (Stautberg et al., 2017)(Gunther et al., 2011). Sabesan et al. (2015) further found that for larger glenoid sizes, a 2Hz frequency was unfeasibly high, as it caused their glenoid samples to shear out of the bone substitute substrate. The original upper limit to velocity of 5000mm/min, chosen for the test rig based on a 2Hz sliding speed on large glenoids, is therefore likely to be damaging to the glenoid samples. The true safe upper limit for this parameter is not known, and bears further investigation. This is discussed in the recommendations for future work Section 6.2.3.

Based on the comparative frequency to the experiments of the researchers listed above, and the fact that it is well below the velocity level expected to be damaging, the chosen test velocity of

1000mm/min is considered reasonable. The possibility of material creep during the endpoint delays does, however, need to be considered. No visible creep was observed during the preliminary rig validation testing. However, it is noted that all samples should be checked after full cyclic testing to ensure there is no surface degradation.

While the final chosen input parameters do result in a longer than desirable test duration (approximately five days for 100,000 cycles), the Glenoid Edge Motion protocol was shown to be able to perform the cyclic testing within the set design requirements.

2.7.2.3. Normal Force Application Validation Discussion

The purpose of the normal load application validation test was to determine the magnitude of the friction and inertial load variations during a typical test and to confirm that these did not cause the load to exceed the limitations set out during the design requirements.

Figure 2-27 compares the total load variations from static load. The widest load variation is in the 750N static run, where up to 70N overall variation is observed. All the measured loads show a larger negative force variation than positive. In the 180N static load runs, the peak normal load in the positive direction is approximately half that in the negative direction. For the 750N, the positive peak is roughly two-thirds of the negative peak. This implies that at some points in the motion, the friction and inertial effects are both working to reduce the load, while at other positions, one is contributing to, while the other detracts from, the load.

To understand the combined forces more clearly, we need to look at **Figure 2-28** and **Figure 2-29**, in which the load is plotted alongside the humeral head position. In both plots, as expected, the positive force peaks occur during the upward motion as the humeral head climbs the glenoid edge and is resisted by downward friction on the vertical bearing rails. To understand the inertial force behaviour in this motion, we can refer to the velocity profile shown in **Figure 2-32**. The profile shows that the HH accelerates during the motion from the edge to the centroid and decelerates from the centroid to the next edge (with inverted directional acceleration during the reverse movement).

While this shear deceleration does not necessarily translate to a normal deceleration due to the varying curve of the glenoid, it appears the action results in a ‘pull’ to slow the deadweight as it moves to a stop close to the top of the curve. The combined effect on the upward motion is, therefore, the addition of load by friction with some detraction by the inertial force. Inversely, on the move down the surface, the friction is working to lift the deadweight, and the load is being

accelerated downwards, again adding an inertial 'pull', and creating the combined effect low peak. This lasts until the centroid, when the load begins to rise again.

While the overall force variation of 70N approaches the 10% threshold of full load, the edge-to-edge load variation is less since it is always the positive peak that occurs on the edge. On the 750N test, the maximum edge loads vary between 15N and 30N (15N range). When the humeral head reaches the edge, the 'pause' in the motion as the controller seeks its setpoint (as discussed in Section 2.4) occurs. During this micromotion around the setpoint, the force either partially or completely reverts to the static load.

Even accounting for the 'settling' variation, the edge loads vary by a maximum of 35N, or 5% of the total load. This is comfortably within the threshold of 10% allowable edge load variation. Further, the force increases for the 750N data set of up to 30N are unlikely to raise the total axial force above 1000N. The forces observed in these tests, therefore, remain within the requirements set. The passively controlled load does produce a wider load range at 750N than the ±7.5N that the standard suggests.

Reported applied force values in the literature range from low (10-400N (Karduna et al., 1997),150N by (Giles et al., 2010)), to higher than recommended (1800N (Junaid et al., 2010)). Few authors give an indication of the variability in their applied loads. Oosterom et al.(2004) reported 750N±10N, achieved on a pneumatic test apparatus. Stautberg et al. (2017) simply stated 'constant 750N axial load'. While it is expected that pneumatic or hydraulic systems would have good active force control, the weight-applied system of Karduna et al. (1998) should experience some of the same frictional and inertial effects observed here. Even though the deadweight in their system is not subjected to the shear motion of this rig design, the normal acceleration as the humeral head or glenoid moves to accommodate the curve and some friction in the system supporting the weight would still occur.

Overall, the load measured did not exceed either of the limits set. Since this variation is 'passively' controlled by the behaviour of the mechanical system, it remains necessary to monitor the force values during the glenoid evaluation experimental work. It is also necessary to check that the force variation between different glenoids remains acceptable, particularly if changes in glenoid design influence the normal force. The final test results should be checked for any influence force variations may have.

2.7.2.4. Temperature Control System Validation Discussion

The goal of the temperature control and lubrication system validation was to confirm that the system keeps the glenoid and Sawbones wet, and that the temperature remains within 37±2°C for the duration of the test.

The short functionality check confirmed that the controller activates the heating or cooling circuits when the temperature deviates from the controller setpoint by more than 0.2°C. The reliability testing showed that the pump and temperature controller maintained functionality at all observed times. The loss of water due to the slow leak at the sample housing catchment reservoir and evaporation from the system necessitated replenishment of the water in the main reservoir. The reservoir water temperature decreased when water was added. However, it was found that refilling twice daily ensures the overall temperature does not fall below the allowable 2°C deviation (a sample of logged values is provided in Appendix A3). The twice-daily check-in is also used to visually confirm that the temperature has been maintained at the setpoint. With this schedule in place, the system maintains the temperature and lubrication of the glenoid and Sawbones base as required.

2.7.3. Deviations from the Standard

While the ASTM F2028 test method has been used as the foundation of the test rig design, some deviations from the standard suggested values have been implemented. These are summarised here.

Firstly, the normal load application by passive deadweight does not result in the normal load during the cyclic motion remaining within the 750N±7.5N suggested by the standard. The final force application is expected to be within 750N±40N. However, the requirement that the forces at each edge under load remain within 10% of each other is still met. The same deadweight will be used for all tests for consistency.

Secondly, the value for the applied shear force is not measured, but rather, the trend in this force is evaluated by comparison to motor torque, from which the subluxation distance is determined. Sample measurements taken using this method showed a good correlation to values reported in the literature. The lack of measurement of the shear force does prevent the calculation of the total resultant force applied to the glenoid. The variation in the resultant force would be used to check the cyclic motion starts at the centroid of the glenoid. The test rig ensures this starting point by a fixed mounting location of the sample housing on the base plate and of the sample within the housing.

Finally, the recommended optional measurement of the humeral head normal translation is not performed. This measurement would determine if any sudden changes in glenoid edge motion occur during the testing when the edge motion is only measured before and after the cyclic loading. The test rig will measure the edge motions throughout the cyclic loading, so the normal translation value was deemed unnecessary.

2.7.4. Summary

Overall, the test rig can perform the DGL test within the design requirements set out. The full list of requirements, with the ASTM standard, recommended values, the implementation method, final implemented values, and the method of verification, are summarised in **Table 2-4**. The glenoid edge motion measurement system can now be added to the rig. Full-length testing of the complete system is performed in the Augmented Test Rig Validation testing.

Table 2-4 *Summary of all DGL test rig requirements, alongside the ASTM F2028 standard recommendations, and the method of implementation of the requirements into the test rig*

Feature/ Variable	Action	ASTM Recommendation	Implemented Value	Implementation Method	Verification	Comments
Normal Load	Controlled Variable	750±7.5N Resultant edge load variation of max 10%	750±30N Normal edge load variation of ~5%	Deadweight	Monitored by load cell behind humeral head	Passively controlled by mechanical system and fixed set of weights in all tests.
Humeral Normal Translation	Free motion	Monitor during testing	Not monitored	Roller blocks on vertical bearing rails		Monitoring not required due to continuous edge motion measurement
Humeral Shear Motion Amplitude	Controlled Variable	Amplitude determined by glenoid size.	Up to ±35mm possible.	Rexroth IndraDrive controlled linear actuator.	Position logged by controller during testing.	
Humeral shear motion start position	Controlled variable	Motion must start ±0.5mm from centroid	Centroid location at 66.5mm actuator absolute position.	Sample implantation and mounting in fixed location.	Normal load at edges does not vary by more than 10%	
Humeral Shear Motion Velocity	Controlled variable	50mm/min for P90 test 2Hz for cyclic testing (Max 6Hz allowable)	50mm/min for P90 test 1000m/min for cyclic testing (up to 5000mm/min allowable)	Rexroth IndraDrive controlled linear actuator.	Velocity logged by controller during validation testing.	Allowable velocity estimated based on 2Hz and expected motion amplitude.
Shear Force Peak Location	Dependant variable	Measure shear force to determined location of peak value	Motor torque variation measured to determined location of peak value	Rexroth IndraDrive controlled linear actuator.	Torque logged by controller during P90 testing.	Clear torque peaks occur, producing subluxation distances which concur with values reported in literature.
Sample Temperature Control	Controlled variable	37±2°C recirculating water bath	37±0.2°C recirculating water flow	Water reservoir temperature controlled and circulated over sample by constant flow pump	Twice daily visual check of temperature controller display	Water levels to be monitored and replenished twice daily to ensure temperature does not drop by more than 2°C.
Sample and substrate lubrication	Physical requirement	Constantly wetted sample and substate surfaces	Constantly wetted sample and substate surfaces	Recirculating water flow from constant flow pump	Twice daily visual check of circulation system	NA
Substrate Properties	Controlled variable	Bone substitute of: E_{Bone} = 193MPa σ_{Bone} = 7.6MPa	Sawbones polyurethane PC20	Use of ASTM accredited material (Sawbones)	Reliant on material certification	NA
Sample implantation	Controlled variable	To mimic actual surgical implantation	Surgical implantation method used	Qualified surgeon, training implantation tool set and PMMA bone cement used.	Reliant on surgeon expertise.	To be performed at Groote Schuur Hospital, Cape Town
Single user interface for test control	Operational requirement	NA	NA	Control of testing co-ordinated via Labview on laboratory PC	Proper execution of protocols checked in validation testing	NA
Uninterrupted electrical power supply	Operational requirement	NA	NA	Test rig power supply linked to generator backup via 6kVA changeover UPS	Installation by qualified UCT electrical technician	NA

Chapter 3

Glenoid Edge Motion Measurement System Design and Development

To investigate the complex motions occurring at the glenoid edges, a method of measuring the vertical, horizontal, and tilting motions of the glenoid edges throughout the DGL test is required. Since such a system does not exist in the literature, the glenoid edge motion measurement system was designed, integrated into the DGL test rig, and the completed system functionally validated as part of this research.

This chapter discusses the design process, which led to the development of 3 prototypes before the final edge motion measurement system was developed. The final design utilises multiple sensors at each glenoid edge, whose readings are converted to edge motion by means of a MATLAB algorithm. The functionality and *in-silico* verification of this algorithm are then described (Objectives 2.1 to 2.3). The Rig Validation Study, using the augmented test rig with the integrated edge motion measurement system, is described and the results discussed (Objectives 3.1 to 3.3 and the conclusion of Objective 1.3).

3.1. Background and Aims

The standard requires the measurement of the vertical edge displacement and suggests this be done by attachment of a small screw in the side of the glenoid surface, on which the measuring point of a sensor can be placed. This suggestion was used as the starting point for the edge motion measurement system design.

In the literature, lever dial indicators are used by Anglin et al. (2000b) and Gunther et al. (2011) to measure the edge displacements before and after cyclic testing. In both of their setups, a pin extends from the side of the glenoid in the direction of the major axis, and the lever of the dial indicator rests on this, oriented perpendicularly to the pin, as indicated in **Figure 3-1**. These setups were moved to a water bath, without the sensors, for cyclic testing.

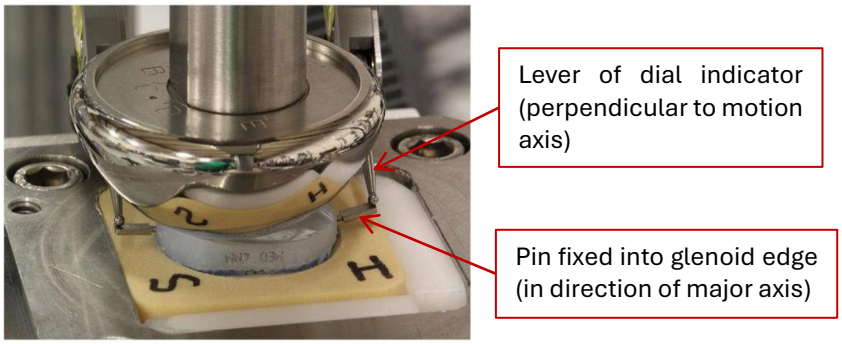

***Figure 3-1**: Experimental setup used by Gunther et al. (2011) to measure vertical glenoid edge deflections before and after cyclic loading. Pins are attached to the sides of the glenoid, on which the levers of a dial indicators rest. (Image adapted from Gunther et al. (2011))*

During initial development, the focus was on achieving a continuous edge motion measurement method that met only the standard requirement of measuring vertical edge displacement. However, during the initial concept evaluation, it was observed that horizontal and/or tilt motions were occurring and confounding the vertical motion measurement methods attempted. The second prototype developed attempted to measure the vertical displacement in a manner that was robust to the horizontal and tilting motions, but it became apparent that these motions were more pronounced than expected.

From this, it was apparent that a system that could quantify these motions was required. The aim of the design was therefore to develop a method of measuring vertical, horizontal, and tilting motion of the glenoid edges motion simultaneously, continuously (i.e. during each cycle) for the full length of the cyclic loading test.

3.2. Design Constraints and Requirements

The design requirements for the edge motion measurement system are set by the expected measurement range, resolution recommendations from the standard, the physical constraints relating to space and environment, and durability of the system in order to survive multiple full-length cyclic tests.

The range of motion for the edge measurement sensors must accommodate the expected motion of the edges, even when the fixation of the component has begun to fail. Reported values for the vertical edge displacement before fixation failure are within ±1.6mm of the starting position (Anglin et al., 2001; Sabesan et al., 2015; Stautberg et al., 2017), and no studies were found in which the horizontal or angular displacements were reported. From this, a required measurement range of ±2mm in each the horizontal and vertical directions, and an angular motion of ±15° from the vertical axis was chosen. Any motions exceeding this range are deemed to be an indication of fixation failure. Within these measurements, a desired resolution of 10μm and 0.1° was chosen. As discussed in Section 2.2.4, the sampling rate for the measurements is at the 5 prescribed locations along the glenoid surface, during each test cycle.

Space constraints on the edge motion measurement are caused by the leading edge of the humeral head as this moves to the edge of the glenoid. The humeral component overhangs the glenoid edge, resulting in a small amount of clearance (usually less than 5mm) at the glenoid edge, as illustrated in **Figure 3-2**. This is problematic for most displacement sensor types, where the sensor body is placed on the same axis as the direction of measurement (e.g. LVDT). This space restriction means that the measurement location either needs to be shifted outwards (e.g. using a long enough pin) for the sensor to be out of the range of the humeral head or by changing

the direction of the measurement to allow the sensor orientation to be changed. Even in the configuration used by Gunther et al. (2011) shown in **Figure 3-1**, where only the dial indicator lever is near the measurement point, the lever is moved slightly away from the edge, along the pin, to avoid clashing with the HH.

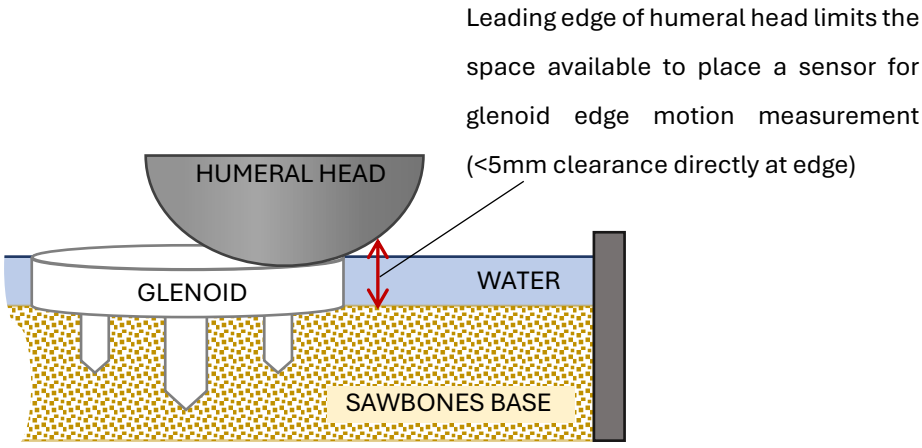

Figure 3-2 *Physical constraints to be considered during the design of the glenoid edge motion measurement system.*

Further, for continuous measurement of edge deflections during the cyclic loading, the standard recommendation of glenoid temperature control and lubrication by a water bath means that electronics need to be moved away from the glenoid edge, or waterproofed.

It is desirable that the sensor itself does not add additional loading only the glenoid edge. In the absence of a specific requirement from the standard, the suggested cyclic loading tolerance (±7.5N) is used as a guide for acceptable load applied by the sensor. It remains desirable for the sensor to apply as little force to the glenoid edge as possible. Minimising the force applied to the point of measurement is also likely to improve the durability of the sensor attachment during the cyclic testing.

The durability of the system must at least be sufficient for a single 100,000 cycle test to be performed. However, it is desirable that individual components, such as the sensors, are able to survive the full expected course of testing (15 tests of 100,000 cycles each), to provide consistency between tests and to prevent unnecessary costs. The design requirements discussed are summarised in **Table 3-1**.

Table 3-1 Summary of glenoid edge measurement system design requirements

Requirement		Value
Measurement Resolution	x	10μm
	y	10μm
	α	0.1°
Measurement Range	x	±2mm
	y	±2mm
	α	±15°
Measurement point space available		5mm in vertical axis
Environment		37°C water
Force applied by sensor to glenoid edge		<7.5N
Sensor longevity		1 500 000 cycles
Sensor Fixation survival		100 000 cycles (minimum)

3.3. Design Considerations and Concept Selection

The edge displacement measurement system was designed by first considering the types of displacement sensors available and evaluating them based on resolution, mode of operation, suitability for use within the physical constraints of the system, and cost. Initial prototypes were then developed to further evaluate the use of selected sensor types. From this, a final concept was chosen.

As discussed, the initial concept design focused on developing a continuous edge measurement system for vertical displacement only. The findings from the initial concepts highlighted the need for and guided the development of the system to measure the horizontal and tilt motions. These initial concepts are therefore included as part of the design process.

3.3.1. Concepts Considered

To measure displacement, a wide variety of sensor types which have the desired measurement sensitivity are available. The main limiting factors for the sensor choice are the presence of the water bath, and the space constraint created by the leading edge of the humeral head as it moves to the glenoid edge. Sensors considered included non-contact types such as Hall Effect sensors, eddy current sensors, and optical sensors. Sensors requiring contact included LVDT sensors, draw-wire sensors or the use of strain gauges to measure the deflection of a plate. Possible configurations of these different sensor types are shown in **Figure 3-3**.

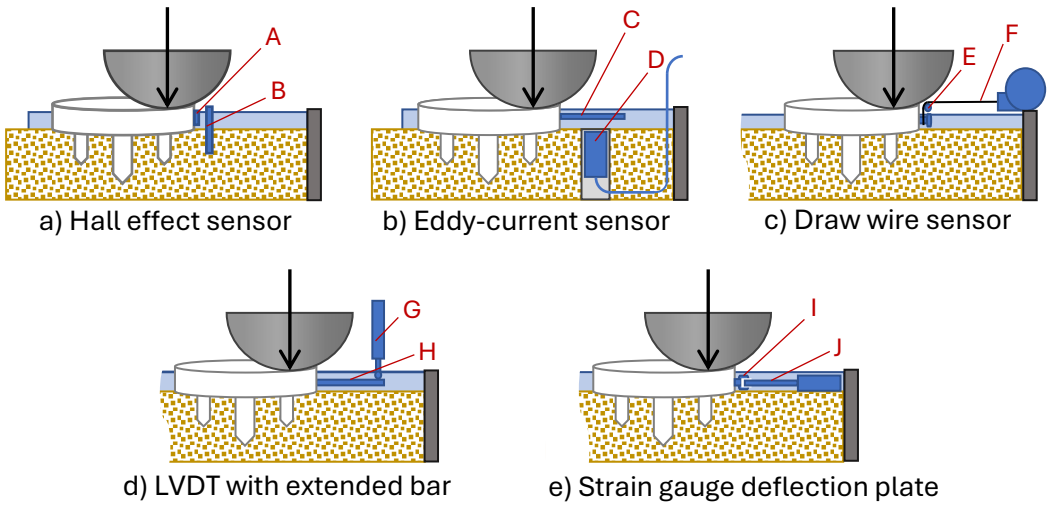

Figure 3-3 *Possible vertical edge displacement measurement sensor types, including: a) A Hall effect sensor where a small magnet (A) is attached to the glenoid edge, and a semiconductor element (B) detects the magnet's motion, b) An eddy current sensor (D) which can detect the motion of a flat plate (C) extended from the side of the glenoid, c) A draw wire sensor (F), in which the wire is direction is converted from vertical to horizontal via a pivot pin (E), d) An LVDT sensor that can detect motion of a plate or pin extended from the side of the glenoid, and e) a thin plate fitted with strain gauges that is deflected by a pin in the glenoid edge.*

Methods of accommodating the space constraint at the glenoid edge include moving the measurement point outwards using a pin (shown for an LVDT sensor), changing the direction of measurement using a pivot point (for draw wire), or placing the main body of the sensor below the surface of the Sawbones (Eddy current, Hall Effect sensors). The pros and cons of each sensor type considered are summarised in **Table 3-2**.

The optical sensor was eliminated as an option due to the presence of water at the glenoid edge, which would obscure the measurement. Of the remaining concepts, the Hall Effect sensor was selected for the first prototype, despite the need for waterproofing, due to its low cost, and because it utilised contactless measurement directly at the glenoid edge. Further prototype development is discussed in the next section.

Table 3-2 *Evaluation of displacement sensor types considered for the glenoid edge motion measurement based on practicality of use and cost.*

Sensor Type	Cost	Pros	Cons
LVDT	Moderate	Sensor electronics remain out of water bath.	Space constraints in vertical direction would require a long bar attachment to glenoid to move measurement point outward.
Optical	Very high	Very high resolution on sensors	Water at edge would obscure measurement
Hall Effect	Low	Magnet can be placed directly on edge of glenoid. Non-contact measurement applies no force to edge.	Electronics would need to be waterproofed
Eddy Current	High	Non-contact measurement applies no force to edge.	Sensor would need to be waterproofed. Plate with sufficiently large surface area for measurement would need to be attached to glenoid edge.
Draw wire	Moderate	Sensor electronics remain out of water bath.	Space constraints directly at edge, measurement point would need to be moved outward or direction of wire changed
Strain gauge bending bar	Low	Height of sensor low enough to allow measurement at edge	A self-built sensor would require validation and calibration. Electronics would need to be waterproofed.

3.3.2. Prototypes Developed

The first two prototypes developed, the Hall effect sensor concepts and the strain gauge bending bar, were still aimed at measuring only the vertical edge deflection. The outcomes of these designs led to the development of the final prototype, the LVDT lever arm assembly, aimed at measuring motions in vertical, horizontal, and tilt directions.

3.3.2.1. Prototype 1: Hall Effect Sensor

The initial prototype comprised a Hall Effect sensor in a sideways detection configuration. This sensor uses a semiconductor element to determine the location of a small magnet as it moves relative to the semiconductor surface. In the prototype the semiconductor surface and circuitry were mounted alongside the glenoid edge, set into the Sawbones surface and the magnet was glued directly to the glenoid edge, as shown in **Figure 3-4**. At this proof-of-concept stage, the water bath was omitted and an 'off the shelf' semiconductor element circuit board, (which was not compact enough to be cleared by the HH) was used.

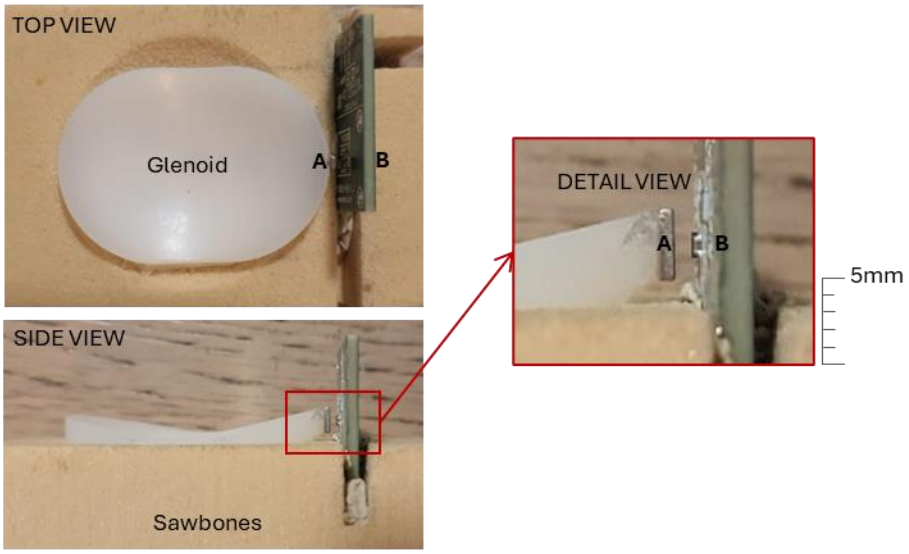

Figure 3-4 *Prototype 1: A Hall Effect sensor semiconductor element circuit (B) is embedded vertically in the Sawbones base adjacent to the implanted glenoid sample and magnet (A) is glued to the side face of the glenoid. The semiconductor element detects any motion of the magnet.*

For the initial sensor prototype, the glenoid edge was normally loaded using a precision drill press. A known deflection was applied rather than a specified load, to verify the sensor deflection measurements. It was found, however, that the sensor was not able to accurately measure the deflection. The Hall effect sensor requires the magnetic field to remain perpendicular to the semiconductor surface for measurement to be taken. Tilting of the glenoid edge under load was observed, which caused the field to misalign. The concept was therefore abandoned.

While the extent of the tilt expected at 750N load was not known at this stage, the fact that some tilt was occurring meant that only concepts that would not be confounded by the tilt were further considered. This caused the Eddy-current sensor to be excluded as these sensors also require their measurement surface to remain parallel to the sensor face.

Further, the horizontal and tilting motions can potentially confound the measurement if the measurement location is moved away from the glenoid edge. An example of this would be when using a pin extending from the glenoid edge, and a measurement location on the pin away from the edge. Tilting motion of the edge, even without any vertical motion, would induce an 'apparent' vertical motion if the sensor rests anywhere but directly against the side face of the glenoid. Placing the sensor at a consistent distance from the edge of the glenoid would help to ensure the amount of apparent motion included by tilt is the same in all repeated measurements (if the same amount of tilt is occurring). However, if a horizontal motion of the edge is also occurring, the distance to the sensor will change, as the edge moves, resulting in an indeterminate contribution of tilt to the vertical motion. Based on these concerns, the LVDT with a pin or plate extending from the glenoid edge was also excluded. Of the remaining options, the strain gauge

deflection plate concept was selected, due to the measurement location, the sensor's vertical compactness, and low cost.

3.3.2.2. Prototype 2: Deflection Plate

The deflection plate sensor concept consists of a strain gauge Wheatstone bridge on a thin spring steel plate. One end of the plate is fixed to the sample housing, and the other is deflected by a pin in the glenoid edge. The low height profile of the plate allows the deflected end to be placed directly at the glenoid edge to measure motion.

The strain gauges are arranged as a full Wheatstone bridge, in a typical 'bending bar' configuration as illustrated in **Figure 3-5**. This configuration allows for maximum amplification of the output signal when the plate is deflected while compensating for temperature-induced strains in the system. The concept utilised a self-built amplification circuit and an Arduino Mega (Arduino, Somerville, MA, USA) for signal acquisition.

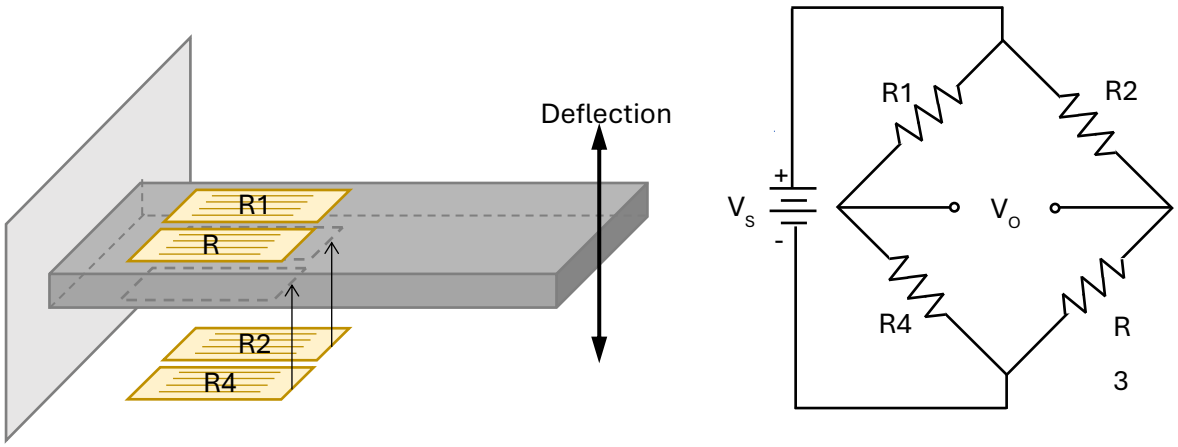

Figure 3-5 *Full Wheatstone bridge strain gauge configuration used for the deflection plate sensor concept.*

The thickness of the plate was chosen by experimentation with a range of spring steel plate samples. The final thickness chosen was 0.25mm, as this was thin enough to deflect easily, minimising the load applied by the sensor to the glenoid edge, while not so thin that the material permanently deformed during the test.

In the first iteration of this concept, the plate end was placed in the groove of a flat-head screw, pinned into the glenoid edge, as illustrated in **Figure 3-6**. This allowed the plate to start in its 'neutral' or undeflected state.

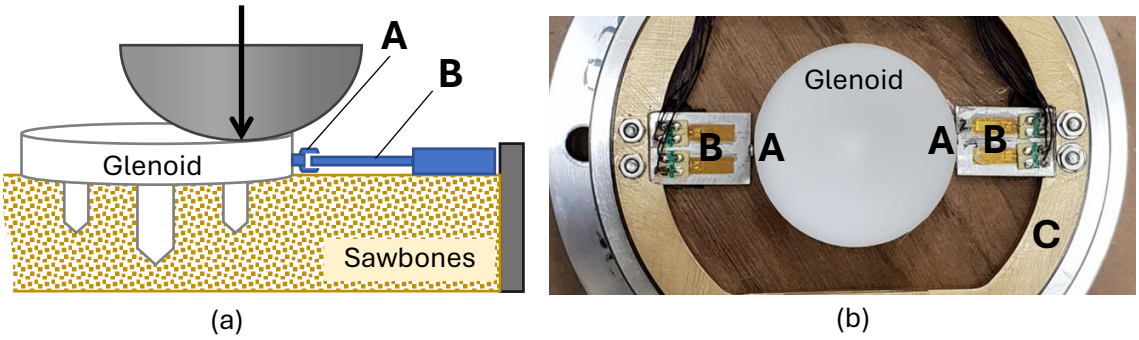

Figure 3-6 *Prototype 2: Deflection plate sensor concept (a) and prototype (b) in which 0.25mm thick spring steel (B) plates are each fitted with four strain gauges in a full Wheatstone bridge configuration. The plates are mounted to a ring (C) attached to the sample housing so that their free ends rest in the grooves of flat head screws (A) fixed to the glenoid edges.*

The depth of the groove in the screw head allowed a small amount (±0.5mm) of horizontal motion at the plate end. It was initially hoped that this would be enough to accommodate the horizontal shift caused by the tilt of the edge. However, preliminary testing showed this horizontal/tilt motion was much more pronounced than expected, causing plates to warp under compression rather than deflect freely.

The concept was then adapted to a configuration in which the plate rests on top of the pin, with an initial upward deflection applied, as Illustrated in **Figure 3-7**. The plate would either deflect further for upward motion or relax for downward motion.

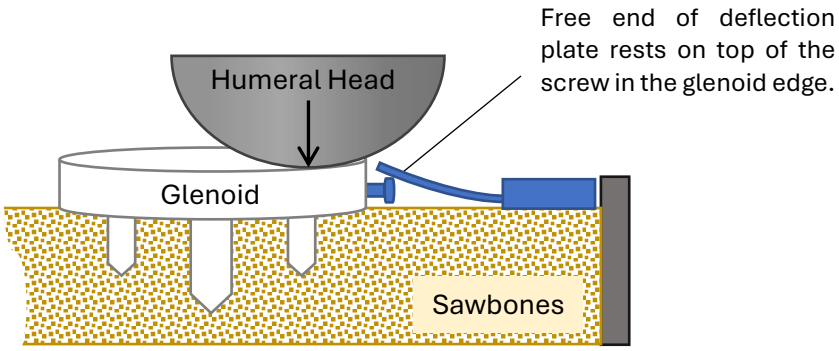

Figure 3-7 *Prototype 2.1: Revised concept of the deflection plate sensor prototype, in which the free end of the plate rests on the top of the screw in the glenoid edge. The plate has an initial upward deflection before any glenoid edge motion occurs.*

The severity of the horizontal motion observed at this point motivated for the addition of a 'tilt bar', to measure this motion. The tilt bar consisted of a bent steel bar, with a flattened front edge placed against the glenoid edge and held there by a pre-deflected additional deflection plate sensor, mounted vertically, as illustrated in **Figure 3-8**. This version of the prototype could

measure the horizontal motion of the edge, but it could not distinguish between pure sideways motion of the edge and motion caused by tilt. To allow testing in a water bath, the plates and associated electronics were coated in marine silicone (except at the point where the head of the screw or the back of the tilt bar contacts the metal plate).

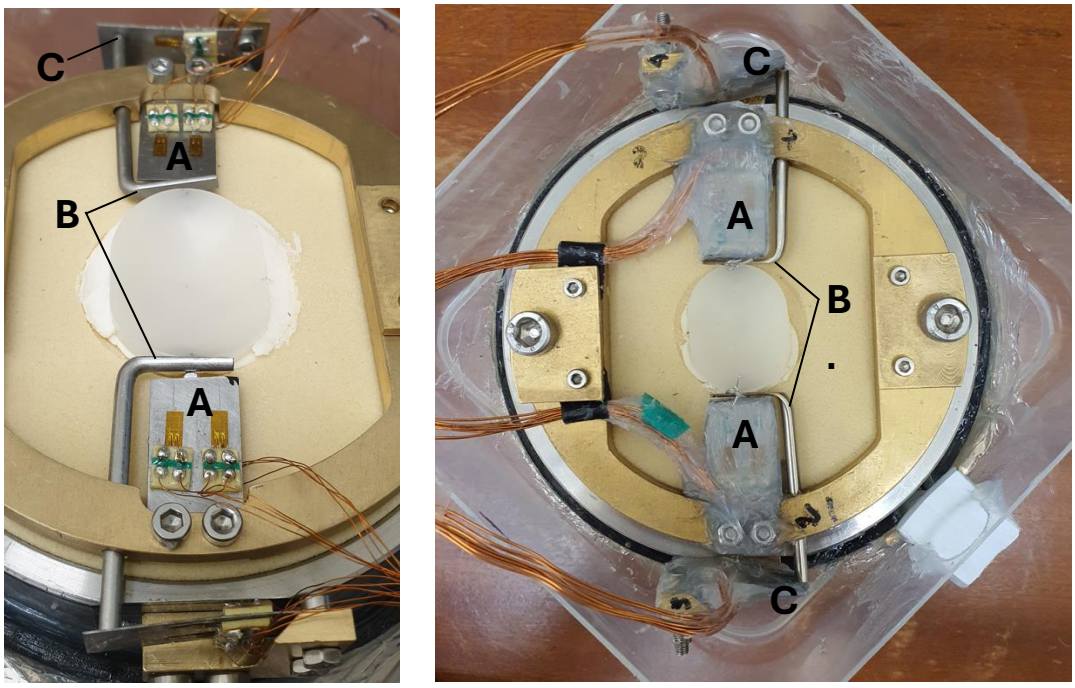

(a) (b)

Figure 3-8 *Prototype 2.2: Horizontal deflection plate sensors (C) which have their free ends resting on top of screws in the glenoid edges measure vertical edge deflection. Tilt bars (A) are pressed against the glenoid edges by additional vertically aligned deflection plates (B), to measure horizontal/tilt motion of the glenoid edge. The system is shown (a) before waterproofing and (b) after waterproofing with marine silicone.*

The sensors were calibrated by deflecting the plate with a known magnitude using the precision drill press at the UCT Medical Campus workshop and recording the output voltage. However, it was found that the sensor outputs were susceptible to variation if the sensor was moved from one assembly to another. Shifting the sensors from the workshop to the lab altered the signal output enough for the workshop calibration to be invalid. To combat this the sensors were assembled to the sample housing (without the glenoid in place) in the testing laboratory and deflected using an electronic micrometer gauge. The voltage output of the amplification circuit was adjusted by changing the amplification and zero point offset potentiometers so that the signal for the expected deflection range utilised the full 5V range of the Arduino. The known applied deflection was used to convert the voltage output to sensor edge deflection.

However, testing of this sensor setup using an expired glenoid sample showed persistent instability in the output signal. The cause of this instability is believed to be temperature ‘hotspots’ occurring in the strain gauges. The thin plate metal combined with the silicone

insulation does not allow good heat dissipation, resulting in inconsistent resistance in the gauges. Additionally, the system showed some susceptibility to signal noise. The poor signal quality achieved at this stage drove the decision to move away from the Arduino to a more reliable data acquisition system.

Even with an improved signal acquisition system, it was decided that the deflection plate sensors were not reliable enough in terms of signal quality and longevity. Further, from the preceding investigations it was clear that the horizontal and tilting motions of the edge are much more pronounced than was initially assumed. A measurement system that is not only robust to the confounding effects of these motions, but that can quantify them, is necessary if the glenoid edge motion is to be understood.

3.3.2.3. Prototype 3: LVDT Lever Arm Assembly

To simultaneously measure all 3 types of motion, a third prototype, the 'LVDT Lever arm assembly' was developed. Like the lever dial gauges used by Gunther et al. (2011), this prototype uses a lever that extends perpendicularly to the major axis (axis of motion) of the glenoid. However, instead of using a pin extending out of the glenoid edge, this concept utilises a pair of levers which each have one end pinned directly against the glenoid edge face. The levers are each supported by a pivot and are fitted with a 'measuring block' on their free ends. A set of 3 LVDT sensors is used to track the motion of each of the measuring blocks.

The lever arm assembly prototype is illustrated in **Figure 3-9**. Each lever arm is fixed to the side face of the glenoid by a screw. The lever pivots through a rod end bearing mounted to the side of the sample housing. This bearing allows free rotational motion in all directions except along the axis of the lever arm.

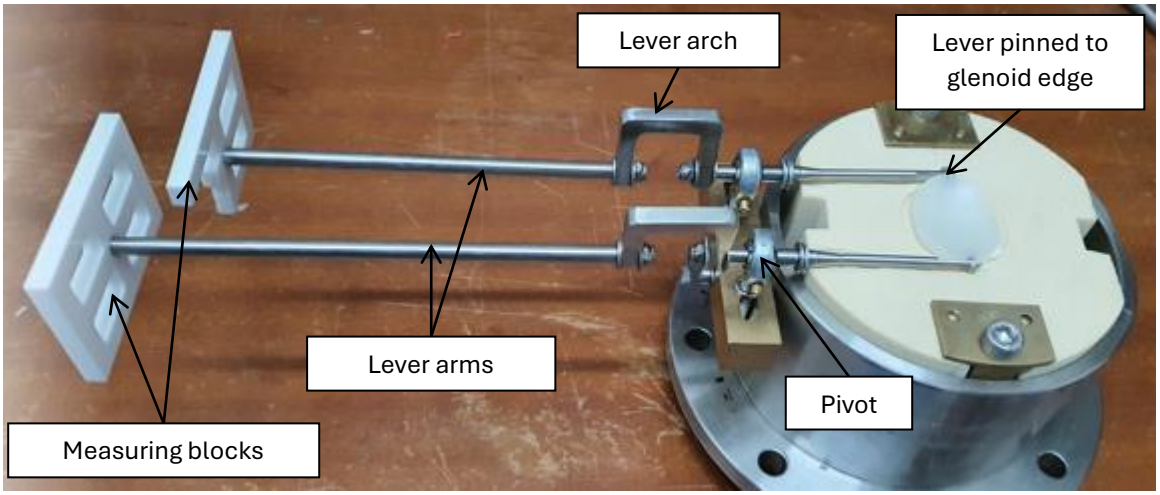

Figure 3-9 *Prototype 3: Lever arm assembly, where two levers are each pinned to the glenoid edges at one end, supported by a pivot point, and fitted with a measuring block on their free end. Each lever has an arch after the pivot point, to allow it to clear the water bath wall (not shown).*

The use of the pivoted lever allows the motion directly at the glenoid edge to cause an amplified, inverted motion at the other end of the lever. This has the benefit of moving the sensors away from both the water bath and the space-constrained zone at the glenoid edge, while still using the edge surface as the motion measurement point.

The lever arms were designed with 'arches' in them to allow the top edge of the water bath to be higher than the glenoid surface and hence allow full submersion of the glenoid sample. The end of the lever was fitted with a lightweight (Perspex) measuring block, against which the LVDT sensors make contact. To prevent clashing of the measuring blocks with each other and with the adjacent lever, the left-hand side (LHS) lever was made 15mm shorter than the right-hand side (RHS) lever. The lower, internal corner of the measuring block on the shorter lever was removed. This surface has no contacting sensor, so the shape adjustment does not affect the motion measurement.

The two sets of 3 LVDT sensors are then mounted in a rigid frame around the measuring blocks, so that the sensor tips contact, but are not affixed to, the measuring block top and outer side surfaces, as shown in **Figure 3-10**. The sensors are fixed to the frame by adjustable mounting clamps, which allow the position of each sensor to be adjusted according to the location of the measuring block, which varies with different glenoid sizes. Each measuring block is marked with three etched lines, to which the sensor tips are aligned, and the clamps fixed in place. The clamps also allow the distance of the sensor from the measuring block to be adjusted, so that each sensor can be positioned at its neutral (0mm deflection) position at the start of each test.

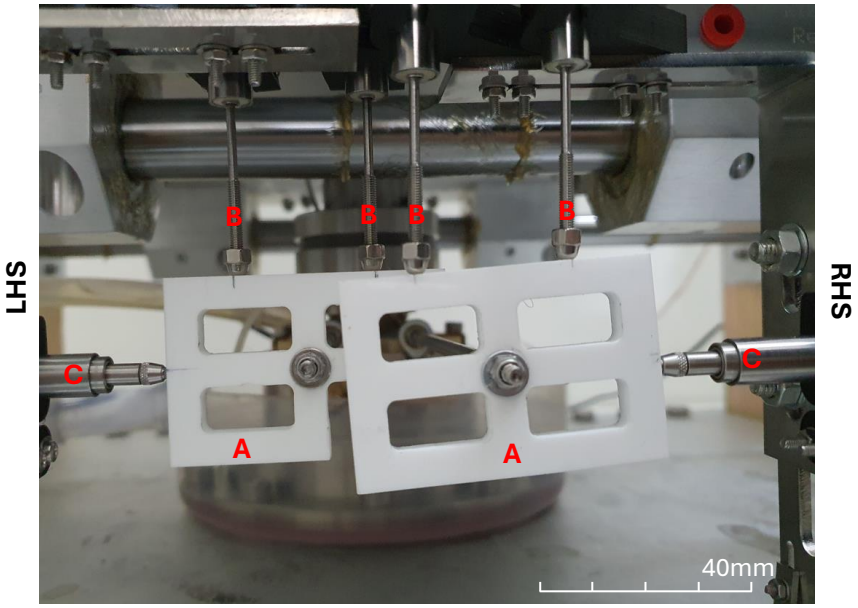

Figure 3-10 *Prototype 3: Sensor setup at the measuring blocks (A), where two vertically mounted unguided LVDT sensors (B) contact the top surface of each measuring block, and one horizontally mounted spring-guided LVDT (C) contacts the outer side surface of each block.*

The LVDT sensors were selected for high measurement resolution, as well as with a focus on minimising the force applied by the sensor tips to the measuring block (as this would be transferred back to the glenoid edge). As the lever arm pivot point location is at approximately 1/3 of the length of the lever, the edge motion will be magnified at the measuring block by a factor of approximately 2 (and inverted in direction) in the vertical and horizontal axes. The tilt will be transferred directly, as the pivot does not affect rotation around the lever axis. The LVDT sensors must therefore be chosen to allow an expected motion at the end of the lever (the centre of the measuring block) of ±4mm for horizontal and vertical, and ±15° tilt (based on the target motion range in the design requirements).

The magnitude of the deflection of the sensors at their locations on the measuring block surface will be determined by the combined motion of the centroid. The most extreme motion that could occur, would be when all three directions of motion 'work together' at the measuring block. This would be achieved by an edge motion that is downwards into the surface, outwards from the centroid, and with rotation towards the centroid. For this motion, the pivot on the lever would cause the measuring block to move upwards, inwards, and with the same inward rotation. This motion is illustrated in **Figure 3-11**, for the LHS measuring block.

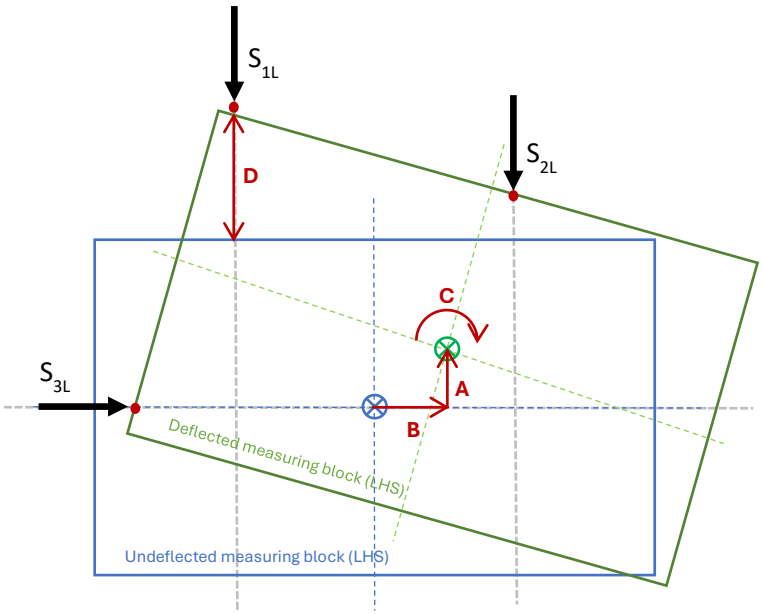

Figure 3-11 *Motion of the LHS measuring block as the LHS glenoid edge is deflected, with the resultant position of the three LVDT sensors (S1l, S2L, and S3L) indicated. An edge deflection downwards into the surface causes the measuring block to be pivoted upwards (A). An edge motion outward from the glenoid centroid (i.e. to the left) causes the measuring block to be pivoted inwards (B, to the right). A rotation towards the glenoid centroid (clockwise), causes a corresponding clockwise rotation (C) of the measuring block. These motions cause the largest combined deflection (D) at vertical sensor S_{1L}.*

The most extreme displacement occurs at the left vertical sensor (S_{1L}) where the combined rotational and horizontal motions add magnitude to the vertical displacement. While this particular combination of the three motions may not occur in the physical testing, it is used to determine the maximum displacement possible for the range of edge motion specified in **Table 3-1**, to guide sensor selection. The details of the final sensor selection are discussed in Section 3.4.2.

The data acquisition system (DAQ) was upgraded during the development of this prototype. Choices considered for this system were data acquisition hardware from Revolution Pi (company name, address), HBK, and National Instruments. The HBK PMX was selected, as described in Chapter 2, as it provided a good balance between ease of use, sensor type versatility by choice of I/O cards, and cost.

The new DAQ was integrated into the main rig, and proof of concept testing of the lever arm system was performed. It was found in these tests that multi-part levers were difficult to assemble consistently without incurring some misalignment in the lever. As the straightness and rigidity of the levers are important to prevent geometric errors in the conversion of sensor readings to glenoid edge motion, it was decided to remove the arcs and have solid lever arms. To allow for the straight levers, the wall height of the water bath was reduced, converting the

immersive water bath to a surface circulation of water for cooling (as illustrated in **Figure 2-13**). The straight lever arm design was then taken forward for development.

3.4. Design Implementation

As for the prototype, the final glenoid edge measurement system comprises two sub-assemblies, the lever arm sample assembly, and the sensor assembly.

3.4.1. Lever Arm Sample Assembly

The lever arm sample assembly with the single-part, straight lever arm is shown in **Figure 3-12**, with the water catchment reservoir (whose walls cross below the lever arms) in place. The same measuring blocks, rod end pivots, and mounting components are used as were used for the prototype. For clarity of discussion, the two levers are distinguished as the LHS, shorter lever, and the RHS lever, based on position when viewed from the measuring blocks.

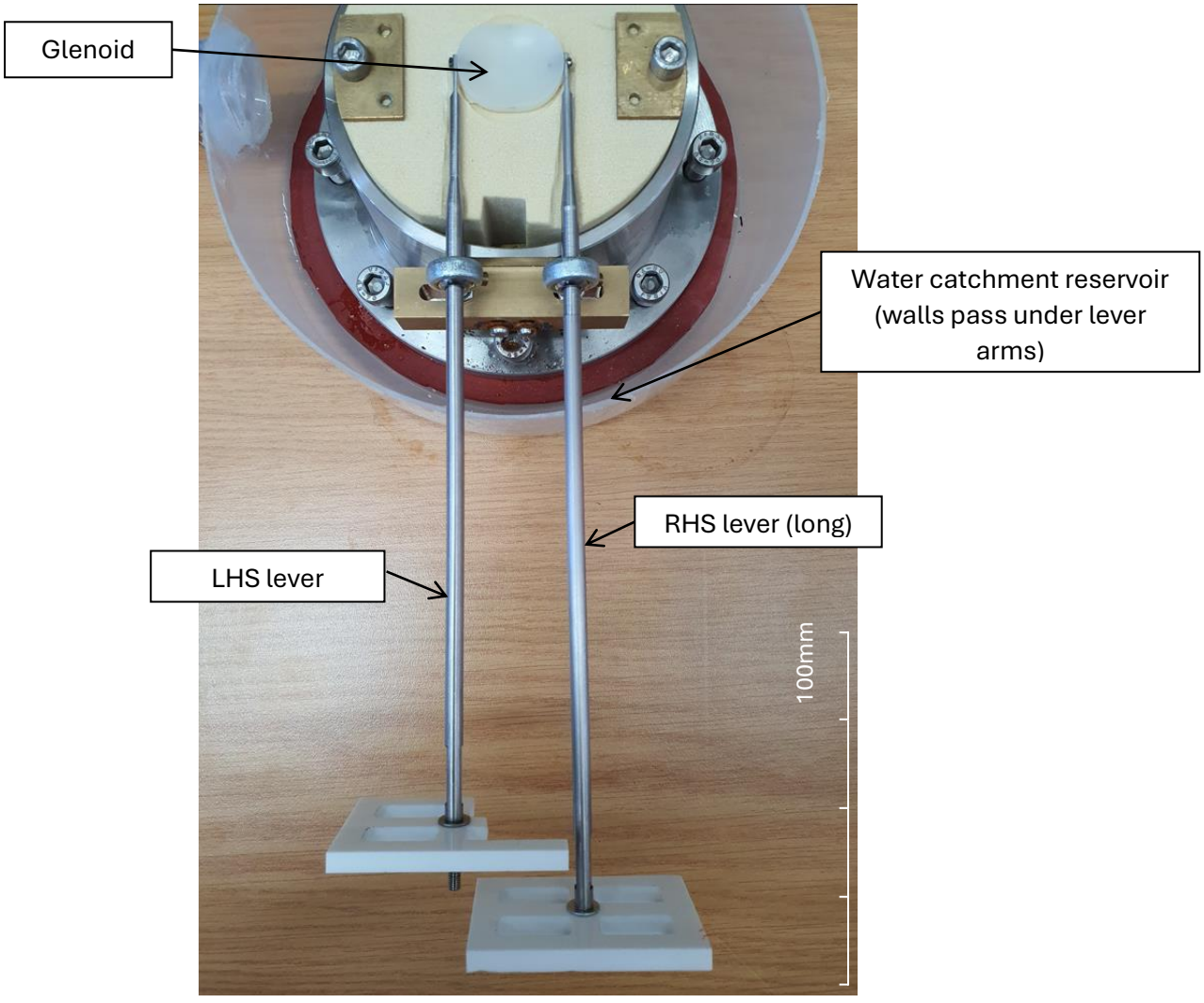

Figure 3-12 *Final design of the LVDT lever arm sample assembly. Straight, single-piece levers are used, while the walls of the water bath are lowered to allow the levers to be positioned horizontally, parallel to the Sawbones surface.*

For rigidity, the levers are made from solid Ø5mm stainless steel rods. The glenoid ends of the levers are narrowed to allow them to clear the Sawbones surface near the attachment point. The attachment points of the levers are ground flat on two sides (vertically) to allow the lever to seat flush against the side of the glenoid edge. To allow vertical motion without interference between the lever and the surface, a groove is filed into the Sawbones, which is shallow at the glenoid edge where the lever is narrowed, and deeper near the pivot point where the lever bar is at full diameter.

The fixation screw is inserted parallel to the glenoid surface (as recommended by the standard) to prevent its end exiting from or approaching the surface, which could cause the humeral head to deflect the pin itself relative to the surface. The hole in the lever for attachment is angled to match the fixation screw so that the lever face seats flat against the glenoid edge, illustrated in **Figure 3-13**.

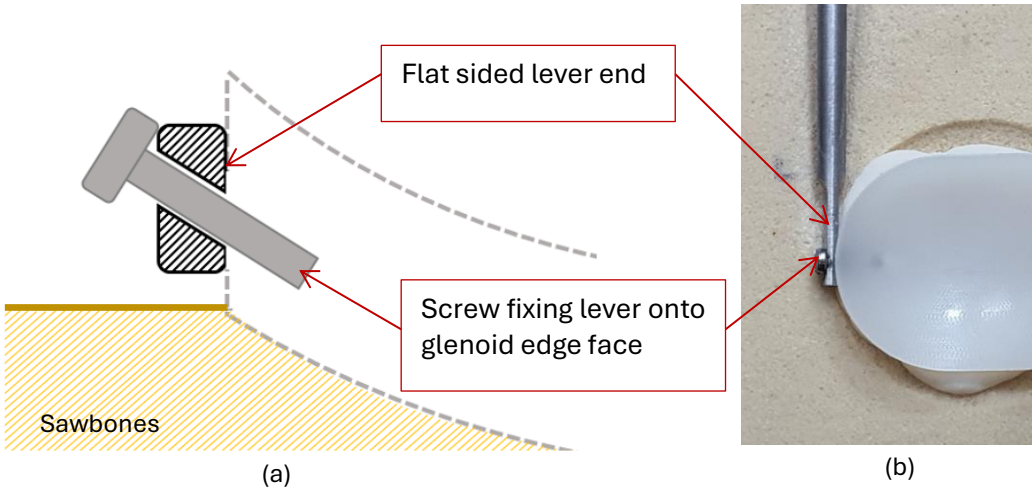

Figure 3-13 *Fixation of the lever end at the glenoid edge by an angled screw in (a) cross-section and (b) top view.*

The accuracy of the measurements taken using the lever arms relies on the fixation of the lever at the glenoid edge being firm and remaining so for the duration of a full cycle test. Using a 'dummy' glenoid machined at the UCT workshop, different combinations of fixation screw to hole size were tested. It was found that a slightly undersized, untapped, hole allowed the screw to 'self-tap' and created a strong bite into the material by the thread. However, if the hole is too undersized then the screw would need to be forced, causing the surrounding material to warp outwards and deform the surface. A final combination of a 1.4mm unthreaded hole and a 1.6mm straight screw was found to be consistently strong without causing surface deformation.

While this connection was found to be firm when the attachment was made, confirming the durability of the connection for a full 100,000 cycle test is one of the primary goals of the Rig Validation testing (to be discussed in Section 3.6).

3.4.2. Sensor Assembly

The final design uses the sensor arrangement developed in the prototype. The LVDT properties were chosen to minimise the force applied to the measuring block (to prevent both the transfer of force to the glenoid edge and to minimise stress on the lever fixation point) and to ensure that the full motion range could be measured while remaining within the goal resolution range. Unguided armature sensors were chosen for the vertical sensors, and spring-guided sensors were used for the horizontal sensors, as indicated in **Figure 3-14**

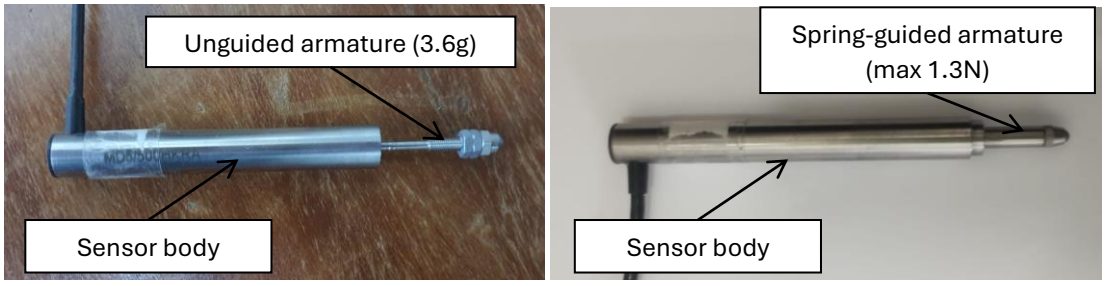

Figure 3-14 *(a) Unguided LVDT sensor and (b) spring-guided LVDT sensor used in the measuring block sensor assembly.*

Unguided armature sensors were chosen for the vertical sensors, as this allows the small light armatures to rest on the top surface of the measuring block, maintaining contact by gravity only, and applying little force (0.035N). The choice of unguided armatures for the vertical sensors had the further benefit of protecting the sensor in the case of motion of the block extreme enough to cause the sensor tip to move off the block surface. In this case, the unsupported armature would fall out of the sensor. No further readings would be taken, but a motion this extreme would be caused by the complete failure of the glenoid fixation (or the lever attachment), and the test would be stopped at this point.

The horizontal sensors need to be spring-guided to maintain surface contact. Sensors were chosen with low spring force values (1.3N at maximum deflection), to minimise force on the measuring block. The spring-guided sensors, however, do not have the inherent self-protection property. If the sensor moves off the edge it would extend to its full length and then potentially clash with the measuring block, perpendicular to the sensor axis. To eliminate possible damage to these sensors, the clamps used in the prototype design were redesigned to be sacrificial (i.e. strong in the direction of measurement, but very weak in the shear direction). This was done by

means of a deep but thin surface between the clamp mounting fixation and the sensor fixation, shown in **Figure 3-15**, which would break if any shear force was applied.

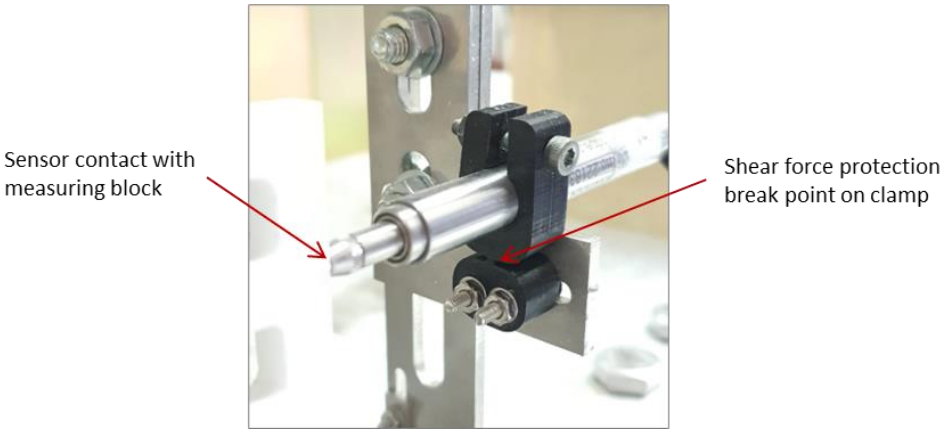

Figure 3-15 *Spring-guided horizontal LVDT sensor with sacrificial mounting clamp*

The sensors were chosen by assuming the extreme motion described in Section 3.3.2.3, with the glenoid edge at 2mm downwards, 2mm outwards, 15° inward rotation of the edge, and calculating the expected position of the sensors using the geometry of the final system. The resultant required sensor range was determined to be ±10.5mm for the vertical sensor and ±3.8mm for the horizontal sensors, by use of a SolidWorks (SolidWorks 2020, Waltham, MA, USA) motion simulation. This simulation was performed in collaboration with Tim Peach, as part of his internship work at UCT. The sensors chosen, and their properties, are listed in **Table 3-3**, below. Sensor data sheets are provided in Appendix B1.

Table 3-3 *Details and properties of the LDVT sensors used in the Sensor Assembly*

Sensor	Product code	Type	Measurement Range	Nominal Sensitivity	Contact Force
Horizontal Sensors	RDP D6/05000ARA	Spring guided	±5mm	700mV/V	0.9N at 0mm 1.3N at ±5mm
Vertical Sensors	RDP MD5/500HKRA	Unguided	±12.5mm	785mV/V	Weight of armature (3.6g)

The 6 sensors were connected to the PMX PX455 measurement cards and set up using the individual calibration data provided by the manufacturer. Signal filtering was applied by setting the PMX filer to a 2000Hz Bessel filter. A basic functionality check was performed by deflecting the sensors using an electronic micrometer, to ensure the calibration data had been correctly applied. The 6 LVDT sensor readings are recorded as part of the Glenoid Edge Motion protocol discussed in Chapter 2. These readings are then converted into glenoid edge motion, as described in the next section.

3.5. Glenoid Edge Motion Calculation

The LVDT sensor readings are converted into edge motion using the geometry of the measurement system. To perform the motion calculation, the geometry of the system is defined, and a global frame of reference is created. The motions of the measuring blocks and the sensors at their edges are then tracked within the frame of reference and converted back to edge motion. This calculation is performed individually for the LHS and RHS edges, as the senor layout is mirrored on the blocks. The geometric calculation is converted to a MATLAB algorithm, which is then validated *in-silico* by means of a SolidWorks motion simulation.

3.5.1. Physical Setup and Frames of Reference

The measuring algorithm must be applied to the physical sensor setup, which consists of two measuring blocks and two sets of sensors, which mirror each other. Due to physical space restraints, the two levers are not the same length. The measuring blocks are the same size. This section defines the geometry of the system, the names and locations of sensors, and the global frame of reference used in the calculations to follow.

The directional frame of reference is defined as shown in **Figure 3-16** below, which views the setup from above. The front of the system is chosen to be the measuring block side, with the LHS and RHS levers, blocks, and glenoid edges defined as shown. The use of LHS and RHS terminology is used rather than referring to the superior or inferior edge of the glenoid, because the glenoid can be implanted in whichever orientation is preferred.

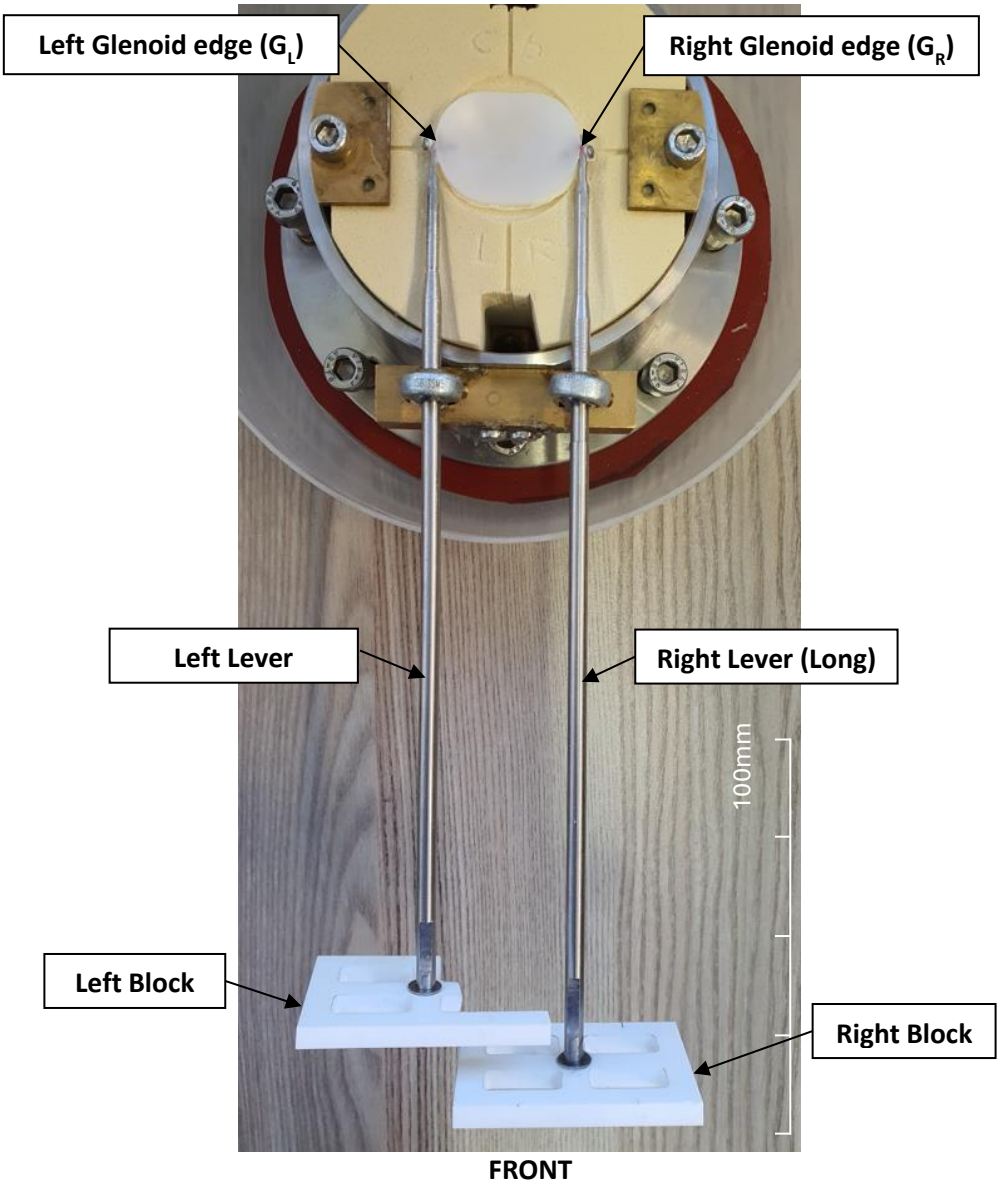

Figure 3-16 *Physical definition of lever arms and glenoid sample assembly for use in the motion calculation.*

The global directional conventions for the system are defined as illustrated in **Figure 3-17**, in which upward vertical motion (out of the surface) is positive, horizontal motion to the right is positive, and clockwise rotation is positive. This directionality is applied to both edges and blocks in the same way. It is noted for future results analysis that the chosen directionality has the effect that for horizontal and tilt motions, the LHS edge will experience positive values when the edge moves 'inwards' toward the centroid of the glenoid, whereas at the RHS a positive motion would be 'outwards', away from the centroid.

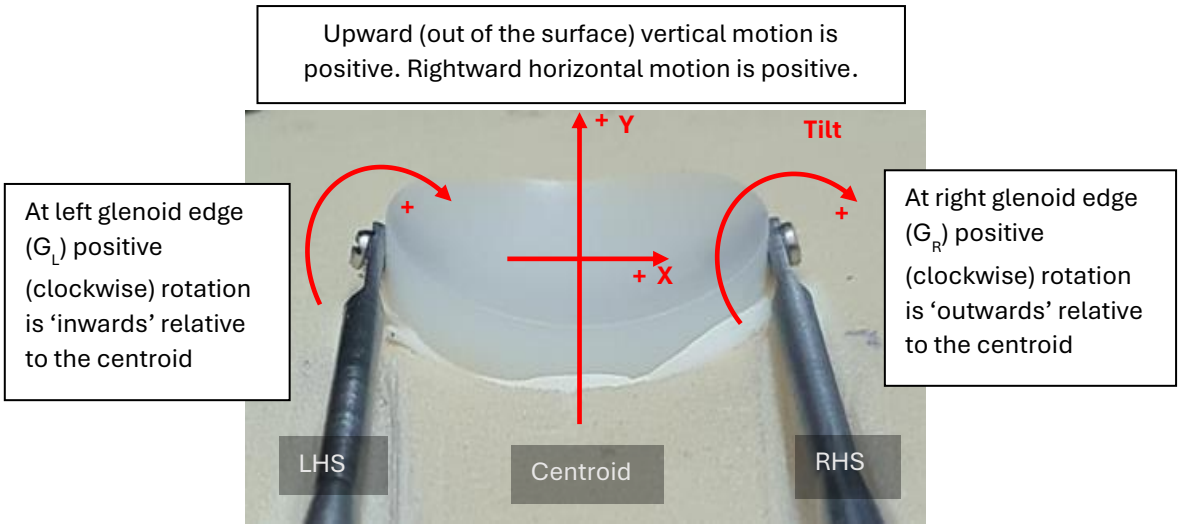

Figure 3-17 *Definition of the global co-ordinate direction conventions used in the edge motion calculation.*

The sensors are designated names based on which measuring block they are associated with and their position on the block, and are defined in **Figure 3-18.** It is noted here that horizontal sensors, S_{3L} and S_{3R}, are mirrored on opposite sides of their respective blocks.

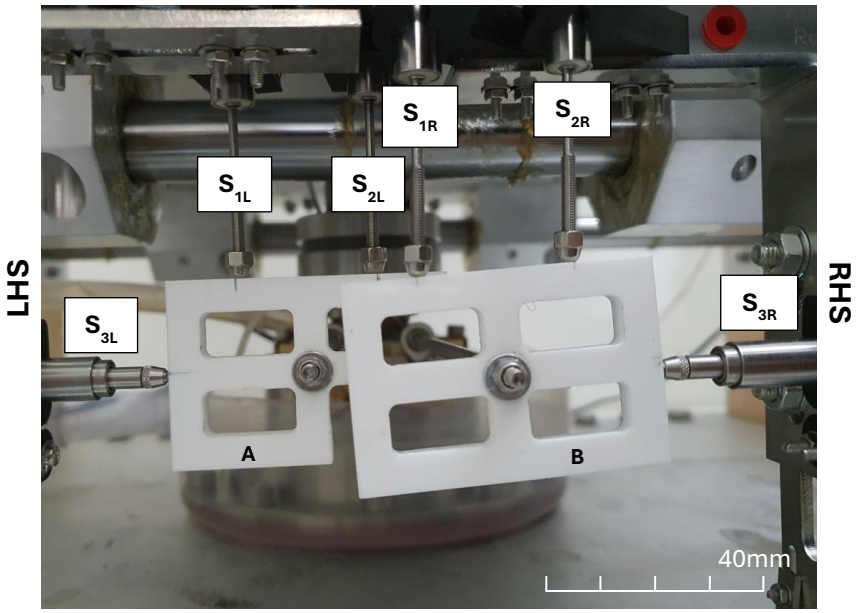

A: LHS Measuring Block
S_{1L}, S_{2L}: LHS Vertical LVDTs
S_{3L}: LHS Horizontal LVDT

B: RHS Measuring Block
S_{1R}, S_{2R}: LHS Vertical LVDTs
S_{3R}: LHS Horizontal LVDT

Figure 3-18 *Sensor assembly layout and LVDT sensor names. Four vertical (unguided) and two horizontal (spring-guided) LVDT sensors are arranged at the two measuring blocks in mirrored configurations.*

The sensor readings are at zero in the initial position of the block. Sensor extension is read by the PMX as positive deflection, and sensor compression is read as negative deflection. This requires the signs of the readings from all but S_{3L} to be inverted to be consistent with the global co-ordinate system, as illustrated in **Figure 3-19**.

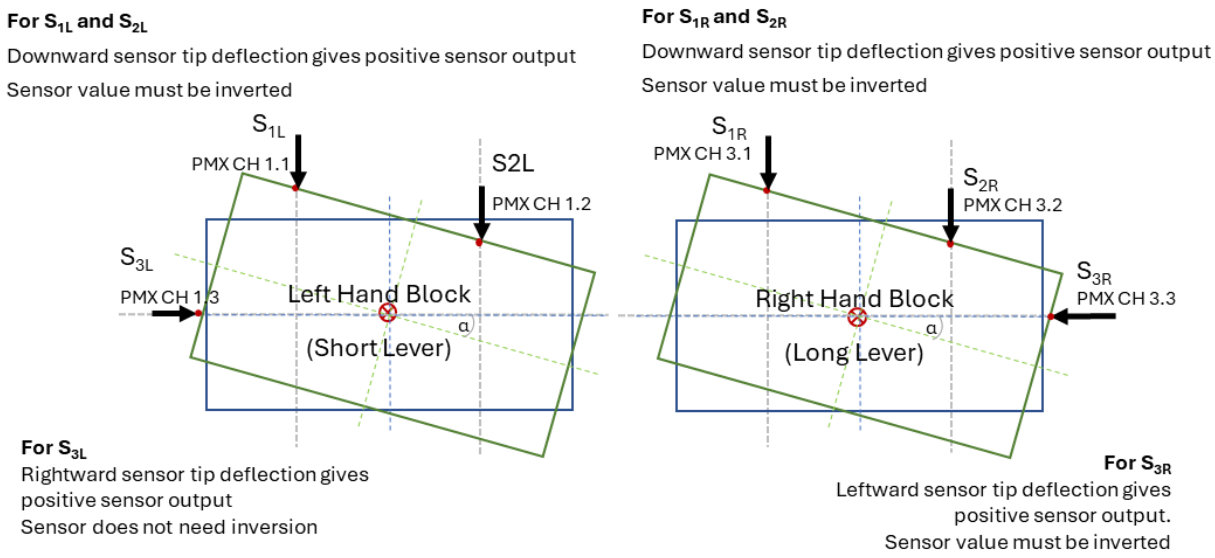

Figure 3-19 *Directionality conversions required for the six LVDT sensors used in the sensor assembly. The directionality conversions ensure that all values used in the data processing scripts conform to the chosen global co-ordinate system.*

While the same global directional conventions are used for both blocks, the edge motion calculation assumes a local origin of axes on each of the blocks, taken as the starting position of the centroid of the block (which is the end of the lever). Around this origin, the co-ordinates of each of the sensor tips are defined. These co-ordinates are known at the starting, undeflected, position of the block, based on the block's physical size, as illustrated in **Figure 3-20** and listed **Table 3-4**, where L_b is the length of the block and H_b is the height.

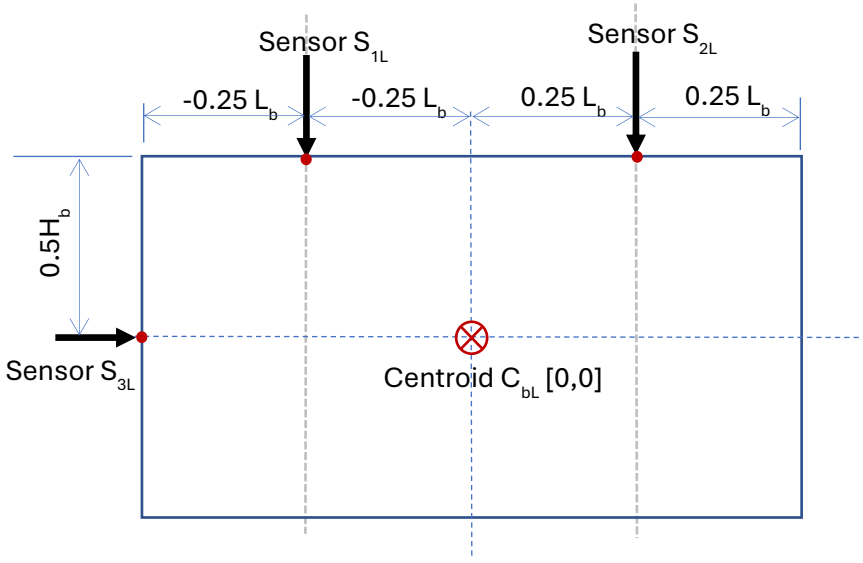

Figure 3-20 *Undeflected sensor and centroid co-ordinates of the LHS measuring block.*

As the block moves, the co-ordinates of the sensors will change in the direction of their measurement axis but remain fixed in the other direction (e.g. S_{1L} will always have an *x*-value of -0.25L_b).

Table 3-4 Co-ordinates of sensors and centroid of the LHS measuring block

Feature	Initial co-ordinates	Co-ordinates during motion	Fixed co-ordinate
Centroid of block	[0, 0]	[C_{bLx}, C_{bLy}]	none
Sensor S_{1L}	[-0.25L_b, 0.5H_b]	[-0.25L_b, S_{1Ly}]	x value
Sensor S_{2L}	[0.25L_b, 0.5H_b]	[-0.25L_b, S_{2Ly}]	x value
Sensor S_{3L}	[-0.5L_b,0]	[S3L_x, 0]	y value

The changing co-ordinate value is determined by the initial position to which the measured sensor values are added. The measured values at each sensor are zeroed at the start of the test. Accounting for initial value zeroing, directionality of the sensor reading, and block geometry, the sensor outputs are converted to sensor position in the global coordinates, relative to their block centroid, as follows for the LHS block:

$$S_{1Ly} = -(S_{1Ly}\_measured - S_{1Ly}\_measured_0) + 0.5H_b \quad [3.1]$$

$$S_{2Ly} = -(S_{2Ly}\_measured - S_{2Ly}\_measured_0) + 0.5H_b \quad [3.2]$$

$$S_{3Lx} = S_{3Lx}\_measured - S_{3Lx}\_measured_0 - 0.5L_b \quad [3.3]$$

In the same way, but with the horizontal sensor location changed, the initial and motion-induced co-ordinates of the RHS block centroid and sensors are given in **Figure 3-21** and **Table 3-5**.

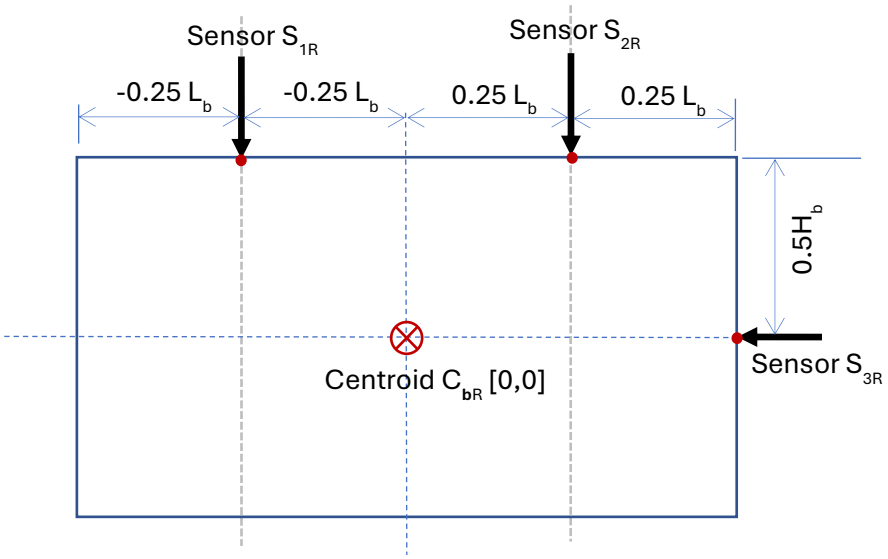

Figure 3-21 Undeflected sensor and centroid co-ordinates of the RHS measuring block

Table 3-5 Co-ordinates of sensors and centroid of the RHS measuring block

Feature	Initial co-ordinates	Co-ordinates during motion	Fixed co-ordinate
Centroid of block	[0, 0]	[C_{bLx}, C_{bLy}]	none
Sensor S_{1R}	[-0.25L_b, 0.5H_b]	[-0.25L_b, S_{1Ry}]	x value
Sensor S_{2R}	[0.25L_b, 0.5H_b]	[-0.25L_b, S_{2Ry}]	x value
Sensor S_{3R}	[0.5L_b,0]	[S_{3Rx}, 0]	y value

Again, sensor outputs are converted to global coordinates relative to their block centroid:

$$S_{1Ry} = -(S_{1Ry}\_measured - S_{1Ry}\_measured_0) + 0.5H_b \quad [3.4]$$

$$S_{2Ry} = -(S_{2Ry}\_measured - S_{2Ry}\_measured_0) + 0.5H_b \quad [3.5]$$

$$S_{3Rx} = -(S_{3Rx}\_measured - S_{3Rx}\_measured_0) + 0.5L_b \quad [3.6]$$

The defined sensor locations can now be used to begin the glenoid edge motion calculation.

3.5.2. Motion Calculation Method

The glenoid edge motion calculation method was developed during this research in collaboration with Tim Peach, as part of his internship under the supervision of the author. The glenoid edge motion will be calculated by first tracking the motion of the centroid of the block, based on changes in the sensor locations, and then converting the block motion to glenoid edge motion.

The tracking of the block motion is done in five stages:

- First by calculating the tilt using the vertical sensor values to determine the gradient of the top line of the block.
- This gradient is then used to define the two straight lines formed by the top and the side of the block on which the horizontal sensor rests.
- The intersection of these lines allows the co-ordinates of the LHS top corner of the block to be found.
- Using these co-ordinates, the known size and tilt of the block, and basic trigonometry, the co-ordinates of the bottom RHS corner are found. This allows the straight line along the diagonal of the block to be defined.
- The midpoint of the diagonal is the centroid of the block.

The motion of the block is then translated back to glenoid edge motion using the lever length and pivot location. This process is described in detail here for the LHS. The calculation for the RHS

follows the same method, with adjustments to account for the location of the horizontal sensor, and is provided in Appendix B2.

For the LHS, **Figure 3-22** shows the starting position of the block in blue (centroid at [0, 0] and no tilt) and a deflected position for an unspecified motion in all three degrees of freedom in green.

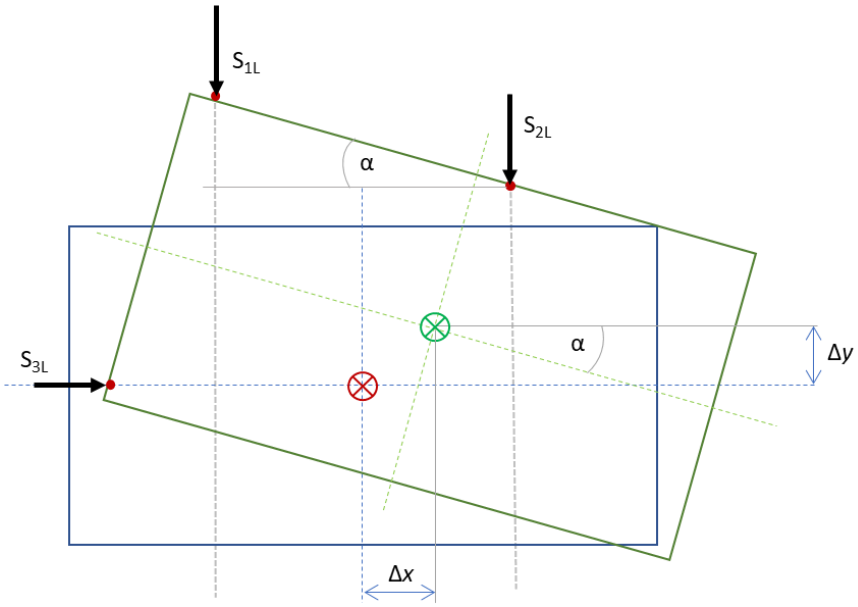

Figure 3-22 *Initial and deflected position of the LHS measuring block for a motion of unknown magnitude, where the block centroid has moved by Δx in the horizontal direction and Δy in the vertical direction, and the block has rotated α°*

As the distance between sensors S_{1L} and S_{2L} is fixed, and the edge of the measuring block is always a straight line, the difference between the sensor readings allows us to calculate the tilt of the block. The gradient of the line formed by the top surface of the block is given by:

$$m_1 = -\left[\frac{S_{1Ly} - S_{2Ly}}{0.5L_b}\right] = -\tan\alpha = \tan(-\alpha) \qquad [3.7]$$

From which we find the degree of clockwise rotation of the block:

$$\alpha = -\tan^{-1}\left(\frac{S_{1Ly} - S_{2Ly}}{0.5L_b}\right) \qquad [3.8]$$

Next, we use the gradient m_1 to define the equation for the top line of the block:

$$y = m_1 x + C_1 \qquad [3.9]$$

Where m_1 is known and the co-ordinates at the sensors $S_{1L} = [-0.25L_b, S_{1Ly}]$ and $S_{2L} = [-0.25L_b, S_{2Ly}]$ are either constants or measured, so are also known.

Using the co-ordinates of sensor S_{1L}:

$$S_{1Ly} = m_1(-0.25L_b) + C_1$$

$$\text{So } C_1 = S_{1Ly} - m_1(-0.25L_b) \quad [3.10]$$

We now define the equation of the straight line formed by the side of the block. The gradient of this line is the inverse of the gradient of the top of the block, since these are rigidly perpendicular to each other, so:

$$m_2 = -\frac{1}{m_1} \quad [3.11]$$

and

$$y = m_2 x + C_2 \quad [3.12]$$

Using the co-ordinates of sensor S_{3L} [S_{3Lx}, 0] we can solve for C_2

$$C_2 = 0 - m_2 S_{3Lx}$$

The point where these two straight lines intersect is the location of the top LHS corner of the block (Corner 1 in **Figure 3-23**):

$$m_1 x_{corner1} + C_1 = m_2 x_{corner1} + C_2 \quad [3.13]$$

$$x_{corner1} = \frac{C_2 - C_1}{m_1 - m_2} \quad [3.14]$$

$$y_{corner1} = m_1 x_{corner1} + C_1 \quad [3.15]$$

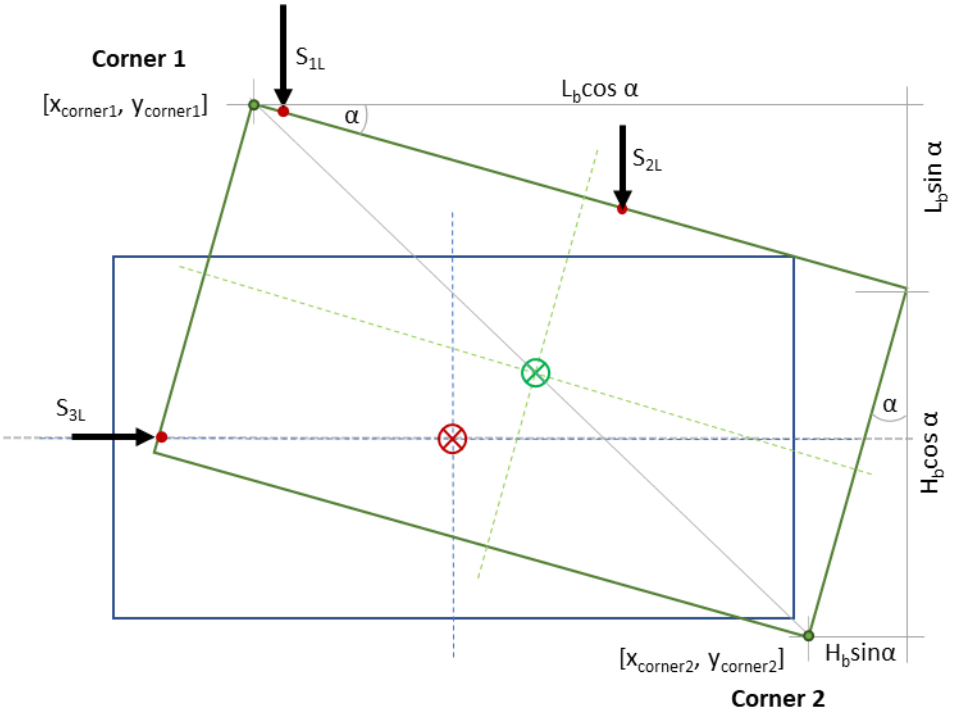

Figure 3-23 *Definition of the diagonal line from Corner 1 to Corner 2 of the LHS measuring block, used to determine the centroid location.*

Using known geometry and trigonometry of the block, the co-ordinates of the diagonally opposite corner (Corner 2) can be calculated using the distances indicated in **Figure 3-23**:

$$x_{corner2} = x_{corner1} + L_b \cos\alpha - H_b \sin\alpha \quad [3.16]$$

$$y_{corner2} = y_{corner1} - H_b \cos\alpha - L_b \sin\alpha \quad [3.17]$$

The centre point of the diagonal line between the two corners is the location of the centroid of the block.

$$C_{BLx} = \frac{x_{corner1}+x_{corner2}}{2} \quad [3.18]$$

$$C_{BLy} = \frac{y_{corner1}+y_{corner2}}{2} \quad [3.19]$$

Since the original position of the centroid was [0,0], the x and y co-ordinate values are the horizontal and vertical deflection of the end of the lever arm. As mentioned, the calculation for the RHS block follows the same method, but with adjustments to account for the different horizontal sensor position, and is provided in Appendix B2.

With the tilt and the new position of the centroid (front end of the lever) known, the position of the glenoid end of the lever can be calculated. The centroid motion is translated back to motion at the glenoid edge using the ratio of lever arm length on either side of the pivot point for each lever, as illustrated in **Figure 3-24**.

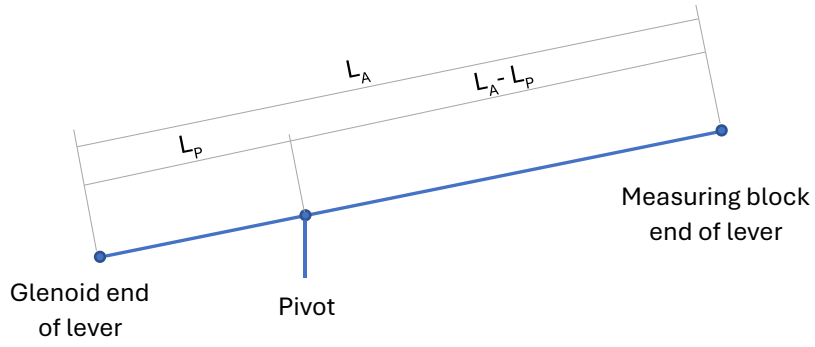

Figure 3-24 *Definition of lever arm lengths with respect to the pivot point location.*

The lever amplifies the deflection at the glenoid by the ratio of the lever lengths before and after the pivot and inverts the motion direction. For a lever arm total length L_A, and a pivot point distance L_P from the glenoid edge, the horizontal motion is given by:

$$\frac{\Delta x_{glenoid}}{\Delta x_{centroid}} = -\frac{L_P}{L_A - L_P}$$

$$\Delta x_{glenoid} = -\Delta x_{centroid} \frac{L_P}{L_A - L_P} = -C_{Bx} \frac{L_P}{L_A - L_P} \quad [3.20]$$

And similarly for the vertical direction:

$$\Delta y_{glenoid} = -C_{By} \frac{L_P}{L_A - L_P} \quad [3.21]$$

Since the lever arms are of different lengths, the values in the calculation are adjusted according to the lever in question, and the *x* and *y* deflections at the edges are determined. The tilt of the edge is not changed by the lever pivot, as it occurs around the lever axis, so is taken directly from the calculation in Equation 3.8.

This method allows the calculation of the three edge motions for every point at which sensor measurements are logged. To perform this calculation for the full length of the cyclic testing, a MATLAB script was developed.

3.5.3. Data Processing

An overview of the MATLAB script used to calculate the edge motion (MotionCalculation.m) program is provided here, illustrated in **Figure 3-25**. The full code is provided in Appendix B2.

The code calls in the data logged by the Glenoid Edge Motion protocol described in Chapter 2 and defines vectors from the variables logged. A for-loop runs for the length of the logged data vector (for a full 100,000 cycle test this is in the order of 900,000 data points per vector). In each step of the for-loop, each sensor value is converted to the measuring block co-ordinate system by subtracting the initial sensor value, inverting the sign where necessary, and adding the appropriate starting location (as described in Equations 3.1 to 3.3).

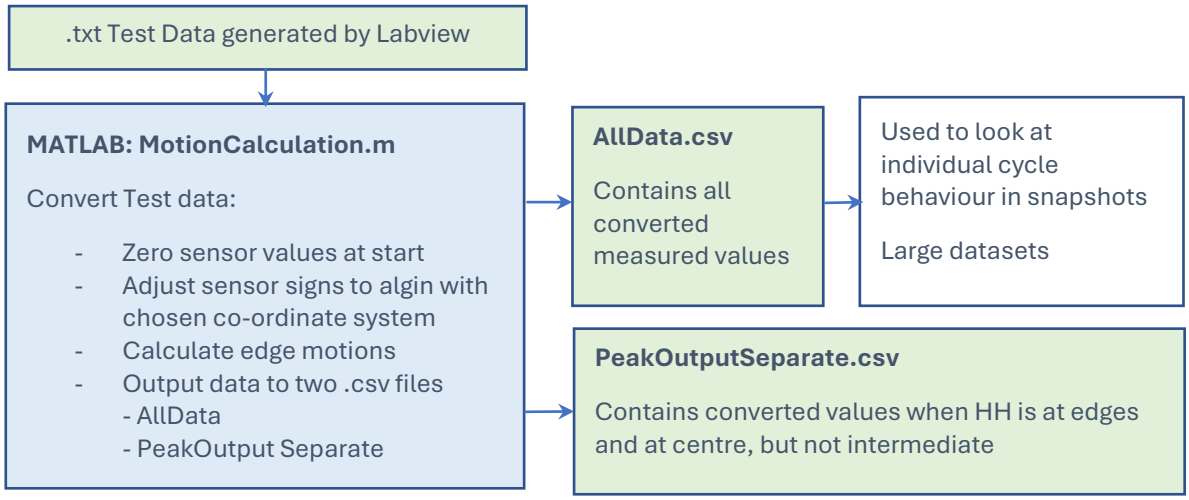

Figure 3-25 *Overview of the MATLAB script used to convert the sensor outputs to glenoid edge motions.*

The program then calculates the glenoid edge motion based on the method described above and logs these values to the output data vectors. Each of these vectors contains the motions at all logged positions on the glenoid. As it is desirable to be able to view the deflections as individual vectors for different positions of the humeral head, particularly the edges, the loop is also used to define separate vectors for motions when the glenoid is at the edges and at the centroid of the glenoid.

Once the loop is completed, the algorithm writes the data to two spreadsheet files, one with the complete data vectors, and another with the edge and centroid motions. The code also automatically plots all edge motion values, and the logged normal contact force for the duration of the test.

3.5.4. Limitations of the Edge Motion Calculation

The edge motion calculation has some limitations, based on physical aspects of the system and assumptions made. Firstly, the vertical and horizontal motions are assumed to occur as straight lines at the measuring block and glenoid edge, when in reality they are arcs. As the angle of motion is small (<15°) the difference between the arc length and a straight line is neglected.

Secondly, the separation of the planar and tilt motions assumes the glenoid edge pivots around its midline, where the lever is attached. The actual pivot point for the tilting motion is unknown. This means the vertical and horizontal values likely include some portion of motion induced by the change in angle, and hence the deflection values should be viewed as new positional values of the centre of the glenoid edge, with associated side face angle.

Finally, the algorithm assumes the sensor point of contact on the block surface to be infinitely small. In reality the sensors have rounded tips, with a radius of approximately 3mm. The use of

finer points on the sensors was avoided to prevent the sensor from digging into or catching on the surface in a way that might prevent the sensor from sliding freely as the surface moved. The effect of this real radius on the deflection measured is neglected.

3.5.5. *In-silico* Validation of Algorithm

Before using the MATLAB algorithm to calculate experimentally measured edge motions, both the calculation method and its implementation into code must be validated. This was done *in-silico* using SolidWorks motion simulation. The simulation contains the sample assembly and sensors, constrained relative to each other as they would be in the physical setup, shown in **Figure 3-26**.

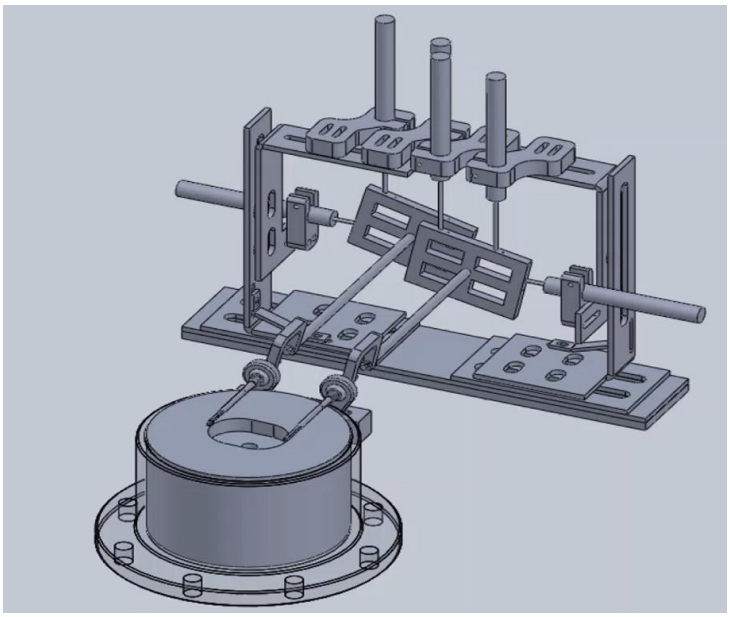

Figure 3-26 *SolidWorks model assembly used for motion simulation. The glenoid edge face was simulated as a point, that was moved through two known motions (each with vertical, horizontal, and tilt components) to simulate an expected tensile and an expected compressive load response. The motion of the tips of each of the 6 simulated sensors in response to the applied motion was tracked.*

In the simulation, the lever pin-hole was assembled to the glenoid edge as a point contact, and the RHS glenoid edge was moved in two separate compound motions, one to simulate compression (downwards and outwards with outward tilt) and the other to simulate tension (upwards and inwards with inward tilt). The directional component motions for each of the compound motions used are listed in **Table 3-6** (in the measurement system frame of reference).

Table 3-6 Compound motions applied to the RHS, simulated glenoid edge in the SolidWorks motion simulation

Overall Motion	Applied Component Motions		
	Vertical (y)	Horizontal (x)	Rotation (α)
Compression	-2.5mm	1mm	5°
Tension	2.5mm	-1mm	-5°

The motions of the sensor tips were tracked during the simulated edge motions and recorded. These tracked sensor motions were then used as the input to the analytical algorithm, and the calculated results were compared to the original simulated edge motion. The results of the comparisons for the tensile and compressive motions are given in **Figure 3-27** and **Figure 3-28** respectively.

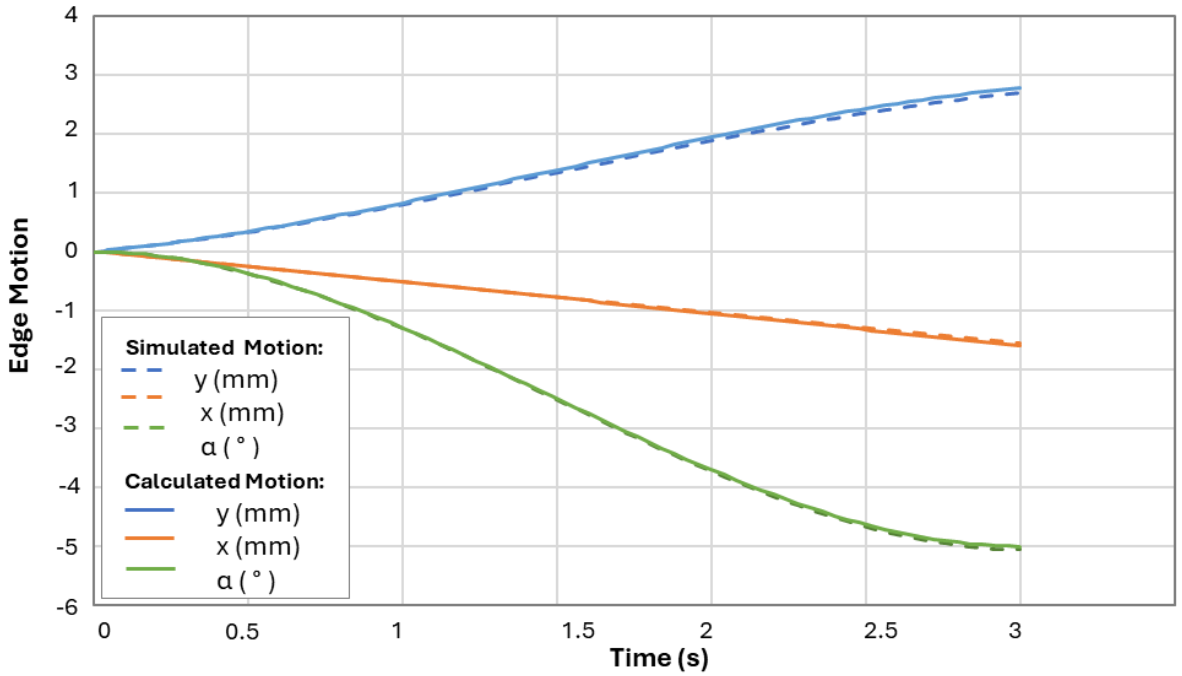

Figure 3-27 Comparison of the simulated and calculated motion of the RHS glenoid edge in tension. The simulated motion of 2.5mm in the vertical, -1mm in the horizontal, and -5° tilt is used as the input to the SolidWorks motion simulation. The simulated sensor tip motions caused by the input edge motion are used as the input to the Motion Calculation script, from which the calculated edge motions are obtained.

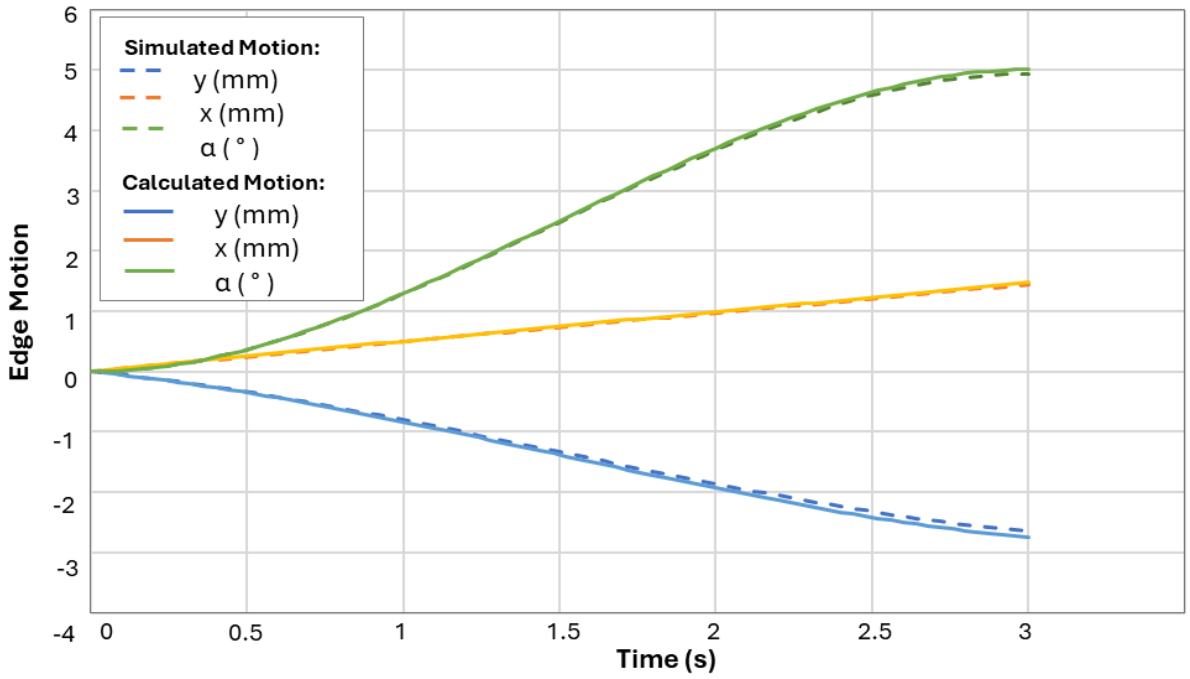

Figure 3-28 *Comparison of the simulated and calculated motion of the RHS glenoid edge in compression. The simulated motion of -2.5mm in the vertical, 1mm in the horizontal, and 5° tilt is used as the input to the SolidWorks motion simulation. The simulated sensor tip motions caused by the input edge motion are used as the input to the Motion Calculation script, from which the calculated edge motions are obtained.*

The calculated and simulated edge motions followed similar trends but with a slight discrepancy in the values. The largest discrepancy was 0.1mm in the vertical (*y*) direction, towards the end of the compressive motion, representing an approximately 1.5% difference between the simulated and calculated values.

The discrepancies are attributed to a combination of the limitations to the accuracy of the SolidWorks tracking of the sensor tip, as well as the effect of the physical radius of the sensor. As mentioned in the limitations (Section 3.5.4), the MATLAB code does not account for the radius of the sensor tip, while the SolidWorks simulation used sensor models with tip radii representative of the real sensor geometry.

A basic error analysis was performed to quantify the maximum expected systematic measurement errors that could occur in the system. In this analysis the systematic errors considered were those resulting from by sensor calibration uncertainty, linearity errors, or drift, as well as from geometrical characteristics of the measurement system, including the effect of the sensor tip radius and the arcing motion of the lever arm on the glenoid edge motion calculation. The combined effect the of the errors at the sensors was then converted back to glenoid edge motion, to predict the maximum systematic error that can occur in the glenoid edge

motions. The details of this analysis are provided in Appendix B2.3. From this analysis it was found that the maximum systematic error that could be induced at the glenoid edge by the errors on the measurement for the expected range of data is 0.03μm in the x-direction, -20μm in the y-direction and 0.07° of rotation, at a glenoid motion of 1.5mm horizontal, -2.8mm vertical and 6.5° of rotation.

Overall, the simulation showed that the calculation method and the MATLAB implementation are valid and can now be used to evaluate the experimental glenoid edge motions in the augmented rig validation testing.

3.6. Augmented DGL Test Rig Validation Testing

The augmented rig validation study was performed to functionally validate the glenoid edge motion measurement system, and to complete the function validation of the base test rig for full-length tests, by performing the augmented DGL test on a selection of glenoid components.

The cost of new glenoid components prevented their use in this phase of the testing, so a selection of expired components was used. The components available were all of the same design (DePuy Global Advantage) but were of various sizes. The humeral head component used for this test stage was a Ø44mm head (DePuy Global Advantage) and was used for all glenoid sizes. Further, for cost-saving, recently expired bone cement was used.

The data from the rig validation study is therefore used only to evaluate the functionality of the equipment and the edge motion measurement system. While basic trends in the edge motion, such as the expected directions of each component motion during tension or compression will be checked to ensure the results are realistic, no conclusions regarding edge motion magnitudes, cycle-dependent changes, or fixation survivability are drawn at this stage.

3.6.1. Aims

The augmented test rig validation testing aimed to ensure that the full DGL protocol could be reliably performed, and the required data were captured by the test setup. The test protocol, therefore, followed the DGL methodology of first determining the P90 distance, and then completing full-length (100,000 cycle) cyclic loading tests. Further, the sensor functionality was checked by confirming that the measured values produce reasonable edge motion results, i.e. the results should be within the range set in the design requirements and have directionality that is physically explainable for the given loading condition (e.g. a compressive load should produce a downward vertical deflection).

In the test rig design discussion (Chapter 2), two checks to be performed in the rig validation testing were identified. Firstly, the normal contact force for the full tests should not vary by more than 10% at the edges. Secondly, the surface of the glenoid should be checked for any creep-related surface damage due to the endpoint pauses of the humeral head. These checks will therefore also be performed as part of this rig validation testing.

In summary, the following objectives were set:

- The test rig must run for 100,000 cycles without any mechanical malfunction.
- All required data (as specified in the Glenoid Edge Moton protocol) must be logged by the system.
- The lever arms must remain firmly fixed to the glenoid edge for the duration of the test.
- The sensors remain in contact with the measuring blocks for the duration of the test.
- The sensors must output reasonable results for the load applied (with respect to directionality).
- The measured normal contact force must remain within the design requirements set during the test rig design.
- The glenoid surface should be inspected for creep-related surface damage.

3.6.2. Methodology

Testing was divided into the estimation of the P90 distance for the range of samples, and cyclic testing. The available samples were prepared for testing by implantation into Sawbones and allocated to the different stages of the rig validation testing as shown in **Table 3-7**. The rationale for the allocation of the samples is described in the test stage descriptions to follow.

Table 3-7 *Expired glenoid samples available for rig validation testing*

Sample size	Qty	Use
40	2	P90 estimate (1), Full Length Cyclic Testing (1)
44	2	Full Length Cyclic Testing
48	2	Full Length Cyclic Testing
52	1	P90 estimate
56	1	P90 Estimate

3.6.2.1. Sample Preparation

The test samples were implanted into the Sawbones bases by a fellowship-trained shoulder surgeon at the Orthopaedic Surgery Department of Groote Schuur Hospital, Cape Town. The implantation was performed using a training set of the surgical tools associated with the glenoid design (DePuy Global Advantage). The first step of the implantation is the drilling of the central peg hole (using the guide hole placed during the manufacture of the sawbones base). The central peg hole is then used as a guide for the reaming of the surface to match the back curvature of the glenoid samples, and the remaining peg holes. The cement is mixed and placed into the peg holes, the glenoid is inserted and held in place with firm pressure until the cement has set. All the sawbones bases were prepared ahead of time, to allow multiple glenoid samples to be implanted from a single batch of cement. Two packets of recently expired cement were used for the 8 glenoids used in the rig validation testing, as well as 2 others that were used during preliminary design and prototype testing.

3.6.2.2. Subluxation Distance Estimate

In the standard test, each glenoid size used would have its subluxation distance determined by performing the P90 test as described in Section 2.2.2, using (and destroying) two samples of the given size. Limitations in available samples prevented this from being done for all the glenoid sizes used in the rig validation testing. Instead, the subluxation distance was approximated by testing 3 individual samples, each of a different size, and using the results to estimate the subluxation distance for other sizes.

The data for the size 52mm glenoid, measured in the P90 test method validation (Section 2.6.1), were used as one sample. In addition to this, the P90 test was performed on one size 40mm sample and one size 56mm sample. These samples covered the minimum and maximum of the sizes available. The two data points generated for each sample (one in each direction) were then plotted against glenoid size, and a linear extrapolation was performed to estimate the subluxation distance for the intermediate glenoid sizes. From these distances, the P90 stroke amplitude was then calculated.

This method is a rough approximation of the subluxation distance, but as the data generated will only be used to evaluate test rig functionality, and not glenoid edge motion or loosening, the approximation is deemed acceptable for the current purpose.

3.6.2.3. Cyclic Testing

The rig validation cyclic testing consisted of five full-length tests, performed on the samples listed in Table 3-7. As per the standard, the tests each consisted of 10 conditioning cycles,

followed by 100,000 load cycles. The cyclic testing comprises five main stages, namely the sample assembly setup, the test rig setup, the conditioning test, the full cycle test, and finally disassembly and maintenance. The procedure for each of these stages is as follows:

1. **Sample Assembly Setup**

   Before the sample is mounted into the housing the glenoid in the Sawbones is checked for excess cement at the lever attachment point, and if present this must be filed away. The grooves for lever clearance of the surface are then filed (positioned based on the location of the glenoid edges, which varies according to glenoid size), and the holes in the glenoid edges are drilled using a Dremel tool. The Sawbones base is then mounted into the sample housing. The levers are attached by first adjusting the pivot mounting positions so that the levers are perpendicular to the glenoid major axis and parallel to the sawbones surface (again dependent on the glenoid size). This is done before the fixation screw is inserted, by holding the lever end in position, to prevent the screw fixation from being disturbed by the pivot adjustment. Once the pivot is properly located, the lever fixation screw is inserted.

2. **Test Setup**

   The sample assembly is mounted to the test rig base plate and bolted in place, the humeral head lowered onto the glenoid while the inner weight housing is empty, and the water bath inlet and outlet pipes are connected. The sensors are mounted around their respective measuring blocks, with the position of the mounting clamps adjusted so that the sensor tips align with the etched location markers on the blocks.

   The PMX interface is then opened, and are weights loaded until the load cell reads 750N. The sensor distance from the blocks is adjusted so that each sensor reading starts within 0.2mm of its zero point, to ensure the full sensor range is available. (This value will be zeroed during data processing).

3. **Conditioning**

   The input parameters for the conditioning test (10 cycles, 500mm/min, Stroke according to the P90 distance for the given glenoid size) are input into the LabView Glenoid Edge Motion protocol. The test is run, and the data generated are saved to a Conditioning Run text file. The test ends with the humeral head at the centroid, allowing the main cyclic testing to begin without any adjustments to the system.

4. **Cyclic Testing**

   The humeral head velocity and cycle number are changed from the conditioning values to the main test values (100,000 cycles, 1000mm/min), while all other parameters remain the same, and the cyclic test is started. The test runs for approximately 100h, and the data is saved to a Full Test text file. During the test, the water bath is refilled (as discussed in Chapter 3) twice a day.

5. **Shut-Down, Disassembly, and Maintenance**

   Once the cyclic test is complete, the data files are immediately backed up to cloud storage. The rig is shut down and the sensors, weights, and sample assembly are removed. The sample assembly is examined to note whether the lever attachment is still strong, whether the glenoid fixation has failed, and any other damage or anomalies in the system.

   The levers and Sawbones block are disassembled from the sample housing and all reusable parts are cleaned and checked for damage. General rig maintenance is also performed, including draining and cleaning the water bath, replacing the filter if it has become discoloured, and performing bearing turnover cycles (cycles that run the full stroke of the linear actuator) to maintain good bearing health.

The rig validation testing provided an opportunity for troubleshooting, particularly for the edge motion measurement system. As the testing of the 5 samples proceeded, adjustments to the design were made and tested on the next sample. These adjustments are described in the results, for the sample at which they were implemented.

3.6.3. Results

The results for each of the stages of the testing are presented here, and design changes made during the testing are noted. The results and changes are interpreted and discussed in Section 3.7.3, as part of the overall chapter discussions.

3.6.3.1. Sample Preparation

During the implantation of the glenoids, the cement setting was found to be generally poor. The cement set un-evenly behind the glenoid face, sometimes forming ‘steps’ where the back face of the glenoid was seated in cement for a portion of its surface, but ‘floating’ where the cement

ended. The glenoids also did not all set evenly, with one edge raised higher than the other due to excess cement.

The initial Sawbones base, used in this testing, had a central guide hole for alignment of the centre peg of the glenoid but did not have the cross-hair guide marks for alignment of the other pegs. The location of the superior peg hole had to be marked out during the implantation to ensure the sample was implanted in the correct direction. Machined cross-hair guides were added for future implantations. However, all glenoids were strongly fixed in the Sawbones, and could be used for the rig functional validation.

3.6.3.2. Subluxation Distance Estimate

The results of the P90 test performed on three glenoid samples (sizes 40, 52, 56mm) are shown in **Figure 3-29**.

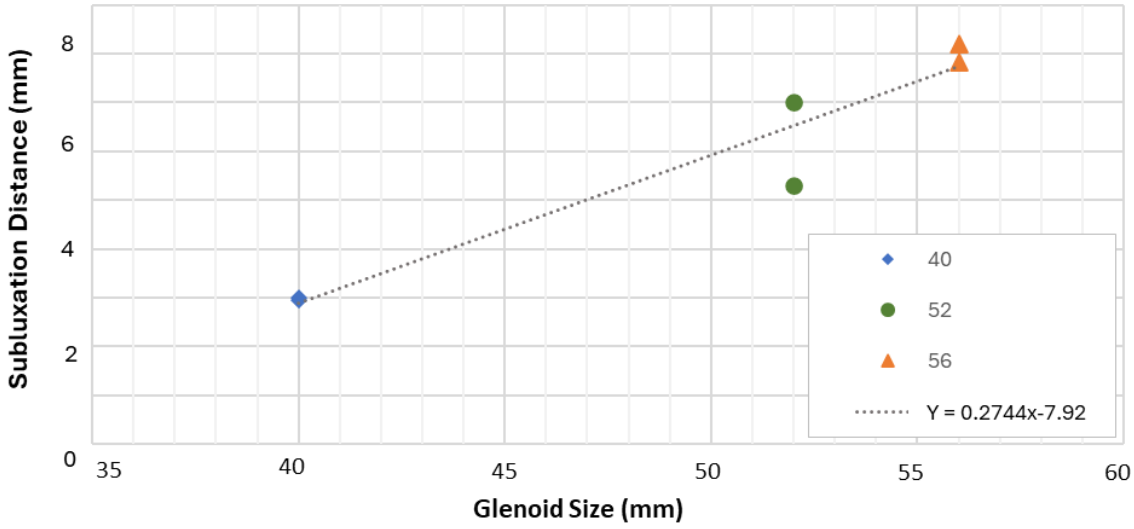

Figure 3-29 *Subluxation distance measurements for three expired glenoid samples tested according to the P90 protocol, and the resultant linear extrapolation formula to determine subluxation distances of intermediate sizes (not tested)*

The subluxation distances were taken as the average values for the three measured sizes. For the intermediate sized glenoid samples, the subluxation distances were estimated using the limited data by linear extrapolation, as listed in **Table 3-8**.

Table 3-8 *Measured and estimated subluxation distances, using linear interpolation for intermediate glenoid sizes.*

Glenoid Size	Subluxation Distance (mm)		P90 (90% of Subluxation distance, mm)
40	3.1	Measured	2.8
44	4.2	Estimated	3.8
48	5.3	Estimated	4.8
52	6.2	Measured	5.6
56	7.8	Measured	7.0

3.6.3.3. Cyclic Testing

The cyclic test results are presented by first discussing each of the five samples tested, noting any failures, glenoid damage, or any other observations, and finally describing any design modifications made. The glenoid edge motion results of one sample (Sample 3) are then presented to confirm the sensor functionality. These results are presented for the full cyclic test to observe overall motion, and as a 'snapshot' of 5 cycles, to observe motions within the cycles. The normal force measurement for this test is also presented.

All tests ran for the full 100,000 cycle count without mechanical failure of the rig, and all data was logged as required. None of the tests experienced edge motion severe enough to cause the sensors to lose contact with the measuring blocks, or exceed their measurement range.

Observations and design adjustments made for the 5 samples are as follows:

Sample 1 (Size 40mm)

The first sample tested was a size 40mm, shown in

Figure 3-30, before and after the test. This sample had a 'step' in the cement that left the RHS front edge unsupported.

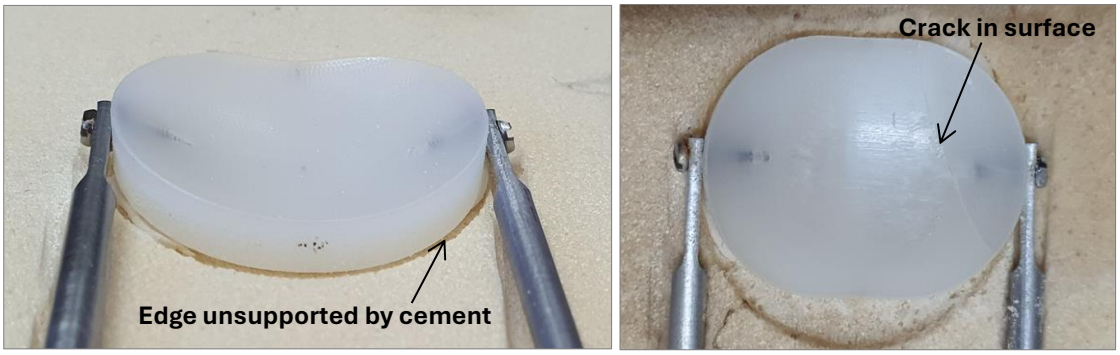

a) Before test b) After test

Figure 3-30 *Rig validation test Sample 1 (size 40mm) before (a) and after (b) testing. This sample had uneven cement leading to an unsupported RHS edge, resulting in a crack through the glenoid surface at the RHS.*

Inspection of the glenoid after testing showed that the sample had cracked near the RHS edge slightly below the pin insertion depth. Further, the glenoid fixation had loosened enough that the component could be 'rocked' slightly by hand after the test, but not so much that it could be pulled out of the Sawbones.

Both levers were still attached at the end of the test, but some slack was noted in the lever fixation against the glenoid edge. Inspection of the lever fixation screws showed that the thread still had grip on the fixation holes, but the screws had begun to turn loose, by an estimated ¾ turn on the LHS and ¼ turn on RHS. To combat this in future tests, it was decided to add an adhesive to the screws to prevent loosening of this type.

Sample 2 (Size 44mm)

The second sample tested was a size 44mm, shown in **Figure 3-31**. This sample had excess cement around the edges, but no noticeable unsupported regions. For this test, a waterproof adhesive was added to the lever screw thread before attachment, as well as to the screw head to form a 'cap' after fixation.

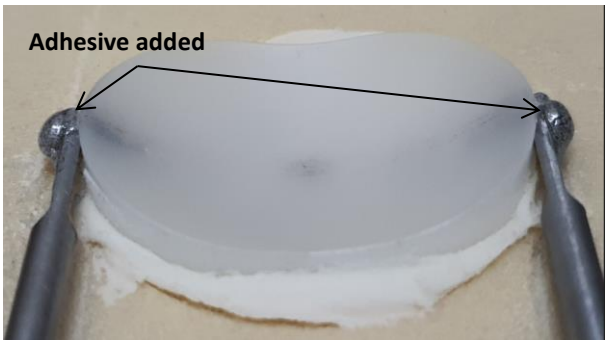

Figure 3-31 *Rig validation test Sample 2 (size 44mm) which has adhesive added to the lever fixation screws to prevent these from turning loose during cyclic testing.*

The glenoid fixation was still firm after the test (i.e. it could not be rocked by hand), and no damage to the component was apparent. Inspection of the levers found the RHS lever to be firm, but the LHS still had slight slack. Both adhesive caps were intact and no noticeable turning of the screws had occurred. A possible cause considered for the slack on the lever was the angled contact of the screw head against the vertical face of the lever end. To solve this, a washer was added between the screw head and the lever.

Sample 3 (Size 44mm)

The third sample tested was a second size 44mm, shown in **Figure 3-32**, with the new washers added. This sample had uneven cementing causing an unsupported section at the LHS edge. The added washers were small sections of polypropylene pipe (ID 1.8mm, OD 3mm), cut by hand at

an angle of approximately 30° to match the pin-to-lever face angle, and placed between the fixation screw head and the outside face of lever end. The screws were again coated with adhesive before attachment, and the head of the screw and washer were coated in an adhesive cap.

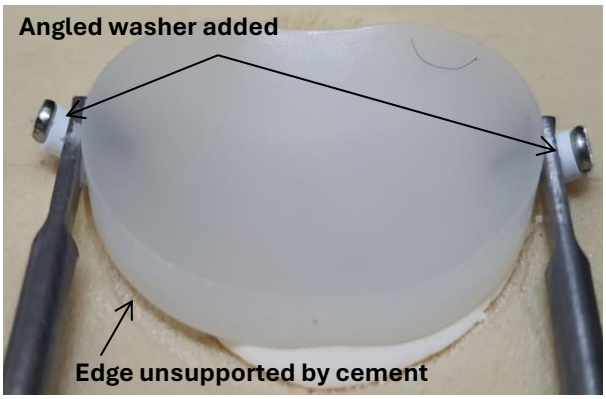

Figure 3-32 *Rig validation test Sample 3 (size 44mm) with angled polypropylene washers at the lever fixation screws (before adhesive is added). This sample had uneven cement leading to the LHS edge being unsupported.*

Inspection of the glenoid sample after the test showed loosening of the fixation (could be rocked by hand), but like Sample 1, the component was still held strongly enough that it could not be removed from the Sawbones by hand. No surface or other damage to the glenoid was noted. The inspection of the levers found the fixation of both levers to be firm. The glue caps and washers were intact and no noticeable turning of the screws had occurred. No further design adjustments were made at this stage.

Sample 4 (Size 48mm)

The fourth sample was a size 48mm, shown in **Figure 3-33**. This sample had uneven cement resulting in a large unsupported region (approximately 1/4 of the glenoid) at the RHS edge.

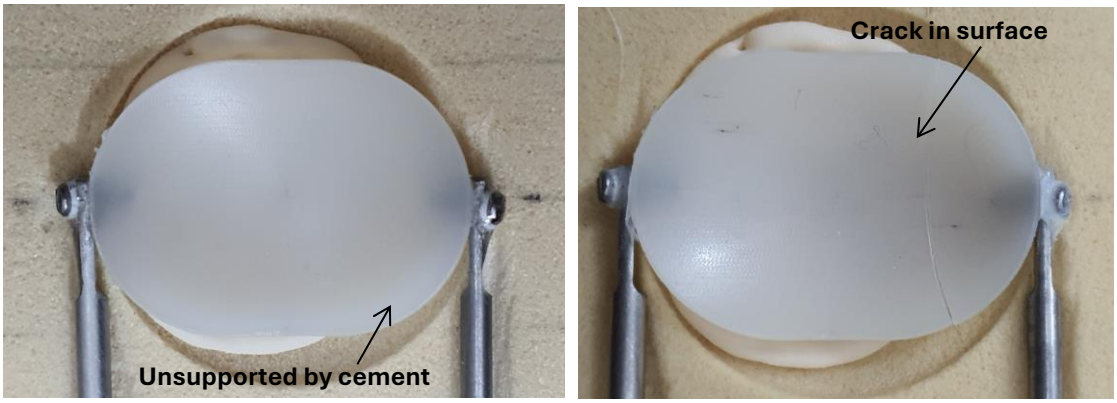

a) Before test b) After test

Figure 3-33 *Rig validation test Sample 4 (size 48mm) before (a) and after (b) test. Uneven cement resulted in the RHS edge of this sample being unsupported, and the sample cracked on this side during the test. The angled washers and adhesive caps were sufficient to keep the lever fixation firm.*

Inspection of the glenoid after the test showed the glenoid fixation was still firm, but the glenoid surface had cracked at the RHS. Inspection of the levers found the LHS to be firm. This was more difficult to discern at the RHS, since moving the lever caused the broken section of the glenoid to move, giving the impression of slack, but the lever fixation itself appeared strong.

Sample 5 (Size 48mm)

The final sample tested was another size 48mm, shown in **Figure 3-34**. This sample had excess cement around the edges, unevenly distributed at the RHS edge.

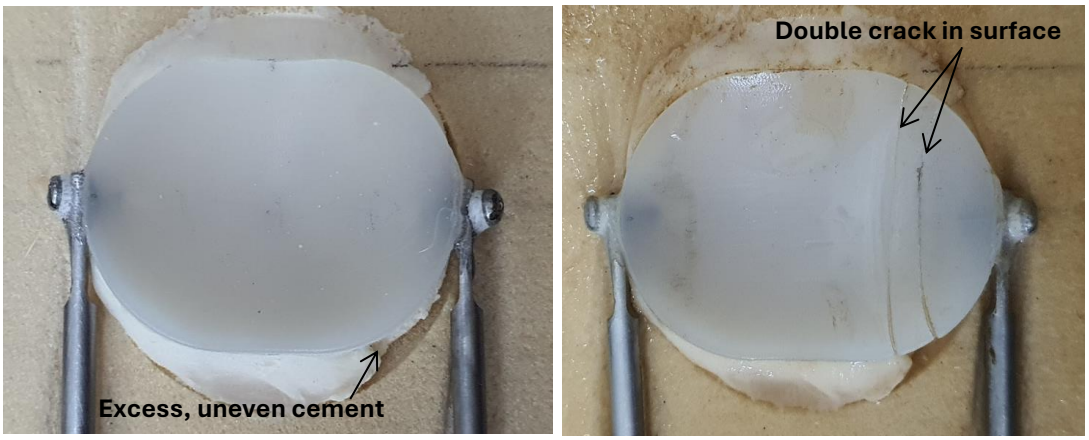

a) Before test b) After test

Figure 3-34 *Rig validation test Sample 5 (size 48mm) before (a) and after (b) test. Excess and uneven cement resulted in the RHS edge of this sample being unsupported, and the sample cracked in two places on this side during the test. The lever fixation remained firm.*

Inspection of the glenoid showed this sample to have broken in two places, possibly during conditioning when a loud cracking noise was noted at the first cycle. The surviving body of the glenoid did not show any fixation failure. Inspections of the levers again showed them to have both remained firm (with the note that the RHS edge of the glenoid was mobile due to the break).

Other adjustments made during testing:

Unrelated to specific sample tests, additional adjustments were made during the rig validation testing. The first of these was that it was noted that using the unguided armature LVDTs without positioning support for the armature was inadvisable. The sensors themselves do not hold the armatures away from the internal walls of the sensor, which is likely to damage the sensor in the long term. The sensors were fitted with resin 3D-printed guide bushings placed over the measurement end of the housing, as shown in **Figure 3-35**. These bushings have a cap section that press-fits over the sensor end, and a 5mm long 'daisy' guide in the cone, to maintain armature alignment.

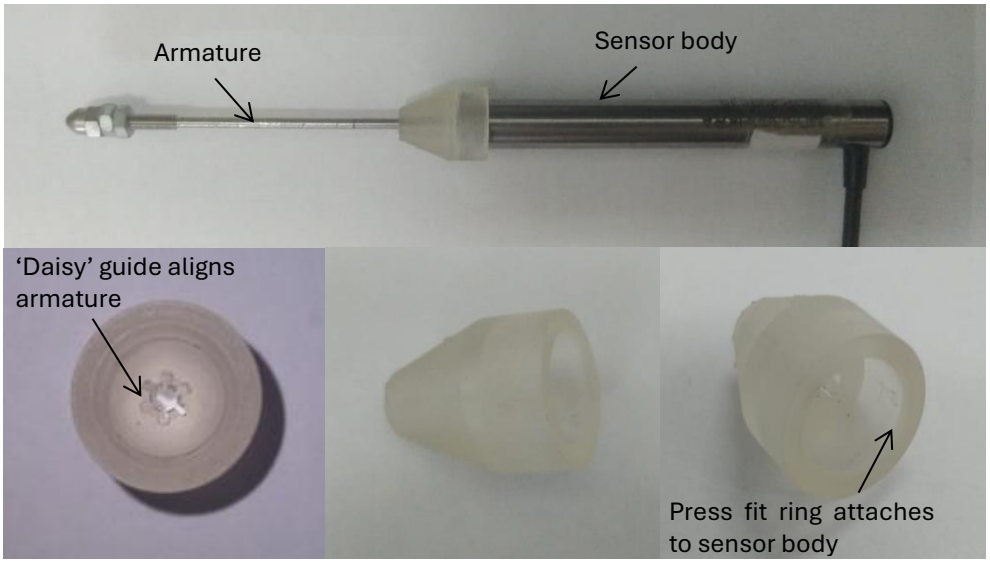

Figure 3-35 *Resin 3D Printed cap bushings used to align the unguided LVDT armatures for the vertical displacement sensors. A guide in the cap tip holds the armature, while the back of the cap press fits onto the front of the sensor body.*

Further, over the course of the testing, some of the tests showed discolouration in the water and at the sample and Sawbones. This was noted to be caused by corrosion on some of the fasteners used. These were replaced with stainless steel parts and where necessary coated in marine silicone.

Glenoid Edge Motion Measurement Results

To confirm that the sensors are functioning correctly the results of Sample 3, which had levers fixed using the polypropylene washers and adhesive, are presented. This sample was chosen because, while the glenoid fixation did show loosening during the test, there were no failures of the lever fixation, and the glenoid component did not break. The data presented here are interpreted and discussed in the chapter closing discussions (Section 3.7.3.3).

The six sensor readings were converted to glenoid edge motions using the Motion Calculation MATLAB protocol. The three motions at each of the edges for the full length of the test are shown in **Figure 3-36**. The figure shows the overall range of motion measured for each of the edges, as the edge moves from tension to compression. In this figure, the density of the data does not allow the intermediate data points measured along the HH to be distinguished. It is used to observe the progression of the tensile and compressive range of deflection as the test proceeded. The data for individual cycles are shown in **Figure 3-37**.

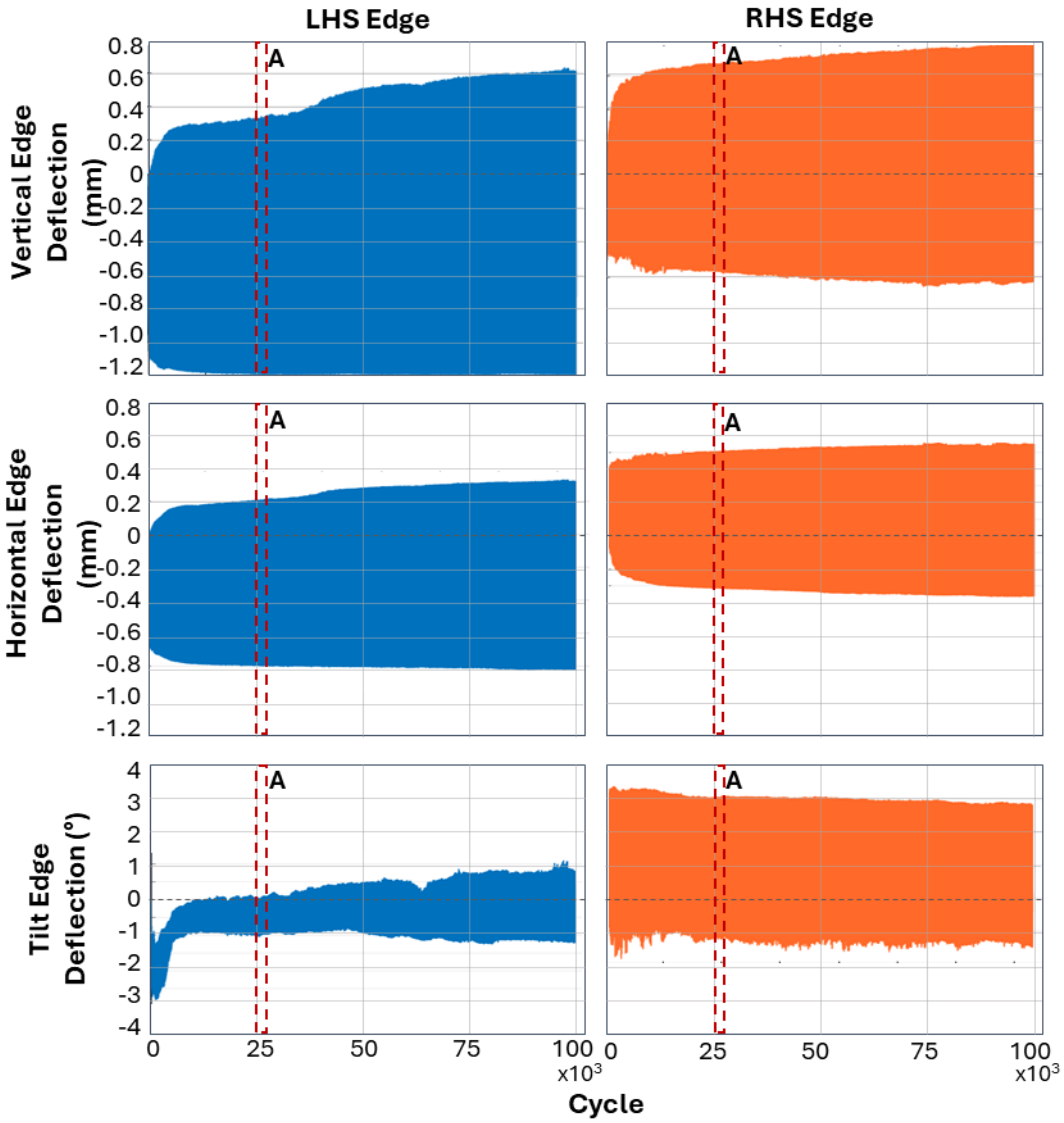

A: Expanded view of all measured data for the 5 cycles indicated is provided in Figure 3.37

Figure 3-36 *All measured glenoid edge motions for the rig validation test Sample 3 for 100,000 cycles. The width of the band of data shown in each plot indicates the total range of motion of the glenoid edges as they are loaded and unloaded. Data at intermediate locations of the HH is obscure by data density. To examine the individual data points relative to the HH position, 5 cycles at A are provided in an expanded view in Figure 3.37.*

The LHS edge showed a vertical deflection ranging between a minimum that reached -1.2mm (i.e. downwards into the surface) in the first quarter of the test and remained at that level for the

remainder of the test. The LHS maximum increased gradually from 0mm to +0.6mm (i.e. out of the surface) as the test proceeded. The RHS vertical motion reached a minimum of approximately -0.65mm for the full duration of the test, and a maximum that ramped quickly to +0.6mm in the beginning of the test and then rose more slowly to approximately +0.8mm.

For the horizontal motion, the LHS moved quickly to a minimum of -0.8mm and remained there, and to a maximum that rose from 0mm to approximately +0.3mm as the test proceeded. The RHS showed a minimum moving from 0 to -0.35mm and a maximum moving from 0.4 to 0.55mm.

The LHS showed an initial dip in the rotation, with a minimum of -3° and a maximum of -1°. The motion then shifted back towards the origin, with the minimum now settling around -1° and the maximum moving from -0.5° to 1°. The RHS edge showed a minimum rotation of between -1° to -1.5°, and a maximum starting at 3.5° and then dropping to 3° as the test proceeded. Interpretation of the feasibility of the combined motion directions seen in Figure 3-36 is discussed in the Section 3.7.3.3. At this point, it is noted that none of the edge motions exceeded the thresholds set in the edge motion measurement system design requirements Section 3.2.

To examine the motions occurring at the intermediate HH positions, within the cycles, the data for five cycles is isolated, allowing individual data points to be observed. The cycles from 25,000 to 25,005 were chosen, as they fall within the portion of the test where the motions had reached more 'steady' levels and are shown in **Figure 3-37**. The results are plotted with reference to the position of the HH. The dashed blue vertical lines indicate that the HH is at the LHS and the dashed orange vertical lines indicate it is at the RHS. The grey vertical lines indicate the estimated point at which the HH is at the centroid. The measurements at the edges are taken very close to the set distance (usually within 0.01mm of the setpoint) because the HH stops at this location. The measurements at the intermediate locations 'lag' slightly as they are taken after the setpoint threshold is crossed (as discussed in Section 2.4.5.3). This can be seen at the centroid, where the log point happens at distances of 1.1mm to 1.5mm after the centroid is crossed, in both directions.

In the vertical direction, the results show the edges moving in opposing directions to each other. As one edge moves upwards the other moves downwards. The amplitude of the motion from minimum to maximum is similar (approximately 2mm for the LHS and 1.5mm for the RHS), but the LHS edge is lower overall, with both minimum and maximum at lower levels than those of the RHS. This indicates the RHS edge of the glenoid is raised compared to the LHS.

The horizontal motion shows the edges moving in concert, where both either move to the left or to the right. Again, the amplitude of motion is similar (approximately 1mm for the LHS and 0.8mm for the RHS), but the LHS edge has overall lower x-values. This indicates the LHS edge has shifted outward to the left relative to the RHS edge.

The tilting motion also shows the edges moving in concert directionally, where both edges tilt in the clockwise or anti-clockwise direction for a given humeral head position. The RHS edge has markedly higher overall amplitude in tilt, moving from 3° when loaded to -1.2° when unloaded, compared to the LHS which moves between -1° when loaded to 0° when unloaded. The higher outward rotation of the RHS side edge could be due to this edge being raised relative to the LHS side, allowing it to be more mobile in tilt.

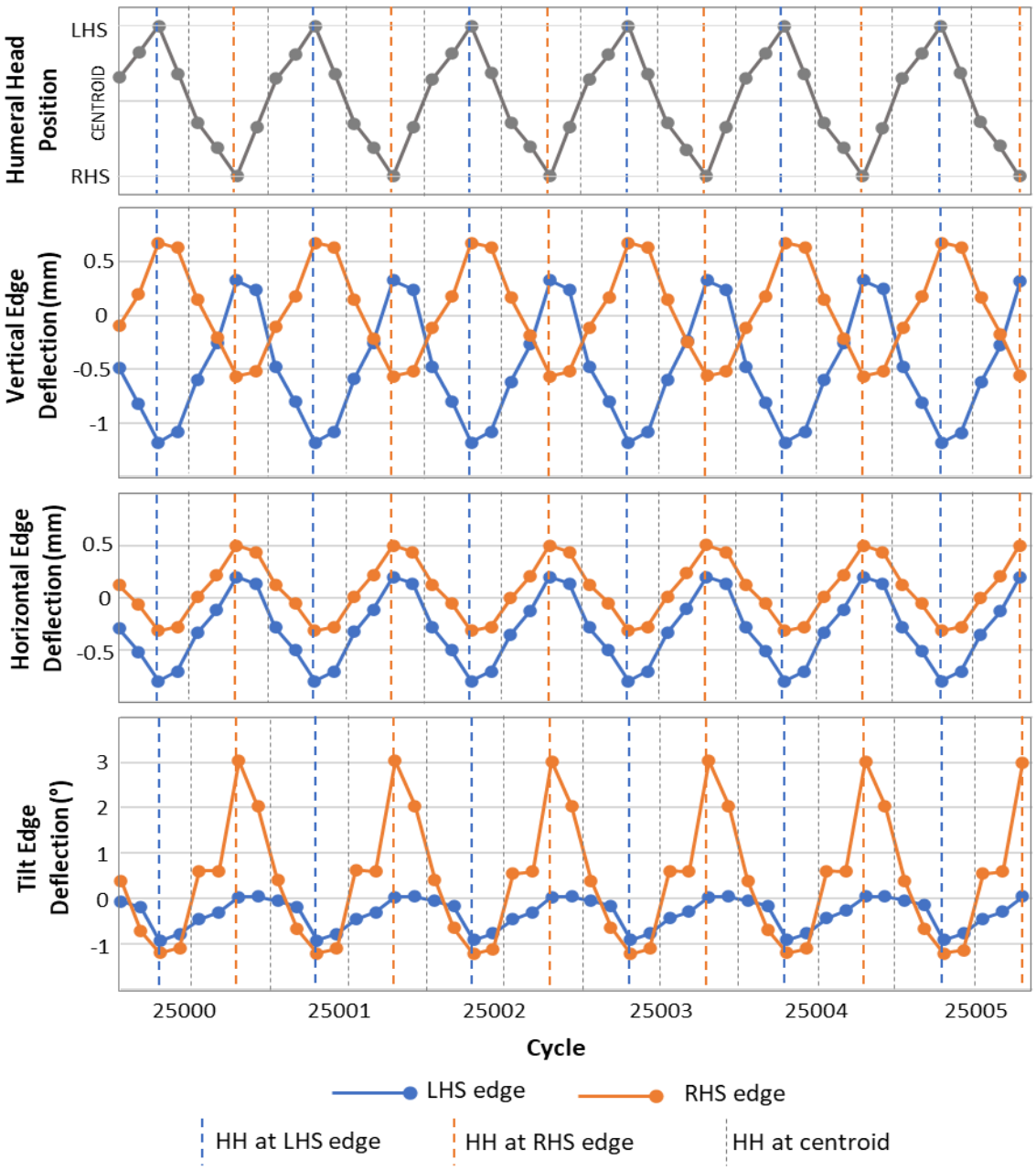

Figure 3-37 *Expanded view of the edge motions for cycles 25,000 to 25,005 for test Sample 3. Vertical, horizontal, and tilt motions are plotted relative to the HH position, indicated by the dashed vertical lines, where orange indicates the HH is at the RHS edge, grey indicates the HH is at the centroid, and blue indicates the HH is at the LHS edge.*

As stated in the rig validation testing aims, the normal contact force must be checked to confirm that force variation remains within the design requirements. The normal contact force measured for the full test is shown in **Figure 3-38**. The normal force maximum was between 780N and 790N for the length of the test. The normal force minimum was between 740N and 745N for the full test.

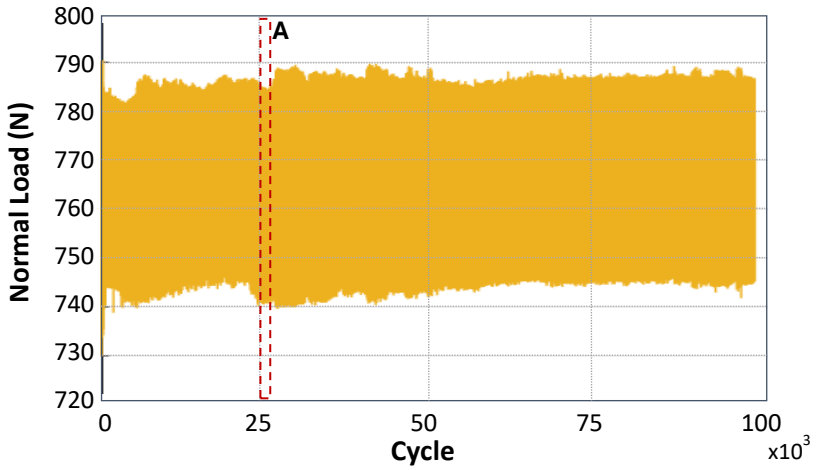

A: Expanded view of all measured data for the 5 cycles indicated is provided in Figure 3.39

Figure 3-38 *Measured normal load for rig validation Sample 3 for 100,000 cycles. The width of the band of data shown in each plot indicates the total range of normal load measured in the cyclic loading. Data at intermediate locations of the HH is obscured by data density. To examine the individual data points relative to the HH position, 5 cycles at A are provided in an expanded view in Figure 3.39.*

As for the edge motions, a snapshot of the five cycles from 25,000 to 25,005 is provided in **Figure 3-39**, to observe the intermediate data points and to relate the measured values to the position of the HH. The normal contact force snapshot shows that the minimum force measurement (745 to 755N in this snapshot) occurs when the humeral head is crossing the centroid, and the maximum forces (773 to 785N) occur at both edges.

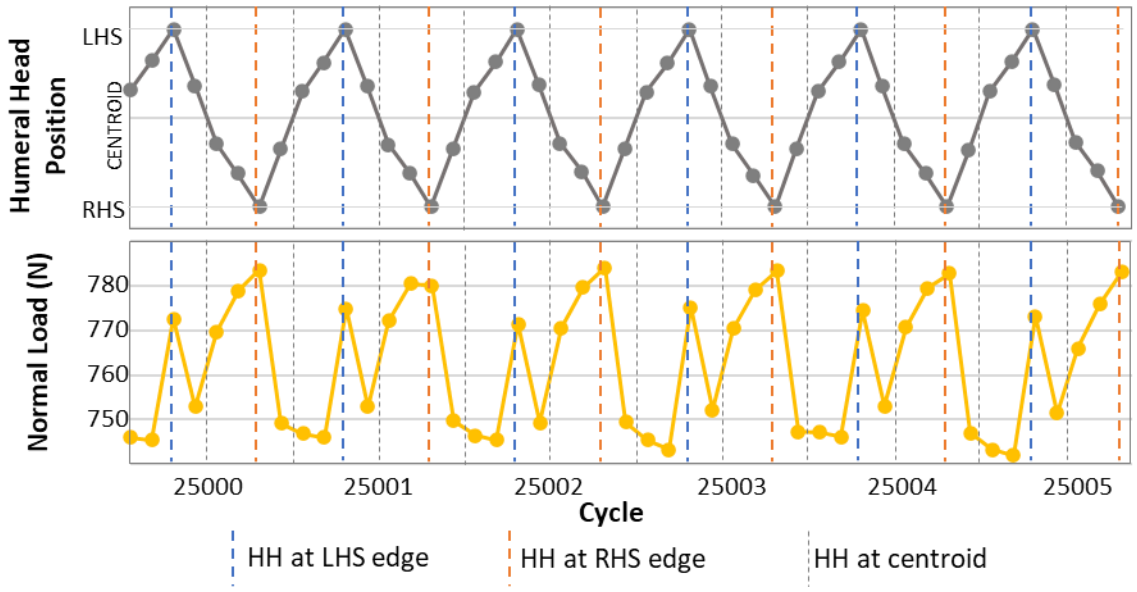

Figure 3-39 *Expanded view of normal load measured for cycles 25,000 to 25,005 for test Sample 3. Maximum and minimum load locations are compared to the HH position, indicated by the dashed vertical lines, where orange indicates the HH is at the RHS edge, grey indicates the HH is at the centroid, and blue indicates the HH is at the LHS edge. The load peaks occur when the HH is at each of the edges, and the load minimums occur as the HH passes the centroid.*

The results presented are used to determine the suitability of the edge motion measurement system and augmented test rig to use in the novel glenoid design evaluation, as discussed in the sections that follow.

3.7. Discussion

The design process, testing, and results are discussed here with the goal of confirming that the aims of the edge motion measurement system design have been met.

3.7.1. Discussion of Concept Selection and Design Implementation

The initial concepts for measurement of the vertical glenoid edge motion, the Hall effect sensor, and the strain gauge bending bar were confounded by the horizontal and tilting motions that also occurred. The investigation of these concepts highlighted the extent to which the additional motions, particularly tilt, occur. This led to the development of the pivoted lever system (shown in Figure 3-9), which can be used to quantify all three directions of motion simultaneously.

The pivoted lever, positioned perpendicularly to the glenoid primary axis, allows the edge motion to be amplified, but in a quantifiable way that is not distorted by tilt. The lever also has the benefit of moving the sensors far from the water bath, removing the need for waterproofing. The fixation of the lever end flat against the side of the glenoid edge ensures the motion that is being amplified by the lever is the motion of the glenoid edge itself. This method does require this fixation to be firm and the fixation pin to not loosen during the testing. The testing and troubleshooting around the lever fixation are discussed in the next Section 3.7.3.2.

3.7.2. Discussion of Motion Calculation Method and *in-silico* Validation

The glenoid edge motion measurement system design implemented requires the readings from the six LVDT sensors to be converted to glenoid edge motions using the known geometry of the system. Since the calculation method developed is novel to this research, it was necessary to validate it *in-silico* using a SolidWorks motion simulation. That the calculation method was developed based on the motion of the glenoid edge that would produce the largest combined motion at the measuring block (referred to as the 'extreme' motion), but it should remain valid for any combination of motions.

To confirm that the calculation remains valid, the *in-silico* validation was performed using two motion combinations that are different from the extreme motion, and which are expected to occur during the cyclic glenoid loading. These were the predicted response to compression and tensile distraction of the RHS edge. The three motion combinations are illustrated in **Figure 3-40**. In the extreme motion, the glenoid edge moves downwards, inwards towards the centroid, and

tilts outwards. In compression, the edge is expected to move downwards, outwards, and with outward tilt, while in tension it would be expected to do the opposite. The resultant motions of the measuring blocks as they are pivoted by the lever are shown in the figure for each edge motion.

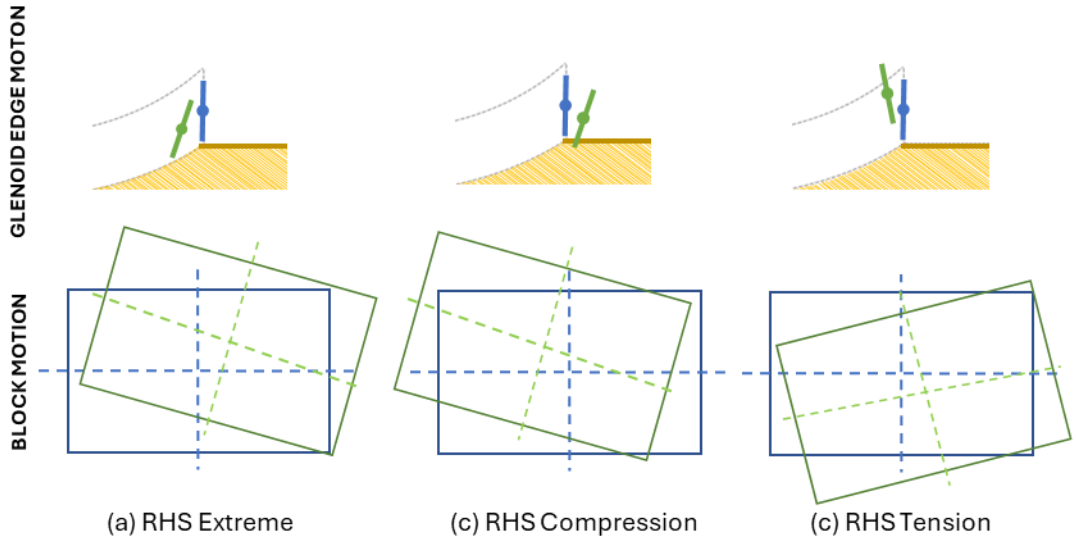

Figure 3-40 *Comparison of the 'extreme' (a) combined edge motion used to develop the edge motion calculation method to the compressive (b) and tensile (c) motions used to validate the calculation method. In the figure, the undeflected glenoid edge and measuring block are shown in blue. For each motion, the new glenoid edge position, and the resultant motion of the block on the pivoted lever are shown in green. The motions are for the RHS edge and are not to scale.*

For both the implemented motions, the *in-silico* validation showed the calculation method to be valid, as discussed in Section 3.5.5. The calculation method is therefore shown to not be limited to a particular combination of motions and can be used with confidence to convert the sensor reading to glenoid edge motions.

3.7.3. Discussion of Augmented Rig Validation Testing

The results of each stage of the rig validation testing are discussed here, to assess the design changes made and to confirm that the aims of the validation testing have been met.

3.7.3.1. Sample Preparation

The rig validation sample preparation brought to attention some areas in which improvement was needed before the novel glenoid evaluation testing could be performed. The primary concern was the uneven cement distribution. This result is attributed to a combination of the use of expired cement and the implantation of multiple glenoid components at the same time. While the novel glenoid evaluation will use non-expired cement, it is still prohibitively expensive to implant only one component from a single pack. To facilitate multiple component implantation, the implantation process needs to be performed more quickly, by employing more people to

compress the glenoids into the bases and clear any excess cement while it is still soft. The surgeon will need to carefully note the cement condition during the implantation, to ensure they do not exceed the drying time.

A second concern was the lack of directional alignment guides on the original sawbones base. The surgical set provides a guide that sets the distance of the inferior peg from the central peg but does not dictate the orientation around the peg in which it should be placed. As it is important for the testing that the primary axis of the glenoid is parallel to the motion of the humeral head, this orientation must be accurately set in relation to the Sawbones mounting clamps, as shown in **Figure 3-41**.

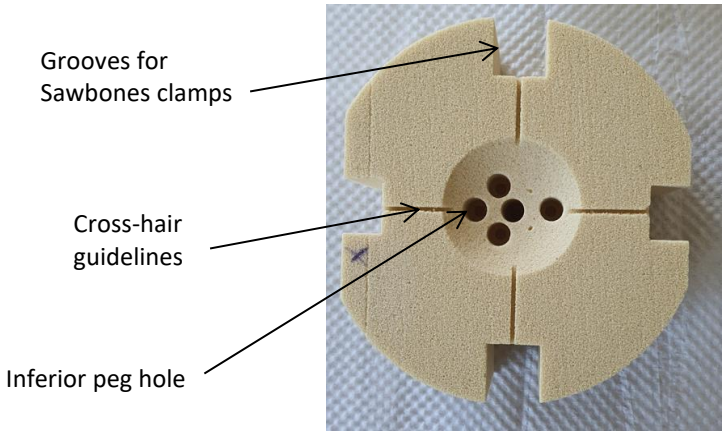

Figure 3-41 *Final Sawbones base after preparing the surface for implantation of the glenoid. Grooves for the mounting clamps and glenoid placement alignment guide cross-hairs were machined before the surgical preparation. The surface was then reamed and drilled using a training set of surgical tools.*

Marking the inferior peg position by hand was onerous and susceptible to human error. This was solved by the addition of the machined cross-hairs, which form a 1mm deep groove that effectively locates the drill bit, ensuring the peg lies on the line the humeral head will follow in the testing.

Overall, the process of using the training set of the surgical tools was effective for mimicking the surgery, and with the guides in place, non-expired cement, and cognizance of the cement drying, the novel glenoid testing components should be successfully implanted.

3.7.3.2. Subluxation Distance Estimate

The subluxation distances were estimated for glenoid sizes for which there were not enough samples for the full P90 test to be performed. This was done either by testing a single component or by extrapolating values for intermediate sizes. To check the validity of the estimates, the analytical subluxation distance is calculated for each size using Equation 2.1. The experimentally

estimated distance is then compared to the subluxation distance range reported by Anglin et al. (2000c) for the given analytical distance, as shown in **Table 3-9**.

Table 3-9 *Comparison of estimated subluxation distance to literature*

Glenoid Size	Analytical Subluxation Distance	Experimental Subluxation Distance (Anglin et al., 2000c)	Experimental and Estimated Subluxation Distance (Rig Validation P90 Tests)	
40	0.7mm	1.8 - 2.2mm	3.1mm	By measuring one sample
44	2.0mm	3.0 - 4.5mm	4.2mm	By extrapolation
48	3.5mm	3.5 – 4.6 mm	5.3mm	By extrapolation
52	5.0mm	4.9 – 6.2mm	6.2mm	By measuring one sample
56	5.8mm	5.5 - 6.2mm	7.8mm	By measuring one sample

The experimentally estimated values for the size 44 and size 52 glenoids fall within the range reported by Anglin et al. (2000c), while those for the other sizes tended to exceed the ranges by 1 – 1.5mm. For the purposes of rig functional validation only, these values are deemed acceptable.

3.7.3.3. Cyclic Testing

The cyclic testing results are used to: evaluate the durability of the measurement system components (particularly the lever fixation), check the rig mechanical and data logging capabilities over the full test, to check the normal contact force remained within the levels set by the design requirements, and to confirm the LVDT sensors are functioning as they should. The mechanical function of the rig showed no errors during the testing and all required data was logged. The observations from the five sample tests are summarised briefly in **Table 3-10**.

Table 3-10 *Summary of rig validation testing results, observations, and adjustments made.*

Glenoid Sample		Fixation Failed?	Comments
1	**Size 40mm**	yes	Lever arm fixation screws turned loose Glenoid surface cracked
2	**Size 44mm**	no	Adhesive add to lever fixation screws Screws remained fixed, but lever still had some slack at end
3	**Size 44mm**	yes	Offset washer added to lever fixation screws Lever fixation firm at end of test
4	**Size 48mm**	no	No further adjustments Glenoid surface cracked, lever fixation firm at end of test
5	**Size 48mm**	no	No further adjustments Glenoid surface cracked twice, lever fixation firm at end of

Although assessing the glenoid fixation survival is not a goal of this set of testing, it is noted that Samples 1 and 3 showed signs of fixation failure. In both cases, the glenoid could be moved by hand after the test but had not dissociated completely from the Sawbones. Three of the samples cracked during the testing, with Sample 5 exhibiting two cracks across the full surface near the RHS edge. Oral et al.(2006) observed that the fatigue strength of conventionally used cross-linked UHMWPE is reduced with age. As the samples tested were expired, age embrittlement of the material likely contributed to these failures. It further noted that the cracks occurred over or near 'unsupported' sections of the glenoid, where uneven cement is present. Sample 3 had uneven cement causing an unsupported section and did not break, but it did loosen. Material embrittlement aside, it is clear from these results that uneven cement is highly undesirable for glenoid fixation survival.

The lever fixation was adjusted during the testing to improve durability. While none of the levers detached from the glenoid edge during the testing, the initial lever fixation method showed loosening due to screws turning loose during the test. Lever fixation survivability and rigidity were improved by the addition of the offset washer and by adding adhesive to the screw, as illustrated in **Figure 3-42**.

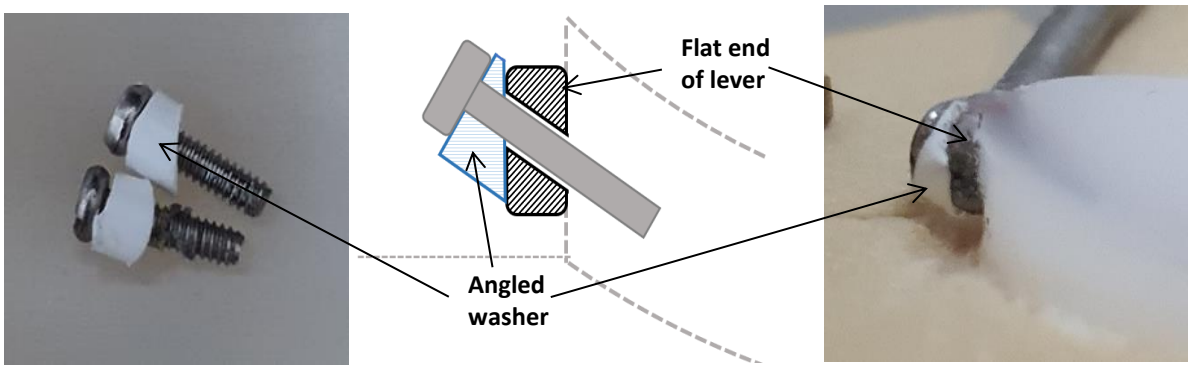

a) Fixation screws with angled washers

b) Cross section of lever fixation

c) Lever end with angled washer and adhesive cap

Figure 3-42 *Detail of the implementation of angled polypropylene washers for improved lever fixation strength. (a) Fixation screws with washers prior to attachment of lever. (b) Cross section of the fixation screw holding the lever end against the glenoid edge with the angled washer in place. (c) Close-up of the lever end fixed by pin with the angled washer.*

The polypropylene material used in the offset washers is moderately rigid but allows limited material deformation. This allows the washer to be compressed between the back face of the fixation screw and the outside face of the lever attachment end, creating a firm pressure holding the lever against the side face of the glenoid. With these adjustments in place, the lever fixation remained firm for the final three 100,000 cycle tests. The levers themselves were not damaged

by the testing, and the measuring blocks had no noticeable wear at their contact surfaces, indicating that these components could be used going forward in future test runs.

The initial sensor setup, in which the armature was placed without an alignment guide, is understood to have the potential to damage the sensors' internal insulation in the long term. Captive bushing LVDT sensors, which have a built-in alignment bearing but still allow free motion of the armature (without a spring guide), would have been a more appropriate choice for this application. However, the good electronic properties and small light armatures of the chosen sensors remained desirable for the sensor setup. It was therefore decided that the 3D-printed cap bushings (as shown in **Figure 3-35**) would be added to maintain alignment of the armatures, and the existing sensors were retained.

The sensor measurements from Sample 3 were chosen to evaluate sensor function, as this test did not have a lever fixation failure, and the glenoid itself did not break. The glenoid did show fixation loosening, but this is a feature that the measurement system should be able to accommodate and evaluate. These measurements were processed using the Motion Calculation algorithm.

The overall amplitudes of the motions in the vertical direction (LHS 0.6 to -1.2mm; RHS 0.8 to -0.65mm) remained within the ±2mm design range. The -1.2mm deflection at the LHS under compression is greater than our predicted range for a component that has not loosened (±1mm), but this component did show some loosening, so the value is not deemed unreasonable. The horizontal motions (LHS 0.3 to -0.8mm; RHS 0.8 to -0.65mm) remained within the estimated range of ±1mm, and the rotation (LHS 1° to -3°; RHS 3.5° to -1.5°) remained well within the design range of ±15°.

The vertical and horizontal motions both showed an initial, moderately rapid increase in amplitude, followed by a slower increase or steady state. This indicates edges becoming more mobile as the tests proceed, which is expected. The rotation, particularly at the LHS edge, showed an unexpected initially large outward deflection, where even in tension the outward deflection lessened, but was still present. This edge was unsupported by cement, so this large outward tilt likely indicates deformation of the unsupported surface.

The outward rotation decreased as the test proceeded, until the edge was shifting from outward (during compression) to inward (in tension) rotation. The timing of the reduction in outward rotation coincides with the end of the rapid increase in vertical and horizontal motion amplitudes. The fixation of this sample was loosened, so it is likely the increased motions are an

indication of the glenoid becoming more mobile, beginning to ‘rock'. In compression, the increased downward motion could be enough to cause the edge to be supported by the Sawbones. Further, the increased outward motion causes the edge to move slightly away from the HH. In combination, these would cause the glenoid surface to deform, or be ‘pushed over’, less severely than the unsupported edge. In tension, the increasing vertical distraction in tension would contribute to increasing the inward rotation occurring as the test proceeds. This trend is therefore an unusual case caused by the high mobility of the unsupported edge but is not concluded to be physically impossible.

Once the test reaches 25,000 cycles, the edge motions are steadier, exhibiting slower changes. The motion of the edges relative to each other, referenced to the centre of the glenoid edge at the start of the test, when the HH is at each of the edges is illustrated in **Figure 3-43**.

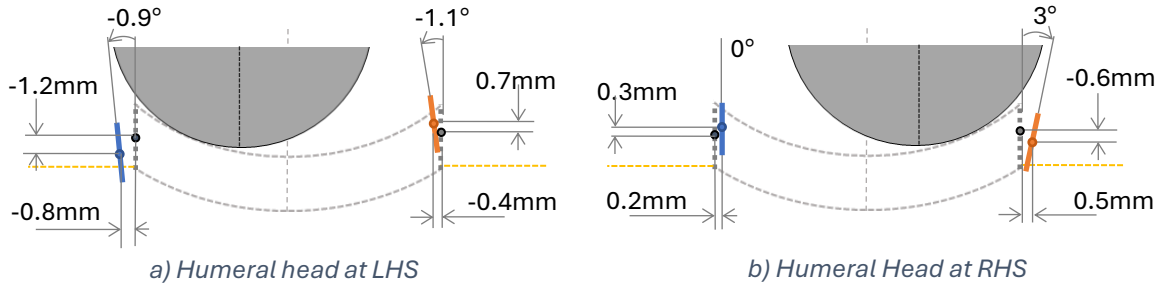

Figure 3-43 *Illustration of the glenoid edge motions in in tension and compression based on the position of the humeral head, at cycle 25,000. The combined effect of the three motions is indicated by the lines representing the new positions of the LHS (blue) and RHS (orange) edges relative to the undeflected edges (grey).*

In the 5-cycle snapshot motion in the vertical direction, the edges were seen to move in alternating directions, indicating that as one edge moved downward in compression, the other tended to distract from the surface in tension, as expected. In the horizontal direction, the edges move in concert, either both in the positive (rightward) or both in the negative (leftward) direction. This is again expected since the whole glenoid would be expected to move in the direction of the loaded edge. In the tilt direction, we again see motion trends in concert (i.e., the edges either rotate outward or inward at the same time.) Again, this is expected since the edges would tilt in the same direction as the glenoid ‘rocks’ in that direction.

The magnitude of the motions, seen in compression and tension at each of the edges differs. Overall, the LHS shows higher amplitudes of vertical and horizontal motion than the RHS but rotates less. The difference in mobility could be due to physical factors such as the edge being unsupported by the uneven cement. To draw proper conclusions regarding the physical behaviour of the glenoid would require more data and is not the goal of this stage of the testing. At this stage, it is concluded only that the observed overall and snapshot glenoid motions are

feasible and within the reasonable measurement range, and the sensor function is thereby confirmed.

Finally, the normal contact force is considered. In the overall test data, the force is seen to vary between a minimum of 740N and a maximum of 780N for the duration of the test. This is within the expected 40N variation determined in the test rig design stage. To meet the design requirements, it must be confirmed that the normal force variation at the edges when they are loaded does not exceed 10% of the edge load. To do this we refer to the snapshot data, in which we see that as expected from the initial force behaviour investigation, the peak forces are measured at the edges, while the minimum forces are measured near the centroid. The variation in the peak force is between 773N and 785N, or 12N, which is well within the 10% requirement.

From the above discussions, it is concluded that the edge motion measurement system and the base test rig function as required, are therefore functionally validated, and the objectives of the rig validation testing have been met.

3.8. Conclusion

The aims of this glenoid edge measurement system design were to develop a method for continuously measuring the vertical, horizontal, and tilt motions at the glenoid edge during the ASTM F2028 test, to integrate this design into the existing test rig, and functionally validate the edge measurement design as well as the test rig for full-length cyclic testing.

The final edge measurement system design utilised pivoted lever arms attached to the glenoid edges and two sets of LVDT sensors to track the motion of blocks attached to the lever ends. The LVDT measurements are converted to glenoid edge motions using a MATLAB algorithm based on changes in the geometry of the system when the glenoid edges are deflected. The functionality of this algorithm was confirmed by *in-silico* verification, using a SolidWorks motion simulation.

The test rig with the integrated edge motion measurement system was then functionally validated by performing the DGL testing on 5 expired glenoid samples. In this testing it was confirmed that the edge motion measurement system (after some adjustments) as well as the test rig itself, are able to perform all required functions in the full-length cyclic tests without failure and that the results achieved in the test are reasonable. The augmented test rig is therefore functionally validated and can now be used to perform the novel glenoid evaluation testing.

Chapter 4

Glenoid Testing and Novel Glenoid Design Evaluation

The glenoid testing is comprised of the DGL test performed on a series of control and novel glenoid components using the augmented test rig. From this testing general trends in the behaviour of the glenoids based on the three edge motions are identified. The novel glenoid design is then evaluated by comparison of the results. The work in this chapter covers Objectives 4.1 to 4.4.

4.1. Overview

The DGL testing was performed as per the method described in Chapter 2.2. The subluxation distance for each design was first determined using two samples, followed by the cyclic loading tests. The standard test calls for, at minimum, measurement of the vertical edge motion before and after the cyclic loading. As per Chapter 3, the vertical, horizontal, and tilting edge motions were measured continuously in the cyclic tests, using the augmented DGL test rig.

The standard test also calls for a minimum of three samples of each design to be tested. For this research, to improve the statistical strength of the results comparison, the goal was to test at least five of each sample. Eight samples were produced for each design to allow for possible failures during the testing. The samples of both designs were manufactured by Computerised Numerical Control (CNC) machining, from medical grade UHMWPE, and subsequently sterilised by ethylene oxide gas.

The measured sensor values from the cyclic testing were converted to edge motions using the motion calculation method described in Chapter 3. The edge motions, and other test parameters, were further processed by an additional MATLAB algorithm, which calculates average and standard deviations of the relevant results, as well as samples and smoothes the very large datasets for ease of analysis. The resultant average motion vectors for the control and novel designs were statistically compared using Statistical Parametric Modelling in 1 Dimension (SPM1D) (Pataky, 2010).

The edge motions of both control and novel designs were interpreted to identify overall glenoid behaviours and how these may affect fixation survival as the cyclic tests proceeded. Finally, the control and novel results were used to evaluate the novel glenoid design, based on the standard ASTM criterion, as well as by comparison to the original design intention and accompanying FE model.

4.2. Novel Glenoid Design

The novel glenoid was developed at the UCT Orthopaedic Biomechanics Laboratory (OBL) by Dey, (2018). Before presenting the experimental testing, the design intention and the FEM analysis performed during the novel design development are described.

4.2.1. Design Intention

In the novel design, the glenoid was 'compartmentalised' by incorporating slots in the surface, which divide the glenoid into an inner, pear-shaped region and an outer 'eccentric' oval-shaped region, shown in **Figure 4-1**.

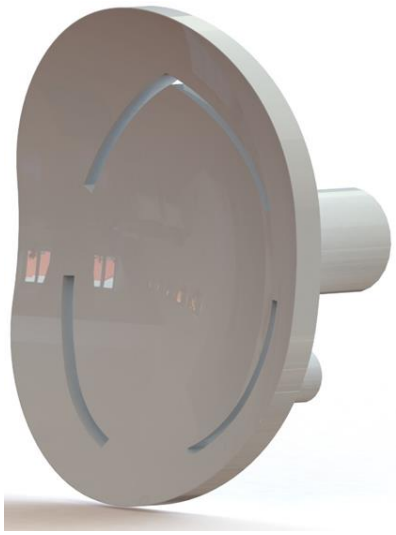

Figure 4-1 *Compartmentalised Glenoid Design (Image adapted from Dey, 2018)*

The forces on the surface of the glenoid component transverse radially outwards, from the point of contact of the humeral head (Buchler et al., 2002; Wang et al., 2005; Zhang et al., 2013). Compartmentalising the glenoid introduces a break in the surface along which the forces are transferred. The surface slots aimed to reduce the tensile force that is transferred to the unloaded edge of the component during compression of the opposing edge, thereby reducing the tensile distraction. The design further aimed to reduce the surface area that is actively supporting the normal load, thereby increasing the pressure on the underlying bone, and promoting bone growth.

4.2.2. FE Model of Novel Design

The stresses induced in the novel glenoid were modelled by Dey (2018) using Abaqus/Standard (v6.14 , SIMULIA, Providence, RI, USA) Finite Element software. A comparative model of a control component with a continuous surface was also made.

Both the control and novel glenoid models were based on a size 56mm, four-peg component. A 28mm humeral head and 2.75mm glenohumeral radial mismatch were used. Material properties for the glenoid UHMWPE were; Young's modulus 1260MPa, density of $1x10^{-11}$ tonnes/mm^3 and Poisson's ratio of 0.4, as has been previously used in FE models in literature (Hopkins et al., 2006; Junaid et al., 2010; Stone et al., 1999; Zhang et al., 2013).

Behind the glenoid, a uniform 1mm thick layer of cement was simulated (Lacroix et al., 2000); Zhang et al., 2013). This cement layer was rigidly fixed to the back of the glenoid component. Properties of PMMA cement were applied as Young's modulus of 2200MPa, a material density of $1.6x10^{-10}$ tonnes/mm^3, and Poisson's ratio of 0.3 (Junaid et al., 2010; Lacroix et al., 2000) .

The underlying bone was modelled using the properties of bone substitute foam, to more closely mimic the ASTM test. Bone substitute properties of a Youngs Modulus of 193MPa, density of 1.13 x 10-3 tonnes/mm3 and Poisson's ratio of 0.3 were applied (Junaid et al., 2010). While many reported FE models will include perfectly bonded cement and underlying bone surfaces (Junaid et al., 2010; Zhang et al., 2013), such an interface does not allow the motion of the component that will occur if tensile loosening has occurred. To allow for glenoid motion, the cement-bone interface was modelled as a sliding contact, with a frictional coefficient of 0.6, based on cement-bone interface studies by (Terrier et al., 2006).

The loading applied in the model mimicked the subluxation test, which has been demonstrated by Zhang et al., (2013), to be sufficient to model the stress characteristics of a glenoid design, and when limited motion is allowed between the glenoid and underlying surface, also the potential for loosening. The analytical subluxation distance was used in the FEM, calculated to be 3.7mm, for the size 52 glenoid and a glenohumeral radial mismatch of 3mm.

At the subluxation distance, the Von Mises stress distribution in the control and novel glenoid design are illustrated in **Figure 4-2**. The locations of the maximum and minimum principal stresses are shown in the red and green circles, respectively. These locations are on the perimeter of the control component but shifted towards the edge of the inner pear-shaped area of the novel design. The maximum principal stress under compression was 9.6% higher in the novel design, than in the control, but occurred away from the outer edge. Both the compressive and tensile edge motions were reduced in the novel compared to the control (by 9.1% and 14.3%) respectively.

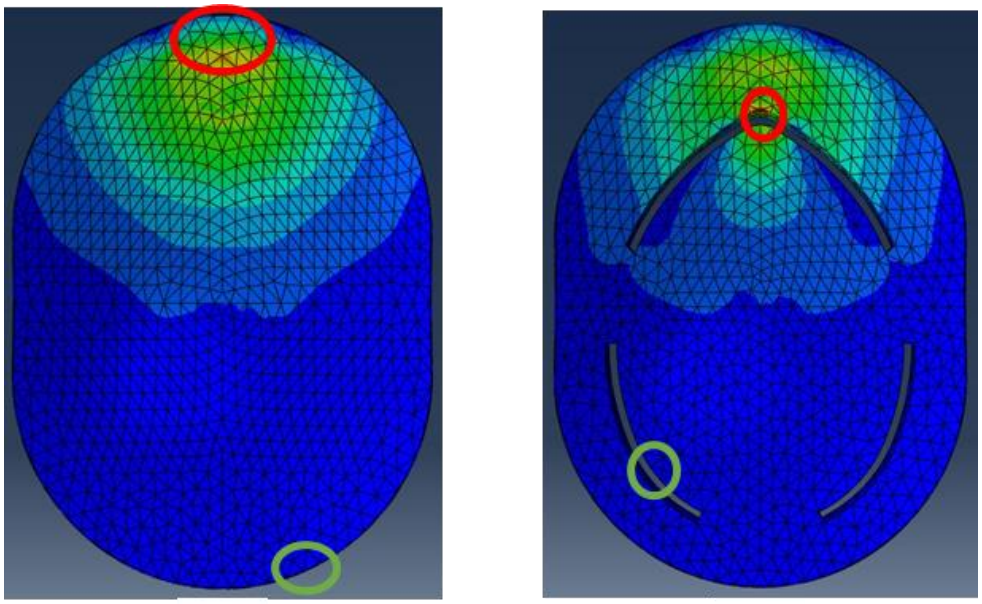

Figure 4-2 *Von Mises stress distribution in (a) the control and (b) the novel glenoid designs at the point of subluxation. The location of the lowest Von Mises stress is indicated by the green circles, and the highest stress by the red circles. (adapted from Dey, 2018)*

4.3. Experimental Testing of Glenoids

The experimental glenoid testing was performed using the augmented DGL test rig, on a series of control and novel glenoid samples, using the test criteria set in the rig validation study.

4.3.1. Aims

The overall aim of the testing is to measure all three directions of edge motion continuously for the duration of the standard test, to analyse the resultant edge motions for overall trends as the test proceeds, and to use the comparative results between the control and novel designs to evaluate the success of the novel design.

The following objectives were defined for the glenoid testing:

- Perform the full DGL test on the control glenoid design and the novel glenoid design. This includes performing the P90 test on two samples of each design, and 100,000 cycle cyclic loading tests on at least 5 samples for each.
- Use the control design results as a baseline against which to evaluate the performance of the novel design, based on the ASTM criterion of equal or lessened vertical edge motion.
- Compare the novel design edge motion to the control results in the horizontal and tilting motions as well and use these to evaluate the overall mobility of the novel design relative to the control.

- Use the measured edge motions from both glenoid designs to interpret trends in the motion and loosening behaviour of the glenoids for the cyclic testing.
- Compare the novel glenoid experimental results to the existing FEM model and discuss any variances in expected behaviour.
- From the combined results, evaluate the overall success of the novel glenoid design, and make recommendations for further development.

4.3.2. Glenoid Test Samples

To ensure comparable tests, it is desirable for the only difference between the control and novel glenoids to be the characteristic design feature of the novel glenoid. In this case, this was an alteration to the glenoid surface. All other design features of the control and novel glenoids, their manufacturing, sterilisation and implantation were held constant.

The control glenoid design was based on existing, clinically established design features and was modelled on a size 48 component. A Ø48mm humeral head was used for this testing. The control utilises 5 peg cemented fixation and has a symmetrical surface with 3mm radial mismatch to the humeral head, illustrated in **Figure 4-3**.

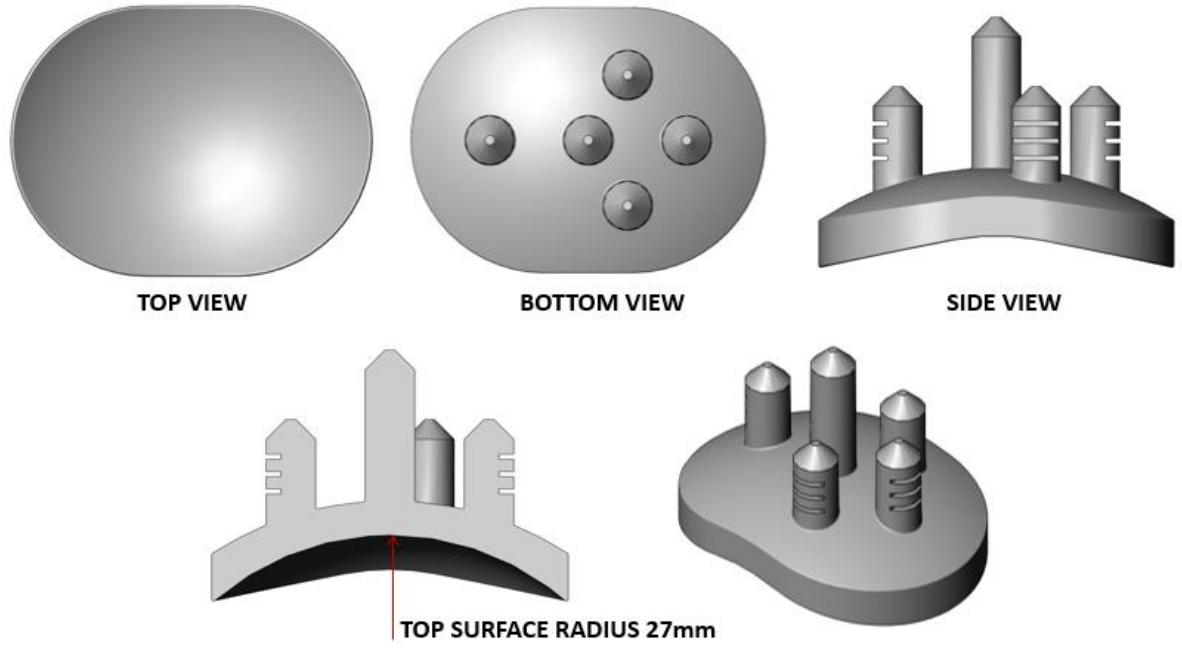

Figure 4-3 *Control glenoid design (All-polyethylene, curve-backed, 5 cemented peg fixation, size 48 with 3mm GH radial mismatch)*

The size 48 glenoid, rather than the size 56 used in the novel component design development, was chosen because it is a moderate size, in comparison to the most widely available sizes (40 to 56). This reduces the comparability of the experimental results to the FEM but was considered

preferable to performing the edge motion study on samples that are on the extreme end of the available size range. The experimental samples further differ from the FEM model in the use of the 5-peg fixation, rather than the modelled 4 pegs. This was driven by necessity, as the only surgical implantation toolset available was for the 5-peg design.

The novel component, illustrated in **Figure 4-4**, uses the control design as the base geometry, to which the design feature of the surface slots was added. The change from four to five fixation pegs necessitated an adjustment to the surface slots compared to the original FEM design. The slot adjustment was made by the original designer, Dr Dey, to ensure the original design intention was maintained. Because of these adjustments, the final comparison of the experimental results to the FEM will be based on observed trends, rather than exact calculated values.

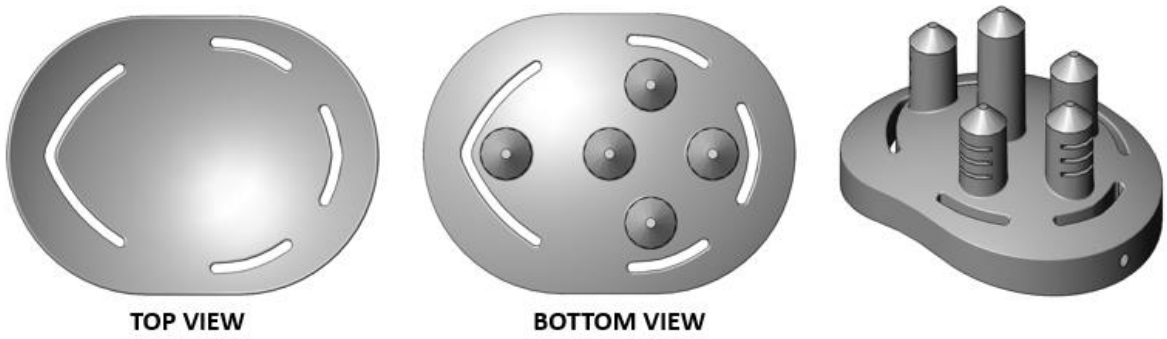

Figure 4-4 *Novel glenoid design (All-polyethylene, curve-backed, 5 cemented peg fixation, size 48 with 3mm GH radial mismatch) with surface slots added. The surface slots create a break in the surface through which stresses are transmitted, centralising the location of maximum stress under load and thereby aiming to reduce the tensile edge motions.*

Ten samples of both the control and novel design were manufactured, two for the subluxation distance test and the remainder for cyclic testing, to achieve the goal of five successful cyclic loading tests while allowing for the possibility of test failures. All samples were manufactured by CNC machining, from medical grade UHMWPE (compression moulded sheet stock, GUR1050, material specification sheets are provided in Appendix C1). The material was not irradiation cross-linked. All manufacturing was performed by TiTamed (Pty) Ltd, (Paardeneiland, Cape Town). As per the standard guidelines, the samples were sterilised prior to testing. Sterilisation by ethylene oxide gas was performed at SupraHealthcare (Montague Gardens, Cape Town). Further, the samples of both control and novel designs were all implanted by the same surgical team, using the same type of bone cement (PMMA) and the same type of bone substitute base (Sawbones PCF20).

4.3.3. Method

As for the rig validation testing, the novel glenoid evaluation is divided into three stages; the implantation, the determination of the subluxation distance, and the cyclic loading testing. Each of these stages was repeated for the control and the novel designs. Due to the availability of samples from the manufacturers, the three stages were not completed linearly for all samples. The control samples were manufactured first, at which stage they were implanted, their P90 test performed, and cyclic testing was begun. While the control cyclic testing was being performed, the novel components were manufactured. Once the novel samples were available, they were implanted and the novel P90 test was performed. The remaining cyclic testing was then performed alternating between novel samples and the remaining control samples. The methodology and results presented here are grouped by stage for clarity.

4.3.3.1. Implantation

As for the augmented rig validation study, the control and novel glenoid samples were implanted in a Sawbones PCF20 base, at the Department of Orthopaedics at Groote Schuur Hospital, Cape Town, using the same training set of implantation surgical tools (DePuy Global Advantage fixation shape). For this implantation, viable (unexpired) bone cement, MectaCem II HV (specification provided in Appendix C1), was used for all samples. The bases, sterilised glenoid components, and cement are shown in **Figure 4-5**.

Figure 4-5 *Materials used in the implantation of the glenoid samples (control glenoid components shown)*

The Sawbones bases were prepared for implantation before the cementing process was started. The implantation was performed in a series of sessions, based on the availability of samples from manufacturing. To minimise the negative outcome of uneven cement setting, the number of samples implanted from one pack of cement was limited to a maximum of six, with the surgeon

remaining cognizant of the cement condition during the implantation and stopping the process if it was deemed to have begun to harden. Additional assistants were enlisted to help with the compression of the glenoid into the cement, to speed up the implantation process.

As a check before testing, the initial levels of the implanted samples were measured using a digital inclinometer. No literature was found indicating what an appropriate limit to the level of the glenoid in the standard test should be. Since the test aims for consistency, the samples should ideally be implanted perfectly level. As the real implantation will always have some variation, the standard criterion of peak edge force variation (used in the standard to confirm the starting point of the motion is within the acceptable distance from the centroid) is used as a measure of acceptable component tilt. On this basis, if the component is level enough that the edge forces remain within 10% of each other, the implantation level is deemed acceptable.

4.3.3.2. P90 Test

The P90 test was performed as per the standard specification using the P90 Test Protocol as described in Chapter 2. The test was performed first on 2 control samples, allowing their cyclic testing to begin, and then on 2 novel samples once these were manufactured.

As described in Section 2.6.1, the measured motor torque values were processed by removing those sections of the data where the humeral head had moved off the glenoid, converting the directional values to absolute values, and then finding the location at which the motor torque peaked using the MATLAB curve fitting toolbox. The average data for the four test runs (two per sample, once in each direction) for each design was taken, to calculate the average subluxation distance. The P90 distance (motion amplitude) is then 90% of the subluxation distance.

4.3.3.3. Cyclic Testing

The cyclic loading testing was set up as per the final rig validation testing samples and tested according to the Glenoid Edge Motion protocol as described in Section 2.4.5.3.

The samples were assembled with the angled attachment pin washers and adhesive cap, a minimum of 12 hours before testing, to ensure the adhesive was set. Further, all samples were mounted in the rig so that the 3-pin (inferior) side of the glenoid was always on the LHS.

The cyclic testing was performed according to the Glenoid Edge Motion test protocol, with:

- 10 cycles at conditioning speed (500mm/min).
- 100,000 cycles at the motion parameters as per Section 2.6.2.3, using the control and novel P90 test results for the motion amplitude.
- Sensor setup was performed as per the rig validation testing.
- Water temperature and levels were checked twice a day.

General test rig maintenance was performed between tests, including:

- Replacing the water, cleaning the water bath, and replacing the filter as required.
- Performing bearing turnover between cyclic tests.
- Intermittent re-greasing of bearing shafts, as required.

The testing was performed as test samples were manufactured, with initial testing on 6 control samples. Before the manufacture of the novel samples, a preliminary feasibility check of the novel glenoid design was performed by converting one of the control samples that had already been tested to the novel shape by cutting the surface slots in by hand. This sample was then tested again, to check that the novel design did not have any inherent weakness that would make it unable to survive the testing. The sample survived the feasibility check, so the novel samples were manufactured, and the novel cyclic testing was performed.

After all the standard cyclic tests were complete, additional extended tests (500,000 cycles) were also performed, to observe the response of the test rig and glenoid fixation to longer tests. The extended testing was performed on one novel and one control sample that had already been tested in the standard test, as well as on one of the novel samples previously excluded due to uneven cement.

4.3.3.4. Data Processing

As discussed in Chapter 3, the Motion Calculation MATLAB script protocol converts the sensor readings to edge motions, represented as ~1,000,000 data point vectors. The 'continuous' data (i.e. data vectors containing nine logged data points per cycle, for each variable) are used to observe snapshots of the data relative to HH position but are unnecessarily large for overall edge motion analysis. The Motion Calculation protocol therefore separates each of the continuous vectors into 3 separate vectors, representing the motions of each edge when the HH is at the edges (i.e. at ±P90), and at the centroid. The measurements at the intermediate positions (HH halfway between ±P90 and the centroid) are omitted from the separated vectors. These separate motion vectors are written to a spreadsheet file (PeakOutputSeparate.xls) for further analysis.

The separation of the vectors reduces the size of the vectors to ~100,000 data points for the motions when the HH is at the edges and ~200,000 data points when it is at the centroid (since this is logged twice per cycle) but increases the number of motion variables.

The separated motion variables relate to the different directions of motion (*x,y,α*), the edge in question (LHS, RHS) and the 'state' of the edge (tension, neutral or compression). The state is based on the position of the humeral head relative to the edge in question, for example when the humeral head is at the LHS, the LHS will be in compression, and the RHS in tension (and vice versa), as illustrated in **Figure 4-6**. When the humeral head is at the centroid of the glenoid, both edges will be in their neutral positions. The combination of edge, state, and edge motion direction results in 18 edge motion variables in the output file of the Motion Calculation script. These motion variable vectors are used in the glenoid edge motion analysis, using a further Data Processing MATLAB script, (DataProcessingAll.m, provided in Appendix C2).

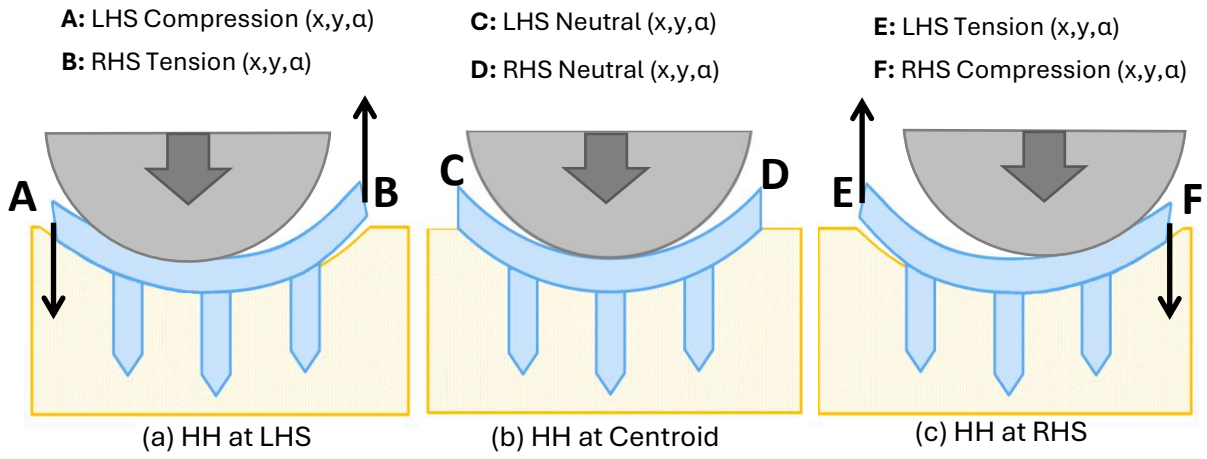

Figure 4-6 *Summary of the motion variables in the output file of the Motion Calculation script (PeakOutputSeparate.xls) for each test run, used as inputs to the Data Processing script. For each edge motion direction (x,y,α), at each of the three HH positions (+P90, centroid, -P90), each edge will be in either tension, compression, or the neutral state.*

The Data Processing script process flow is illustrated in **Figure 4-7**. The script first calls in the edge motion variable vectors from all the test samples (6 control and 6 novel data sets). Next, it reduces the vector sizes further by sampling out every 100th data point, after which the data is smoothed. The smoothing is performed using a Robust Loess method, with a 1% span, which was found to reduce high frequency noise in the data without obscuring data trends. The resultant vectors are then used to calculate the average edge motion vectors of the control and novel glenoid test runs.

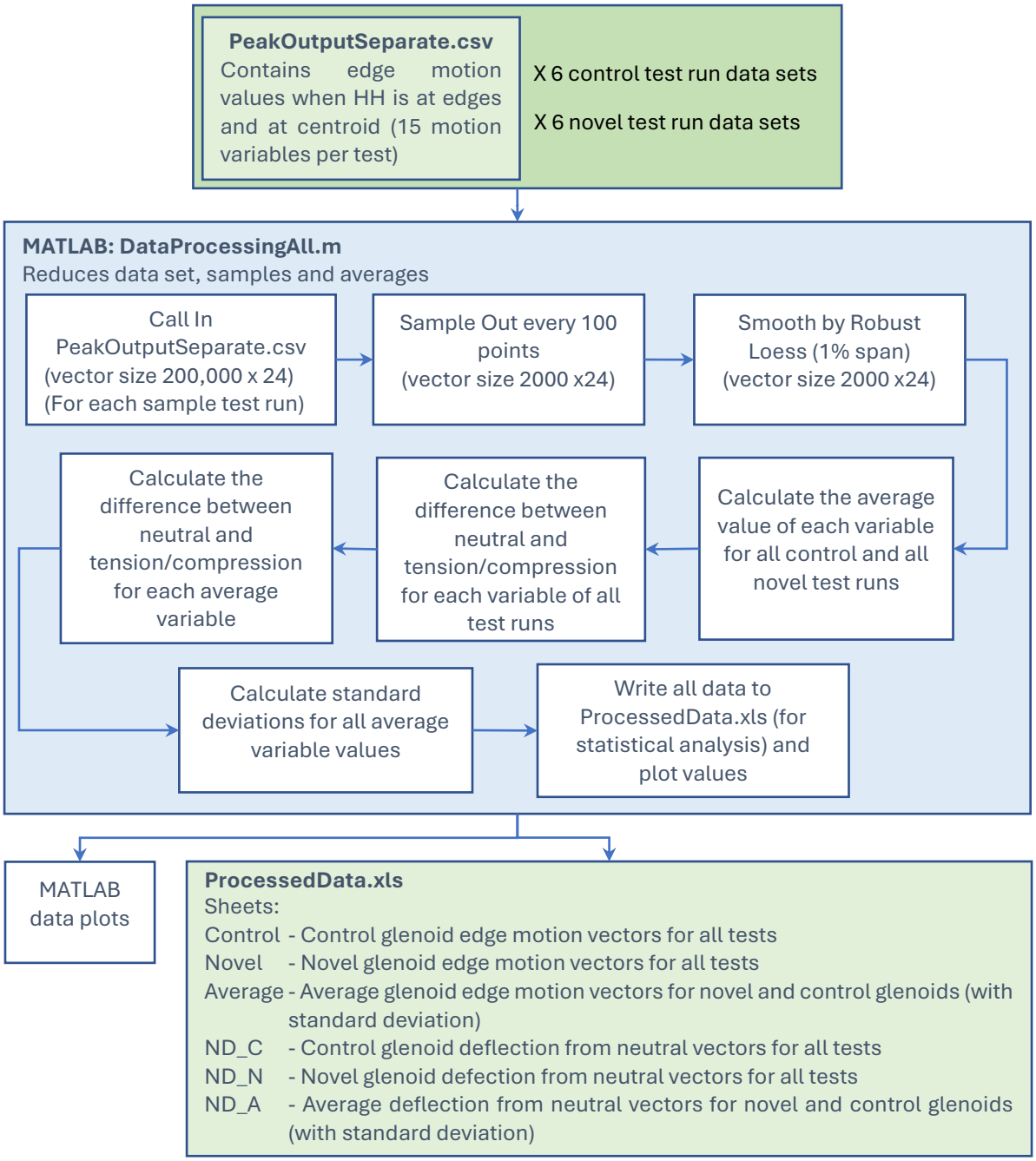

Figure 4-7 *Process flow for the Data Processing MATLAB script, which calls in all individual test data, and outputs combined data to be used in the statistical analysis.*

In the standard, the pass criterion for glenoid design performance is reduced vertical edge motion. This motion is defined as the difference between the position of the edge when loaded in tension, relative to its unloaded position. As the unloaded (neutral) position may vary during the testing, a further variable, neutral deflection (ND), is defined. This expresses the compressive or tensile deflection relative to the current neutral condition for the length of the test. The Data Processing script calculates the ND for each of the motion variables, and then the average and standard deviation for the control and novel glenoid data.

Finally, the protocol writes all calculated values to an output file (ProcessedData.xls) and plots the results. The data in the output file is used as the input into the statistical analysis of the motion trends.

4.3.3.5. Statistical Analysis

Statistical comparison of the novel data to the control data was performed using Statistical Parametric Mapping in 1 dimension (SPM1D). This method uses random field theory to compare two continuous 1D trajectory datasets over their full length. The method was developed by (Pataky, 2010), and is appropriate for comparing 1D datasets that represent a specifically repeated biomechanical action, which in this case is the set 100,000 load cycles. Scripts to perform the analysis are available at https://spm1D.org, which provides MATLAB and PYTHON code for various types of statistical tests for 1D vectors.

As differences between the control and novel edge motions were unknown, a two-sided t-test was used in this research. The datasets were first checked for normality of distribution using the test for normality script in the SPM1D package. Datasets that were normally distributed were analysed using a parametric two-sided t-test. Datasets that were not normally distributed were analysed using a non-parametric two-sided t-test, with 924 permutations (the maximum number of possible permutations for 6 data sets). Both tests plot the threshold t-value for significance, and the alpha (probability (P) for Type 1 error) values when the difference is statistically significant. An alpha value of $P < 0.05$ was used as the threshold for significance in this study.

4.3.4. Results

The results of the sample preparation, P90 test, and cyclic testing are presented here. These results are subsequently discussed in Section 4.4.

4.3.4.1. Sample Preparation

The measures implemented during the implantation of the control and novel glenoid samples (i.e. use of viable cement, limiting the number of samples implanted per pack of cement, and enlisting additional personnel) improved the overall implantation quality in comparison to the rig validation study samples.

The cement distribution for the control glenoids was even, with a thin layer of cement behind the glenoid surface and no obvious raised or unsupported sections of the glenoid. Excess cement around the edges of the glenoids was removed during the implantation before setting. Some samples still required the removal of cement edges to ensure a completely clean surface at the

lever attachment edge. This removal was performed by sanding carefully by hand to ensure the glenoid edge was not damaged.

The cement distribution for the novel glenoids was affected by the surface slots. When the cement was compressed behind the surface, and reached the slots, it tended to fill the slots, and in some cases did not continue evenly to the other side of the slot. This resulted in two samples with unsupported outer edges. Considering the surface fractures associated with unsupported edges in the rig validation study, these two samples were deemed undesirable and excluded for use in the testing.

Further, the novel glenoids were manufactured with the attachment pin-hole already in place. This pin-hole is open to the slot on the inside, and the cement also moved into these holes when it filled the slot. Both the slot and the pin holes were cleared as much as possible while the cement was still hardening, but both required further clearing during the sample assembly stage. This clearing was done by carefully removing the unwanted cement with a pin.

The implantation levels of the glenoids were measured when they were assembled in the sample assembly. The level was measured across the highest points of the glenoid edges. A clockwise rotation around the centroid was taken as a positive implantation angle, and anticlockwise as negative, as indicated in **Figure 4-8**.

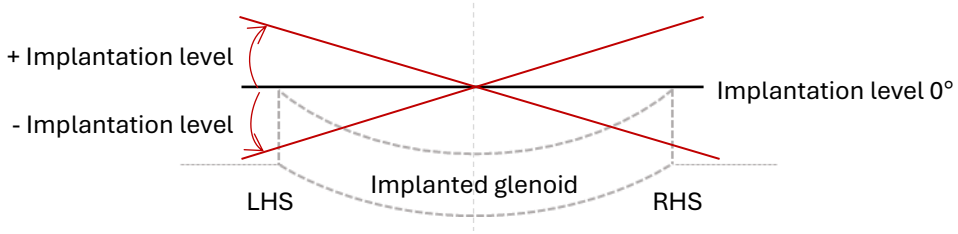

Figure 4-8 *Definition and directionality of glenoid implantation level.*

The measured implantation levels were all within 1.8° of level as listed in **Table 4-1**. Most samples were <0.5° from level, four samples between 0.5° and 1.5° (C4, C1, C5, N3) and one sample (C8) at 1.7°. An additional sample (N7) was 1.74° off level, but this sample was one of those excluded due to unsupported edges (it was measured as it was used in the additional extended testing).

Table 4-1 *Summary of Implantation levels for all control and novel glenoid samples*

Control Glenoids (C)		Novel Glenoids (N)	
Sample No	**Implantation Level**	**Sample No**	**Implantation Level**
C P90 1	-0.08°	**N P90 1**	0.37°
C P90 2	0.31°	**N P90 2**	-0.04°
C1	1.12°	**N1**	-0.07°
C2	-0.18°	**N2**	-0.01°
C3	0.17°	**N3**	-1.39°
C4	-1.25° (data lost, lever failure)	**N4**	0.19°
C5	0.68° (data lost, lever failure)	**N5**	0.44°
C6	0.43°	**N6**	-0.07°
C7	0.46°	**N7**	-1.74 (excluded, used in extended test)
C8	-1.7°	**N8**	Not measured (excluded, uneven cement)

The acceptability of the levels is gauged by whether the edge loading forces remain within 10% of each other, for each sample. From the results shown, the three samples with the largest starting level variation were C1 (1.12°), C8 (-1.7°), and N3(-1.39°). The peak edge forces for these three samples are shown in **Figure 4-9**, where the maximum variation between the peak edge forces is 2.1%, seen at 21,561 cycles for sample C1. The comparative edge forces for the remaining samples were all also within the 10% variation criterion.

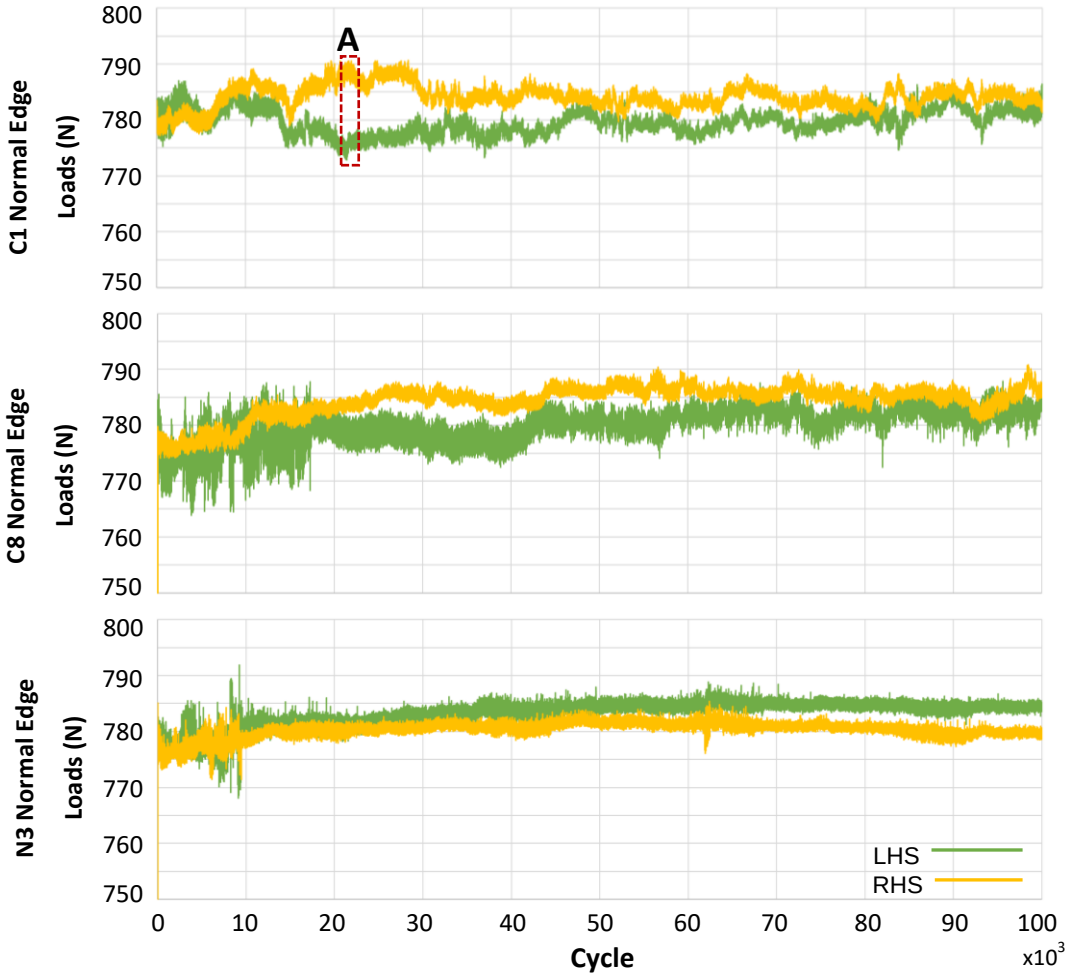

A: Maximum variation in normal load between LHS and RHS is 2.1% at cycle 21,561 for sample C1

Figure 4-9 *Normal load at the edges for samples C1, C8 and N3 which had the least level implantation. The largest difference in measured normal load between the LHS and RHS edges was for sample C1, where a 2.1% variation occurred at cycle 21,561.*

4.3.4.2. Control and Novel P90 Tests

The P90 test was performed on two control glenoid samples, and two novel glenoid samples. The test resulted in material creep deformation of the edges of the glenoids as expected. The before and after shapes of the glenoid are shown for one of each of the control and the novel samples, in **Figure 4-10** and **Figure 4-11**, respectively. The control sample exhibits a local 'cold flow' deformation at the glenoid edge. The novel sample also has the 'cold flow' edge deformation, but there is a noticeable 'stretching' deformation resulting in elongation of the sample body, not seen in the control.

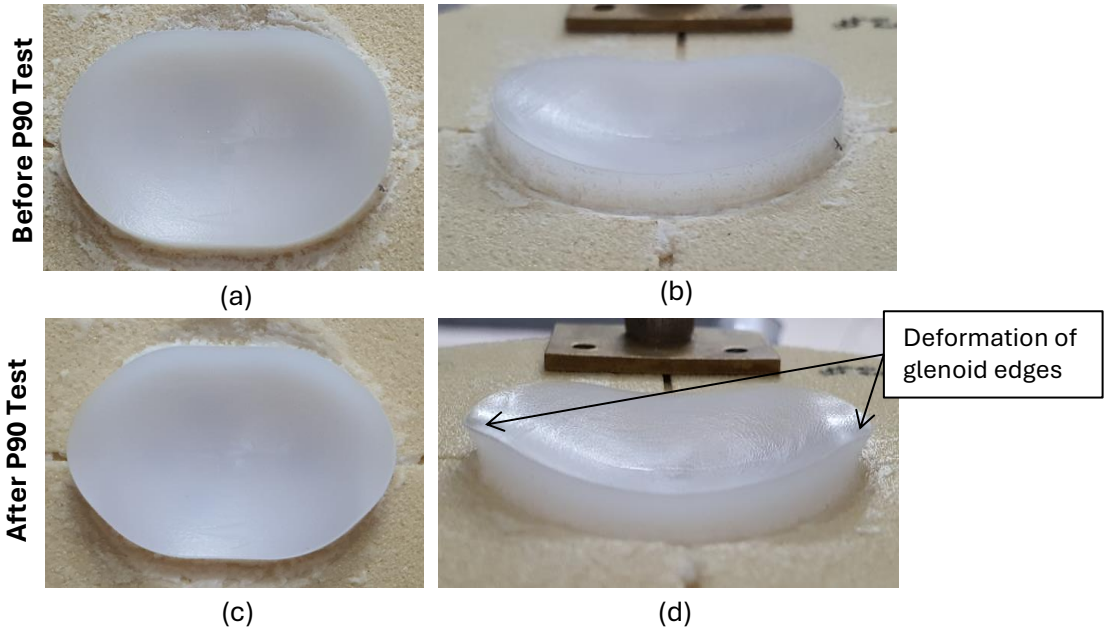

Figure 4-10 *Top and side view of sample C P90 2 before (a,b) and after (c,d) the P90 test. The edges of the sample are deformed, as is expected after this test.*

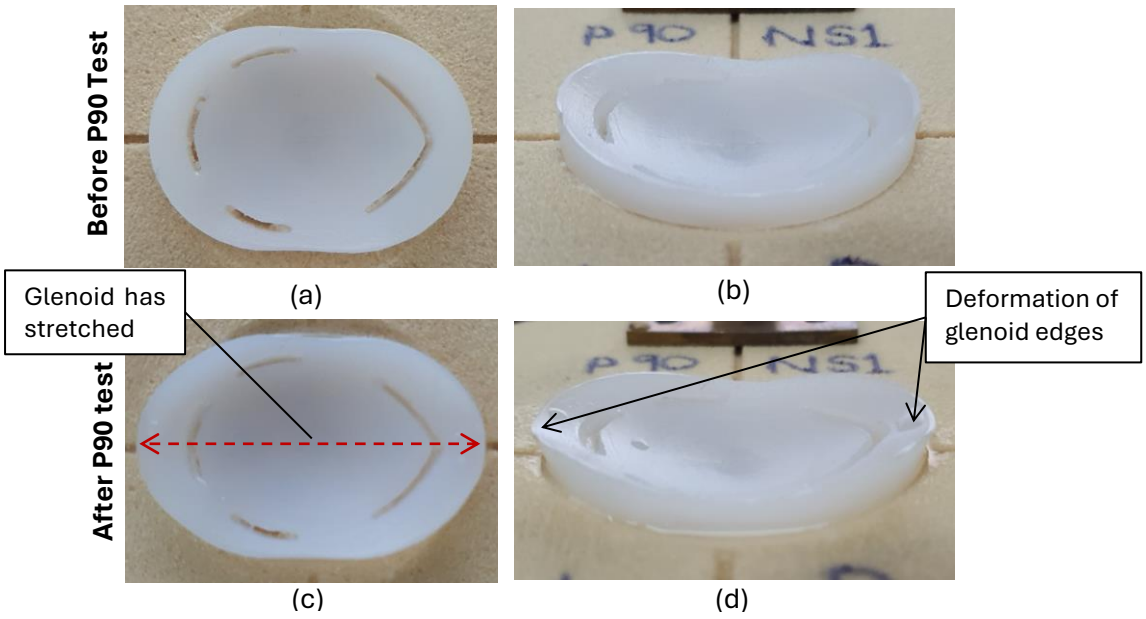

Figure 4-11 *Top and side view of sample N P90 1 before (a,b) and after (c,d) the P90 test. The edges of the sample are deformed, as is expected after this test. The sample is also stretched along the axis of motion, shown in (c).*

The control and novel subluxation distance results are shown in **Figure 4-12**, for both directions of the two samples of each design. The data are truncated and normalised to absolute values of torque and distance from the centroid, as per the P90 data processing protocol discussed in Section 2.6.1.

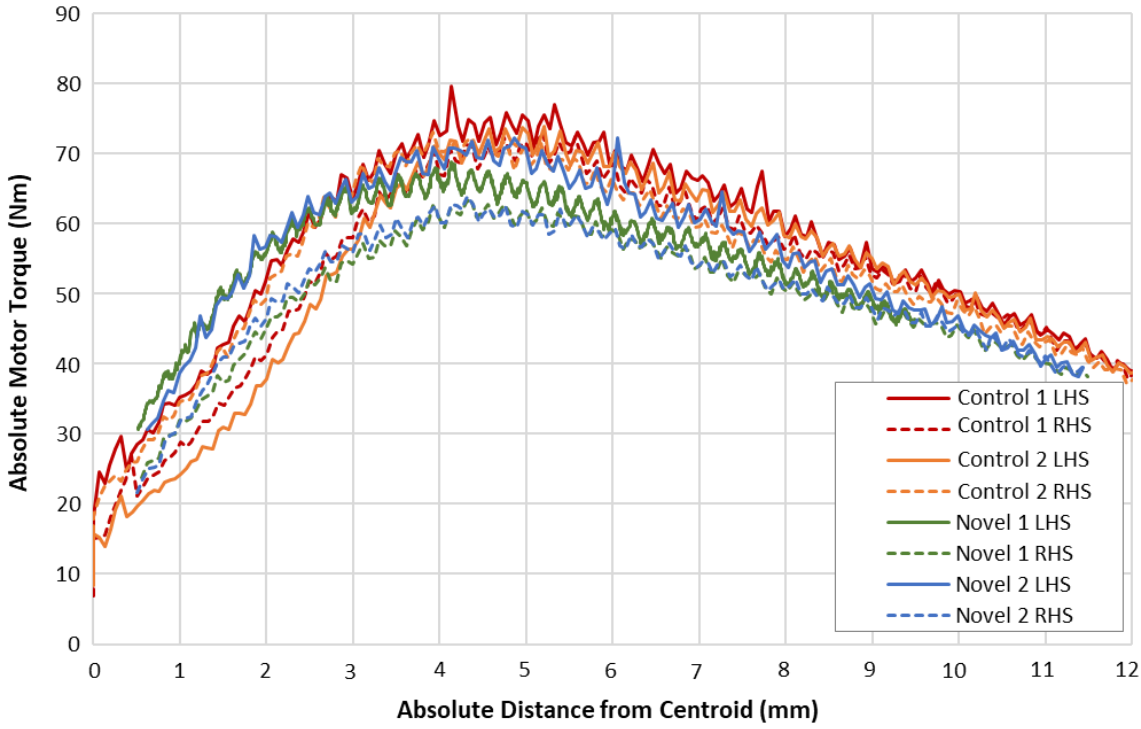

Figure 4-12 *Absolute motor torque for two control and two novel samples, each of which was tested in both directions. The data are truncated to include only the portion of the test before the HH has moved out of contact with the glenoid and are normalised to absolute values of motor torque and distance from the centroid.*

The data were fitted using the MATLAB Curve fit toolbox, to determine the fit with the minimum root mean squares error for each curve. From this, the peak location for each of the runs was determined as listed in **Table 4-2**. The control data was collected first, from which the subluxation distance of 4.6mm, and corresponding P90 distance of 4.2mm, were determined and used in the control testing.

Table 4-2 *Measured subluxation distances for the two tested control glenoid samples*

Subluxation Distances for Sample C P90 1		**Subluxation Distances for Sample C P90 2**		**Average Subluxation Distance**
LHS	RHS	LHS	RHS	4.6 (±0.2) mm
4.6mm	4.75mm	4.8mm	4.25mm	

Once the novel samples became available, their P90 test was performed. The results from the novel test produced a subluxation distance of 4.4mm, from which a P90 of 4.0mm is determined, as listed in **Table 4-3**.

Table 4-3 Measured subluxation distances for the two tested novel glenoid samples

Subluxation Distances for Sample N P90 1		Subluxation Distances for Sample N P90 2		Average Subluxation Distances
LHS	RHS	LHS	RHS	4.4mm(±0.2mm)
4.13mm	4.64mm	4.35mm	4.42m	

Since the 0.2mm variation is within the standard deviation of the overall test results, and less than the allowable starting point variation of ±0.5mm set by the standard, it was determined that for consistency between the cyclic tests, the same P90 distance (4.2mm) would be used for the novel testing as well.

4.3.4.3. Cyclic Testing Results

The cyclic test results are presented first by giving a general summary of the testing performed, and the observations made before and after the tests, with a focus on lever and glenoid fixation survival, and troubleshooting performed during the testing. The resultant edge motions for all the tests, as well as the deflection from neutral values, are presented as comparative average values for each motion direction and state, for both edges. The edge motion data for each of the individual glenoid samples is provided in Appendix C3. Finally, the results of the additional, extended tests are given.

For the standard-length tests, 8 controls were tested, from which two data sets were discarded due to lever fixation failures. Six novel glenoids were tested, with no failed tests. This gives 6 data sets per design, which is double the standard minimum requirement and the same sample size used by Stautberg et al. (2017) in their ASTM F2028 based evaluation of glenoids with differing peg numbers.

All glenoids were checked to note if fixation failure had occurred, or begun to occur, resulting in the glenoid being loose enough to move perceptibly when alternating pressure was applied by thumbs to the glenoid edges. No glenoids (control or novel) showed observable loosening during the standard-length test, including the re-tested control, C1. The survival of all the samples' fixation motivated the extended testing.

Two tests, C4 and C5, suffered complete lever detachment of one of the levers during the test. Both these samples were flagged for poor lever fixation before the testing started, but the tests were attempted anyway. The poor fixation was due to errors made during the pin-hole drilling by hand with a Dremel. The pin-hole on sample C4 was too wide to allow the thread of the pin to

take at all. An attempt was made to close the hole using a '3D-pen' with PLA material to create a plug around the pin. This showed initial promise but failed entirely at 5640 cycles. The initial fix of the lever on sample C5 was not as severely compromised, but the fixation pin felt like it had 'stripped' the material inside the pinhole (i.e. it did not reach a point where it would no longer turn without force). This lever survived longer but suffered fixation failure at around 35,000 cycles. To avoid future failures caused by human error in the hole drilling, the pinhole was added to the CNC design of all samples not yet manufactured. This included all the novel samples, and two additional control samples (C7 and C8) manufactured to replace the lost data. The validity of the previously hand-drilled data was judged based on the final lever fixation integrity after testing was completed, as listed in **Table 4-4**.

During testing, as data processing was performed, it was noted that a signal 'short' was occurring in some data sets (C1, C6, N1), where the measured sensor deflection was hitting the sensor rail (i.e. it read $1x10^6$ mm). This short was isolated to sensor S_{1L}. The sensor was replaced by a captive bushing LVDT sensor of similar electronic properties (datasheet provided in Appendix B1) from test N3 onwards. A filter was added to the edge motion calculation that excluded the short values, and the remaining data were retained for analysis. The standard-length cyclic tests performed are summarised in **Table 4-4**, in the order of testing, with observations from the testing noted. These results are discussed in Section 4.4.3.

Table 4-4 *Summary of standard-length (100,000 cycle) glenoid loading tests, in the order of testing.*

Sample	Cycles	Notes at Setup	Observations after Test	Comments
C1	100,000	Both levers have firm fix	Levers still firm, glenoid fixation still firm	3 'short' data points filtered out of S1L data
C2	100,000	Both levers have firm fix	Levers still firm, glenoid fixation still firm	
C1 (mod)	100,000	Sample C1 modified by hand to novel design, lever pinholes re-used	Levers still firm, glenoid fixation still firm Sample did not break	Modified sample was tested as 'first pass' check to ensure the novel design could survive 100,000 cycles, before prototype manufacture.
C3	100,000	Both levers have firm fix	Levers still firm, glenoid fixation still firm	
C4	100,000	LHS lever fix compromised – pin hole badly drilled. Attempted to attach using '3D pens' PLA plug.	LHS lever detached completely at 5640 cycles. Data set discarded.	Data Not used.
C5	100,000	LHS lever firm, RHS lever slightly compromised (thread felt like it started to strip on assembly).	RHS lever detached at 35 700 cycles. Data set discarded	Data not used. Additional control samples manufactured to make up for lost data. Pin holes to be added by CNC to prevent further human error.
C6	100,000	Both levers have firm fix	Levers still firm, glenoid fixation still firm	57 'short' data points filtered out of S1L data
N1	100,000	Both levers have firm fix	Levers still firm, glenoid fixation still firm	34 'short' data points filtered out of S1L data
N2	100,000	Both levers have firm fix	Levers still firm, glenoid fixation still firm	
N3	100,000	Both levers have firm fix	Levers still firm, glenoid fixation still firm	New sensor S1L assembled to rig.
N4	100,000	Both levers have firm fix	Levers still firm, glenoid fixation still firm	
N5	100,000	Both levers have firm fix	Levers still firm, glenoid fixation still firm	
N6	100,000	Both levers have firm fix	Levers still firm, glenoid fixation still firm	
C7	100,000	Both levers have firm fix	Levers still firm, glenoid fixation still firm	
C8	100,000	Both levers have firm fix	Levers still firm, glenoid fixation still firm	

The measured glenoid edge motions are presented in this section based on the condition (compression, neutral, or tension) experienced by each edge, which depends on the location of the humeral head relative to that edge. As discussed in Section 3.5.1, the direction of motion induced at the two edges for the same condition will not always be the same, since the overall direction of motion is held to the chosen global convention. This is illustrated in **Figure 4-13**, for a compressive motion at each edge. In this condition, the LHS edge will be expected to have negative vertical (y), horizontal (x), and tilt (α) motions, while the RHS edge would be expected to have a negative y-motion, but positive x and α motions.

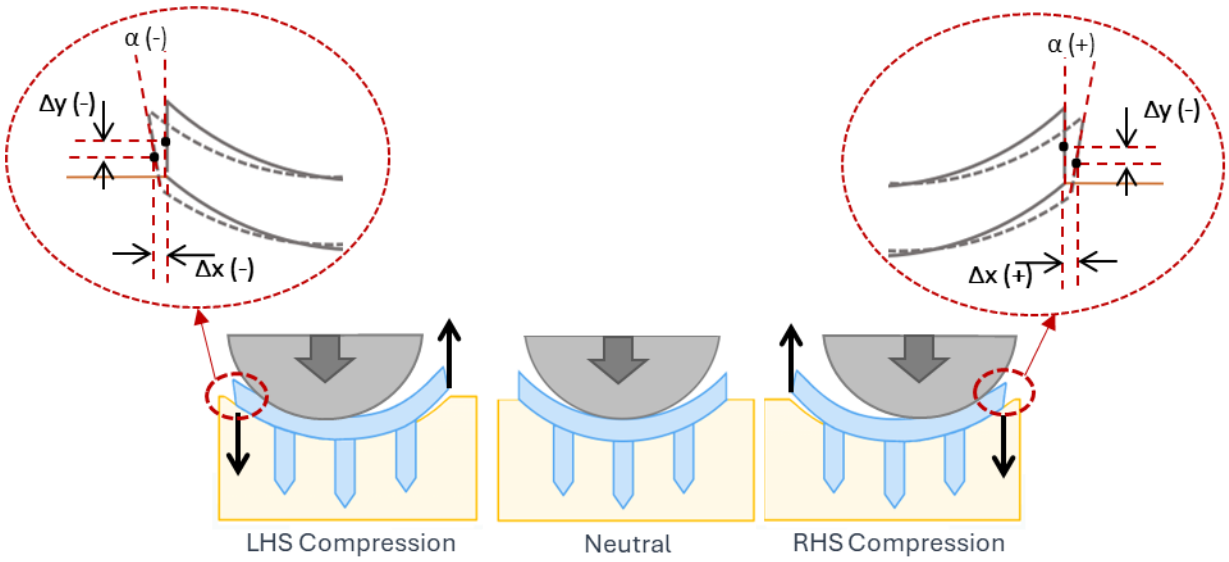

Figure 4-13 *Expected motion directions for compression at the LHS and RHS edges. The LHS edge under compression is expected to move downwards into the Sawbones (-Δy), leftward away from the centroid (-Δx) and with an outward, anti-clockwise tilt (-α). The RHS edge under compression is expected to move downwards (-Δy), rightwards away from the centroid (+Δx) and with an outward clockwise tilt (+α).*

The average edge motions in each direction (vertical, horizontal, and tilt) for the control and novel data are plotted for the three conditions (tension, neutral, compression), for each edge. Standard deviations of the average data are shown as shade plots on each curve. Where statistical significance ($P<0.05$) between the respective curves of the control and novel data was found, it is indicated by bars on the plots, for the cycle duration that significance persists. The motions plotted begin with a zero-position taken after the 10 cycles of conditioning are completed.

In this section, the motion results are described and general trends in the data are observed. These results are interpreted in the discussion section at the end of this chapter (Section 4.4.3).

VERTICAL GLENOID EDGE MOTION:

The vertical glenoid edge motion is shown in **Figure 4-14**. Looking at overall trends in the motion for both designs, we see that in the early stage of the test (first 200 cycles), there is a movement down into the surface for all states.

The neutral position drops from 0mm (initial position) to -0.2mm for the control and -0.25mm for the novel on the LHS, and -0.15mm for both the control and novel on the RHS. After this, the downward movement continues at a slower rate for 10,000 to 20,000 cycles, until the samples 'settle' at a near equilibrium position. For the LHS control, the neutral position reaches -0.26mm at 20,000 cycles, and then takes the remainder of the 100,000 cycles to drop a further -0.04mm, ending the test -0.3mm below the starting point. The LHS novel neutral position runs almost parallel to the control, approximately -0.05mm lower. The RHS control neutral position drops to -0.2mm after 20,000 cycles, and then a further -0.05mm for the remainder of the test. The RHS novel neutral position again runs almost parallel to the control, approximately -0.05mm lower. *In summary, both edges in the **neutral position** sink down into the Sawbones, rapidly at first, before reaching a steady state position. On both edges, the novel sinks down further than the control.*

The tension and compression deflections follow a similar trend to the neutral position, with an early drop, followed by settling to almost equilibrium for the remainder of the tests. *The position of each edge in **tensile** distraction lifts 'above' the neutral position of the edge but remains below the starting (zero) position for the duration of the test*. This drop below the starting position is between -0.15mm and -0.3mm for the LHS of control and novel respectively, and approximately -0.15mm for the RHS of both novel and control.

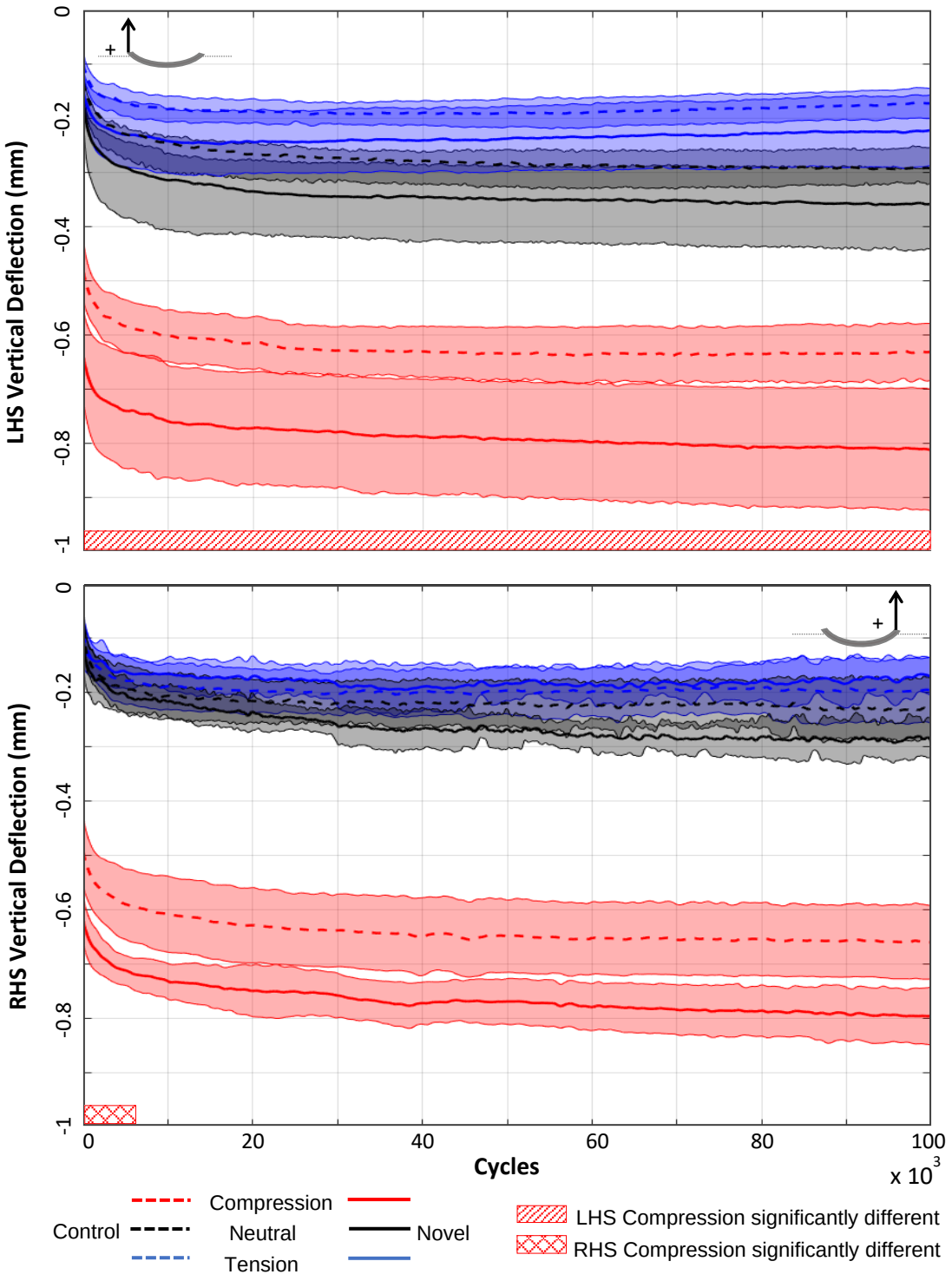

Figure 4-14 *Mean vertical edge deflection of the control and novel glenoids for 100,000 load cycles. The compressive (red), neutral (black), and tensile (blue) deflections are shown for the LHS edge (above) and RHS edge (below). All edge motions exhibit an initial fast change as the edges sink down into the surface, after which a relatively steady or slowly decreasing position is maintained for each state. Statistically significant differences between the control and novel glenoids are indicated for the LHS compressive deflection over the length of the test, and for the RHS compressive deflection for the first 7,000 cycles.*

The compressive position drops almost immediately to -0.5mm for the control and -0.65mm for the novel for both edges It levels out at approximately -0.65mm for the control and slowly decreases to -0.8mm for the novel, again for both edges. The difference between the control and novel glenoids in vertical compression on the LHS is significantly different ($P<0.05$) for the full length of the test. On the RHS, a significant difference ($P<0.05$) was found for approximately the first 7,000 cycles. *In summary, in* ***compression****, both edges sink deeper into the surface than their neutral positions. The downward motion of the novel glenoid is greater than the control glenoid for both edges*.

The vertical deflections in tension and compression normalised to the prevailing neutral position (neutral deflections (ND)) are shown in **Figure 4-15**. The ND plots are shown on the same scale as the overall edge motion plots (approximately 1mm on the y-axis), for comparison of the ND amplitudes to the overall edge motion.

In tension for the LHS, the distraction above neutral starts at approximately +0.05mm for both glenoid designs, and increases gradually as the test proceeds, approaching +0.1mm above the neutral at the end of the test. There was no statistical difference between the control and novel motion on this edge. For the RHS, the tensile distraction again starts near +0.05mm and increases to +0.1mm for the novel glenoid, while for the control the motion starts at 0mm and increases to +0.25mm. These RHS vertical deflections from neutral were significantly different ($P <0.05$) from approximately 15,000 cycles and remained so for the duration of the test. *In summary, the* ***ND in tension*** *increases gradually for the duration of the test for both edges. At the RHS edge to novel glenoid distracts further upward from its neutral than the control glenoid does*.

In compression on the LHS, both the novel and control ND remained moderately constant for the duration of the test, with the control -0.35mm below the neutral and the novel -0.45 below the neutral. This difference was sporadically statistically significant for brief periods along the length of the test (as indicated by the bars on the LHS plot in **Figure 4-15**), but was largely not statistically significant. For the RHS the compressive ND showed a similar trend to the LHS but was approximately -0.05mm lower than the LHS for the respective glenoids. For the first 18,000 cycles, the RHS compressive ND was significantly different ($P<0.05$) between the control and the novel glenoids. *In summary, in* ***compression****, the* ***ND*** *is relatively constant for the duration of the test for both edges, with the novel glenoid deflecting further down from its neutral than the control*.

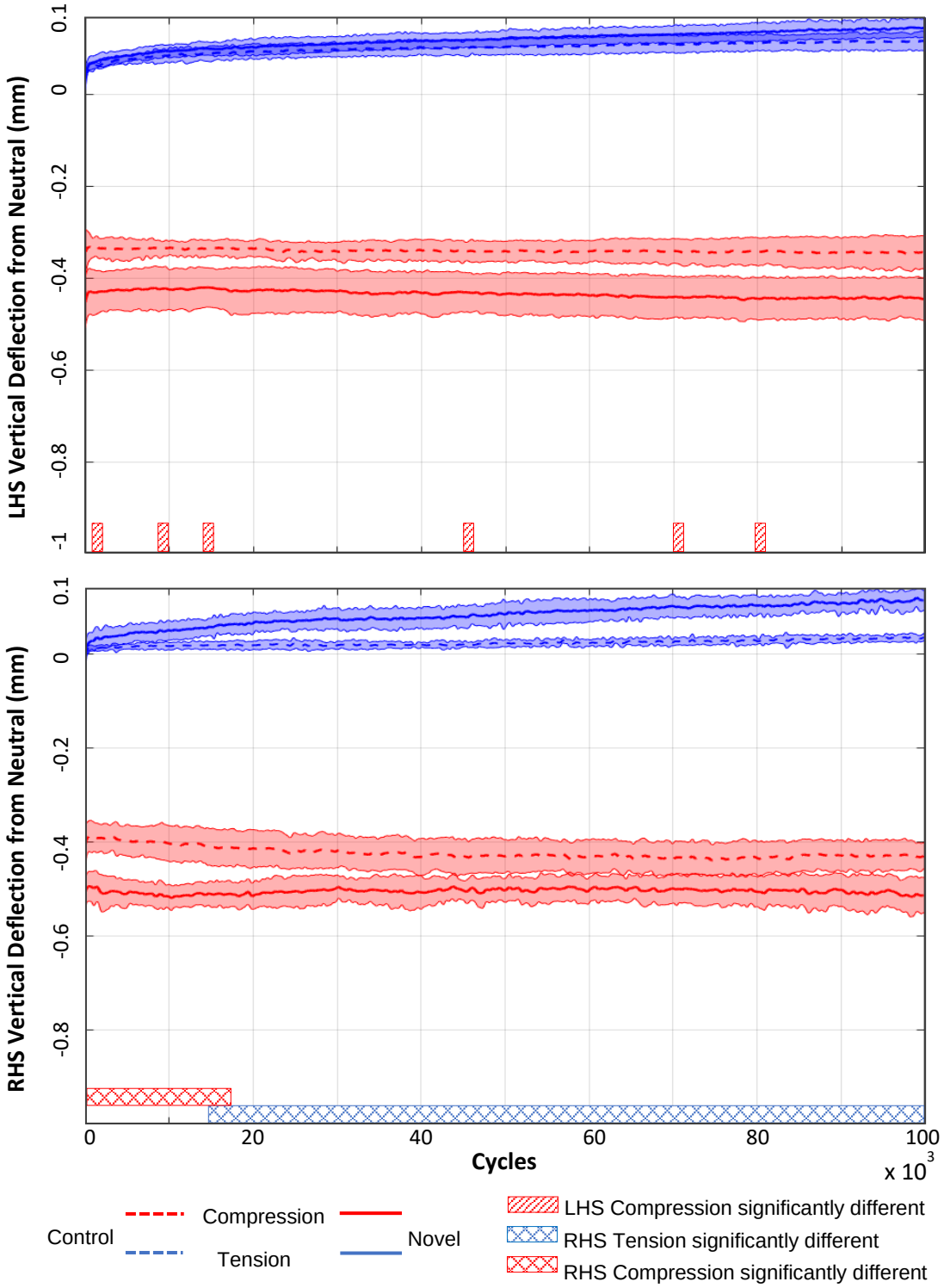

Figure 4-15 *Vertical ND for the novel and control glenoids. In the figure, the origin of the y-axis represents the prevailing position of the glenoid edge when the HH is at the centroid, and the ND in tension (blue) and compression (red), represent the motion of the edges away from the neutral position. The positive tensile ND indicates the edges are lifting above the neutral, with a gradually increasing magnitude. The negative compressive ND indicates the edges are depressing further into the Sawbones surface.*

HORIZONTAL MOTION

The horizontal deflections for the three edge conditions are shown in **Figure 4-16**. As for the vertical motion, the neutral position of the edge is seen to change initially before settling into an equilibrium position, with the tensile and compressive motions moving around the neutral. For the horizontal motions, no significant difference was found between the control and novel glenoids for any of the edge conditions.

For the LHS, the neutral shift of the edge is in the negative direction, i.e. outwards to the left, reaching -0.15mm and -0.18mm for the control and novel respectively at 20 000cycles, and then both dropping a further -0.03mm by the end of the test. The RHS neutral position shows a similar pattern but moves in the positive (outward to the right) direction. The control and novel reach +0.2mm and 0.24mm respectively by 20,000 cycles, and both end the test at +0.24mm. *In summary, the **neutral position** of both edges, for both glenoid designs, moves outward away from the centroid as the test proceeds*.

The tensile motions at the LHS for the control and novel follow each other very closely, both reaching -0.21mm at 20,000 cycles, and remaining at this position for the duration of the test. On the RHS, the control moves to +0.15mm and the novel to +0.2mm by 20,000 cycles, and both remain at this level for the remainder of the test. As was observed for the vertical tensile motions, it is again noted that *even though the **tensile** distractions are 'inwards' relative to the neutral position for both edges, they remain 'outward' of their starting positions for the full test*.

The edges both move distinctly outward in compression. The LHS control and novel reach -0.53mm and -0.59mm respectively at 20,000 cycles and then move outward (to the left) another -0.03mm for the remainder of the test. For the RHS, the control and novel follow each other closely, both reaching +0.48mm at 20,000 cycles and then moving outward (to the right) by a further +0.02mm by the end of the test. *In summary, in **compression**, both edges for both designs move even further outwards away from the centroid*.

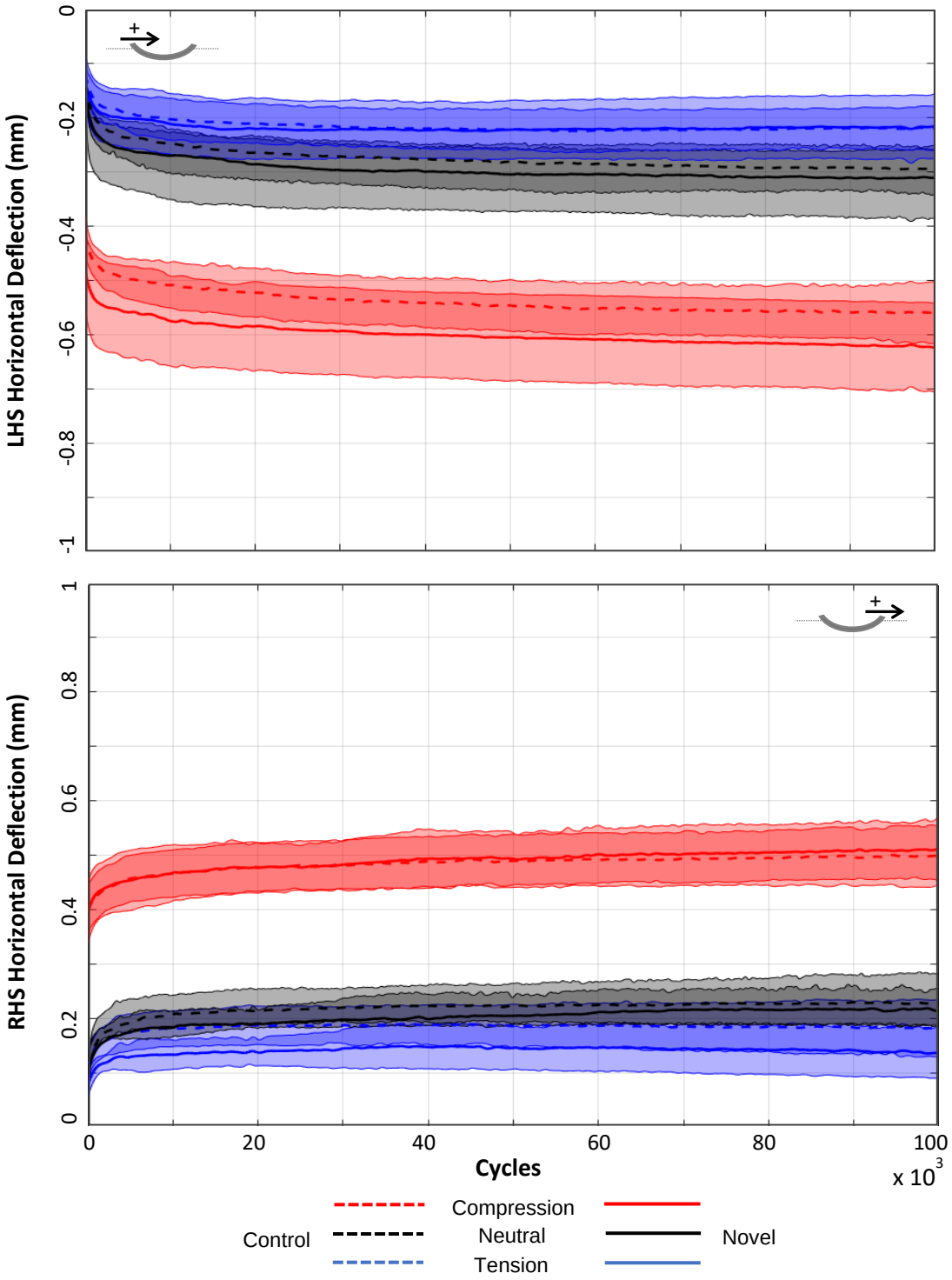

Figure 4-16 *Mean horizontal edge deflection of the control and novel glenoids for 100,000 load cycles. The compressive (red), neutral (black), and tensile (blue) deflections are shown for the LHS edge (above) and RHS edge (below). All edge motions exhibit an initial fast change as the edges move outwards from the centroid, after which a relatively steady position is maintained for each state. No statistically significant differences between the control and novel glenoids were observed.*

The horizontal ND motions are shown in **Figure 4-17**. As observed for the overall motions, no statistical difference was found for the horizontal ND motions.

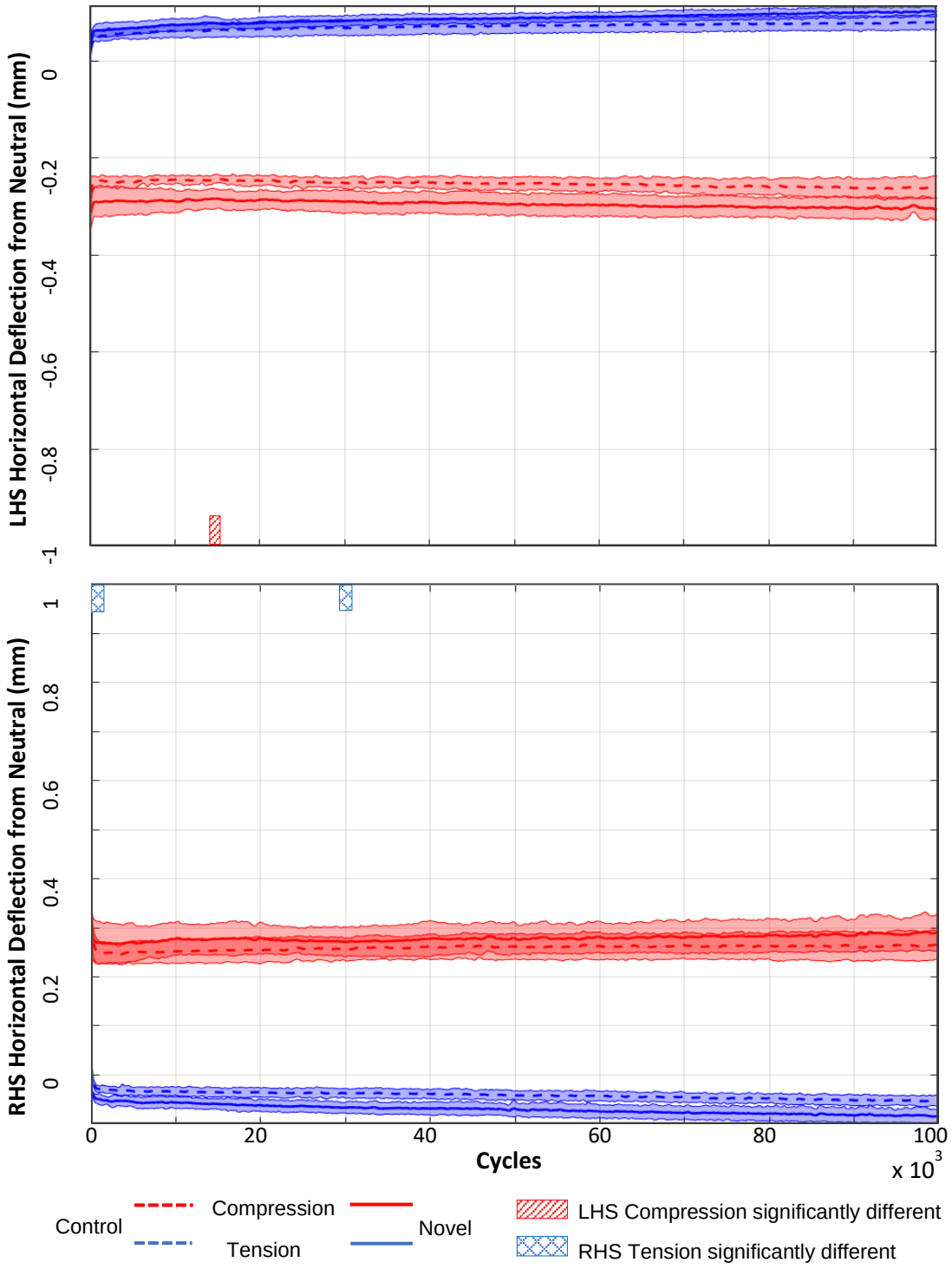

Figure 4-17 *Horizontal deflection from neutral for the control and novel glenoids. In the figure the origin of the y-axis represents the prevailing position of the glenoid edge when the HH is at the centroid, and the ND in tension (blue) and compression (red), represent the motion of the edges away from the neutral position. Both edges move slightly inward of the neutral position in tension and outwards from the neutral in compression.*

For tension on the LHS both the control and novel start at approximately +0.05mm, and then steadily approach +0.1mm by the end of the test. On the RHS the control moves from -0.025mm to -0.5mm, while the novel data moves from approximately -0.05mm to -0.1mm. For the LHS compressive ND, the control maintains an outward (to the left) motion of around -0.25mm for the duration of the test, and the novel maintains a motion of -0.3mm. At the RHS the compressive ND for both the novel and control remain near +0.35 for the duration of the test. *In summary, for both the LHS and the RHS for both glenoid designs, there is a small but gradually increasing inward **ND** motion during **tension**, and a level, larger, outward **ND** motion in **compression**.*

TILT MOTION

The tilting motion for the three edge states is shown in **Figure 4-18**. As for the other motions, there is again an initial period of rapid change, followed by a levelling-off of the deflections.

For the LHS neutral position, the control reaches a tilt of -1° (i.e. 1° outwards to the left) within 10,000 cycles and maintains this tilt for the remainder of the test. The LHS novel design neutral tilt position shifts to -2° within 10,000 cycles and also remains constant for the remainder of the test. The RHS neutral position of the control glenoid moves 0.9° (i.e. outwards to the right) in the first 10,000 cycles, and then slowly decreases to 0.8° at the end of the test. The RHS novel neutral position moves to 1.3° in the first 10,000 cycles and remains at this tilt for the remainder of the test. The difference between the control and novel tilt in neutral was found to be significant ($P<0.05$) for approximately the first 5000 cycles. *In summary, the **neutral position** of both edges **tilts** outwards in the early stages of the test and then remains that way or decreases slightly (RHS control) as the test proceeds.*

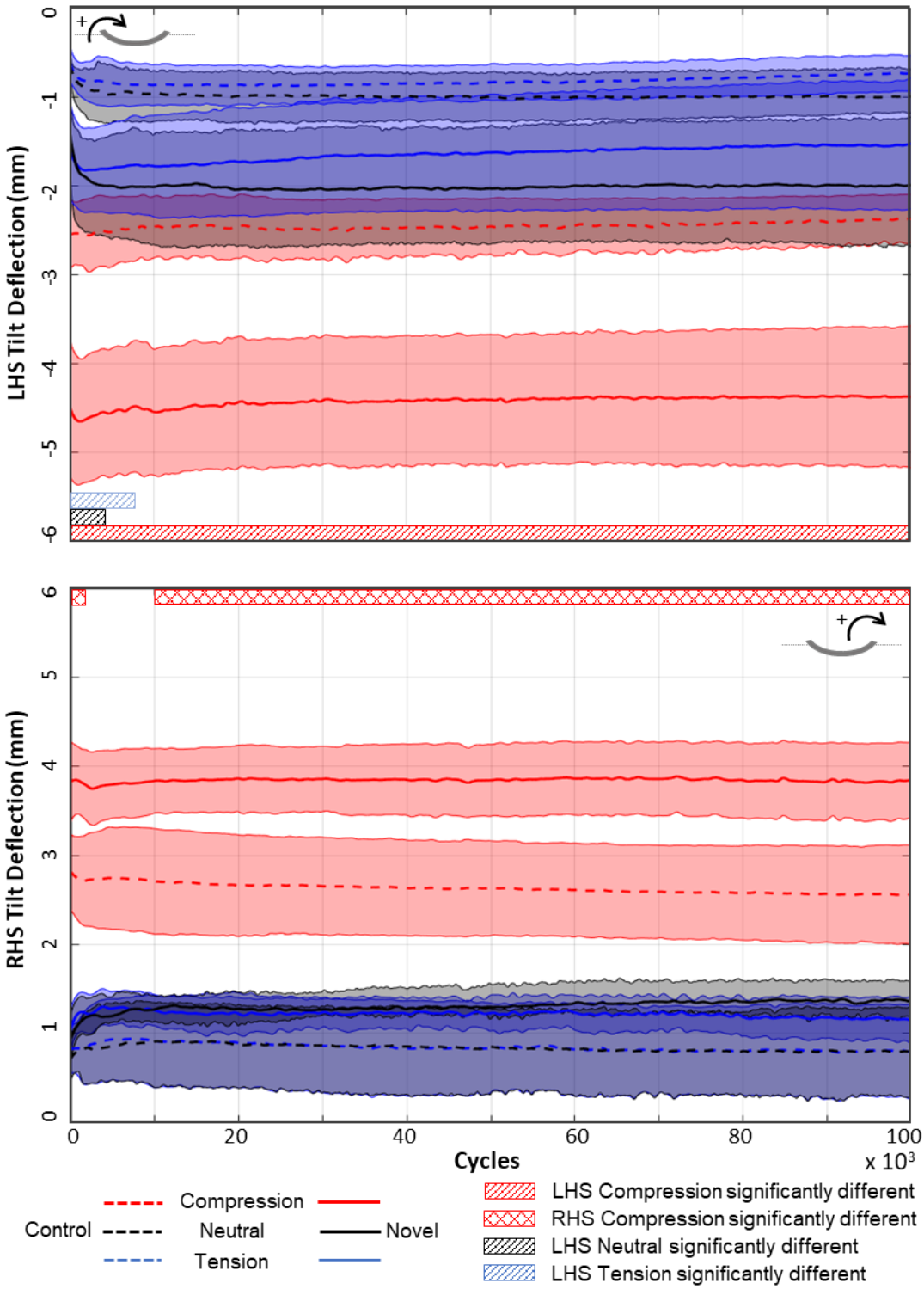

Figure 4-18 *Mean tilt deflection of control and novel glenoids for 100,000 load cycles. The compressive (red), neutral (black), and tensile (blue) deflections are shown for the LHS edge (above) and RHS edge (below). All edge motions exhibit an initial fast outward tilt, which then remains relatively steady for the remainder of the test. Statistically significant differences between the control and novel glenoids were found for all motions at the LHS at the start of the test, as indicated. The compressive motions were found to be significantly different at both edges for the duration of the test, except for the period of 2000 to 10,000 cycles on the RHS)*

On the LHS, the tensile tilt of the control glenoid reaches -0.8° in the first 10,000 cycles, and then slowly increases to -0.6° by the end of the test (i.e. the amount of total outward rotation decreases as the test proceeds). The LHS novel glenoid tilt moves with the neutral position to -1.8° at approximately 2000 cycles, after which it steadily increases to -1.5° at the end of the test. The LHS tensile tilt levels of the control and novel glenoids were found to be significantly different for the first 8000 cycles. On the RHS of the control glenoid, the tilt in tension follows the tilt in the neutral state closely, reaching a maximum of 0.95° within the first 10,000 cycles and then gradually decreasing to 0.8°. On the RHS of the novel glenoid, the tilt in tension also follows the neutral position closely reaching a maximum of 1.3° within the first 5000 cycles, but with a very gradual decrease in outward tilt as the test proceeds, to a final position of 1.2°. *In summary, both edges remain **tilted** outwards in **tension** relative to their starting position, by a gradually decreasing amount towards the end of the test.*

The compressive tilt shows a distinct outward rotation at both edges and for both designs. The LHS control glenoid compressive tilt moves almost immediately to -2.5° and remains at this level for the duration of the test. The LHS novel glenoid tilts outward by -4.5° at the start of the test. The edge tilts further outward to -4.7°, in the first 2000 cycles, after which it slowly returns to -4.5° and remains so for the rest of the test. The larger degree of outward tilt of the novel glenoid at the LHS was significantly different from the control for the duration of the test.

The RHS control glenoid edge tilts immediately to 2.8° in compression, and slowly decreases to 2.6° by the end of the test. The RHS novel also shows a small peak and dip in the first 2000 cycles, where the tilt moves at first to 3.8°, then briefly up to 3.9°, before dropping back to 3.8° and finally slowly moving back to 3.9° by 20,000 cycles, where it remains until the end of the test. The novel and control overall compressive tilt on the RHS were found to be significantly different except for the period between 2000 and 10,000 cycles. *In summary, in **compression**, both edges of both glenoid designs **tilt** distinctly outward from the start of the test, with the novel glenoid exhibiting a significantly larger tilt than the control. A brief outward tilt peak is seen at or near the start of the test (except at the LHS control), after which the tilt remains constant or gradually decreases as the test proceeds.*

The tilt deflections from the prevailing neutral position are given in **Figure 4-19**. In tension on the LHS, the control glenoid ND tilt is inward by 0.2° for the whole test, while the novel glenoid ND tilt starts at 0.2°, and slowly increases to 0.4° by the end of the test. On the RHS in tension, the control glenoid exhibits almost no ND tilt, remaining steadily at 0° for the duration of the test. The novel glenoid ND tilt starts at 0° and reaches -0.4° by the end of the test. There was no statistical

difference between the control and novel glenoid ND tilt on the LHS, but on the RHS the novel ND tilt was significantly more than the control from 53,000 cycles until the end of the test.

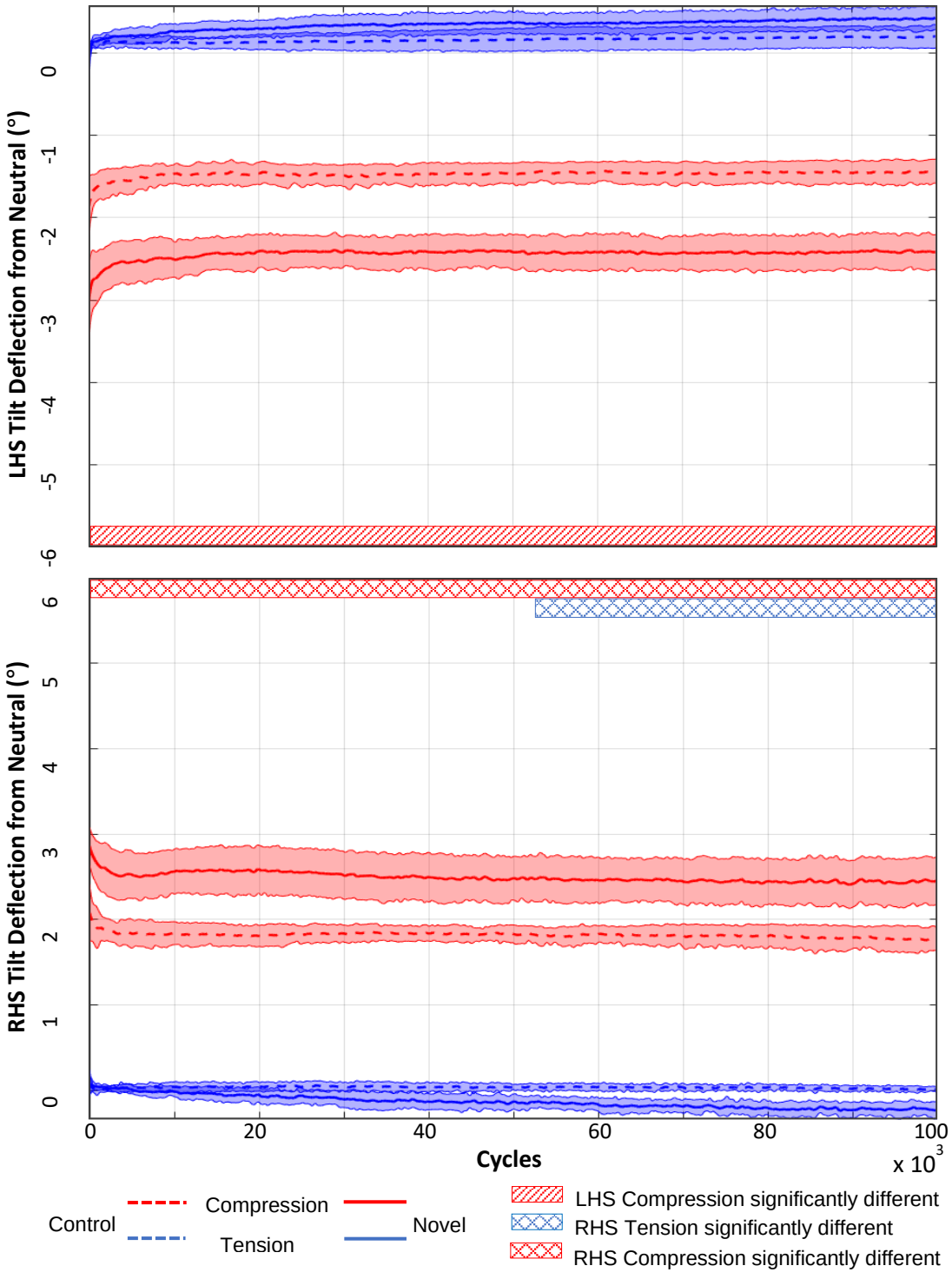

Figure 4-19 *Tilt ND for the control and novel glenoids. In the figure, the origin of the y-axis represents the prevailing position of the glenoid edge when the HH is at the centroid, and the ND in tension (blue) and compression (red), represent the motion of the edges away from the neutral position. Both edges rotate slightly inward of the neutral position or remain unchanged in tension. A distinct outward rotation is observed in compression.*

In compression, the LHS ND tilt for the control glenoid is outward (to the left) by -2° initially but decreases in outward tilt to -1.5° by 10,000 cycles, where it remains for the rest of the test. The novel glenoid behaves similarly, moving from -3° outward from the neutral, to -2.5° after 10,000 cycles. The novel glenoid compressive ND tilt is significantly larger than that of the control glenoid for the full length of the test.

At the RHS, the control glenoid again has an initially higher outward (to the right) ND tilt, starting at 3°, which then decreases to 2.5° by 10,000 cycles and remains steady at this level. The novel glenoid compressive ND tilt starts at 2.1° outwards and decreases slightly to 1.8° after 5000 cycles, where it remains for the rest of the test. The control and novel compressive tilt deflection from neutral are sporadically significantly different along the length of the test, as indicated in **Figure 4-19**.

*In summary, for both edges and glenoid designs the **ND tilt** is zero or slightly inwards of the neutral in **tension**, with a comparatively larger outward tilt during **compression**. The outward ND tilt of the novel is greater than that of the control for both edges.*

EXTENDED TEST RESULTS

As none of the samples tested in the standard-length test showed clear signs of glenoid fixation failure, additional, longer cycle count tests were performed (summarised in **Table 4-5**). The first was a 500,000-cycle test on the previously excluded sample N7, followed by re-testing of earlier samples of a control sample (C8) and another novel sample (N1).

***Table 4-5** Summary of the Extended Cyclic Testing performed to attempt to achieve glenoid fixation failure.*

Sample	Cycles	Notes at Setup	Observations after Test	Comments
N7	500 000	This sample has uneven cement. Both levers have firm fix	Levers still firm. Glenoid fixation loose	
C8 (ext)	400 000	Extended re-test of sample. Previous pin holes re-used. Both levers have firm fix	Levers still firm, glenoid fixation barely perceptibly loose	
N1 (ext)	500 000	Extended re-test of sample. Previous pin holes re-used. Both levers have firm fix	Levers still firm, glenoid fixation firm	
N1 (ext 2)	320 000	Second re-test of sample N1. Levers were not disassembled after previous test, re-used here.	Levers still firm, glenoid barely perceptibly loose	Levers fixed into previously used holes have survived 820 000 cycles without loosening

The fixation of sample N7 was loosened enough after the extended test that it could be noticeably ‘rocked’ by hand, but it was still fast to the Sawbones (i.e. it could not be pulled completely out of the base). The control sample C8, which was re-tested for an additional 400,000 cycles (to bring the full cyclic load on the sample up to 500,000 cycles), did not show the same clear signs of loosening. This sample could just barely perceptibly be moved by hand after the test.

To try to ensure loosening, the next novel sample, the already tested N1, was tested for an additional 500,000 cycles (bringing the total cyclic load on this sample to 600,000 cycles). The sample was dismounted from the rig and checked after the test but did not show any sign of loosening. It was therefore re-mounted, with the lever attachment from the previous test still in place, and another 500,000 cycle test was begun. This test was cut short by a malfunction of the lab PC (crashed) at just past 320,000 cycles. The sample was dismounted from the rig and checked again for loosening. A just perceptible motion was noted at this stage. It is also noted that the lever fixation remained firm for all samples in the extended tests, even those of sample N1 which were subjected to a total of 820,000 cycles.

The results for the extended tests are shown in **Figure 4-20**, where all test runs are plotted together. As there were not enough samples tested for a meaningful statistical comparison, these results are presented for observation of general trends only.

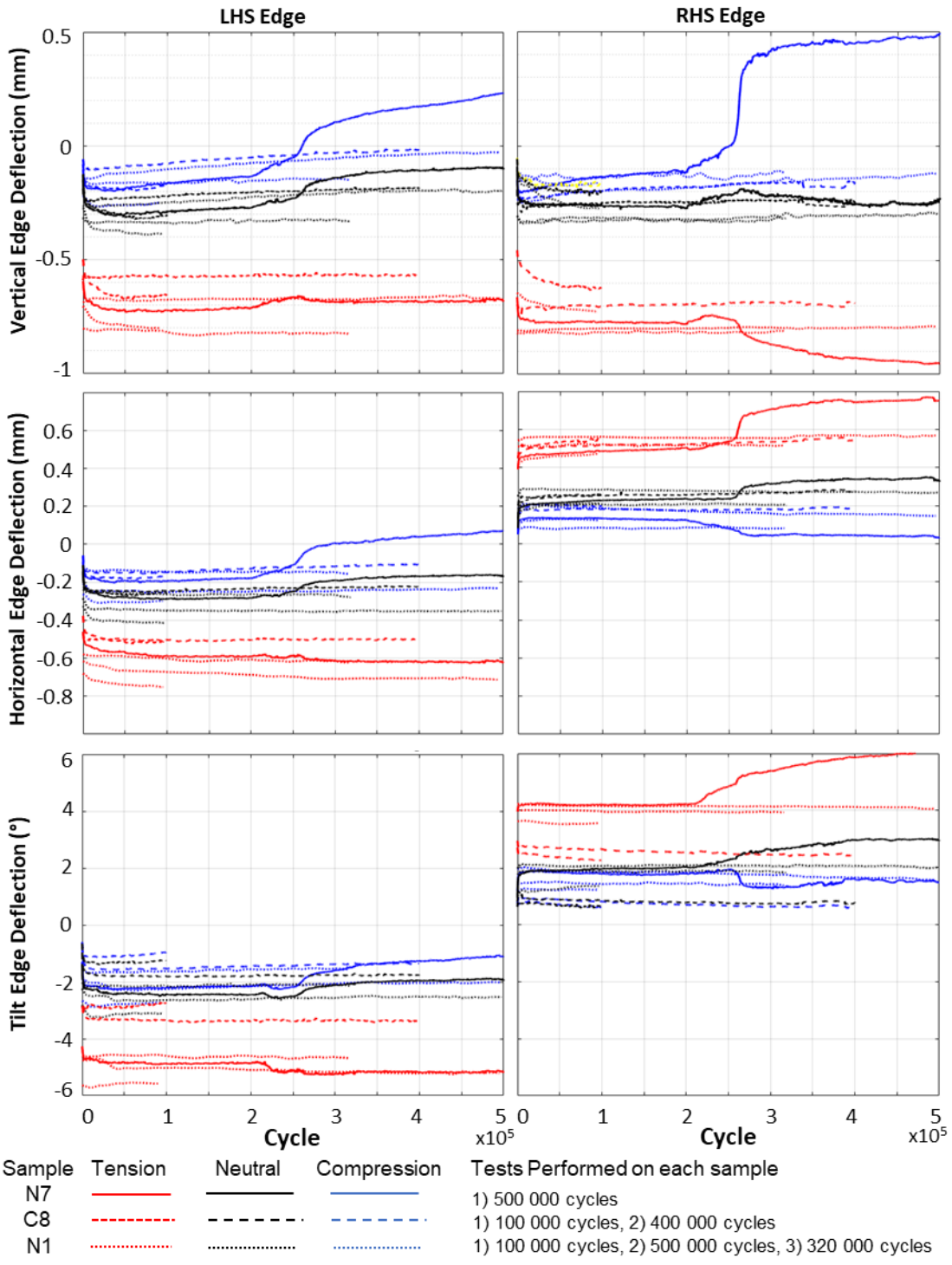

Figure 4-20 *All Extended Test Edge Deflections. Sample N7, previously excluded from testing because of poor cement distribution, was tested once for 500,00 cycles and exhibited loosening of fixation at 250,000 cycles. Samples C8 and N1 had been previously tested for 100,000 cycles each. The starting position of the glenoid edges was zeroed at the start of each test, and the first cycle of repeated tests reset to cycle zero in the plot.*

The results from these tests showed the same general trends as for the standard-length cyclic testing, with an initial rapid shift in the neutral positions of the edges to a downward and outward, with outward tilt, position at each edge. After the settling period, the levels of deflection remain relatively constant for all but sample N7, and the vertical motion of the LHS of sample C8. In the

vertical motion of sample C8, there is a gradual increase in the neutral and tensile deflections for the length of the test. This sample was just perceptibly loose at the end of the extended test.

The trends in motions for sample N7 are examined in some detail, as this was the only sample that was unambiguously loosened at the end of the extended test. For this sample dramatic increase in motion amplitude occurs between 200,000 and 300,000 cycles, after which the amplitudes become steadier again. On the LHS the neutral position shifts upward, inward, and with internal rotation relative to the previous 'steady' neutral position, and the tensile motions show the same trend in change. The tensile motions in the vertical and horizontal directions are large enough that the edge moves above and inwards of the starting (zero) position. The LHS vertical compressive motion shows a similar but lesser upward trend, while the horizontal shows little change, and the tilt indicates an increase in outward rotation.

On the RHS of N7 the neutral position does not change notably in the vertical direction (but does show some instability in the 200,000 to 300,000 cycle zone), while the horizontal and rotational neutral positions change with an outward and outward-tilting motion. On the RHS under compression, the edge moves strongly downwards, outwards, and with an outward tilt. In tension, the RHS edge moves upwards, inwards, and with inward tilt (relative to the previous steady state position). The tensile vertical motion on the RHS is notable both in its large magnitude compared to other tensile motions, and that despite the neutral position of this edge remaining below the initial starting point (0mm), the tensile distraction is lifting the edge upwards to 0.5mm out of the surface.

The ND for all the extended tests is shown in **Figure 4-21**. As for the standard-length tests, the ND for all measured values shifts quickly at the start of the test, to a value that then remains relatively steady for the remainder of the test (except N7, as it began to loosen). For the unloosened samples, overall, the amplitudes of the ND are; for vertical motion between 0mm and 0.2mm in tension, and -0.3mm and -0.5mm in compression; for horizontal motion between 0mm and (±)0.12mm in tension and (±)0.22mm and (±)0.35mm in compression; and for tilt between 0° and (±)0.6° in tension and (±)1.5° and (±)3° in compression. The tilt in compression again shows an initially highest outward motion at the start of the test, which reduces toward the steady value. The ND around 250,000 cycles in sample N7 increases distinctly in all measured motions except for the LHS tensile tilt, which shows only a small increase (from ~ 0.4° to ~ 0.8°).

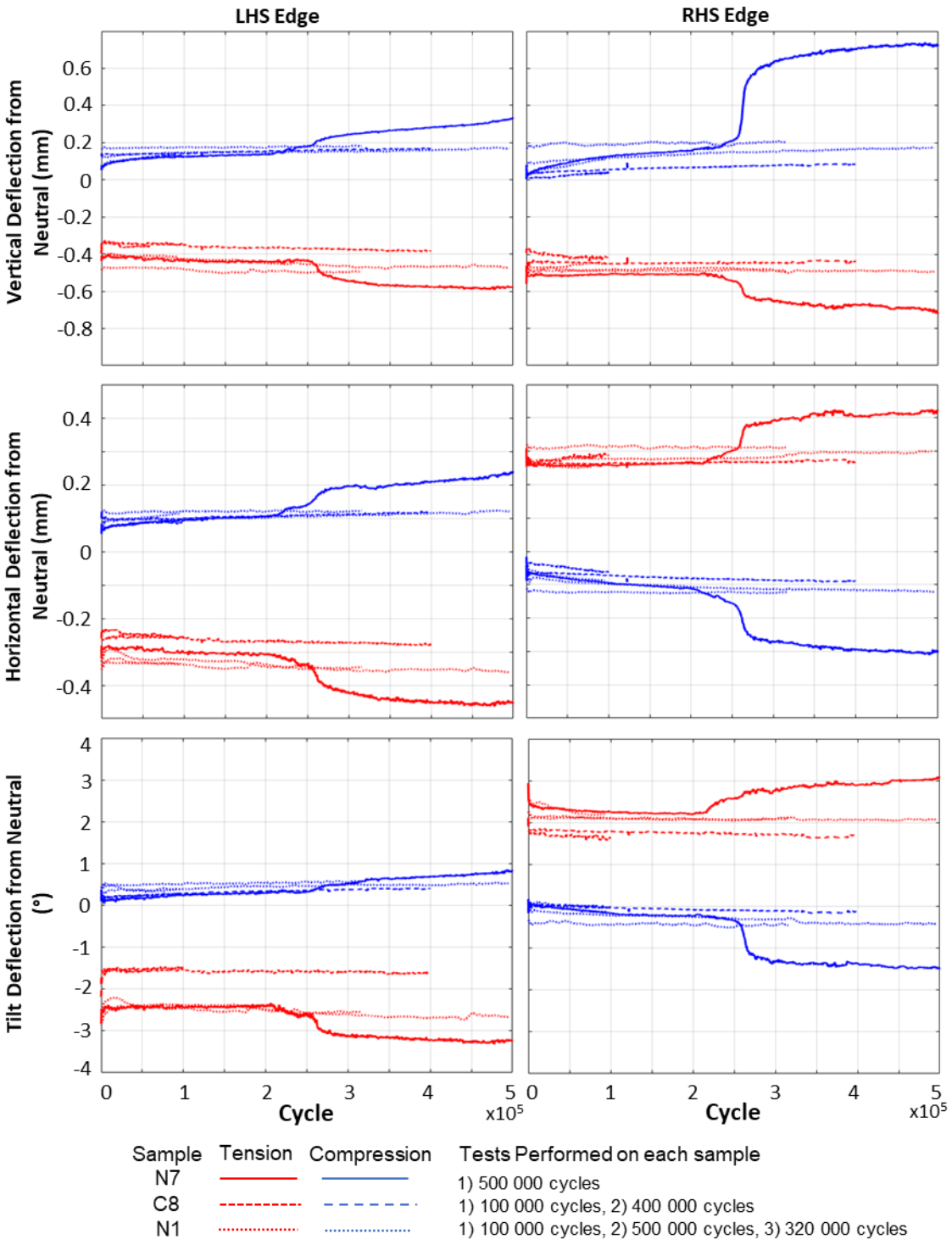

Figure 4-21 *All Extended Test Deflections from Neutral. A clear increase in the amplitude of both the tensile and compressive motions around the neutral position at both edges is seen for Sample N7 after at approximately 250,000 cycles.*

4.4. Discussion

The results presented in this chapter are discussed in four stages, first relating to the sample implantation, next to the subluxation tests, and then the general trends in the cyclic test results. Finally, a comparison is made between the control and novel results, to evaluate the novel glenoid design based on the standard pass criteria, and the original design intention. The implications these results may have for future testing, glenoid designs, and clinical evaluations are discussed separately in Chapter 5.

4.4.1. Discussion of Glenoid Samples and Implantation

Overall, the sample preparation was much improved compared to the rig validation testing samples. However, the novel glenoid introduced new variables into the cement setting pattern due to the surface slots.

The control glenoids showed better cement distribution than the samples tested in the augmented rig validation test. To achieve this improved cement distribution for multiple glenoids before the cement hardened, the glenoids were implanted into the Sawbones by a senior shoulder surgeon and then held in compression while the cement set by experienced shoulder fellows and registrars at Groote Schuur Hospital. A thin layer of cement was still present behind the glenoid surface, but this layer was in most cases evenly distributed. While Lazarus et al. (2002) defines any part of the glenoid back surface that is not in direct contact with the underlying bone (e.g. if there is cement between the glenoid and the bone) as ‘unsupported’ and unfavourable Matsen et al. (2008) and Terrier et al. (2005) found that a thin layer of cement (up to 1.5mm) can be beneficial to the implantation. For the samples implanted here, an evenly distributed layer of cement behind the surface was not considered to be a reason for the exclusion of the sample.

The novel glenoid surface slot (and pre-drilled pin holes) complicated the cementing process, as the cement tended to fill the slots and the pin holes (which ‘bridge’ the outer region of the surface between the slot and the external edge). These were cleared as much as possible during the implantation process while the cement was still soft. Final clearing of any excess cement, particularly inside the pin holes, had to be performed after the cement had set. A further consequence of the cement moving into the slot was that it did not always then travel fully out to the edges (rather moving upward into the slot). This resulted in two samples (N7 and N8) that had outer edges raised off the Sawbones surface due to the uneven cement layer, causing them to be excluded from the main cyclic testing.

To eliminate these cementing complications, a component such as this novel design would require an implantation tool similar to the curved pressure applicator in the surgical set, but with positive extrusions that match the slots of the novel glenoid. These extrusions would fill the slots while the component is held under pressure and the cement sets, preventing cement from moving into the grooves, and promoting even distribution to the edges. The pinholes being filled with cement is a test sample problem only, as an actual component would not have this feature. Overall, enough glenoids of both the control and novel designs with good cement quality were available for the planned cyclic testing.

4.4.2. Discussion of P90 Test Results

The average measured subluxation distance for the control and novel glenoids was 4.6±0.2mm and 4.4±0.2mm, respectively. The analytical subluxation distance for the humeral/glenoid geometry of both glenoid designs is the same since it is based on the relative curvatures of the humeral head and glenoid, and the overall glenoid size, which are consistent for the two designs. Using Equation 2.1, a humeral radius r_{HH} = 24mm, a glenoid radius of $r_{glenoid}$ = 27mm, and the distance to the glenoid edge of d_{edge} = 18.75mm, the analytical subluxation distance for these components would be $d_{subluxation}$ = 2.1mm.

$$d_{subluxation} = d_{Edge}\left(1 - \frac{r_{HH}}{r_{glenoid}}\right) \qquad [2.1]$$

For this range of analytical subluxation distance, Anglin et al. (2000c) reported measured subluxation distances of ~4.5mm (based on graphically presented data). Stautberg et al. (2017) reported 90% subluxation distance values of 6.16mm (inferior) and 5.66mm (superior) for a 'medium-sized' glenoid tested (the exact size and glenohumeral mismatch was not reported). Sabesan et al. (2015) reported an experimental subluxation distance of 3.8±0.3mm for a size 48 glenoid with a Ø44mm humeral head. Since the values measured in this research correlate well with the expected result using the analytical calculations and fall within values for similar (but not identical) implant pairs reported, they are reasonable based on the literature.

Despite having the same curvature and surface geometry, the subluxation distances measured for the control and novel samples were not identical, with the control average measured at 4.6mm±0.2mm and the novel at 4.4mm±0.2mm. At the time that the novel glenoid P90 testing was performed, the control glenoid cyclic testing had already begun, using a P90 distance of 4.2mm based on the control glenoid subluxation distance of 4.6mm. Since the average difference in subluxation distance of 0.2mm was within the standard deviation of the novel data and was less than the 0.5mm tolerance on the initial position of the humeral head specified by

the standard, it was decided to use the same P90 distance of 4.2mm for both glenoid designs, to ensure consistency between the tests.

Examination of the samples after the tests showed the expected surface deformation on the control glenoid, caused by the humeral head smearing the material on the outer edge. On the novel samples, in addition to this smearing, a 'stretching' of the outer edges was observed. This is likely due to the material on the outside of the slot being less supported than the continuous edge of the control glenoid. While this effect will be exaggerated in the case of the humeral head moving fully out over the edge of the novel glenoid in the P90 test, it is of interest to note whether an increase in horizontal outward deformation is also observed in the cyclic testing, when the humeral head moves only to the 90% of the subluxation distance.

4.4.3. Discussion of Cyclic Testing

The discussion of the cyclic testing includes first a discussion of the experimental testing itself, followed by interpretation of the testing results to identify overall motion trends for both the control and novel glenoid designs.

4.4.3.1. Discussion of Test Methodology

While the cyclic testing was overall successfully performed, there were two notable problems encountered, namely the fixation failure of two of the levers, and the shorting of sensor S_{1L} on the LHS measuring block. The validity of the data measured is dependent on a firm connection of the lever to the glenoid edge, such that any motion of the lever can be taken as the motion of the edge. While the data from the tests with a failed lever was discarded, the cause of the failure warrants some discussion, to be confident that the remaining data is valid.

The integrity of lever fixation was ensured by using the angled polypropylene washers, and the adhesive added to the fixation. The polypropylene tubing used for the washers was moderately rigid but could be deformed slightly under compression during the fixation. The fixation screws were always tightened to the point that the washer began to deform, to ensure there was a tight compression of the lever face against the glenoid side. This rigidity was checked gently by hand in all tests, both before and after the cyclic testing. The 'by-feel' hand check did not provide a quantified value for the strength of the fixation but was chosen because even a properly assembled lever fixation could be damaged by excessive force.

The only forces applied to the block are the weights of the vertical sensor armatures and the spring force of the horizontal sensors (≤1N). The failure of the lever fixation is therefore more likely

due to fatigue on a compromised screw thread fixation than from an excessive force applied to the end block.

Both the levers that failed were noted to have poor fixation at the start of the test, in both cases due to human error during the drilling of the holes by hand using a Dremel. While this method had been used successfully for the samples in the rig validation study, and the preceding control samples (C1, C2, C3), the two consecutive failures drove the decision to have all the subsequent lever fixation holes added by CNC during the manufacture of the components. None of the samples produced by CNC suffered lever loosening, even the samples used in the extended tests. Sample N7 in particular, which had levers attached twice in the same holes, first for 100,000 cycles and subsequently for two consecutive extended tests, totalling an additional 820,000 cycles, still had firmly attached levers at the end of the final test. These results indicate that the fixation of the levers in the CNC-created holes is consistently reliable.

Of the samples that had hand-drilled holes (C1 to C3), C1 was re-used for the novel design check testing, and the levers attached into the previously used holes survived the second 100,000 cycles. This indicates the holes were correctly drilled. The remaining hand-drilled samples are evaluated solely by the pre- and post-testing check by hand, in which neither showed any indication of loosening.

The levers that failed were noticeably compromised from the start, and these failed completely. Considering this, and that those that remained fixed all passed the 'firmness check', (even after 820,000 cycles in the case of N7), the lever motion is confidently said to be representative of edge motion.

The second problem encountered during the testing was the malfunction of sensor S_{1L}, which began to give readings on the rail of the applied voltage, indicating an electrical short circuit occurring. This sensor is believed to have suffered damage to its internal electrical insulation layer during the rig validation testing, and possibly still after, due to the unguided armature not being held away from the sides of the sensor body. The end cap bushings were added to align the armatures, but they could not be too tightly toleranced, or they risked preventing free motion of the armatures under gravity. This may have allowed the back of the armature to wear against the inside of the sensor. If a small spot of broken insulation developed, and the armature intermittently touched it, it would cause a short in the sensor for that reading.

Short values were noted in data sets C1, C6, and N1 (as listed in **Table 4-4**). The measured values were filtered out in the MATLAB algorithm if they were physically impossible, with a threshold of

100mm used (the maximum sensor displacement is ±12.5mm) and the program returned a warning, reporting the number of data points filtered. A second filter was applied with a value of 15mm, to determine if the sensor was reading incorrect but 'reasonable' values, which might imply distortion of the actual measurements. No additional data points were filtered at this value. This confirms that when the fault was occurring, it always produced a distinctly physically impossible reading (most of the short data measurements were $1x10^6$mm). This filter was also applied to all the other sensor readings. No sensors other than S_{1L} returned filtered data points. Even in the most badly affected test, C6, only 57 out of 900,000 data points were compromised by this shorting behaviour. This implies the damaged area was small, and there is no reason to believe the data recorded when the armature was not in contact with this area is compromised.

However, since the end cap bushings are not high-precision, it is possible that the other sensors could eventually be damaged in the same way. The sensor was therefore replaced with captive bushing sensor, to ensure longevity. For future studies, it would be recommended to replace all sensors with the captive bushing type. The replacement sensor was physically larger than the existing sensors (to accommodate the internal bearings) but had similar electronic performance and the armature remained free to move under gravity. No noticeable change was observed in general data collected after the change in sensor, other than that no further short data points occurred.

4.4.3.2. Discussion of Glenoid Edge Motions

The cyclic testing results are discussed in three stages. First, the overall trends in the motions, presented in Section 4.3.4.3, are interpreted to understand how the components react as the tests proceed. Focus is given to how the neutral positions of the edges change during the tests. The deflection of the edges around the neutral point is then discussed to understand the changes in amplitude of the motions around their prevailing neutral 'undeflected' state. Finally, the extended test results, in which a clear fixation failure of sample N7 was observed, are examined and the implications of the results are discussed.

OVERALL COMPONENT MOTION TRENDS

The results presented in Section 4.3.4.3, show the edge motions reached an absolute maximum amplitude of approximately -0.8mm in y-direction, 0.6mm in the x-direction and 4.5° of rotation. These motions are within the assumed maximum range of motion that was specified for the edge motion measurement design. At these motion amplitudes the maximum systematic error in the glenoid edge motions, as calculated in Appendix B.2.3, would be -1.7μm in the y-direction, 0.2 μm in the x-direction and 0.06° of rotation. As these values are below the original goal

measurement resolution of 10 μm for linear and 0.1° for rotational measurements, set out in **Table 3-1,** these errors can be neglected.

The results show that for both the control and novel glenoids, at both the component edges, there is a general trend of moving down into the Sawbones surface, while simultaneously stretching outwards, and tilting outwards as the test proceeds, even when the edges are in the unloaded neutral state. On both sides, these motions are exaggerated in compression and reduced in tension. That both edges show the downward, outward stretch and tilt indicates that there has been a deformation of the glenoid component, rather than a shift of the glenoid to one side or the other. This is visualised (not to scale) in **Figure 4-22**, for the neutral position of the edges. It is also noted that the deformation is a change in the shape of the component overall, and not localised surface damage as was observed in the P90 test samples.

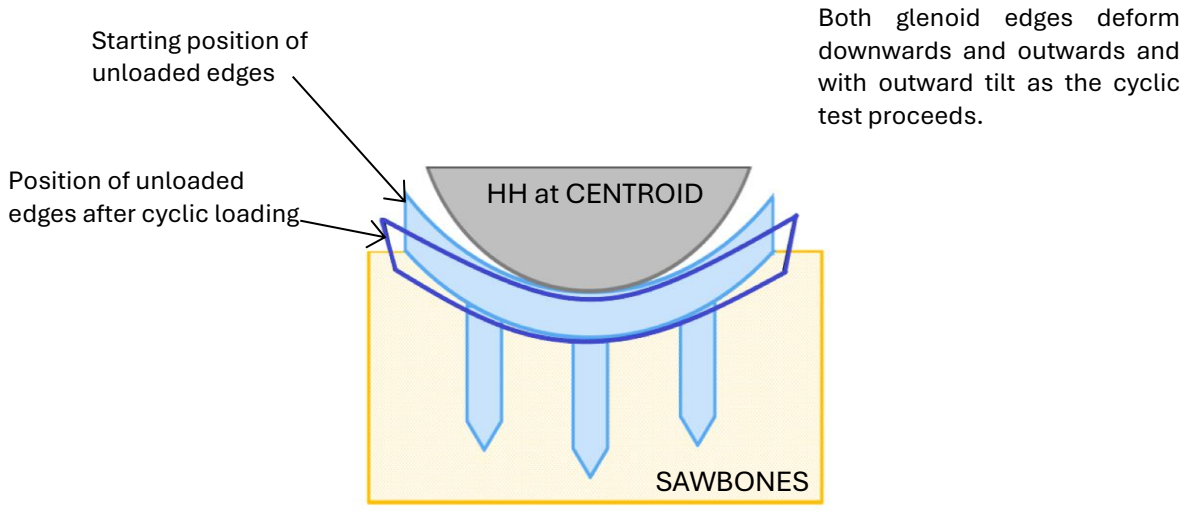

***Figure 4-22** Simple visualisation of the deformation of the glenoid component during cyclic testing.* For both the control and novel glenoids, both edges of the component in the unloaded (neutral) state compress down into the Sawbones and stretch and tilt outwards.

The edge motions increase in amplitude quickly at the start of the test, before reaching an equilibrium or near equilibrium state around 10,000 cycles, except for compressive tilt. For this tilt, the control moves immediately to its equilibrium position and remains there for the duration of the test. The novel shows a small increase in outward deflection at both edges at the beginning of the test, which then lessens to an equilibrium state, again around 10,000 cycles. This implies that as the edges move downwards and outwards, the amount of outward tilt in compression reduces slightly (or remains steady), even though the outward tilt in the unloaded state is increasing at the same time. This is believed to be due to the edge of the glenoid being slightly further from the humeral head as the component 'stretches' out, reducing the effect the humeral head has on the angle of the edge.

The rate at which the edges change position is best reflected by the shift of the neutral position as the test proceeds. The position of the neutral point at each of the edges of the glenoid at 10 cycles, 2000 cycles, and 100,000 cycles (not to scale) is illustrated in **Figure 4-23** for the control glenoids. The magnitudes of the motions relative to the final edge deflection are provided in **Table 4-6**.

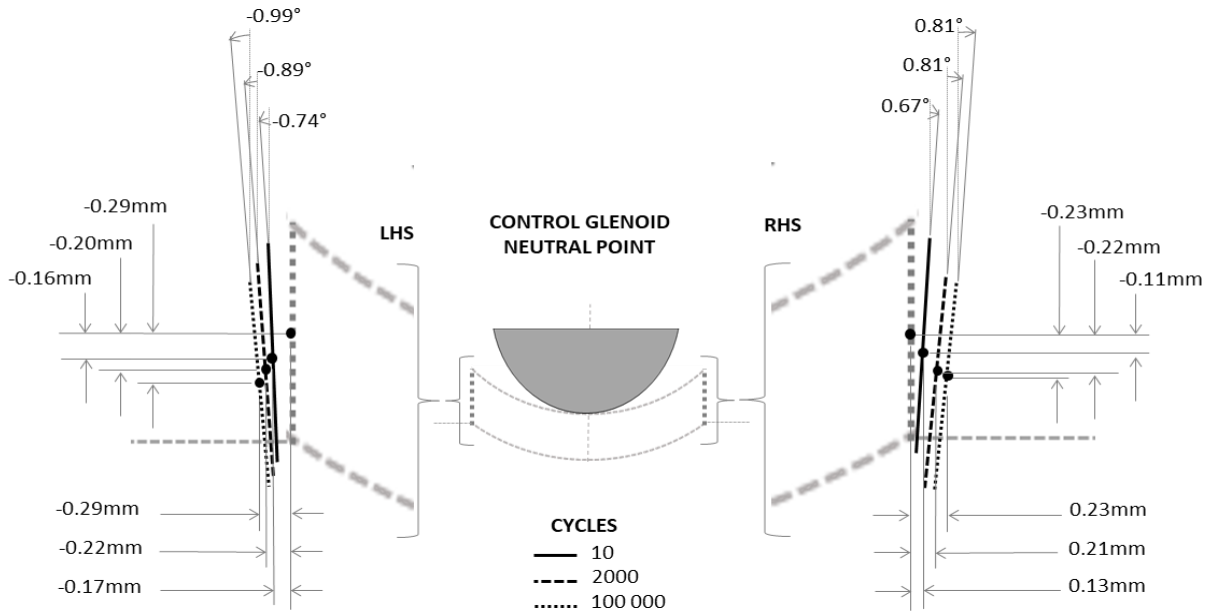

Figure 4-23 *Progression of the position of the control glenoid edges in the neutral state, at 10 cycles, 2000 cycles, and 100,000 cycles, relative to the edge starting position. The majority of the shift in the neutral position of the edges is seen in the first 10 cycles.*

Table 4-6 *Progression of the position of the control glenoid edges in the neutral state, at 10 cycles, 2000 cycles, 5000 cycles, and 100,000 cycles relative to the final position of the edges for each motion.*

Control	LHS						RHS					
Cycle	y (mm)	%y	x (mm)	%x	α (°)	%α	y (mm)	%y	x (mm)	%x	α (°)	%α
10	-0.16	56	-0.17	59	-0.74	74	-0.11	48	0.13	55	0.67	83
2000	-0.20	69	-0.22	74	-0.89	90	-0.22	94	0.21	94	0.81	100
5000	-0.22	76	-0.23	80	-0.95	96	-0.22	95	0.22	98	0.86	107
100 000	-0.29	100	-0.29	100	-0.99	100	-0.23	100	0.23	100	0.81	100

For the control glenoid, we see that the first 10 cycles account for a minimum of 48% (RHS y) and a maximum of 83% (RHS α) of the total motion. By 2000 cycles a minimum of 69% (LHS y) and a maximum of 94% (RHS x) of the final deflection has been reached. By 5000 cycles this is 76% (LHS y) to 98% (RHS α) of the final value. It is clear from these results that the majority of the neutral shift is occurring within the first 10 cycles, and after 5000 cycles little change is seen.

For novel glenoid neutral point shift, shown in **Figure 4-24**, a slight reduction in the overall percentage is seen in the first 10 cycles, but by 2000 cycles, similar values are noted (**Table 4-7**).

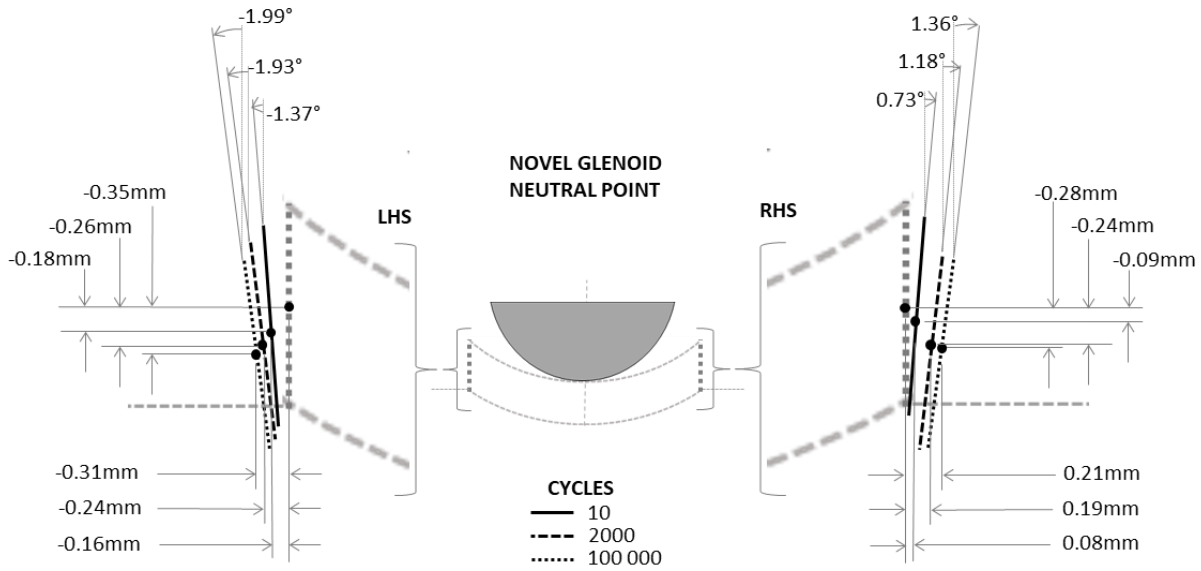

Figure 4-24 *Progression of the position of the novel glenoid edges in the neutral state, at 10 cycles, 2000 cycles, and 100,000 cycles, relative to the edge starting position. The majority of the shift in the neutral position of the edges is seen in the first 10 cycles.*

Table 4-7 *Progression of the position of the control glenoid edges in the neutral state, at 10 cycles, 2000 cycles, 5000 cycles, and 100,000 cycles relative to the final position of the edges for each motion.*

Novel	LHS						RHS					
Cycle	y (mm)	%y	x (mm)	%x	α (°)	%α	y (mm)	%y	x (mm)	%x	α(°)	%α
10	-0.18	49	-0.16	51	-1.37	69	-0.09	30	0.08	38	0.73	53
2000	-0.26	73	-0.24	77	-1.93	97	-0.24	84	0.19	89	1.18	87
5000	-0.29	81	-0.26	84	-2.01	101	-0.27	94	0.21	96	1.20	88
100 000	-0.36	100	-0.31	100	-1.99	100	-0.28	100	0.21	100	1.36	100

The first 10 cycles account for a minimum of 38% (RHS x) and a maximum of 73% (RHS α) of the total motion. By 2000 cycles a minimum of 73% (LHS y) and a maximum of 97% (LHS α) of the final deflection has been reached. By 5000 cycles this reaches 81% (LHS y) to 101% (LHS α, due to fluctuation in the 'steady state' value) of the final value.

Since the first 10 cycles account for half or more of the final motion measured, it is worth noting that these motions are measured after the 10-cycle conditioning run. The motions induced by the conditioning are zeroed out of the main test, so they are not captured by the main test data. The conditioning test was performed shortly before the main cyclic testing, with only the time taken to enter the main test parameters and start the main test (approximately 5min), between the

tests. The total motion of the glenoid edges from implantation would therefore be the sum of the preconditioning and main cyclic testing.

Since the conditioning test is controlled with the same protocol (Glenoid Edge Motion), the same data was recorded by default for the conditioning cycles as for the full test. This data was processed in the same way as the main test data. The average motions of the control and novel data, for the position of the neutral point at the final cycle of the conditioning are provided in **Table 4-8**.

Table 4-8 *Average vertical, horizontal and tilt positions of the control and novel glenoid edges in the neutral state after 10 conditioning cycles*

Conditioning Cycle 10	LHS			RHS		
	y (mm)	x (mm)	α (°)	y (mm)	x (mm)	α (°)
Control	-0.16 (±0.04)	-0.16 (±0.02)	-1.26 (±0.45)	-0.17 (±0.04)	0.14 (±0.02)	1.03 (±0.30)
Novel	-0.16 (±0.06)	-0.17 (±0.05)	-1.85 (±0.53)	-0.24 (±0.07)	0.15 (±0.03)	1.30 (±0.33)

The control shows a similar amplitude of motion induced in the 10-cycle conditioning as in the next 10 cycles (the cyclic test values in 10 cycles all fall within the SD of the conditioning amplitude). In the novel data, less additional motion is seen on the RHS in the first 10 cyclic test cycles than in the conditioning for the x and y motions (-0.09mm y and 0.08mm x vs -0.17mm y and 0.14mm x), while the RHS rotation and all the LHS motions remain comparable.

The purpose of performing the conditioning (and disregarding the changes that might occur during this stage) in the standard, is to allow the glenoid to 'settle' before investigating design-related differences in motion. The substantial amount of 'settling' seen in the 10 cycles after conditioning could therefore be a motivation for extending the conditioning to at least 20 cycles for testing consistency. However, from a clinical perspective, the motions occurring in both the conditioning and the early test represent a real shift from the position of the component at implantation, which may be of clinical relevance. The implications of this on the test method and methods of clinical evaluation are discussed further in Chapter 5.

MOTION OF THE EDGES AROUND THE NEUTRAL POSITION

We now look at the deflection of the edges around the neutral position as it moves during the tests, to understand how the amplitude of the motion is changing as the testing proceeds. As seen for the overall motions, there are overall trends and exceptions seen in the results.

The most notable overall trend is the large discrepancy between the relative amplitudes of the tensile and compressive motions around the neutral, for both designs. In the vertical direction, the compressive motion amplitude is in the order of 5 times the magnitude of that of the tensile motion, as listed in **Table 4-9**. In the horizontal direction, it is in the order of 3 times the amplitude, and in the tilting motion in the order of 5 to 6 times the amplitude. This discrepancy indicates a relatively small amount of tensile distraction is being transferred back to the unloaded edge, compared to the compression under load.

Table 4-9 *Average vertical distraction and compression ND at the start and end of cyclic testing for the control and novel glenoid designs*

Cycle	LHS				RHS			
	Tension (mm)		Compression (mm)		Tension (mm)		Compression (mm)	
	Novel	Control	Novel	Control	Novel	Control	Novel	Control
1	0.03 (±0.03)	0.04 (±0.11)	-0.45 (±0.06)	-0.34 (±0.05)	0.01 (±0.02)	0.00 (±0.02)	-0.50 (±0.03)	-0.40 (±0.04)
100 000	0.14 (±0.02)	0.14 (±0.04)	-0.45 (±0.05)	-0.34 (±0.04)	0.11 (±0.02)	0.04 (±0.01)	-0.51 (±0.04)	-0.43 (±0.03)

The deflections from neutral are comparable to values reported by Anglin et al. (2001), in which a series of glenoid design pairs were tested. Maximum tensile displacements (relative to the undeflected state) were reported graphically to be between approximately 0.06mm and 0.21 mm for all components that did not delaminate. Chamseddine et al. (2019) reported mean tensile distractions of 0.18mm and 0.33mm for pegged glenoid components implanted in cadaveric bone after 23,000 load cycles. Sabesan et al. (2015) reported tensile distractions of 0.1mm to 0.69mm after 50,000 cycles. The tensile ND results seen here, ranging from 0.04mm to 0.14mm, are therefore reasonable based on the literature.

Also noted is that the compressive ND for both designs, in both vertical and horizontal directions, moves almost immediately to its equilibrium. For the same motions, the tensile deflection from neutral increases in amplitude slowly but continuously for the duration of the test. This indicates a more time-dependent behaviour in the ND tensile distraction, while ND compression is steady. It is noted that in the global co-ordinates, the neutral position and the compressive motion are moving gradually further down into the Sawbones surface, while the position of the edges in tension remains steady (refer to **Figure 4-14** and **Figure 4-16**). The increasing tensile ND is therefore caused by the edge reverting to the same global position in tension while the neutral sinks downwards, rather than an increasing lift of the edge in tension.

In contrast to the constant compressive x and y motions, the ND tilting motion in compression shows a quick move to a local maximum amplitude of motion (outwards from the neutral) at the

beginning of the test, which then slowly decreases towards the equilibrium outward tilt of 1.5° (control) and 2.5° (novel). This lessening of the outward ND tilt indicates that rotational deflections in compression are 'absorbed' by the global movement of the neutral position. When the glenoid edge is in its original state, the compressive motion causes the outward stretch and tilt. As the component edge moves steadily into that new position and orientation, the compressive load has less of an effect on the tilt than it did in the starting position. It is notable that the compressive rotation decreases not only around the neutral, but overall, as the edge is deformed outward, meaning the tilting motion is lessened globally as the edge stretches away from the humeral head.

From these discussions, it is clear that there are complex motions occurring at the glenoid edges that are not captured by only the vertical ND values reported in the literature. How these complex motions may affect glenoid fixation survival is not clear from standard-length test results obtained in this research, because the samples tested for 100,000 cycles did not fail.

EXTENDED CYCLIC TESTING

The extended cyclic testing showed that well-implanted samples did not clearly fail even at five to eight times the standard test duration. Both un-failed components did show a barely perceptible motion when rocked by hand after their respective final tests (C8 at a total of 500,000 cycles and N1 after a total of 830,000 cycles). The measured edge motions for these components remained relatively steady throughout their tests, except for the global vertical tensile deflection and neutral position of both edges, which slowly increased. This indicates the edges start to move back upwards towards the surface after long enough test times (although they remained firmly below the starting level).

Sample N7, which failed at around 250,000 cycles, was the only sample in which the global tensile position moved higher than the starting level (with the RHS edge reaching >0.6mm). This is a clear indication that this component is 'rocking' as is widely expected under eccentric loading. However, this rocking did not begin until the fixation failed. Before this point, the deformation of the surfaces for this, and all the other components tested, appears to be the more relevant factor in edge motion.

Sample N7 also showed a shift in neutral position suggesting the whole glenoid had tilted to the right (the LHS edge moved up, to the right, and with inward rotation, while the RHS stayed steady in the vertical direction but moved to the right, and with outward rotation). Around this neutral,

the amplitudes of the tensile (upward, inward, inward-tilting) and compressive (downward, outward, outward-tilting) increased at the failure point. The RHS edge had much larger relative motion amplitudes than the LHS, likely due to this being the single-pegged side, giving it more mobility. After the loosening event, the glenoid settled again, at a new nearly steady state, indicating the motion was the most extreme likely to be produced by this test rig (i.e. steady state for a loosened glenoid in this particular loading condition). It is again noted that this glenoid, although definitely mobile after the test, was still firmly enough attached to the Sawbones that it could not be pulled out by hand.

Also notable in the extended test results is that for samples that were tested repeatedly, the initial early settling to a new neutral position is evident in the repeat tests. All measurement values were zeroed at the start of each individual test, so if the deflection induced in the previous test was still in effect on the samples, they should already be at or near the equilibrium position and hence remain close to zero deflection in the repeated tests. *That samples C8 and N1, which were tested on two and three separate test runs respectively, showed a similar amplitude of settling, in a similar time frame, in each of their test runs, indicates that the deflection of the edges to the new neutral position is not a permanent effect*. In the time between the repeated tests, the edges move back towards their initial positions. This material response is supported by UHMWPE material studies which indicate that the polymer material exhibits viscoelastic strain behaviour, and even when cyclically loaded some strain recovery is expected (Avanzini, 2011; Meyer & Pruitt, 2001) .

Looking at, for example, the vertical neutral position shift of both N1 and C8, we see that for the LHS, the amount of settling is steadily decreasing for each consecutive test (from -0.4mm, to -0.33 to -0.2mm for N1 and from -0.3mm to -0.2 for C8). This implies a small amount of permanent deformation has occurred in each test. However, on the RHS, both samples show less settling on the first test than on subsequent tests and, in the case of N1 the two subsequent tests show almost identical settling. This could indicate that the samples did not reach their equilibrium position in the first test (which is supported by the curves of the first test for both samples, which do not fully flatten out). In each case, after being compressed down into the surface during the test, the edges subsequently rise back toward their original positions.

Physical inspection of components after the standard test showed a slight gap between the cement and the back of the glenoids at the edges, indicating delamination at the cement/polyethylene interface. This delamination could be caused by the glenoid recovering its original shape, while the underlying Sawbones and cement remain permanently compressed.

From a study of retrieved samples, Gregory et al (2009) observed that in some samples failure of the polyethylene-cement bond behind the glenoid surface occurred, but no failure of the cement-bone interface around the pegs. The results obtained in this research indicate a debonding of the glenoid back from the cement that occurs within the standard test duration, while the pegs remain fixed. The failure modes observed here therefore correspond to the 'mixed failure' type reported by Gregory.

Overall, there are too few samples tested repeatedly (and the time between tests was not a controlled variable) to be able to make firm conclusions about the response of a sample to being re-tested. It is however clear that the deformation of the samples observed in the standard test has a time dependent element to it. That the equilibrium position of the neutral point is a temporary deflection, rather than a permanent deformation, raises questions as to how this may influence the movements around the neutral point, particularly in the tensile state.

As the humeral head moves away and the edge is unloaded, the relaxation of the downward and outward deflection would already begin. Takahashi et al. (2016) report a logarithmic strain deformation recovery rate in Vitamin E-infused UHMWPE hip prostheses. In their research, approximately half of the strain recovery occurred in the first 5min after unloading, and almost all deformation was recovered after 300 min. While the geometries and material are not identical in this research, it is reasonable to conclude that in the seconds between the compressive and tensile loading states, active strain recovery is occurring at the glenoid edge. The 'rocking horse effect' assumes that the edge motion when the humeral head reaches the opposite edge is purely tensile distraction. However, since there is still a deflection of the neutral point, and this deflection is still in the process of relaxing back towards its initial position, a portion of the 'tensile' motion may well be caused by the relaxation and *would occur even with no tensile load applied*.

In this particular test rig, the end-point delay in the cyclic testing, discussed in Chapter 2, may be contributing to this behaviour. The humeral head resting on the loaded edge for a few seconds may allow additional time-dependent deflection to occur. At the same time, the opposing edge remaining unloaded for these few seconds would allow a longer period for relaxation, allowing more 'recovery' motion than a higher frequency test (e.g. 2Hz as recommended by the standard). The endpoint delay and slower loading frequency are, however, more physiologically likely. Everyday actions capable of causing the applied load, such as supporting oneself on an arm as you push out of a chair, or holding a heavy object at shoulder height, would likely apply a load for a few seconds. A load applied in this way could be relevant to a real implanted component's

survival. In contradiction, the real-life loading would not occur in high enough repetitions to reach the equilibrium neutral positions seen in the tests, as these aim to apply 10 years' worth of load cycles in a single test. However, since approximately half the deformation of the neutral position occurs within the first 10 cycles of the test, and 10 repetitions of a high load activity (at the <0.5Hz applied in the test) is not unreasonable as part of an exercise regime, the cyclically induced deformation and subsequent relaxation could well be clinically relevant. The test as performed here does not adequately investigate the time dependency of the deformation and relaxation of the surface, and this aspect requires further study.

A further factor relevant to the deformation of the component is the material used. In this study medical grade UHMWPE was used, but it was not gamma-irradiated to cross-link the material. Cross-linked UHMWPE has better wear resistance, but also usually lower rigidity than the material used in this research (Lewis, 2001). The implications of these material differences are discussed further in Section 5.2.

The overall understanding of the response of the glenoids tested to the cyclic testing now allows us to evaluate the novel design.

4.4.4. Evaluation of the Novel Glenoid Design

The novel glenoid design is evaluated by comparing the control and novel edge motions. The difference between these motions is compared to the expected difference based on the design intention and the FE model. The ASTM criterion of equal or less vertical edge motion is applied to assess how well the design performs in the standard test. Finally, the overall trends in all motions measured are discussed, to predict fixation survivability and make design recommendations.

As set out in Section 4.2, the novel design aimed to reduce the forces experienced at the edges of the component, particularly in tension, by shifting the location of peak stress away from the outer edges, and onto the edge inside the surface slots. This movement of the peak Von Mises stress location is observed in the FE model of the novel design, created as part of the design development. The reduction in stress was further associated with reduced maximum tensile and compressive edge motions in the FE model of the novel glenoid, compared to a control.

The results of the control and novel glenoids are compared first based on the overall motion trends. In the results presented in Section 4.3.4, it was seen that there was a persistent significant difference between the control and the novel glenoids for the LHS vertical and tilting edge motions in compression, and for the RHS tilting motion in compression. This higher mobility of the novel glenoid edge in compression this is likely due to the eccentric section of the novel

glenoid being more flexible than the continuous surface of the control glenoid when the humeral head is at or near the edge.

It was noted in the subluxation distance discussion that the novel glenoids used in the P90 test were visibly stretched rather than just deformed at the edges after the test. Looking at the global results for the compressive horizontal motions, we see no significant difference in the amplitude of motion between the novel and control glenoids. This implies the permanent deformation in the P90 test is occurring as or after the humeral head reaches the subluxation point, but not at the cyclic testing motion distance. *Based on the global motions, the novel glenoid design has more mobile edges in compression, while in tension the control and novel glenoids have equivalent performance*.

However, the standard test criterion for evaluating performance is vertical deflection of the edge, around its undeflected position, before and after the cyclic testing. The deflections from neutral are therefore a better measure of the design performance from the standard perspective. In the motions around neutral, a significant difference developed in the RHS vertical ND motion after 15,000 cycles and persisted for the remainder of the test. A persistent significant difference was seen at both edges in the compressive ND tilting motion. Additionally, the RHS tensile ND tilt motion showed a significant difference from approximately 53,000 cycles until the end of the test. In all cases, the novel glenoid showed greater edge motions than the control glenoid.

The higher mobility of the edges of the novel glenoid in compression is not surprising, since the eccentric edges (on the outside of the surface slot) do not have the support of the continuous control surface when directly loaded by the humeral head. The difference in this case between the experimental results and the FEM could be explained by the difference in the subluxation distance used. The FEM used a 3.7mm motion amplitude, compared to the 4.2mm in the tests. This may have moved the humeral head further onto the less supported outer ring, increasing the compressive deflection.

The increased tensile ND motions for the novel glenoid are unexpected, as the design aimed to transfer the distracting forces to the inner, concentric region of the component, as indicated in the FE model. The significant and continuously increasing difference in tensile ND is of particular interest, as this is the design evaluation criterion used by the standard. *Based on these results, the novel glenoid does not pass the standard test and is not considered to be more reliable than the control*.

A possible reason for this discrepancy between the experimental and FEM results is the complex motion induced by the time-dependent deformation noted for both glenoid types. The FE model included the stresses induced by the tensile distraction but did not account for the, as yet not fully defined, dynamic material changes. If the glenoid edges are relaxing out of their deformed state while the edge is unloaded, there will be an upward and inward motion caused by the relaxation that will add to the tensile distraction motion. The relative contributions of the tension and the deformation are not known but considering that the global shift in the position of the neutral is consistently larger than the deflection around neutral for all tensile motions, it is reasonable to assume that the relaxation out of the shifted neutral position is not trivial.

Overall, based on the standard DGL test criterion, the design of the novel glenoid is not considered to be more reliable or to exceed the performance of the existing control. A redesign iteration would therefore be recommended before attempting to proceed with any next steps towards commercialisation.

It is worth noting, however, that none of the samples (novel or control) suffered fixation failure within the 100,000 cycle standard test. Being the only standardised measure of glenoid loosening, this test is by necessity the starting point in a mechanical design evaluation. The results obtained here do raise the question of whether a design such as the novel glenoid, which has more mobile edges inherent to the design, is appropriately assessed by this test. Possible alternative criteria by which this and other future designs could be evaluated are discussed in Chapter 5.

4.5. Conclusion

The augmented DGL test rig was used to measure the three directions of edge motion on a series of control and novel glenoid components, as intended. The results for subluxation distance and vertical tensile distraction from the neutral position, correlate with reported values in the literature, giving confidence in the overall test method.

The additional motions measured allowed us to observe that in the global frame of reference, before loosening occurs, the dominant factor in the motion of the edges is the deformation of the glenoid surfaces. The component as a whole is compressed downward into the underlying bone substitute and stretched and tilted outwards at both edges. In this state, the tensile distractions caused by eccentric edge loading lessen the downward compression but were never large enough to bring the component edges back to their starting position (i.e. the component remained below the starting level for the duration of the test).

In the standard-length tests, none of the test samples suffered a fixation failure, so extended-length tests were performed on previously excluded or already tested samples. In these tests, only the excluded, very poorly cemented, sample showed a clear fixation failure, at approximately 2.5 times the length of the standard test. At the onset of this failure, the glenoid began to exhibit the classical ‘rocking horse’ motion generally associated with eccentric edge loading.

In the re-testing of the components during the extended test series, it was noted that the downward and outward shift of the edges seen in the standard-length tests occurred again for each consecutive test of the same sample. As the starting positions of the glenoid are zeroed at the beginning of each test, the repeated settling indicates that between the tests, the deformation that occurred has been removed. This indicates that these surface deformations are not permanent, and there is a tendency for the component to relax back toward its starting position. The speed of the relaxation is not known, but it is likely that the few seconds between test cycles are enough for some relaxation of the edges to occur. This would contribute to the apparent distraction motion of the edges, as they will always be moved upwards back to the starting level. The relative contribution of tensile distraction and upward relaxation motion to the overall tensile vertical deflection would be of interest to learn.

The comparative results of the two glenoid designs tested indicated that the novel design has greater vertical edge motion in tension, despite the FE model predicting the opposite. The presence of a time-dependent deformation effect, not accounted for by the FE model, is the likely cause of this unexpected result. By the standard criterion, the novel design should be re-evaluated before any further development is considered. However, the experimental results indicate that before fixation fails, the edge motion is largely driven by surface deformation, which may not be relevant to the fixation survival. It is possible that the limited criterion of the standard test will not always be the most appropriate predictor of fixation failure.

5. Discussion

In the preceding chapters, the design of the test rig, the design of the edge motion measurement system and the comparative testing of the control and novel glenoid designs were presented and individually discussed. In this chapter, the broader implications the research may have on glenoid fixation testing, new glenoid design considerations and clinical evaluation of surgical outcomes is discussed.

5.1. Implications for Glenoid Loosening Test Methods

The DGL test provides a standardised and highly repeatable method by which to evaluate the fixation survival of new glenoid designs. In the literature, the DGL test has been implemented using varied physical designs and has been used as the basis for multiple FEM studies, as discussed in Chapter 1. The results obtained in this research, however, suggest some areas in which the test may benefit from adjustments. These relate to the ability of the standard test to break the glenoid fixation, the criteria used to evaluate new designs, and the inclusion of measures to account for time dependent deformations of components tested.

The first question raised by the results of this research is simply, is the standard test onerous enough? Of the 12 glenoids tested for the standard test length, none exhibited fixation failure. Of the three samples tested for extended periods of time, only one very poorly cemented sample actually loosened, and that occurred after 250,000 cycles. While the standard test does not require the components to actually fail to perform the comparative evaluation, it would provide a more definitive measure of fixation performance if the test showed loosening for one component design and not the other.

Possible methods to increase the probability of failure include an increase in the applied load or an increase in the number of load cycles performed. However, the opportunity for increasing the applied load is limited by the need to keep the forces within the physiologically likely range, and increasing the number of load cycles will increase the test duration. The latter could be offset by performing the test at the higher limits of the standard recommended cyclic frequency (up to 6Hz). However, the higher frequency will also move the simulated motion further from physiologically feasible actions and may not produce a clinically relevant response from the component. This was observed by Sabesan et al. (2015) when testing larger glenoids at 2Hz resulted in shearing of the fixation pegs. Other researchers who have used lower cyclic frequency when implementing the DGL test include Stautberg et al. (2017) who tested at 1.5Hz, and Junaid et al., (2017) who tested at 0.5Hz. The testing performed in this study had a slower frequency (~0.25Hz) than both the standard recommended 2Hz and the values reported in the

literature, which may have improved the survival of the fixation. A large increase in cycle count does increase the number of loads to higher than is physiologically likely to occur within the 10 years proposed by the standard, but it doesn't induce extreme component behaviour the way increased load or speed does. Performing the tests at both a slower loading frequency and for more load cycles may well be worth the extra time cost that these changes incur.

In the absence of an unambiguous fixation failure, the measure of performance that is used by the DGL test, the vertical ND edge motion before and after cyclic testing, provides limited understanding of glenoid behaviour. For the samples tested here, the first and last values of the vertical ND (provided in **Table 4-9**) indicate edge motions in tension that start at 0mm and increase up to 0.15mm, but provide no insight into how this increase occurred, what other motions occur along with it, or whether the ND values observed will be reliable predictors of fixation failure.

The addition of continuous measurement of the edge motions during the cyclic loading allows us to observe the variation within the test. When looking at only the vertical ND motions (**Figure 4-15**), there is a general trend that in tension there is a quick rise above the neutral at the test start followed by a steadily increasing tensile ND, and that this is accompanied by a much larger compressive ND motion down into the surface which almost immediately reaches equilibrium. These trends are placed into further context by the continuous measurement of the global edge positions. If looking at the ND alone, the trends described imply a glenoid edge that is starting to lift slightly more in tension as the test proceeds, while reaching a maximum compressive depth down into the surface. However, the global trends (**Figure 4-14**) show firstly that for all edges the vertical neutral position compresses down into the surface at the start of the test, amplifying the overall compression of the surface. Further, looking specifically at the LHS novel edge motion, we see the neutral position never reaches a true equilibrium, but continues to compress downwards. The constant compressive vertical ND observed for this measurement is therefore not an indication that the edge has stopped moving down into, and likely damaging, the underlying surface. If before and after measurements are taken relative to the neutral but without a global reference, such interactions of the glenoid with the surface would be obscured. The additional effect of time-dependent strain recovery of the glenoid edges also should be considered when taking before and after edge deflection measurements. The final measurement should either be taken as the last cycle is performed (as continuous measurement allows), or long enough after the test that all strain recovery has occurred, to prevent unquantified contributions of the recovery to the edge deflection amplitudes.

Using only the vertical ND results can also be misleading when identifying trends in the overall glenoid component motion. For example, if we look at the control glenoid at the end of the test, the LHS has a higher lift above its neutral, and a shallower drop below its neutral than the RHS does (LHS: 0.06mm (T)and -0.35mm (C) vs RHS: 0.03mm(T) and -0.43mm (C)). If we had only the vertical values, this result could imply that the glenoid component as a whole had tilted over towards the right. However, when we look at the global horizontal and tilting motions, it is clear that the component is deforming outward in both directions, rather than tilting as a whole. The addition of the horizontal and tilting motions, while tracking the overall neutral positions, allows us to distinguish in this case between deformation and 'rocking' of the component.

A further shortcoming of using only the difference in vertical ND is that, at least in the results of this study, it has not shown itself to be a clear predictor of loosening before the fixation has failed. Once fixation failure has occurred (based on the single instance in which this was observed in sample N7), the sudden increase in the amplitude of this deflection in both tension and compression clearly indicates the failure. However, leading up to this increase (at ~250,000 cycles for N7), the motions measured followed similar trends to other samples, which did not clearly fail even in their extended tests. While the re-tested samples C8 and N1 did have just perceptible motion when rocked by hand after their extended tests, this was at a total of 500,000 cycles for C8 and 830,000 cycles for N1. At 600,000 cycles (between tests 2 and 3 of this sample) N1 did not show any loosening but had larger tensile ND motions than the loosened C8. Again, the limited number of tests does not allow a firm conclusion to be made from these results, but they do suggest *it is possible for a still well-fixed component to have larger tensile distraction motions than one that has begun to loosen*. In this case measuring the additional motion directions did not add further insight, as the trends in these are also not noticeably different before the failure begins. The standard DGL test, even without continuous monitoring, would capture the sudden change in vertical tensile motion, and hence the loosening event, if the recommended humeral head axial motion measurement was included. It is in the cases where loosening has not occurred that the metric of vertical edge deflection becomes less useful.

There is clearly a certain amount of edge motion that will occur in all glenoid components, which is not an indication of the component fixation beginning to fail. The amplitude of this motion will be different for different designs. In the case, of the novel design evaluated here, the increased mobility of the edges is likely influenced by the presence of the surface slot, and may not be related to the condition of the peg fixation. Another example of a design difference would be related to material properties. The components tested here were of medical grade UHMWPE, but not cross-linked UHMWPE. The cross-linked material generally has a lower Young's Modulus

(Lewis, 2001) and so components made from this would likely show more pronounced edge motion than was observed here. Again, this would not be an indication that the more flexible components were at higher risk of fixation failure, only that more deformation of the component was occurring.

A possible better predictor leading up to loosening would be a variation of the edge motions within the design itself. Once the component has settled into its equilibrium condition, a percentage increase in motion from this stable motion inherent to the design could indicate the probability of future loosening. Comparing the percentage of motion change in the two designs, rather than the amplitude of the motion, may be a more relevant evaluation metric. The single failed component dataset in this research is insufficient to make a recommendation as to what an appropriate percentage should be. Junaid et al. (2018) performed a comparative study of *in-vitro* monitoring techniques (measured vertical edge displacement, clinical CT and visual inspections) and found that an increase in measured vertical edge deflection from ~0.25mm to ~0.5mm correlated with initial visual and CT detection of implant failure. Measured edge displacements of ~0.7mm were observed after implant failure. There is no intermediate data provided to indicate the progression of the displacement prior to the initial failure, but based on their reported values a doubling of the displacement could be used as an indicator of the component starting to fail.

A more direct metric of predicting fixation failure would be to measure motion on the fixation pegs themselves, although this would need to be done with cognizance of any disturbance to the fixation itself that might change the results. In the absence of fixation peg motion measurement, radiographic evaluation of the condition of the fixation cement in conjunction with component motion measurements, in the manner of Junaid et al. (2018), allows comparison between the mechanical testing and clinical evaluation methods to be made.

The most direct evaluation method would of course be to simply extend all tests until the fixation fails. This has the potential to increase testing duration considerably if the design has favourable fixation. A more clinically comparable method of evaluating fixation survival would be to perform a test to failure in a shoulder simulator, using an anatomical shoulder motion at physiologically representative rates. This would both extend the test duration and add a requirement for highly specialised equipment. It would therefore still be beneficial to develop a method of evaluating components prior to loosening, that does not rely on the 'stable' edge motions of the comparative designs being equivalent, and which does not compromise the repeatability of, or add unreasonable complexity to, the standard test.

5.2. Implications for New Glenoid Designs

There is a great deal of literature focused on the 'rocking' motion expected when the glenoid edges are eccentrically loaded, but less so on the temporary or permanent deformation of the surface that occurs during the same loading, and how this may impact glenoid survival.

The addition of the horizontal and tilting motion measurements in this study allowed us to identify the complex motions of the edges relative to each other, to the original starting location, and to their prevailing unloaded positions. From these, it was clear that before loosening occurs the deformation of the surfaces contributes more to the motion of the component edges than the tensile distraction does. This is evidenced by the position of the edge in tension remaining below the starting level in the un-failed samples.

The continuous measurements of all three motions indicate there is a certain amount of stable motion that will occur in even a well-fixed glenoid. It would be useful for designers to define this characteristic motion for their component, which would then allow the design to be tested based on a deviation from this baseline. Factors likely to influence the overall motion would be glenohumeral mismatch (Matsen et al., 2008; Sabesan et al., 2015) and material variations, such as using cross linked UHMWPE (instead of the un-cross-linked material used in this research).

A wide range of cross-linked UHMWPE materials have been developed, with varying material properties (Fung et al., 2018; Lewis, 2001; Slouf et al., 2021; Sobieraj et al., 2013). Most of the reported material characteristics relate to the wear resistance of the material. In this research, the elastic modulus of the material is of interest, as it would influence how much of the compressive edge motion could absorbed by stable deflection of the surface, and how much would be rigidly transferred back to the opposing edge as tensile distraction. Lewis (2001) performed a comprehensive review of existing cross-linked and non-cross-linked materials, from which a 'mean of the mean' overview of material properties was calculated. Other than wear resistance, the material properties of cross-linked material are generally poorer. They report a reduction of elastic modulus when cross-linking is applied, as well as reduced ultimate tensile strength, and reduced elongation to failure.

In this case, the reduced elastic modulus may imply that a cross-linked material component would exhibit even greater stable edge motion in compression, compared to the results reported here, but would tend to transfer less motion rigidly back to the opposing edge in tension. Anglin et al. (2001) observed a small increase in tensile distraction when comparing an all-polyethylene

component to one of the same designs that had a titanium mesh backing, which increased the rigidity. The less rigid material would also improve the force transfer from the humeral head to the underlying bone.

There is, however, a limit to how much compression can be applied to the underlying bone before the implant damages the bone surface rather than promoting bone growth. Junaid et al. (2018) visually observed bone loss under the compressive edge of *in-vitro* loaded glenoid components. Terrier et al. (2012) simulated the effects of different polyethylene thicknesses of the glenoid component (from 2mm to 6mm) and found portions of the cement mantle exceeding the fatigue limit of 5MPa at thinner surface thicknesses and almost none at 6mm thickness. A small increase in bone volume (from 294mm^3 to 631mm^3) exceeding the failure limit of 1% was also observed as the surface thickness decreased.

The optimal amount of relative motion between the bone and the surface would be that which promotes bone growth. Bone ingrowth onto cementless implants occurs when the micromotions remain below a threshold of 40μm to 150μm (Sukjamsri et al., 2015). To relate this to the current research we can compare this motion threshold to the movement of the glenoid edge neutral position in only the 10 conditioning cycles, which could feasibly represent a real patient action. In the 10 cycles of conditioning the neutral position of the glenoid edges moved -0.16±0.04mm to -0.24±0.07mm. Even excluding the additional compressive and tensile motions around this neutral, these motions exceed the threshold for bone ingrowth. Ignoring the complexity of adding the horizontal and tilting motions, and looking at vertical only, the total amplitude of vertical motions measured (i.e. height of tension to depth of compression) varies between approximately 0.4mm and 0.55mm, which far exceeds the micromotion value promoting ingrowth.

While Sawbones may compress and form a stable surface, the living bone would be traumatised by this level of compression, particularly if it was applied and released as the time-dependent deformation and strain recovery indicates it would be. The underlying bone could be damaged and produce an unsupported glenoid surface, which would then promote loosening. This could be a reason why the components that had durable fixation in this *in-vitro* test, still perform badly *in-vivo*. Szabo et al. (2005) compared the fixation stability of keeled components implanted in glenoid bone that had been prepared by standard methods and by the addition of bone compaction prior to implantation. They found a decrease in immediate postoperative keel radiolucencies (11% vs 38%) and a reduction in the progression of periglenoid radiolucencies for the components implanted in compacted bone. Designers should consider the progression of

compressive motions occurring in cyclic loading when simulating new glenoid designs, to properly account for potential damage to the underlying bone.

Quinci et al. (2014) investigated the inclusion of viscoelastic and creep behaviour in models predicting wear of a unicondylar knee prosthesis. They found that models which included only elastoplastic properties underpredicted the deformations of the component compared to the viscoelastic model and to their experiment. Another time-dependent material property that should be considered is fatigue resistance, which has been shown to be lower for cross-linked UHMWPE. For a prosthesis such as the glenoid, which experiences repeated eccentric loading causing repeated material deflection, this reduction in fatigue resistance is particularly concerning as a possible cause of component fracture. Research related to the properties and improvement of cross-linked materials by, for example, vitamin E infusion (Oral et al., 2008), is ongoing (Scholz et al., 2018; Sirimamilla & Rimnac, 2019; Slouf et al., 2021).

Overall, new glenoid designs should aim to balance the component to be flexible enough to prevent stress shielding and to reduce tensile stress transfer to the unloaded edge, while also low enough to prevent excessive compression of the underlying bone and cement mantle and limit fatigue damage. Modelling methods that include the time variable material properties including creep, cyclic strain recovery and fatigue should be developed to properly assess new designs. The test method developed in this research could be used to verify such models by means of the continuous complex edge motion measurement. Being able to quantify the complex deformation of the component during loading puts the designer in a better position to identify and pre-empt potential modes of failure other than the 'rocking horse'.

5.3. Implications for Surgical Techniques and Evaluation of Outcomes

From a clinical perspective, the most unambiguous outcome of this research is the reiteration of the conclusions of Matsen et al. (2008), Nyffeler et al. (2003), Terrier et al. (2005), and others that good surface preparation and good cement technique are crucial to the long-term survival of the glenoid prosthesis. In this research, poor cement distribution resulted in the only clear fixation failure of a new glenoid component, and multiple catastrophic surface fractures in age embrittled components in the rig validation testing. While our experimental results support the conclusion of Nyffeler, Meyer, et al. (2006), that some cement behind the surface is acceptable, this layer must be evenly distributed and leave no section of the back surface of the glenoid unsupported.

The incidence of radiolucent lines immediately after surgery was reported by (Grob et al., 2021) to be up to 90% for 147 patients with pegged glenoids. This implies the back of the glenoid may

very quickly show a gap relative to the underlying cement/bone, even if the peg fixation is still intact. In contrast, Everding et al. (2016) performed a retrospective analysis of 100 pegged glenoid TSA surgeries and found none to have postoperative radiolucent lines. They attribute this result to surgical technique, including careful reaming of the bone to match the glenoid surface, placing cement on the back of the glenoid, and pressurising the cement.

Understanding how important the support of the component is to its survival, makes it clear how problematic the observed stable edge motions are from the perspective of post-surgical evaluation. If the surface deformation edge motions such as those measured were to occur in a real implant, a radiolucent line would develop behind the surface, implying an unsupported component, even if the cement was well distributed. The severity of, and time taken to induce these surface deformations is hard to gauge from this research, because of the time-dependent relaxation which would likely be different in a patient than in the mechanical test.

For surgeons monitoring patients by radiographic study, at what point should the level of radiolucency behind the glenoid become concerning? The results of this study indicate that a noticeable increase/change in the level of radiolucency could be used as an indicator of loosening, as this would be evidence of the increase in edge motions postulated in the previous section to be a good indicator of initial loosening. However, the settling period seen in the test results, which was not an indicator of loosening, would need to be completed before a change in radiolucency would necessarily be concerning. It is also unclear how this settling period would be affected by the intermittent loading that would be expected in daily life, rather than the condensed loading of the mechanical test that does not allow time for the full relaxation of the material between load cycles. A more useful measure might be the level of motion expected during a small number of initial cycles, such as was seen in the 10 conditioning cycles, which is physiologically likely as part of the patient's daily life and surgical rehabilitation programme. Further, is the motion of the glenoid edges likely to induce the same amount of pain, a common reason for a TSA revision (Australian Orthopaedic Association, 2022), as motion around the peg fixation would? If it is, then it would be a cause for revision even if it is not an indication that actual fixation failure will occur.

Further, while the loosened sample indicated that an increase in deflection around the neutral (unloaded) position is very evident when the component has loosened, the actual change in the neutral position was not prominent in the vertical direction (the LHS rose by 0.2mm across the loosening event, while RHS showed no noticeable change). A radiograph taken while the shoulder is resting may therefore not capture the mobility of a loosened component under load.

Taking a radiograph with the shoulder in a loaded state would provide a better indication of loosening, but would require great care to replicate accurately, and has the further disadvantage of exposing the patient to multiple X-ray doses instead of just one at each stage of evaluation.

Radiolucency around the pegs themselves is a clear indicator of loosening (Lazarus et al., 2002) but is difficult to relate to the edge motions prior to the onset of loosening. Radiolucency behind the surface appears likely, and possibly unavoidable, even when loosening has not occurred. More and more detailed comparative studies such as that of Junaid et al. (2018) are needed, characterising the more easily measured edge motions leading up to loosening, comparing them *in-vitro* to the incidence of loosening by extended testing, and *in-vivo* to reported pain for comparable motions. In this way, the clinical feedback can be translated into improved designs, based on overall glenoid behaviour, even prior to the onset of loosening.

5.4. Limitations

The current study had several limitations, related to the test equipment and samples.

Firstly, as discussed in Section 2.7.3 Deviations from the Standard, in the final design of the ASTM DGL test rig the application of the cyclic load by deadweight did not provide the level of control over the normal load that is recommended by the standard. Further, the test rig did not directly monitor of control shear load applied. This prevents the total load on the glenoid from being monitored and controlled by this iteration of the test rig. Improvements to the design are suggested in Section 6.2.1.

Secondly, the rig validation study was performed using expired glenoids ranging from size 42 to size 56, in combination with a single Ø44 humeral head. The radial mismatch between these glenoids and the humeral head was therefore both varied and not according to standard surgical recommendations. This non-standard glenohumeral mismatch, and unknown material condition of the glenoids, limits the use of the DGL test rig validation results to the evaluation of the test rig functionality only.

Thirdly, there was no statistical *a-priori* sample size calculation performed to select the sizes of the novel and control glenoid groups. The number of glenoids available for testing in each group was limited by financial and time constraints. The choice of sample size was based on the recommended minimum of three samples in the standard combined with the resources available to acquire additional samples.

The fourth limitation of this thesis was the use of self-manufactured glenoid samples made from non-cross-linked UHMWPE, rather than commercially available (clinically approved)

components. The choice to manufacture the control components was made to maintain consistency between the control and novel glenoids, since the novel component is not commercially available. While using non-cross-linked UHMWPE is a deviation from current clinically used glenoids, it improves the comparative analysis performed on the two distinct designs.

6. Conclusion and Future Perspectives

6.1. Conclusion

The work presented here aimed to test whether it is possible to continuously measure the edge motion of the glenoid in three degrees of freedom during the ASTM F2028 test, if doing this provides deeper insight into the behaviour of the glenoid component during the test, and how this behaviour may influence the fixation failure.

For the first part, the ASTM F2028 DGL test rig was designed and validated according to the standard's requirements and several improvements to the testing processes of novel shoulder implants. The test rig utilises a linear actuator to apply the shear motion and a deadweight to apply the normal load. The basic functionality of the test rig was validated against the design criteria during the edge motion measurements system prototyping phase.

Early edge motion measurement system prototypes were intended to measure only the vertical motion as specified by the standard. However, horizontal and tilting motions confounded the vertical measurements by shifting the displacement sensors' orientation. This served to highlight the extent to which these motions occur. The LVDT lever arm measurement system was designed to be robust to the effect of the additional motions and to quantify all three motions for the duration of the cyclic testing.

The LVDT lever arm system uses a lever with one end pinned directly to the glenoid edge and pivoted through a rod end bearing at approximately 1/3 of its length, to amplify the edge motion at the free end of the lever. A rigid lightweight (Perspex) measuring block is mounted perpendicular to the lever axis on the free end. Against the sides of this measuring block, three LVDT sensors are mounted, two vertically and one horizontally. The sensors were chosen to apply minimal force to the block, with the vertical sensors having free armatures, held on the surface by gravity, and the horizontal sensor spring guided with a spring force of 1N. In this way, force transfer back to the lever fixation is minimised, and the sensors themselves do not move the block.

The combined readings of the three sensors were converted to motion at the glenoid edge using an analytical algorithm, based on the geometry of the system. This algorithm was solved for the edge motions using MATLAB. The conversion of LVDT readings to edge motion using the algorithm was validated *in-silico* by means of a SolidWorks motion simulation. Two edge motions (indicative of a tensile and a compressive motion) were input into the SolidWorks model, and the motion of the model sensor tips was recorded. The recorded motions were then input into the

MATLAB algorithm, and the edge motions were calculated. These were then compared to the original motion inputs, and good correlation was observed. Therefore, the motion calculation algorithm and its solution using MATLAB were considered to be valid. To finally validate the measurement system, the physical system needed to be tested to ensure it could endure the full cyclic testing without failure of components or fixation of the levers.

The measurement system functional validation was performed in combination with the final functional testing of the test rig itself, by performing the ASTM DGL test, including subluxation distance tests and the cyclic loading test, on a series of expired glenoid components. During this testing modifications were made, particularly to improve the rigidity and durability of the lever fixation. These modifications included adding an adhesive and an angled washer, to ensure the flat edge of the lever end sat flush against the vertical outer glenoid edge and the fixation survived the cyclic test. With these modifications, it was found that if the initial fixation was firm, the lever would remain firm for the full cyclic test.

The validated motion calculation method, combined with a physical system capable of performing the required measurements, is used to confirm the first part of the research question, that *the measurement of all three edge motions for the duration of the ASTM F2028 DGL test is feasible and valid*.

For the second part of the research question, *'Are the horizontal and tilt motions also significantly influencing the loosening of the glenoid component, and will quantifying the tilt and horizontal motion provide a more comprehensive understanding of the loosening mechanisms of the component?'* the augmented test rig was used to perform the comparative DGL test on the control and novel glenoid designs.

The results of this testing were used both to evaluate the novel design, as well as to investigate the loosening behaviour of both designs and to try to gain insight into the complex glenoid edge motions. Data from six samples of each design, tested for the standard 100,000 cycles, was used in the analysis. None of these samples showed fixation failure, so additional extended testing was performed on a previously excluded (poorly cemented) novel sample, and two previously tested (one novel and one control) samples. In these extended tests, only the poorly cemented sample showed clear fixation failure, indicated by a dramatic change in edge motion amplitudes. It is further noted that in the rig validation testing, multiple poorly cemented samples fractured completely. While age embrittlement likely contributed to these fractures, the results confirm the widely reported assertion in the literature that the back surface of the glenoid should be evenly and completely supported, to promote fixation survival.

Comparison of the subluxation distances measured and the vertical deflection from the neutral (unloaded) edge at the start and end of the tests correlated well with values reported in the literature. The continuously measured motions in the three directions indicated deformation of the glenoid edges occurred as the tests proceeded. This deformation was quick at the start of the test, particularly in the first 10 cycles, and then reached a relatively stable position, usually after 10,000 cycles. The combined motions indicate the component surfaces were being deformed downwards and outwards with an outward edge tilt, at both edges. This overall deflection was present even when the humeral head was at the centroid and the edges were unloaded.

That both the edges are deforming with this downward and outward motion indicates that, in the global frame of reference, the component is not 'rocking' as is generally expected to occur in the literature. Within the overall deformation, tensile and compressive motions decreased or increased the deformations around the prevailing unloaded edge position. This local 'rocking' motion was not large enough to bring the edges of the glenoids back up to their starting levels, indicating that the deformation of the component has a larger influence on the overall edge motion than the tensile distraction caused by loading of the opposite edge. The novel glenoid sample that failed in the extended test did show the classic 'rocking' motion. In this component alone the edge in tension rose above the starting level. The rocking motion is therefore clearly evident in a component that has loosened but is not the main factor in the overall edge motion of a component that is still well-fixed.

Further observed in the extended testing, for the components that were re-tested, was that the initial quick move to a new neutral position was seen for the second and third tests of the same sample. This means that between the tests, the deformation of the surface has relaxed back toward its original position. The surface deformation is therefore, at least partially, not a permanent effect. This behaviour is in keeping with strain recovery characteristics of UHMPE reported in the literature. The rate of relaxation is not known, but strain recovery at a logarithmically decreasing rate has been reported, which indicates that a large portion of the strain recovery will happen shortly after the edge is unloaded. This raises questions as to how the relaxation of the component may influence the tensile motions measured. Even in the case of no opposing edge loading, the relaxation would add an upward and inward motion as the glenoid reverted to its original shape. The rate of the relaxation, and how the test parameters may be inducing and holding a deformation of the glenoid, compared to how this would be induced in a physiological manner, warrant further study.

When the control and novel data were compared, the novel glenoid did not out-perform the control by the standard test criteria. The vertical ND of the novel was statistically larger than that of the control and continued to increase gradually over the duration of the test. This contradicted the FE model developed by the original designer of the novel glenoid, which predicted reduced tensile edge deflection when loaded under DGL test conditions. It is believed that the relaxation motions are adding to the tensile distraction motions in the experimental results, making them larger than expected in the model which does not include the time-dependent material behaviours induced by the cyclic loading. Further study of the novel glenoid is recommended, to more unambiguously evaluate its potential for fixation failure.

The presence of the time-dependent deformation motions, which combine with the tensile distraction transferred by eccentric loading, raises the question of whether the comparison of tensile deflection between designs is the best predictor of future loosening. Although tensile distraction by rocking is a clear indicator that loosening has occurred, while the component is still well fixed it may be more strongly influenced by material deformation than by the rocking of the component. It is difficult to draw conclusions in this regard because only one sample failed, and that was certainly a result of poor cement distribution. It would be useful to measure the three motion directions continuously using the same test method, but in which all tests are run to fixation failure. This would allow correlation to be made between the complex motions and the likelihood of failure, and could further be compared to radiographic studies and clinical outcomes.

Even if the vertical deflection remains the best predictor of loosening by the rocking horse effect, the addition of the horizontal and tilting motions, while tracking the overall neutral positions, provides a more comprehensive picture of the overall component motion. It allows us to distinguish between deformation and rocking of the component, without adding undue complexity to the standard test. Understanding the overall response of the glenoid further allows designers to make better-informed choices around other design criteria, such as material properties. For example, quantifying the cyclic deformation would help gauge the potential response and failure of a material based on fatigue resistance, known to be reduced in modern cross-linked materials. Quantifying the global compressive interaction of components with the underlying bone would help to evaluate the potential for bone and cement mantle damage.

While the results presented do not conclusively show that the additional motions can be used to predict fixation loosening, largely due to the lack of failed components in the experimental testing from which to draw data, it is clear that with only the vertical motion measured, the response of

the glenoid to the loading is poorly understood. There is much literature regarding the 'rocking' of the glenoid when eccentrically loaded, but little regarding the complex, time-dependent deformations which also occur. Understanding the overall response of the glenoid would allow designers to make better-informed design choices, predict more potential failure modes, and ultimately improve the longevity of the designs.

6.2. Recommendations for Future Work

The results presented here raise many questions related to the factors influencing glenoid survival, as well as the test methods currently used to evaluate it. For example, how would the time-dependent deformation be different in a faster-cycled test? How would cross-linked material influence the edge deflection? Does the time-dependent deformation play a role in TSA in patients, where the patient would never load their shoulder with such sustained frequency? How do the settling and the relaxing of the edges affect the formation of radiolucent lines in patients?

Based on the results of this research, further research is suggested, firstly related to the design of the testing equipment, and then to how this (or similar) equipment could be used to better the understanding of glenoid behaviour.

6.2.1. Suggested Improvements to Test Rig Functionality

While the test rig built for this study performed within the design criteria set, there are some aspects which could be improved for use in future studies.

The application of the normal force by passive deadweight did not allow as fine a tolerance as the ASTM standard suggests and has overall variation during the cycle that is a function of the motion of the system rather than a controlled input. Despite the additional cost, it is recommended that the inner weight housing unit be replaced by a second linear actuator, with force feedback control, mounted within the outer weight housing, to which the humeral head would be mounted. This would give the operator more precise control over the force applied. Further, a load cell should be added between the outer housing and horizontal linear actuator to determine the shear force directly.

Finally, the source of the noted endpoint delay should be determined and eliminated. It is crucial for any study comparing the effect of surface speed and cyclic frequency that all aspects of the horizontal motion are fully defined. For the edge motion measurement system, it is recommended that all sensors be converted to captive bushing types, to eliminate the possibility

of future sensor damage. Using the improved test rig, a number of future studies would be of interest, both for the novel design evaluated in this research, and general glenoid prostheses.

6.2.2. Further Novel Glenoid Design Development

The results of the standard ASTM test indicate that the novel glenoid is likely to be less durable than the control. Additional design work is therefore required before further development or commercialisation of the novel design should be considered. However, since the novel designs tested did not fail in the experimental testing performed, even after 600,000 cycles in the case of N1, would be worth performing further testing on the design as it stands, to unequivocally evaluate the loosening likely to occur, before redesign is performed.

In this case, it is recommended that a series of novel samples are tested to failure, using the same test parameters used in this research. The actual occurrence of failure could then be compared to the early edge motion behaviours, and used to judge the best route forward for redesign.

6.2.3. Comparison of Effect of Varied ASTM F2028 Test Parameters

The ASTM F2028 DGL test sets a number of recommendations for parameters at which testing is performed but does not stipulate exact requirements for, for example, normal load applied or cyclic testing speed. This allows freedom within the research space but does make the comparison of results between studies more complex. It would be of interest to see how the variation of these parameters affects the test results for a given design. The most relevant of the parameters based on the results of this research is the speed at which the test is performed, both related to surface sliding speed and overall cyclic frequency.

The ASTM recommendation in this regard, of 2Hz, is particularly vague as it results in dramatically different sliding speeds for different glenoid sizes and subluxation distances. Sabesan et al. (2015) reported the consequences of this in their research, where at 2Hz the larger glenoids tested were sheared out of the bone substitute, suffering massive fixation peg deformation.

The first recommendation for further study in this regard would therefore be to perform the standard DGL test, with the added edge motion measurements, on identical glenoid components, at increasing surface sliding speeds, but with little to no delay between cyclic motions.

The second recommendation would be to perform the test in the same way but with a set surface speed, and increasing delays between the cycles, (with the humeral head pausing at the centroid of the glenoid) to investigate the time taken for the edges to relax out of their deformed state.

A third possibility would be to create a loading speed, and cyclic frequency for a given period (e.g. one day) that represents a 'typical' day in the life of a TSA recipient and apply this in the test.

The goal of these tests would be to try to refine the standard test parameters to more closely represent the daily life loading the glenoid would experience, particularly by taking into account the time-dependent deformations that can be induced by this loading.

The test rig could further be used to individually investigate the effect of variables within the sample setup, such as differing bone quality or positioning of the implant to simulate improperly located glenoids in surgery, and how implants with these properties respond to variations in loading and cyclic motion speeds.

6.2.4. Comparison of the Same Design in Different Materials

Directly investigating the influence of using different materials would also be of interest. The popularity of cross-linked UHMWPE because of its improved wear properties makes studies of the fixation survival and fatigue resistance of glenoids of this material crucial. A comparative study of the same glenoid design, using un-cross-linked vs different options of cross-linked materials (including the vitamin E-infused material which claims better fatigue resistance) should be performed.

In such a study the augmented test rig could be used to determine:

- How does the deformation of the component change?
- How does the fixation durability change (is loosening by 'rocking horse' influenced)?
- Does another failure mode come into play (e.g. fatigue failure)?
- What is the rate at which strain recovery occurs, is any permanent deformation induced by the loading, and at how many cycles does this occur?

6.2.5. Companion Radiographic and Clinical Comparisons

Any, or all, of the above studies could be accompanied by radiographic analysis of the *in-vitro* test samples. Careful choice of the glenoids chosen in the *in-vitro* tests, to match well-documented components in the literature, would allow a continuous study of the progression of radiolucent lines with a known applied load and loosening occurrence, to clinically observed radiolucency and its associated clinical outcomes.

6.2.6. Companion FEM Analyses

Finally, like the companion radiographic analysis, any or all of the above experiments could be accompanied by a dynamic FE model of the experimental conditions. A starting point in this study could be to update the FEM of Dey (2018) to include the viscoelastic behaviour of the UHMWPE, and then re-compare the results of the FEM to the experimental results obtained in this research.

Another consideration for the FE models is to revisit the cement/UHMPE and cement/bone interface characteristics, with the knowledge that the glenoid surface deformation may cause delamination at the cement/UHMWPE interface due to mismatched elongation properties between these materials.

A comprehensive FE model with the above characteristics could then be adapted to assess the stress in the bone during the various loading conditions suggested in Section 3.2.3.

References

Ackland, D. C., Patel, M., & Knox, D. (2015). Prosthesis design and placement in reverse total shoulder arthroplasty. *Journal of Orthopaedic Surgery and Research*, *10*(1), 101. https://doi.org/10.1186/s13018-015-0244-2

American Society for Testing and Materials. (2009). *F1829-98 (2009) Standard Test Method for Static Evaluation of Glenoid Locking Mechanism in Shear 1*. American Society for Testing and Materials. https://doi.org/10.1520/F1829-98R09

American Society for Testing and Materials. (2017). *Standard Test Methods for Dynamic Evaluation of Glenoid Loosening or Disassociation (ASTM Standard No. F2028-17)*. https://doi.org/10.1520/F2028-17

American Society for Testing and Materials. (2018). *Standard specification for shoulder prostheses (ASTM Standard No. F1378-18e1)*. https://doi.org/10.1520/F1378-18E01

American Society for Testing and Materials. (2020). *Standard Test Method for Determining the Axial Disassembly Force of Taper Connections of Modular Prostheses (ASTM Standard No. F2009-20)*. https://doi.org/10.1520/F2009-20

American Society for Testing and Materials. (2021). *Standard Specification for Rigid Polyurethane Foam for Use as a Standard Material for Testing Orthopaedic Devices and Instruments (ASTM Standard No. 1839-08)*. https://compass.astm.org/document/?contentCode=ASTM%7CF1839-08R21

Anglin, C., Wyss, U. P., Nyffeler, R. W., & Gerber, C. (2001). Loosening performance of cemented glenoid prosthesis design pairs. *Clinical Biomechanics*, *16*(2), 144–150. https://doi.org/10.1016/S0268-0033(00)00078-4

Anglin, C., Wyss, U. P., & Pichora, D. R. (2000a). Glenohumeral contact forces. *Proceedings of the Institution of Mechanical Engineers, Part H: Journal of Engineering in Medicine*, *214*(6), 637–644. https://doi.org/10.1243/0954411001535660

Anglin, C., Wyss, U. P., & Pichora, D. R. (2000b). Mechanical testing of shoulder prostheses and recommendations for glenoid design. *Journal of Shoulder and Elbow Surgery*, *9*(4), 323–331. https://doi.org/10.1067/mse.2000.105451

Anglin, C., Wyss, U. P., & Pichora, D. R. (2000c). Shoulder prosthesis subluxation: Theory and experiment. *Journal of Shoulder and Elbow Surgery*, *9*(2).

https://doi.org/10.1067/mse.2000.105

Ansari, F., Ries, M. D., & Pruitt, L. (2016). Effect of processing, sterilization and crosslinking on UHMWPE fatigue fracture and fatigue wear mechanisms in joint arthroplasty. *Journal of the Mechanical Behavior of Biomedical Materials*, *53*, 329–340. https://doi.org/10.1016/j.jmbbm.2015.08.026

Asadi Nikooyan, A., Veeger, H. E. J., Chadwick, E. K. J., Praagman, M., & Van Der Helm, F. C. T. (2011). Development of a comprehensive musculoskeletal model of the shoulder and elbow. *Medical and Biological Engineering and Computing*, *49*(12), 1425–1435. https://doi.org/10.1007/s11517-011-0839-7

Australian Orthopaedic Association. (2022). Australian Orthopaedic Association National Joint Replacement Registry. Hip, Knee & Shoulder Arthroplasty: 2022. *Annual Report*, 1–430.

Avanzini, A. (2011). Effect of cyclic strain on the mechanical behavior of virgin ultra-high molecular weight polyethylene. *Journal of the Mechanical Behavior of Biomedical Materials*, *4*(7), 1242–1256. https://doi.org/10.1016/j.jmbbm.2011.04.010

Bohsali, K. I., Wirth, M. A., & Rockwood, C. A. (2006). Complications of Total Shoulder Arthroplasty. *Journal Of Bone and Joint Surgery*, *88-A*(10), 2279–2290.

Boileau, P. (2011). Biographical Sketch: Paul M Grammont, MD (1940). *Clinical Orthopaedics and Related Research*, *469*, 2422–2423. https://doi.org/10.1007/s11999-011-1959-y

Braman, J. P., Falicov, A., Boorman, R., & Matsen, F. A. (2006). Alterations in surface geometry in retrieved polyethylene glenoid component. *Journal of Orthopaedic Research*, *24*(6), 1249–1260. https://doi.org/10.1002/jor.20158

Buchler, P., Ramaniraka, N. A., Rakotomanana, L. R., Iannotti, J. P., & Farron, A. (2002). A finite element model of the shoulder: application to the comparison of normal and osteoarthritic joints. *Clinical Biomechanics*, *17*(9–10), 630–639.

Chamseddine, M., Breden, S., Pietschmann, M. F., Müller, P. E., & Chevalier, Y. (2019). Periprosthetic bone quality affects the fixation of anatomic glenoids in total shoulder arthroplasty: in vitro study. *Journal of Shoulder and Elbow Surgery*, *28*(1), e18–e28. https://doi.org/10.1016/j.jse.2018.07.012

Charlton, I. W., & Johnson, G. R. (2006). A model for the prediction of the forces at the glenohumeral joint. *Proceedings of the Institution of Mechanical Engineers, Part H: Journal of Engineering in Medicine*, *220*(8), 801–812. https://doi.org/10.1243/09544119JEIM147

Chin, P. Y. K., Sperling, J. W., Cofield, R. H., & Schleck, C. (2006). Complications of total shoulder arthroplasty: Are they fewer or different? *Journal of Shoulder and Elbow Surgery*, *15*(1), 19–22. https://doi.org/10.1016/j.jse.2005.05.005

Churchill, R. S., Boorman, R. S., Fehringer, E. V., & Matsen, F. A. (2004). Glenoid Cementing May Generate Sufficient Heat to Endanger the Surrounding Bone. *Clinical Orthopaedics and Related Research*, *419*, 76–79. https://doi.org/10.1097/00003086-200402000-00013

Cofield, R. H. (1994). Uncemented total shoulder arthroplasty. A review. *Clinical Orthopaedics and Related Research*, *307*, 86–93.

Collins, D., Tencer, A., Sidles, J., & Matsen, F. (1992). Edge displacement and deformation of glenoid components in response to eccentric loading. The effect of preparation of the glenoid bone. *Journal of Bone and Joint Surgery - Series A*, *74*(4), 501–507. https://doi.org/10.2106/00004623-199274040-00005

Constant, C. R., Gerber, C., Emery, R. J. H., Søjbjerg, J. O., Gohlke, F., & Boileau, P. (2008). A review of the Constant score: Modifications and guidelines for its use. *Journal of Shoulder and Elbow Surgery*, *17*(2), 355–361. https://doi.org/10.1016/j.jse.2007.06.022

Damsgaard, M., Rasmussen, J., Christensen, S. T., Surma, E., & de Zee, M. (2006). Analysis of musculoskeletal systems in the AnyBody Modeling System. *Simulation Modelling Practice and Theory*, *14*(8), 1100–1111. https://doi.org/10.1016/j.simpat.2006.09.001

Delp, S. L., Anderson, F. C., Arnold, A. S., Loan, P., Habib, A., John, C. T., Guendelman, E., & Thelen, D. G. (2007). OpenSim: Open-source software to create and analyze dynamic simulations of movement. *IEEE Transactions on Biomedical Engineering*, *54*(11), 1940–1950. https://doi.org/10.1109/TBME.2007.901024

Dey, R. (2018). *Design and Development Towards a Novel Prosthesis for Total Shoulder Arthroplasty to Reduce Aseptic Glenoid Loosening* [University of Cape Town]. http://hdl.handle.net/11427/36748

Edwards, T. B., Labriola, J. E., Stanley, R. J., O'Connor, D. P., Elkousy, H. A., & Gartsman, G. M. (2010). Radiographic comparison of pegged and keeled glenoid components using modern cementing techniques: A prospective randomized study. *Journal of Shoulder and Elbow Surgery*, *19*(2), 251–257. https://doi.org/10.1016/j.jse.2009.10.013

Everding, N., Levy, J., Formaini, N., Blum, S., Gil, C., & Verde, K. (2016). Observation of initial postoperative radiolucent lines using a modern pegged-glenoid design. *International*

Journal of Shoulder Surgery, *10*(2), 67–71. https://doi.org/10.4103/0973-6042.180718

Farron, A., Terrier, A., & Büchler, P. (2006). Risks of loosening of a prosthetic glenoid implanted in retroversion. *Journal of Shoulder and Elbow Surgery*, *15*(4), 521–526. https://doi.org/10.1016/j.jse.2005.10.003

Ferguson, M., Aaron, D. L., Lang, P., Rubín, C. G., Surgery, O., York, N., & York, N. (2013). Medium- and Long-Term Radiographic Evaluation of Sur vivorship of Pegged Versus Keeled Glenoid Components. *University of New Mexico Orthopaedics Research Journal*, *2*(1), 45–49.

Flatow, E. L., & Harrison, A. K. (2011). A history of reverse total shoulder arthroplasty. *Clinical Orthopaedics and Related Research*, *469*(9), 2432–2439. https://doi.org/10.1007/s11999-010-1733-6

Franklin, J. L., Barret, W. P., Jackins, S. E., & Matsen, F. A. (1988). Glenoid loosening in total shoulder arthroplasty: Associatio with rotator cuff deficiency. *The Journal of Arthroplasty*, *3*(1), 39–46. https://doi.org/10.1016/S0883-5403(88)80051-2.

Fung, M., Bowsher, J. G., & Van Citters, D. W. (2018). Variation of mechanical properties and oxidation with radiation dose and source in highly crosslinked remelted UHMWPE. *Journal of the Mechanical Behavior of Biomedical Materials*, *82*(March), 112–119. https://doi.org/10.1016/j.jmbbm.2018.03.005

Garreau De Loubresse, C., Norton, M. R., Piriou, P., & Walch, G. (2004). Replacement arthroplasty in the weight-bearing shoulder of paraplegic patients. *Journal of Shoulder and Elbow Surgery*, *13*(4), 369–372. https://doi.org/10.1016/j.jse.2004.01.019

Giles, J., Glennie, A., Ferreira, L., Athwal, G., Faber, K., & Johnson, J. (2010). Mechanisms of Load Transfer between a Polyethylene Glenoid Implant and Bone : Implications for Loosening in Total Shoulder Arthroplasty Poster No . 1835 • 56th Annual Meeting of the Orthopaedic Research Society. *56th Annual Meeting of the Orthopaedic Research Society*, *Poster No*, 1835.

Glenday, J., Kontaxis, A., Roche, S., & Sivarasu, S. (2019). Effect of humeral tray placement on impingement-free range of motion and muscle moment arms in reverse shoulder arthroplasty. *Clinical Biomechanics*, *62*(February), 136–143. https://doi.org/10.1016/j.clinbiomech.2019.02.002

Gorica, Z., McFarland, K., O'Neill, C. N., Vanderbeck, J., & Vap, A. R. (2023). Anatomic Shoulder Arthroplasty in the Setting of Concurrent or Prior Rotator Cuff Repair: A Systematic Review.

Journal of Shoulder and Elbow Arthroplasty, *7*, 247154922311527. https://doi.org/10.1177/24715492231152733

Government Gazette 40480 (2016): Medicines and Related Substances Act (101/1965): Regulations relating to medical Devices and In-Vitro Diagnostic Medical Devices (IVDS) (SAHPRA, 2017).

Grammont, P. M., & Baulot, E. (1993). Delta Shoulder Prosthesis for Rotator Cuff Rupture. *Orthopedics*, *16*, 65–68. https://doi.org/10.1007/s11999-011-1960-5

Gregory, T., Hansen, U., Taillieu, F., Baring, T., Brassart, N., Mutchler, C., Amis, A., Augereau, B., & Emery, R. (2009). Glenoid loosening after total shoulder arthroplasty: An in vitro CT-scan study. *Journal of Orthopaedic Research*, *27*(12), 1589–1595. https://doi.org/10.1002/jor.20912

Grob, A., Freislederer, F., Marzel, A., Audigé, L., Schwyzer, H. K., & Scheibel, M. (2021). Glenoid component loosening in anatomic total shoulder arthroplasty: Association between radiological predictors and clinical parameters—an observational study. *Journal of Clinical Medicine*, *10*(2), 1–13. https://doi.org/10.3390/jcm10020234

Gulotta, L. V., Choi, D., Marinello, P., Knutson, Z., Lipman, J., Wright, T., Cordasco, F. A., Craig, E. V., & Warren, R. F. (2012). Humeral component retroversion in reverse total shoulder arthroplasty: a biomechanical study. *Journal of Shoulder and Elbow Surgery*, *21*(9), 1121–1127. https://doi.org/10.1016/j.jse.2011.07.027

Gunther, S. B., Graham, J., Norris, T. R., Ries, M. D., & Pruitt, L. (2002). Retrieved glenoid components: A classification system for surface damage analysis. *Journal of Arthroplasty*, *17*(1), 95–100. https://doi.org/10.1054/arth.2002.27671

Gunther, S. B., Lynch, T. L., O'Farrell, D., Calyore, C., & Rodenhouse, A. (2011). Finite element analysis and physiologic testing of a novel, inset glenoid fixation technique. *Journal of Shoulder and Elbow Surgery*, *21*(6), 795–803. https://doi.org/10.1016/j.jse.2011.08.073

Gupta, S., Van Der Helm, F. C. T., & Van Keulen, F. (2004). Stress analysis of cemented glenoid prostheses in Total Shoulder Arthroplasty. *Journal of Biomechanics*, *37*(11), 1777–1786. https://doi.org/10.1016/j.jbiomech.2004.02.001

Hopkins, A. R., Hansen, U. N., Amis, A. A., Knight, L., Taylor, M., Levy, O., & Copeland, S. A. (2007). Wear in the prosthetic shoulder: Association with design parameters. *Journal of Biomechanical Engineering*, *129*, 223–230. https://doi.org/10.1115/1.2486060

Hopkins, A. R., Hansen, U. N., Amis, A. A., Taylor, M., Gronau, N., & Anglin, C. (2006). Finite element modelling of glenohumeral kinematics following total shoulder arthroplasty. *Journal of Biomechanics*, *39*(13), 2476–2483. https://doi.org/10.1016/j.jbiomech.2005.07.031

Iannotti, J. P., Spencer, E. E., Winter, U., Deffenbaugh, D., & Williams, G. (2005). Prosthetic positioning in total shoulder arthroplasty. *Journal of Shoulder and Elbow Surgery*, *14*(1 SUPPL.), S111–S121. https://doi.org/10.1016/j.jse.2004.09.026

International Organisation for Standardization. (2016). *Medical devcies - Quality management systems - requirements for regulatory purposes (ISO Standard No. 13485:2016)*. https://www.iso.org/standard/59752.html

International Organisation for Standardization. (2018). *Implants for surgery - Essential principles of safety and perfomance (ISO/TR Standard N0. 14283:2018)*. https://www.iso.org/standard/68007.html

International Organisation for Standardization. (2019). *Medical Devcies - Application of risk management to medical devices (ISO Standard No. 14971:2019)*. https://www.iso.org/standard/72704.html

International Organization for Standardization. (2007). *Non-active surgical implants- Joint replacement implants (ISO Standrad No. 21534:2007)*. https://www.iso.org/standard/39024.html

International Organization for Standardization. (2012). *Non-active surgical implants - General Requriements (ISO Standard No. 14630:2012)*. https://www.iso.org/standard/61749.html

International Organization for Standardization. (2020). *Clinical investigation of medical devices for human subjects- Good clinical practice (ISO Standard 14155:2020*. https://www.iso.org/standard/71690.html

Junaid, S., Gregory, T., Fetherston, S., Emery, R., Amis, A. A., & Hansen, U. (2018). Cadaveric study validating in vitro monitoring techniques to measure the failure mechanism of glenoid implants against clinical CT. *Journal of Orthopaedic Research*, *36*(9), 2524–2532. https://doi.org/10.1002/jor.23899

Junaid, S., Gupta, S., Sanghavi, S., Anglin, C., Roger, E., Amis, A., & Hansen, U. (2010). Failure mechanism of the all-polyethylene glenoid implant. *Journal of Biomechanics*, *43*(4), 714–719. https://doi.org/10.1016/j.jbiomech.2009.10.019

Junaid, S., Sanghavi, S., Anglin, C., Bull, A., Emery, R., Amis, A. A., & Hansen, U. (2017). Treatment of the Fixation Surface Improves Glenoid Prosthesis Longevity in vitro. *Journal of Biomechanics*, *61*, 81–87. https://doi.org/10.1016/j.jbiomech.2017.07.008

Karduna, A. R., Williams, G. R., Iannotti, J. P., & Williams, J. L. (1998). Total shoulder arthroplasty biomechanics: A study of the forces and strains at the glenoid component. *Journal of Biomechanical Engineering*, *120*(1), 92–99. https://doi.org/10.1115/1.2834312

Karduna, A. R., Williams, G. R., Williams, J. L., & Iannotti, J. P. (1997). Glenohumeral joint translations before and after total shoulder arthroplasty. A study in Cadavera. *Journal of Bone and Joint Surgery*, *79*(8), 1166–1174. https://doi.org/10.2106/00004623-199708000-00008

Karssiens, T. J., Gill, J. R., Sunil Kumar, K. H., & Sjolin, S. U. (2021). Clinical results and survivorship of the Mathys Affinis Short, Short Stem Total Shoulder Prosthesis. *Bone and Joint Open*, *2*(1), 58–65. https://doi.org/10.1302/2633-1462.21.BJO-2020-0184

Kim, S. H., Wise, B. L., Zhang, Y., & Szabo, R. M. (2011). Increasing incidence of shoulder arthroplasty in the United States. *Journal of Bone and Joint Surgery*, *93*(24), 2249–2254. https://doi.org/10.2106/JBJS.J.01994

Kleim, B. D., Garving, C., & Brunner, U. H. (2021). RSA, TSA and PyC hemi-prostheses: comparing indications and clinical outcomes using a second-generation modular short-stem shoulder prosthesis. *Archives of Orthopaedic and Trauma Surgery*, *141*(10), 1639–1648. https://doi.org/10.1007/s00402-020-03529-w

Klepps, S., Chiang, A. S., Miller, S., Jiang, C. Y., Hazrati, Y., & Flatow, E. L. (2005). Incidence of early radiolucent glenoid lines in patients having total shoulder replacements. *Clinical Orthopaedics and Related Research*, *435*, 118–125. https://doi.org/10.1097/01.blo.0000155080.37228.65

Lacroix, D., Murphy, L. A., & Prendergast, P. J. (2000). Three-dimensional finite element analysis of glenoid replacement prostheses: A comparison of keeled and pegged anchorage systems. *Journal of Biomechanical Engineering*, *122*(4), 430–436. https://doi.org/10.1115/1.1286318

Lazarus, M. D., Jensen, K. L., Southworth, C., & Iii, F. A. M. (2002). The Radiographic Evaluation of Keeled and Pegged Glenoid Component Insertion. *Journal of Bone and Joint Surgery*, *84-A*(7). www.jbjs.org.

Lewis, G. (2001). Properties of crosslinked ultra-high-molecular-weight polyethylene. In *Biomaterials* (Vol. 22, Issue 4). https://doi.org/10.1016/S0142-9612(00)00195-2

Li, T., Levy, K. H., Duey, A. H., Patel, A. V., White, C. A., Cirino, C. M., Williams, A., Whitelaw, K., Shukla, D., Parsons, B. O., Flatow, E. L., & Cagle, P. J. (2023). Does humeral fixation technique affect long-term outcomes of total shoulder arthroplasty? *Clinics in Shoulder and Elbow*, *26*(3), 245–251. https://doi.org/10.5397/cise.2023.00199

Lugli, T. (1978). Artificial Shoulder joint by Pean (1893): The facts of an exceptional intervention and the prosthetic method. *Clinical Orthopaedics and Related Research*, *133*, 215–218.

Malahias, M. A., Chytas, D., Kostretzis, L., Trellopoulos, A., Brilakis, E., & Antonogiannakis, E. (2021). Modern trabecular metal-backed glenoid components in total shoulder arthroplasty: What is the evidence? A systematic review. *Shoulder and Elbow*, *13*(1), 29–37. https://doi.org/10.1177/1758573220914277

Marigi, E. M., Elahi, M. A., Cancio-bello, A. M., Duquin, T. R., & Sperling, J. W. (2022). Stemless anatomic total shoulder arthroplasty : surgical technique and review of the literature. *JSES Reviews , Reports , and Techniques*, *2*, 442–450. https://doi.org/10.1016/j.xrrt.2022.08.001

Matsen, F. A., Clinton, J., Lynch, J., Bertelsen, A., & Richardson, M. L. (2008). Glenoid component failure in total shoulder arthroplasty. In *Journal of Bone and Joint Surgery* (Vol. 90, Issue 4, pp. 885–896). https://doi.org/10.2106/JBJS.G.01263

Meyer, R. W., & Pruitt, L. A. (2001). The effect of cyclic true strain on the morphology, structure, and relaxation behavior of ultra high molecular weight polyethylene. *Polymer*, *42*(12), 5293–5306. https://doi.org/10.1016/S0032-3861(00)00626-1

Nagels, J., Valstar, E. R., & Rozing, P. M. (2002). Patterns of Loosening of the Glenoid Component. *Journal of Bone and Joint Surgery [Br]*, *84-B*(1), 83–87. https://www.researchgate.net/publication/2571927

Neer, C. S. I. (1955). Articular Replacement for the humeral head. *Journal of Bone and Joint Surgery*, *37*(2), 215–228.

NJR. (2023). 20th Annual Report. *National Joint Joint Registry, UK*, *December 2022*.

Norris, T. R., & Iannotti, J. P. (2002). Functional outcome after shoulder arthroplasty for primary osteoarthritis: A multicenter study. *Journal of Shoulder and Elbow Surgery*, *11*(2), 130–135. https://doi.org/10.1067/mse.2002.121146

Noyes, M. P., Meccia, B., & Spencer, E. E. (2015). Five- to ten-year follow-up with a partially cemented all-polyethylene bone-ingrowth glenoid component. *Journal of Shoulder and Elbow Surgery*, *24*(9), 1458–1462. https://doi.org/10.1016/j.jse.2015.02.018

Nyffeler, R. W., Anglin, C., Sheikh, R., & Gerber, C. (2003). Influence of peg design and cement mantle thickness on pull-out strength of glenoid component pegs. *Journal of Bone and Joint Surgery - Series B*, *85*(5), 748–752. https://doi.org/10.1302/0301-620x.85b5.12580

Nyffeler, R. W., Meyer, D., Sheikh, R., Koller, B. J., & Gerber, C. (2006). The effect of cementing technique on structural fixation of pegged glenoid components in total shoulder arthroplasty. *Journal of Shoulder and Elbow Surgery*, *15*(1), 106–111. https://doi.org/10.1016/j.jse.2005.05.002

Nyffeler, R. W., Sheikh, R., Atkinson, T. S., Jacob, H. A. C., Favre, P., & Gerber, C. (2006). Effects of glenoid component version on humeral head displacement and joint reaction forces: An experimental study. *Journal of Shoulder and Elbow Surgery*, *15*(5), 625–629. https://doi.org/10.1016/j.jse.2005.09.016

Oosterom, R., Rozing, P. M., Verdonschot, N., & Bersee, H. E. N. (2004). Effect of joint conformity on glenoid component fixation in total shoulder arthroplasty. *Proceedings of the Institution of Mechanical Engineers, Part H: Journal of Engineering in Medicine*, *218*(5), 339–347. https://doi.org/10.1243/0954411041932818

Oral, E., Malhi, A. S., & Muratoglu, O. K. (2006). Mechanisms of decrease in fatigue crack propagation resistance in irradiated and melted UHMWPE. *Biomaterials*, *27*(6), 917–925. https://doi.org/10.1016/j.biomaterials.2005.06.025

Oral, E., Malhi, A. S., Wannomae, K. K., & Muratoglu, O. K. (2008). Highly Cross-Linked Ultrahigh Molecular Weight Polyethylene With Improved Fatigue Resistance for Total Joint Arthroplasty. Recipient of the 2006 Hap Paul Award. *Journal of Arthroplasty*, *23*(7), 1037–1044. https://doi.org/10.1016/j.arth.2007.09.027

Papadonikolakis, A., & Matsen, F. A. (2014). Metal-backed glenoid components have a higher rate of failure and fail by different modes in comparison with all-polyethylene components: A systematic review. *Journal of Bone and Joint Surgery*, *96*(12), 1041–1047. https://doi.org/10.2106/JBJS.M.00674

Pataky, T. C. (2010). Generalized n-dimensional biomechanical field analysis using statistical parametric mapping. *Journal of Biomechanics*, *43*(10), 1976–1982.

https://doi.org/10.1016/j.jbiomech.2010.03.008

Prinold, J. A. I., Masjedi, M., Johnson, G. R., & Bull, A. M. J. (2013). Musculoskeletal shoulder models: A technical review and proposals for research foci. *Proceedings of the Institution of Mechanical Engineers, Part H: Journal of Engineering in Medicine*, *227*(10), 1041–1057. https://doi.org/10.1177/0954411913492303

Quinci, F., Dressler, M., Strickland, A. M., & Limbert, G. (2014). Towards an accurate understanding of UHMWPE visco-dynamic behaviour for numerical modelling of implants. *Journal of the Mechanical Behavior of Biomedical Materials*, *32*, 62–75. https://doi.org/10.1016/j.jmbbm.2013.12.023

Raniga, S., Arenas-Miquelez, A., & Bokor, D. J. (2022). Anatomic total shoulder arthroplasty in patients under 50 and over 80 years of age. Part 1. *Obere Extremitat*, *17*(4), 259–266. https://doi.org/10.1007/s11678-022-00708-6

Roberson, T. A., Bentley, J. C., Griscom, J. T., Kissenberth, M. J., Tolan, S. J., Hawkins, R. J., & Tokish, J. M. (2017). Outcomes of total shoulder arthroplasty in patients younger than 65 years: a systematic review. *Journal of Shoulder and Elbow Surgery*, *26*(7), 1298–1306. https://doi.org/10.1016/j.jse.2016.12.069

Rockwood, C. A., & Wirth, M. A. (2002). Observation on retrieved Hylamer glenoids in shoulder arthroplasty: Problems associated with sterilization by gamma irradiation in air. *Journal of Shoulder and Elbow Surgery*, *11*(2), 191–197. https://doi.org/10.1067/mse.2002.121480

Rubin, C. G., Rubin, C. G., & Rubin, P. G. (2013). *Radiographic Evaluation of Glenoid Components and its Survivorship Radiographic Evaluation of Glenoid Components and its Survivorship*. 1–7.

Sabesan, V. J., Ackerman, J., Sharma, V., Baker, K. C., Kurdziel, M. D., & Wiater, J. M. (2015). Glenohumeral mismatch affects micromotion of cemented glenoid components in total shoulder arthroplasty. *Journal of Shoulder and Elbow Surgery*, *24*(5), 814–822. https://doi.org/10.1016/j.jse.2014.10.004

Scholz, R., Knyazeva, M., Porchetta, D., Wegner, N., Senatov, F., Salimon, A., Kaloshkin, S., & Walther, F. (2018). Development of biomimetic in vitro fatigue assessment for UHMWPE implant materials. *Journal of the Mechanical Behavior of Biomedical Materials*, *85*(May), 94–101. https://doi.org/10.1016/j.jmbbm.2018.05.034

Sharplin, P. K., Frampton, C. M. A., & Hirner, M. (2020). Cemented vs. uncemented glenoid

fixation in total shoulder arthroplasty for osteoarthritis: a New Zealand Joint Registry study. *Journal of Shoulder and Elbow Surgery*, *29*(10), 2097–2103. https://doi.org/10.1016/j.jse.2020.03.008

Sirimamilla, A., & Rimnac, C. M. (2019). Crack initiation from a clinically relevant notch in a highly-crosslinked UHMWPE subjected to static and cyclic loading. *Journal of the Mechanical Behavior of Biomedical Materials*, *91*(August 2018), 366–372. https://doi.org/10.1016/j.jmbbm.2018.12.032

Slouf, M., Arevalo, S., Vlkova, H., Gajdosova, V., Kralik, V., & Pruitt, L. (2021). Comparison of macro-, micro- and nanomechanical properties of clinically-relevant UHMWPE formulations. *Journal of the Mechanical Behavior of Biomedical Materials*, *120*(November 2020). https://doi.org/10.1016/j.jmbbm.2020.104205

Smith, S. L., Li, B. L., Buniya, A., Ho Lin, S., Scholes, S. C., Johnson, G., & Joyce, T. J. (2015). In vitro wear testing of a contemporary design of reverse shoulder prosthesis. *Journal of Biomechanics*, *48*(12), 3072–3079. https://doi.org/10.1016/j.jbiomech.2015.07.022

Sobieraj, M. C., Murphy, J. E., Brinkman, J. G., Kurtz, S. M., & Rimnac, C. M. (2013). Monotonic and fatigue behavior of five clinically relevant conventional and highly crosslinked UHMWPEs in the presence of stress concentrations. *Journal of the Mechanical Behavior of Biomedical Materials*, *28*, 244–253. https://doi.org/10.1016/j.jmbbm.2013.07.024

Stautberg, E. F., Jupiter, D. C., Amin, A., Qadeer, A. A., & Ilahi, O. A. (2017). Stability of two versus three peripheral pegs of the glenoid component in modern total shoulder arthroplasty. *International Orthopaedics*, *41*(11), 2345–2351. https://doi.org/10.1007/s00264-017-3599-7

Stone, K. D., Grabowski, J. J., Cofield, R. H., Morrey, B. F., & An, K. N. (1999). Stress analyses of glenoid components in total shoulder arthroplasty. *Journal of Shoulder and Elbow Surgery*, *8*(2), 151–158. https://doi.org/10.1016/S1058-2746(99)90009-5

Sukjamsri, C., Geraldes, D. M., Gregory, T., Ahmed, F., Hollis, D., Schenk, S., Amis, A., Emery, R., & Hansen, U. (2015). Digital volume correlation and micro-CT: An in-vitro technique for measuring full-field interface micromotion around polyethylene implants. *Journal of Biomechanics*, *48*(12), 3447–3454. https://doi.org/10.1016/j.jbiomech.2015.05.024

Szabo, I., Buscayret, F., Edwards, T. B., Nemoz, C., Boileau, P., & Walch, G. (2005). Radiographic comparison of flat-back and convex-back glenoid components in total shoulder

arthroplasty. *Journal of Shoulder and Elbow Surgery*, *14*(6), 636–642. https://doi.org/10.1016/j.jse.2005.05.004

Takahashi, Y., Tateiwa, T., Shishido, T., Masaoka, T., Kubo, K., & Yamamoto, K. (2016). Post-deformation shape-recovery behavior of vitamin E-diffused, radiation crosslinked polyethylene acetabular components. *Journal of the Mechanical Behavior of Biomedical Materials*, *63*, 399–406. https://doi.org/10.1016/j.jmbbm.2016.07.015

Terrier, A., Brighenti, V., Pioletti, D. P., & Farron, A. (2012). Importance of polyethylene thickness in total shoulder arthroplasty: A finite element analysis. *Clinical Biomechanics*, *27*(5), 443–448. https://doi.org/10.1016/j.clinbiomech.2011.12.003

Terrier, A., Büchler, P., & Farron, A. (2005). Bone-cement interface of the glenoid component: Stress analysis for varying cement thickness. *Clinical Biomechanics*, *20*, 710–717. https://doi.org/10.1016/j.clinbiomech.2005.03.010

Terrier, A., Büchler, P., & Farron, A. (2006). Influence of glenohumeral conformity on glenoid stresses after total shoulder arthroplasty. *Journal of Shoulder and Elbow Surgery*, *15*(4), 515–520. https://doi.org/10.1016/j.jse.2005.09.021

Wagner, E. R., Farley, K. X., Higgins, I., Wilson, J. M., Daly, C. A., & Gottschalk, M. B. (2020). The incidence of shoulder arthroplasty: rise and future projections compared with hip and knee arthroplasty. *Journal of Shoulder and Elbow Surgery*, *29*(12), 2601–2609. https://doi.org/10.1016/j.jse.2020.03.049

Wahab, A. H. A., Kadir, M. R. A., Harun, M. N., Kamarul, T., & Syahrom, A. (2017). Number of pegs influence focal stress distributions and micromotion in glenoid implants: a finite element study. *Medical and Biological Engineering and Computing*, *55*(3), 439–447. https://doi.org/10.1007/s11517-016-1525-6

Walch, G., Edwards, T. B., Boulahia, A., Boileau, P., Mole, D., & Adeleine, P. (2002). The Influence of Glenohumeral Prosthetic Mismatch on Glenoid Radiolucent Lines. *Journal of Bone and Joint Surgery*, *84-A*(12), 2186–2191.

Wang, V. M., Krishnan, R., Ugwonali, O. F. C., Flatow, E. L., Bigliani, L. U., & Ateshian, G. A. (2005). Biomechanical evaluation of a novel glenoid design in total shoulder arthroplasty. *J Shoulder Elbow Surg*, *14*(15), 129–140. https://doi.org/10.1016/j.jse.2004.09.029

Wiater, J. M., & Fabing, M. H. (2009). Shoulder arthroplasty. *Journal of the American Academy of Orthopaedic Surgeons*, *17*, 415–425. https://doi.org/10.1007/s00330-008-1093-8

Williams, G. R., & Abboud, J. A. J. a. (2005). Total shoulder arthroplasty: glenoid component design. *Journal of Shoulder and Elbow Surgery*, *14*(1), S122–S128. https://doi.org/10.1016/j.jse.2005.09.028

Wirth, M. A., Korvick, D. L., Basamania, C. J., Toro, F., Aufdemorte, T. B., & Rockwood, C. A. (2001). Radiologic, mechanical, and histologic evaluation of 2 glenoid prosthesis designs in a canine model. *Journal of Shoulder and Elbow Surgery*, *10*(2), 140–148. https://doi.org/10.1067/mse.2001.112021

Wirth, M. A., Mauli Agrawal, C., Mabrey, J. D., Dean, D. D., Blanchard, C. R., Miller, M. A., & Rockwood, C. A. (1999). Isolation and characterization of polyethylene wear debris associated with osteolysis following total shoulder arthroplasty. *Journal of Bone and Joint Surgery*, *81*(1), 29–37. https://doi.org/10.2106/00004623-199901000-00005

Wirth, M. A., Rockwood, C. A., & Antonio, S. (1996). Current Concepts Review - Complications of Total Shoulder-Replacement Arthroplasty. *The Journal of Bone & Joint Surgery*, *78-A*(4), 603–613. https://journals.lww.com/jbjsjournal

Zhang, J., Yongpravat, C., Mike Kim, H., Levine, W. N., Bigliani, L. U., Gardner, T. R., & Ahmad, C. S. (2013). Glenoid articular conformity affects stress distributions in total shoulder arthroplasty. *Journal of Shoulder and Elbow Surgery*, *22*, 350–356. https://doi.org/10.1016/j.jse.2012.08.025

A. APPENDIX A: ASTM TEST RIG DESIGN FILES

A1 Mechanical Components

A1.1 Mechanical Components Summary

Table A- 1 *Summary of purchased mechanical components used in the DGL Test Rig*

Component	Product Code	Description
Rexroth Ball Runner Block	R165181320 KWD-020-FNS-C1-H-1	Inner weight housing mounting
Rexroth Guide Rail	R16505803	
Rexroth Linear Roller Bearings	R103562520	Outer weight housing mounting
Rexroth Linear bearing shaft	R100002531	
Rexroth Anti-torque bushing	R072523000	Humeral head assembly mounting
Rexroth Anti-torque bushing	R072403089	

A1.2 Technical Data Sheets

The information regarding the technical data of the Rexroth Ball Rail system were obtained from the catalogues *BSHP_R999000485_2020_10_EN Rexroth rail bearing systems* and *R999000488_2015-02_KBF_EN Linear Bushings*. Extracts of the information are presented below along with their page numbers.

Rexroth Ball Runner Block R165181320 KWD-020-FNS-C1-H-1 Datasheet

Ball runner blocks		Page		Size	15	20	25	30	35	45	55	65
					Load ratings (N) and load moments (Nm)							
Standard, heavy duty, ball runner blocks[7] made of steel[3] Resist NR[4] Resist CR[6]	FNS R1651[3][6] R2001[4]	48[3] 99[4]	106[6]	C 1)	9860	23400	28600	36500	51800	86400	109000	172000
				C 2)	8 850	22 200	26 700	34 800	49 400	82 400	–	–
				C_0 1)	12700	29800	35900	48100	80900	132000	174000	280000
				C_0 2)	10 800	27 700	32 300	44 700	75 200	123 000	–	–
	SNS R1622[3][6] R2011[4]	54[3] 99[4]	106[6]	M_t 1)	95	300	410	630	1110	2330	3480	6810
				M_t 2)	85	280	380	600	1060	2 220	–	–
				M_{t0} 1)	120	380	510	830	1740	3560	5550	11100
				M_{t0} 2)	100	350	460	780	1 620	3 320	–	–
	SNH R1621[3][6]	60[3]		M_L 1)	68	200	290	440	720	1540	2320	4560
				M_L 2)	62	190	270	420	700	1 480	–	–
				M_{L0} 1)	87	260	360	580	1130	2350	3690	7400
				M_{L0} 2)	76	240	330	540	1060	2 210	–	–

Bosch Rexroth AG, R999000485/2022-03
Pg 12

FNS – Flanged, normal, standard height R1651 ... 2.

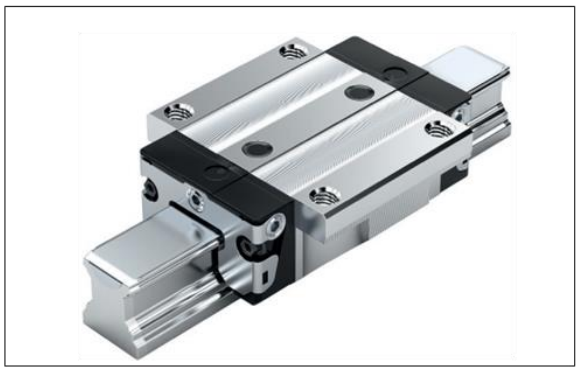

Dynamic characteristics

Travel speed: $v_{max} = 5\,m/s$

m/s Acceleration: $a_{max} = 500\,m/s^2$

(If $F_{comb} > 2.8 \cdot F_{pr}$: $a_{max} = 50\,m/s^2$)

Note on lubrication

► Pre-lubricated

Note

Can be used on all SNS/SNO ball guide rails. Ball runner blocks of size 55 and size 65 can be found in chapter "Heavy-duty ball runner block BSHP made of steel" after this chapter.

Options and material numbers

Size	Ball runner blocks with size	Preload class				Accuracy class						Seals on ball runner blocks					
												without ball chain			with ball chain		
		C0	C1	C2	C3	N	H	P	XP	SP	UP	SS	LS[1]	DS	SS	LS[1]	DS
15	R1651 1	9				4	3	–	–	–	–	20	21	–	22	23	–
			1			4	3	2	8	1	9	20	21	2Z	22	23	2Y
				2		–	3	2	8	1	9	20	21	2Z	22	23	2Y
					3	–	–	–	8	1	9	20	21	2Z	22	23	2Y
20	R1651 8	9				4	3	–	–	–	–	20	21	–	22	23	–
			1			4	3	2	8	1	9	20	21	2Z	22	23	2Y
				2		–	3	2	8	1	9	20	21	2Z	22	23	2Y
					3	–	–	–	8	1	9	20	21	2Z	22	23	2Y
25	R1651 2	9				4	3	–	–	–	–	20	21	–	22	23	–
			1			4	3	2	8	1	9	20	21	2Z	22	23	2Y
				2		–	3	2	8	1	9	20	21	2Z	22	23	2Y
					3	–	–	–	8	1	9	20	21	2Z	22	23	2Y
E.g.:	R1651 7		1				3					20					

1) Only for accuracy classes N and H and for XP in preload class C1.

Preload classes
C0 = Without preload (clearance)
C1 = Moderate preload
C2 = Average preload
C3 = High preload

Seals
SS = Standard seal
LS = Low-friction seal
DS = Double-lip seal

Key
gray numbers
= No preferred variant / combination
(partially longer delivery times)

Rexroth Guide Rail R16505803

SNS/SNO with plastic mounting hole plugs

R1605 .0. ../ R1605 .C. ..

For mounting from above with plastic mounting hole plugs

Notes

- Plastic mounting hole plugs included in scope of supply.
- Observe the instruction for mounting! Please request the "Mounting instructions for ball rail systems."
- Composite ball guide rail also available.

Further ball guide rails SNS and accessories

- Corrosion resistant ball guide rails Resist NR, Resist CR
- Mounting hole plugs made of plastic, see accessories for ball guide rails

Options and material numbers

Size	Ball guide rail with size	Accuracy class					Number of partial sections., Rail length L (mm), ...		Spacing T (mm)	Recommended rail length in accordance with formula $L = n_B \cdot T - 4$ mm
		N	H	P	SP	UP	One-piece	Composite		Maximum number of holes n_B
15	R1605 10	4	3	2	1	9	31, ...	3., ...	60	64
20	R1605 80	4	3	2	1	9	31, ...	3., ...	60	64
25	R1605 20	4	3	2	1	9	31, ...	3., ...	60	64
30	R1605 70	4	3	2	1	9	31, ...	3., ...	80	48
35	R1605 30	4	3	2	1	9	31, ...	3., ...	80	48
45	R1605 40	4	3	2	1	9	31, ...	3., ...	105	36
55	R1605 50	4	3	2	1	9	31, ...	3., ...	120	32
65	R1605 60	4	3	2	1	9	31, ...	3., ...	150	25
E.g.:	R1605 70	3					31, 1676			

Rexroth Ball Runner Block Frictional Characteristics

Friction

The friction coefficient μ of Rexroth's ball rail system is approximately 0.002 to 0.003 (without the friction of the seal).

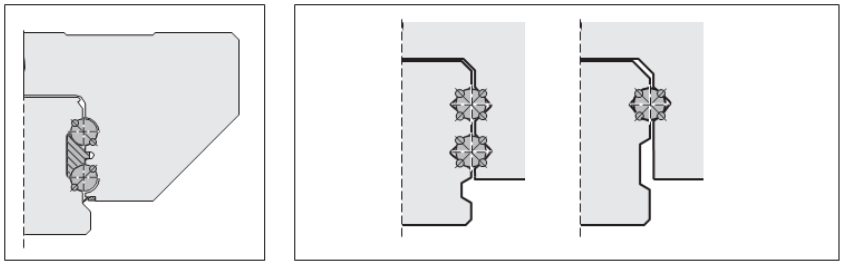

Due to the Rexroth design with four rows of balls, there are always **two points of contact** in all the directions of loading. This reduces the friction to a minimum.

Other ball rails with two or four rows of balls with **four points of contact** have multiple friction: due to the differential slip with lateral loading and with a comparable preload without load, the gothic raceway profile causes higher friction (depending on the conformity and the load, up to five times the friction coefficient). This high friction leads correspondingly to greater heat.

Seals

Seals are use to prevent dirt, chips and coolants, etc. from working their way into the inside of the ball runner block, thereby preventing reductions to its service life. For further information, see “Selection criteria/seals”.

Standard seal (SS)

Universal seals are fitted as standard in Rexroth ball runner blocks. They have a uniform sealing effect for ball guide rails with and without cover strips. Low friction and a good sealing effect have both been taken into account in the design. For applications where effective sealing is required.

R999000485/2022-03, **Bosch Rexroth AG**
Pg 19

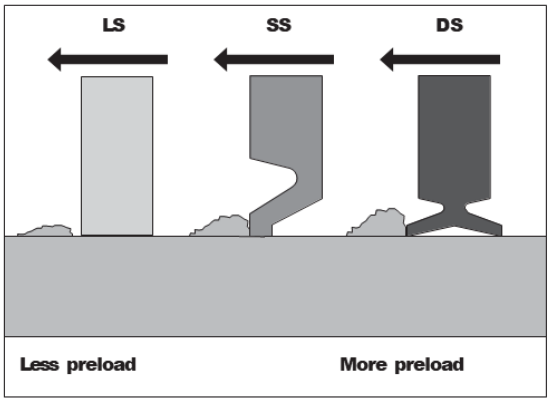

R999000485/2022-03, **Bosch Rexroth AG**
Pg 35

Fluctuation of friction forces

Definition

The overall driving force of a ball runner block consist of the following components:

1 Ball friction

2 Sealing friction

3 Friction in the ball deflections and ball returns

In operation, the fluctuations of the friction force can be particularly disturbing.

These fluctuations are essentially impacted by the following effect:

The balls need to be brought into the loaded load-bearing zone from the load-free zone. The harmonic entry zone and the innovative ball feed are used to reduce the fluctuations to a minimum, which means that the linear drive will also be easier to control.

Friction force comparison of ball runner block size 35 with an external load of 10,000 N

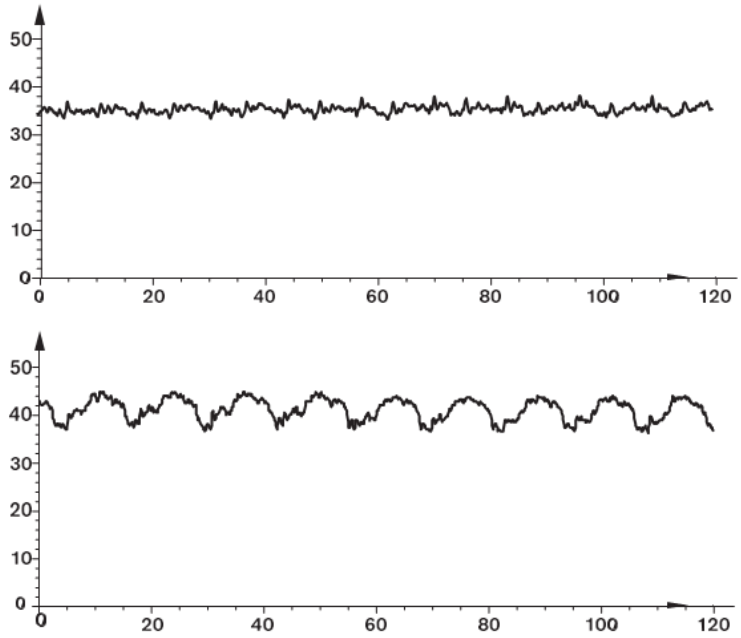

⇒ Reduced friction force value

⇒ Significantly reduced fluctuation of friction forces

Friction

The friction coefficient μ of Rexroth's ball rail system is approximately 0.002 to 0.003 (without the friction of the seal).

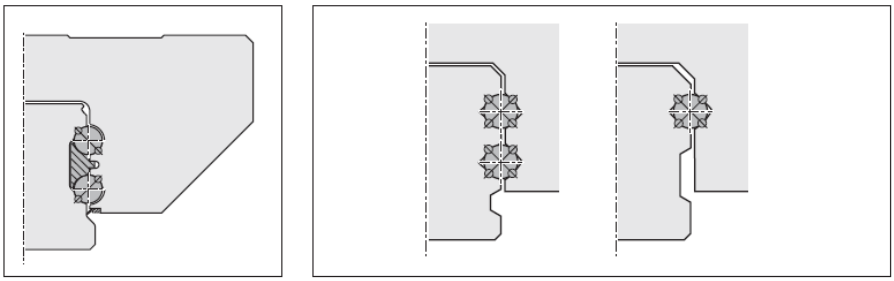

Due to the Rexroth design with four rows of balls, there are always **two points of contact** in all directions of loading. This reduces the friction to a minimum.

Other ball rails with two or four rows of balls with **four points of contact** have multiple friction: due to the differential slip with lateral loading and with a comparable preload without load, the gothic raceway profile causes higher friction (depending on the conformity and the load, up to five times the friction coefficient). This high friction leads correspondingly to greater heat.

Seals

Seals are used to prevent dirt, chips and coolants, etc. from working their way into the inside of the ball runner block, thereby preventing reductions to its service life.
For more information, see "Selection criteria / Seals".

Standard seal (SS)

Universal seals are fitted as standard in Rexroth ball runner blocks. They have a uniform sealing effect for ball guide rails with and without cover strips. Low friction and a good sealing effect have both been taken into account in the design. For applications where effective sealing is required.

Low-friction (LS)

For special requirements with regard to ease of movement.

Double-lip seal (DS)

For increased exposure to media

Front seal

For applications in environments with fine dirt or metal particles, as well as coolants or cutting fluids.
Interchangeable during servicing.
Front seals are available as accessories for mounting by the customer.

FKM seal

For applications in extreme environments with fine dirt or metal particles, as well as heavy use of coolants or cutting fluids.
Interchangeable during servicing.
FKM front seals are available as accessories for mounting by the customer.

Cover plate wiper

For use in environments with coarse dirt or chips.
Cover plate wipers are available as accessories for mounting by the customer.

Ball chain

Rexroth recommends the ball chain especially for applications where a low noise level is required.

Ball runner blocks including ball chain (1) are available as an option. The ball chain prevents the balls from colliding with each other and helps to achieve a calmer and smoother running. A lower noise level is achieved.
Due to the smaller number of load-bearing balls in the ball runner block with ball chain, lower load capacities and load moments can result ("Product overview with load capacities and load moments").

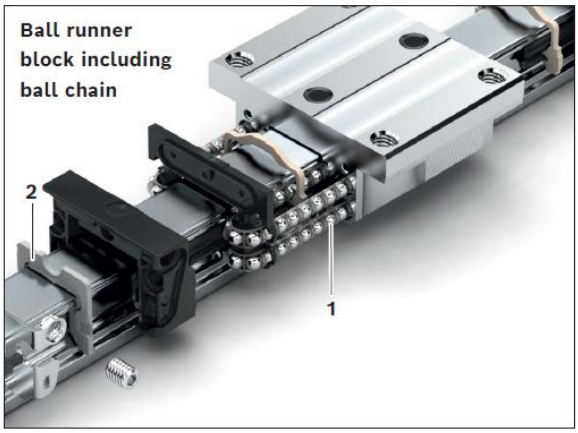

Seals

The sealing plate on the end face (2) protects the interior of the ball runner block against dirt, chips and fluids. Additionally, it prevents the discharge of lubricant. Due to the optimized form of the sealing lips, the occurring friction is reduced to a minimum. Sealing plates are optionally available with black standard seals (SS), beige low-friction seals (LS) or green double-lip seals (DS).

Low-friction seal (LS) (seal with very low friction)
For special requirements with regard to ease of movement and reduced lubricant application, the low-friction seal has been developed. It consists of an open-pored polyurethane foam and features only limited wiping action.

Standard seal (SS) (universal sealing with good sealing effect)
For most application cases, the standard seal is suitable. It comprises of a good wiping action but also enables long relubrication intervals.

Double-lip seal (DS) (sealing with very good sealing effect)
For applications in which the rail guide is heavily charged with chips, wood dust, cooling lubricants etc., Rexroth recommends the double-lip seal. It comprises an excellent wiping action but a greater friction force and lower relubrication interval.

Sealing effect and displacement resistance
The displacement resistance can be impacted by the geometry and the material. The diagram shows the effects of different sealing versions on the sealing effect and the displacement resistance.

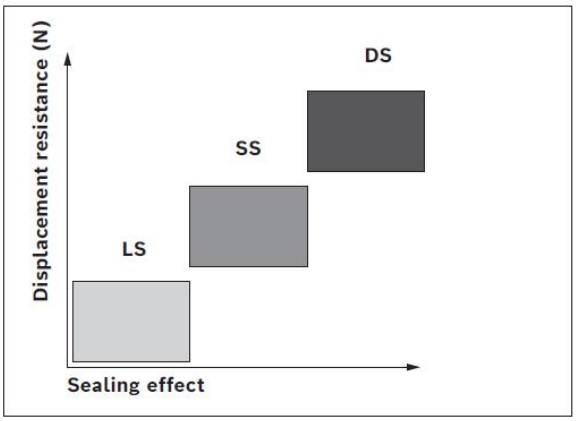

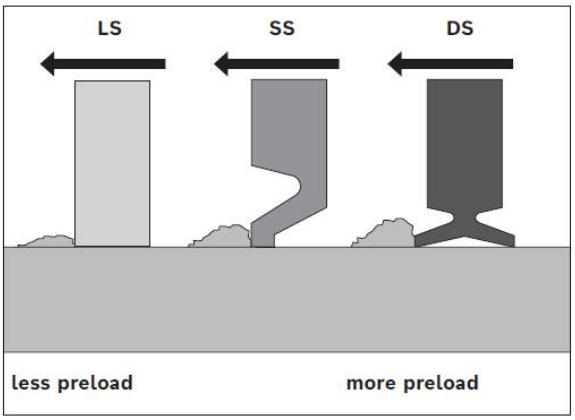

Rexroth Linear Roller Bearings R103562520

Dimensions

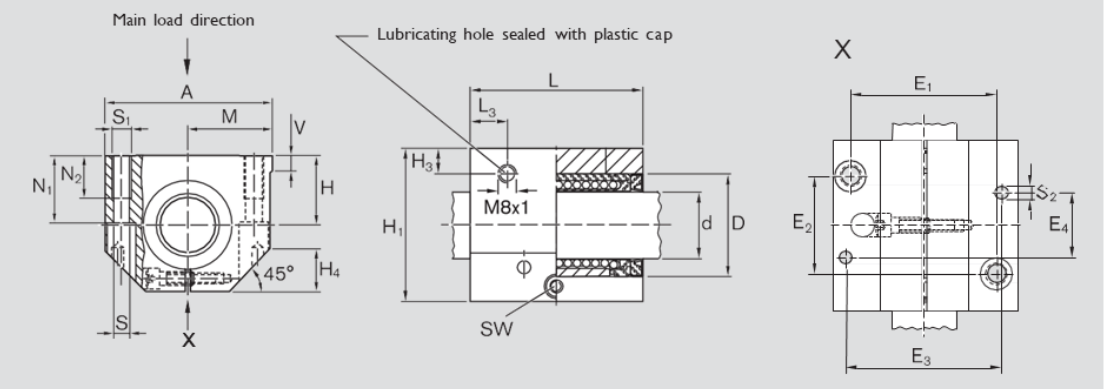

Dimensions (mm)

Ø d	D	H[1] +0.008 −0.016	H1	M[1] ±0.01	A	L	E1	E2	E3	E4	S[2]	S1	S2[3]	N1	N2	H3	L3	V	SW	H4
10	19	16	31.5	20.0	40	36	29±0.15	20±0.15	31	29	4.3	M5	4	15.0	11	10.0	10.5	5.0	2.5	10
12	22	18	35.0	21.5	43	39	32±0.15	23±0.15	34	32	4.3	M5	4	16.5	11	10.0	10.5	5.0	2.5	10
16	26	22	42.0	26.5	53	43	40±0.15	26±0.15	42	35	5.3	M6	4	21.0	13	10.0	11.5	5.0	3.0	13
20	32	25	50.0	30.0	60	54	45±0.15	32±0.15	50	45	6.6	M8	5	24.0	18	10.0	13.5	5.0	4.0	16
25	40	30	60.0	39.0	78	67	60±0.15	40±0.15	64	20	8.4	M10	6	29.0	22	10.0	15.0	6.5	5.0	20
30	47	35	70.0	43.5	87	79	68±0.15	45±0.15	72	30	8.4	M10	6	34.0	22	11.5	16.0	8.0	5.0	22
40	62	45	90.0	54.0	108	91	86±0.15	58±0.15	90	35	10.5	M12	8	44.0	26	14.0	18.0	10.0	6.0	28
50	75	50	105.0	66.0	132	113	108±0.20	50±0.20	108	42	13.5	M16	10	49.0	34	12.5	22.0	12.0	8.0	37

Ø d	Radial clearance (µm)		Load ratings[4] (N)	
	R1035	R1036		
(mm)	h6 shaft		dyn. C	stat. C_0
10	+36 +9	Comes clamped to h5 shaft (lower limit) and set to zero clearance	730	380
12	+38 +10		1,020	490
16	+38 +10		1,250	620
20	+43 +11		2,470	1,340
25	+43 +11		4,820	2,790
30	+43 +11		5,860	3,570
40	+50 +12		10,070	5,570
50	+50 +12		14,730	8,280

The dynamic load ratings are based on a total travel of 100,000 m.
When based on 50,000 m, the C values in the table are multiplied by 1.26.

1) Clamped (fastened) in relation to Ø d.
2) ISO 4762-8.8 fastening bolts.
3) Pin centering.
4) The load ratings apply for the main load direction.
If the load direction is not the main load direction, the load ratings must be multiplied by the following factors:

Ø d 10 to 16: $f = 0.82$, $f_0 = 0.86$

Ø d 20 to 50: $f = 0.82$, $f_0 = 0.78$

Rexroth Linear Bearing Shaft R100002531

Dimensions

Shaft Ø d	Part numbers for solid shafts								
	Heat-treated Cf53		Max. usable Length	X46Cr13		Max. usable Length	X90CrMoV18		Max. usable Length
	h6[1]	h7[1]		h6[1]	h7[1]		h6[1]	h7[1]	
(mm)			(mm)			(mm)			(mm)
3	R1000 003 00	–	400	–	–		R1000 003 20	–	400
4	–	–	–	R1000 004 30	R1000 004 31	3,450	–	–	–
5	R1000 005 00	R1000 005 01	3,900	R1000 005 30	R1000 005 31	3,450	–	–	–
6	R1000 006 00	R1000 006 01	5,650	R1000 006 30	R1000 006 31	3,450	–	–	–
8	R1000 008 00	R1000 008 01	5,900	R1000 008 30	R1000 008 31	5,900	–	–	–
10	R1000 010 00	R1000 010 01	5,900	R1000 010 30	R1000 010 31	3,450	–	–	–
12	R1000 012 00	R1000 012 01	5,900	R1000 012 30	R1000 012 31	5,900	R1000 012 20	R1000 012 21	5,900
14	R1000 014 00	R1000 014 01	5,900	R1000 014 30	R1000 014 31	5,900	–	–	–
15	R1000 015 00	R1000 015 01	5,900	–	–	–	–	–	–
16	R1000 016 00	R1000 016 01	5,900	R1000 016 30	R1000 016 31	5,900	R1000 016 20	R1000 016 21	5,900
18	R1000 018 00	R1000 018 01	5,900	–	–	–	–	–	–
20	R1000 020 00	R1000 020 01	5,900	R1000 020 30	R1000 020 31	5,900	R1000 020 20	R1000 020 21	5,900
22	R1000 022 00	R1000 022 01	5,900	–	–	–	–	–	–
24	R1000 024 00	R1000 024 01	5,900	–	–	–	–	–	–
25	R1000 025 00	R1000 025 01	5,900	R1000 025 30	R1000 025 31	5,900	R1000 025 20	R1000 025 21	5,900
30	R1000 030 00	R1000 030 01	5,900	R1000 030 30	R1000 030 31	5,900	R1000 030 20	R1000 030 21	5,900

Precision steel shafts

Technical data

Dimensional accuracy and tolerance zones

The diameters of the precision steel shafts come in h6 and h7 tolerance zones. The adjacent table shows information on dimensional accuracy. The diameter tolerance of annealed shaft cross-sections vary slightly from the specified tolerance zone.

Nominal size ranges d	(mm)	Over	1	3	6	10	18	30	50	80
		Up to	3	6	10	18	30	50	80	120
Diameter tolerance	(µm)	h6	0	0	0	0	0	0	0	0
			–6	–8	–9	–11	–13	–16	–19	–22
		h7	0	0	0	0	0	0	0	0
			–10	–12	–15	–18	–21	–25	–30	–35
Roundness tolerance t_1	(µm)	h6	3	4	4	5	6	7	8	10
		h7	4	5	6	8	9	11	13	15
Cylindricity t_2[1]	(µm)	h6	4	5	6	8	9	11	13	15
		h7	6	8	9	11	13	16	19	22
Straightness t_3[2]	(µm/m)		150	150	120	100	100	100	100	100
Surface roughness (Ra)	(µm)		0.32	0.32	0.32	0.32	0.32	0.32	0.32	0.32

1) Differences in diameter
2) The smallest possible value is 40 µm for lengths under 1 m. Straightness is measured based on ISO 13012.

Straightness based on ISO 13012
The measuring points are evenly distributed between the support points and the shaft sections protruding past them. More supports are used accordingly for long, thin shafts. Straightness is half of the gauge measurement when turning the shaft 360°.

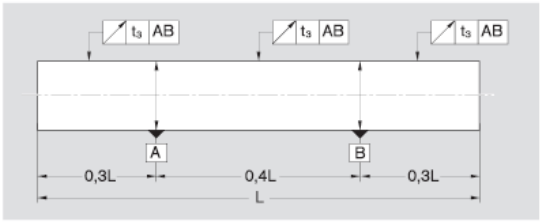

Roundness
The drawing shows the roundness of a raw shaft compared to a precision steel shaft.

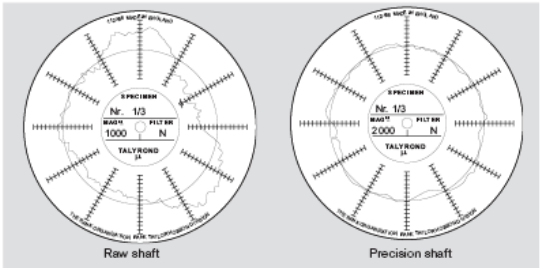

Raw shaft
Precision shaft

Rexroth Anti-torque Bushing R072523000 and Bearing shaft R072403089

Design
- Hardened and machined outer sleeve
- POM ball retainer
- Balls made of rolling bearing steel
- **Integrated wiper seals**
- Relubricatable

Size	Material number KBDR4-F- ...DD	Weight (kg)
6	R0725 206 00	0.037
8	R0725 208 00	0.042
10	R0725 210 00	0.094
13	R0725 213 00	0.100
16	R0725 216 00	0.200
20	R0725 220 00	0.220
25	R0725 225 00	0.320
30	R0725 230 00	0.510
40	R0725 240 00	1.150
50	R0725 250 00	2.100

Dimensions for R0725

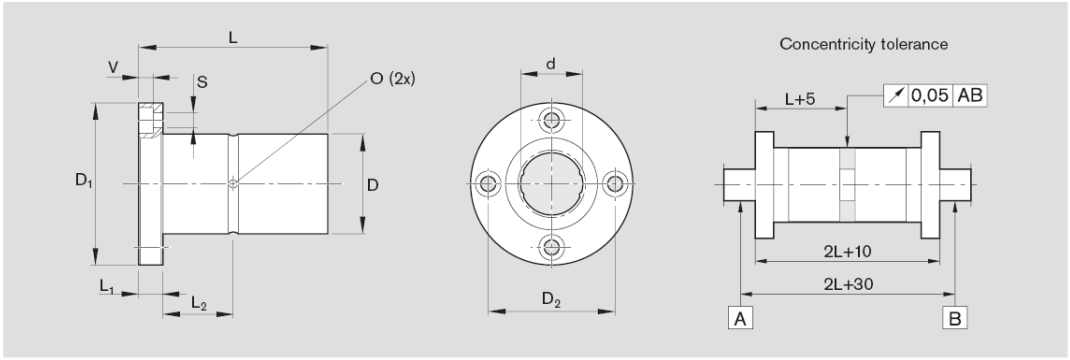

Size[1]	Dimensions (mm) Ø d	D h6	D_1	D_2	L	L_1	L_2	V	S[3]	O	Torsional load moment (Nm) dyn. M_t	stat. M_{t0}	Load ratings[2] (N) dyn. C	stat. C_0
6	6.0	14	30	22	$25_{-0.2}$	5	7.5	3.3	3.4	1.0	1.2	2.4	970	2,280
8	8.0	16	32	24	$25_{-0.2}$	5	7.5	3.3	3.4	1.5	1.7	3.7	1,150	2,870
10	10.0	21	42	32	$33_{-0.2}$	6	10.5	4.4	4.5	1.5	3.5	8.2	2,170	5,070
13	13.0	24	43	33	$36_{-0.2}$	7	11.0	4.4	4.5	1.5	16.7	39.2	2,120	4,890
16	16.0	31	50	40	$50_{-0.2}$	7	18.0	4.4	4.5	2.0	48.0	110.0	4,860	11,200
20	18.2	32	51	40	$60_{-0.2}$	7	23.0	4.4	4.5	2.0	66.0	133.0	6,200	11,300
25	23.0	37	60	47	$70_{-0.3}$	9	26.0	5.4	5.5	3.0	129.0	239.0	9,800	16,100
30	28.0	45	70	54	$80_{-0.3}$	10	30.0	6.5	6.6	3.0	229.0	412.0	14,800	23,200
40	37.4	60	90	72	$100_{-0.3}$	14	36.0	8.6	9.0	4.0	500.0	882.0	24,400	37,500
50	47.0	75	113	91	$112_{-0.3}$	16	40.0	11.0	11.0	4.0	1,100.0	3,180.0	36,600	74,200

1) Shaft diameter varies
2) The load ratings indicated are minimal values as the load direction cannot always be clearly defined.
3) ISO 4762-8.8 fastening bolts

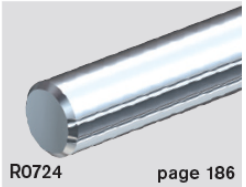

R0724 page 186

Precision steel shaft with four ball guide grooves

Sample shaft:

Shaft, torque-resistant linear bushing
WVDR4-20-1200

Definition of codes			WV	DR	4	20	1200
Type	Shaft	= WV					
	Hollow shaft	= WO					
Series	Torque	= DR					
Track	4 ball guide grooves	= 4					
Size[1]		= 20					
Shaft length (mm)		= 1200					

1) Shaft diameter varies (see dimension table)

A2 Electronic and Electromechanical Components

A2.1 Electronic and Electromechanical Components Summary

Table A- 2 *Summary of electrical and electronic components used in the DGL test rig*

Component	Product Code	Description
Motor controller	HCS01.1E-W0009, Firmware version FWA-INDRV*-MPB-18VRS-D5-1-NNN-NN-NN-FW	Motor controller. Full details provided in
Linear Actuator and motor	R911344214, EMC-032-NN-2	Linear Actuator and motor
DAQ	HBK PMX	DAQ
Compression load cell	TE Connectivity FX1901	Load cell measuring normal contact load
Temperature controller (with thermocouple)	STC-1000	Digital Temperature controller (with thermocouple)
Water circulation pump	Waterfall SP600 pump	Water circulation pump (hMax 0.45m, QMax 260l/h, 5V)

A2.2 Electronic and Electromechanical Components Technical Datasheets

Motor Controller HCS01 Specification Sheet

Full motor controller manual *DOK-INDRV*-HSC01*UL***-IB07-EN-P* can be found at:

https://www.google.com/url?sa=t&source=web&rct=j&opi=89978449&url=https://www.boschrexroth.com/media/700a64a4-f4e4-4113-b2ab-5ee41e92a2cb&ved=2ahUKEwjtz7Oy9rWHAxU2QUEAHZ_RDCoQFnoECBIQAQ&usg=AOvVaw1o3dLyqpITYZO3lnAs-igq

Motor R911344214Datasheet

SERVOMOTOR MSM031B-0300-NN-M5-MH1

R911344214

Product attributes	
Motor type	With holding brake
Maximum torque [Nm]	1.91
Maximum speed [rpm]	5000
Flange size [mm]	60
Cooling type	Self-cooling
electrical connection	Cable tail, circular connector M17
ctrlX Configurator	https://www.boschrexroth.com/ctrlx-configurator/
Encoder design	Optical encoder, multi turn-absolute (20 Bit)
Continuous torque (int. cooling) 60k [Nm]	0.64
Rotor inertia (with brake) value [kg/m²]	0.0000158
Weight [kg]	1.55

Linear Actuator EMC 032 NN Data

Bosch Rexroth Electromechanical cylinder EMC-032-NN-2 R030523525

Table 19: Operating conditions

Ambient temperature	Cylinder mechanism: −10 °C ... 50 °C Cylinder with Rexroth Servomotor: 0 °C ... 40 °C, performance degradation over 40 °C	ϑ
Travel speed	max 1.6 m/s	v
Maximum travel range	100 to 1500 mm	

HBK PMX Datasheet

Full HBX PMX datasheet (*B03579 10 E00 05*) can be found at https://www.hbm.com/en/2981/pmx-modular-measuring-amplifier-system-for-the-iot/?product_type_no=PMX%20Multi%20Channel%20Data%20Acquisition%20System.

Relevant excerpts provided here.

DATA SHEET

PMX
Modular measuring amplifier system

SPECIAL FEATURES

- Up to 16 measurement inputs with TEDS sensor detection
- 24-bit A/D converter and 19200 Hz or 38400 Hz sample rate per channel
- Automatic synchronization of several devices
- 32 calculated channels with peak values, limit values and mathematical functions
- Digital inputs/outputs, analog outputs
- Fast PROFINET®, EtherCAT®, EtherNet/IP™
- Optional: CODESYS SoftPLC and CANopen interface
- Rugged DIN rail or wall mounting
- Operation via integrated web server with user navigation on three levels (Operator, Maintenance, Administrator)

BLOCK DIAGRAM

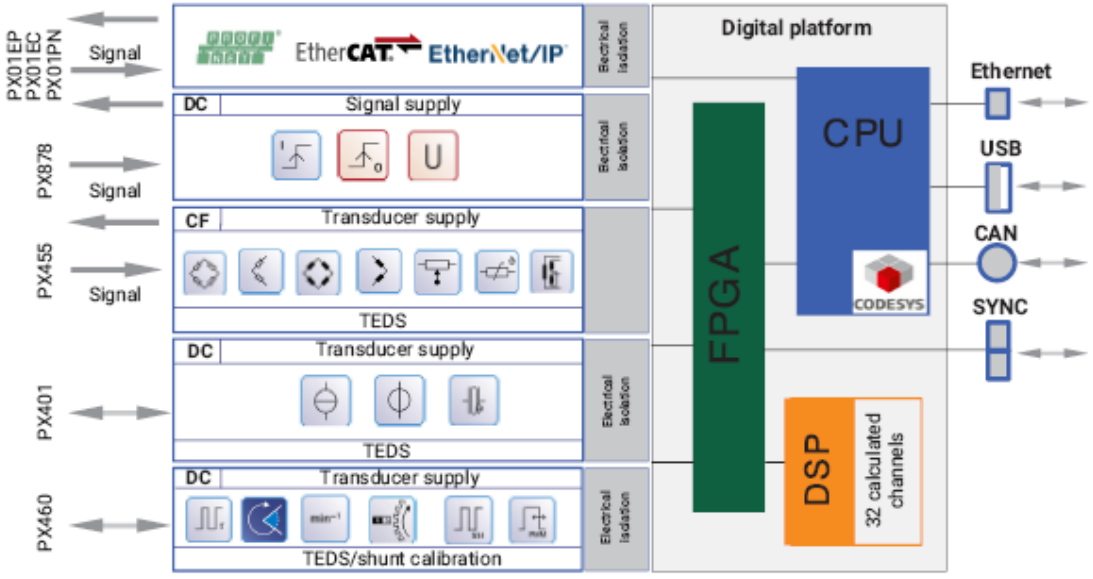

SPECIFICATIONS FOR THE BASIC DEVICE

Basic device		WGX001/002
Modules	Number	1 communication card, 4 measurement cards
Supply voltage range	V_{DC}	10 ... 30 (nominal (rated) voltage 24 V)
Supply voltage interruption (based on PLC standard DIN EN 61131-2)		
24 V (- 10 %)	ms	10
12 V (- 10 %)	ms	1
Power consumption at 24 V supply voltage		
Basic device	W	3
Per PX455	W	1.6
Per PX401	W	0.75
Per PX460	W	2
Per PX878	W	2
EtherCAT®[1] communication card PX01EC	W	1.9
PROFINET® communication card PX01PN	W	2.3
EtherNet/IP™[2] communication card PX01EP	W	2.2
Ethernet (data link)		IEEE802.3.; 10 Base-T/100 Base-TX
Protocol/addressing		TCP/IP (direct IP address or DHCP)
Plug connection		RJ45, 8-pin
Cable type		Standard LAN, CAT 5, SFTP
Max. cable length to module	m	100
Synchronization		
NTP protocol		Time over Ethernet
HBM protocol		Measured values in measurement grid and carrier frequency (module to module)
Plug connection		RJ45, 8-pin
Cable type		Standard LAN, CAT 5, SFTP
Number of devices		20
Line lengths between neighboring devices, max.	m	30
USB connection		USB 2.0 Host
Function		Resets all device parameters to the factory settings, sets the device name and network settings, resets user passwords, backs up measurement data (using the free CODESYS application)
CAN connection		CANopen interface only with WGX001 (CAN ISO11898)
Real-time calculation in the device		CAN 2.0b
Total sample rate	MW/s	400,000
Calculated channels	Number	32 in real time (max. 48 for internal calculations)
Update rate	Hz	19,200
Function		Peak values, Limit values, Mean values, Root mean square (RMS) values, Tolerance bands, Mathematical calculated channels, Logical functions, Signal characteristic, Signal generators, 2-point scaling, 2-state controller, PID controller, CASMA filter, Bessel and Butterworth filters (IIR, high-pass and low-pass), Moving average (FIR), Multiplexer, Sample and Hold, Time calculation, Counter, Trigger, 6x6 matrix calculation, Strain gauge rosette calculation, Coordinate calculation (polar <-> Cartesian), Pulse-width measurement, Edge detector, Checkweigher, Connection to CODESYS
Peak-value memory		
Number		32
Reference level		All measurement signals, all calculated channels
Function		Min./Max., peak-to-peak
Update time	µs	52
Clear		
Via digital inputs	ms	1
Via fieldbus	ms	20

[1] EtherCAT® is a registered brand and patented technology, licensed by Beckhoff Automation GmbH, Germany.

[2] EtherNet/IP™ is a trademark of ODVA Inc. For more information regarding ODVA, visit www.odva.org.

SPECIFICATIONS (BASIC DEVICE CONTINUED)

Limit switches		
Number		32, via fieldbus and Ethernet data link 8 via digital outputs per PX878 (max. 2 PX878 can be inserted)
Reference level		All measurement signals, all calculated channels
Function		Exceeding or falling below a level Inside/outside a tolerance band
Typical response time	µs	300
Digital inputs		
Number		32 max. 17 ... 32 via fieldbus and Ethernet data link 1 ... 8 via digital signals per PX878 (max. 2 PX878 can be inserted)
Function		Zero balance, tare, reset limit value, digital output, parameter set selection (bit-coded), calculated channel flags, CODESYS flags
Typical response time	ms	1
Digital outputs		
Number		16, via fieldbus and Ethernet data link 8 signals per PX878 (max. 2 PX878 can be inserted). Designed as high-side switches.
Function		Measured value/system status, digital input, fieldbus flag, limit value switch, current parameter set number (bit-coded), flags, calculated channels, CODESYS flags)
Typical response time	ms	1
Parameter Sets		
Number		100, each parameter set comprises 4 parameter subsets
Parameter subsets		Sensor settings, measurement acquisition, limit values, digital outputs
Switching time	ms	**Sensor data / Measurement acquisition / Limit values / Digital outputs / st*)** 1,200 / - / - / - / 1,200 - / 950 / - / - / 950 1,200 / 950 / - / - / 2,150 - / - / 100 / - / 100 1,200 / 950 / 100 / - / 2,250 - / - / - / 80 / 80 1,200 / 950 / 100 / 80 / 2,330 *) Typical average switching time (in ms)
Log file		For logging all parameter changes and (error) messages of all users
Storage location		In the device
File size, max.	MB	20
Optional		Parallel transfer via network profile (RCF5424) to a network PC/server
Nominal (rated) temperature range	°C	0 ... 50
Operating temperature range (no condensation allowed/ module not immune to water condensation)	°C	-10 ... +60
Storage temperature range	°C	-20 ... +70
Relative humidity	%	5 ... 95 (non-condensing)
Protection class (height up to 2,000 m, degree of contamination 2)		III
Equipment protection level		IP 20 per EN60529
Mechanical tests (test similar to IEC/EN 60068, Part 2-6)		
Oscillation (30 min in each direction)	m/s^2	25 (5 ... 65 Hz)
Impact (3 times in each direction; impact duration 11 ms) (test similar to IEC/EN 60068, Part 2-27)	m/s^2	200

SPECIFICATIONS (BASIC DEVICE CONTINUED)

EMC requirements		As per EN 61326 and EN 55011 (Class B) **Relevant directives:** 2004/108/EC **Relevant standards:** Immunity to interference: DIN EN61326-1, Issue 2006-10 Table 2 (industrial environments) Emissions & Immunity (EME): DIN EN61326-1, Issue 2006-10, Class B
Proof of quality		
Declaration of compliance with the order		A PDF document of the manufacturer's certificate as per EN10204 2.1 is stored in the PMX device memory and can be downloaded via the PMX browser.
EMC update		The scope of inspection was updated with the requirements of the "EMC integration guideline for achieving electromagnetic compatibility in electrical systems in the automotive industry" version 1-03: EN61000-4-4: Burst test 2 kV EN55022: Interference current, interference voltage: expansion of frequency range 9 kHz ... 30 MHz
Quality requirements EMC requirements Long-term stability		 Evaluation criteria A are met in all EMC tests. This means that operating behavior, i.e. accuracy and functions, remains in line with the specifications of the data sheet, even when subject to electromagnetic interference. All PMX components are pre-aged for 7 hours in an oven run to improve long-term stability.
Fuses Automatic current limiter Short-circuit resistance		 Per device and per device card Synchronization/fieldbus/input and output signals are secured against mix-ups and short circuits
Dimensions (H x W x D)	mm	200 x 200 x 122
Weight (fully equipped), approx.	g	2,750
SoftPLC control (with WGX001)		**CODESYS**
Programming language		IEC61131-3
RAM	MB	10
Flash memory	MB	100
Timer resolution	Hz	300, for timer-controlled tasks (3.33 ms)
Number of tasks		100
Usable CODESYS channels in PMX		30 to 14 depending on the hardware configuration, (available number = 30 minus number of installed measurement channels)
Available channels in CODESYS	16 32 1 1 32 4	Measurement channels and status Calculated channels and status 64bit timestamp System status Limit value status Slot status
CODESYS web visualization		Creates the web visualization with CODESYS software as an application suitable for running in PMX. The visualization can be used on all browser-based devices via the PMX Ethernet TCP/IP interface.

SPECIFICATIONS (BASIC DEVICE CONTINUED)

CAN interface (with WGX001)								
Number of CAN interfaces		1						
Bus link		Two-wire as per ISO11898-2						
Electrical isolation		60 V DC voltage to supply and measurement ground						
Protocol with CODESYS		CANopen 2.0, CiA301, 302, 405, 401, 306						
CANopen		Node guarding, sync producing/consuming						
Usable CAN channels in PMX Internal in CODESYS, max. Can be used in calculated channels or mapped on analog output, fieldbus or Ethernet		128, freely programmable 30 to 14, depending on the hardware configuration						
CAN signal types		USINT, INT UINT, DINT UDINT, LINT ULINT, REAL SINT, LREAL						
Baud rate	bit/s	20k	50k	100k	125k	250k	500k	1M
Line length	m	1,000	1,000	1,000	500	250	100	25
CAN master (CODESYS), signal input		Several SDO channels, EDS and DCF file import; no DBC format, PDO mapping CiA401 (module-dependent), low-level CAN library						
CAN slave (CODESYS), signal output		Static PDO mapping, SDO parameter ranges, EDS file generation with the CODESYS programming system						
Number of PDOs, send or receive		Max. 16 PDO streams with max. total data size 128 bytes						
PDO transfer		Timer-controlled up to max. 300 Hz, measure value-controlled up to max. 1.2 kHz or via SYNC message (type: external, event: MeasVal/Event)						
Number of SDOs		Max. 199 x 255 subIDs						
PDO, SDO generation		In the CODESYS programming environment						
Connection technique		1 x M12						
Transmit/receive CAN data								
Number of signals to be received/transmitted		128 maximum						
Number of signals for 1 Mbit/s, REAL format, 32-bit								
Signals		Reading/ transmission rate (Hz)		Measured value-controlled (Hz)		Timer-controlled (ms)		
2		1,200		1,200		-		
4		160		-		6		
8		160		-		6		
16		160		-		6		
24		100		-		10		
32		80		-		12		

SPECIFICATIONS FOR PX455

Strain gauge and inductive full/half bridge, 4.8 kHz CF		PX455
Accuracy class Full bridge Half bridge		 0.05 0.1
Carrier frequency (sine)	Hz	4800 ± 0.1 %
Bridge excitation voltage (effective)	V	2.5 ±5 %
Connectable transducers[1), 2)] in six or five-wire configuration Strain gauge half and full bridges Inductive half and full bridges, LVDTs	 Ω mH	 120 ... 1000 4 ... 33
Potentiometer Cable length	 m	Deviations in accuracy class 1
Resistance value 1 kΩ Resistance value 5 kΩ	% %	< 0.1 < 0.1
PT100 resistance thermometer (in conjunction with a 100 Ω completion resistor as a half bridge circuit)	°C	-100 ... +500
Measurement frequency range (-3 dB)	kHz	2
Data rate, max.	Hz	19200 per channel
Resolution of D/A converter	bit	24
Active low-pass filter (Bessel/Butterworth) 6th order, IIR	Hz	0.1 ... 2000
Transducer connection		Plug terminals 4 x 7-pin
TEDS, IEEE1451.4		Zero-wire[3), 4)]
Permissible cable length between PX455 and transducer	m	100[4)]
Measurement ranges Strain gauge Inductive LVDT	 mV/V mV/V mV/V	 ± 4 ± 100, ± 1000 ± 500
Nominal (rated) temperature range	°C	0 ... 50
Operating temperature range (no condensation allowed/module not immune to water condensation)	°C	-10 ... +60
Storage temperature range	°C	-20 ... +70
Relative humidity	%	5 ... 95 (non-condensing)
Protection class (height up to 2,000 m, degree of contamination 2)		III
Equipment protection level		IP 20 per EN60529
EMC requirements		As per EN 61326 and EN 55011 (Class B)
Non-linearity	%	0.03
Zero drift (excitation, 2.5 V) at 4 mV/V rel. to full-scale value	%/10 K	Full bridge: 0.05; half bridge: 0.1
Full-scale drift (excitation, 2.5 V) at 4 mV/V rel. to measured value	%/10 K	Full bridge: 0.05; half bridge: 0.05
Half bridge offset[5)] (at 350 Ω and a cable length of < 5 m)	µV/V	< ± 50
Accuracy class of full bridge strain gauge with Zener barrier SD01A, 350 Ω, cable length of up to 100m	%	0.5

1) For bridge resistance from RB > 500 Ω or cable lengths >30 m: insert transducer-side resistors RB/2 in the feedback lines.
2) With transducers >350 Ω, the zero point must be calibrated with cables >50 m (tare/zero balance).
3) When using transducers with integrated zero-wire TEDS, RB/2 must be reduced by 100 Ω in each sense lead.
4) Transducer-side TEDS cannot be read after RB/2 > 300 Ω.
5) The zero point for half bridges is heavily dependent on the test setup, the line length and the line type and should be tared or set to zero by the user.

SPECIFICATIONS (PX455 CONTINUED)

Proof of quality		
Calibration certificate		A PDF document of the card calibration certificate as per ISO 10012 is stored in the PMX device memory as a PDF document and can be downloaded via the device browser.
Strain gauge full bridge 4 mV/V		
Noise at 25 °C and 2.5 V bridge excitation (peak-to-peak)		
With 0.1 Hz Bessel filter	µV/V	0.1
With 1 Hz Bessel filter	µV/V	0.2
With 10 Hz Bessel filter	µV/V	0.3
With 100 Hz Bessel filter	µV/V	0.5
With 1 kHz Bessel filter	µV/V	1.5
With 2 kHz Bessel filter	µV/V	3
Inductive full bridge 100 mV/V		
Noise at 25 °C and 2.5 V bridge excitation (peak-to-peak)		
With 0.1 Hz Bessel filter	µV/V	2
With 1 Hz Bessel filter	µV/V	3
With 10 Hz Bessel filter	µV/V	4
With 100 Hz Bessel filter	µV/V	5
With 1 kHz Bessel filter	µV/V	10
With 2 kHz Bessel filter	µV/V	15
Inductive full bridge 1,000 mV/V		
Noise at 25 °C and 2.5 V bridge excitation (peak-to-peak)		
With 0.1 Hz Bessel filter	µV/V	20
With 1 Hz Bessel filter	µV/V	30
With 10 Hz Bessel filter	µV/V	40
With 100 Hz Bessel filter	µV/V	50
With 1 kHz Bessel filter	µV/V	100
With 2 kHz Bessel filter	µV/V	200
Strain gauge half bridge 4 m/V		
Noise at 25 °C and 2.5 V bridge excitation (peak-to-peak)		
With 0.1 Hz Bessel filter	µV/V	1
With 1 Hz Bessel filter	µV/V	2
With 10 Hz Bessel filter	µV/V	3
With 100 Hz Bessel filter	µV/V	4
With 1 kHz Bessel filter	µV/V	5
With 2 kHz Bessel filter	µV/V	10
Inductive half bridge 100 m/V		
Noise at 25 °C and 2.5 V bridge excitation (peak-to-peak)		
With 0.1 Hz Bessel filter	µV/V	2
With 1 Hz Bessel filter	µV/V	3
With 10 Hz Bessel filter	µV/V	4
With 100 Hz Bessel filter	µV/V	5
With 1 kHz Bessel filter	µV/V	15
With 2 kHz Bessel filter	µV/V	30
Inductive half bridge 500 m/V, LVDT, potentiometer		
Noise at 25 °C and 2.5 V bridge excitation (peak-to-peak)		
With 0.1 Hz Bessel filter	µV/V	20
With 1 Hz Bessel filter	µV/V	30
With 10 Hz Bessel filter	µV/V	40
With 100 Hz Bessel filter	µV/V	50
With 1 kHz Bessel filter	µV/V	100
With 2 kHz Bessel filter	µV/V	200

SPECIFICATIONS (PX455 CONTINUED)

Cut-off frequency (Hz, -3dB)		Runtime (ms)	
		Bessel	Butterworth
2000		0.16	0.23
1000		0.42	0.60
500		0.85	1.24
200		2.00	3.10
100		4.15	6.17
50		8.45	12.5
20		21.4	30.7
10		39	47
5		74	91
2		174	216
1		340	430
0.5		680	840
0.2		1,680	2,090
0.1		3,360	4,200

TE Connectivity Load Cell FX 1901

FX1901
Compression Load Cell

STANDARD RANGES

Range	lbf
0 to 0010	•
0 to 0025	•
0 to 0050	•
0 to 0100	•
0 to 0200	•

PERFORMANCE SPECIFICATIONS

Supply Voltage: 5.0V, Ambient Temperature: 25°C (unless otherwise specified)

PARAMETERS	MIN	TYP	MAX	UNITS	NOTES
Recommended Excitation		5		V	
Full Scale Output Span	16	20	24	mV/V	
Full Scale Output Span (200lbf)	34.2	36	37.8	mV/V	
Zero Offset	-15		15	mV/V	
Non-Linearity	-1		1	%Span	
Hysteresis	-0.80		0.80	%Span	
Thermal Zero Shift	-0.05		0.05	%Span / °C	
Thermal Sensitivity Shift	-0.05		0.05	%Span / °C	
Insulation Resistance	50			MΩ	@500V_{DC}
Maximum Overload		250		%FS	
Maximum Overload (200lbf)		150		%FS	
Operating Temperature	0		50	°C	
Storage Temperature	-40		+85	°C	
Creeping			0.5	%Span	F.S. span in 3min
Zero Drift			0.5	%Span	Load F.S. 3min
Zero Return	-0.8		0.8	%Span	
Span Repeat	-0.8		0.8	%Span	
Humidity	0		90	%R.H.	
Deflection		0.05		mm	At Rated Load
Input Resistance	2.4	3	3.6	kΩ	
Output Resistance	1.76	2.2	2.64	kΩ	

For custom configurations, consult factory.

CE Compliance
IEC61000-4-2 [4 kV/ 4 kV (Air/Contact)]
IEC61000-4-3 (3 V/m)
IEC55022 Class A

FX1901-0001

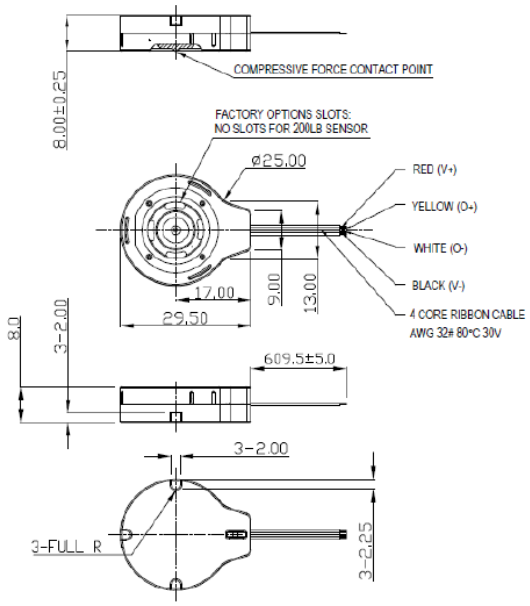

STC 1000 Digital Temperature Controller Datasheet

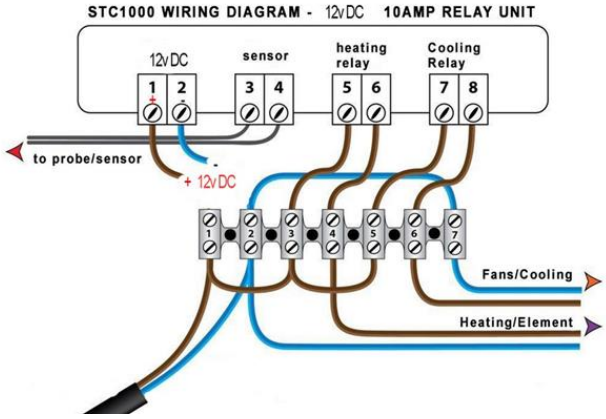

Description:
Digital STC-1000 12VDC All-Purpose Temperature Controller Thermostat with Sensor

Features:
- Switch the modes between cool and heat
- Control temperature by setting the temperature setting value and the difference value
- Temperature calibration
- Refrigerating control output delay protection
- Alarm when the temperature exceeds temperature limit or when sensor error

Specifications and size:
- Front panel size: 75(L) x 34.5(W) (mm)
- Mounting size: 71(L) x 29(W) mm
- Sensor length: 1m (include the probe)
- Product size: 75(L) x 34.5(W) x 85(D) mm

Technical Parameters:
- Temperature measuring range: -50 - 99 degrees C
- Resolution: 0.1 degrees C
- Accuracy: +/- 1 degrees C (-50 - 70 degrees C)
- Sensor error delay: 1 minute
- Power supply: 12VDC +/- 10%, 50/60Hz
- Power consumption: - Sensor: NTC sensor (1PC)
- Relay contact capacity: Cool 10A/250VAC; Heat 10A/250VAC
- Ambient temperature: 0 - 60 degrees C
- Storage temperature: -30 - 75 degrees C
- Relative humidity: 20% - 85% (No condensate)
- Weight: 178g

A2.3 Calibration Data

The TE Connectivity compression load cell was not provided with a calibration certificate at purchase. The calibration of the load cell was performed by applying an excitation voltage of 5V using an oscilloscope, loading the sensor with known loads using a Testometric Universal Testing Machine (Testometric X350-5, The Testometric Co Ltd, Rochdale, UK), and recording the output voltage using a voltmeter. The applied loads spanned the range expected in the glenoid edge motion testing (650N-850N), at 50N intervals. The test was repeated 4 times.

The recorded output voltage (mV), converted to mV/V and averaged for the 5 tests is shown for each applied load in **Table A- 3**. The HBK PMX allows 2-point sensor setup, so the sensor was programmed using the values of 27.77mV/V at 650N and 36.57mV/V at 850N (highlighted in green).

Table A- 3 *TE Connectivity Load Cell calibration testing results. Output voltage measured from the sensor for 5V excitation and known applied forces over the expected DGL test normal force range are recorded. The mean mV/V values at 650N and 850N (green) were used to set the sensor up in the HBK PMX.*

Applied Force (N)	**Measured voltage at 5V excitation, converted to mV/V and mV/V/N**	**Test no.**				**Mean**
		1	**2**	**3**	**4**	
650	mV (measured)	138	139		139.5	138.83
	mV/V	27.6	27.8		27.9	27.77
	mV/V/N	0.0425	0.0428		0.0429	0.0427
700	mV (measured)	150	151.5	152	151.5	151.25
	mV/V	30	30.3	30.4	30.3	30.25
	mV/V/N	0.0429	0.0433	0.0434	0.0433	0.0432
750	mV (measured)	162	162.5	162.5	163	162.50
	mV/V	32.4	32.5	32.5	32.6	32.50
	mV/V/N	0.0432	0.0433	0.0433	0.0435	0.0433
800	mV (measured)	172	173	172.5	172.5	172.50
	mV/V	34.4	34.6	34.5	34.5	34.50
	mV/V/N	0.0430	0.0433	0.0431	0.0431	0.0431
850	mV (measured)	183	183.5	182		182.83
	mV/V	36.6	36.7	36.4		36.57
	mV/V/N	0.0431	0.0432	0.0428		0.0430

A3 Preliminary Functional Validation Testing Results

Samples of the logged data for the two LabView Scripts, the P90 Test Protocol and the Glenoid Edge Motion Protocol script are provided.

A3.1 P90 Test Protocol

A sample of save file data from the P90 Test Protocol LabView script for the Size 52 glenoid, for the motion from centroid to LHS edge is provided below:

Position	Clock	Torque
66,500000	12401084	10,000000
66,501700	12401160	18,100000
66,567600	12401236	24,600000
66,630000	12401310	23,000000
66,690400	12401384	25,500000
66,751900	12401461	27,900000
66,813400	12401536	29,700000
66,883600	12401613	24,800000
66,941000	12401690	27,200000
67,002600	12401764	28,500000

{central data omitted for brevity]

90,054900	12429394	-7,100000
90,117400	12429470	-7,500000
90,180200	12429544	-7,900000
90,242000	12429620	-8,000000
90,306500	12429696	-7,700000
90,370200	12429772	-8,300000
90,431300	12429846	-8,700000
90,494600	12429922	-8,500000
90,559300	12429998	-8,300000
90,622700	12430074	-9,500000
90,686200	12430150	-9,900000
90,747300	12430226	-9,200000
90,812900	12430302	-10,300000
90,877000	12430378	-10,600000
90,939200	12430454	-10,100000

A3.2 Glenoid Edge Motion Protocol

A sample of save file test data from the Glenoid Edge Motion Protocol LabView script for the expired Size 44 glenoid conditioning test is provided below:

Position	Clock	Torque	Cycle	PMX 1.1	PMX 1.2	PMX 1.3	PMX 1.4	PMX 3.1	PMX 3.2	PMX 3.3
66,500000	8346141	2,300000	1	-0,093319	-0,110335	0,094219	759,378910	0,013457	0,082346	-0,041328
66,500000	8346218	2,600000	0	-0,093801	-0,111067	0,094282	759,341800	0,011797	0,081611	-0,041313
68,734200	8346535	63,500000	0	-0,245489	-0,287918	0,249359	788,158390	0,106506	0,123684	-0,075530
70,503300	8346851	66,800000	0	-0,747722	-2,011797	1,102733	786,520750	0,166970	0,154173	-0,102420
68,200400	8347755	13,600000	0	-0,393302	-1,177642	0,614247	740,609310	0,106635	0,129821	-0,088499
66,267300	8347991	-25,900000	0	-0,078876	-0,698605	0,257660	744,125310	0,052507	0,097371	-0,060186
63,986600	8348269	-74,300000	0	0,042940	-0,546187	0,161333	788,945310	-0,364677	-0,203847	0,189779
62,496000	8348505	-68,500000	0	0,074858	-0,505748	0,132740	781,371030	-2,347593	-0,431164	0,664629
64,758400	8349295	-19,200000	1	0,077420	-0,498971	0,126623	744,052120	-1,394415	-0,445854	0,484865
66,727100	8349535	23,400000	1	0,036805	-0,548294	0,150570	756,724850	-0,466973	-0,225302	0,171714
68,672500	8349771	59,800000	1	-0,085413	-0,682160	0,299983	788,723880	-0,231246	-0,064322	0,080488
70,504200	8350090	68,300000	1	-0,703893	-2,091674	1,138802	786,651980	-0,115656	0,019122	0,043403
68,215700	8350889	13,900000	1	-0,397597	-1,268654	0,660268	738,869320	-0,108427	0,019770	0,043397
66,282400	8351125	-27,000000	1	-0,080476	-0,765433	0,289743	744,904360	-0,146905	0,003814	0,046677
64,346000	8351361	-63,300000	1	0,019059	-0,639438	0,203209	779,055790	-0,414435	-0,252091	0,228544
62,496300	8351675	-65,900000	1	0,066061	-0,570611	0,164861	784,701840	-2,573084	-0,528011	0,748632
64,797400	8352467	-17,900000	2	0,067284	-0,560550	0,156687	745,416560	-1,404797	-0,496159	0,510660
66,724900	8352703	23,400000	2	0,028546	-0,607439	0,183594	755,678960	-0,544699	-0,295517	0,209908
68,661800	8352939	58,900000	2	-0,090968	-0,741400	0,329826	788,125730	-0,330374	-0,162006	0,117133
70,504200	8353255	68,400000	2	-0,707768	-2,122632	1,155989	787,074400	-0,196502	-0,033529	0,081195
68,217200	8354053	13,200000	2	-0,405472	-1,296862	0,675959	743,739380	-0,182634	-0,029095	0,082331
66,258200	8354293	-22,200000	2	-0,089951	-0,791914	0,309998	746,906680	-0,216733	-0,044815	0,091940
64,287400	8354531	-61,400000	2	0,012428	-0,663451	0,222802	781,519900	-0,490884	-0,312918	0,277637
62,497700	8354849	-64,100000	2	0,060456	-0,591679	0,183124	786,937740	-2,635761	-0,592772	0,768240

[Central data omitted for brevity]

64,778700	8377481	-15,300000	8	0,027629	-0,667407	0,249258	744,054750	-1,603832	-0,673536	0,619587
66,710300	8377717	20,600000	8	-0,010631	-0,717178	0,287204	749,333980	-0,808169	-0,424269	0,342014
68,671700	8377956	56,400000	8	-0,152975	-0,883458	0,429316	785,631230	-0,579538	-0,289742	0,234643
70,505400	8378275	67,400000	8	-0,716055	-2,259402	1,230611	787,503230	-0,438026	-0,145332	0,152246
68,216800	8378993	12,100000	8	-0,400809	-1,402631	0,721718	742,783140	-0,443644	-0,146973	0,174191
66,260900	8379231	-20,300000	8	-0,086863	-0,939702	0,376316	747,107180	-0,470622	-0,158952	0,204253
64,342600	8379465	-59,100000	8	0,000319	-0,816556	0,290696	782,770080	-0,712849	-0,416159	0,368640
62,496400	8379779	-64,200000	8	0,045325	-0,652929	0,230004	783,505490	-2,697797	-0,741777	0,878776
64,787700	8381232	-15,200000	9	0,029184	-0,665811	0,251006	746,969540	-1,594673	-0,694855	0,623013
66,710300	8381466	20,500000	9	-0,010125	-0,717034	0,288245	752,247010	-0,825238	-0,436887	0,345136
68,662900	8381704	54,900000	9	-0,153543	-0,888172	0,429485	786,252320	-0,601289	-0,306294	0,246096
70,505700	8382020	65,500000	9	-0,713272	-2,251242	1,227913	788,856320	-0,465026	-0,170022	0,164133
68,225700	8383836	12,400000	9	-0,431091	-1,457551	0,765429	742,931400	-0,415493	-0,149662	0,167581
66,271200	8384075	-20,500000	9	-0,122409	-0,984902	0,418336	746,980160	-0,443640	-0,161670	0,199421
64,344000	8384310	-58,500000	9	-0,028257	-0,860700	0,330788	781,331970	-0,696660	-0,424847	0,367188
62,496500	8384624	-64,000000	9	0,024798	-0,708190	0,264986	785,364620	-2,703977	-0,753769	0,883395
66,500000	8387638	0,500000	9	-0,026447	-0,756292	0,308781	751,924190	-0,591090	-0,354067	0,281686

A3.3 Normal Load application

For the estimate of inertial force contribution of the motion of the deadweight in the vertical direction (as the HH moves up the curve of the glenoid), the following assumptions were made:

1. The humeral head climb is 3mm in the vertical direction.
2. The climb is up a straight surface (i.e. neglect acceleration variations due to the curvature of the glenoid).
3. The horizontal motion is 90% of the largest predicted subluxation distance, 13.5mm x 0.9 = 12.5mm
4. Horizontal motion speed is 2Hz, on a glenoid with a subluxation distance of 13.5mm.
5. The horizontal motion has a constant acceleration for the first half of the motion, and constant deceleration for the second half of the motion.
6. This results in the same effect, but at different acceleration value, in the vertical motion.
7. The vertical motion of the humeral head as it crosses the centroid is zero.

The force required to accelerate the deadweight upward will occur for the first half of the motion to the edge. To calculate this, we use:

$$F_{inertia} = ma \qquad \text{[A1]}$$

where *m* is the weight of the deadweight, and *a* is the upward acceleration of the deadweight. To calculate the upward acceleration, we use:

$$s = ut + 0.5at^2 \qquad \text{[A2]}$$

Where s is the vertical distance travelled when the HH has moved half the horizontal distance to the edge. Based on the assumptions 2 and 5, *s* will be half the total vertical motion, s= 1.5mm, based on assumption 1. From assumption 7, the initial vertical velocity, *u* = 0. The time *t* is the time taken for the HH to move hallway between the centroid and the P90 distance in the horizontal direction. In one cycle the HH must move four times the distance from the centroid to P90 (Centroid -> +P90 -> Centroid->-P90-> Centroid). At 2Hz the HH must travel this distance 8 times. The time taken to reach P90 is therefore t_{P90}= 1/8=0.125s, and *t* In Equation A2 will be half of this, or *t* = 0.063s. We now calculate the upward acceleration:

$$a = \frac{2(s-ut)}{t^2} = \frac{2(0.015-0)}{0.063^2} = 0.768ms^{-2} \qquad \text{[A3]}$$

From which the upward inertial force is found to be:

$$F_{inertia} = \frac{750}{9.81}0.768 = 58.72N \qquad \text{[A4]}$$

A3.4 Temperature Control and Lubrication System

Sample data of five days of water bath temperature, before and after the water bath was refilled, are provided in **Table A- 4**. The addition of cold water caused the water temperature to drop near but not below the 35°C minimum temperature range.

Table A- 4 *Water bath temperature log, before and after twice daily refilling of water bath.*

Day	Time	Water Batch Temperature (°C)	
		Before water bath refilled	After water bath refilled
06 May 2022	09:31	37.0	35.1
	17:30	36.8	36.5
07 May 2022	11:11	36.7	35.5
	17:22	36.8	36.5
08 May 2022	11:30	36.7	35.0
	18:19	36.8	36.2
09 May 2022	13:22	36.8	35.1
	15:33	37.0	36.7
10 May 2022	08:06	37.0	35.6
	16:57	37.0	35.9

B. APPENDIX B: GLENOID EDGE MOTION MEASURMENT SYSTEM

B1 LVDT Sensors

B1.1 Summary of LVDT Sensors

Table B- 1 *Summary of LVDT sensors used in the glenoid edge motion measurement system*

Sensor	**Product code**	**Type**	**Measurement Range**	**Nominal Sensitivity**
Horizontal Sensors	RDP D6/05000ARA	Spring guided	±5mm	700mV/V
Vertical Sensors	RDP MD5/500HKRA	Unguided	±12.5mm	775mV/V
Vertical Sensor replacement (S_{L1})	ACT500C	Captive guided	±12.5mm	700mV/V

RDP MD5/500HKRA Datasheet

DISPLACEMENT

D5 & D6 LVDT Displacement Transducer

- High cycle life
- Stainless steel
- High accuracy
- Infinite resolution
- Miniature

These transducers are for displacement / position measurement. They make an accurate position measurement of the movement of the armature (the sliding part) relative to the body of the displacement transducer.
This transducer uses the Linear Variable Differential Transformer (LVDT) principle which means that it is probably the most robust and reliable position sensor type available. The strength of the LVDT sensor's principle is that there is no electrical contact across the transducer position sensing element which for the user of the sensor means clean data, infinite resolution and a very long life.
The LVDTs are available as either unguided or spring return versions.

Unguided version.

On our D5-D6 unguided LVDTs the armature assembly is a separate component, to make a measurement the user must guide the armature inside the body without touching the sides. Our D5-D6 unguided position measurement transducers are appropriate where external guidance is available and give truly non-contact operation

End (axial) exit cable.

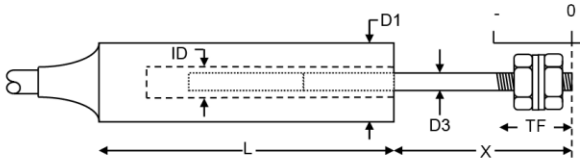

D1=0.374" (0.370" to 0.374")
D3=0.079"
TGF=M3x0.5
X=Center of range

Type	Range	Linearity error (% F.S.)	L	X (nom)	ID	Total weight	Armature weight	TF	Inward over-travel	Sensitivity (nom)
D6/02500U	±2.5mm (±0.1")	±0.5/±0.25/±0.1	1.69"	0.8"	0.114"	0.6oz	0.06oz	0.60"	0.06"	375mV/V
D6/05000U	±5mm (±0.2")	±0.5/±0.25/±0.1	2.20"	1.0"	0.114"	0.7oz	0.06oz	0.73"	0.08"	700mV/V
D5/300HK	±7.5mm (±0.3")	±0.5/±0.25/±0.1	2.28"	1.2"	0.100"	0.7oz	0.06oz	0.73"	0.15"	502mV/V
D5/400HK	±10mm (±0.4")	±0.5/±0.25	2.48"	1.3"	0.100"	0.9oz	0.07oz	0.73"	0.17"	576mV/V
MD5/500HK	±12.5mm (±0.5")	±0.5/±0.25	3.11"	1.4"	0.100"	1.2oz	0.08oz	0.73"	0.17"	775mV/V
MD5/1000HK	±25mm (±1")	±0.5/±0.25	4.50"	1.9"	0.100"	1.2oz	0.11oz	0.72"	0.16"	475mV/V
MD5/2000HK	±50mm (±2")	±0.5/±0.25	8.25"	2.9"	0.100"	2.2oz	0.19oz	0.73"	0.20"	535mV/V
MD5/3000HK	±75mm (±3")	±0.5/±0.25	11.75"	3.9"	0.100"	3.1oz	0.26oz	0.73"	0.20"	525mV/V

Side (radial) exit cable.

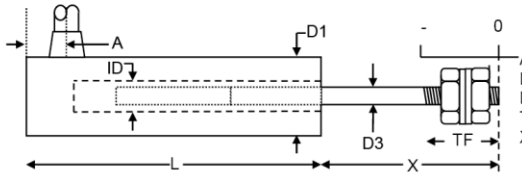

A=0.2" (nominal)
D1=0.374" (0.370" to 0.374")
D3=0.079"
TGF=M3x0.5
X=Center of range

Type	Range	Linearity error (% F.S.)	L	X (nom)	ID	Total weight	Armature weight	TF	Inward over-travel	Sensitivity (nom)
D6/02500URA	±2.5mm (±0.1")	±0.5/±0.25/±0.1	1.77"	0.8"	0.115"	0.6oz	0.06oz	0.60"	0.06"	375mV/V
D6/05000URA	±5mm (±0.2")	±0.5/±0.25/±0.1	2.34"	1.0"	0.115"	0.7oz	0.06oz	0.73"	0.08"	700mV/V
D5/300HKRA	±7.5mm (±0.3")	±0.5/±0.25/±0.1	2.37"	1.2"	0.100"	0.7oz	0.06oz	0.73"	0.15"	502mV/V
D5/400HKRA	±10mm (±0.4")	±0.5/±0.25	2.57"	1.3"	0.100"	0.9oz	0.07oz	0.73"	0.17"	576mV/V
MD5/500HKRA	±12.5mm (±0.5")	±0.5/±0.25	3.20"	1.4"	0.100"	1.2oz	0.08oz	0.73"	0.17"	775mV/V
MD5/1000HKRA	±25mm (±1")	±0.5/±0.25	4.59"	1.9"	0.100"	1.2oz	0.11oz	0.73"	0.16"	475mV/V
MD5/2000HKRA	±50mm (±2")	±0.5/±0.25	8.34"	2.9"	0.100"	2.2oz	0.19oz	0.73"	0.20"	535mV/V
MD5/3000HKRA	±75mm (±3")	±0.5/±0.25	11.84"	3.9"	0.100"	3.1oz	0.26oz	0.73"	0.20"	525mV/V

RDP D6/05000ARA Datasheet

Spring return version.

Our D5-D6 spring displacement transducer has bearings to guide the armature inside the measurement sensor and a spring which pushes the armature to the fully out position. Our D5-D6 spring return LVDTs are appropriate where it is not possible to connect the transducer armature to the moving component being measured.

End (axial) exit cable.

Type	Range	Linearity error (% F.S.)	L	X (nom)	Total weight	Spring force at X	Spring rate	Inward over-travel	Outward over-travel	Sensitivity (nom)
D6/00250A	±0.25mm (±0.01")	±0.5/±0.25	1.94"	0.5"	0.4oz	2oz	11oz/inch	0.02"	0.02"	38mV/V
D6/00500A	±0.5mm (±0.02")	±0.5/±0.25	1.94"	0.5"	0.4oz	2oz	11oz/inch	0.01"	0.01"	75mV/V
D6/01000A	±1mm (±0.04")	±0.5/±0.25/±0.1	2.06"	0.5"	0.4oz	1oz	11oz/inch	0.07"	0.03"	150mV/V
D6/02500A	±2.5mm (±0.1")	±0.5/±0.25/±0.1	2.39"	0.5"	0.9oz	3oz	9oz/inch	0.05"	0.05"	375mV/V
D6/05000A	±5mm (±0.2")	±0.5/±0.25/±0.1	3.08"	0.5"	1.1oz	3oz	7oz/inch	0.04"	0.05"	700mV/V
D5/300AG	±7.5mm (±0.3")	±0.5/±0.25/±0.1	3.44"	0.6"	1.2oz	4oz	6oz/inch	0.04"	0.06"	502mV/V
D5/400AG	±10mm (±0.4")	±0.5/±0.25	3.88"	0.7"	1.4oz	5oz	4oz/inch	0.10"	0.05"	576mV/V
MD5/500AG	±12.5mm (±0.5")	±0.5/±0.25	4.76"	0.9"	1.7oz	5oz	4oz/inch	0.10"	0.05"	775mV/V
MD5/1000AG	±25mm (±1")	±0.5/±0.25	7.56"	1.4"	2.7oz	10oz	4oz/inch	0.05"	0.11"	475mV/V
MD5/2000AG	±50mm (±2")	±0.5/±0.25	13.74"	2.6"	4.9oz	1lbs	4oz/inch	0.17"	0.13"	535mV/V
MD5/3000AG	±75mm (±3")	±0.5/±0.25	20.67"	3.9"	7.3oz	1lbs	3oz/inch	0.20"	0.20"	525mV/V

Side (radial) exit cable.

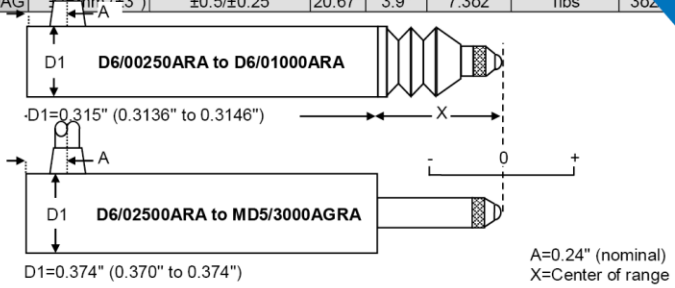

Type	Range	Linearity error (% F.S.)	L	X (nom)	Total weight	Spring force at X	Spring rate	Inward over-travel	Outward over-travel	Sensitivity (nom)
D6/00250ARA	±0.25mm (±0.01")	±0.5/±0.25	1.98"	0.5"	0.4oz	2oz	11oz/inch	0.02"	0.02"	38mV/V
D6/00500ARA	±0.5mm (±0.02")	±0.5/±0.25	1.98"	0.5"	0.4oz	2oz	11oz/inch	0.01"	0.01"	75mV/V
D6/01000ARA	±1mm (±0.04")	±0.5/±0.25/±0.1	2.10"	0.5"	0.4oz	1oz	11oz/inch	0.07"	0.03"	150mV/V
D6/02500ARA	±2.5mm (±0.1")	±0.5/±0.25/±0.1	2.50"	0.5"	0.9oz	3oz	9oz/inch	0.05"	0.05"	375mV/V
D6/05000ARA	±5mm (±0.2")	±0.5/±0.25/±0.1	3.27"	0.5"	1.1oz	3oz	7oz/inch	0.04"	0.05"	700mV/V
D5/300AGRA	±7.5mm (±0.3")	±0.5/±0.25/±0.1	3.54"	0.6"	1.2oz	4oz	6oz/inch	0.04"	0.06"	502mV/V
D5/400AGRA	±10mm (±0.4")	±0.5/±0.25	4.00"	0.7"	1.4oz	5oz	4oz/inch	0.10"	0.05"	576mV/V
MD5/500AGRA	±12.5mm (±0.5")	±0.5/±0.25	4.88"	0.9"	1.7oz	5oz	4oz/inch	0.10"	0.05"	775mV/V
MD5/1000AGRA	±25mm (±1")	±0.5/±0.25	7.68"	1.4"	2.7oz	10oz	4oz/inch	0.05"	0.11"	535mV/V
MD5/2000AGRA	±50mm (±2")	±0.5/±0.25	13.82"	2.6"	4.9oz	1lbs	4oz/inch	0.17"	0.13"	535mV/V
MD5/3000AGRA	±75mm (±3")	±0.5/±0.25	20.81"	3.9"	7.3oz	1lbs	3oz/inch	0.20"	0.20"	525mV/V

RDP ACT500C Datasheet

DISPLACEMENT

ACT LVDT Displacement Transducer

- High accuracy
- High cycle life
- Infinite resolution
- Stainless steel

The ACT series displacement transducers form part of our industrial series of LVDTs. Because they use the LVDT principle they have a very long life as there is no electrical contact across the sensing element which means clean, reliable data. The ACT transducer gives an output proportional to the position of the armature assembly with respect to the body of the transducer. ACT series transducers are available in three versions as detailed below.
RDP are the designers and manufactures of the ACT series and so in addition to the range of standard options (higher temperature, IP rating, radiation tolerance etc) we can offer tailor made mechanical solutions to mounting and installing the transducer.

Unguided version.

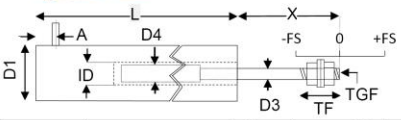

A=0.35"
D1=0.811" ±0.005"
D3=0.187"
D4=0.235"
ID=0.268"
TGF=M5x0.8

On our ACT unguided LVDTs the armature assembly is a separate component, to make a measurement the user must guide the armature inside the body without touching the sides. Our ACT unguided position measurement transducers are appropriate where external guidance is available and give truly non-contact operation

Type	Range	Linearity error (% F.S.)	L	X (nom)	Total weight	Armature weight	TF	Inward over-travel	Sensitivity (nom)
ACT500	±12.5mm (±0.5")	±0.5/±0.25/±0.1	5.00"	1.7"	6.0oz	0.60oz	0.59"	0.6"	0.7V/V
ACT1000	±25mm (±1")	±0.5/±0.25/±0.1	6.10"	2.7"	8.0oz	0.81oz	0.59"	0.9"	0.9V/V
ACT2000	±50mm (±2")	±0.5/±0.25/±0.1	10.63"	3.2"	11.3oz	1.31oz	0.59"	0.6"	1.5V/V
ACT3000	±75mm (±3")	±0.5/±0.25/±0.1	14.96"	4.7"	1.0lb	1.94oz	0.59"	1.1"	1.5V/V
ACT4000	±100mm (±4")	±0.5/±0.25/±0.1	16.81"	5.2"	1.3lb	2.50oz	0.59"	0.6"	3.2V/V
ACT6000	±150mm (±6")	±0.5/±0.25	24.29"	7.2"	1.8lb	3.53oz	0.59"	0.6"	2.4V/V
ACT8000	±200mm (±8")	±0.5/±0.25	31.81"	10.2"	2.6lb	4.94oz	1.15"	1.1"	1.5V/V

Captive guided version.

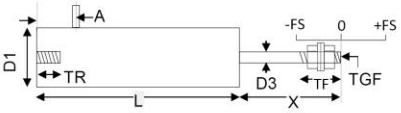

A=0.94"
D1=0.811" ±0.005"
TGF=M5x0.8
TGR=M5x0.8
TR=0.43"

Our ACT captive guided displacement transducer has bearings to guide the armature inside the measurement sensor. Our ACT captive LVDTs are for position measurement applications where guidance may be poor and end bearings may be required.

Type	Range	Linearity error (% F.S.)	L	X (nom)	D3	Total weight	TF	Inward over-travel	Outward over-travel	Sensitivity (nom)
ACT500C	±12.5mm (±0.5")	±0.5/±0.25/±0.1	5.98"	1.5"	0.187"	10.0oz	0.59"	0.4"	0.47"	0.7V/V
ACT1000C	±25mm (±1")	±0.5/±0.25/±0.1	7.09"	2.5"	0.187"	12.0oz	0.59"	0.5"	0.39"	0.9V/V
ACT2000C	±50mm (±2")	±0.5/±0.25/±0.1	11.61"	3.0"	0.187"	1.1lb	0.59"	0.4"	0.55"	1.5V/V
ACT3000C	±75mm (±3")	±0.5/±0.25/±0.1	15.98"	4.5"	0.187"	1.4lb	0.59"	0.9"	0.59"	1.5V/V
ACT4000C	±100mm (±4")	±0.5/±0.25/±0.1	17.80"	5.0"	0.187"	1.6lb	0.59"	0.3"	0.55"	3.2V/V
ACT6000C	±150mm (±6")	±0.5/±0.25	25.31"	7.0"	0.187"	2.3lb	0.59"	0.5"	0.67"	2.4V/V
ACT8000C	±200mm (±8")	±0.5/±0.25	32.80"	10.0"	0.187"	3.1lb	1.25"	0.9"	0.98"	1.5V/V
ACT10000C	±250mm (±10")	±0.5/±0.25	40.55"	12.0"	0.187"	3.5lb	1.05"	1.3"	1.38"	2.0V/V
ACT15000C	±380mm (±15")	±0.5	56.50"	16.0"	0.187"	4.7lb	0.75"	0.5"	0.51"	3.2V/V
ACT18500C	±470mm (±18.5")	±0.5	67.01"	20.0"	0.236"	5.6lb	1.05"	0.2"	1.30"	3.6V/V

B1.3 Sensor Calibration Data

Table B- 2 *Calibration certificates for RDP LVDT sensors*

Sensor	Calibration certificate
S_{1L}	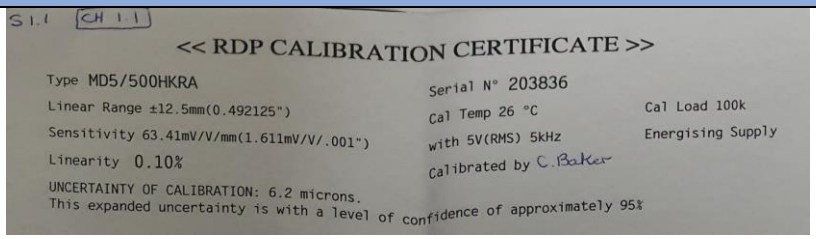 S1.1 CH 1.1 << RDP CALIBRATION CERTIFICATE >> Type MD5/500HKRA Serial N° 203836 Linear Range ±12.5mm(0.492125") Cal Temp 26 °C Cal Load 100k Sensitivity 63.41mV/V/mm(1.611mV/V/.001") with 5V(RMS) 5kHz Energising Supply Linearity 0.10% Calibrated by C.Baker UNCERTAINTY OF CALIBRATION: 6.2 microns. This expanded uncertainty is with a level of confidence of approximately 95%
S_{2L}	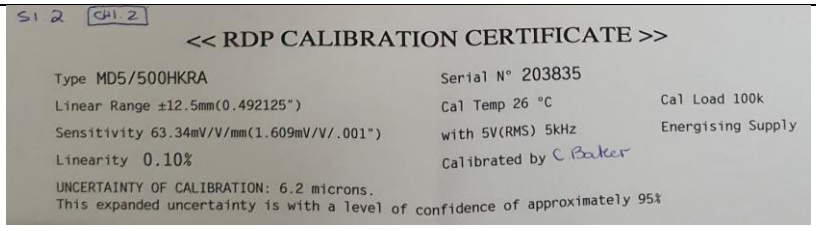 S1.2 CH1.2 << RDP CALIBRATION CERTIFICATE >> Type MD5/500HKRA Serial N° 203835 Linear Range ±12.5mm(0.492125") Cal Temp 26 °C Cal Load 100k Sensitivity 63.34mV/V/mm(1.609mV/V/.001") with 5V(RMS) 5kHz Energising Supply Linearity 0.10% Calibrated by C Baker UNCERTAINTY OF CALIBRATION: 6.2 microns. This expanded uncertainty is with a level of confidence of approximately 95%
S_{3L}	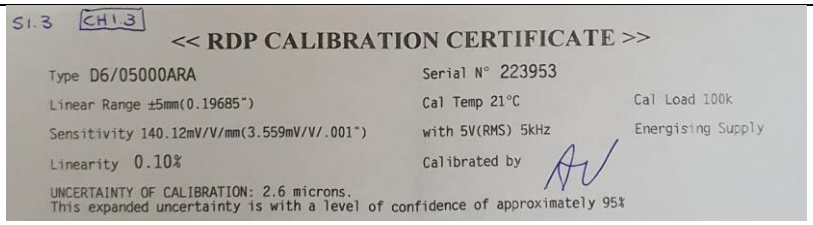 S1.3 CH1.3 << RDP CALIBRATION CERTIFICATE >> Type D6/05000ARA Serial N° 223953 Linear Range ±5mm(0.19685") Cal Temp 21°C Cal Load 100k Sensitivity 140.12mV/V/mm(3.559mV/V/.001") with 5V(RMS) 5kHz Energising Supply Linearity 0.10% Calibrated by AV UNCERTAINTY OF CALIBRATION: 2.6 microns. This expanded uncertainty is with a level of confidence of approximately 95%
S_{1R}	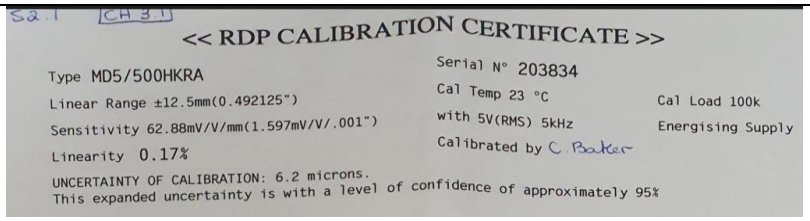 S2.1 CH 3.1 << RDP CALIBRATION CERTIFICATE >> Type MD5/500HKRA Serial N° 203834 Linear Range ±12.5mm(0.492125") Cal Temp 23 °C Cal Load 100k Sensitivity 62.88mV/V/mm(1.597mV/V/.001") with 5V(RMS) 5kHz Energising Supply Linearity 0.17% Calibrated by C. Baker UNCERTAINTY OF CALIBRATION: 6.2 microns. This expanded uncertainty is with a level of confidence of approximately 95%
S_{2R}	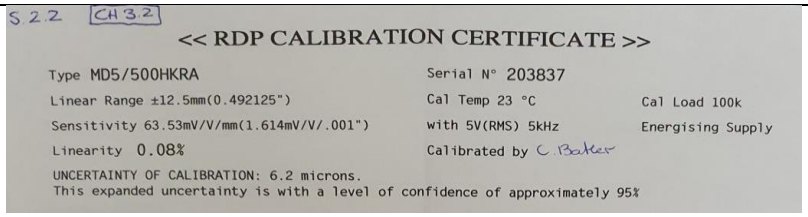 S 2.2 CH 3.2 << RDP CALIBRATION CERTIFICATE >> Type MD5/500HKRA Serial N° 203837 Linear Range ±12.5mm(0.492125") Cal Temp 23 °C Cal Load 100k Sensitivity 63.53mV/V/mm(1.614mV/V/.001") with 5V(RMS) 5kHz Energising Supply Linearity 0.08% Calibrated by C. Baker UNCERTAINTY OF CALIBRATION: 6.2 microns. This expanded uncertainty is with a level of confidence of approximately 95%
S_{3R}	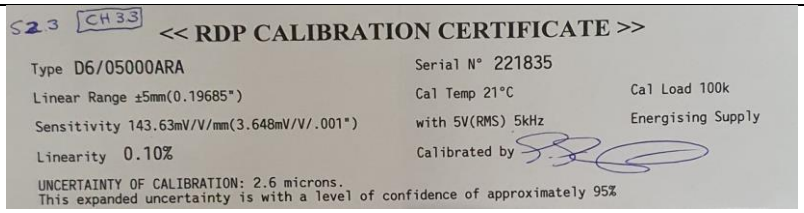 S2.3 CH 3.3 << RDP CALIBRATION CERTIFICATE >> Type D6/05000ARA Serial N° 221835 Linear Range ±5mm(0.19685") Cal Temp 21°C Cal Load 100k Sensitivity 143.63mV/V/mm(3.648mV/V/.001") with 5V(RMS) 5kHz Energising Supply Linearity 0.10% Calibrated by UNCERTAINTY OF CALIBRATION: 2.6 microns. This expanded uncertainty is with a level of confidence of approximately 95%
S_{1L} **(replacement)**	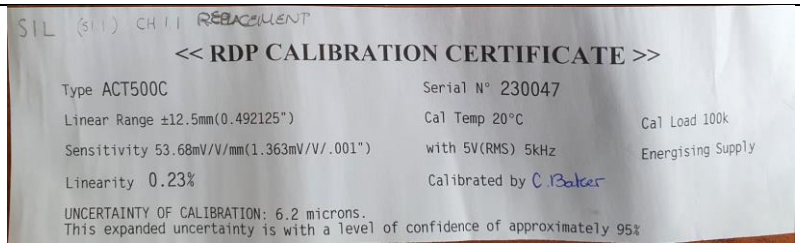 S1L (S1.1) CH 1.1 REPLACEMENT << RDP CALIBRATION CERTIFICATE >> Type ACT500C Serial N° 230047 Linear Range ±12.5mm(0.492125") Cal Temp 20°C Cal Load 100k Sensitivity 53.68mV/V/mm(1.363mV/V/.001") with 5V(RMS) 5kHz Energising Supply Linearity 0.23% Calibrated by C.Baker UNCERTAINTY OF CALIBRATION: 6.2 microns. This expanded uncertainty is with a level of confidence of approximately 95%

B2 Glenoid Edge Motion Calculation

B2.1 Glenoid Edge Motion Calculation Method (RHS)

The calculation of the RHS glenoid edge motion, based on the motion of the RHS measuring block, follows a similar method to what was applied to the LHS block in Chapter 3, but adjusted for the location of sensor S_{3R}, as shown in **Figure B-1**.

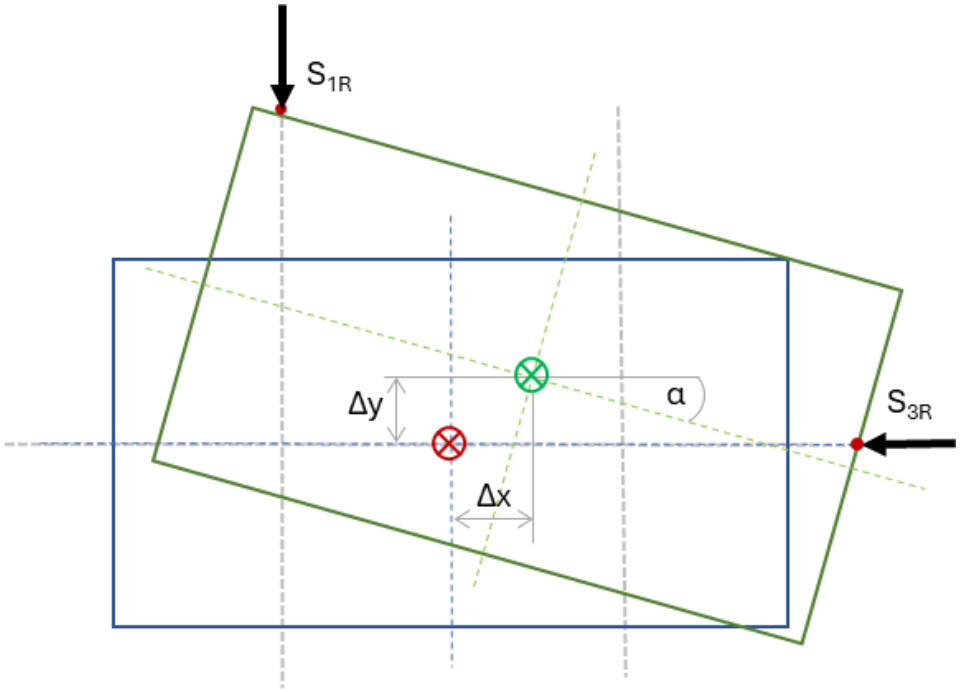

Figure B-1 *Initial and deflected position of the RHS measuring block for a motion of unknown magnitude, where the block centroid has moved by Δx in the horizontal direction and Δy in the vertical direction, and the block has rotated α°*

First, we find the gradient of the line formed by the top surface of the block the value of, m_3, and α_R:

$$m_3 = -\left[\frac{S_{1Ry} - S_{2Ry}}{0.5L_b}\right] = -\tan\alpha \qquad [B1]$$

From which we find the degree of rotation of the block

$$\alpha_R = -\tan^{-1}\left(\frac{S_{1Ry} - S_{2Ry}}{0.5L_b}\right) \qquad [B2]$$

Next, we use the gradient m_3 to define the equation for the top line of the block:

$$y = m_3 x + C_3 \qquad [B3]$$

Where m1 is known and the co-ordinates at the sensors S1R = [$-0.25L_b$, $S1R_y$] and S2R = [$-0.25L_b$, $S2R_y$] are either constants or measured, so are also known.

Using the co-ordinates of sensor S1R

$$S_{1Ry} = m_3(-0.25L_b) + C_3 \quad \text{[B5]}$$

So $C_3 = S_{1Ry} - m_3(-0.25L_b)$

We now define the equation of the straight line formed by the side of the block.

The gradient of this line is the inverse of the gradient of the top of the block, since these are rigidly perpendicular to each other.

$$m_4 = -\frac{1}{m_3} \quad \text{[B6]}$$

and

$$y = m_4 x + C_4 \quad \text{[B7]}$$

Using the co-ordinates of sensor S_3 [S3Rx, 0] we can solve for C_2

$$C_4 = 0 - m_4 S_{3Rx} \quad \text{[B8]}$$

The point where these two straight lines intersect is the location of the top right-hand corner (Corner 3) of the block

$$m_3 x_{corner3} + C_3 = m_4 x_{corner3} + C_4 \quad \text{[B9]}$$

$$x_{corner3} = \frac{C_4 - C_3}{m_3 - m_4} \quad \text{[B10]}$$

$$y_{corner3} = m_3 x_{corner3} + C_3 \quad \text{[B11]}$$

Using known geometry and trigonometry of the block, as shown in **Figure B-2**, the co-ordinates of the opposite (lower, left) corner (Corner 4) can be calculated.

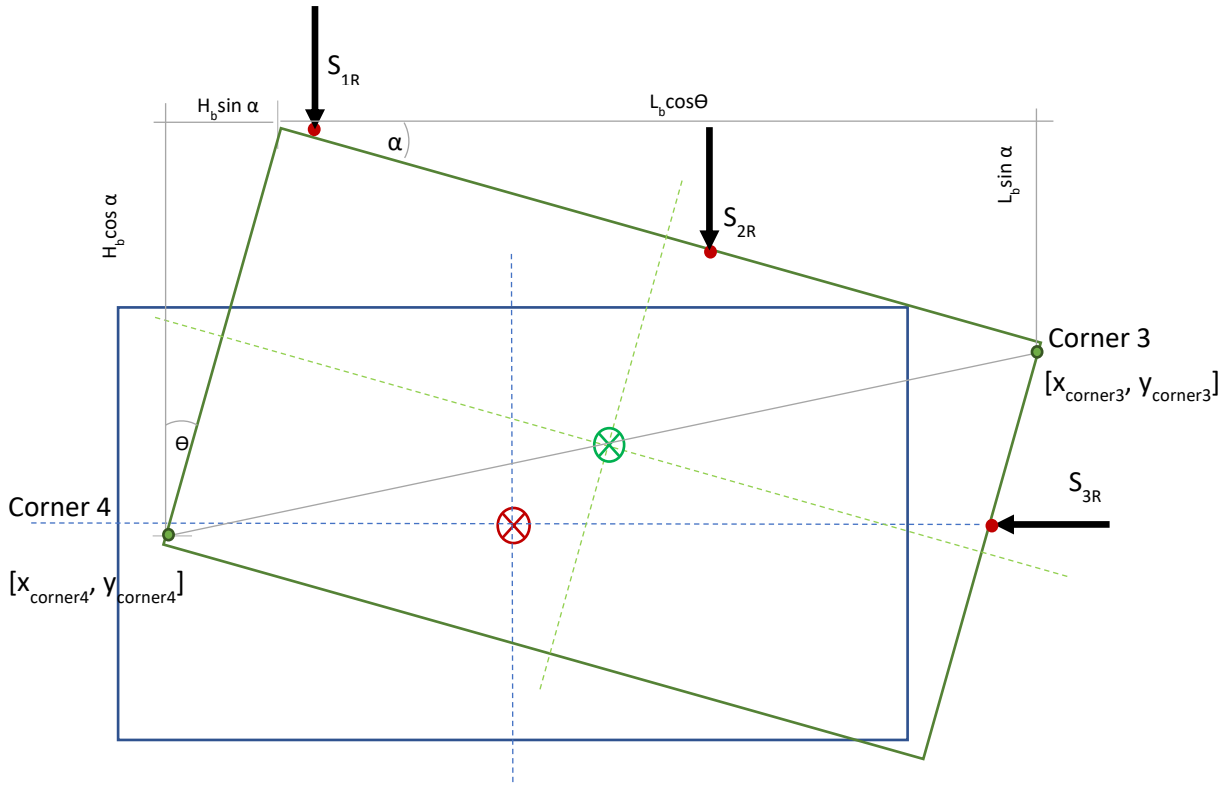

Figure B-2 *Definition of the diagonal line from Corner 3 to Corner 4 of the RHS measuring block, used to determine the centroid location.*

$$x_{corner4} = x_{corner3} - L_b \cos\theta - H_b \sin\theta \quad \text{[B12]}$$

$$y_{corner4} = y_{corner3} + L_b \sin\theta - H_b \cos\theta \quad \text{[B13]}$$

The centre point of the diagonal line between the two corners is the location of the centroid of the block.

$$C_{BRx} = \frac{x_{corner3} + x_{corner4}}{2} \quad \text{[B14]}$$

$$C_{BRy} = \frac{y_{corner3} + y_{corner4}}{2} \quad \text{[B15]}$$

Since the original position of the centroid was [0,0], the x and y co-ordinate values give an indication of the x and y deflection of the end of the lever arm. Yhe block motion is converted to glenoid edge motion at the RHS using the level geometry as described in Equation 3.20 and Equation 3.21.

B2.2 Motion Calculation MATLAB Script

The Motion Calculation Matlab script, converts sensor readings into glenoid edge motion, separates the edge motion into tensile, compressive and neutral load condition vectors and outputs excel data files for analysis. The code used is given here.

MOTION CLACULATON REV 3 MATLAB SCRIPT

```
clear all
close all
clc
format long;
digits(20);

%Geometric Constants and initial values (mm)
CbxL = 0;             % Left Block center x coordinate
CbyL = 0;             % Left Block center y coordinate
CbxR = 0;             % Right Block center x coordinate
CbyR = 0;             % Right Block center y coordinate


Lb = 60;             % Block length
Hb = 40;             % Block heigth

LPL = 60;            % Glenoid connector 1 length
LPR = 60;            % Glenoid connector 2 length
LAL = 215;           % Lever Arm 1 length
LAR = 235;           % Lever arm 2 lenght

Stroke = 4.15;         %Stroke lengrht for glenoid head size NB CHECK FOR EACH DATA
SET

%Constant sensor values
%Left Block
 S1Lx = -Lb/4;
 S2Lx = Lb/4;
 S3Ly = 0;
 %Right Block
 S1Rx = -Lb/4;
 S2Rx = Lb/4;
 S3Ry = 0;

%Distance between sensors S1 and S2
 L_S1S2L = S2Lx - S1Lx;
 L_S1S2R = S2Rx - S1Rx;

 %Import all Measured test Data
 Test_Data = readtable('allData.csv','Format', 'auto');
 %Check vector size
 disp('All Data table imported')
 disp('All Data Table Size =')
 disp(size(Test_Data))

 %Left Block sensor values
 S1Ly_measured = Test_Data(:,5);
 S2Ly_measured = Test_Data(:,6);
 S3Lx_measured = Test_Data(:,7);

 %Right Block sensor values
 S1Ry_measured = Test_Data(:,9);
 S2Ry_measured = Test_Data(:,10);
 S3Rx_measured = Test_Data(:,11);


 %Check vector size
```

```
 disp('Data vector size')
 disp('Sensor 1 =')
 disp(size(S1Ly_measured))

 count = height(S1Ly_measured);

%Pre allocate arrays to be built in loop
Time = zeros(1,count);
HHP = zeros(1,count);
Force = zeros(1,count);
Cycle = zeros(1,count);
alphadL = zeros(1,count);
DeltaxGL = zeros(1,count);
DeltayGL = zeros(1,count);
alphadR = zeros(1,count);
DeltaxGR = zeros(1,count);
DeltayGR = zeros(1,count);

%start values of indeces and other loop values
waitingFor = 10;
peakposition = Stroke;
j=1;
k=1;
n=1;
move = 1;
shortfilter = 0;
shortfilterR1 = 0;
shortfilterR2 = 0;

 disp('Loop start')

   for i = 1 :  (count)

    %Sensor Displacement data (current co-ordinate position)
    %Invert where required, tear to initial sensor position value and add
    %geometry of block to locate on global co-ordinate system
        %Left Block
        S1Ly_i = -(S1Ly_measured{i,1}-S1Ly_measured{1,1}) + 0.5*Hb;
   %Check S1 has not shorted to rail, remove data point if it has and log event
     if -100 > S1Ly_i
         S1Ly_i = NaN;
         shortfilter = shortfilter +1;
     elseif 100 < S1Ly_measured{i,1}
         S1Ly_measured{i,1}= NaN;
          shortfilter = shortfilter +1;
     end

        S2Ly_i = -(S2Ly_measured{i,1}-S2Ly_measured{1,1}) + 0.5*Hb;
        S3Lx_i = S3Lx_measured{i,1}-S3Lx_measured{1,1} - 0.5*Lb;

        %Right Block with short filters on S1R and S2R
        S1Ry_i = -(S1Ry_measured{i,1}-S1Ry_measured{1,1}) + 0.5*Hb;
        if -15 > S1Ry_i
         S1Ry_i = NaN;
         shortfilterR1 = shortfilterR1 +1;
        elseif 15 < S1Ry_measured{i,1}
         S1Ry_measured{i,1}= NaN;
          shortfilterR1 = shortfilterR1 +1;
        end

        S2Ry_i = -(S2Ry_measured{i,1}-S2Ry_measured{1,1}) + 0.5*Hb;
         if -15 > S2Ry_i
         S2Ry_i = NaN;
         shortfilterR2 = shortfilterR2 +1;
        elseif 15 < S2Ry_measured{i,1}
         S2Ry_measured{i,1}= NaN;
          shortfilterR2 = shortfilterR2 +1;
         end
```

```
        S3Rx_i = -(S3Rx_measured{i,1}-S3Rx_measured{1,1}) + 0.5*Lb;

   %Create local test time vector (tear clock values)convert ms to s
   Time(i) = (Test_Data{i,2}-Test_Data{1,2})/1000;
   %Create humeral head position vector centred on centoid of glenoid
   HHP(i) = Test_Data{i,1}-Test_Data{1,1};

   %collect other variables from initial file
    Force(i) = Test_Data{i,8};
    Cycle(i) = Test_Data{i,4};
   %Force(i) = Test_Data{i,8};

   %CALCULATE GELNOID EDGE MOTION FOR THE LEFT BLOCK
        %Gradient of top line of block
        m1 = -(S1Ly_i - S2Ly_i)/(L_S1S2L);

        %Rotation of the block
        alphaL = -atan(m1);
        alphadL(i) = alphaL * 180/pi;

        %Solve for C1, Constant of straight line equationfor top of block using
        %the co-ocdinates of Sensor S1
        C1 = (S1Ly_i) - m1*(S1Lx) ;

        %Calculate the gradient of the side of the block (inverse of the top of
        %the block)
        m2 = -(1/m1);

        %Solve for C2, the constant for the straight line equation of the side
        %of the block
        C2 = S3Ly - m2*(S3Lx_i);

        % Use the intersection of the two lines m1x1 + C1 = m1x2 + C2 to locate left
top corner
        x_corner1 = (C2-C1)/(m1-m2);
        y_corner1 = m1*x_corner1 + C1;

        %Calculate the co ordinates of the bottom right corner
        x_corner2 = x_corner1 + Lb*cos(alphaL)-Hb*sin(alphaL);
        y_corner2 = y_corner1 -Hb*cos(alphaL) -Lb*sin(alphaL);

        %Calculate the position of the centroid of the block
        CbxL = (x_corner2 + x_corner1)/2;
        CbyL = (y_corner2 + y_corner1)/2;

        %Convert block motion to glenoid edge motion
        DeltaxGL(i) = -CbxL*(LPL/(LAL-LPL));
        DeltayGL(i) = -CbyL*(LPL/(LAL-LPL));

     %CALCULATE GELNOID EDGE MOTION FOR THE RIGHT BLOCK
        %Gradient of top line of block
        m3 = -(S1Ry_i - S2Ry_i)/(L_S1S2R);

        %Rotation of the block
        alphaR = -atan(m3);
        alphadR(i) = alphaR * 180/pi;

        %Solve for C1, Constant of straight line equationfor top of block using
        %the co-ocdinates of Sensor S1
        C3 = (S1Ry_i) - m3*(S1Rx) ;

        %Calculate the gradient of the side of the block (inverse of the top of
        %the block)
        m4 = -(1/m3);

        %Solve for C2, the constant for the straight line equation of the side
        %of the block
```

```
        C4 = S3Ry - m4*(S3Rx_i);

        % Use the intersection of the two lines m1x1 + C1 = m1x2 + C2 to locate left
top corner
        x_corner3 = (C4-C3)/(m3-m4);
        y_corner3 = m3*x_corner3 + C3;

        %Calculate the co ordinates of the bottom right corner
        x_corner4 = x_corner3 - Lb*cos(alphaR)-Hb*sin(alphaR);
        y_corner4 = y_corner3 + Lb*sin(alphaR) -Hb*cos(alphaR);

        %Calculate the position of the centroid of the block
        CbxR = (x_corner3 + x_corner4)/2;
        CbyR = (y_corner3 + y_corner4)/2;

        %Convert block motion to glenoid edge motion
        DeltaxGR(i) = -CbxR*(LPR/(LAR-LPR));
        DeltayGR(i) = -CbyR*(LPR/(LAR-LPR));

%display progress
    progress = (i / count) * 100;

    if(progress > waitingFor)
        disp(waitingFor);
        waitingFor = waitingFor + 10;
    end

 %log peak and centre values as separate tables
 %move = indicates current humeral head motion section

  if HHP(i) >= peakposition
    if move == 1
        DeltayGR_PMAX(j) = DeltayGR(i);
        DeltaxGR_PMAX(j) = DeltaxGR(i);
        alphadR_PMAX(j) = alphadR(i);
        DeltayGL_PMAX(j) = DeltayGL(i);
        DeltaxGL_PMAX(j) = DeltaxGL(i);
        alphadL_PMAX(j) = alphadL(i);
        HHP_PMAX(j) = HHP(i);
        Cycle_PMAX(j) = Cycle(i);
        j = j+1;
        peakposition = HHP(1);
        move = 2;
    end
  end

  if HHP(i) <= peakposition
      if move == 2
      DeltayGR_P0(k) = DeltayGR(i);
      DeltaxGR_P0(k) = DeltaxGR(i);
      alphadR_P0(k) = alphadR(i);
      DeltayGL_P0(k) = DeltayGL(i);
      DeltaxGL_P0(k) = DeltaxGL(i);
      alphadL_P0(k) = alphadL(i);
      HHP_P0(k) = HHP(i);
      Cycle_P0(k) = Cycle(i);
      k = k+1;
      peakposition = HHP(1)-0.95*Stroke;
      move = 3;
      end
  end

  if HHP(i) <= peakposition
      if move == 3
      DeltayGR_PMIN(n) = DeltayGR(i);
      DeltaxGR_PMIN(n) = DeltaxGR(i);
      alphadR_PMIN(n) = alphadR(i);
      DeltayGL_PMIN(n) = DeltayGL(i);
```

```
        DeltaxGL_PMIN(n) = DeltaxGL(i);
        alphadL_PMIN(n) = alphadL(i);
        HHP_PMIN(n) = HHP(i);
        Cycle_PMIN(n) = Cycle(i);
        n = n+1;
        peakposition = HHP(1);
        move = 4;
        end
    end

    if HHP(i) >= peakposition
        if move == 4
        DeltayGR_P0(k) = DeltayGR(i);
        DeltaxGR_P0(k) = DeltaxGR(i);
        alphadR_P0(k) = alphadR(i);
        DeltayGL_P0(k) = DeltayGL(i);
        DeltaxGL_P0(k) = DeltaxGL(i);
        alphadL_P0(k) = alphadL(i);
        HHP_P0(k) = HHP(i);
        Cycle_P0(k) = Cycle(i);
        k = k+1;
        peakposition = HHP(1) + 0.95*Stroke;
        move = 1;
        end
    end

%
     end
     disp('Loop Finished')
     disp('short data points filtered=')
     disp(shortfilter)
     disp('short data points filtered SR1=')
     disp(shortfilterR1)
     disp('short data points filtered SR2=')
     disp(shortfilterR2)

     %Invert vector values for glenoid motion
      alphadL  = alphadL';
      DeltaxGL = DeltaxGL';
      DeltayGL = DeltayGL';

      alphadR  = alphadR';
      DeltaxGR = DeltaxGR';
      DeltayGR = DeltayGR';

      Time = Time';
      HHP = HHP';
      Force = Force';
      Cycle = Cycle';


      HHP_PMAX = HHP_PMAX';
      HHP_PMIN = HHP_PMIN';
      HHP_P0 = HHP_P0';

      DeltayGR_PMAX = DeltayGR_PMAX';
      DeltayGR_PMIN = DeltayGR_PMIN';
      DeltayGR_P0 = DeltayGR_P0';

      DeltaxGR_PMAX = DeltaxGR_PMAX';
      DeltaxGR_PMIN = DeltaxGR_PMIN';
      DeltaxGR_P0 = DeltaxGR_P0';

      alphadR_PMAX  = alphadR_PMAX';
      alphadR_PMIN  = alphadR_PMIN';
      alphadR_P0  = alphadR_P0';

      DeltayGL_PMAX = DeltayGL_PMAX';
```

```
    DeltayGL_PMIN = DeltayGL_PMIN';
    DeltayGL_P0 = DeltayGL_P0';

    DeltaxGL_PMAX = DeltaxGL_PMAX';
    DeltaxGL_PMIN = DeltaxGL_PMIN';
    DeltaxGL_P0 = DeltaxGL_P0';

    alphadL_PMAX  = alphadL_PMAX';
    alphadL_PMIN  = alphadL_PMIN';
    alphadL_P0  = alphadL_P0';

    Cycle_PMAX = Cycle_PMAX';
    Cycle_PMIN = Cycle_PMIN';
    Cycle_P0 = Cycle_P0';


figure(1);
P1 = plot(Time,DeltaxGL','LineWidth',1);
P1.Color = 'm';
%ylim([-1 1]);
title('x motion of LEFT glenoid edge');
ylabel('x (mm) ');
xlabel('Time (s)');
grid on;

figure(2);
P2 = plot(Time,DeltayGL','LineWidth',1);
P2.Color = 'r';
title('y motion of LEFT glenoid edge (mm)');
%ylim([-1 1]);
ylabel('y (mm)');
%xlim([0 200000]);
xlabel(' ');
grid on;

figure(3);
P3 = plot(Time,alphadL','LineWidth',1);
P3.Color = 'b';
title('Rotation of LEFT glenoid edge');
ylabel('rotation (degrees)');
xlabel('Time (s)');
%ylim([-5 5]);
grid on;

figure(4);
P4 = plot(Time,DeltaxGR','LineWidth',1);
P4.Color = 'c';
%ylim([-1 1]);
title('x motion of RIGHT glenoid edge');
ylabel('x (mm) ');
xlabel('Time (s)');
grid on;

figure(5);
P5 = plot(Time,DeltayGR','LineWidth',1);
P5.Color = 'g';
title('y motion of Right glenoid edge (mm)');
%ylim([-1 1]);
ylabel('y (mm)');
%xlim([0 200000]);
xlabel('Time (s)');
grid on;

figure(6);
P6 = plot(Time,alphadR','LineWidth',1);
P6.Color = 'b';
title('Rotation of RIGHT glenoid edge');
ylabel('rotation (degrees)');
```

```
xlabel('Time (s)');
%ylim([-5 5]);
grid on;

figure(7);
P7 = plot(Time,HHP,'LineWidth',1);
P7.Color = [0.13 0.47 0.17];
title('Humeral Head Position');
ylabel('Humeral head position (mm)');
xlabel('Time (s)');
grid on;

figure(8);
P8 = plot(Time,Force,'LineWidth',1);
%P8.Color = [0.13 0.47 0.17];
title('Glenoid Contact Force');
ylabel('Force (N)');
xlabel('Time (s) ');
grid on;

%OUTPUT
%write processed data to excel sheet
ProcessedData                                                                    =
table(Time,Cycle,HHP,DeltaxGL,DeltayGL,alphadL,DeltaxGR,DeltayGR,alphadR,Force);
DataOutput = 'DataOutput.xlsx';
%writetable(ProcessedData,DataOutput,'sheet',1,'Range','A1:J800001')
writetable(ProcessedData,DataOutput)


%OUTPUT 2 - Analysis
%Determine further values of interest and write to streamlined output file

%Peak values
%PeakData                                                                        =
table(HHP_peak,Cycle_peak,DeltayGR_peak,DeltaxGR_peak,alphadR_peak,DeltayGL_peak,De
ltaxGL_peak,alphadR_peak);
PeakOutputSeparate = 'PeakOutputSeparate.xlsx';
headings                                                                         =
{'HHP_MAX','Cycle_PMAX','DeltayGR_PMAX','DeltaxGR_PMAX','alphadR_PMAX','DeltayGL_PM
AX','DeltaxGL_PMAX','alphadL_PMAX','HHP_P0','Cycle_P0','DeltayGR_P0','DeltaxGR_P0',
'alphadR_P0','DeltayGL_P0','DeltaxGL_P0','alphadL_P0','HHP_MIN','Cycle_PMIN','Delta
yGR_PMIN','DeltaxGR_PMIN','alphadR_PMIN','DeltayGL_PMIN','DeltaxGL_PMIN','alphadL_P
MIN'};
writecell(headings,PeakOutputSeparate,'Range','A1')


disp('Writing Pmax values')
writematrix(HHP_PMAX,PeakOutputSeparate,'Range','A2')
writematrix(Cycle_PMAX,PeakOutputSeparate,'Range','B2')
writematrix(DeltayGR_PMAX,PeakOutputSeparate,'Range','C2')
writematrix(DeltaxGR_PMAX,PeakOutputSeparate,'Range','D2')
writematrix(alphadR_PMAX,PeakOutputSeparate,'Range','E2')
writematrix(DeltayGL_PMAX,PeakOutputSeparate,'Range','F2')
writematrix(DeltaxGL_PMAX,PeakOutputSeparate,'Range','G2')
writematrix(alphadL_PMAX,PeakOutputSeparate,'Range','H2')

disp('Writing RH P0 values')
writematrix(HHP_P0,PeakOutputSeparate,'Range','I2')
writematrix(Cycle_P0,PeakOutputSeparate,'Range','J2')
writematrix(DeltayGR_P0,PeakOutputSeparate,'Range','K2')
writematrix(DeltaxGR_P0,PeakOutputSeparate,'Range','L2')
writematrix(alphadR_P0,PeakOutputSeparate,'Range','M2')
writematrix(DeltayGL_P0,PeakOutputSeparate,'Range','N2')
writematrix(DeltaxGL_P0,PeakOutputSeparate,'Range','O2')
writematrix(alphadL_P0,PeakOutputSeparate,'Range','P2')

disp('Writing RH Pmin values')
writematrix(HHP_PMIN,PeakOutputSeparate,'Range','Q2')
```

```
writematrix(Cycle_PMIN,PeakOutputSeparate,'Range','R2')
writematrix(DeltayGR_PMIN,PeakOutputSeparate,'Range','S2')
writematrix(DeltaxGR_PMIN,PeakOutputSeparate,'Range','T2')
writematrix(alphadR_PMIN,PeakOutputSeparate,'Range','U2')
writematrix(DeltayGL_PMIN,PeakOutputSeparate,'Range','V2')
writematrix(DeltaxGL_PMIN,PeakOutputSeparate,'Range','W2')
writematrix(alphadL_PMIN,PeakOutputSeparate,'Range','X2')
```

B2.3 Basic Error Analysis

The sources of measurement errors in data can be either systematic or random. In this analysis the systematic errors considered were those resulting from by sensor calibration uncertainty, linearity errors, or drift, as well as from geometrical characteristics of the measurement system, including the effect of the sensor tip radius and the arcing motion of the lever arm on the glenoid edge motion calculation.

Random errors are usually quantified by taking repeated measurements of the same values, to determine. This was not possible with the current research due to the time dependent nature of the motions measured as the tests proceeded. The degree of random error is assessed by observing the overall variability between subsequent measurements in each vector. The data remained consistent, with no sudden variations, other than a limited amount of signal noise noted, except in one dataset (LHSyT). The effect of the signal noise was reduced by smoothing of the data as discussed in Section 4.3.3.4, and the single unusual data spike, possibly caused by sensor drift, was filtered from the data and omitted from all calculations. The data otherwise do not show evidence of any sensor drift. The sensors chosen are recommended by their manufacturer to be robust against drift, except in the case of extreme shock or temperature variations. The drift error is therefore neglected.

The remaining systematic errors are estimated at the sensors, and then the adjusted sensor readings are used to calculate the glenoid edge motion over the full applied motion of the motion simulation. This is then compared to the glenoid edge motion calculated for the same motion, but without sensor adjustments, to determine the effect of the error on the glenoid edge motions themselves.

Broadly, the systematic errors are accounted for at the sensor readings as follows:

1: Zero out the sensor starting measurement before the calculation begins. This eliminates the effect of any calibration uncertainty, as well as any offset in the starting position of the sensor.

2: Add the effect of the sensor tip radius to the measurements. This effect tends to cause the sensors to exaggerate the motion of the block, so accounting for it will reduce the absolute value of the displacement measured.

3: Further adjust the measured sensor value by including the effect of the arced motion of the lever. This motion tends to cause the sensor to underestimate the motion of the centroid, due to the angle induced on the measuring block.

4: Add the linearity error specific to each sensor by multiplying (or reducing) each sensor value in the combination that would cause the largest change to the motion of the block.

Each of these steps is described in detail below:

1 Adjustment for Calibration Uncertainty:

The zeroing of the sensor readings at the start of the motion calculation removes the contribution of any calibration uncertainty (as it is zeroed out), along with any initial offset in the sensor starting value. The sensors are set to start within 0.5mm of their zero position, to ensure each sensor operating in the linear portion of its range. No additional changes are to the sensor readings are required to accommodate the calibration uncertainty.

2 Adjustment for effect of real sensor tip radius:

The effect of the real sensor tip radius, as opposed to the infinitely small point of contact assumed by the motion calculation algorithm, is illustrated in **Figure B-3** below, where the sensor radius and surface tilt have been exaggerated for clarity. The yellow line represents an infinitely small sensor contact, while the circle represents the tip of a sensor with a real radius. When the surface on which the sensor rests is not level, the point of contact with the real sensor will move to the tangent of the circle representing the sensor tip. This has the effect that sensor with a real radius will give a reading that is higher off the surface that the infinitely smaller sensor would have.

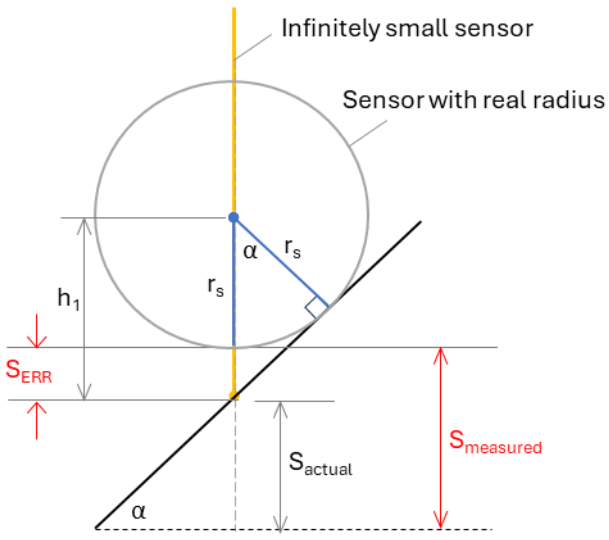

Figure B-3 *Illustration of the effect of real sensor tip radius, r_s, when the sensor rests on a surface tilted by α°, used to calculate the measurement error, S_{ERR} induced by this effect.*

The size of the error is dependent only on the radius of the sensor and the angle of the contact surface, and is given by:

$$S_{ERR} = h_1 - r_s = \frac{r_s}{\cos\propto} - r_s \qquad \text{[B16]}$$

To convert the real sensor reading $S_{measured}$, to the value that represents the surface of the block in the line of the sensor S_{actual}, the S_{ERR} should be subtracted from all vertical sensor readings in the global co-ordinate system, subtracted from the horizontal sensor at the RHS block, and added to the horizontal sensor at the LHS block (due to these acting in different directions).

3 Adjustment for Arcing Motion of the Lever:

The second error introduced by the geometry of the system is the change in the height of the block caused by the block tilting as the lever moves in an arc, rather than directly uprads or sideways as assumed by the motion calculation algorithm. This height difference is illustrated in **Figure B-4** below, which illustrates the case for the vertical direction. The figure represents a side view of the lever, as it is deflected at the glenoid edge and rotates through the pivot point. Again, the motion is exaggerated in the figure for clarity.

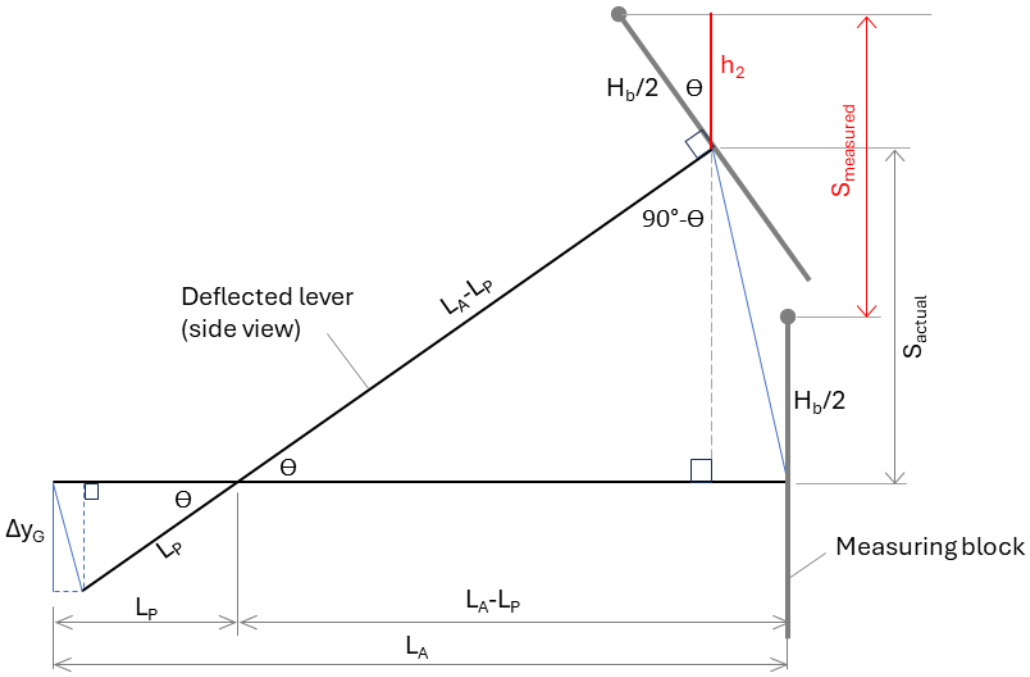

Figure B-4 *Illustration of the effect of the arcing motion of the lever on the systematic measurement error for a sensor resting on the top surface of a measuring block. The lever is illustrated in side view, for a downward (y-direction) glenoid edge motion, which induces a level angle of Θ from level.*

For a given downward motion of the lever at the glenoid end, the is a vertical motion of the centroid of the measuring block, $S_{actual.}$ However, this vertical motion is accompanied by a backward curve, which will cause the measuring block to become tilted. The height of the top

surface of the measuring block (in the vertical direction) is reduced by the backward tilt of the block. Since the sensor tips rest on the surface of the measuring block, the value measured by the sensor, $S_{measured}$ will be less than the motion of the centroid.

From the figure, we see that:

$$S_{actual} - {}^{H_b}/_2 = S_{measured} - h_2 \quad \text{[B17]}$$

Where

$$h_2 = {}^{H_b}/_2 \cos\theta \quad \text{[B18]}$$

So

$$S_{actual} = S_{measured} - {}^{H_b}/_2 \cos\theta + {}^{H_b}/_2 \quad \text{[B19]}$$

This will hold for all vertical sensors. The same phenomenon will happen in the horizontal direction, but $H_b/2$ would be replaced by $L_b/2$, or half the block length.

To apply this to the measured sensor values, it is necessary to know the angle of rotation of the lever (Θ), which can only be known when the S_{actual} is also known. To overcome this the angle was approximated in the motion calculation by using the angle in the previous motion position, calculating the new S_{actual}, and then using this to calculate Θ for the next value. As the simulated sensor measurements are continuous (smooth) functions, this is considered a reasonable approximation.

4 Adjustment for linearity uncertainty:

The final systematic error present in the measurements is the linearity error of the sensors. To determine the maximum systematic error that can be induced by the linearity error, the readings from each of the sensors is amplified or reduced in such a way as to cause the errors to induce an exaggerated motion (i.e the errors all stack instead of cancelling each other out). This combination is illustrated for the RHS block when the glenoid edge is experiencing a compression induced motion.

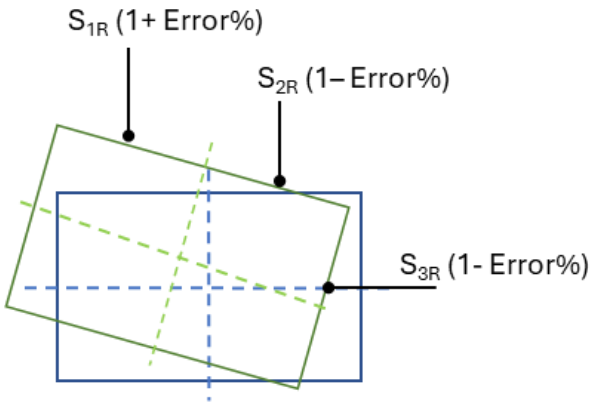

Figure B-5 *Combined sensor linearity error directionality that produces the maximum motion error, by causing the individual sensor errors to stack, for the RHS block when the RHS glenoid edge is in compression.*

For the vertical sensors the linearity error is 0.23% (as per the calibration certificates), and for the horizontal sensors it is 0.1%.

Combined Systematic Errors:

To determine the worst case combined systematic error, all three of the above error sources are used to adjust the sensor readings at the RHS block while the glenoid is under compression. For the three sensors this adjustment is:

$$S_{1R\_actual} = S_{1R\_measured}(1 + 0.0023) - {}^{H_b}/_{2}\cos\theta + {}^{H_b}/_{2} - \left(\frac{r_s}{\cos\propto} - r_s\right) \quad \text{[B20]}$$

$$S_{2R\_actual} = S_{2R\_measured}(1 - 0.0023) - {}^{H_b}/_{2}\cos\theta + {}^{H_b}/_{2} - \left(\frac{r_s}{\cos\propto} - r_s\right) \quad \text{[B21]}$$

$$S_{3R\_actual} = S_{3R\_measured}(1 - 0.0023) - {}^{L_b}/_{2}\cos\theta + {}^{L_b}/_{2} - \left(\frac{r_s}{\cos\propto} - r_s\right) \quad \text{[B22]}$$

These sensor value adjustments are now applied to the simulated sensor readings for the compressive motion of the SolidWorks Motion simulation, to determine the effect these errors have on the glenoid edge motions. **Figure B-6** shows the three glenoid edge motions calculated before and after the sensor errors were applied to simulated sensor readings. **Figure B-7** shows the value of the error in each motion for the duration of the simulation.

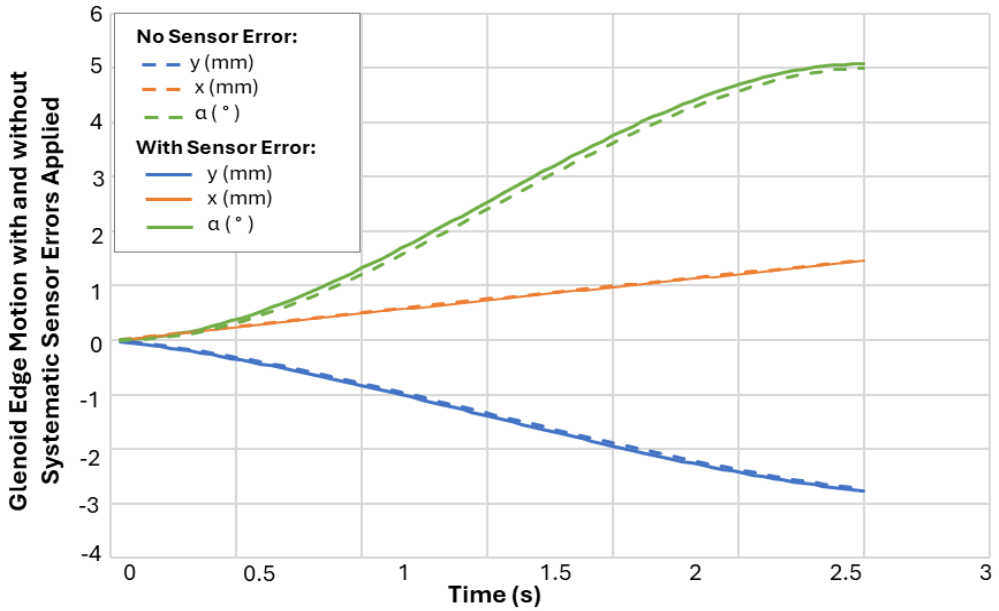

Figure B-6 *Glenoid edge motions calculated using the edge motion calculation algorithm with the sensor motions tracked during the SolidWorks motion simulation as the input. The combined maximum possible systematic errors are then applied to the input sensor motions and the glenoid edge motions calculated again, to quantify the effect of the possible sensor errors on the glenoid edge motion.*

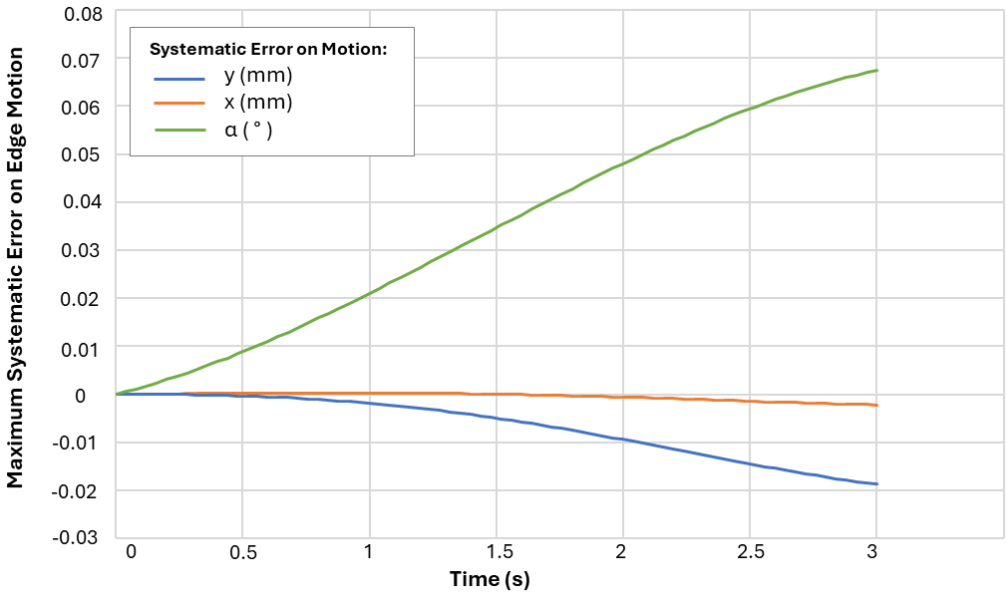

Figure B-7 *The difference between the glenoid edge motions calculated with and without the systematic sensor errors applied to the simulated sensor inputs for the duration of the motion simulation. (i.e the errors induced at the glenoid edge motions by the possible systematic measurement errors).*

Based on these results, the maximum systematic error that could be induced at the glenoid edge by the errors on the measurement for the expected range of data is 0.03μm in the x-direction, -20μm in the y-direction and 0.07° of rotation, at a glenoid motion of 1.5mm horizontal, -2.8mm vertical and 6.5° of rotation.

C. APPENDIX C: NOVEL GLENOID EVALUATION TEST DATA

C1 Test Materials

Table C- 1 *Summary of materials used for glenoid samples and sample preparation in the glenoid edge motion testing.*

Item	Material	Product code
Control and Novel Glenoid Test Samples	UHMWPE GUR1050	NA
Bone Substitute	Solid Polyurethane Foam	Sawbones 20PCF
Bone Cement	Polymethylmethacrylate Bone cement	MectaCem II HV

UHMWPE GUR1050 Specification and Certificate of Conformance

RMP Restoration Medical Polymers	Restoration Medical Polymers; LLC				An ISO 13485 Registered Company
	Certificate of Processing and Compliance				4474 E Park 30 Drive, Columbia City IN 46725
	Consolidation Process		Compression Molded Sheet		
Customer Name	NA	Account #	NA	PO #	NA
RMP Part Number	CMS-500-3210-021	PO Line #	NA	RMP Sales Order #	NA
RMP Lot Number	10487	Customer PN	NA	Part Quantity	1 Sheet

Raw Material Information

Manufacturer:	Celenese	Property	Units	Requirement	Actual
Powder Description	GUR1050	Aluminum	mg/kg	≤ 20	3
RMP Powder Part Number	RES-500-021	Titanium	mg/kg	≤ 40	9
Powder Lot Number	974957	Calcium	mg/kg	≤ 5	0
Customer Specification	NA	Chlorine	mg/kg	≤ 30	10
Standard Reference (ASTM)	ASTM F648	Ash wt	mg/kg	≤ 125	30
Standard Reference (ISO)	NA	Viscosity Number	mL/g	>3200	3660
		Elongation Stress	N/mm^2	≥ .42	0.53
		Extraneous Matter per 300 g	No.	≤ 3	2

Fabricated Form

No stabilizers or processing aids added to virgin powder during manufacture of fabricated form

Material was annealed to RMP's internal specification

F) Date of Manufacture: 31-Jul-18

Physical Property	Unit	Requirement	Actual
Extraneous Matter per 5,000cm^2	particle count	≤ 10	0
Morphology Index	count	≤ 10	0

Mechanical Properties

Property	Test Method	Units	Requirement	Actual
Yield Strength	F648	MPa	≥ 19	20.82
Ultimate Strength	F648	MPa	≥ 40	62.36
Elongation at Break	F648	%	≥ 340	405
Izod Impact Strength	F648 Annex 1	kJ/m^2	≥ 73	106.97
Density	D792	g/cm^2	0.927-0.944	933
Certification Prepared By:	Tim Tilbury		Date:	17-Dec-18

Dia 38 – PE-08

RMP Restoration Medical Polymers	Restoration Medical Polymers; LLC				An ISO 13485 Registered Company
	Certificate of Processing and Compliance				4474 E Park 30 Drive, Columbia City IN 46725
	Consolidation Process		Compression Molded Sheet		
Customer Name	TPI	Account #	47	PO #	26247623
RMP Part Number	0047-C1050-1500-1M	PO Line #	3	RMP Sales Order #	92
RMP Lot Number	10635	Customer PN	UHR01500NAT000015	Part Quantity	~~196~~ 1 meter

1 meter TMP 1/13/2021

Certification Statement:

Material meets the following mechanical property requirements of ASTM F648 GUR 1050 Type II:

Property	Units	Requirement	Pass/Fail
Yield Strength	MPa	≥ 19	Pass
Ultimate Strength	MPa	≥ 40	Pass
Elongation at Break	%	≥ 340	Pass
Izod Impact Strength	kJ/m^2	≥ 73	Pass
Density	g/cm^2	0.927-0.944	Pass

Material meets the following physical property requirements of ASTM F648 GUR 1050 Type II:

Property	Units	Requirement	Pass/Fail
Extraneous Matter per 5,000cm^2	particle count	≤ 10	Pass
Morphology Index	count	≤ 10	Pass

Material meets the following dimensional requirements:

Dimension	Requirement	Pass/Fail
Diameter	1.50 +0.040-0.000" (38.1+1.016-0mm)	Pass
Length	39.370+0.250-0.000" (1000+6.35-0.00mm)	Pass
Bar Bow	0.328" max (8.33mm max)	Pass

This finished goods lot consists of the following consolidation lots:

Lot #	Resin Lot #
10487	974957
10492	974957
10512	925261
10557	974957
10559	974957
10561	974957
10563	974957
10565	974957
10587	974957
10603	974957
10605	974957
10604	974957

Certification Prepared By:	Tim Tilbury		Date:	21 Dec 2018

Westlake plastics
LIFE IN POLYMERS

PE - 10
Dia 63.5

Certificate Of Manufacturing Conformance
Doc.ID: 2103121056160

Customer Order Information

Bill to: TOTAL PLASTICS - LIFE SCIENCE 7508 HONEYWELL DR FORT WAYNE, IN 46825 USA	**Ship to:** TOTAL PLASTICS - LIFE SCIENCE 7508 HONEYWELL DR FORT WAYNE, IN 46825 USA
Customer P.O. # 26289265	**WPC Order #** 274982

Product Information

Product Name	Lennite GUR 1050 Natural RE WM	**Product Dimensions**	ROD 2.5"D x 60"L
Polymer	UHMW Polyethylene	**Manufacture Date**	02/09/2021
Resin Lot #	0001201429	**Shop Order #**	00180954
Qty:30 Serial #s	WA308, WA310, WA311, WA313, WA314, WA315, WA316, WA317, WA318, WA319, WA320, WA321, WA322, WA323, WB308, WB309, WB310, WB311, WB312, WB313, WB314, WB315, WB316, WB317, WB318, WB319, WB320, WB321, WB322, WB323		

1 PC TMP 1-13-22

Compliance Information

FDA	ASTM	USP Class VI	ISO 10993
21 CFR 177.1520 Resin	ASTM F648 Resin & Stock Shape ISO 5834 Resin & Stock Shape	Compliant Resin	Chapters 3, 4, 5, 6, 10, 11 Resin

End user is responsible for biocompatibility evaluations appropriate for the intended applications.

Products were manufactured under processes that were tested and verified to yield products that meet the compliance masterbatch referenced above.

No stabilizers, antioxidants, or processing aids were added to the polymer during manufacture.

Westlake Plastics Company certifies that Lennite products are annealed and free of annealing agents and additional additives. Lennite products are uniform in color and free of voids. Westlake Plastics Company ensures the product consistency of Lennite through change notification agreements with our suppliers, internal process control procedures and stringent quality control.

Thank you.

Yared Mengistu, Director of Quality

TOTAL PLASTICS INT'L
Company: Ti-tamed Pty
PO# : 9112
S/O# : 1065604
Approved by : TMP 1-13-2022
Cut in half
CP 1-13-22

Westlake plastics
LIFE IN POLYMERS

Lennite UHMW-PE Certificate of Analysis Doc.ID: 0001201429 176614

Westlake Plastics Company produces Lennite Ultra-High Molecular Weight Polyethylene (UHMW-PE) product in compliance to ASTM F648-14 and ISO 5834-1/2.

Celanese Product Information		Lennite Product Information	
Product Name	GUR 1050 Type 2	**Product Name**	Lennite UHMW-PE
Resin Lot #	0001201429	**Test Reference #**	176614

Properties of GUR 1050 Tested by Celanese, LTD.

Property	Unit	Test Method		Requirement	Result
		ASTM F648-14	ISO 5834 (2019)		
Viscosity Number	mL/g	ASTM D4020	ISO 1628-3	≥3200	3550
Elongational Stress	MPa	ASTM D4020	ISO 11542-2	≥0.42	0.52
Ash	ppm		ISO 3451-1	≤125	39
Extraneous Matter	count	ASTM F648-14	ISO 5834-1 (2019)	≤3	.3
Trace Element: Titanium	ppm			≤40	4
Trace Element: Aluminum	ppm			≤20	1
Trace Element: Calcium	ppm			≤5	1
Trace Element: Chlorine	ppm			≤30	10

Properties of Lennite UHMW-PE RAM Extruded Rod Produced From GUR 1050 Tested by Westlake Plastics

Property	Unit	Test Method		Requirement	Result
		ASTM F648-14	ISO 5834 (2019)		
Density	kg/m³	ASTM D792-13	ISO 1183 (2012)	927-944	929
Tensile Strength, Yield	MPa	ASTM D638-14	ISO 5834-2 (2019)	≥19	23
Elongation at Break	%	ASTM D638-14	ISO 5834-2 (2019)	≥340	345
Tensile Strength, Ultimate	MPa	ASTM D638-14	ISO 5834-2 (2019)	≥40	48
Izod Double-Notched Impact Strength	kJ/m²	ASTM F648-14	ISO 5834-2 (2019)	≥73	104
Morphology Index		ASTM F648-14	ISO 5834-5 (2011)	report	
Total Type A	count	ASTM F648-14		report	0
Total Type B	count	ASTM F648-14		report	0
Total Surface Area Examined	cm²	ASTM F648-14		report	5000

Test date: 12/20/19

Greg Lambert Sr. Quality Engineer

Westlake Plastics Company is ISO 13485: 2016 and ISO 9001: 2015 certified.

490 Lenni Road | Lenni, PA 19052-0127 | USA www.westlakeplastics.com

Solid Rigid Polyurethane Foam

Solid rigid polyurethane foam provides a uniform structure with only +/-10% variation in density. Material properties cover a broad range of human bone qualities allowing you to select an appropriate density for your study. This closed cell foam
conforms to ASTM F-1839-08 "Standard Specification for Rigid Polyurethane Foam for Use as a Standard Material for Testing Orthopaedic Devices and Instruments" and has the largest density range available from 0.08g/cc up to 0.80g/cc (5pcf to 50pcf).

For more information see our Biomechanical Validation Studies page.

DENSITY			COMPRESSION		TENSION		SHEAR		Shore D Hardness
ASTM D1622		Volume Fraction	ASTM D1621		ASTM D1623		ASTM C273		
(pcf)	(g/cc)		Strength (MPa)	Modulus (MPa)	Strength (MPa)	Modulus (MPa)	Strength (MPa)	Modulus (MPa)	
5*	0.08	0.07	0.6	16	1.0	32	.59	7.1	10
8	0.13	0.11	1.5	38	1.3	56	1.2	14	14
10*	0.16	0.14	2.2	58	2.1	86	1.6	19	15
12*	0.19	0.16	3.2	81	2.5	112	2.1	24	21
15*	0.24	0.20	4.9	123	3.7	173	2.8	33	25
17**	0.27	0.23	6.2	155	4.6	205	3.4	39	29
20*	0.32	0.27	8.4	210	5.6	284	4.3	49	35
25*	0.40	0.34	13	317	8.8	399	5.9	68	43
30*	0.48	0.41	18	445	12	592	7.6	87	55
35*	0.56	0.47	24	592	16	713	9.4	108	59
40*	0.64	0.54	31	759	19	1000	11	130	65
50*	0.80	0.68	48	1148	27	1469	16	178	85

*Solid rigid polyurethane foam meets ASTM F1839-08 material specification
**standard cancellous foam used in absolute™ bones

Our foam is available in sizes up to 24" x 24" x 4" thick.

SOLID FOAM BLOCK TOLERANCES:	
Foam density	± 10%
Block dimensions	± 2mm
Sheet thickness	± 0.3mm

SAWBONES®

MectaCem II HV Specification

english

MectaCem II LV/HV with Gentamicin

TO THE MEDICAL STAFF'S ATTENTION

DESCRIPTION

MectaCem II LV/HV with Gentamicin are disposable and sterile medical devices consisting of one 16g sterile liquid ampoule and one 40g sterile powder with Gentamicin bag. The package consists of an aluminium wrapping containing a hermetically sealed blister pack whose contents (40 g sachet of powder and 16 g vial of liquid) are sterilized by ethylene oxide. The liquid is sterilized by filtration and the powder by ethylene oxide.

MectaCem II LV/HV with Gentamicin is radiopaque and is supplied in two versions: MectaCem II HV with Gentamicin is a high viscosity bone cement, it can be prepared and handled rapidly and is ideal for manual application, MectaCem II LV with Gentamicin is a low viscosity bone cement and is ideal for syringe application.

COMPOSITION OF MECTACEM II LV/HV WITH GENTAMICIN:

Liquid Component

Bone cement liquid is a colourless, flammable liquid with a distinctive odour.

Its major component is methyl methacrylate. Hydroquinone is added as a stabilizer to prevent premature polymerization, which may occur under conditions such as heat or direct light.

N,N-Dimethyl-p-toluidine is added to promote polymerization following the mixing of the liquid and the powder components.

Powder Component

Bone cement powder is a white, finely divided powder. Its major component is the polymethylmethacrylate. The polymer contains benzoyl peroxide which initiates polymerization when the powder and liquid components are mixed. The barium sulphate is present as a radiopaque agent.

The Gentamicin Sulphate is present as antibiotic agent.

Composition

Liquid components	
Methyl Methacrylate	99,10% w/w
N,N-Dimethyl-p-toluidine	0,90% w/w
Hydroquinone	75 ppm
Powder components	
Polymethylmethacrylate	82,78% w/w
Barium Sulphate	10% w/w
Gentamicin Sulphate	4,22% w/w*
Benzoyl Peroxide	3% w/w

*Equivalent to 1,0g (1,0 M.I.U.), 2,5% Gentamicin base in 40g unit.

C2 Data Processing Script

Data Processing All RLoess1% Matlab script

```
clear all
close all
clc
format long;
digits(20);

%%%%%%%%%%%%%%%%%%%%%%%%%%%%%%%%%%
%STEP 1 IMPORT DATA AND SET UP VARIABLE VECTORS
%Import data files for peak data output
C1_Data = readtable('PeakOutputSeparateC1A.xlsx','Range', 'A1:X200000');
C2_Data = readtable('PeakOutputSeparateC2A.xlsx','Range', 'A1:X200000');
C3_Data = readtable('PeakOutputSeparateC3A.xlsx','Range', 'A1:X200000');
C6_Data = readtable('PeakOutputSeparateC6A.xlsx','Range', 'A1:X200000');
C7_Data = readtable('PeakOutputSeparateC7.xlsx','Range', 'A1:X200000');
C8_Data = readtable('PeakOutputSeparateC8.xlsx','Range', 'A1:X200000');

N1_Data = readtable('PeakOutputSeparateN1.xlsx','Range', 'A1:X200000');
N2_Data = readtable('PeakOutputSeparateN2.xlsx','Range', 'A1:X200000');
N3_Data = readtable('PeakOutputSeparateN3.xlsx','Range', 'A1:X200000');
N4_Data = readtable('PeakOutputSeparateN4.xlsx','Range', 'A1:X200000');
N5_Data = readtable('PeakOutputSeparateN5.xlsx','Range', 'A1:X200000');
N6_Data = readtable('PeakOutputSeparateN6.xlsx','Range', 'A1:X200000');

vector_length = 200000/100;

%Check vector size
 disp('All Data tables imported')
 disp('C6 Table Size =')
 disp(size(C6_Data))
 disp('N1 Table Size =')
 disp(size(N1_Data))

% %Create emtpy vectors for all data to be generated
 C1_HHP_Max= NaN(1, vector_length);  C1_Cycle_MaxMin= NaN(1,vector_length);
 C1_RHSy_Max= NaN(1, vector_length); C1_RHSx_Max= NaN(1, vector_length);
 C1_RHSa_Max= NaN(1, vector_length); C1_LHSy_Max= NaN(1, vector_length);
 C1_LHSx_Max= NaN(1, vector_length); C1_LHSa_Max= NaN(1, vector_length);

 C1_HHP_0 = NaN(1, vector_length);  C1_Cycle_0 = NaN(1, vector_length);
 C1_RHSy_0 = NaN(1, vector_length); C1_RHSx_0= NaN(1, vector_length);
 C1_RHSa_0= NaN(1, vector_length);  C1_LHSy_0= NaN(1, vector_length);
 C1_LHSx_0 = NaN(1, vector_length); C1_LHSa_0= NaN(1, vector_length);

 C1_HHP_Min = NaN(1, vector_length);  C1_RHSy_Min = NaN(1, vector_length);
 C1_RHSx_Min = NaN(1, vector_length); C1_RHSa_Min = NaN(1, vector_length);
 C1_LHSy_Min = NaN(1, vector_length); C1_LHSx_Min = NaN(1, vector_length);
 C1_LHSa_Min = NaN(1, vector_length);

 C2_HHP_Max= NaN(1, vector_length);  C2_Cycle_MaxMin= NaN(1, vector_length);
 C2_RHSy_Max= NaN(1, vector_length); C2_RHSx_Max= NaN(1, vector_length);
 C2_RHSa_Max= NaN(1, vector_length); C2_LHSy_Max= NaN(1, vector_length);
 C2_LHSx_Max= NaN(1, vector_length); C2_LHSa_Max= NaN(1, vector_length);

 C2_HHP_0 = NaN(1, vector_length);  C2_Cycle_0 = NaN(1, vector_length);
 C2_RHSy_0 = NaN(1, vector_length); C2_RHSx_0= NaN(1, vector_length);
 C2_RHSa_0= NaN(1, vector_length);  C2_LHSy_0= NaN(1, vector_length);
 C2_LHSx_0 = NaN(1, vector_length); C2_LHSa_0 = NaN(1, vector_length);

 C2_HHP_Min = NaN(1, vector_length);  C2_RHSy_Min = NaN(1, vector_length);
 C2_RHSx_Min = NaN(1, vector_length); C2_RHSa_Min = NaN(1, vector_length);
 C2_LHSy_Min = NaN(1, vector_length); C2_LHSx_Min = NaN(1, vector_length);
 C2_LHSa_Min = NaN(1, vector_length);

 C3_HHP_Max= NaN(1, vector_length);  C3_Cycle_MaxMin= NaN(1, vector_length);
 C3_RHSy_Max= NaN(1, vector_length); C3_RHSx_Max= NaN(1, vector_length);
 C3_RHSa_Max= NaN(1, vector_length); C3_LHSy_Max= NaN(1, vector_length);
 C3_LHSx_Max= NaN(1, vector_length); C3_LHSa_Max= NaN(1, vector_length);

 C3_HHP_0 = NaN(1, vector_length);  C3_Cycle_0 = NaN(1, vector_length);
 C3_RHSy_0 = NaN(1, vector_length); C3_RHSx_0= NaN(1, vector_length);
 C3_RHSa_0= NaN(1, vector_length);  C3_LHSy_0= NaN(1, vector_length);
```

```
C3_LHSx_0 = NaN(1, vector_length); C3_LHSa_0 = NaN(1, vector_length);

C3_HHP_Min = NaN(1, vector_length);  C3_RHSy_Min = NaN(1, vector_length);
C3_RHSx_Min = NaN(1, vector_length); C3_RHSa_Min = NaN(1, vector_length);
C3_LHSy_Min = NaN(1, vector_length); C3_LHSx_Min = NaN(1, vector_length);
C3_LHSa_Min = NaN(1, vector_length);

C6_HHP_Max= NaN(1, vector_length);  C6_Cycle_MaxMin= NaN(1, vector_length);
C6_RHSy_Max= NaN(1, vector_length); C6_RHSx_Max= NaN(1, vector_length);
C6_RHSa_Max= NaN(1, vector_length); C6_LHSy_Max= NaN(1, vector_length);
C6_LHSx_Max= NaN(1, vector_length); C6_LHSa_Max= NaN(1, vector_length);

C6_HHP_0 = NaN(1, vector_length);  C6_Cycle_0 = NaN(1, vector_length);
C6_RHSy_0 = NaN(1, vector_length); C6_RHSx_0= NaN(1, vector_length);
C6_RHSa_0= NaN(1, vector_length);  C6_LHSy_0= NaN(1, vector_length);
C6_LHSx_0 = NaN(1, vector_length); C6_LHSa_0 = NaN(1, vector_length);

C6_HHP_Min = NaN(1, vector_length);  C6_RHSy_Min = NaN(1, vector_length);
C6_RHSx_Min = NaN(1, vector_length); C6_RHSa_Min = NaN(1, vector_length);
C6_LHSy_Min = NaN(1, vector_length); C6_LHSx_Min = NaN(1, vector_length);
C6_LHSa_Min = NaN(1, vector_length);

C7_HHP_Max= NaN(1, vector_length);  C7_Cycle_MaxMin= NaN(1, vector_length);
C7_RHSy_Max= NaN(1, vector_length); C7_RHSx_Max= NaN(1, vector_length);
C7_RHSa_Max= NaN(1, vector_length); C7_LHSy_Max= NaN(1, vector_length);
C7_LHSx_Max= NaN(1, vector_length); C7_LHSa_Max= NaN(1, vector_length);

C7_HHP_0 = NaN(1, vector_length);  C7_Cycle_0 = NaN(1, vector_length);
C7_RHSy_0 = NaN(1, vector_length); C7_RHSx_0= NaN(1, vector_length);
C7_RHSa_0= NaN(1, vector_length);  C7_LHSy_0= NaN(1, vector_length);
C7_LHSx_0 = NaN(1, vector_length); C7_LHSa_0 = NaN(1, vector_length);

C7_HHP_Min = NaN(1, vector_length);  C7_RHSy_Min = NaN(1, vector_length);
C7_RHSx_Min = NaN(1, vector_length); C7_RHSa_Min = NaN(1, vector_length);
C7_LHSy_Min = NaN(1, vector_length); C7_LHSx_Min = NaN(1, vector_length);
C7_LHSa_Min = NaN(1, vector_length);

C8_HHP_Max= NaN(1, vector_length);  C8_Cycle_MaxMin= NaN(1, vector_length);
C8_RHSy_Max= NaN(1, vector_length); C8_RHSx_Max= NaN(1, vector_length);
C8_RHSa_Max= NaN(1, vector_length); C8_LHSy_Max= NaN(1, vector_length);
C8_LHSx_Max= NaN(1, vector_length); C8_LHSa_Max= NaN(1, vector_length);

C8_HHP_0 = NaN(1, vector_length);  C8_Cycle_0 = NaN(1, vector_length);
C8_RHSy_0 = NaN(1, vector_length); C8_RHSx_0= NaN(1, vector_length);
C8_RHSa_0= NaN(1, vector_length);  C8_LHSy_0= NaN(1, vector_length);
C8_LHSx_0 = NaN(1, vector_length); C8_LHSa_0 = NaN(1, vector_length);

C8_HHP_Min = NaN(1, vector_length);  C8_RHSy_Min = NaN(1, vector_length);
C8_RHSx_Min = NaN(1, vector_length); C8_RHSa_Min = NaN(1, vector_length);
C8_LHSy_Min = NaN(1, vector_length); C8_LHSx_Min = NaN(1, vector_length);
C8_LHSa_Min = NaN(1, vector_length);

N1_HHP_Max= NaN(1, vector_length);  N1_Cycle_MaxMin= NaN(1, vector_length);
N1_RHSy_Max= NaN(1, vector_length); N1_RHSx_Max= NaN(1, vector_length);
N1_RHSa_Max= NaN(1, vector_length); N1_LHSy_Max= NaN(1, vector_length);
N1_LHSx_Max= NaN(1, vector_length); N1_LHSa_Max= NaN(1, vector_length);

N1_HHP_0 = NaN(1, vector_length);  N1_Cycle_0 = NaN(1, vector_length);
N1_RHSy_0 = NaN(1, vector_length); N1_RHSx_0= NaN(1, vector_length);
N1_RHSa_0= NaN(1, vector_length);  N1_LHSy_0= NaN(1, vector_length);
N1_LHSx_0 = NaN(1, vector_length); N1_LHSa_0= NaN(1, vector_length);

N1_HHP_Min = NaN(1, vector_length);  N1_RHSy_Min = NaN(1, vector_length);
N1_RHSx_Min = NaN(1, vector_length); N1_RHSa_Min = NaN(1, vector_length);
N1_LHSy_Min = NaN(1, vector_length); N1_LHSx_Min = NaN(1, vector_length);
N1_LHSa_Min = NaN(1, vector_length);

N2_HHP_Max= NaN(1, vector_length);  N2_Cycle_MaxMin= NaN(1, vector_length);
N2_RHSy_Max= NaN(1, vector_length); N2_RHSx_Max= NaN(1, vector_length);
N2_RHSa_Max= NaN(1, vector_length); N2_LHSy_Max= NaN(1, vector_length);
N2_LHSx_Max= NaN(1, vector_length); N2_LHSa_Max= NaN(1, vector_length);

N2_HHP_0 = NaN(1, vector_length);  N2_Cycle_0 = NaN(1, vector_length);
N2_RHSy_0 = NaN(1, vector_length); N2_RHSx_0= NaN(1, vector_length);
N2_RHSa_0= NaN(1, vector_length);  N2_LHSy_0= NaN(1, vector_length);
N2_LHSx_0 = NaN(1, vector_length); N2_LHSa_0 = NaN(1, vector_length);
```

```
 N2_HHP_Min = NaN(1, vector_length);  N2_RHSy_Min = NaN(1, vector_length);
 N2_RHSx_Min = NaN(1, vector_length); N2_RHSa_Min = NaN(1, vector_length);
 N2_LHSy_Min = NaN(1, vector_length); N2_LHSx_Min = NaN(1, vector_length);
 N2_LHSa_Min = NaN(1, vector_length);

 N3_HHP_Max= NaN(1, vector_length);  N3_Cycle_MaxMin= NaN(1, vector_length);
 N3_RHSy_Max= NaN(1, vector_length); N3_RHSx_Max= NaN(1, vector_length);
 N3_RHSa_Max= NaN(1, vector_length); N3_LHSy_Max= NaN(1, vector_length);
 N3_LHSx_Max= NaN(1, vector_length); N3_LHSa_Max= NaN(1, vector_length);

 N3_HHP_0 = NaN(1, vector_length);  N3_Cycle_0 = NaN(1, vector_length);
 N3_RHSy_0 = NaN(1, vector_length); N3_RHSx_0= NaN(1, vector_length);
 N3_RHSa_0= NaN(1, vector_length);  N3_LHSy_0= NaN(1, vector_length);
 N3_LHSx_0 = NaN(1, vector_length); N3_LHSa_0 = NaN(1, vector_length);

 N3_HHP_Min = NaN(1, vector_length);  N3_RHSy_Min = NaN(1, vector_length);
 N3_RHSx_Min = NaN(1, vector_length); N3_RHSa_Min = NaN(1, vector_length);
 N3_LHSy_Min = NaN(1, vector_length); N3_LHSx_Min = NaN(1, vector_length);
 N3_LHSa_Min = NaN(1, vector_length);

 N4_HHP_Max= NaN(1, vector_length);  N4_Cycle_MaxMin= NaN(1, vector_length);
 N4_RHSy_Max= NaN(1, vector_length); N4_RHSx_Max= NaN(1, vector_length);
 N4_RHSa_Max= NaN(1, vector_length); N4_LHSy_Max= NaN(1, vector_length);
 N4_LHSx_Max= NaN(1, vector_length); N4_LHSa_Max= NaN(1, vector_length);

 N4_HHP_0 = NaN(1, vector_length);  N4_Cycle_0 = NaN(1, vector_length);
 N4_RHSy_0 = NaN(1, vector_length); N4_RHSx_0= NaN(1, vector_length);
 N4_RHSa_0= NaN(1, vector_length);  N4_LHSy_0= NaN(1, vector_length);
 N4_LHSx_0 = NaN(1, vector_length); N4_LHSa_0 = NaN(1, vector_length);

 N4_HHP_Min = NaN(1, vector_length);  N4_RHSy_Min = NaN(1, vector_length);
 N4_RHSx_Min = NaN(1, vector_length); N4_RHSa_Min = NaN(1, vector_length);
 N4_LHSy_Min = NaN(1, vector_length); N4_LHSx_Min = NaN(1, vector_length);
 N4_LHSa_Min = NaN(1, vector_length);

 N5_HHP_Max= NaN(1, vector_length);  N5_Cycle_MaxMin= NaN(1, vector_length);
 N5_RHSy_Max= NaN(1, vector_length); N5_RHSx_Max= NaN(1, vector_length);
 N5_RHSa_Max= NaN(1, vector_length); N5_LHSy_Max= NaN(1, vector_length);
 N5_LHSx_Max= NaN(1, vector_length); N5_LHSa_Max= NaN(1, vector_length);

 N5_HHP_0 = NaN(1, vector_length);  N5_Cycle_0 = NaN(1, vector_length);
 N5_RHSy_0 = NaN(1, vector_length); N5_RHSx_0= NaN(1, vector_length);
 N5_RHSa_0= NaN(1, vector_length);  N5_LHSy_0= NaN(1, vector_length);
 N5_LHSx_0 = NaN(1, vector_length); N5_LHSa_0 = NaN(1, vector_length);

 N5_HHP_Min = NaN(1, vector_length);  N5_RHSy_Min = NaN(1, vector_length);
 N5_RHSx_Min = NaN(1, vector_length); N5_RHSa_Min = NaN(1, vector_length);
 N5_LHSy_Min = NaN(1, vector_length); N5_LHSx_Min = NaN(1, vector_length);
 N5_LHSa_Min = NaN(1, vector_length);

 N6_HHP_Max= NaN(1, vector_length);  N6_Cycle_MaxMin= NaN(1, vector_length);
 N6_RHSy_Max= NaN(1, vector_length); N6_RHSx_Max= NaN(1, vector_length);
 N6_RHSa_Max= NaN(1, vector_length); N6_LHSy_Max= NaN(1, vector_length);
 N6_LHSx_Max= NaN(1, vector_length); N6_LHSa_Max= NaN(1, vector_length);

 N6_HHP_0 = NaN(1, vector_length);  N6_Cycle_0 = NaN(1, vector_length);
 N6_RHSy_0 = NaN(1, vector_length); N6_RHSx_0= NaN(1, vector_length);
 N6_RHSa_0= NaN(1, vector_length);  N6_LHSy_0= NaN(1, vector_length);
 N6_LHSx_0 = NaN(1, vector_length); N6_LHSa_0 = NaN(1, vector_length);

 N6_HHP_Min = NaN(1, vector_length);  N6_RHSy_Min = NaN(1, vector_length);
 N6_RHSx_Min = NaN(1, vector_length); N6_RHSa_Min = NaN(1, vector_length);
 N6_LHSy_Min = NaN(1, vector_length); N6_LHSx_Min = NaN(1, vector_length);
 N6_LHSa_Min = NaN(1, vector_length);

%%%%%%%%%%%%%%%%%%%%%%%%%%%%%%%%%%
 %STEP 2
 %CONVERT TABLES INTO INDIVIDUAL ARRAYS AND CALCULATE Robust Loess Smoothed
 %DEFLECTIONS

%Set Robust Loess filter span (percentage of total data points)
FP = 0.01;

 %For Control Glenoid C1
 %Reduce data set size
 C1_HHP_0FULL =  C1_Data{:,9}';
 sampleC1 = 1;
```

```
j =1;
 for i = 1:length(C1_HHP_0FULL)
    if i == sampleC1
        sampleC1 = sampleC1 +100;
C1_HHP_Max(j) =  C1_Data{i,1};
C1_Cycle_MaxMin(j) = C1_Data{i,2};
C1_RHSy_Max(j)= C1_Data{i,3};
C1_RHSx_Max(j) = C1_Data{i,4};
C1_RHSa_Max(j) = C1_Data{i,5};
C1_LHSy_Max(j) = C1_Data{i,6};
C1_LHSx_Max(j) = C1_Data{i,7};
C1_LHSa_Max(j) = C1_Data{i,8};

C1_HHP_0(j) =  C1_Data{i,9};
C1_Cycle_0(j) = C1_Data{i,10};
C1_RHSy_0(j) = C1_Data{i,11};
C1_RHSx_0(j) = C1_Data{i,12};
C1_RHSa_0(j) = C1_Data{i,13};
C1_LHSy_0(j) = C1_Data{i,14};
C1_LHSx_0(j) = C1_Data{i,15};
C1_LHSa_0(j) = C1_Data{i,16};

C1_HHP_Min(j) =  C1_Data{i,17};
C1_RHSy_Min(j) = C1_Data{i,19};
C1_RHSx_Min(j) = C1_Data{i,20};
C1_RHSa_Min(j) = C1_Data{i,21};
C1_LHSy_Min(j) = C1_Data{i,22};
C1_LHSx_Min(j) = C1_Data{i,23};
C1_LHSa_Min(j) = C1_Data{i,24};
j=j+1;
    end
end

%Calculate Robust Loess smoothed vectors of C1 motions
%RHS
C1_RHSy_Max_MA = smooth(C1_Cycle_MaxMin,C1_RHSy_Max,  FP, 'rloess' );
C1_RHSx_Max_MA = smooth(C1_Cycle_MaxMin,C1_RHSx_Max,  FP, 'rloess' );
C1_RHSa_Max_MA = smooth(C1_Cycle_MaxMin,C1_RHSa_Max,  FP, 'rloess' );
C1_RHSy_0_MA = smooth(C1_Cycle_0,C1_RHSy_0,  FP, 'rloess' );
C1_RHSx_0_MA = smooth(C1_Cycle_0,C1_RHSx_0,  FP, 'rloess' );
C1_RHSa_0_MA = smooth(C1_Cycle_0,C1_RHSa_0,  FP, 'rloess' );
C1_RHSy_Min_MA = smooth(C1_Cycle_MaxMin,C1_RHSy_Min,  FP, 'rloess' );
C1_RHSx_Min_MA = smooth(C1_Cycle_MaxMin,C1_RHSx_Min,  FP, 'rloess' );
C1_RHSa_Min_MA = smooth(C1_Cycle_MaxMin,C1_RHSa_Min,  FP, 'rloess' );
%LHS
C1_LHSy_Max_MA = smooth(C1_Cycle_MaxMin,C1_LHSy_Max,  FP, 'rloess' );
C1_LHSx_Max_MA = smooth( C1_Cycle_MaxMin,C1_LHSx_Max, FP, 'rloess' );
C1_LHSa_Max_MA = smooth(C1_Cycle_MaxMin,C1_LHSa_Max,  FP, 'rloess' );
C1_LHSy_0_MA = smooth(C1_Cycle_0,C1_LHSy_0,  FP, 'rloess' );
C1_LHSx_0_MA = smooth(C1_Cycle_0,C1_LHSx_0,  FP, 'rloess' );
C1_LHSa_0_MA = smooth(C1_Cycle_0,C1_LHSa_0,  FP, 'rloess' );
C1_LHSy_Min_MA = smooth(C1_Cycle_MaxMin,C1_LHSy_Min,  FP, 'rloess' );
C1_LHSx_Min_MA = smooth(C1_Cycle_MaxMin,C1_LHSx_Min,  FP, 'rloess' );
C1_LHSa_Min_MA = smooth(C1_Cycle_MaxMin,C1_LHSa_Min,  FP, 'rloess' );

%Control Glenoid C2
%Reduce data set size
C2_HHP_0FULL =  C2_Data{:,9}';
sampleC2 = 1;
j =1;
 for i = 1:length(C2_HHP_0FULL)
    if i == sampleC2
        sampleC2 = sampleC2 +100;
C2_HHP_Max(j) =  C2_Data{i,1};
C2_Cycle_MaxMin(j) = C2_Data{i,2};
C2_RHSy_Max(j) = C2_Data{i,3};
C2_RHSx_Max(j) = C2_Data{i,4};
C2_RHSa_Max(j) = C2_Data{i,5};
C2_LHSy_Max(j) = C2_Data{i,6};
C2_LHSx_Max(j) = C2_Data{i,7};
C2_LHSa_Max(j) = C2_Data{i,8};

C2_HHP_0(j) =  C2_Data{i,9};
C2_Cycle_0(j) = C2_Data{i,10};
C2_RHSy_0(j) = C2_Data{i,11};
C2_RHSx_0(j) = C2_Data{i,12};
C2_RHSa_0(j) = C2_Data{i,13};
```

```
C2_LHSy_0(j) = C2_Data{i,14};
C2_LHSx_0(j) = C2_Data{i,15};
C2_LHSa_0(j) = C2_Data{i,16};

C2_HHP_Min(j) =  C2_Data{i,17};
C2_RHSy_Min(j) = C2_Data{i,19};
C2_RHSx_Min(j) = C2_Data{i,20};
C2_RHSa_Min(j) = C2_Data{i,21};
C2_LHSy_Min(j) = C2_Data{i,22};
C2_LHSx_Min(j) = C2_Data{i,23};
C2_LHSa_Min(j) = C2_Data{i,24};
j=j+1;
    end
 end

%Calculate Robust Loess smoothed vectors of C2 motions
%RHS
C2_RHSy_Max_MA = smooth(C2_Cycle_MaxMin,C2_RHSy_Max,  FP, 'rloess' );
C2_RHSx_Max_MA = smooth(C2_Cycle_MaxMin,C2_RHSx_Max,  FP, 'rloess' );
C2_RHSa_Max_MA = smooth(C2_Cycle_MaxMin,C2_RHSa_Max,  FP, 'rloess' );
C2_RHSy_0_MA = smooth(C2_Cycle_0,C2_RHSy_0,  FP, 'rloess' );
C2_RHSx_0_MA = smooth(C2_Cycle_0,C2_RHSx_0,  FP, 'rloess' );
C2_RHSa_0_MA = smooth(C2_Cycle_0,C2_RHSa_0,  FP, 'rloess' );
C2_RHSy_Min_MA = smooth(C2_Cycle_MaxMin,C2_RHSy_Min,  FP, 'rloess' );
C2_RHSx_Min_MA = smooth(C2_Cycle_MaxMin,C2_RHSx_Min,  FP, 'rloess' );
C2_RHSa_Min_MA = smooth(C2_Cycle_MaxMin,C2_RHSa_Min,  FP, 'rloess' );
%LHS
C2_LHSy_Max_MA = smooth(C2_Cycle_MaxMin,C2_LHSy_Max,  FP, 'rloess' );
C2_LHSx_Max_MA = smooth(C2_Cycle_MaxMin,C2_LHSx_Max,  FP, 'rloess' );
C2_LHSa_Max_MA = smooth(C2_Cycle_MaxMin,C2_LHSa_Max,  FP, 'rloess' );
C2_LHSy_0_MA = smooth( C2_Cycle_0,C2_LHSy_0, FP, 'rloess' );
C2_LHSx_0_MA = smooth(C2_Cycle_0,C2_LHSx_0,  FP, 'rloess' );
C2_LHSa_0_MA = smooth(C2_Cycle_0,C2_LHSa_0,  FP, 'rloess' );
C2_LHSy_Min_MA = smooth(C2_Cycle_MaxMin,C2_LHSy_Min,  FP, 'rloess' );
C2_LHSx_Min_MA = smooth(C2_Cycle_MaxMin,C2_LHSx_Min,  FP, 'rloess' );
C2_LHSa_Min_MA = smooth(C2_Cycle_MaxMin,C2_LHSa_Min,  FP, 'rloess' );

%Control Glenoid C3

%Reduce data set size
C3_HHP_0FULL =  C3_Data{:,9}';
sampleC3 = 1;
j =1;
 for i = 1:length(C3_HHP_0FULL)
    if i == sampleC3
        sampleC3 = sampleC3 +100;
C3_HHP_Max(j) =  C3_Data{i,1};
C3_Cycle_MaxMin(j) = C3_Data{i,2};
C3_RHSy_Max(j) = C3_Data{i,3};
C3_RHSx_Max(j) = C3_Data{i,4};
C3_RHSa_Max(j) = C3_Data{i,5};
C3_LHSy_Max(j) = C3_Data{i,6};
C3_LHSx_Max(j) = C3_Data{i,7};
C3_LHSa_Max(j) = C3_Data{i,8};

C3_HHP_0(j) =  C3_Data{i,9};
C3_Cycle_0(j) = C3_Data{i,10};
C3_RHSy_0(j)= C3_Data{i,11};
C3_RHSx_0(j) = C3_Data{i,12};
C3_RHSa_0(j) = C3_Data{i,13};
C3_LHSy_0(j) = C3_Data{i,14};
C3_LHSx_0(j) = C3_Data{i,15};
C3_LHSa_0(j) = C3_Data{i,16};

C3_HHP_Min(j) =  C3_Data{i,17};
C3_RHSy_Min(j) = C3_Data{i,19};
C3_RHSx_Min(j) = C3_Data{i,20};
C3_RHSa_Min(j) = C3_Data{i,21};
C3_LHSy_Min(j)= C3_Data{i,22};
C3_LHSx_Min(j) = C3_Data{i,23};
C3_LHSa_Min(j) = C3_Data{i,24};
j=j+1;
    end
 end

%Calculate Robust Loess smoothed vectors of C3 motions
%RHS
```

```
C3_RHSy_Max_MA = smooth(C3_Cycle_MaxMin,C3_RHSy_Max,  FP, 'rloess' );
C3_RHSx_Max_MA = smooth(C3_Cycle_MaxMin,C3_RHSx_Max,  FP, 'rloess' );
C3_RHSa_Max_MA = smooth(C3_Cycle_MaxMin,C3_RHSa_Max,  FP, 'rloess' );
C3_RHSy_0_MA = smooth(C3_Cycle_0, C3_RHSy_0,  FP, 'rloess' );
C3_RHSx_0_MA = smooth(C3_Cycle_0 ,C3_RHSx_0,  FP, 'rloess' );
C3_RHSa_0_MA = smooth(C3_Cycle_0 ,C3_RHSa_0,  FP, 'rloess' );
C3_RHSy_Min_MA = smooth(C3_Cycle_MaxMin,C3_RHSy_Min,  FP, 'rloess' );
C3_RHSx_Min_MA = smooth(C3_Cycle_MaxMin,C3_RHSx_Min,  FP, 'rloess' );
C3_RHSa_Min_MA = smooth(C3_Cycle_MaxMin,C3_RHSa_Min,  FP, 'rloess' );
%LHS
C3_LHSy_Max_MA = smooth(C3_Cycle_MaxMin,C3_LHSy_Max,  FP, 'rloess' );
C3_LHSx_Max_MA = smooth(C3_Cycle_MaxMin,C3_LHSx_Max,  FP, 'rloess' );
C3_LHSa_Max_MA = smooth(C3_Cycle_MaxMin,C3_LHSa_Max,  FP, 'rloess' );
C3_LHSy_0_MA = smooth(C3_Cycle_0,C3_LHSy_0,  FP, 'rloess' );
C3_LHSx_0_MA = smooth(C3_Cycle_0,C3_LHSx_0,  FP, 'rloess' );
C3_LHSa_0_MA = smooth(C3_Cycle_0,C3_LHSa_0,  FP, 'rloess' );
C3_LHSy_Min_MA = smooth(C3_Cycle_MaxMin,C3_LHSy_Min,  FP, 'rloess' );
C3_LHSx_Min_MA = smooth(C3_Cycle_MaxMin,C3_LHSx_Min,  FP, 'rloess' );
C3_LHSa_Min_MA = smooth(C3_Cycle_MaxMin,C3_LHSa_Min,  FP, 'rloess' );


%Control glenoid C6
 C6_HHP_0FULL =  C6_Data{:,9}';
%Reduce data set size
 sampleC6 = 1;
j =1;
 for i = 1:length(C6_HHP_0FULL)
    if i == sampleC6
        sampleC6 = sampleC6 +100;
C6_HHP_Max(j) =  C6_Data{i,1};
C6_Cycle_MaxMin(j) = C6_Data{i,2};
C6_RHSy_Max(j) = C6_Data{i,3};
C6_RHSx_Max(j) = C6_Data{i,4};
C6_RHSa_Max(j) = C6_Data{i,5};
C6_LHSy_Max(j) = C6_Data{i,6};
C6_LHSx_Max(j) = C6_Data{i,7};
C6_LHSa_Max(j) = C6_Data{i,8};

C6_HHP_0(j) =  C6_Data{i,9};
C6_Cycle_0(j) = C6_Data{i,10};
C6_RHSy_0(j) = C6_Data{i,11};
C6_RHSx_0(j) = C6_Data{i,12};
C6_RHSa_0(j) = C6_Data{i,13};
C6_LHSy_0(j) = C6_Data{i,14};
C6_LHSx_0(j) = C6_Data{i,15};
C6_LHSa_0(j) = C6_Data{i,16};

C6_HHP_Min(j) =  C6_Data{i,17};
C6_RHSy_Min(j) = C6_Data{i,19};
C6_RHSx_Min(j) = C6_Data{i,20};
C6_RHSa_Min(j) = C6_Data{i,21};
C6_LHSy_Min(j) = C6_Data{i,22};
C6_LHSx_Min(j) = C6_Data{i,23};
C6_LHSa_Min(j) = C6_Data{i,24};
j=j+1;
    end
 end

%Calculate Robust Loess smoothed vectors of C6 motions
%RHS
C6_RHSy_Max_MA = smooth(C6_Cycle_MaxMin,C6_RHSy_Max, FP, 'rloess' );
C6_RHSx_Max_MA = smooth(C6_Cycle_MaxMin,C6_RHSx_Max, FP, 'rloess' );
C6_RHSa_Max_MA = smooth(C6_Cycle_MaxMin,C6_RHSa_Max, FP, 'rloess' );
C6_RHSy_0_MA = smooth(C6_Cycle_0,C6_RHSy_0, FP, 'rloess' );
C6_RHSx_0_MA = smooth(C6_Cycle_0,C6_RHSx_0, FP, 'rloess' );
C6_RHSa_0_MA = smooth(C6_Cycle_0,C6_RHSa_0, FP, 'rloess' );
C6_RHSy_Min_MA = smooth(C6_Cycle_MaxMin,C6_RHSy_Min, FP, 'rloess' );
C6_RHSx_Min_MA = smooth(C6_Cycle_MaxMin,C6_RHSx_Min, FP, 'rloess' );
C6_RHSa_Min_MA = smooth(C6_Cycle_MaxMin,C6_RHSa_Min, FP, 'rloess' );
%LHS
C6_LHSy_Max_MA = smooth(C6_Cycle_MaxMin,C6_LHSy_Max, FP, 'rloess' );
C6_LHSx_Max_MA = smooth(C6_Cycle_MaxMin,C6_LHSx_Max, FP, 'rloess' );
C6_LHSa_Max_MA = smooth(C6_Cycle_MaxMin,C6_LHSa_Max, FP, 'rloess' );
C6_LHSy_0_MA = smooth(C6_Cycle_0,C6_LHSy_0, FP, 'rloess' );
C6_LHSx_0_MA = smooth(C6_Cycle_0,C6_LHSx_0, FP, 'rloess' );
C6_LHSa_0_MA = smooth(C6_Cycle_0,C6_LHSa_0, FP, 'rloess' );
C6_LHSy_Min_MA = smooth(C6_Cycle_MaxMin,C6_LHSy_Min, FP, 'rloess' );
```

```
C6_LHSx_Min_MA = smooth(C6_Cycle_MaxMin,C6_LHSx_Min, FP, 'rloess' );
C6_LHSa_Min_MA = smooth(C6_Cycle_MaxMin,C6_LHSa_Min, FP, 'rloess' );

%For Control Glenoid C7
%Reduce data set size
C7_HHP_0FULL =  C7_Data{:,9}';
sampleC7 = 1;
j =1;
 for i = 1:length(C7_HHP_0FULL)
    if i == sampleC7
        sampleC7 = sampleC7 +100;
C7_HHP_Max(j) =  C7_Data{i,1};
C7_Cycle_MaxMin(j) = C7_Data{i,2};
C7_RHSy_Max(j)= C7_Data{i,3};
C7_RHSx_Max(j) = C7_Data{i,4};
C7_RHSa_Max(j) = C7_Data{i,5};
C7_LHSy_Max(j) = C7_Data{i,6};
C7_LHSx_Max(j) = C7_Data{i,7};
C7_LHSa_Max(j) = C7_Data{i,8};

C7_HHP_0(j) =  C7_Data{i,9};
C7_Cycle_0(j) = C7_Data{i,10};
C7_RHSy_0(j) = C7_Data{i,11};
C7_RHSx_0(j) = C7_Data{i,12};
C7_RHSa_0(j) = C7_Data{i,13};
C7_LHSy_0(j) = C7_Data{i,14};
C7_LHSx_0(j) = C7_Data{i,15};
C7_LHSa_0(j) = C7_Data{i,16};

C7_HHP_Min(j) =  C7_Data{i,17};
C7_RHSy_Min(j) = C7_Data{i,19};
C7_RHSx_Min(j) = C7_Data{i,20};
C7_RHSa_Min(j) = C7_Data{i,21};
C7_LHSy_Min(j) = C7_Data{i,22};
C7_LHSx_Min(j) = C7_Data{i,23};
C7_LHSa_Min(j) = C7_Data{i,24};
j=j+1;
    end
end

%Calculate Robust Loess smoothed vectors of C7 motions
%RHS
C7_RHSy_Max_MA = smooth(C7_Cycle_MaxMin,C7_RHSy_Max, FP, 'rloess' );
C7_RHSx_Max_MA = smooth(C7_Cycle_MaxMin,C7_RHSx_Max, FP, 'rloess' );
C7_RHSa_Max_MA = smooth(C7_Cycle_MaxMin,C7_RHSa_Max, FP, 'rloess' );
C7_RHSy_0_MA = smooth(C7_Cycle_0,C7_RHSy_0, FP, 'rloess' );
C7_RHSx_0_MA = smooth(C7_Cycle_0,C7_RHSx_0, FP, 'rloess' );
C7_RHSa_0_MA = smooth(C7_Cycle_0,C7_RHSa_0, FP, 'rloess' );
C7_RHSy_Min_MA = smooth(C7_Cycle_MaxMin,C7_RHSy_Min, FP, 'rloess' );
C7_RHSx_Min_MA = smooth(C7_Cycle_MaxMin,C7_RHSx_Min, FP, 'rloess' );
C7_RHSa_Min_MA = smooth(C7_Cycle_MaxMin,C7_RHSa_Min, FP, 'rloess' );
%LHS
C7_LHSy_Max_MA = smooth(C7_Cycle_MaxMin,C7_LHSy_Max, FP, 'rloess' );
C7_LHSx_Max_MA = smooth(C7_Cycle_MaxMin,C7_LHSx_Max, FP, 'rloess' );
C7_LHSa_Max_MA = smooth(C7_Cycle_MaxMin,C7_LHSa_Max, FP, 'rloess' );
C7_LHSy_0_MA = smooth(C7_Cycle_0,C7_LHSy_0, FP, 'rloess' );
C7_LHSx_0_MA = smooth(C7_Cycle_0,C7_LHSx_0, FP, 'rloess' );
C7_LHSa_0_MA = smooth(C7_Cycle_0,C7_LHSa_0, FP, 'rloess' );
C7_LHSy_Min_MA = smooth(C7_Cycle_MaxMin,C7_LHSy_Min, FP, 'rloess' );
C7_LHSx_Min_MA = smooth(C7_Cycle_MaxMin,C7_LHSx_Min, FP, 'rloess' );
C7_LHSa_Min_MA = smooth(C7_Cycle_MaxMin,C7_LHSa_Min, FP, 'rloess' );

%For Control Glenoid C8
 %Reduce data set size
 C8_HHP_0FULL =  C8_Data{:,9}';
 sampleC8 = 1;
 j =1;
  for i = 1:length(C8_HHP_0FULL)
     if i == sampleC8
         sampleC8 = sampleC8 +100;
 C8_HHP_Max(j) =  C8_Data{i,1};
 C8_Cycle_MaxMin(j) = C8_Data{i,2};
 C8_RHSy_Max(j)= C8_Data{i,3};
 C8_RHSx_Max(j) = C8_Data{i,4};
 C8_RHSa_Max(j) = C8_Data{i,5};
 C8_LHSy_Max(j) = C8_Data{i,6};
 C8_LHSx_Max(j) = C8_Data{i,7};
```

```
C8_LHSa_Max(j) = C8_Data{i,8};

C8_HHP_0(j) =  C8_Data{i,9};
C8_Cycle_0(j) = C8_Data{i,10};
C8_RHSy_0(j) = C8_Data{i,11};
C8_RHSx_0(j) = C8_Data{i,12};
C8_RHSa_0(j) = C8_Data{i,13};
C8_LHSy_0(j) = C8_Data{i,14};
C8_LHSx_0(j) = C8_Data{i,15};
C8_LHSa_0(j) = C8_Data{i,16};

C8_HHP_Min(j) =  C8_Data{i,17};
C8_RHSy_Min(j) = C8_Data{i,19};
C8_RHSx_Min(j) = C8_Data{i,20};
C8_RHSa_Min(j) = C8_Data{i,21};
C8_LHSy_Min(j) = C8_Data{i,22};
C8_LHSx_Min(j) = C8_Data{i,23};
C8_LHSa_Min(j) = C8_Data{i,24};
j=j+1;
    end
end

%Calculate Robust Loess smoothed vectors of C8 motions
%RHS
C8_RHSy_Max_MA = smooth(C8_Cycle_MaxMin,C8_RHSy_Max, FP, 'rloess' );
C8_RHSx_Max_MA = smooth(C8_Cycle_MaxMin,C8_RHSx_Max, FP, 'rloess' );
C8_RHSa_Max_MA = smooth(C8_Cycle_MaxMin,C8_RHSa_Max, FP, 'rloess' );
C8_RHSy_0_MA = smooth(C8_Cycle_0,C8_RHSy_0, FP, 'rloess' );
C8_RHSx_0_MA = smooth(C8_Cycle_0,C8_RHSx_0, FP, 'rloess' );
C8_RHSa_0_MA = smooth(C8_Cycle_0,C8_RHSa_0, FP, 'rloess' );
C8_RHSy_Min_MA = smooth(C8_Cycle_MaxMin,C8_RHSy_Min, FP, 'rloess' );
C8_RHSx_Min_MA = smooth(C8_Cycle_MaxMin,C8_RHSx_Min, FP, 'rloess' );
C8_RHSa_Min_MA = smooth(C8_Cycle_MaxMin,C8_RHSa_Min, FP, 'rloess' );
%LHS
C8_LHSy_Max_MA = smooth(C8_Cycle_MaxMin,C8_LHSy_Max, FP, 'rloess' );
C8_LHSx_Max_MA = smooth(C8_Cycle_MaxMin,C8_LHSx_Max, FP, 'rloess' );
C8_LHSa_Max_MA = smooth(C8_Cycle_MaxMin,C8_LHSa_Max, FP, 'rloess' );
C8_LHSy_0_MA = smooth(C8_Cycle_0,C8_LHSy_0, FP, 'rloess' );
C8_LHSx_0_MA = smooth(C8_Cycle_0,C8_LHSx_0, FP, 'rloess' );
C8_LHSa_0_MA = smooth(C8_Cycle_0,C8_LHSa_0, FP, 'rloess' );
C8_LHSy_Min_MA = smooth(C8_Cycle_MaxMin,C8_LHSy_Min, FP, 'rloess' );
C8_LHSx_Min_MA = smooth(C8_Cycle_MaxMin,C8_LHSx_Min, FP, 'rloess' );
C8_LHSa_Min_MA = smooth(C8_Cycle_MaxMin,C8_LHSa_Min, FP, 'rloess' );

 %Novel glenoid N1
N1_HHP_0FULL =  N1_Data{:,9}';
 sampleN1 = 1;
j =1;
 for i = 1:length(N1_HHP_0FULL)
    if i == sampleN1
        sampleN1 = sampleN1 +100;
N1_HHP_Max(j) =  N1_Data{i,1};
N1_Cycle_MaxMin(j) = N1_Data{i,2};
N1_RHSy_Max(j)= N1_Data{i,3};
N1_RHSx_Max(j) = N1_Data{i,4};
N1_RHSa_Max(j) = N1_Data{i,5};
N1_LHSy_Max(j) = N1_Data{i,6};
N1_LHSx_Max(j) = N1_Data{i,7};
N1_LHSa_Max(j) = N1_Data{i,8};

N1_HHP_0(j) =  N1_Data{i,9};
N1_Cycle_0(j) = N1_Data{i,10};
N1_RHSy_0(j) = N1_Data{i,11};
N1_RHSx_0(j) = N1_Data{i,12};
N1_RHSa_0(j) = N1_Data{i,13};
N1_LHSy_0(j) = N1_Data{i,14};
N1_LHSx_0(j) = N1_Data{i,15};
N1_LHSa_0(j) = N1_Data{i,16};

N1_HHP_Min(j) =  N1_Data{i,17};
N1_RHSy_Min(j) = N1_Data{i,19};
N1_RHSx_Min(j) = N1_Data{i,20};
N1_RHSa_Min(j) = N1_Data{i,21};
N1_LHSy_Min(j) = N1_Data{i,22};
N1_LHSx_Min(j) = N1_Data{i,23};
N1_LHSa_Min(j) = N1_Data{i,24};
j=j+1;
```

```
    end
 end

%Calculate Robust Loess smoothed vectors of N1 motions
%RHS
N1_RHSy_Max_MA = smooth(N1_Cycle_MaxMin, N1_RHSy_Max, FP, 'rloess' );
N1_RHSx_Max_MA = smooth(N1_Cycle_MaxMin,N1_RHSx_Max, FP, 'rloess' );
N1_RHSa_Max_MA = smooth(N1_Cycle_MaxMin,N1_RHSa_Max, FP, 'rloess' );
N1_RHSy_0_MA = smooth(N1_Cycle_0,N1_RHSy_0, FP, 'rloess' );
N1_RHSx_0_MA = smooth(N1_Cycle_0,N1_RHSx_0, FP, 'rloess' );
N1_RHSa_0_MA = smooth(N1_Cycle_0,N1_RHSa_0, FP, 'rloess' );
N1_RHSy_Min_MA = smooth(N1_Cycle_MaxMin,N1_RHSy_Min, FP, 'rloess' );
N1_RHSx_Min_MA = smooth(N1_Cycle_MaxMin,N1_RHSx_Min, FP, 'rloess' );
N1_RHSa_Min_MA = smooth(N1_Cycle_MaxMin,N1_RHSa_Min, FP, 'rloess' );

%LHS
N1_LHSy_Max_MA = smooth(N1_Cycle_MaxMin,N1_LHSy_Max, FP, 'rloess' );
N1_LHSx_Max_MA = smooth(N1_Cycle_MaxMin,N1_LHSx_Max, FP, 'rloess' );
N1_LHSa_Max_MA = smooth(N1_Cycle_MaxMin,N1_LHSa_Max, FP, 'rloess' );
N1_LHSy_0_MA = smooth(N1_Cycle_0,N1_LHSy_0, FP, 'rloess' );
N1_LHSx_0_MA = smooth(N1_Cycle_0,N1_LHSx_0, FP, 'rloess' );
N1_LHSa_0_MA = smooth(N1_Cycle_0,N1_LHSa_0, FP, 'rloess' );
N1_LHSy_Min_MA = smooth(N1_Cycle_MaxMin,N1_LHSy_Min, FP, 'rloess' );
N1_LHSx_Min_MA = smooth(N1_Cycle_MaxMin,N1_LHSx_Min, FP, 'rloess' );
N1_LHSa_Min_MA = smooth(N1_Cycle_MaxMin,N1_LHSa_Min, FP, 'rloess' );

%Novel glenoid N2
N2_HHP_0FULL =  N2_Data{:,9}';
 sampleN2 = 1;
j =1;
 for i = 1:length(N2_HHP_0FULL)
    if i == sampleN2
        sampleN2 = sampleN2 +100;
N2_HHP_Max(j) =  N2_Data{i,1};
N2_Cycle_MaxMin(j) = N2_Data{i,2};
N2_RHSy_Max(j) = N2_Data{i,3};
N2_RHSx_Max(j) = N2_Data{i,4};
N2_RHSa_Max(j) = N2_Data{i,5};
N2_LHSy_Max(j) = N2_Data{i,6};
N2_LHSx_Max(j) = N2_Data{i,7};
N2_LHSa_Max(j) = N2_Data{i,8};

N2_HHP_0(j) =  N2_Data{i,9};
N2_Cycle_0(j) = N2_Data{i,10};
N2_RHSy_0(j) = N2_Data{i,11};
N2_RHSx_0(j) = N2_Data{i,12};
N2_RHSa_0(j) = N2_Data{i,13};
N2_LHSy_0(j) = N2_Data{i,14};
N2_LHSx_0(j) = N2_Data{i,15};
N2_LHSa_0(j) = N2_Data{i,16};

N2_HHP_Min(j) =  N2_Data{i,17};
N2_RHSy_Min(j) = N2_Data{i,19};
N2_RHSx_Min(j) = N2_Data{i,20};
N2_RHSa_Min(j) = N2_Data{i,21};
N2_LHSy_Min(j) = N2_Data{i,22};
N2_LHSx_Min(j) = N2_Data{i,23};
N2_LHSa_Min(j) = N2_Data{i,24};
j=j+1;
    end
 end

%Calculate Robust Loess smoothed vectors of N2 motions
%RHS
N2_RHSy_Max_MA = smooth(N2_Cycle_MaxMin,N2_RHSy_Max, FP, 'rloess' );
N2_RHSx_Max_MA = smooth(N2_Cycle_MaxMin,N2_RHSx_Max, FP, 'rloess' );
N2_RHSa_Max_MA = smooth(N2_Cycle_MaxMin,N2_RHSa_Max, FP, 'rloess' );
N2_RHSy_0_MA = smooth(N2_Cycle_0,N2_RHSy_0, FP, 'rloess' );
N2_RHSx_0_MA = smooth(N2_Cycle_0,N2_RHSx_0, FP, 'rloess' );
N2_RHSa_0_MA = smooth(N2_Cycle_0,N2_RHSa_0, FP, 'rloess' );
N2_RHSy_Min_MA = smooth(N2_Cycle_MaxMin,N2_RHSy_Min, FP, 'rloess' );
N2_RHSx_Min_MA = smooth(N2_Cycle_MaxMin,N2_RHSx_Min, FP, 'rloess' );
N2_RHSa_Min_MA = smooth(N2_Cycle_MaxMin,N2_RHSa_Min, FP, 'rloess' );
%LHS
N2_LHSy_Max_MA = smooth(N2_Cycle_MaxMin,N2_LHSy_Max, FP, 'rloess' );
N2_LHSx_Max_MA = smooth(N2_Cycle_MaxMin,N2_LHSx_Max, FP, 'rloess' );
N2_LHSa_Max_MA = smooth(N2_Cycle_MaxMin,N2_LHSa_Max, FP, 'rloess' );
```

```
N2_LHSy_0_MA = smooth(N2_Cycle_0,N2_LHSy_0, FP, 'rloess' );
N2_LHSx_0_MA = smooth(N2_Cycle_0,N2_LHSx_0, FP, 'rloess' );
N2_LHSa_0_MA = smooth(N2_Cycle_0,N2_LHSa_0, FP, 'rloess' );
N2_LHSy_Min_MA = smooth(N2_Cycle_MaxMin,N2_LHSy_Min, FP, 'rloess' );
N2_LHSx_Min_MA = smooth(N2_Cycle_MaxMin,N2_LHSx_Min, FP, 'rloess' );
N2_LHSa_Min_MA = smooth(N2_Cycle_MaxMin,N2_LHSa_Min, FP, 'rloess' );

%For Novel Glenoid N3
%Reduce data set size
N3_HHP_0FULL =  N3_Data{:,9}';
sampleN3 = 1;
j =1;
 for i = 1:length(N3_HHP_0FULL)
    if i == sampleN3
        sampleN3 = sampleN3 +100;
N3_HHP_Max(j) =  N3_Data{i,1};
N3_Cycle_MaxMin(j) = N3_Data{i,2};
N3_RHSy_Max(j)= N3_Data{i,3};
N3_RHSx_Max(j) = N3_Data{i,4};
N3_RHSa_Max(j) = N3_Data{i,5};
N3_LHSy_Max(j) = N3_Data{i,6};
N3_LHSx_Max(j) = N3_Data{i,7};
N3_LHSa_Max(j) = N3_Data{i,8};

N3_HHP_0(j) =  N3_Data{i,9};
N3_Cycle_0(j) = N3_Data{i,10};
N3_RHSy_0(j) = N3_Data{i,11};
N3_RHSx_0(j) = N3_Data{i,12};
N3_RHSa_0(j) = N3_Data{i,13};
N3_LHSy_0(j) = N3_Data{i,14};
N3_LHSx_0(j) = N3_Data{i,15};
N3_LHSa_0(j) = N3_Data{i,16};

N3_HHP_Min(j) =  N3_Data{i,17};
N3_RHSy_Min(j) = N3_Data{i,19};
N3_RHSx_Min(j) = N3_Data{i,20};
N3_RHSa_Min(j) = N3_Data{i,21};
N3_LHSy_Min(j) = N3_Data{i,22};
N3_LHSx_Min(j) = N3_Data{i,23};
N3_LHSa_Min(j) = N3_Data{i,24};
j=j+1;
    end
end

%Calculate Robust Loess smoothed vectors of N3 motions
%RHS
N3_RHSy_Max_MA = smooth(N3_Cycle_MaxMin,N3_RHSy_Max, FP, 'rloess' );
N3_RHSx_Max_MA = smooth(N3_Cycle_MaxMin,N3_RHSx_Max, FP, 'rloess' );
N3_RHSa_Max_MA = smooth(N3_Cycle_MaxMin,N3_RHSa_Max, FP, 'rloess' );
N3_RHSy_0_MA = smooth(N3_Cycle_0,N3_RHSy_0, FP, 'rloess' );
N3_RHSx_0_MA = smooth(N3_Cycle_0,N3_RHSx_0, FP, 'rloess' );
N3_RHSa_0_MA = smooth(N3_Cycle_0,N3_RHSa_0, FP, 'rloess' );
N3_RHSy_Min_MA = smooth(N3_Cycle_MaxMin,N3_RHSy_Min, FP, 'rloess' );
N3_RHSx_Min_MA = smooth(N3_Cycle_MaxMin,N3_RHSx_Min, FP, 'rloess' );
N3_RHSa_Min_MA = smooth(N3_Cycle_MaxMin,N3_RHSa_Min, FP, 'rloess' );
%LHS
N3_LHSy_Max_MA = smooth(N3_Cycle_MaxMin,N3_LHSy_Max, FP, 'rloess' );
N3_LHSx_Max_MA = smooth(N3_Cycle_MaxMin,N3_LHSx_Max, FP, 'rloess' );
N3_LHSa_Max_MA = smooth(N3_Cycle_MaxMin,N3_LHSa_Max, FP, 'rloess' );
N3_LHSy_0_MA = smooth(N3_Cycle_0,N3_LHSy_0, FP, 'rloess' );
N3_LHSx_0_MA = smooth(N3_Cycle_0,N3_LHSx_0, FP, 'rloess' );
N3_LHSa_0_MA = smooth(N3_Cycle_0,N3_LHSa_0, FP, 'rloess' );
N3_LHSy_Min_MA = smooth(N3_Cycle_MaxMin,N3_LHSy_Min, FP, 'rloess' );
N3_LHSx_Min_MA = smooth(N3_Cycle_MaxMin,N3_LHSx_Min, FP, 'rloess' );
N3_LHSa_Min_MA = smooth(N3_Cycle_MaxMin,N3_LHSa_Min, FP, 'rloess' );

%For Novel Glenoid N4
%Reduce data set size
N4_HHP_0FULL =  N4_Data{:,9}';
sampleN4 = 1;
j =1;
 for i = 1:length(N4_HHP_0FULL)
    if i == sampleN4
        sampleN4 = sampleN4 +100;
N4_HHP_Max(j) =  N4_Data{i,1};
N4_Cycle_MaxMin(j) = N4_Data{i,2};
N4_RHSy_Max(j)= N4_Data{i,3};
```

```
N4_RHSx_Max(j) = N4_Data{i,4};
N4_RHSa_Max(j) = N4_Data{i,5};
N4_LHSy_Max(j) = N4_Data{i,6};
N4_LHSx_Max(j) = N4_Data{i,7};
N4_LHSa_Max(j) = N4_Data{i,8};

N4_HHP_0(j) =  N4_Data{i,9};
N4_Cycle_0(j) = N4_Data{i,10};
N4_RHSy_0(j) = N4_Data{i,11};
N4_RHSx_0(j) = N4_Data{i,12};
N4_RHSa_0(j) = N4_Data{i,13};
N4_LHSy_0(j) = N4_Data{i,14};
N4_LHSx_0(j) = N4_Data{i,15};
N4_LHSa_0(j) = N4_Data{i,16};

N4_HHP_Min(j) =  N4_Data{i,17};
N4_RHSy_Min(j) = N4_Data{i,19};
N4_RHSx_Min(j) = N4_Data{i,20};
N4_RHSa_Min(j) = N4_Data{i,21};
N4_LHSy_Min(j) = N4_Data{i,22};
N4_LHSx_Min(j) = N4_Data{i,23};
N4_LHSa_Min(j) = N4_Data{i,24};
j=j+1;
    end
end

%Calculate Robust Loess smoothed vectors of N4 motions
%RHS
N4_RHSy_Max_MA = smooth(N4_Cycle_MaxMin,N4_RHSy_Max, FP, 'rloess' );
N4_RHSx_Max_MA = smooth(N4_Cycle_MaxMin,N4_RHSx_Max, FP, 'rloess' );
N4_RHSa_Max_MA = smooth(N4_Cycle_MaxMin,N4_RHSa_Max, FP, 'rloess' );
N4_RHSy_0_MA = smooth(N4_Cycle_0,N4_RHSy_0, FP, 'rloess' );
N4_RHSx_0_MA = smooth(N4_Cycle_0,N4_RHSx_0, FP, 'rloess' );
N4_RHSa_0_MA = smooth(N4_Cycle_0,N4_RHSa_0, FP, 'rloess' );
N4_RHSy_Min_MA = smooth(N4_Cycle_MaxMin,N4_RHSy_Min, FP, 'rloess' );
N4_RHSx_Min_MA = smooth(N4_Cycle_MaxMin,N4_RHSx_Min, FP, 'rloess' );
N4_RHSa_Min_MA = smooth(N4_Cycle_MaxMin,N4_RHSa_Min, FP, 'rloess' );
%LHS
N4_LHSy_Max_MA = smooth(N4_Cycle_MaxMin,N4_LHSy_Max, FP, 'rloess' );
N4_LHSx_Max_MA = smooth(N4_Cycle_MaxMin,N4_LHSx_Max, FP, 'rloess' );
N4_LHSa_Max_MA = smooth(N4_Cycle_MaxMin,N4_LHSa_Max, FP, 'rloess' );
N4_LHSy_0_MA = smooth(N4_Cycle_0,N4_LHSy_0, FP, 'rloess' );
N4_LHSx_0_MA = smooth(N4_Cycle_0,N4_LHSx_0, FP, 'rloess' );
N4_LHSa_0_MA = smooth(N4_Cycle_0,N4_LHSa_0, FP, 'rloess' );
N4_LHSy_Min_MA = smooth(N4_Cycle_MaxMin,N4_LHSy_Min, FP, 'rloess' );
N4_LHSx_Min_MA = smooth(N4_Cycle_MaxMin,N4_LHSx_Min, FP, 'rloess' );
N4_LHSa_Min_MA = smooth(N4_Cycle_MaxMin,N4_LHSa_Min, FP, 'rloess' );

%For Novel Glenoid N5
%Reduce data set size
N5_HHP_0FULL =  N5_Data{:,9}';
sampleN5 = 1;
j =1;
 for i = 1:length(N5_HHP_0FULL)
    if i == sampleN5
        sampleN5 = sampleN5 +100;
N5_HHP_Max(j) =  N5_Data{i,1};
N5_Cycle_MaxMin(j) = N5_Data{i,2};
N5_RHSy_Max(j)= N5_Data{i,3};
N5_RHSx_Max(j) = N5_Data{i,4};
N5_RHSa_Max(j) = N5_Data{i,5};
N5_LHSy_Max(j) = N5_Data{i,6};
N5_LHSx_Max(j) = N5_Data{i,7};
N5_LHSa_Max(j) = N5_Data{i,8};

N5_HHP_0(j) =  N5_Data{i,9};
N5_Cycle_0(j) = N5_Data{i,10};
N5_RHSy_0(j) = N5_Data{i,11};
N5_RHSx_0(j) = N5_Data{i,12};
N5_RHSa_0(j) = N5_Data{i,13};
N5_LHSy_0(j) = N5_Data{i,14};
N5_LHSx_0(j) = N5_Data{i,15};
N5_LHSa_0(j) = N5_Data{i,16};

N5_HHP_Min(j) =  N5_Data{i,17};
N5_RHSy_Min(j) = N5_Data{i,19};
N5_RHSx_Min(j) = N5_Data{i,20};
```

```
N5_RHSa_Min(j) = N5_Data{i,21};
N5_LHSy_Min(j) = N5_Data{i,22};
N5_LHSx_Min(j) = N5_Data{i,23};
N5_LHSa_Min(j) = N5_Data{i,24};
j=j+1;
    end
end

%Calculate Robust Loess smoothed vectors of N5 motions
%RHS
N5_RHSy_Max_MA = smooth(N5_Cycle_MaxMin,N5_RHSy_Max, FP, 'rloess' );
N5_RHSx_Max_MA = smooth(N5_Cycle_MaxMin,N5_RHSx_Max, FP, 'rloess' );
N5_RHSa_Max_MA = smooth(N5_Cycle_MaxMin,N5_RHSa_Max, FP, 'rloess' );
N5_RHSy_0_MA = smooth(N5_Cycle_0,N5_RHSy_0, FP, 'rloess' );
N5_RHSx_0_MA = smooth(N5_Cycle_0,N5_RHSx_0, FP, 'rloess' );
N5_RHSa_0_MA = smooth(N5_Cycle_0,N5_RHSa_0, FP, 'rloess' );
N5_RHSy_Min_MA = smooth(N5_Cycle_MaxMin,N5_RHSy_Min, FP, 'rloess' );
N5_RHSx_Min_MA = smooth(N5_Cycle_MaxMin,N5_RHSx_Min, FP, 'rloess' );
N5_RHSa_Min_MA = smooth(N5_Cycle_MaxMin,N5_RHSa_Min, FP, 'rloess' );
%LHS
N5_LHSy_Max_MA = smooth(N5_Cycle_MaxMin,N5_LHSy_Max, FP, 'rloess' );
N5_LHSx_Max_MA = smooth(N5_Cycle_MaxMin,N5_LHSx_Max, FP, 'rloess' );
N5_LHSa_Max_MA = smooth(N5_Cycle_MaxMin,N5_LHSa_Max, FP, 'rloess' );
N5_LHSy_0_MA = smooth(N5_Cycle_0,N5_LHSy_0, FP, 'rloess' );
N5_LHSx_0_MA = smooth(N5_Cycle_0,N5_LHSx_0, FP, 'rloess' );
N5_LHSa_0_MA = smooth(N5_Cycle_0,N5_LHSa_0, FP, 'rloess' );
N5_LHSy_Min_MA = smooth(N5_Cycle_MaxMin,N5_LHSy_Min, FP, 'rloess' );
N5_LHSx_Min_MA = smooth(N5_Cycle_MaxMin,N5_LHSx_Min, FP, 'rloess' );
N5_LHSa_Min_MA = smooth(N5_Cycle_MaxMin,N5_LHSa_Min, FP, 'rloess' );

%For Novel Glenoid N6
%Reduce data set size
N6_HHP_0FULL =  N6_Data{:,9}';
sampleN6 = 1;
j =1;
 for i = 1:length(N6_HHP_0FULL)
    if i == sampleN6
        sampleN6 = sampleN6 +100;
N6_HHP_Max(j) =  N6_Data{i,1};
N6_Cycle_MaxMin(j) = N6_Data{i,2};
N6_RHSy_Max(j)= N6_Data{i,3};
N6_RHSx_Max(j) = N6_Data{i,4};
N6_RHSa_Max(j) = N6_Data{i,5};
N6_LHSy_Max(j) = N6_Data{i,6};
N6_LHSx_Max(j) = N6_Data{i,7};
N6_LHSa_Max(j) = N6_Data{i,8};

N6_HHP_0(j) =  N6_Data{i,9};
N6_Cycle_0(j) = N6_Data{i,10};
N6_RHSy_0(j) = N6_Data{i,11};
N6_RHSx_0(j) = N6_Data{i,12};
N6_RHSa_0(j) = N6_Data{i,13};
N6_LHSy_0(j) = N6_Data{i,14};
N6_LHSx_0(j) = N6_Data{i,15};
N6_LHSa_0(j) = N6_Data{i,16};

N6_HHP_Min(j) =  N6_Data{i,17};
N6_RHSy_Min(j) = N6_Data{i,19};
N6_RHSx_Min(j) = N6_Data{i,20};
N6_RHSa_Min(j) = N6_Data{i,21};
N6_LHSy_Min(j) = N6_Data{i,22};
N6_LHSx_Min(j) = N6_Data{i,23};
N6_LHSa_Min(j) = N6_Data{i,24};
j=j+1;
    end
end

%Calculate Robust Loess smoothed vectors of N6 motions
%RHS
N6_RHSy_Max_MA = smooth(N6_Cycle_MaxMin,N6_RHSy_Max, FP, 'rloess' );
N6_RHSx_Max_MA = smooth(N6_Cycle_MaxMin,N6_RHSx_Max, FP, 'rloess' );
N6_RHSa_Max_MA = smooth(N6_Cycle_MaxMin,N6_RHSa_Max, FP, 'rloess' );
N6_RHSy_0_MA = smooth(N6_Cycle_0,N6_RHSy_0, FP, 'rloess' );
N6_RHSx_0_MA = smooth(N6_Cycle_0,N6_RHSx_0, FP, 'rloess' );
N6_RHSa_0_MA = smooth(N6_Cycle_0,N6_RHSa_0, FP, 'rloess' );
N6_RHSy_Min_MA = smooth(N6_Cycle_MaxMin,N6_RHSy_Min, FP, 'rloess' );
N6_RHSx_Min_MA = smooth(N6_Cycle_MaxMin,N6_RHSx_Min, FP, 'rloess' );
```

```
 N6_RHSa_Min_MA = smooth(N6_Cycle_MaxMin,N6_RHSa_Min, FP, 'rloess' );
 %LHS
 N6_LHSy_Max_MA = smooth(N6_Cycle_MaxMin,N6_LHSy_Max, FP, 'rloess' );
 N6_LHSx_Max_MA = smooth(N6_Cycle_MaxMin,N6_LHSx_Max, FP, 'rloess' );
 N6_LHSa_Max_MA = smooth(N6_Cycle_MaxMin,N6_LHSa_Max, FP, 'rloess' );
 N6_LHSy_0_MA = smooth(N6_Cycle_0,N6_LHSy_0, FP, 'rloess' );
 N6_LHSx_0_MA = smooth(N6_Cycle_0,N6_LHSx_0, FP, 'rloess' );
 N6_LHSa_0_MA = smooth(N6_Cycle_0,N6_LHSa_0, FP, 'rloess' );
 N6_LHSy_Min_MA = smooth(N6_Cycle_MaxMin,N6_LHSy_Min, FP, 'rloess' );
 N6_LHSx_Min_MA = smooth(N6_Cycle_MaxMin,N6_LHSx_Min, FP, 'rloess' );
 N6_LHSa_Min_MA = smooth(N6_Cycle_MaxMin,N6_LHSa_Min, FP, 'rloess' );
%%%%%%%%%%%%%%%%%%%%%%%%%%%%%%%%%%%%%%%%%%%%%%%%%%%%%%%%%%%%%%%%

%%%%%%%%%%%%%%%%%%%%%%%%%%%%%%%%%%%%%%%%%%%%%%%%%%%%%%%%%%%%%%%%
%STEP 3
%CALCULATE AVERAGE and standard Deviation VALUES OF CONTROL AND NOVEL DATA SETS
%Calculate average of smoothed Controls
 CAll_RHSy_Max                                =                                [C1_RHSy_Max_MA';
C2_RHSy_Max_MA';C3_RHSy_Max_MA';C6_RHSy_Max_MA';C7_RHSy_Max_MA';C8_RHSy_Max_MA'];
  CAV_RHSy_Max = mean(CAll_RHSy_Max,'omitnan');
 CAll_RHSy_0                                                                                                =
[C1_RHSy_0_MA';C2_RHSy_0_MA';C3_RHSy_0_MA';C6_RHSy_0_MA';C7_RHSy_0_MA';C8_RHSy_0_MA'];
  CAV_RHSy_0 = mean(CAll_RHSy_0,'omitnan');
 CAll_RHSy_Min                                                                                              =
[C1_RHSy_Min_MA';C2_RHSy_Min_MA';C3_RHSy_Min_MA';C6_RHSy_Min_MA';C7_RHSy_Min_MA';C8_RHSy_Min_M
A'];
  CAV_RHSy_Min = mean(CAll_RHSy_Min,'omitnan');

  CAll_RHSx_Max                                                                                              =
[C1_RHSx_Max_MA';C2_RHSx_Max_MA';C3_RHSx_Max_MA';C6_RHSx_Max_MA';C7_RHSx_Max_MA';C8_RHSx_Max_M
A'];
  CAV_RHSx_Max = mean(CAll_RHSx_Max,'omitnan');
 CAll_RHSx_0                                                                                                =
[C1_RHSx_0_MA';C2_RHSx_0_MA';C3_RHSx_0_MA';C6_RHSx_0_MA';C7_RHSx_0_MA';C8_RHSx_0_MA'];
  CAV_RHSx_0 = mean(CAll_RHSx_0,'omitnan');
 CAll_RHSx_Min                                                                                              =
[C1_RHSx_Min_MA';C2_RHSx_Min_MA';C3_RHSx_Min_MA';C6_RHSx_Min_MA';C7_RHSx_Min_MA';C8_RHSx_Min_M
A'];
   CAV_RHSx_Min = mean(CAll_RHSx_Min,'omitnan');

CAll_RHSa_Max                                                                                              =
[C1_RHSa_Max_MA';C2_RHSa_Max_MA';C3_RHSa_Max_MA';C6_RHSa_Max_MA';C7_RHSa_Max_MA';C8_RHSa_Max_M
A'];
  CAV_RHSa_Max = mean(CAll_RHSa_Max,'omitnan');
 CAll_RHSa_0                                                                                                =
[C1_RHSa_0_MA';C2_RHSa_0_MA';C3_RHSa_0_MA';C6_RHSa_0_MA';C7_RHSa_0_MA';C8_RHSa_0_MA'];
  CAV_RHSa_0 = mean(CAll_RHSa_0,'omitnan');
 CAll_RHSa_Min                                                                                              =
[C1_RHSa_Min_MA';C2_RHSa_Min_MA';C3_RHSa_Min_MA';C6_RHSa_Min_MA';C7_RHSa_Min_MA';C8_RHSa_Min_M
A'];
   CAV_RHSa_Min = mean(CAll_RHSa_Min,'omitnan');

CAll_LHSy_Max                                                                                              =
[C1_LHSy_Max_MA';C2_LHSy_Max_MA';C3_LHSy_Max_MA';C6_LHSy_Max_MA';C7_LHSy_Max_MA';C8_LHSy_Max_M
A'];
  CAV_LHSy_Max = mean(CAll_LHSy_Max,'omitnan');
 CAll_LHSy_0                                                                                                =
[C1_LHSy_0_MA';C2_LHSy_0_MA';C3_LHSy_0_MA';C6_LHSy_0_MA';C7_LHSy_0_MA';C8_LHSy_0_MA'];
  CAV_LHSy_0 = mean(CAll_LHSy_0,'omitnan');
 CAll_LHSy_Min                                                                                              =
[C1_LHSy_Min_MA';C2_LHSy_Min_MA';C3_LHSy_Min_MA';C6_LHSy_Min_MA';C7_LHSy_Min_MA';C8_LHSy_Min_M
A'];
   CAV_LHSy_Min = mean(CAll_LHSy_Min,'omitnan');

  CAll_LHSx_Max                                                                                              =
[C1_LHSx_Max_MA';C2_LHSx_Max_MA';C3_LHSx_Max_MA';C6_LHSx_Max_MA';C7_LHSx_Max_MA';C8_LHSx_Max_M
A'];
  CAV_LHSx_Max = mean(CAll_LHSx_Max,'omitnan');
 CAll_LHSx_0                                                                                                =
[C1_LHSx_0_MA';C2_LHSx_0_MA';C3_LHSx_0_MA';C6_LHSx_0_MA';C7_LHSx_0_MA';C8_LHSx_0_MA'];
  CAV_LHSx_0 = mean(CAll_LHSx_0,'omitnan');
 CAll_LHSx_Min                                                                                              =
[C1_LHSx_Min_MA';C2_LHSx_Min_MA';C3_LHSx_Min_MA';C6_LHSx_Min_MA';C7_LHSx_Min_MA';C8_LHSx_Min_M
A'];
   CAV_LHSx_Min = mean(CAll_LHSx_Min,'omitnan');
```

```
CAll_LHSa_Max                                                                    =
[C1_LHSa_Max_MA';C2_LHSa_Max_MA';C3_LHSa_Max_MA';C6_LHSa_Max_MA';C7_LHSa_Max_MA';C8_LHSa_Max_M
A'];
  CAV_LHSa_Max = mean(CAll_LHSa_Max,'omitnan');
 CAll_LHSa_0                                                                     =
[C1_LHSa_0_MA';C2_LHSa_0_MA';C3_LHSa_0_MA';C6_LHSa_0_MA';C7_LHSa_0_MA';C8_LHSa_0_MA'];
  CAV_LHSa_0 = mean(CAll_LHSa_0,'omitnan');
 CAll_LHSa_Min                                                                   =
[C1_LHSa_Min_MA';C2_LHSa_Min_MA';C3_LHSa_Min_MA';C6_LHSa_Min_MA';C7_LHSa_Min_MA';C8_LHSa_Min_M
A'];
   CAV_LHSa_Min = mean(CAll_LHSa_Min,'omitnan');

%Calculate average of average Novels
 NALL_RHSy_Max                                                                   =
[N1_RHSy_Max_MA';N2_RHSy_Max_MA';N3_RHSy_Max_MA';N4_RHSy_Max_MA';N5_RHSy_Max_MA';N6_RHSy_Max_M
A'];
  NAV_RHSy_Max = mean(NALL_RHSy_Max,'omitnan');
 NALL_RHSy_0                                                                     =
[N1_RHSy_0_MA';N2_RHSy_0_MA';N3_RHSy_0_MA';N4_RHSy_0_MA';N5_RHSy_0_MA';N6_RHSy_0_MA'];
  NAV_RHSy_0 = mean(NALL_RHSy_0,'omitnan');
 NALL_RHSy_Min                                                                   =
[N1_RHSy_Min_MA';N2_RHSy_Min_MA';N3_RHSy_Min_MA';N4_RHSy_Min_MA';N5_RHSy_Min_MA';N6_RHSy_Min_M
A'];
   NAV_RHSy_Min = mean(NALL_RHSy_Min,'omitnan');

  NALL_RHSx_Max                                                                  =
[N1_RHSx_Max_MA';N2_RHSx_Max_MA';N3_RHSx_Max_MA';N4_RHSx_Max_MA';N5_RHSx_Max_MA';N6_RHSx_Max_M
A'];
  NAV_RHSx_Max = mean(NALL_RHSx_Max,'omitnan');
 NALL_RHSx_0                                                                     =
[N1_RHSx_0_MA';N2_RHSx_0_MA';N3_RHSx_0_MA';N4_RHSx_0_MA';N5_RHSx_0_MA';N6_RHSx_0_MA'];
  NAV_RHSx_0 = mean(NALL_RHSx_0,'omitnan');
 NALL_RHSx_Min                                                                   =
[N1_RHSx_Min_MA';N2_RHSx_Min_MA';N3_RHSx_Min_MA';N4_RHSx_Min_MA';N5_RHSx_Min_MA';N6_RHSx_Min_M
A'];
   NAV_RHSx_Min = mean(NALL_RHSx_Min,'omitnan');

NALL_RHSa_Max                                                                    =
[N1_RHSa_Max_MA';N2_RHSa_Max_MA';N3_RHSa_Max_MA';N4_RHSa_Max_MA';N5_RHSa_Max_MA';N6_RHSa_Max_M
A'];
  NAV_RHSa_Max = mean(NALL_RHSa_Max,'omitnan');
 NALL_RHSa_0                                  =                                  [N1_RHSa_0_MA';
N2_RHSa_0_MA';N3_RHSa_0_MA';N4_RHSa_0_MA';N5_RHSa_0_MA';N6_RHSa_0_MA'];
  NAV_RHSa_0 = mean(NALL_RHSa_0,'omitnan');
 NALL_RHSa_Min                                                                   =
[N1_RHSa_Min_MA';N2_RHSa_Min_MA';N3_RHSa_Min_MA';N4_RHSa_Min_MA';N5_RHSa_Min_MA';N6_RHSa_Min_M
A'];
   NAV_RHSa_Min = mean(NALL_RHSa_Min,'omitnan');

NALL_LHSy_Max                                                                    =
[N1_LHSy_Max_MA';N2_LHSy_Max_MA';N3_LHSy_Max_MA';N4_LHSy_Max_MA';N5_LHSy_Max_MA';N6_LHSy_Max_M
A'];
  NAV_LHSy_Max = mean(NALL_LHSy_Max,'omitnan');
 NALL_LHSy_0                                                                     =
[N1_LHSy_0_MA';N2_LHSy_0_MA';N3_LHSy_0_MA';N4_LHSy_0_MA';N5_LHSy_0_MA';N6_LHSy_0_MA'];
  NAV_LHSy_0 = mean(NALL_LHSy_0,'omitnan');
 NALL_LHSy_Min                                                                   =
[N1_LHSy_Min_MA';N2_LHSy_Min_MA';N3_LHSy_Min_MA';N4_LHSy_Min_MA';N5_LHSy_Min_MA';N6_LHSy_Min_M
A'];
   NAV_LHSy_Min = mean(NALL_LHSy_Min,'omitnan');

  NALL_LHSx_Max                                                                  =
[N1_LHSx_Max_MA';N2_LHSx_Max_MA';N3_LHSx_Max_MA';N4_LHSx_Max_MA';N5_LHSx_Max_MA';N6_LHSx_Max_M
A'];
  NAV_LHSx_Max = mean(NALL_LHSx_Max,'omitnan');
 NALL_LHSx_0                                                                     =
[N1_LHSx_0_MA';N2_LHSx_0_MA';N3_LHSx_0_MA';N4_LHSx_0_MA';N5_LHSx_0_MA';N6_LHSx_0_MA'];
  NAV_LHSx_0 = mean(NALL_LHSx_0,'omitnan');
 NALL_LHSx_Min                                                                   =
[N1_LHSx_Min_MA';N2_LHSx_Min_MA';N3_LHSx_Min_MA';N4_LHSx_Min_MA';N5_LHSx_Min_MA';N6_LHSx_Min_M
A'];
   NAV_LHSx_Min = mean(NALL_LHSx_Min,'omitnan');

NALL_LHSa_Max                                                                    =
[N1_LHSa_Max_MA';N2_LHSa_Max_MA';N3_LHSa_Max_MA';N4_LHSa_Max_MA';N5_LHSa_Max_MA';N6_LHSa_Max_M
A'];
  NAV_LHSa_Max = mean(NALL_LHSa_Max,'omitnan');
```

```
 NALL_LHSa_0                                                                                    =
[N1_LHSa_0_MA';N2_LHSa_0_MA';N3_LHSa_0_MA';N4_LHSa_0_MA';N5_LHSa_0_MA';N6_LHSa_0_MA'];
  NAV_LHSa_0 = mean(NALL_LHSa_0,'omitnan');
 NALL_LHSa_Min                                                                                  =
[N1_LHSa_Min_MA';N2_LHSa_Min_MA';N3_LHSa_Min_MA';N4_LHSa_Min_MA';N5_LHSa_Min_MA';N6_LHSa_Min_M
A'];
   NAV_LHSa_Min = mean(NALL_LHSa_Min,'omitnan');

 %Calculate standard deviations of all average vectors

   CSTD_RHSy_Max = std(CAll_RHSy_Max,1,'omitnan');
   CSTD_RHSy_0 = std(CAll_RHSy_0,1,'omitnan');
   CSTD_RHSy_Min = std(CAll_RHSy_Min,1,'omitnan');

   CSTD_RHSx_Max = std(CAll_RHSx_Max,1,'omitnan');
   CSTD_RHSx_0 = std(CAll_RHSx_0,1,1,'omitnan');
   CSTD_RHSx_Min = std(CAll_RHSx_Min,1,1,'omitnan');

   CSTD_RHSa_Max = std(CAll_RHSa_Max,1,'omitnan');
   CSTD_RHSa_0 = std(CAll_RHSa_0,1,'omitnan');
   CSTD_RHSa_Min = std(CAll_RHSa_Min,1,'omitnan');

   CSTD_LHSy_Max = std(CAll_LHSy_Max,1,'omitnan');
   CSTD_LHSy_0 = std(CAll_LHSy_0,1,'omitnan');
   CSTD_LHSy_Min = std(CAll_LHSy_Min,1,'omitnan');

   CSTD_LHSx_Max = std(CAll_LHSx_Max,1,'omitnan');
   CSTD_LHSx_0 = std(CAll_LHSx_0,1,'omitnan');
   CSTD_LHSx_Min = std(CAll_LHSx_Min,1,'omitnan');

   CSTD_LHSa_Max = std(CAll_LHSa_Max,1,'omitnan');
   CSTD_LHSa_0 = std(CAll_LHSa_0,1,'omitnan');
   CSTD_LHSa_Min = std(CAll_LHSa_Min,1,'omitnan');

   NSTD_RHSy_Max = std(NALL_RHSy_Max,1,'omitnan');
   NSTD_RHSy_0 = std(NALL_RHSy_0,1,'omitnan');
   NSTD_RHSy_Min = std(NALL_RHSy_Min,1,'omitnan');

   NSTD_RHSx_Max = std(NALL_RHSx_Max,1,'omitnan');
   NSTD_RHSx_0 = std(NALL_RHSx_0,1,'omitnan');
   NSTD_RHSx_Min = std(NALL_RHSx_Min,1,'omitnan');

   NSTD_RHSa_Max = std(NALL_RHSa_Max,'omitnan');
   NSTD_RHSa_0 = std(NALL_RHSa_0,1,'omitnan');
   NSTD_RHSa_Min = std(NALL_RHSa_Min,1,'omitnan');

   NSTD_LHSy_Max = std(NALL_LHSy_Max,1,'omitnan');
   NSTD_LHSy_0 = std(NALL_LHSy_0,1,'omitnan');
   NSTD_LHSy_Min = std(NALL_LHSy_Min,1,'omitnan');

   NSTD_LHSx_Max = std(NALL_LHSx_Max,1,'omitnan');
   NSTD_LHSx_0 = std(NALL_LHSx_0,1,'omitnan');
   NSTD_LHSx_Min = std(NALL_LHSx_Min,1,'omitnan');

   NSTD_LHSa_Max = std(NALL_LHSa_Max,1,'omitnan');
   NSTD_LHSa_0 = std(NALL_LHSa_0,1,'omitnan');
   NSTD_LHSa_Min = std(NALL_LHSa_Min,1,'omitnan');

  %Calculate + and - std vectors for max and min positions
  shade_vector_length = 1;

  for i = 1:vector_length
      if shade_vector_length == 1
       if isnan(C1_Cycle_MaxMin(i))
          shade_vector_length = i-1;
       end
      end
  end

  %STD plusminus vectors for edges

  for i = 1:shade_vector_length

  CSTD_RHSy_Max_PLUS(i) = CAV_RHSy_Max(i) + CSTD_RHSy_Max(i);
  CSTD_RHSy_Max_MINUS(i) = CAV_RHSy_Max(i) - CSTD_RHSy_Max(i);
  CSTD_RHSy_Min_PLUS(i) = CAV_RHSy_Min(i) + CSTD_RHSy_Min(i);
  CSTD_RHSy_Min_MINUS(i) = CAV_RHSy_Min(i) - CSTD_RHSy_Min(i);
```

```
if isnan(CSTD_RHSy_Max_PLUS(i))
CSTD_RHSy_Max_PLUS(i)= CSTD_RHSy_Max_PLUS(i-1);
end
if isnan(CSTD_RHSy_Max_MINUS(i))
CSTD_RHSy_Max_MINUS(i)= CSTD_RHSy_Max_MINUS(i-1);
end
if isnan(CSTD_RHSy_Min_PLUS(i))
CSTD_RHSy_Min_PLUS(i)= CSTD_RHSy_Min_PLUS(i-1);
end
if isnan(CSTD_RHSy_Min_MINUS(i))
CSTD_RHSy_Min_MINUS(i)= CSTD_RHSy_Min_MINUS(i-1);
end

  CSTD_RHSx_Max_PLUS(i) = CAV_RHSx_Max(i) + CSTD_RHSx_Max(i);
  CSTD_RHSx_Max_MINUS(i) = CAV_RHSx_Max(i) - CSTD_RHSx_Max(i);
  CSTD_RHSx_Min_PLUS(i) = CAV_RHSx_Min(i) + CSTD_RHSx_Min(i);
  CSTD_RHSx_Min_MINUS(i) = CAV_RHSx_Min(i) - CSTD_RHSx_Min(i);

if isnan(CSTD_RHSx_Max_PLUS(i))
CSTD_RHSx_Max_PLUS(i)= CSTD_RHSx_Max_PLUS(i-1);
end
if isnan(CSTD_RHSx_Max_MINUS(i))
CSTD_RHSx_Max_MINUS(i)= CSTD_RHSx_Max_MINUS(i-1);
end
if isnan(CSTD_RHSx_Min_PLUS(i))
CSTD_RHSx_Min_PLUS(i)= CSTD_RHSx_Min_PLUS(i-1);
end
if isnan(CSTD_RHSx_Min_MINUS(i))
CSTD_RHSx_Min_MINUS(i)= CSTD_RHSx_Min_MINUS(i-1);
end
  CSTD_RHSa_Max_PLUS(i) = CAV_RHSa_Max(i) + CSTD_RHSa_Max(i);
  CSTD_RHSa_Max_MINUS(i) = CAV_RHSa_Max(i) - CSTD_RHSa_Max(i);
  CSTD_RHSa_Min_PLUS(i) = CAV_RHSa_Min(i) + CSTD_RHSa_Min(i);
  CSTD_RHSa_Min_MINUS(i) = CAV_RHSa_Min(i) - CSTD_RHSa_Min(i);

if isnan(CSTD_RHSa_Max_PLUS(i))
CSTD_RHSa_Max_PLUS(i)= CSTD_RHSa_Max_PLUS(i-1);
end
if isnan(CSTD_RHSa_Max_MINUS(i))
CSTD_RHSa_Max_MINUS(i)= CSTD_RHSa_Max_MINUS(i-1);
end
if isnan(CSTD_RHSa_Min_PLUS(i))
CSTD_RHSa_Min_PLUS(i)= CSTD_RHSa_Min_PLUS(i-1);
end
if isnan(CSTD_RHSa_Min_MINUS(i))
CSTD_RHSa_Min_MINUS(i)= CSTD_RHSa_Min_MINUS(i-1);
end

  CSTD_LHSy_Max_PLUS(i) = CAV_LHSy_Max(i) + CSTD_LHSy_Max(i);
  CSTD_LHSy_Max_MINUS(i) = CAV_LHSy_Max(i) - CSTD_LHSy_Max(i);
  CSTD_LHSy_Min_PLUS(i) = CAV_LHSy_Min(i) + CSTD_LHSy_Min(i);
  CSTD_LHSy_Min_MINUS(i) = CAV_LHSy_Min(i) - CSTD_LHSy_Min(i);

if isnan(CSTD_LHSy_Max_PLUS(i))
CSTD_LHSy_Max_PLUS(i)= CSTD_LHSy_Max_PLUS(i-1);
end
if isnan(CSTD_LHSy_Max_MINUS(i))
CSTD_LHSy_Max_MINUS(i)= CSTD_LHSy_Max_MINUS(i-1);
end
if isnan(CSTD_LHSy_Min_PLUS(i))
CSTD_LHSy_Min_PLUS(i)= CSTD_LHSy_Min_PLUS(i-1);
end
if isnan(CSTD_LHSy_Min_MINUS(i))
CSTD_LHSy_Min_MINUS(i)= CSTD_LHSy_Min_MINUS(i-1);
end

  CSTD_LHSx_Max_PLUS(i) = CAV_LHSx_Max(i) + CSTD_LHSx_Max(i);
  CSTD_LHSx_Max_MINUS(i) = CAV_LHSx_Max(i) - CSTD_LHSx_Max(i);
  CSTD_LHSx_Min_PLUS(i) = CAV_LHSx_Min(i) + CSTD_LHSx_Min(i);
  CSTD_LHSx_Min_MINUS(i) = CAV_LHSx_Min(i) - CSTD_LHSx_Min(i);

if isnan(CSTD_LHSx_Max_PLUS(i))
CSTD_LHSx_Max_PLUS(i)= CSTD_LHSx_Max_PLUS(i-1);
end
if isnan(CSTD_LHSx_Max_MINUS(i))
CSTD_LHSx_Max_MINUS(i)= CSTD_LHSx_Max_MINUS(i-1);
```

```
end
if isnan(CSTD_LHSx_Min_PLUS(i))
CSTD_LHSx_Min_PLUS(i)= CSTD_LHSx_Min_PLUS(i-1);
end
if isnan(CSTD_LHSx_Min_MINUS(i))
CSTD_LHSx_Min_MINUS(i)= CSTD_LHSx_Min_MINUS(i-1);
end
  CSTD_LHSa_Max_PLUS(i) = CAV_LHSa_Max(i) + CSTD_LHSa_Max(i);
  CSTD_LHSa_Max_MINUS(i) = CAV_LHSa_Max(i) - CSTD_LHSa_Max(i);
  CSTD_LHSa_Min_PLUS(i) = CAV_LHSa_Min(i) + CSTD_LHSa_Min(i);
  CSTD_LHSa_Min_MINUS(i) = CAV_LHSa_Min(i) - CSTD_LHSa_Min(i);

if isnan(CSTD_LHSa_Max_PLUS(i))
CSTD_LHSa_Max_PLUS(i)= CSTD_LHSa_Max_PLUS(i-1);
end
if isnan(CSTD_LHSa_Max_MINUS(i))
CSTD_LHSa_Max_MINUS(i)= CSTD_LHSa_Max_MINUS(i-1);
end
if isnan(CSTD_LHSa_Min_PLUS(i))
CSTD_LHSa_Min_PLUS(i)= CSTD_LHSa_Min_PLUS(i-1);
end
if isnan(CSTD_LHSa_Min_MINUS(i))
CSTD_LHSa_Min_MINUS(i)= CSTD_LHSa_Min_MINUS(i-1);
end

NSTD_RHSy_Max_PLUS(i) = NAV_RHSy_Max(i) + NSTD_RHSy_Max(i);
  NSTD_RHSy_Max_MINUS(i) = NAV_RHSy_Max(i) - NSTD_RHSy_Max(i);
  NSTD_RHSy_Min_PLUS(i) = NAV_RHSy_Min(i) + NSTD_RHSy_Min(i);
  NSTD_RHSy_Min_MINUS(i) = NAV_RHSy_Min(i) - NSTD_RHSy_Min(i);

if isnan(NSTD_RHSy_Max_PLUS(i))
NSTD_RHSy_Max_PLUS(i)= NSTD_RHSy_Max_PLUS(i-1);
end
if isnan(NSTD_RHSy_Max_MINUS(i))
NSTD_RHSy_Max_MINUS(i)= NSTD_RHSy_Max_MINUS(i-1);
end
if isnan(NSTD_RHSy_Min_PLUS(i))
NSTD_RHSy_Min_PLUS(i)= NSTD_RHSy_Min_PLUS(i-1);
end
if isnan(NSTD_RHSy_Min_MINUS(i))
NSTD_RHSy_Min_MINUS(i)= NSTD_RHSy_Min_MINUS(i-1);
end

  NSTD_RHSx_Max_PLUS(i) = NAV_RHSx_Max(i) + NSTD_RHSx_Max(i);
  NSTD_RHSx_Max_MINUS(i) = NAV_RHSx_Max(i) - NSTD_RHSx_Max(i);
  NSTD_RHSx_Min_PLUS(i) = NAV_RHSx_Min(i) + NSTD_RHSx_Min(i);
  NSTD_RHSx_Min_MINUS(i) = NAV_RHSx_Min(i) - NSTD_RHSx_Min(i);

if isnan(NSTD_RHSx_Max_PLUS(i))
NSTD_RHSx_Max_PLUS(i)= NSTD_RHSx_Max_PLUS(i-1);
end
if isnan(NSTD_RHSx_Max_MINUS(i))
NSTD_RHSx_Max_MINUS(i)= NSTD_RHSx_Max_MINUS(i-1);
end
if isnan(NSTD_RHSx_Min_PLUS(i))
NSTD_RHSx_Min_PLUS(i)= NSTD_RHSx_Min_PLUS(i-1);
end
if isnan(NSTD_RHSx_Min_MINUS(i))
NSTD_RHSx_Min_MINUS(i)= NSTD_RHSx_Min_MINUS(i-1);
end
  NSTD_RHSa_Max_PLUS(i) = NAV_RHSa_Max(i) + NSTD_RHSa_Max(i);
  NSTD_RHSa_Max_MINUS(i) = NAV_RHSa_Max(i) - NSTD_RHSa_Max(i);
  NSTD_RHSa_Min_PLUS(i) = NAV_RHSa_Min(i) + NSTD_RHSa_Min(i);
  NSTD_RHSa_Min_MINUS(i) = NAV_RHSa_Min(i) - NSTD_RHSa_Min(i);

if isnan(NSTD_RHSa_Max_PLUS(i))
NSTD_RHSa_Max_PLUS(i)= NSTD_RHSa_Max_PLUS(i-1);
end
if isnan(NSTD_RHSa_Max_MINUS(i))
NSTD_RHSa_Max_MINUS(i)= NSTD_RHSa_Max_MINUS(i-1);
end
if isnan(NSTD_RHSa_Min_PLUS(i))
NSTD_RHSa_Min_PLUS(i)= NSTD_RHSa_Min_PLUS(i-1);
end
if isnan(NSTD_RHSa_Min_MINUS(i))
NSTD_RHSa_Min_MINUS(i)= NSTD_RHSa_Min_MINUS(i-1);
end
```

```
  NSTD_LHSy_Max_PLUS(i) = NAV_LHSy_Max(i) + NSTD_LHSy_Max(i);
  NSTD_LHSy_Max_MINUS(i) = NAV_LHSy_Max(i) - NSTD_LHSy_Max(i);
  NSTD_LHSy_Min_PLUS(i) = NAV_LHSy_Min(i) + NSTD_LHSy_Min(i);
  NSTD_LHSy_Min_MINUS(i) = NAV_LHSy_Min(i) - NSTD_LHSy_Min(i);

if isnan(NSTD_LHSy_Max_PLUS(i))
NSTD_LHSy_Max_PLUS(i)= NSTD_LHSy_Max_PLUS(i-1);
end
if isnan(NSTD_LHSy_Max_MINUS(i))
NSTD_LHSy_Max_MINUS(i)= NSTD_LHSy_Max_MINUS(i-1);
end
if isnan(NSTD_LHSy_Min_PLUS(i))
NSTD_LHSy_Min_PLUS(i)= NSTD_LHSy_Min_PLUS(i-1);
end
if isnan(NSTD_LHSy_Min_MINUS(i))
NSTD_LHSy_Min_MINUS(i)= NSTD_LHSy_Min_MINUS(i-1);
end

  NSTD_LHSx_Max_PLUS(i) = NAV_LHSx_Max(i) + NSTD_LHSx_Max(i);
  NSTD_LHSx_Max_MINUS(i) = NAV_LHSx_Max(i) - NSTD_LHSx_Max(i);
  NSTD_LHSx_Min_PLUS(i) = NAV_LHSx_Min(i) + NSTD_LHSx_Min(i);
  NSTD_LHSx_Min_MINUS(i) = NAV_LHSx_Min(i) - NSTD_LHSx_Min(i);

if isnan(NSTD_LHSx_Max_PLUS(i))
NSTD_LHSx_Max_PLUS(i)= NSTD_LHSx_Max_PLUS(i-1);
end
if isnan(NSTD_LHSx_Max_MINUS(i))
NSTD_LHSx_Max_MINUS(i)= NSTD_LHSx_Max_MINUS(i-1);
end
if isnan(NSTD_LHSx_Min_PLUS(i))
NSTD_LHSx_Min_PLUS(i)= NSTD_LHSx_Min_PLUS(i-1);
end
if isnan(NSTD_LHSx_Min_MINUS(i))
NSTD_LHSx_Min_MINUS(i)= NSTD_LHSx_Min_MINUS(i-1);
end
  NSTD_LHSa_Max_PLUS(i) = NAV_LHSa_Max(i) + NSTD_LHSa_Max(i);
  NSTD_LHSa_Max_MINUS(i) = NAV_LHSa_Max(i) - NSTD_LHSa_Max(i);
  NSTD_LHSa_Min_PLUS(i) = NAV_LHSa_Min(i) + NSTD_LHSa_Min(i);
  NSTD_LHSa_Min_MINUS(i) = NAV_LHSa_Min(i) - NSTD_LHSa_Min(i);

if isnan(NSTD_LHSa_Max_PLUS(i))
NSTD_LHSa_Max_PLUS(i)= NSTD_LHSa_Max_PLUS(i-1);
end
if isnan(NSTD_LHSa_Max_MINUS(i))
NSTD_LHSa_Max_MINUS(i)= NSTD_LHSa_Max_MINUS(i-1);
end
if isnan(NSTD_LHSa_Min_PLUS(i))
NSTD_LHSa_Min_PLUS(i)= NSTD_LHSa_Min_PLUS(i-1);
end
if isnan(NSTD_LHSa_Min_MINUS(i))
NSTD_LHSa_Min_MINUS(i)= NSTD_LHSa_Min_MINUS(i-1);
end

%Create cycle vectors for shade plot
Cycle_shade_MaxMin(i) = C1_Cycle_MaxMin(i);
if isnan(Cycle_shade_MaxMin(i))
    Cycle_shade_MaxMin(i) = 100000;
end
  end

  %Calculate + and - std vectors for 0 position

  for i = 1:vector_length
       if isnan(C1_Cycle_0(i))
          shade_vector_length_0 = i-1;
          i = vector_length;
       else
           shade_vector_length_0 = vector_length;
       end
  end

  %STD plusminus vectors for centroid
  for i = 1:shade_vector_length_0

CSTD_RHSy_0_PLUS(i) = CAV_RHSy_0(i) + CSTD_RHSy_0(i);
CSTD_RHSy_0_MINUS(i) = CAV_RHSy_0(i) - CSTD_RHSy_0(i);
```

```
if isnan(CSTD_RHSy_0_PLUS(i))
CSTD_RHSy_0_PLUS(i)= CSTD_RHSy_0_PLUS(i-1);
end
if isnan(CSTD_RHSy_0_MINUS(i))
CSTD_RHSy_0_MINUS(i)= CSTD_RHSy_0_MINUS(i-1);
end

  CSTD_RHSx_0_PLUS(i) = CAV_RHSx_0(i) + CSTD_RHSx_0(i);
  CSTD_RHSx_0_MINUS(i) = CAV_RHSx_0(i) - CSTD_RHSx_0(i);

if isnan(CSTD_RHSx_0_PLUS(i))
CSTD_RHSx_0_PLUS(i)= CSTD_RHSx_0_PLUS(i-1);
end
if isnan(CSTD_RHSx_0_MINUS(i))
CSTD_RHSx_0_MINUS(i)= CSTD_RHSx_0_MINUS(i-1);
end

  CSTD_RHSa_0_PLUS(i) = CAV_RHSa_0(i) + CSTD_RHSa_0(i);
  CSTD_RHSa_0_MINUS(i) = CAV_RHSa_0(i) - CSTD_RHSa_0(i);

if isnan(CSTD_RHSa_0_PLUS(i))
CSTD_RHSa_0_PLUS(i)= CSTD_RHSa_0_PLUS(i-1);
end
if isnan(CSTD_RHSa_0_MINUS(i))
CSTD_RHSa_0_MINUS(i)= CSTD_RHSa_0_MINUS(i-1);
end

  CSTD_LHSy_0_PLUS(i) = CAV_LHSy_0(i) + CSTD_LHSy_0(i);
  CSTD_LHSy_0_MINUS(i) = CAV_LHSy_0(i) - CSTD_LHSy_0(i);

if isnan(CSTD_LHSy_0_PLUS(i))
CSTD_LHSy_0_PLUS(i)= CSTD_LHSy_0_PLUS(i-1);
end
if isnan(CSTD_LHSy_0_MINUS(i))
CSTD_LHSy_0_MINUS(i)= CSTD_LHSy_0_MINUS(i-1);
end

  CSTD_LHSx_0_PLUS(i) = CAV_LHSx_0(i) + CSTD_LHSx_0(i);
  CSTD_LHSx_0_MINUS(i) = CAV_LHSx_0(i) - CSTD_LHSx_0(i);

if isnan(CSTD_LHSx_0_PLUS(i))
CSTD_LHSx_0_PLUS(i)= CSTD_LHSx_0_PLUS(i-1);
end
if isnan(CSTD_LHSx_0_MINUS(i))
CSTD_LHSx_0_MINUS(i)= CSTD_LHSx_0_MINUS(i-1);
end

  CSTD_LHSa_0_PLUS(i) = CAV_LHSa_0(i) + CSTD_LHSa_0(i);
  CSTD_LHSa_0_MINUS(i) = CAV_LHSa_0(i) - CSTD_LHSa_0(i);

if isnan(CSTD_LHSa_0_PLUS(i))
CSTD_LHSa_0_PLUS(i)= CSTD_LHSa_0_PLUS(i-1);
end
if isnan(CSTD_LHSa_0_MINUS(i))
CSTD_LHSa_0_MINUS(i)= CSTD_LHSa_0_MINUS(i-1);
end

  NSTD_RHSy_0_PLUS(i) = NAV_RHSy_0(i) + NSTD_RHSy_0(i);
  NSTD_RHSy_0_MINUS(i) = NAV_RHSy_0(i) - NSTD_RHSy_0(i);

if isnan(NSTD_RHSy_0_PLUS(i))
NSTD_RHSy_0_PLUS(i)= NSTD_RHSy_0_PLUS(i-1);
end
if isnan(NSTD_RHSy_0_MINUS(i))
NSTD_RHSy_0_MINUS(i)= NSTD_RHSy_0_MINUS(i-1);
end

  NSTD_RHSx_0_PLUS(i) = NAV_RHSx_0(i) + NSTD_RHSx_0(i);
  NSTD_RHSx_0_MINUS(i) = NAV_RHSx_0(i) - NSTD_RHSx_0(i);

if isnan(NSTD_RHSx_0_PLUS(i))
NSTD_RHSx_0_PLUS(i)= NSTD_RHSx_0_PLUS(i-1);
end
if isnan(NSTD_RHSx_0_MINUS(i))
NSTD_RHSx_0_MINUS(i)= NSTD_RHSx_0_MINUS(i-1);
```

```
end

  NSTD_RHSa_0_PLUS(i) = NAV_RHSa_0(i) + NSTD_RHSa_0(i);
  NSTD_RHSa_0_MINUS(i) = NAV_RHSa_0(i) - NSTD_RHSa_0(i);

if isnan(NSTD_RHSa_0_PLUS(i))
NSTD_RHSa_0_PLUS(i)= NSTD_RHSa_0_PLUS(i-1);
end
if isnan(NSTD_RHSa_0_MINUS(i))
NSTD_RHSa_0_MINUS(i)= NSTD_RHSa_0_MINUS(i-1);
end

  NSTD_LHSy_0_PLUS(i) = NAV_LHSy_0(i) + NSTD_LHSy_0(i);
  NSTD_LHSy_0_MINUS(i) = NAV_LHSy_0(i) - NSTD_LHSy_0(i);

if isnan(NSTD_LHSy_0_PLUS(i))
NSTD_LHSy_0_PLUS(i)= NSTD_LHSy_0_PLUS(i-1);
end
if isnan(NSTD_LHSy_0_MINUS(i))
NSTD_LHSy_0_MINUS(i)= NSTD_LHSy_0_MINUS(i-1);
end

  NSTD_LHSx_0_PLUS(i) = NAV_LHSx_0(i) + NSTD_LHSx_0(i);
  NSTD_LHSx_0_MINUS(i) = NAV_LHSx_0(i) - NSTD_LHSx_0(i);

if isnan(NSTD_LHSx_0_PLUS(i))
NSTD_LHSx_0_PLUS(i)= NSTD_LHSx_0_PLUS(i-1);
end
if isnan(NSTD_LHSx_0_MINUS(i))
NSTD_LHSx_0_MINUS(i)= NSTD_LHSx_0_MINUS(i-1);
end

  NSTD_LHSa_0_PLUS(i) = NAV_LHSa_0(i) + NSTD_LHSa_0(i);
  NSTD_LHSa_0_MINUS(i) = NAV_LHSa_0(i) - NSTD_LHSa_0(i);

if isnan(NSTD_LHSa_0_PLUS(i))
NSTD_LHSa_0_PLUS(i)= NSTD_LHSa_0_PLUS(i-1);
end
if isnan(NSTD_LHSa_0_MINUS(i))
NSTD_LHSa_0_MINUS(i)= NSTD_LHSa_0_MINUS(i-1);
end


Cycle_shade_0(i) = C1_Cycle_0(i);
if isnan(Cycle_shade_0(i))
    Cycle_shade_0(i) = 100000;
end
  end

%%%%%%%%%%%%%%%%%%%%%%%%%%%%%%%%%%%%%%%%%%%%%%%%%%%%%%%%%%%%
%STEP 4
%CALCULATE DEFLECTION AROUND THE NEUTRAL VALUES FOR CONTROL AND NOVEL

%Calculate control tension and compression deflections

%Control C1
%Specify matrix sizes to account for double measurement at centre

C1_RHSy_deltaT = NaN(1, vector_length/2);
C1_RHSy_deltaC = NaN(1, vector_length/2);
C1_LHSy_deltaT = NaN(1, vector_length/2);
C1_LHSy_deltaC = NaN(1, vector_length/2);

C1_RHSx_deltaT = NaN(1, vector_length/2);
C1_RHSx_deltaC = NaN(1, vector_length/2);
C1_LHSx_deltaT = NaN(1, vector_length/2);
C1_LHSx_deltaC = NaN(1, vector_length/2);

C1_RHSa_deltaT = NaN(1, vector_length/2);
C1_RHSa_deltaC = NaN(1, vector_length/2);
C1_LHSa_deltaT = NaN(1, vector_length/2);
C1_LHSa_deltaC = NaN(1, vector_length/2);

C2_RHSy_deltaT = NaN(1, vector_length/2);
C2_RHSy_deltaC = NaN(1, vector_length/2);
C2_LHSy_deltaT = NaN(1, vector_length/2);
C2_LHSy_deltaC = NaN(1, vector_length/2);
```

```
C2_RHSx_deltaT = NaN(1, vector_length/2);
C2_RHSx_deltaC = NaN(1, vector_length/2);
C2_LHSx_deltaT = NaN(1, vector_length/2);
C2_LHSx_deltaC = NaN(1, vector_length/2);

C2_RHSa_deltaT = NaN(1, vector_length/2);
C2_RHSa_deltaC = NaN(1, vector_length/2);
C2_LHSa_deltaT = NaN(1, vector_length/2);
C2_LHSa_deltaC = NaN(1, vector_length/2);

C3_RHSy_deltaT = NaN(1, vector_length/2);
C3_RHSy_deltaC = NaN(1, vector_length/2);
C3_LHSy_deltaT = NaN(1, vector_length/2);
C3_LHSy_deltaC = NaN(1, vector_length/2);

C3_RHSx_deltaT = NaN(1, vector_length/2);
C3_RHSx_deltaC = NaN(1, vector_length/2);
C3_LHSx_deltaT = NaN(1, vector_length/2);
C3_LHSx_deltaC = NaN(1, vector_length/2);

C3_RHSa_deltaT = NaN(1, vector_length/2);
C3_RHSa_deltaC = NaN(1, vector_length/2);
C3_LHSa_deltaT = NaN(1, vector_length/2);
C3_LHSa_deltaC = NaN(1, vector_length/2);

C6_RHSy_deltaT = NaN(1, vector_length/2);
C6_RHSy_deltaC = NaN(1, vector_length/2);
C6_LHSy_deltaT = NaN(1, vector_length/2);
C6_LHSy_deltaC = NaN(1, vector_length/2);

C6_RHSx_deltaT = NaN(1, vector_length/2);
C6_RHSx_deltaC = NaN(1, vector_length/2);
C6_LHSx_deltaT = NaN(1, vector_length/2);
C6_LHSx_deltaC = NaN(1, vector_length/2);

C6_RHSa_deltaT = NaN(1, vector_length/2);
C6_RHSa_deltaC = NaN(1, vector_length/2);
C6_LHSa_deltaT = NaN(1, vector_length/2);
C6_LHSa_deltaC = NaN(1, vector_length/2);

C7_RHSy_deltaT = NaN(1, vector_length/2);
C7_RHSy_deltaC = NaN(1, vector_length/2);
C7_LHSy_deltaT = NaN(1, vector_length/2);
C7_LHSy_deltaC = NaN(1, vector_length/2);

C7_RHSx_deltaT = NaN(1, vector_length/2);
C7_RHSx_deltaC = NaN(1, vector_length/2);
C7_LHSx_deltaT = NaN(1, vector_length/2);
C7_LHSx_deltaC = NaN(1, vector_length/2);

C7_RHSa_deltaT = NaN(1, vector_length/2);
C7_RHSa_deltaC = NaN(1, vector_length/2);
C7_LHSa_deltaT = NaN(1, vector_length/2);
C7_LHSa_deltaC = NaN(1, vector_length/2);

C8_RHSy_deltaT = NaN(1, vector_length/2);
C8_RHSy_deltaC = NaN(1, vector_length/2);
C8_LHSy_deltaT = NaN(1, vector_length/2);
C8_LHSy_deltaC = NaN(1, vector_length/2);

C8_RHSx_deltaT = NaN(1, vector_length/2);
C8_RHSx_deltaC = NaN(1, vector_length/2);
C8_LHSx_deltaT = NaN(1, vector_length/2);
C8_LHSx_deltaC = NaN(1, vector_length/2);

C8_RHSa_deltaT = NaN(1, vector_length/2);
C8_RHSa_deltaC = NaN(1, vector_length/2);
C8_LHSa_deltaT = NaN(1, vector_length/2);
C8_LHSa_deltaC = NaN(1, vector_length/2);

N1_RHSy_deltaT = NaN(1, vector_length/2);
N1_RHSy_deltaC = NaN(1, vector_length/2);
N1_LHSy_deltaT = NaN(1, vector_length/2);
N1_LHSy_deltaC = NaN(1, vector_length/2);

N1_RHSx_deltaT = NaN(1, vector_length/2);
```

```
N1_RHSx_deltaC = NaN(1, vector_length/2);
N1_LHSx_deltaT = NaN(1, vector_length/2);
N1_LHSx_deltaC = NaN(1, vector_length/2);

N1_RHSa_deltaT = NaN(1, vector_length/2);
N1_RHSa_deltaC = NaN(1, vector_length/2);
N1_LHSa_deltaT = NaN(1, vector_length/2);
N1_LHSa_deltaC = NaN(1, vector_length/2);

N2_RHSy_deltaT = NaN(1, vector_length/2);
N2_RHSy_deltaC = NaN(1, vector_length/2);
N2_LHSy_deltaT = NaN(1, vector_length/2);
N2_LHSy_deltaC = NaN(1, vector_length/2);

N2_RHSx_deltaT = NaN(1, vector_length/2);
N2_RHSx_deltaC = NaN(1, vector_length/2);
N2_LHSx_deltaT = NaN(1, vector_length/2);
N2_LHSx_deltaC = NaN(1, vector_length/2);

N2_RHSa_deltaT = NaN(1, vector_length/2);
N2_RHSa_deltaC = NaN(1, vector_length/2);
N2_LHSa_deltaT = NaN(1, vector_length/2);
N2_LHSa_deltaC = NaN(1, vector_length/2);

N3_RHSy_deltaT = NaN(1, vector_length/2);
N3_RHSy_deltaC = NaN(1, vector_length/2);
N3_LHSy_deltaT = NaN(1, vector_length/2);
N3_LHSy_deltaC = NaN(1, vector_length/2);

N3_RHSx_deltaT = NaN(1, vector_length/2);
N3_RHSx_deltaC = NaN(1, vector_length/2);
N3_LHSx_deltaT = NaN(1, vector_length/2);
N3_LHSx_deltaC = NaN(1, vector_length/2);

N3_RHSa_deltaT = NaN(1, vector_length/2);
N3_RHSa_deltaC = NaN(1, vector_length/2);
N3_LHSa_deltaT = NaN(1, vector_length/2);
N3_LHSa_deltaC = NaN(1, vector_length/2);

N4_RHSy_deltaT = NaN(1, vector_length/2);
N4_RHSy_deltaC = NaN(1, vector_length/2);
N4_LHSy_deltaT = NaN(1, vector_length/2);
N4_LHSy_deltaC = NaN(1, vector_length/2);

N4_RHSx_deltaT = NaN(1, vector_length/2);
N4_RHSx_deltaC = NaN(1, vector_length/2);
N4_LHSx_deltaT = NaN(1, vector_length/2);
N4_LHSx_deltaC = NaN(1, vector_length/2);

N4_RHSa_deltaT = NaN(1, vector_length/2);
N4_RHSa_deltaC = NaN(1, vector_length/2);
N4_LHSa_deltaT = NaN(1, vector_length/2);
N4_LHSa_deltaC = NaN(1, vector_length/2);

N5_RHSy_deltaT = NaN(1, vector_length/2);
N5_RHSy_deltaC = NaN(1, vector_length/2);
N5_LHSy_deltaT = NaN(1, vector_length/2);
N5_LHSy_deltaC = NaN(1, vector_length/2);

N5_RHSx_deltaT = NaN(1, vector_length/2);
N5_RHSx_deltaC = NaN(1, vector_length/2);
N5_LHSx_deltaT = NaN(1, vector_length/2);
N5_LHSx_deltaC = NaN(1, vector_length/2);

N5_RHSa_deltaT = NaN(1, vector_length/2);
N5_RHSa_deltaC = NaN(1, vector_length/2);
N5_LHSa_deltaT = NaN(1, vector_length/2);
N5_LHSa_deltaC = NaN(1, vector_length/2);

N6_RHSy_deltaT = NaN(1, vector_length/2);
N6_RHSy_deltaC = NaN(1, vector_length/2);
N6_LHSy_deltaT = NaN(1, vector_length/2);
N6_LHSy_deltaC = NaN(1, vector_length/2);

N6_RHSx_deltaT = NaN(1, vector_length/2);
N6_RHSx_deltaC = NaN(1, vector_length/2);
N6_LHSx_deltaT = NaN(1, vector_length/2);
```

```
N6_LHSx_deltaC = NaN(1, vector_length/2);

N6_RHSa_deltaT = NaN(1, vector_length/2);
N6_RHSa_deltaC = NaN(1, vector_length/2);
N6_LHSa_deltaT = NaN(1, vector_length/2);
N6_LHSa_deltaC = NaN(1, vector_length/2);

C1_Cycle_delta = C1_Cycle_MaxMin(1:vector_length/2);
C2_Cycle_delta = C2_Cycle_MaxMin(1:vector_length/2);
C3_Cycle_delta = C3_Cycle_MaxMin(1:vector_length/2);
C6_Cycle_delta = C6_Cycle_MaxMin(1:vector_length/2);
C7_Cycle_delta = C7_Cycle_MaxMin(1:vector_length/2);
C8_Cycle_delta = C8_Cycle_MaxMin(1:vector_length/2);

N1_Cycle_delta = N1_Cycle_MaxMin(1:vector_length/2);
N2_Cycle_delta = N2_Cycle_MaxMin(1:vector_length/2);
N3_Cycle_delta = N3_Cycle_MaxMin(1:vector_length/2);
N4_Cycle_delta = N4_Cycle_MaxMin(1:vector_length/2);
N5_Cycle_delta = N5_Cycle_MaxMin(1:vector_length/2);
N6_Cycle_delta = N6_Cycle_MaxMin(1:vector_length/2);


loop_length = vector_length/2 - 1;
 for i = 1:loop_length
    C1_RHSy_deltaT(i) = C1_RHSy_Max_MA(i) - C1_RHSy_0_MA(2*i);
    C1_RHSy_deltaC(i) = C1_RHSy_Min_MA(i) - C1_RHSy_0_MA(2*i);
    C1_LHSy_deltaT(i) = C1_LHSy_Min_MA(i) - C1_LHSy_0_MA(2*i);
    C1_LHSy_deltaC(i) = C1_LHSy_Max_MA(i) - C1_LHSy_0_MA(2*i);

    C1_RHSx_deltaT(i) = C1_RHSx_Max_MA(i) - C1_RHSx_0_MA(2*i);
    C1_RHSx_deltaC(i) = C1_RHSx_Min_MA(i) - C1_RHSx_0_MA(2*i);
    C1_LHSx_deltaT(i) = C1_LHSx_Min_MA(i) - C1_LHSx_0_MA(2*i);
    C1_LHSx_deltaC(i) = C1_LHSx_Max_MA(i) - C1_LHSx_0_MA(2*i);

    C1_RHSa_deltaT(i) = C1_RHSa_Max_MA(i) - C1_RHSa_0_MA(2*i);
    C1_RHSa_deltaC(i) = C1_RHSa_Min_MA(i) - C1_RHSa_0_MA(2*i);
    C1_LHSa_deltaT(i) = C1_LHSa_Min_MA(i) - C1_LHSa_0_MA(2*i);
    C1_LHSa_deltaC(i) = C1_LHSa_Max_MA(i) - C1_LHSa_0_MA(2*i);

    C2_RHSy_deltaT(i) = C2_RHSy_Max_MA(i) - C2_RHSy_0_MA(2*i);
    C2_RHSy_deltaC(i) = C2_RHSy_Min_MA(i) - C2_RHSy_0_MA(2*i);
    C2_LHSy_deltaT(i) = C2_LHSy_Min_MA(i) - C2_LHSy_0_MA(2*i);
    C2_LHSy_deltaC(i) = C2_LHSy_Max_MA(i) - C2_LHSy_0_MA(2*i);

    C2_RHSx_deltaT(i) = C2_RHSx_Max_MA(i) - C2_RHSx_0_MA(2*i);
    C2_RHSx_deltaC(i) = C2_RHSx_Min_MA(i) - C2_RHSx_0_MA(2*i);
    C2_LHSx_deltaT(i) = C2_LHSx_Min_MA(i) - C2_LHSx_0_MA(2*i);
    C2_LHSx_deltaC(i) = C2_LHSx_Max_MA(i) - C2_LHSx_0_MA(2*i);

    C2_RHSa_deltaT(i) = C2_RHSa_Max_MA(i) - C2_RHSa_0_MA(2*i);
    C2_RHSa_deltaC(i) = C2_RHSa_Min_MA(i) - C2_RHSa_0_MA(2*i);
    C2_LHSa_deltaT(i) = C2_LHSa_Min_MA(i) - C2_LHSa_0_MA(2*i);
    C2_LHSa_deltaC(i) = C2_LHSa_Max_MA(i) - C2_LHSa_0_MA(2*i);

    C3_RHSy_deltaT(i) = C3_RHSy_Max_MA(i) - C3_RHSy_0_MA(2*i);
    C3_RHSy_deltaC(i) = C3_RHSy_Min_MA(i) - C3_RHSy_0_MA(2*i);
    C3_LHSy_deltaT(i) = C3_LHSy_Min_MA(i) - C3_LHSy_0_MA(2*i);
    C3_LHSy_deltaC(i) = C3_LHSy_Max_MA(i) - C3_LHSy_0_MA(2*i);

    C3_RHSx_deltaT(i) = C3_RHSx_Max_MA(i) - C3_RHSx_0_MA(2*i);
    C3_RHSx_deltaC(i) = C3_RHSx_Min_MA(i) - C3_RHSx_0_MA(2*i);
    C3_LHSx_deltaT(i) = C3_LHSx_Min_MA(i) - C3_LHSx_0_MA(2*i);
    C3_LHSx_deltaC(i) = C3_LHSx_Max_MA(i) - C3_LHSx_0_MA(2*i);

    C3_RHSa_deltaT(i) = C3_RHSa_Max_MA(i) - C3_RHSa_0_MA(2*i);
    C3_RHSa_deltaC(i) = C3_RHSa_Min_MA(i) - C3_RHSa_0_MA(2*i);
    C3_LHSa_deltaT(i) = C3_LHSa_Min_MA(i) - C3_LHSa_0_MA(2*i);
    C3_LHSa_deltaC(i) = C3_LHSa_Max_MA(i) - C3_LHSa_0_MA(2*i);

    C6_RHSy_deltaT(i) = C6_RHSy_Max_MA(i) - C6_RHSy_0_MA(2*i);
    C6_RHSy_deltaC(i) = C6_RHSy_Min_MA(i) - C6_RHSy_0_MA(2*i);
    C6_LHSy_deltaT(i) = C6_LHSy_Min_MA(i) - C6_LHSy_0_MA(2*i);
    C6_LHSy_deltaC(i) = C6_LHSy_Max_MA(i) - C6_LHSy_0_MA(2*i);

    C6_RHSx_deltaT(i) = C6_RHSx_Max_MA(i) - C6_RHSx_0_MA(2*i);
    C6_RHSx_deltaC(i) = C6_RHSx_Min_MA(i) - C6_RHSx_0_MA(2*i);
    C6_LHSx_deltaT(i) = C6_LHSx_Min_MA(i) - C6_LHSx_0_MA(2*i);
```

```
C6_LHSx_deltaC(i) = C6_LHSx_Max_MA(i) - C6_LHSx_0_MA(2*i);

C6_RHSa_deltaT(i) = C6_RHSa_Max_MA(i) - C6_RHSa_0_MA(2*i);
C6_RHSa_deltaC(i) = C6_RHSa_Min_MA(i) - C6_RHSa_0_MA(2*i);
C6_LHSa_deltaT(i) = C6_LHSa_Min_MA(i) - C6_LHSa_0_MA(2*i);
C6_LHSa_deltaC(i) = C6_LHSa_Max_MA(i) - C6_LHSa_0_MA(2*i);

C7_RHSy_deltaT(i) = C7_RHSy_Max_MA(i) - C7_RHSy_0_MA(2*i);
C7_RHSy_deltaC(i) = C7_RHSy_Min_MA(i) - C7_RHSy_0_MA(2*i);
C7_LHSy_deltaT(i) = C7_LHSy_Min_MA(i) - C7_LHSy_0_MA(2*i);
C7_LHSy_deltaC(i) = C7_LHSy_Max_MA(i) - C7_LHSy_0_MA(2*i);

C7_RHSx_deltaT(i) = C7_RHSx_Max_MA(i) - C7_RHSx_0_MA(2*i);
C7_RHSx_deltaC(i) = C7_RHSx_Min_MA(i) - C7_RHSx_0_MA(2*i);
C7_LHSx_deltaT(i) = C7_LHSx_Min_MA(i) - C7_LHSx_0_MA(2*i);
C7_LHSx_deltaC(i) = C7_LHSx_Max_MA(i) - C7_LHSx_0_MA(2*i);

C7_RHSa_deltaT(i) = C7_RHSa_Max_MA(i) - C7_RHSa_0_MA(2*i);
C7_RHSa_deltaC(i) = C7_RHSa_Min_MA(i) - C7_RHSa_0_MA(2*i);
C7_LHSa_deltaT(i) = C7_LHSa_Min_MA(i) - C7_LHSa_0_MA(2*i);
C7_LHSa_deltaC(i) = C7_LHSa_Max_MA(i) - C7_LHSa_0_MA(2*i);

C8_RHSy_deltaT(i) = C8_RHSy_Max_MA(i) - C8_RHSy_0_MA(2*i);
C8_RHSy_deltaC(i) = C8_RHSy_Min_MA(i) - C8_RHSy_0_MA(2*i);
C8_LHSy_deltaT(i) = C8_LHSy_Min_MA(i) - C8_LHSy_0_MA(2*i);
C8_LHSy_deltaC(i) = C8_LHSy_Max_MA(i) - C8_LHSy_0_MA(2*i);

C8_RHSx_deltaT(i) = C8_RHSx_Max_MA(i) - C8_RHSx_0_MA(2*i);
C8_RHSx_deltaC(i) = C8_RHSx_Min_MA(i) - C8_RHSx_0_MA(2*i);
C8_LHSx_deltaT(i) = C8_LHSx_Min_MA(i) - C8_LHSx_0_MA(2*i);
C8_LHSx_deltaC(i) = C8_LHSx_Max_MA(i) - C8_LHSx_0_MA(2*i);

C8_RHSa_deltaT(i) = C8_RHSa_Max_MA(i) - C8_RHSa_0_MA(2*i);
C8_RHSa_deltaC(i) = C8_RHSa_Min_MA(i) - C8_RHSa_0_MA(2*i);
C8_LHSa_deltaT(i) = C8_LHSa_Min_MA(i) - C8_LHSa_0_MA(2*i);
C8_LHSa_deltaC(i) = C8_LHSa_Max_MA(i) - C8_LHSa_0_MA(2*i);

N1_RHSy_deltaT(i) = N1_RHSy_Max_MA(i) - N1_RHSy_0_MA(2*i);
N1_RHSy_deltaC(i) = N1_RHSy_Min_MA(i) - N1_RHSy_0_MA(2*i);
N1_LHSy_deltaT(i) = N1_LHSy_Min_MA(i) - N1_LHSy_0_MA(2*i);
N1_LHSy_deltaC(i) = N1_LHSy_Max_MA(i) - N1_LHSy_0_MA(2*i);

N1_RHSx_deltaT(i) = N1_RHSx_Max_MA(i) - N1_RHSx_0_MA(2*i);
N1_RHSx_deltaC(i) = N1_RHSx_Min_MA(i) - N1_RHSx_0_MA(2*i);
N1_LHSx_deltaT(i) = N1_LHSx_Min_MA(i) - N1_LHSx_0_MA(2*i);
N1_LHSx_deltaC(i) = N1_LHSx_Max_MA(i) - N1_LHSx_0_MA(2*i);

N1_RHSa_deltaT(i) = N1_RHSa_Max_MA(i) - N1_RHSa_0_MA(2*i);
N1_RHSa_deltaC(i) = N1_RHSa_Min_MA(i) - N1_RHSa_0_MA(2*i);
N1_LHSa_deltaT(i) = N1_LHSa_Min_MA(i) - N1_LHSa_0_MA(2*i);
N1_LHSa_deltaC(i) = N1_LHSa_Max_MA(i) - N1_LHSa_0_MA(2*i);

N2_RHSy_deltaT(i) = N2_RHSy_Max_MA(i) - N2_RHSy_0_MA(2*i);
N2_RHSy_deltaC(i) = N2_RHSy_Min_MA(i) - N2_RHSy_0_MA(2*i);
N2_LHSy_deltaT(i) = N2_LHSy_Min_MA(i) - N2_LHSy_0_MA(2*i);
N2_LHSy_deltaC(i) = N2_LHSy_Max_MA(i) - N2_LHSy_0_MA(2*i);

N2_RHSx_deltaT(i) = N2_RHSx_Max_MA(i) - N2_RHSx_0_MA(2*i);
N2_RHSx_deltaC(i) = N2_RHSx_Min_MA(i) - N2_RHSx_0_MA(2*i);
N2_LHSx_deltaT(i) = N2_LHSx_Min_MA(i) - N2_LHSx_0_MA(2*i);
N2_LHSx_deltaC(i) = N2_LHSx_Max_MA(i) - N2_LHSx_0_MA(2*i);

N2_RHSa_deltaT(i) = N2_RHSa_Max_MA(i) - N2_RHSa_0_MA(2*i);
N2_RHSa_deltaC(i) = N2_RHSa_Min_MA(i) - N2_RHSa_0_MA(2*i);
N2_LHSa_deltaT(i) = N2_LHSa_Min_MA(i) - N2_LHSa_0_MA(2*i);
N2_LHSa_deltaC(i) = N2_LHSa_Max_MA(i) - N2_LHSa_0_MA(2*i);

N3_RHSy_deltaT(i) = N3_RHSy_Max_MA(i) - N3_RHSy_0_MA(2*i);
N3_RHSy_deltaC(i) = N3_RHSy_Min_MA(i) - N3_RHSy_0_MA(2*i);
N3_LHSy_deltaT(i) = N3_LHSy_Min_MA(i) - N3_LHSy_0_MA(2*i);
N3_LHSy_deltaC(i) = N3_LHSy_Max_MA(i) - N3_LHSy_0_MA(2*i);

N3_RHSx_deltaT(i) = N3_RHSx_Max_MA(i) - N3_RHSx_0_MA(2*i);
N3_RHSx_deltaC(i) = N3_RHSx_Min_MA(i) - N3_RHSx_0_MA(2*i);
N3_LHSx_deltaT(i) = N3_LHSx_Min_MA(i) - N3_LHSx_0_MA(2*i);
N3_LHSx_deltaC(i) = N3_LHSx_Max_MA(i) - N3_LHSx_0_MA(2*i);
```

```
    N3_RHSa_deltaT(i) = N3_RHSa_Max_MA(i) - N3_RHSa_0_MA(2*i);
    N3_RHSa_deltaC(i) = N3_RHSa_Min_MA(i) - N3_RHSa_0_MA(2*i);
    N3_LHSa_deltaT(i) = N3_LHSa_Min_MA(i) - N3_LHSa_0_MA(2*i);
    N3_LHSa_deltaC(i) = N3_LHSa_Max_MA(i) - N3_LHSa_0_MA(2*i);

    N4_RHSy_deltaT(i) = N4_RHSy_Max_MA(i) - N4_RHSy_0_MA(2*i);
    N4_RHSy_deltaC(i) = N4_RHSy_Min_MA(i) - N4_RHSy_0_MA(2*i);
    N4_LHSy_deltaT(i) = N4_LHSy_Min_MA(i) - N4_LHSy_0_MA(2*i);
    N4_LHSy_deltaC(i) = N4_LHSy_Max_MA(i) - N4_LHSy_0_MA(2*i);

    N4_RHSx_deltaT(i) = N4_RHSx_Max_MA(i) - N4_RHSx_0_MA(2*i);
    N4_RHSx_deltaC(i) = N4_RHSx_Min_MA(i) - N4_RHSx_0_MA(2*i);
    N4_LHSx_deltaT(i) = N4_LHSx_Min_MA(i) - N4_LHSx_0_MA(2*i);
    N4_LHSx_deltaC(i) = N4_LHSx_Max_MA(i) - N4_LHSx_0_MA(2*i);

    N4_RHSa_deltaT(i) = N4_RHSa_Max_MA(i) - N4_RHSa_0_MA(2*i);
    N4_RHSa_deltaC(i) = N4_RHSa_Min_MA(i) - N4_RHSa_0_MA(2*i);
    N4_LHSa_deltaT(i) = N4_LHSa_Min_MA(i) - N4_LHSa_0_MA(2*i);
    N4_LHSa_deltaC(i) = N4_LHSa_Max_MA(i) - N4_LHSa_0_MA(2*i);

    N5_RHSy_deltaT(i) = N5_RHSy_Max_MA(i) - N5_RHSy_0_MA(2*i);
    N5_RHSy_deltaC(i) = N5_RHSy_Min_MA(i) - N5_RHSy_0_MA(2*i);
    N5_LHSy_deltaT(i) = N5_LHSy_Min_MA(i) - N5_LHSy_0_MA(2*i);
    N5_LHSy_deltaC(i) = N5_LHSy_Max_MA(i) - N5_LHSy_0_MA(2*i);

    N5_RHSx_deltaT(i) = N5_RHSx_Max_MA(i) - N5_RHSx_0_MA(2*i);
    N5_RHSx_deltaC(i) = N5_RHSx_Min_MA(i) - N5_RHSx_0_MA(2*i);
    N5_LHSx_deltaT(i) = N5_LHSx_Min_MA(i) - N5_LHSx_0_MA(2*i);
    N5_LHSx_deltaC(i) = N5_LHSx_Max_MA(i) - N5_LHSx_0_MA(2*i);

    N5_RHSa_deltaT(i) = N5_RHSa_Max_MA(i) - N5_RHSa_0_MA(2*i);
    N5_RHSa_deltaC(i) = N5_RHSa_Min_MA(i) - N5_RHSa_0_MA(2*i);
    N5_LHSa_deltaT(i) = N5_LHSa_Min_MA(i) - N5_LHSa_0_MA(2*i);
    N5_LHSa_deltaC(i) = N5_LHSa_Max_MA(i) - N5_LHSa_0_MA(2*i);

    N6_RHSy_deltaT(i) = N6_RHSy_Max_MA(i) - N6_RHSy_0_MA(2*i);
    N6_RHSy_deltaC(i) = N6_RHSy_Min_MA(i) - N6_RHSy_0_MA(2*i);
    N6_LHSy_deltaT(i) = N6_LHSy_Min_MA(i) - N6_LHSy_0_MA(2*i);
    N6_LHSy_deltaC(i) = N6_LHSy_Max_MA(i) - N6_LHSy_0_MA(2*i);

    N6_RHSx_deltaT(i) = N6_RHSx_Max_MA(i) - N6_RHSx_0_MA(2*i);
    N6_RHSx_deltaC(i) = N6_RHSx_Min_MA(i) - N6_RHSx_0_MA(2*i);
    N6_LHSx_deltaT(i) = N6_LHSx_Min_MA(i) - N6_LHSx_0_MA(2*i);
    N6_LHSx_deltaC(i) = N6_LHSx_Max_MA(i) - N6_LHSx_0_MA(2*i);

    N6_RHSa_deltaT(i) = N6_RHSa_Max_MA(i) - N6_RHSa_0_MA(2*i);
    N6_RHSa_deltaC(i) = N6_RHSa_Min_MA(i) - N6_RHSa_0_MA(2*i);
    N6_LHSa_deltaT(i) = N6_LHSa_Min_MA(i) - N6_LHSa_0_MA(2*i);
    N6_LHSa_deltaC(i) = N6_LHSa_Max_MA(i) - N6_LHSa_0_MA(2*i);
    end

%Calculate average neutral deflection for controls
%RHS
 CAll_RHSy_deltaT                                =                                [C1_RHSy_deltaT;
C2_RHSy_deltaT;C3_RHSy_deltaT;C6_RHSy_deltaT;C7_RHSy_deltaT;C8_RHSy_deltaT];
  CAV_RHSy_deltaT = mean(CAll_RHSy_deltaT,'omitnan');
 CAll_RHSy_deltaC                                                                =
[C1_RHSy_deltaC;C2_RHSy_deltaC;C3_RHSy_deltaC;C6_RHSy_deltaC;C7_RHSy_deltaC;C8_RHSy_deltaC];
  CAV_RHSy_deltaC = mean(CAll_RHSy_deltaC,'omitnan');

  CAll_RHSx_deltaT                                                                =
[C1_RHSx_deltaT;C2_RHSx_deltaT;C3_RHSx_deltaT;C6_RHSx_deltaT;C7_RHSx_deltaT;C8_RHSx_deltaT];
  CAV_RHSx_deltaT = mean(CAll_RHSx_deltaT,'omitnan');
 CAll_RHSx_deltaC                                                                =
[C1_RHSx_deltaC;C2_RHSx_deltaC;C3_RHSx_deltaC;C6_RHSx_deltaC;C7_RHSx_deltaC;C8_RHSx_deltaC];
  CAV_RHSx_deltaC = mean(CAll_RHSx_deltaC,'omitnan');

CAll_RHSa_deltaT                                                                =
[C1_RHSa_deltaT;C2_RHSa_deltaT;C3_RHSa_deltaT;C6_RHSa_deltaT;C7_RHSa_deltaT;C8_RHSa_deltaT];
  CAV_RHSa_deltaT = mean(CAll_RHSa_deltaT,'omitnan');
 CAll_RHSa_deltaC                                                                =
[C1_RHSa_deltaC;C2_RHSa_deltaC;C3_RHSa_deltaC;C6_RHSa_deltaC;C7_RHSa_deltaC;C8_RHSa_deltaC];
  CAV_RHSa_deltaC = mean(CAll_RHSa_deltaC,'omitnan');

%LHS
CAll_LHSy_deltaT                                                                =
[C1_LHSy_deltaT;C2_LHSy_deltaT;C3_LHSy_deltaT;C6_LHSy_deltaT;C7_LHSy_deltaT;C8_LHSy_deltaT];
```

```
  CAV_LHSy_deltaT = mean(CAll_LHSy_deltaT,'omitnan');
 CAll_LHSy_deltaC                                                                    =
[C1_LHSy_deltaC;C2_LHSy_deltaC;C3_LHSy_deltaC;C6_LHSy_deltaC;C7_LHSy_deltaC;C8_LHSy_deltaC];
  CAV_LHSy_deltaC = mean(CAll_LHSy_deltaC,'omitnan');

  CAll_LHSx_deltaT                                                                    =
[C1_LHSx_deltaT;C2_LHSx_deltaT;C3_LHSx_deltaT;C6_LHSx_deltaT;C7_LHSx_deltaT;C8_LHSx_deltaT];
  CAV_LHSx_deltaT = mean(CAll_LHSx_deltaT,'omitnan');
 CAll_LHSx_deltaC                                                                    =
[C1_LHSx_deltaC;C2_LHSx_deltaC;C3_LHSx_deltaC;C6_LHSx_deltaC;C7_LHSx_deltaC;C8_LHSx_deltaC];
  CAV_LHSx_deltaC = mean(CAll_LHSx_deltaC,'omitnan');

 CAll_LHSa_deltaT                                                                    =
[C1_LHSa_deltaT;C2_LHSa_deltaT;C3_LHSa_deltaT;C6_LHSa_deltaT;C7_LHSa_deltaT;C8_LHSa_deltaT];
  CAV_LHSa_deltaT = mean(CAll_LHSa_deltaT,'omitnan');
 CAll_LHSa_deltaC                                                                    =
[C1_LHSa_deltaC;C2_LHSa_deltaC;C3_LHSa_deltaC;C6_LHSa_deltaC;C7_LHSa_deltaC;C8_LHSa_deltaC];
  CAV_LHSa_deltaC = mean(CAll_LHSa_deltaC,'omitnan');

 %Calculate standard deviation of controls
  CSTD_RHSy_deltaT = std(CAll_RHSy_deltaT,'omitnan');
   CSTD_RHSy_deltaC = std(CAll_RHSy_deltaC,'omitnan');

   CSTD_RHSx_deltaT = std(CAll_RHSx_deltaT,'omitnan');
   CSTD_RHSx_deltaC = std(CAll_RHSx_deltaC,'omitnan');

   CSTD_RHSa_deltaT = std(CAll_RHSa_deltaT,'omitnan');
   CSTD_RHSa_deltaC = std(CAll_RHSa_deltaC,'omitnan');

   CSTD_LHSy_deltaT = std(CAll_LHSy_deltaT,'omitnan');
   CSTD_LHSy_deltaC = std(CAll_LHSy_deltaC,'omitnan');

   CSTD_LHSx_deltaT = std(CAll_LHSx_deltaT,'omitnan');
   CSTD_LHSx_deltaC = std(CAll_LHSx_deltaC,'omitnan');

   CSTD_LHSa_deltaT = std(CAll_LHSa_deltaT,'omitnan');
   CSTD_LHSa_deltaC = std(CAll_LHSa_deltaC,'omitnan');

%Calculate average neutral deflection of Novels
%RHS
  NALL_RHSy_deltaT                                                                    =
[N1_RHSy_deltaT;N2_RHSy_deltaT;N3_RHSy_deltaT;N4_RHSy_deltaT;N5_RHSy_deltaT;N6_RHSy_deltaT];
  NAV_RHSy_deltaT = mean(NALL_RHSy_deltaT,'omitnan');
  NALL_RHSy_deltaC                                                                    =
[N1_RHSy_deltaC;N2_RHSy_deltaC;N3_RHSy_deltaC;N4_RHSy_deltaC;N5_RHSy_deltaC;N6_RHSy_deltaC];
  NAV_RHSy_deltaC = mean(NALL_RHSy_deltaC,'omitnan');

  NALL_RHSx_deltaT                                                                    =
[N1_RHSx_deltaT;N2_RHSx_deltaT;N3_RHSx_deltaT;N4_RHSx_deltaT;N5_RHSx_deltaT;N6_RHSx_deltaT];
  NAV_RHSx_deltaT = mean(NALL_RHSx_deltaT,'omitnan');
  NALL_RHSx_deltaC                                                                    =
[N1_RHSx_deltaC;N2_RHSx_deltaC;N3_RHSx_deltaC;N4_RHSx_deltaC;N5_RHSx_deltaC;N6_RHSx_deltaC];
  NAV_RHSx_deltaC = mean(NALL_RHSx_deltaC,'omitnan');

  NALL_RHSa_deltaT                                                                    =
[N1_RHSa_deltaT;N2_RHSa_deltaT;N3_RHSa_deltaT;N4_RHSa_deltaT;N5_RHSa_deltaT;N6_RHSa_deltaT];
  NAV_RHSa_deltaT = mean(NALL_RHSa_deltaT,'omitnan');
  NALL_RHSa_deltaC                                                                    =
[N1_RHSa_deltaC;N2_RHSa_deltaC;N3_RHSa_deltaC;N4_RHSa_deltaC;N5_RHSa_deltaC;N6_RHSa_deltaC];
  NAV_RHSa_deltaC = mean(NALL_RHSa_deltaC,'omitnan');

%LHS
  NALL_LHSy_deltaT                                                                    =
[N1_LHSy_deltaT;N2_LHSy_deltaT;N3_LHSy_deltaT;N4_LHSy_deltaT;N5_LHSy_deltaT;N6_LHSy_deltaT];
  NAV_LHSy_deltaT = mean(NALL_LHSy_deltaT,'omitnan');
  NALL_LHSy_deltaC                                                                    =
[N1_LHSy_deltaC;N2_LHSy_deltaC;N3_LHSy_deltaC;N4_LHSy_deltaC;N5_LHSy_deltaC;N6_LHSy_deltaC];
  NAV_LHSy_deltaC = mean(NALL_LHSy_deltaC,'omitnan');

  NALL_LHSx_deltaT                                                                    =
[N1_LHSx_deltaT;N2_LHSx_deltaT;N3_LHSx_deltaT;N4_LHSx_deltaT;N5_LHSx_deltaT;N6_LHSx_deltaT];
  NAV_LHSx_deltaT = mean(NALL_LHSx_deltaT,'omitnan');
  NALL_LHSx_deltaC                                                                    =
[N1_LHSx_deltaC;N2_LHSx_deltaC;N3_LHSx_deltaC;N4_LHSx_deltaC;N5_LHSx_deltaC;N6_LHSx_deltaC];
  NAV_LHSx_deltaC = mean(NALL_LHSx_deltaC,'omitnan');
```

```
  NALL_LHSa_deltaT                                                                    =
[N1_LHSa_deltaT;N2_LHSa_deltaT;N3_LHSa_deltaT;N4_LHSa_deltaT;N5_LHSa_deltaT;N6_LHSa_deltaT];
  NAV_LHSa_deltaT = mean(NALL_LHSa_deltaT,'omitnan');
  NALL_LHSa_deltaC                                                                    =
[N1_LHSa_deltaC;N2_LHSa_deltaC;N3_LHSa_deltaC;N4_LHSa_deltaC;N5_LHSa_deltaC;N6_LHSa_deltaC];
  NAV_LHSa_deltaC = mean(NALL_LHSa_deltaC,'omitnan');

  %Calculate the standard deviation of the novels
   NSTD_RHSy_deltaT = std(NALL_RHSy_deltaT,'omitnan');
   NSTD_RHSy_deltaC = std(NALL_RHSy_deltaC,'omitnan');
   NSTD_RHSx_deltaT = std(NALL_RHSx_deltaT,'omitnan');
   NSTD_RHSx_deltaC = std(NALL_RHSx_deltaC,'omitnan');
   NSTD_RHSa_deltaT = std(NALL_RHSa_deltaT,'omitnan');
   NSTD_RHSa_deltaC = std(NALL_RHSa_deltaC,'omitnan');
   NSTD_LHSy_deltaT = std(NALL_LHSy_deltaT,'omitnan');
   NSTD_LHSy_deltaC = std(NALL_LHSy_deltaC,'omitnan');
   NSTD_LHSx_deltaT = std(NALL_LHSx_deltaT,'omitnan');
   NSTD_LHSx_deltaC = std(NALL_LHSx_deltaC,'omitnan');
   NSTD_LHSa_deltaT = std(NALL_LHSa_deltaT,'omitnan');
   NSTD_LHSa_deltaC = std(NALL_LHSa_deltaC,'omitnan');

 %%%%%%%%%%%%%%%%%%%%%%%%%%%%%%%%%%%%%%%%%%%%%%%%%%%%%%%%%%%%
 %STEP 5
 %WRITE PROCESSED DATA TO FILES FOR CONTROL, NOVEL AND AVERAGE DATA

 %Create control file and headings
 ProcessedData = 'ProcessedData.xlsx';
 headings
={'C1_RHSy_Max','C2_RHSy_Max','C3_RHSy_Max','C6_RHSy_Max','C7_RHSy_Max','C8_RHSy_Max','C1_RHSx
_Max','C2_RHSx_Max','C3_RHSx_Max','C6_RHSx_Max','C7_RHSx_Max','C8_RHSx_Max','C1_RHSa_Max','C2_
RHSa_Max','C3_RHSa_Max','C6_RHSa_Max','C7_RHSa_Max','C8_RHSa_Max','C1_RHSy_0','C2_RHSy_0','C3_
RHSy_0','C6_RHSy_0','C7_RHSy_0','C8_RHSy_0','C1_RHSx_0','C2_RHSx_0','C3_RHSx_0','C6_RHSx_0','C
7_RHSx_0','C8_RHSx_0','C1_RHSa_0','C2_RHSa_0','C3_RHSa_0','C6_RHSa_0','C7_RHSa_0','C8_RHSa_0',
'C1_RHSy_MIN','C2_RHSy_MIN','C3_RHSy_MIN','C6_RHSy_MIN','C7_RHSy_MIN','C8_RHSy_MIN','C1_RHSx_M
IN','C2_RHSx_MIN','C3_RHSx_MIN','C6_RHSx_MIN','C7_RHSx_MIN','C8_RHSx_MIN','C1_RHSa_MIN','C2_RH
Sa_MIN','C3_RHSa_MIN','C6_RHSa_MIN','C7_RHSa_MIN','C8_RHSa_MIN','C1_LHSy_Max','C2_LHSy_Max','C
3_LHSy_Max','C6_LHSy_Max','C7_LHSy_Max','C8_LHSy_Max','C1_LHSx_Max','C2_LHSx_Max','C3_LHSx_Max
','C6_LHSx_Max','C7_LHSx_Max','C8_LHSx_Max','C1_LHSa_Max','C2_LHSa_Max','C3_LHSa_Max','C6_LHSa
_Max','C7_LHSa_Max','C8_LHSa_Max','C1_LHSy_0','C2_LHSy_0','C3_LHSy_0','C6_LHSy_0','C7_LHSy_0',
'C8_LHSy_0','C1_LHSx_0','C2_LHSx_0','C3_LHSx_0','C6_LHSx_0','C7_LHSx_0','C8_LHSx_0','C1_LHSa_0
','C2_LHSa_0','C3_LHSa_0','C6_LHSa_0','C7_LHSa_0','C8_LHSa_0','C1_LHSy_MIN','C2_LHSy_MIN','C3_
LHSy_MIN','C6_LHSy_MIN','C7_LHSy_MIN','C8_LHSy_MIN','C1_LHSx_MIN','C2_LHSx_MIN','C3_LHSx_MIN',
'C6_LHSx_MIN','C7_LHSx_MIN','C8_LHSx_MIN','C1_LHSa_MIN','C2_LHSa_MIN','C3_LHSa_MIN','C6_LHSa_M
IN','C7_LHSa_MIN','C8_LHSa_MIN'};
 writecell(headings,ProcessedData,'Sheet','Control','Range','A1')
 disp('Writing Control values')

%Write control data Max values RHS
writematrix(C1_RHSy_Max_MA,ProcessedData,'Sheet','Control','Range','A2')
writematrix(C2_RHSy_Max_MA,ProcessedData,'Sheet','Control','Range','B2')
writematrix(C3_RHSy_Max_MA,ProcessedData,'Sheet','Control','Range','C2')
writematrix(C6_RHSy_Max_MA,ProcessedData,'Sheet','Control','Range','D2')
writematrix(C7_RHSy_Max_MA,ProcessedData,'Sheet','Control','Range','E2')
writematrix(C8_RHSy_Max_MA,ProcessedData,'Sheet','Control','Range','F2')

writematrix(C1_RHSx_Max_MA,ProcessedData,'Sheet','Control','Range','G2')
writematrix(C2_RHSx_Max_MA,ProcessedData,'Sheet','Control','Range','H2')
writematrix(C3_RHSx_Max_MA,ProcessedData,'Sheet','Control','Range','I2')
writematrix(C6_RHSx_Max_MA,ProcessedData,'Sheet','Control','Range','J2')
writematrix(C7_RHSx_Max_MA,ProcessedData,'Sheet','Control','Range','K2')
writematrix(C8_RHSx_Max_MA,ProcessedData,'Sheet','Control','Range','L2')

writematrix(C1_RHSa_Max_MA,ProcessedData,'Sheet','Control','Range','M2')
writematrix(C2_RHSa_Max_MA,ProcessedData,'Sheet','Control','Range','N2')
writematrix(C3_RHSa_Max_MA,ProcessedData,'Sheet','Control','Range','O2')
writematrix(C6_RHSa_Max_MA,ProcessedData,'Sheet','Control','Range','P2')
writematrix(C7_RHSa_Max_MA,ProcessedData,'Sheet','Control','Range','Q2')
writematrix(C8_RHSa_Max_MA,ProcessedData,'Sheet','Control','Range','R2')

%Write control data centre values RHS
writematrix(C1_RHSy_0_MA,ProcessedData,'Sheet','Control','Range','S2')
writematrix(C2_RHSy_0_MA,ProcessedData,'Sheet','Control','Range','T2')
writematrix(C3_RHSy_0_MA,ProcessedData,'Sheet','Control','Range','U2')
writematrix(C6_RHSy_0_MA,ProcessedData,'Sheet','Control','Range','V2')
writematrix(C7_RHSy_0_MA,ProcessedData,'Sheet','Control','Range','W2')
writematrix(C8_RHSy_0_MA,ProcessedData,'Sheet','Control','Range','X2')
```

```
writematrix(C1_RHSx_0_MA,ProcessedData,'Sheet','Control','Range','Y2')
writematrix(C2_RHSx_0_MA,ProcessedData,'Sheet','Control','Range','Z2')
writematrix(C3_RHSx_0_MA,ProcessedData,'Sheet','Control','Range','AA2')
writematrix(C6_RHSx_0_MA,ProcessedData,'Sheet','Control','Range','AB2')
writematrix(C7_RHSx_0_MA,ProcessedData,'Sheet','Control','Range','AC2')
writematrix(C8_RHSx_0_MA,ProcessedData,'Sheet','Control','Range','AD2')

writematrix(C1_RHSa_0_MA,ProcessedData,'Sheet','Control','Range','AE2')
writematrix(C2_RHSa_0_MA,ProcessedData,'Sheet','Control','Range','AF2')
writematrix(C3_RHSa_0_MA,ProcessedData,'Sheet','Control','Range','AG2')
writematrix(C6_RHSa_0_MA,ProcessedData,'Sheet','Control','Range','AH2')
writematrix(C7_RHSa_0_MA,ProcessedData,'Sheet','Control','Range','AI2')
writematrix(C8_RHSa_0_MA,ProcessedData,'Sheet','Control','Range','AJ2')

%Write control data Min values RHS
writematrix(C1_RHSy_Min_MA,ProcessedData,'Sheet','Control','Range','AK2')
writematrix(C2_RHSy_Min_MA,ProcessedData,'Sheet','Control','Range','AL2')
writematrix(C3_RHSy_Min_MA,ProcessedData,'Sheet','Control','Range','AM2')
writematrix(C6_RHSy_Min_MA,ProcessedData,'Sheet','Control','Range','AN2')
writematrix(C7_RHSy_Min_MA,ProcessedData,'Sheet','Control','Range','AO2')
writematrix(C8_RHSy_Min_MA,ProcessedData,'Sheet','Control','Range','AP2')

writematrix(C1_RHSx_Min_MA,ProcessedData,'Sheet','Control','Range','AQ2')
writematrix(C2_RHSx_Min_MA,ProcessedData,'Sheet','Control','Range','AR2')
writematrix(C3_RHSx_Min_MA,ProcessedData,'Sheet','Control','Range','AS2')
writematrix(C6_RHSx_Min_MA,ProcessedData,'Sheet','Control','Range','AT2')
writematrix(C7_RHSx_Min_MA,ProcessedData,'Sheet','Control','Range','AU2')
writematrix(C8_RHSx_Min_MA,ProcessedData,'Sheet','Control','Range','AV2')

writematrix(C1_RHSa_Min_MA,ProcessedData,'Sheet','Control','Range','AW2')
writematrix(C2_RHSa_Min_MA,ProcessedData,'Sheet','Control','Range','AX2')
writematrix(C3_RHSa_Min_MA,ProcessedData,'Sheet','Control','Range','AY2')
writematrix(C6_RHSa_Min_MA,ProcessedData,'Sheet','Control','Range','AZ2')
writematrix(C7_RHSa_Min_MA,ProcessedData,'Sheet','Control','Range','BA2')
writematrix(C8_RHSa_Min_MA,ProcessedData,'Sheet','Control','Range','BB2')

%Write control data Max values LHS
writematrix(C1_LHSy_Max_MA,ProcessedData,'Sheet','Control','Range','BC2')
writematrix(C2_LHSy_Max_MA,ProcessedData,'Sheet','Control','Range','BD2')
writematrix(C3_LHSy_Max_MA,ProcessedData,'Sheet','Control','Range','BE2')
writematrix(C6_LHSy_Max_MA,ProcessedData,'Sheet','Control','Range','BF2')
writematrix(C7_LHSy_Max_MA,ProcessedData,'Sheet','Control','Range','BG2')
writematrix(C8_LHSy_Max_MA,ProcessedData,'Sheet','Control','Range','BH2')

writematrix(C1_LHSx_Max_MA,ProcessedData,'Sheet','Control','Range','BI2')
writematrix(C2_LHSx_Max_MA,ProcessedData,'Sheet','Control','Range','BJ2')
writematrix(C3_LHSx_Max_MA,ProcessedData,'Sheet','Control','Range','BK2')
writematrix(C6_LHSx_Max_MA,ProcessedData,'Sheet','Control','Range','BL2')
writematrix(C7_LHSx_Max_MA,ProcessedData,'Sheet','Control','Range','BM2')
writematrix(C8_LHSx_Max_MA,ProcessedData,'Sheet','Control','Range','BN2')

writematrix(C1_LHSa_Max_MA,ProcessedData,'Sheet','Control','Range','BO2')
writematrix(C2_LHSa_Max_MA,ProcessedData,'Sheet','Control','Range','BP2')
writematrix(C3_LHSa_Max_MA,ProcessedData,'Sheet','Control','Range','BQ2')
writematrix(C6_LHSa_Max_MA,ProcessedData,'Sheet','Control','Range','BR2')
writematrix(C7_LHSa_Max_MA,ProcessedData,'Sheet','Control','Range','BS2')
writematrix(C8_LHSa_Max_MA,ProcessedData,'Sheet','Control','Range','BT2')

%Write control data centre values LHS
writematrix(C1_LHSy_0_MA,ProcessedData,'Sheet','Control','Range','BU2')
writematrix(C2_LHSy_0_MA,ProcessedData,'Sheet','Control','Range','BV2')
writematrix(C3_LHSy_0_MA,ProcessedData,'Sheet','Control','Range','BW2')
writematrix(C6_LHSy_0_MA,ProcessedData,'Sheet','Control','Range','BX2')
writematrix(C7_LHSy_0_MA,ProcessedData,'Sheet','Control','Range','BY2')
writematrix(C8_LHSy_0_MA,ProcessedData,'Sheet','Control','Range','BZ2')

writematrix(C1_LHSx_0_MA,ProcessedData,'Sheet','Control','Range','CA2')
writematrix(C2_LHSx_0_MA,ProcessedData,'Sheet','Control','Range','CB2')
writematrix(C3_LHSx_0_MA,ProcessedData,'Sheet','Control','Range','CC2')
writematrix(C6_LHSx_0_MA,ProcessedData,'Sheet','Control','Range','CD2')
writematrix(C7_LHSx_0_MA,ProcessedData,'Sheet','Control','Range','CE2')
writematrix(C8_LHSx_0_MA,ProcessedData,'Sheet','Control','Range','CF2')

writematrix(C1_LHSa_0_MA,ProcessedData,'Sheet','Control','Range','CG2')
writematrix(C2_LHSa_0_MA,ProcessedData,'Sheet','Control','Range','CH2')
writematrix(C3_LHSa_0_MA,ProcessedData,'Sheet','Control','Range','CI2')
writematrix(C6_LHSa_0_MA,ProcessedData,'Sheet','Control','Range','CJ2')
```

```
writematrix(C7_LHSa_0_MA,ProcessedData,'Sheet','Control','Range','CK2')
writematrix(C8_LHSa_0_MA,ProcessedData,'Sheet','Control','Range','CL2')

%Write control data Min values LHS
writematrix(C1_LHSy_Min_MA,ProcessedData,'Sheet','Control','Range','CM2')
writematrix(C2_LHSy_Min_MA,ProcessedData,'Sheet','Control','Range','CN2')
writematrix(C3_LHSy_Min_MA,ProcessedData,'Sheet','Control','Range','CO2')
writematrix(C6_LHSy_Min_MA,ProcessedData,'Sheet','Control','Range','CP2')
writematrix(C7_LHSy_Min_MA,ProcessedData,'Sheet','Control','Range','CQ2')
writematrix(C8_LHSy_Min_MA,ProcessedData,'Sheet','Control','Range','CR2')

writematrix(C1_LHSx_Min_MA,ProcessedData,'Sheet','Control','Range','CS2')
writematrix(C2_LHSx_Min_MA,ProcessedData,'Sheet','Control','Range','CT2')
writematrix(C3_LHSx_Min_MA,ProcessedData,'Sheet','Control','Range','CU2')
writematrix(C6_LHSx_Min_MA,ProcessedData,'Sheet','Control','Range','CV2')
writematrix(C7_LHSx_Min_MA,ProcessedData,'Sheet','Control','Range','CW2')
writematrix(C8_LHSx_Min_MA,ProcessedData,'Sheet','Control','Range','CX2')

writematrix(C1_LHSa_Min_MA,ProcessedData,'Sheet','Control','Range','CY2')
writematrix(C2_LHSa_Min_MA,ProcessedData,'Sheet','Control','Range','CZ2')
writematrix(C3_LHSa_Min_MA,ProcessedData,'Sheet','Control','Range','DA2')
writematrix(C6_LHSa_Min_MA,ProcessedData,'Sheet','Control','Range','DB2')
writematrix(C7_LHSa_Min_MA,ProcessedData,'Sheet','Control','Range','DC2')
writematrix(C8_LHSa_Min_MA,ProcessedData,'Sheet','Control','Range','DD2')

%Create Novel file and headings
 %ProcessedData,'Sheet','Novel', = 'ProcessedData,'Sheet','Novel',.xlsx';
 N_headings
={'N1_RHSy_Max','N2_RHSy_Max','N3_RHSy_Max','N4_RHSy_Max','N5_RHSy_Max','N6_RHSy_Max','N1_RHSx
_Max','N2_RHSx_Max','N3_RHSx_Max','N4_RHSx_Max','N5_RHSx_Max','N6_RHSx_Max','N1_RHSa_Max','N2_
RHSa_Max','N3_RHSa_Max','N4_RHSa_Max','N5_RHSa_Max','N6_RHSa_Max','N1_RHSy_0','N2_RHSy_0','N3_
RHSy_0','N4_RHSy_0','N5_RHSy_0','N6_RHSy_0','N1_RHSx_0','N2_RHSx_0','N3_RHSx_0','N4_RHSx_0','N
5_RHSx_0','N6_RHSx_0','N1_RHSa_0','N2_RHSa_0','N3_RHSa_0','N4_RHSa_0','N5_RHSa_0','N6_RHSa_0',
'N1_RHSy_MIN','N2_RHSy_MIN','N3_RHSy_MIN','N4_RHSy_MIN','N5_RHSy_MIN','N6_RHSy_MIN','N1_RHSx_M
IN','N2_RHSx_MIN','N3_RHSx_MIN','N4_RHSx_MIN','N5_RHSx_MIN','N6_RHSx_MIN','N1_RHSa_MIN','N2_RH
Sa_MIN','N3_RHSa_MIN','N4_RHSa_MIN','N5_RHSa_MIN','N6_RHSa_MIN','N1_LHSy_Max','N2_LHSy_Max','N
3_LHSy_Max','N4_LHSy_Max','N5_LHSy_Max','N6_LHSy_Max','N1_LHSx_Max','N2_LHSx_Max','N3_LHSx_Max
','N4_LHSx_Max','N5_LHSx_Max','N6_LHSx_Max','N1_LHSa_Max','N2_LHSa_Max','N3_LHSa_Max','N4_LHSa
_Max','N5_LHSa_Max','N6_LHSa_Max','N1_LHSy_0','N2_LHSy_0','N3_LHSy_0','N4_LHSy_0','N5_LHSy_0',
'N6_LHSy_0','N1_LHSx_0','N2_LHSx_0','N3_LHSx_0','N4_LHSx_0','N5_LHSx_0','N6_LHSx_0','N1_LHSa_0
','N2_LHSa_0','N3_LHSa_0','N4_LHSa_0','N5_LHSa_0','N6_LHSa_0','N1_LHSy_MIN','N2_LHSy_MIN','N3_
LHSy_MIN','N4_LHSy_MIN','N5_LHSy_MIN','N6_LHSy_MIN','N1_LHSx_MIN','N2_LHSx_MIN','N3_LHSx_MIN',
'N4_LHSx_MIN','N5_LHSx_MIN','N6_LHSx_MIN','N1_LHSa_MIN','N2_LHSa_MIN','N3_LHSa_MIN','N4_LHSa_M
IN','N5_LHSa_MIN','N6_LHSa_MIN'};
 writecell(N_headings,ProcessedData,'Sheet','Novel','Range','A1')
 disp('Writing Novel values')

%Write Novel data Max values RHS
writematrix(N1_RHSy_Max_MA,ProcessedData,'Sheet','Novel','Range','A2')
writematrix(N2_RHSy_Max_MA,ProcessedData,'Sheet','Novel','Range','B2')
writematrix(N3_RHSy_Max_MA,ProcessedData,'Sheet','Novel','Range','C2')
writematrix(N4_RHSy_Max_MA,ProcessedData,'Sheet','Novel','Range','D2')
writematrix(N5_RHSy_Max_MA,ProcessedData,'Sheet','Novel','Range','E2')
writematrix(N6_RHSy_Max_MA,ProcessedData,'Sheet','Novel','Range','F2')

writematrix(N1_RHSx_Max_MA,ProcessedData,'Sheet','Novel','Range','G2')
writematrix(N2_RHSx_Max_MA,ProcessedData,'Sheet','Novel','Range','H2')
writematrix(N3_RHSx_Max_MA,ProcessedData,'Sheet','Novel','Range','I2')
writematrix(N4_RHSx_Max_MA,ProcessedData,'Sheet','Novel','Range','J2')
writematrix(N5_RHSx_Max_MA,ProcessedData,'Sheet','Novel','Range','K2')
writematrix(N6_RHSx_Max_MA,ProcessedData,'Sheet','Novel','Range','L2')

writematrix(N1_RHSa_Max_MA,ProcessedData,'Sheet','Novel','Range','M2')
writematrix(N2_RHSa_Max_MA,ProcessedData,'Sheet','Novel','Range','N2')
writematrix(N3_RHSa_Max_MA,ProcessedData,'Sheet','Novel','Range','O2')
writematrix(N4_RHSa_Max_MA,ProcessedData,'Sheet','Novel','Range','P2')
writematrix(N5_RHSa_Max_MA,ProcessedData,'Sheet','Novel','Range','Q2')
writematrix(N6_RHSa_Max_MA,ProcessedData,'Sheet','Novel','Range','R2')

%Write Novel data centre values RHS
writematrix(N1_RHSy_0_MA,ProcessedData,'Sheet','Novel','Range','S2')
writematrix(N2_RHSy_0_MA,ProcessedData,'Sheet','Novel','Range','T2')
writematrix(N3_RHSy_0_MA,ProcessedData,'Sheet','Novel','Range','U2')
writematrix(N4_RHSy_0_MA,ProcessedData,'Sheet','Novel','Range','V2')
writematrix(N5_RHSy_0_MA,ProcessedData,'Sheet','Novel','Range','W2')
writematrix(N6_RHSy_0_MA,ProcessedData,'Sheet','Novel','Range','X2')
```

```
writematrix(N1_RHSx_0_MA,ProcessedData,'Sheet','Novel','Range','Y2')
writematrix(N2_RHSx_0_MA,ProcessedData,'Sheet','Novel','Range','Z2')
writematrix(N3_RHSx_0_MA,ProcessedData,'Sheet','Novel','Range','AA2')
writematrix(N4_RHSx_0_MA,ProcessedData,'Sheet','Novel','Range','AB2')
writematrix(N5_RHSx_0_MA,ProcessedData,'Sheet','Novel','Range','AC2')
writematrix(N6_RHSx_0_MA,ProcessedData,'Sheet','Novel','Range','AD2')

writematrix(N1_RHSa_0_MA,ProcessedData,'Sheet','Novel','Range','AE2')
writematrix(N2_RHSa_0_MA,ProcessedData,'Sheet','Novel','Range','AF2')
writematrix(N3_RHSa_0_MA,ProcessedData,'Sheet','Novel','Range','AG2')
writematrix(N4_RHSa_0_MA,ProcessedData,'Sheet','Novel','Range','AH2')
writematrix(N5_RHSa_0_MA,ProcessedData,'Sheet','Novel','Range','AI2')
writematrix(N6_RHSa_0_MA,ProcessedData,'Sheet','Novel','Range','AJ2')

%Write Novel data Min values RHS
writematrix(N1_RHSy_Min_MA,ProcessedData,'Sheet','Novel','Range','AK2')
writematrix(N2_RHSy_Min_MA,ProcessedData,'Sheet','Novel','Range','AL2')
writematrix(N3_RHSy_Min_MA,ProcessedData,'Sheet','Novel','Range','AM2')
writematrix(N4_RHSy_Min_MA,ProcessedData,'Sheet','Novel','Range','AN2')
writematrix(N5_RHSy_Min_MA,ProcessedData,'Sheet','Novel','Range','AO2')
writematrix(N6_RHSy_Min_MA,ProcessedData,'Sheet','Novel','Range','AP2')

writematrix(N1_RHSx_Min_MA,ProcessedData,'Sheet','Novel','Range','AQ2')
writematrix(N2_RHSx_Min_MA,ProcessedData,'Sheet','Novel','Range','AR2')
writematrix(N3_RHSx_Min_MA,ProcessedData,'Sheet','Novel','Range','AS2')
writematrix(N4_RHSx_Min_MA,ProcessedData,'Sheet','Novel','Range','AT2')
writematrix(N5_RHSx_Min_MA,ProcessedData,'Sheet','Novel','Range','AU2')
writematrix(N6_RHSx_Min_MA,ProcessedData,'Sheet','Novel','Range','AV2')

writematrix(N1_RHSa_Min_MA,ProcessedData,'Sheet','Novel','Range','AW2')
writematrix(N2_RHSa_Min_MA,ProcessedData,'Sheet','Novel','Range','AX2')
writematrix(N3_RHSa_Min_MA,ProcessedData,'Sheet','Novel','Range','AY2')
writematrix(N4_RHSa_Min_MA,ProcessedData,'Sheet','Novel','Range','AZ2')
writematrix(N5_RHSa_Min_MA,ProcessedData,'Sheet','Novel','Range','BA2')
writematrix(N6_RHSa_Min_MA,ProcessedData,'Sheet','Novel','Range','BB2')

%Write Novel data Max values LHS
writematrix(N1_LHSy_Max_MA,ProcessedData,'Sheet','Novel','Range','BC2')
writematrix(N2_LHSy_Max_MA,ProcessedData,'Sheet','Novel','Range','BD2')
writematrix(N3_LHSy_Max_MA,ProcessedData,'Sheet','Novel','Range','BE2')
writematrix(N4_LHSy_Max_MA,ProcessedData,'Sheet','Novel','Range','BF2')
writematrix(N5_LHSy_Max_MA,ProcessedData,'Sheet','Novel','Range','BG2')
writematrix(N6_LHSy_Max_MA,ProcessedData,'Sheet','Novel','Range','BH2')

writematrix(N1_LHSx_Max_MA,ProcessedData,'Sheet','Novel','Range','BI2')
writematrix(N2_LHSx_Max_MA,ProcessedData,'Sheet','Novel','Range','BJ2')
writematrix(N3_LHSx_Max_MA,ProcessedData,'Sheet','Novel','Range','BK2')
writematrix(N4_LHSx_Max_MA,ProcessedData,'Sheet','Novel','Range','BL2')
writematrix(N5_LHSx_Max_MA,ProcessedData,'Sheet','Novel','Range','BM2')
writematrix(N6_LHSx_Max_MA,ProcessedData,'Sheet','Novel','Range','BN2')

writematrix(N1_LHSa_Max_MA,ProcessedData,'Sheet','Novel','Range','BO2')
writematrix(N2_LHSa_Max_MA,ProcessedData,'Sheet','Novel','Range','BP2')
writematrix(N3_LHSa_Max_MA,ProcessedData,'Sheet','Novel','Range','BQ2')
writematrix(N4_LHSa_Max_MA,ProcessedData,'Sheet','Novel','Range','BR2')
writematrix(N5_LHSa_Max_MA,ProcessedData,'Sheet','Novel','Range','BS2')
writematrix(N6_LHSa_Max_MA,ProcessedData,'Sheet','Novel','Range','BT2')

%Write Novel data centre values LHS
writematrix(N1_LHSy_0_MA,ProcessedData,'Sheet','Novel','Range','BU2')
writematrix(N2_LHSy_0_MA,ProcessedData,'Sheet','Novel','Range','BV2')
writematrix(N3_LHSy_0_MA,ProcessedData,'Sheet','Novel','Range','BW2')
writematrix(N4_LHSy_0_MA,ProcessedData,'Sheet','Novel','Range','BX2')
writematrix(N5_LHSy_0_MA,ProcessedData,'Sheet','Novel','Range','BY2')
writematrix(N6_LHSy_0_MA,ProcessedData,'Sheet','Novel','Range','BZ2')

writematrix(N1_LHSx_0_MA,ProcessedData,'Sheet','Novel','Range','CA2')
writematrix(N2_LHSx_0_MA,ProcessedData,'Sheet','Novel','Range','CB2')
writematrix(N3_LHSx_0_MA,ProcessedData,'Sheet','Novel','Range','CC2')
writematrix(N4_LHSx_0_MA,ProcessedData,'Sheet','Novel','Range','CD2')
writematrix(N5_LHSx_0_MA,ProcessedData,'Sheet','Novel','Range','CE2')
writematrix(N6_LHSx_0_MA,ProcessedData,'Sheet','Novel','Range','CF2')

writematrix(N1_LHSa_0_MA,ProcessedData,'Sheet','Novel','Range','CG2')
writematrix(N2_LHSa_0_MA,ProcessedData,'Sheet','Novel','Range','CH2')
writematrix(N3_LHSa_0_MA,ProcessedData,'Sheet','Novel','Range','CI2')
writematrix(N4_LHSa_0_MA,ProcessedData,'Sheet','Novel','Range','CJ2')
```

```
writematrix(N5_LHSa_0_MA,ProcessedData,'Sheet','Novel','Range','CK2')
writematrix(N6_LHSa_0_MA,ProcessedData,'Sheet','Novel','Range','CL2')

%Write Novel data Min values LHS
writematrix(N1_LHSy_Min_MA,ProcessedData,'Sheet','Novel','Range','CM2')
writematrix(N2_LHSy_Min_MA,ProcessedData,'Sheet','Novel','Range','CN2')
writematrix(N3_LHSy_Min_MA,ProcessedData,'Sheet','Novel','Range','CO2')
writematrix(N4_LHSy_Min_MA,ProcessedData,'Sheet','Novel','Range','CP2')
writematrix(N5_LHSy_Min_MA,ProcessedData,'Sheet','Novel','Range','CQ2')
writematrix(N6_LHSy_Min_MA,ProcessedData,'Sheet','Novel','Range','CR2')

writematrix(N1_LHSx_Min_MA,ProcessedData,'Sheet','Novel','Range','CS2')
writematrix(N2_LHSx_Min_MA,ProcessedData,'Sheet','Novel','Range','CT2')
writematrix(N3_LHSx_Min_MA,ProcessedData,'Sheet','Novel','Range','CU2')
writematrix(N4_LHSx_Min_MA,ProcessedData,'Sheet','Novel','Range','CV2')
writematrix(N5_LHSx_Min_MA,ProcessedData,'Sheet','Novel','Range','CW2')
writematrix(N6_LHSx_Min_MA,ProcessedData,'Sheet','Novel','Range','CX2')

writematrix(N1_LHSa_Min_MA,ProcessedData,'Sheet','Novel','Range','CY2')
writematrix(N2_LHSa_Min_MA,ProcessedData,'Sheet','Novel','Range','CZ2')
writematrix(N3_LHSa_Min_MA,ProcessedData,'Sheet','Novel','Range','DA2')
writematrix(N4_LHSa_Min_MA,ProcessedData,'Sheet','Novel','Range','DB2')
writematrix(N5_LHSa_Min_MA,ProcessedData,'Sheet','Novel','Range','DC2')
writematrix(N6_LHSa_Min_MA,ProcessedData,'Sheet','Novel','Range','DD2')

%Create Average file and headings
 %ProcessedData,'Sheet','Average' = 'ProcessedData,'Sheet','Average'.xlsx';
 NAV_headings                    ={'NAV_RHSy_Max','CAV_RHSy_Max','NAV_RHSx_Max','CAV_RHSx_Max',
'NAV_RHSa_Max','CAV_RHSa_Max','NAV_RHSy_0','CAV_RHSy_0','NAV_RHSx_0','CAV_RHSx_0','NAV_RHSa_0'
,'CAV_RHSa_0','NAV_RHSy_MIN','CAV_RHSy_MIN','NAV_RHSx_MIN','CAV_RHSx_MIN','NAV_RHSa_MIN','CAV_
RHSa_MIN','NAV_LHSy_Max','CAV_LHSy_Max','NAV_LHSx_Max','CAV_LHSx_Max','NAV_LHSa_Max','CAV_LHSa
_Max','NAV_LHSy_0','CAV_LHSy_0','NAV_LHSx_0','CAV_LHSx_0','NAV_LHSa_0','CAV_LHSa_0','NAV_LHSy_
MIN','CAV_LHSy_MIN','NAV_LHSx_MIN','CAV_LHSx_MIN','NAV_LHSa_MIN','CAV_LHSa_MIN'};
 writecell(NAV_headings,ProcessedData,'Sheet','Average','Range','A1')
 disp('Writing Average values')

%Write Average data Max values RHS
writematrix(NAV_RHSy_Max',ProcessedData,'Sheet','Average','Range','A2')
writematrix(CAV_RHSy_Max',ProcessedData,'Sheet','Average','Range','B2')
writematrix(NAV_RHSx_Max',ProcessedData,'Sheet','Average','Range','C2')
writematrix(CAV_RHSx_Max',ProcessedData,'Sheet','Average','Range','D2')
writematrix(NAV_RHSa_Max',ProcessedData,'Sheet','Average','Range','E2')
writematrix(CAV_RHSa_Max',ProcessedData,'Sheet','Average','Range','F2')

%Write Average data centre values RHS
writematrix(NAV_RHSy_0',ProcessedData,'Sheet','Average','Range','G2')
writematrix(CAV_RHSy_0',ProcessedData,'Sheet','Average','Range','H2')
writematrix(NAV_RHSx_0',ProcessedData,'Sheet','Average','Range','I2')
writematrix(CAV_RHSx_0',ProcessedData,'Sheet','Average','Range','J2')
writematrix(NAV_RHSa_0',ProcessedData,'Sheet','Average','Range','K2')
writematrix(CAV_RHSa_0',ProcessedData,'Sheet','Average','Range','L2')

%Write Average data Min values RHS
writematrix(NAV_RHSy_Min',ProcessedData,'Sheet','Average','Range','M2')
writematrix(CAV_RHSy_Min',ProcessedData,'Sheet','Average','Range','N2')
writematrix(NAV_RHSx_Min',ProcessedData,'Sheet','Average','Range','O2')
writematrix(CAV_RHSx_Min',ProcessedData,'Sheet','Average','Range','P2')
writematrix(NAV_RHSa_Min',ProcessedData,'Sheet','Average','Range','Q2')
writematrix(CAV_RHSa_Min',ProcessedData,'Sheet','Average','Range','R2')

%Write Average data Max values LHS
writematrix(NAV_LHSy_Max',ProcessedData,'Sheet','Average','Range','S2')
writematrix(CAV_LHSy_Max',ProcessedData,'Sheet','Average','Range','T2')
writematrix(NAV_LHSx_Max',ProcessedData,'Sheet','Average','Range','U2')
writematrix(CAV_LHSx_Max',ProcessedData,'Sheet','Average','Range','V2')
writematrix(NAV_LHSa_Max',ProcessedData,'Sheet','Average','Range','W2')
writematrix(CAV_LHSa_Max',ProcessedData,'Sheet','Average','Range','X2')

%Write Average data centre values LHS
writematrix(NAV_LHSy_0',ProcessedData,'Sheet','Average','Range','Y2')
writematrix(CAV_LHSy_0',ProcessedData,'Sheet','Average','Range','Z2')
writematrix(NAV_LHSx_0',ProcessedData,'Sheet','Average','Range','AA2')
writematrix(CAV_LHSx_0',ProcessedData,'Sheet','Average','Range','AB2')
writematrix(NAV_LHSa_0',ProcessedData,'Sheet','Average','Range','AC2')
writematrix(CAV_LHSa_0',ProcessedData,'Sheet','Average','Range','AD2')

%Write Average data Min values LHS
```

```
writematrix(NAV_LHSy_Min',ProcessedData,'Sheet','Average','Range','AE2')
writematrix(CAV_LHSy_Min',ProcessedData,'Sheet','Average','Range','AF2')
writematrix(NAV_LHSx_Min',ProcessedData,'Sheet','Average','Range','AG2')
writematrix(CAV_LHSx_Min',ProcessedData,'Sheet','Average','Range','AH2')
writematrix(NAV_LHSa_Min',ProcessedData,'Sheet','Average','Range','AI2')
writematrix(CAV_LHSa_Min',ProcessedData,'Sheet','Average','Range','AJ2')


% Write Average NEUTRAL DEFLECTION TO SHEET ND_A

 NAV_nd_headings
={'NAV_RHSy_deltaT','CAV_RHSy_deltaT','NAV_RHSx_deltaT','CAV_RHSx_deltaT','NAV_RHSa_deltaT','C
AV_RHSa_deltaT','NAV_RHSy_deltaC','CAV_RHSy_deltaC','NAV_RHSx_deltaC','CAV_RHSx_deltaC','NAV_R
HSa_deltaC','CAV_RHSa_deltaC','NAV_LHSy_deltaT','CAV_LHSy_deltaT','NAV_LHSx_deltaT','CAV_LHSx_
deltaT','NAV_LHSa_deltaT','CAV_LHSa_deltaT','NAV_LHSy_deltaC','CAV_LHSy_deltaC','NAV_LHSx_delt
aC','CAV_LHSx_deltaC','NAV_LHSa_deltaC','CAV_LHSa_deltaC'};
 writecell(NAV_nd_headings,ProcessedData,'Sheet', 'ND_A','Range','A1')
 disp('Writing Average ND values')

%Write Average data tension neutral deflection values RHS
writematrix(NAV_RHSy_deltaT',ProcessedData,'Sheet', 'ND_A','Range','A2')
writematrix(CAV_RHSy_deltaT',ProcessedData,'Sheet', 'ND_A','Range','B2')
writematrix(NAV_RHSx_deltaT',ProcessedData,'Sheet', 'ND_A','Range','C2')
writematrix(CAV_RHSx_deltaT',ProcessedData,'Sheet', 'ND_A','Range','D2')
writematrix(NAV_RHSa_deltaT',ProcessedData,'Sheet', 'ND_A','Range','E2')
writematrix(CAV_RHSa_deltaT',ProcessedData,'Sheet', 'ND_A','Range','F2')

%Write Average data compression neutral deflection values RHS
writematrix(NAV_RHSy_deltaC',ProcessedData,'Sheet', 'ND_A','Range','G2')
writematrix(CAV_RHSy_deltaC',ProcessedData,'Sheet', 'ND_A','Range','H2')

writematrix(NAV_RHSx_deltaC',ProcessedData,'Sheet', 'ND_A','Range','I2')
writematrix(CAV_RHSx_deltaC',ProcessedData,'Sheet', 'ND_A','Range','J2')
writematrix(NAV_RHSa_deltaC',ProcessedData,'Sheet', 'ND_A','Range','K2')
writematrix(CAV_RHSa_deltaC',ProcessedData,'Sheet', 'ND_A','Range','L2')

%Write Average data tension neutral deflection values LHS
writematrix(NAV_LHSy_deltaT',ProcessedData,'Sheet', 'ND_A','Range','M2')
writematrix(CAV_LHSy_deltaT',ProcessedData,'Sheet', 'ND_A','Range','N2')
writematrix(NAV_LHSx_deltaT',ProcessedData,'Sheet', 'ND_A','Range','O2')
writematrix(CAV_LHSx_deltaT',ProcessedData,'Sheet', 'ND_A','Range','P2')
writematrix(NAV_LHSa_deltaT',ProcessedData,'Sheet', 'ND_A','Range','Q2')
writematrix(CAV_LHSa_deltaT',ProcessedData,'Sheet', 'ND_A','Range','R2')

%Write Average data compression neutral deflection values LHS
writematrix(NAV_LHSy_deltaC',ProcessedData,'Sheet', 'ND_A','Range','S2')
writematrix(CAV_LHSy_deltaC',ProcessedData,'Sheet', 'ND_A','Range','T2')
writematrix(NAV_LHSx_deltaC',ProcessedData,'Sheet', 'ND_A','Range','U2')
writematrix(CAV_LHSx_deltaC',ProcessedData,'Sheet', 'ND_A','Range','V2')
writematrix(NAV_LHSa_deltaC',ProcessedData,'Sheet', 'ND_A','Range','W2')
writematrix(CAV_LHSa_deltaC',ProcessedData,'Sheet', 'ND_A','Range','X2')

%Create  NEUTRAL DEFLECTION file and headings
% NeutralDeflection = 'NeutralDeflection.xlsx';
 %Witre novel values to sheet 1
 N_nd_headings
={'N1_RHSy_deltaT','N2_RHSy_deltaT','N3_RHSy_deltaT','N4_RHSy_deltaT','N5_RHSy_deltaT','N6_RHS
y_deltaT','N1_RHSx_deltaT','N2_RHSx_deltaT','N3_RHSx_deltaT','N4_RHSx_deltaT','N5_RHSx_deltaT'
,'N6_RHSx_deltaT','N1_RHSa_deltaT','N2_RHSa_deltaT','N3_RHSa_deltaT','N4_RHSa_deltaT','N5_RHSa
_deltaT','N6_RHSa_deltaT','N1_RHSy_deltaC','N2_RHSy_deltaC','N3_RHSy_deltaC','N4_RHSy_deltaC',
'N5_RHSy_deltaC','N6_RHSy_deltaC','N1_RHSx_deltaC','N2_RHSx_deltaC','N3_RHSx_deltaC','N4_RHSx_
deltaC','N5_RHSx_deltaC','N6_RHSx_deltaC','N1_RHSa_deltaC','N2_RHSa_deltaC','N3_RHSa_deltaC','
N4_RHSa_deltaC','N5_RHSa_deltaC','N6_RHSa_deltaC','N1_LHSy_deltaT','N2_LHSy_deltaT','N3_LHSy_d
eltaT','N4_LHSy_deltaT','N5_LHSy_deltaT','N6_LHSy_deltaT','N1_LHSx_deltaT','N2_LHSx_deltaT','N
3_LHSx_deltaT','N4_LHSx_deltaT','N5_LHSx_deltaT','N6_LHSx_deltaT','N1_LHSa_deltaT','N2_LHSa_de
ltaT','N3_LHSa_deltaT','N4_LHSa_deltaT','N5_LHSa_deltaT','N6_LHSa_deltaT','N1_LHSy_deltaC','N2
_LHSy_deltaC','N3_LHSy_deltaC','N4_LHSy_deltaC','N5_LHSy_deltaC','N6_LHSy_deltaC','N1_LHSx_del
taC','N2_LHSx_deltaC','N3_LHSx_deltaC','N4_LHSx_deltaC','N5_LHSx_deltaC','N6_LHSx_deltaC','N1_
LHSa_deltaC','N2_LHSa_deltaC','N3_LHSa_deltaC','N4_LHSa_deltaC','N5_LHSa_deltaC','N6_LHSa_delt
aC' };
 writecell(N_nd_headings,ProcessedData,'Sheet','ND_N','Range','A1')
 disp('Writing Novel ND values')

%Write Novel neutral deflection values RHS
%Tension
writematrix(N1_RHSy_deltaT',ProcessedData,'Sheet','ND_N','Range','A2')
writematrix(N2_RHSy_deltaT',ProcessedData,'Sheet','ND_N','Range','B2')
```

```
writematrix(N3_RHSy_deltaT',ProcessedData,'Sheet','ND_N','Range','C2')
writematrix(N4_RHSy_deltaT',ProcessedData,'Sheet','ND_N','Range','D2')
writematrix(N5_RHSy_deltaT',ProcessedData,'Sheet','ND_N','Range','E2')
writematrix(N6_RHSy_deltaT',ProcessedData,'Sheet','ND_N','Range','F2')

writematrix(N1_RHSx_deltaT',ProcessedData,'Sheet','ND_N','Range','G2')
writematrix(N2_RHSx_deltaT',ProcessedData,'Sheet','ND_N','Range','H2')
writematrix(N3_RHSx_deltaT',ProcessedData,'Sheet','ND_N','Range','I2')
writematrix(N4_RHSx_deltaT',ProcessedData,'Sheet','ND_N','Range','J2')
writematrix(N5_RHSx_deltaT',ProcessedData,'Sheet','ND_N','Range','K2')
writematrix(N6_RHSx_deltaT',ProcessedData,'Sheet','ND_N','Range','L2')

writematrix(N1_RHSa_deltaT',ProcessedData,'Sheet','ND_N','Range','M2')
writematrix(N2_RHSa_deltaT',ProcessedData,'Sheet','ND_N','Range','N2')
writematrix(N3_RHSa_deltaT',ProcessedData,'Sheet','ND_N','Range','O2')
writematrix(N4_RHSa_deltaT',ProcessedData,'Sheet','ND_N','Range','P2')
writematrix(N5_RHSa_deltaT',ProcessedData,'Sheet','ND_N','Range','Q2')
writematrix(N6_RHSa_deltaT',ProcessedData,'Sheet','ND_N','Range','R2')

%Compression
writematrix(N1_RHSy_deltaC',ProcessedData,'Sheet','ND_N','Range','S2')
writematrix(N2_RHSy_deltaC',ProcessedData,'Sheet','ND_N','Range','T2')
writematrix(N3_RHSy_deltaC',ProcessedData,'Sheet','ND_N','Range','U2')
writematrix(N4_RHSy_deltaC',ProcessedData,'Sheet','ND_N','Range','V2')
writematrix(N5_RHSy_deltaC',ProcessedData,'Sheet','ND_N','Range','W2')
writematrix(N6_RHSy_deltaC',ProcessedData,'Sheet','ND_N','Range','X2')

writematrix(N1_RHSx_deltaC',ProcessedData,'Sheet','ND_N','Range','Y2')
writematrix(N2_RHSx_deltaC',ProcessedData,'Sheet','ND_N','Range','Z2')
writematrix(N3_RHSx_deltaC',ProcessedData,'Sheet','ND_N','Range','AA2')
writematrix(N4_RHSx_deltaC',ProcessedData,'Sheet','ND_N','Range','AB2')
writematrix(N5_RHSx_deltaC',ProcessedData,'Sheet','ND_N','Range','AC2')
writematrix(N6_RHSx_deltaC',ProcessedData,'Sheet','ND_N','Range','AD2')

writematrix(N1_RHSa_deltaC',ProcessedData,'Sheet','ND_N','Range','AE2')
writematrix(N2_RHSa_deltaC',ProcessedData,'Sheet','ND_N','Range','AF2')
writematrix(N3_RHSa_deltaC',ProcessedData,'Sheet','ND_N','Range','AG2')
writematrix(N4_RHSa_deltaC',ProcessedData,'Sheet','ND_N','Range','AH2')
writematrix(N5_RHSa_deltaC',ProcessedData,'Sheet','ND_N','Range','AI2')
writematrix(N6_RHSa_deltaC',ProcessedData,'Sheet','ND_N','Range','AJ2')

%Write neutral deflection values LHS
%Tension
writematrix(N1_LHSy_deltaT',ProcessedData,'Sheet','ND_N','Range','AK2')
writematrix(N2_LHSy_deltaT',ProcessedData,'Sheet','ND_N','Range','AL2')
writematrix(N3_LHSy_deltaT',ProcessedData,'Sheet','ND_N','Range','AM2')
writematrix(N4_LHSy_deltaT',ProcessedData,'Sheet','ND_N','Range','AN2')
writematrix(N5_LHSy_deltaT',ProcessedData,'Sheet','ND_N','Range','AO2')
writematrix(N6_LHSy_deltaT',ProcessedData,'Sheet','ND_N','Range','AP2')

writematrix(N1_LHSx_deltaT',ProcessedData,'Sheet','ND_N','Range','AQ2')
writematrix(N2_LHSx_deltaT',ProcessedData,'Sheet','ND_N','Range','AR2')
writematrix(N3_LHSx_deltaT',ProcessedData,'Sheet','ND_N','Range','AS2')
writematrix(N4_LHSx_deltaT',ProcessedData,'Sheet','ND_N','Range','AT2')
writematrix(N5_LHSx_deltaT',ProcessedData,'Sheet','ND_N','Range','AU2')
writematrix(N6_LHSx_deltaT',ProcessedData,'Sheet','ND_N','Range','AV2')

writematrix(N1_LHSa_deltaT',ProcessedData,'Sheet','ND_N','Range','AW2')
writematrix(N2_LHSa_deltaT',ProcessedData,'Sheet','ND_N','Range','AX2')
writematrix(N3_LHSa_deltaT',ProcessedData,'Sheet','ND_N','Range','AY2')
writematrix(N4_LHSa_deltaT',ProcessedData,'Sheet','ND_N','Range','AZ2')
writematrix(N5_LHSa_deltaT',ProcessedData,'Sheet','ND_N','Range','BA2')
writematrix(N6_LHSa_deltaT',ProcessedData,'Sheet','ND_N','Range','BB2')

%Compression
writematrix(N1_LHSy_deltaC',ProcessedData,'Sheet','ND_N','Range','BC2')
writematrix(N2_LHSy_deltaC',ProcessedData,'Sheet','ND_N','Range','BD2')
writematrix(N3_LHSy_deltaC',ProcessedData,'Sheet','ND_N','Range','BE2')
writematrix(N4_LHSy_deltaC',ProcessedData,'Sheet','ND_N','Range','BF2')
writematrix(N5_LHSy_deltaC',ProcessedData,'Sheet','ND_N','Range','BG2')
writematrix(N6_LHSy_deltaC',ProcessedData,'Sheet','ND_N','Range','BH2')

writematrix(N1_LHSx_deltaC',ProcessedData,'Sheet','ND_N','Range','BI2')
writematrix(N2_LHSx_deltaC',ProcessedData,'Sheet','ND_N','Range','BJ2')
writematrix(N3_LHSx_deltaC',ProcessedData,'Sheet','ND_N','Range','BK2')
writematrix(N4_LHSx_deltaC',ProcessedData,'Sheet','ND_N','Range','BL2')
writematrix(N5_LHSx_deltaC',ProcessedData,'Sheet','ND_N','Range','BM2')
```

```
writematrix(N6_LHSx_deltaC',ProcessedData,'Sheet','ND_N','Range','BN2')

writematrix(N1_LHSa_deltaC',ProcessedData,'Sheet','ND_N','Range','BO2')
writematrix(N2_LHSa_deltaC',ProcessedData,'Sheet','ND_N','Range','BP2')
writematrix(N3_LHSa_deltaC',ProcessedData,'Sheet','ND_N','Range','BQ2')
writematrix(N4_LHSa_deltaC',ProcessedData,'Sheet','ND_N','Range','BR2')
writematrix(N5_LHSa_deltaC',ProcessedData,'Sheet','ND_N','Range','BS2')
writematrix(N6_LHSa_deltaC',ProcessedData,'Sheet','ND_N','Range','BT2')

%Create control sheet in neutral deflection file and headings
%NeutralDeflection = 'NeutralDeflection.xlsx';
 C_nd_headings
={'C1_RHSy_deltaT','C2_RHSy_deltaT','C3_RHSy_deltaT','C6_RHSy_deltaT','C7_RHSy_deltaT','C8_RHS
y_deltaT','C1_RHSx_deltaT','C2_RHSx_deltaT','C3_RHSx_deltaT','C6_RHSx_deltaT','C7_RHSx_deltaT'
,'C8_RHSx_deltaT','C1_RHSa_deltaT','C2_RHSa_deltaT','C3_RHSa_deltaT','C6_RHSa_deltaT','C7_RHSa
_deltaT','C8_RHSa_deltaT','C1_RHSy_deltaC','C2_RHSy_deltaC','C3_RHSy_deltaC','C6_RHSy_deltaC',
'C7_RHSy_deltaC','C8_RHSy_deltaC','C1_RHSx_deltaC','C2_RHSx_deltaC','C3_RHSx_deltaC','C6_RHSx_
deltaC','C7_RHSx_deltaC','C8_RHSx_deltaC','C1_RHSa_deltaC','C2_RHSa_deltaC','C3_RHSa_deltaC','
C6_RHSa_deltaC','C7_RHSa_deltaC','C8_RHSa_deltaC','C1_LHSy_deltaT','C2_LHSy_deltaT','C3_LHSy_d
eltaT','C6_LHSy_deltaT','C7_LHSy_deltaT','C8_LHSy_deltaT','C1_LHSx_deltaT','C2_LHSx_deltaT','C
3_LHSx_deltaT','C6_LHSx_deltaT','C7_LHSx_deltaT','C8_LHSx_deltaT','C1_LHSa_deltaT','C2_LHSa_de
ltaT','C3_LHSa_deltaT','C6_LHSa_deltaT','C7_LHSa_deltaT','C8_LHSa_deltaT','C1_LHSy_deltaC','C2
_LHSy_deltaC','C3_LHSy_deltaC','C6_LHSy_deltaC','C7_LHSy_deltaC','C8_LHSy_deltaC','C1_LHSx_del
taC','C2_LHSx_deltaC','C3_LHSx_deltaC','C6_LHSx_deltaC','C7_LHSx_deltaC','C8_LHSx_deltaC','C1_
LHSa_deltaC','C2_LHSa_deltaC','C3_LHSa_deltaC','C6_LHSa_deltaC','C7_LHSa_deltaC','C8_LHSa_delt
aC' };
 writecell(C_nd_headings,ProcessedData,'Sheet','ND_C','Range','A1')
 disp('Writing Control ND values')

%Write Control neutral deflection values RHS
%Tension
writematrix(C1_RHSy_deltaT',ProcessedData,'Sheet','ND_C','Range','A2')
writematrix(C2_RHSy_deltaT',ProcessedData,'Sheet','ND_C','Range','B2')
writematrix(C3_RHSy_deltaT',ProcessedData,'Sheet','ND_C','Range','C2')
writematrix(C6_RHSy_deltaT',ProcessedData,'Sheet','ND_C','Range','D2')
writematrix(C7_RHSy_deltaT',ProcessedData,'Sheet','ND_C','Range','E2')
writematrix(C8_RHSy_deltaT',ProcessedData,'Sheet','ND_C','Range','F2')

writematrix(C1_RHSx_deltaT',ProcessedData,'Sheet','ND_C','Range','G2')
writematrix(C2_RHSx_deltaT',ProcessedData,'Sheet','ND_C','Range','H2')
writematrix(C3_RHSx_deltaT',ProcessedData,'Sheet','ND_C','Range','I2')
writematrix(C6_RHSx_deltaT',ProcessedData,'Sheet','ND_C','Range','J2')
writematrix(C7_RHSx_deltaT',ProcessedData,'Sheet','ND_C','Range','K2')
writematrix(C8_RHSx_deltaT',ProcessedData,'Sheet','ND_C','Range','L2')

writematrix(C1_RHSa_deltaT',ProcessedData,'Sheet','ND_C','Range','M2')
writematrix(C2_RHSa_deltaT',ProcessedData,'Sheet','ND_C','Range','N2')
writematrix(C3_RHSa_deltaT',ProcessedData,'Sheet','ND_C','Range','O2')
writematrix(C6_RHSa_deltaT',ProcessedData,'Sheet','ND_C','Range','P2')
writematrix(C7_RHSa_deltaT',ProcessedData,'Sheet','ND_C','Range','Q2')
writematrix(C8_RHSa_deltaT',ProcessedData,'Sheet','ND_C','Range','R2')

%Compression
writematrix(C1_RHSy_deltaC',ProcessedData,'Sheet','ND_C','Range','S2')
writematrix(C2_RHSy_deltaC',ProcessedData,'Sheet','ND_C','Range','T2')
writematrix(C3_RHSy_deltaC',ProcessedData,'Sheet','ND_C','Range','U2')
writematrix(C6_RHSy_deltaC',ProcessedData,'Sheet','ND_C','Range','V2')
writematrix(C7_RHSy_deltaC',ProcessedData,'Sheet','ND_C','Range','W2')
writematrix(C8_RHSy_deltaC',ProcessedData,'Sheet','ND_C','Range','X2')

writematrix(C1_RHSx_deltaC',ProcessedData,'Sheet','ND_C','Range','Y2')
writematrix(C2_RHSx_deltaC',ProcessedData,'Sheet','ND_C','Range','Z2')
writematrix(C3_RHSx_deltaC',ProcessedData,'Sheet','ND_C','Range','AA2')
writematrix(C6_RHSx_deltaC',ProcessedData,'Sheet','ND_C','Range','AB2')
writematrix(C7_RHSx_deltaC',ProcessedData,'Sheet','ND_C','Range','AC2')
writematrix(C8_RHSx_deltaC',ProcessedData,'Sheet','ND_C','Range','AD2')

writematrix(C1_RHSa_deltaC',ProcessedData,'Sheet','ND_C','Range','AE2')
writematrix(C2_RHSa_deltaC',ProcessedData,'Sheet','ND_C','Range','AF2')
writematrix(C3_RHSa_deltaC',ProcessedData,'Sheet','ND_C','Range','AG2')
writematrix(C6_RHSa_deltaC',ProcessedData,'Sheet','ND_C','Range','AH2')
writematrix(C7_RHSa_deltaC',ProcessedData,'Sheet','ND_C','Range','AI2')
writematrix(C8_RHSa_deltaC',ProcessedData,'Sheet','ND_C','Range','AJ2')

%Write neutral deflection values LHS
%Tension
writematrix(C1_LHSy_deltaT',ProcessedData,'Sheet','ND_C','Range','AK2')
```

```
writematrix(C2_LHSy_deltaT',ProcessedData,'Sheet','ND_C','Range','AL2')
writematrix(C3_LHSy_deltaT',ProcessedData,'Sheet','ND_C','Range','AM2')
writematrix(C6_LHSy_deltaT',ProcessedData,'Sheet','ND_C','Range','AN2')
writematrix(C7_LHSy_deltaT',ProcessedData,'Sheet','ND_C','Range','AO2')
writematrix(C8_LHSy_deltaT',ProcessedData,'Sheet','ND_C','Range','AP2')

writematrix(C1_LHSx_deltaT',ProcessedData,'Sheet','ND_C','Range','AQ2')
writematrix(C2_LHSx_deltaT',ProcessedData,'Sheet','ND_C','Range','AR2')
writematrix(C3_LHSx_deltaT',ProcessedData,'Sheet','ND_C','Range','AS2')
writematrix(C6_LHSx_deltaT',ProcessedData,'Sheet','ND_C','Range','AT2')
writematrix(C7_LHSx_deltaT',ProcessedData,'Sheet','ND_C','Range','AU2')
writematrix(C8_LHSx_deltaT',ProcessedData,'Sheet','ND_C','Range','AV2')

writematrix(C1_LHSa_deltaT',ProcessedData,'Sheet','ND_C','Range','AW2')
writematrix(C2_LHSa_deltaT',ProcessedData,'Sheet','ND_C','Range','AX2')
writematrix(C3_LHSa_deltaT',ProcessedData,'Sheet','ND_C','Range','AY2')
writematrix(C6_LHSa_deltaT',ProcessedData,'Sheet','ND_C','Range','AZ2')
writematrix(C7_LHSa_deltaT',ProcessedData,'Sheet','ND_C','Range','BA2')
writematrix(C8_LHSa_deltaT',ProcessedData,'Sheet','ND_C','Range','BB2')

%Compression
writematrix(C1_LHSy_deltaC',ProcessedData,'Sheet','ND_C','Range','BC2')
writematrix(C2_LHSy_deltaC',ProcessedData,'Sheet','ND_C','Range','BD2')
writematrix(C3_LHSy_deltaC',ProcessedData,'Sheet','ND_C','Range','BE2')
writematrix(C6_LHSy_deltaC',ProcessedData,'Sheet','ND_C','Range','BF2')
writematrix(C7_LHSy_deltaC',ProcessedData,'Sheet','ND_C','Range','BG2')
writematrix(C8_LHSy_deltaC',ProcessedData,'Sheet','ND_C','Range','BH2')

writematrix(C1_LHSx_deltaC',ProcessedData,'Sheet','ND_C','Range','BI2')
writematrix(C2_LHSx_deltaC',ProcessedData,'Sheet','ND_C','Range','BJ2')
writematrix(C3_LHSx_deltaC',ProcessedData,'Sheet','ND_C','Range','BK2')
writematrix(C6_LHSx_deltaC',ProcessedData,'Sheet','ND_C','Range','BL2')
writematrix(C7_LHSx_deltaC',ProcessedData,'Sheet','ND_C','Range','BM2')
writematrix(C8_LHSx_deltaC',ProcessedData,'Sheet','ND_C','Range','BN2')

writematrix(C1_LHSa_deltaC',ProcessedData,'Sheet','ND_C','Range','BO2')
writematrix(C2_LHSa_deltaC',ProcessedData,'Sheet','ND_C','Range','BP2')
writematrix(C3_LHSa_deltaC',ProcessedData,'Sheet','ND_C','Range','BQ2')
writematrix(C6_LHSa_deltaC',ProcessedData,'Sheet','ND_C','Range','BR2')
writematrix(C7_LHSa_deltaC',ProcessedData,'Sheet','ND_C','Range','BS2')
writematrix(C8_LHSa_deltaC',ProcessedData,'Sheet','ND_C','Range','BT2')

 %%%%%%%%%%%%%%%%%%%%%%%%%%%%%%%%%%%%%%%%%%%%%%%%%%%%%%%%
 %CALCULATE  + AND - STD CURVES FOR ALL AVERAGE VECTORS
 %For motion vectors
  %For neutral deflection vectors
 for i = 1: vector_length/2

   CSTD_RHSy_deltaT_PLUS(i) = CAV_RHSy_deltaT(i) + CSTD_RHSy_deltaT(i);
   CSTD_RHSy_deltaT_MINUS(i) = CAV_RHSy_deltaT(i) - CSTD_RHSy_deltaT(i);
   CSTD_RHSy_deltaC_PLUS(i) = CAV_RHSy_deltaC(i) + CSTD_RHSy_deltaC(i);
   CSTD_RHSy_deltaC_MINUS(i) = CAV_RHSy_deltaC(i) - CSTD_RHSy_deltaC(i);

   CSTD_RHSx_deltaT_PLUS(i) = CAV_RHSx_deltaT(i) + CSTD_RHSx_deltaT(i);
   CSTD_RHSx_deltaT_MINUS(i) = CAV_RHSx_deltaT(i) - CSTD_RHSx_deltaT(i);
   CSTD_RHSx_deltaC_PLUS(i) = CAV_RHSx_deltaC(i) + CSTD_RHSx_deltaC(i);
   CSTD_RHSx_deltaC_MINUS(i) = CAV_RHSx_deltaC(i) - CSTD_RHSx_deltaC(i);

   CSTD_RHSa_deltaT_PLUS(i) = CAV_RHSa_deltaT(i) + CSTD_RHSa_deltaT(i);
   CSTD_RHSa_deltaT_MINUS(i) = CAV_RHSa_deltaT(i) - CSTD_RHSa_deltaT(i);
   CSTD_RHSa_deltaC_PLUS(i) = CAV_RHSa_deltaC(i) + CSTD_RHSa_deltaC(i);
   CSTD_RHSa_deltaC_MINUS(i) = CAV_RHSa_deltaC(i) - CSTD_RHSa_deltaC(i);

   CSTD_LHSy_deltaT_PLUS(i) = CAV_LHSy_deltaT(i) + CSTD_LHSy_deltaT(i);
   CSTD_LHSy_deltaT_MINUS(i) = CAV_LHSy_deltaT(i) - CSTD_LHSy_deltaT(i);
   CSTD_LHSy_deltaC_PLUS(i) = CAV_LHSy_deltaC(i) + CSTD_LHSy_deltaC(i);
   CSTD_LHSy_deltaC_MINUS(i) = CAV_LHSy_deltaC(i) - CSTD_LHSy_deltaC(i);

   CSTD_LHSx_deltaT_PLUS(i) = CAV_LHSx_deltaT(i) + CSTD_LHSx_deltaT(i);
   CSTD_LHSx_deltaT_MINUS(i) = CAV_LHSx_deltaT(i) - CSTD_LHSx_deltaT(i);
   CSTD_LHSx_deltaC_PLUS(i) = CAV_LHSx_deltaC(i) + CSTD_LHSx_deltaC(i);
   CSTD_LHSx_deltaC_MINUS(i) = CAV_LHSx_deltaC(i) - CSTD_LHSx_deltaC(i);

   CSTD_LHSa_deltaT_PLUS(i) = CAV_LHSa_deltaT(i) + CSTD_LHSa_deltaT(i);
   CSTD_LHSa_deltaT_MINUS(i) = CAV_LHSa_deltaT(i) - CSTD_LHSa_deltaT(i);
   CSTD_LHSa_deltaC_PLUS(i) = CAV_LHSa_deltaC(i) + CSTD_LHSa_deltaC(i);
   CSTD_LHSa_deltaC_MINUS(i) = CAV_LHSa_deltaC(i) - CSTD_LHSa_deltaC(i);
```

```
NSTD_RHSy_deltaT_PLUS(i) = NAV_RHSy_deltaT(i) + NSTD_RHSy_deltaT(i);
NSTD_RHSy_deltaT_MINUS(i) = NAV_RHSy_deltaT(i) - NSTD_RHSy_deltaT(i);
NSTD_RHSy_deltaC_PLUS(i) = NAV_RHSy_deltaC(i) + NSTD_RHSy_deltaC(i);
NSTD_RHSy_deltaC_MINUS(i) = NAV_RHSy_deltaC(i) - NSTD_RHSy_deltaC(i);

NSTD_RHSx_deltaT_PLUS(i) = NAV_RHSx_deltaT(i) + NSTD_RHSx_deltaT(i);
NSTD_RHSx_deltaT_MINUS(i) = NAV_RHSx_deltaT(i) - NSTD_RHSx_deltaT(i);
NSTD_RHSx_deltaC_PLUS(i) = NAV_RHSx_deltaC(i) + NSTD_RHSx_deltaC(i);
NSTD_RHSx_deltaC_MINUS(i) = NAV_RHSx_deltaC(i) - NSTD_RHSx_deltaC(i);

NSTD_RHSa_deltaT_PLUS(i) = NAV_RHSa_deltaT(i) + NSTD_RHSa_deltaT(i);
NSTD_RHSa_deltaT_MINUS(i) = NAV_RHSa_deltaT(i) - NSTD_RHSa_deltaT(i);
NSTD_RHSa_deltaC_PLUS(i) = NAV_RHSa_deltaC(i) + NSTD_RHSa_deltaC(i);
NSTD_RHSa_deltaC_MINUS(i) = NAV_RHSa_deltaC(i) - NSTD_RHSa_deltaC(i);

NSTD_LHSy_deltaT_PLUS(i) = NAV_LHSy_deltaT(i) + NSTD_LHSy_deltaT(i);
NSTD_LHSy_deltaT_MINUS(i) = NAV_LHSy_deltaT(i) - NSTD_LHSy_deltaT(i);
NSTD_LHSy_deltaC_PLUS(i) = NAV_LHSy_deltaC(i) + NSTD_LHSy_deltaC(i);
NSTD_LHSy_deltaC_MINUS(i) = NAV_LHSy_deltaC(i) - NSTD_LHSy_deltaC(i);

NSTD_LHSx_deltaT_PLUS(i) = NAV_LHSx_deltaT(i) + NSTD_LHSx_deltaT(i);
NSTD_LHSx_deltaT_MINUS(i) = NAV_LHSx_deltaT(i) - NSTD_LHSx_deltaT(i);
NSTD_LHSx_deltaC_PLUS(i) = NAV_LHSx_deltaC(i) + NSTD_LHSx_deltaC(i);
NSTD_LHSx_deltaC_MINUS(i) = NAV_LHSx_deltaC(i) - NSTD_LHSx_deltaC(i);

NSTD_LHSa_deltaT_PLUS(i) = NAV_LHSa_deltaT(i) + NSTD_LHSa_deltaT(i);
NSTD_LHSa_deltaT_MINUS(i) = NAV_LHSa_deltaT(i) - NSTD_LHSa_deltaT(i);
NSTD_LHSa_deltaC_PLUS(i) = NAV_LHSa_deltaC(i) + NSTD_LHSa_deltaC(i);
NSTD_LHSa_deltaC_MINUS(i) = NAV_LHSa_deltaC(i) - NSTD_LHSa_deltaC(i);

%eliminate NaN values
  if isnan(CSTD_RHSy_deltaT_PLUS(i))
      CSTD_RHSy_deltaT_PLUS(i)= CSTD_RHSy_deltaT_PLUS(i-1);
  end
   if isnan(CSTD_RHSx_deltaT_PLUS(i))
      CSTD_RHSx_deltaT_PLUS(i)= CSTD_RHSx_deltaT_PLUS(i-1);
  end
   if isnan(CSTD_RHSa_deltaT_PLUS(i))
      CSTD_RHSa_deltaT_PLUS(i)= CSTD_RHSa_deltaT_PLUS(i-1);
   end
   if isnan(CSTD_LHSy_deltaT_PLUS(i))
      CSTD_LHSy_deltaT_PLUS(i)= CSTD_LHSy_deltaT_PLUS(i-1);
  end
   if isnan(CSTD_LHSx_deltaT_PLUS(i))
      CSTD_LHSx_deltaT_PLUS(i)= CSTD_LHSx_deltaT_PLUS(i-1);
  end
   if isnan(CSTD_LHSa_deltaT_PLUS(i))
      CSTD_LHSa_deltaT_PLUS(i)= CSTD_LHSa_deltaT_PLUS(i-1);
   end
 if isnan(NSTD_RHSy_deltaT_PLUS(i))
      NSTD_RHSy_deltaT_PLUS(i)= NSTD_RHSy_deltaT_PLUS(i-1);
  end
   if isnan(NSTD_RHSx_deltaT_PLUS(i))
      NSTD_RHSx_deltaT_PLUS(i)= NSTD_RHSx_deltaT_PLUS(i-1);
  end
   if isnan(NSTD_RHSa_deltaT_PLUS(i))
      NSTD_RHSa_deltaT_PLUS(i)= NSTD_RHSa_deltaT_PLUS(i-1);
   end
   if isnan(NSTD_LHSy_deltaT_PLUS(i))
      NSTD_LHSy_deltaT_PLUS(i)= NSTD_LHSy_deltaT_PLUS(i-1);
  end
   if isnan(NSTD_LHSx_deltaT_PLUS(i))
      NSTD_LHSx_deltaT_PLUS(i)= NSTD_LHSx_deltaT_PLUS(i-1);
  end
   if isnan(NSTD_LHSa_deltaT_PLUS(i))
      NSTD_LHSa_deltaT_PLUS(i)= NSTD_LHSa_deltaT_PLUS(i-1);
   end
  if isnan(CSTD_RHSy_deltaC_PLUS(i))
      CSTD_RHSy_deltaC_PLUS(i)= CSTD_RHSy_deltaC_PLUS(i-1);
  end
   if isnan(CSTD_RHSx_deltaC_PLUS(i))
      CSTD_RHSx_deltaC_PLUS(i)= CSTD_RHSx_deltaC_PLUS(i-1);
  end
   if isnan(CSTD_RHSa_deltaC_PLUS(i))
      CSTD_RHSa_deltaC_PLUS(i)= CSTD_RHSa_deltaC_PLUS(i-1);
   end
```

```
  if isnan(CSTD_LHSy_deltaC_PLUS(i))
     CSTD_LHSy_deltaC_PLUS(i)= CSTD_LHSy_deltaC_PLUS(i-1);
 end
  if isnan(CSTD_LHSx_deltaC_PLUS(i))
     CSTD_LHSx_deltaC_PLUS(i)= CSTD_LHSx_deltaC_PLUS(i-1);
 end
  if isnan(CSTD_LHSa_deltaC_PLUS(i))
     CSTD_LHSa_deltaC_PLUS(i)= CSTD_LHSa_deltaC_PLUS(i-1);
  end
if isnan(NSTD_RHSy_deltaC_PLUS(i))
     NSTD_RHSy_deltaC_PLUS(i)= NSTD_RHSy_deltaC_PLUS(i-1);
 end
  if isnan(NSTD_RHSx_deltaC_PLUS(i))
     NSTD_RHSx_deltaC_PLUS(i)= NSTD_RHSx_deltaC_PLUS(i-1);
 end
  if isnan(NSTD_RHSa_deltaC_PLUS(i))
     NSTD_RHSa_deltaC_PLUS(i)= NSTD_RHSa_deltaC_PLUS(i-1);
  end
  if isnan(NSTD_LHSy_deltaC_PLUS(i))
     NSTD_LHSy_deltaC_PLUS(i)= NSTD_LHSy_deltaC_PLUS(i-1);
 end
  if isnan(NSTD_LHSx_deltaC_PLUS(i))
     NSTD_LHSx_deltaC_PLUS(i)= NSTD_LHSx_deltaC_PLUS(i-1);
 end
  if isnan(NSTD_LHSa_deltaC_PLUS(i))
     NSTD_LHSa_deltaC_PLUS(i)= NSTD_LHSa_deltaC_PLUS(i-1);
  end
       if isnan(CSTD_RHSy_deltaT_MINUS(i))
     CSTD_RHSy_deltaT_MINUS(i)= CSTD_RHSy_deltaT_MINUS(i-1);
 end
  if isnan(CSTD_RHSx_deltaT_MINUS(i))
     CSTD_RHSx_deltaT_MINUS(i)= CSTD_RHSx_deltaT_MINUS(i-1);
 end
  if isnan(CSTD_RHSa_deltaT_MINUS(i))
     CSTD_RHSa_deltaT_MINUS(i)= CSTD_RHSa_deltaT_MINUS(i-1);
  end
  if isnan(CSTD_LHSy_deltaT_MINUS(i))
     CSTD_LHSy_deltaT_MINUS(i)= CSTD_LHSy_deltaT_MINUS(i-1);
 end
  if isnan(CSTD_LHSx_deltaT_MINUS(i))
     CSTD_LHSx_deltaT_MINUS(i)= CSTD_LHSx_deltaT_MINUS(i-1);
 end
  if isnan(CSTD_LHSa_deltaT_MINUS(i))
     CSTD_LHSa_deltaT_MINUS(i)= CSTD_LHSa_deltaT_MINUS(i-1);
  end
if isnan(NSTD_RHSy_deltaT_MINUS(i))
     NSTD_RHSy_deltaT_MINUS(i)= NSTD_RHSy_deltaT_MINUS(i-1);
 end
  if isnan(NSTD_RHSx_deltaT_MINUS(i))
     NSTD_RHSx_deltaT_MINUS(i)= NSTD_RHSx_deltaT_MINUS(i-1);
 end
  if isnan(NSTD_RHSa_deltaT_MINUS(i))
     NSTD_RHSa_deltaT_MINUS(i)= NSTD_RHSa_deltaT_MINUS(i-1);
  end
  if isnan(NSTD_LHSy_deltaT_MINUS(i))
     NSTD_LHSy_deltaT_MINUS(i)= NSTD_LHSy_deltaT_MINUS(i-1);
 end
  if isnan(NSTD_LHSx_deltaT_MINUS(i))
     NSTD_LHSx_deltaT_MINUS(i)= NSTD_LHSx_deltaT_MINUS(i-1);
 end
  if isnan(NSTD_LHSa_deltaT_MINUS(i))
     NSTD_LHSa_deltaT_MINUS(i)= NSTD_LHSa_deltaT_MINUS(i-1);
  end
 if isnan(CSTD_RHSy_deltaC_MINUS(i))
     CSTD_RHSy_deltaC_MINUS(i)= CSTD_RHSy_deltaC_MINUS(i-1);
 end
  if isnan(CSTD_RHSx_deltaC_MINUS(i))
     CSTD_RHSx_deltaC_MINUS(i)= CSTD_RHSx_deltaC_MINUS(i-1);
 end
  if isnan(CSTD_RHSa_deltaC_MINUS(i))
     CSTD_RHSa_deltaC_MINUS(i)= CSTD_RHSa_deltaC_MINUS(i-1);
  end
  if isnan(CSTD_LHSy_deltaC_MINUS(i))
     CSTD_LHSy_deltaC_MINUS(i)= CSTD_LHSy_deltaC_MINUS(i-1);
 end
  if isnan(CSTD_LHSx_deltaC_MINUS(i))
     CSTD_LHSx_deltaC_MINUS(i)= CSTD_LHSx_deltaC_MINUS(i-1);
```

```
     end
      if isnan(CSTD_LHSa_deltaC_MINUS(i))
         CSTD_LHSa_deltaC_MINUS(i)= CSTD_LHSa_deltaC_MINUS(i-1);
      end
     if isnan(NSTD_RHSy_deltaC_MINUS(i))
         NSTD_RHSy_deltaC_MINUS(i)= NSTD_RHSy_deltaC_MINUS(i-1);
     end
      if isnan(NSTD_RHSx_deltaC_MINUS(i))
         NSTD_RHSx_deltaC_MINUS(i)= NSTD_RHSx_deltaC_MINUS(i-1);
     end
      if isnan(NSTD_RHSa_deltaC_MINUS(i))
         NSTD_RHSa_deltaC_MINUS(i)= NSTD_RHSa_deltaC_MINUS(i-1);
      end
      if isnan(NSTD_LHSy_deltaC_MINUS(i))
         NSTD_LHSy_deltaC_MINUS(i)= NSTD_LHSy_deltaC_MINUS(i-1);
     end
      if isnan(NSTD_LHSx_deltaC_MINUS(i))
         NSTD_LHSx_deltaC_MINUS(i)= NSTD_LHSx_deltaC_MINUS(i-1);
     end
      if isnan(NSTD_LHSa_deltaC_MINUS(i))
         NSTD_LHSa_deltaC_MINUS(i)= NSTD_LHSa_deltaC_MINUS(i-1);
      end
 end
 %%%%%%%%%%%%%%%%%%%%%%%%%%%%%%%%%%%%%%%%%%%%%%%%%%%%%%%%
 %STEP 4
 %PLOT VALUES
figure(13);
shade(Cycle_shade_MaxMin,CSTD_RHSy_Max_PLUS,'b',Cycle_shade_MaxMin,CSTD_RHSy_Max_MINUS,'b','Li
newidth', 0.5 ,'FillType',[1 2]);
hold on
shade(Cycle_shade_MaxMin,NSTD_RHSy_Max_PLUS,'b',Cycle_shade_MaxMin,NSTD_RHSy_Max_MINUS,'b','Li
newidth', 0.5 ,'FillType',[1 2]);
shade(Cycle_shade_0,CSTD_RHSy_0_PLUS,'k',Cycle_shade_0,CSTD_RHSy_0_MINUS,'k','Linewidth',  0.5
,'FillType',[1 2]);
shade(Cycle_shade_0,NSTD_RHSy_0_PLUS,'k',Cycle_shade_0,NSTD_RHSy_0_MINUS,'k','Linewidth',  0.5
,'FillType',[1 2]);
shade(Cycle_shade_MaxMin,CSTD_RHSy_Min_PLUS,'r',Cycle_shade_MaxMin,CSTD_RHSy_Min_MINUS,'r','Li
newidth', 0.5 ,'FillType',[1 2]);
shade(Cycle_shade_MaxMin,NSTD_RHSy_Min_PLUS,'r',Cycle_shade_MaxMin,NSTD_RHSy_Min_MINUS,'r','Li
newidth', 0.5 ,'FillType',[1 2]);
%Tension
CAll_RHSy_Tension = plot(C1_Cycle_MaxMin,CAV_RHSy_Max,'--b','LineWidth',2);
NAll_RHSy_Tension = plot(N1_Cycle_MaxMin,NAV_RHSy_Max,'b','LineWidth',2);
%neutral
CAll_RHSy_neutral = plot(C1_Cycle_0,CAV_RHSy_0,'--k','LineWidth',2);
NAll_RHSy_neutral = plot(N1_Cycle_0,NAV_RHSy_0,'k','LineWidth',2);
%Compression
CAll_RHSy_Compression = plot(C1_Cycle_MaxMin,CAV_RHSy_Min,'--r','LineWidth',2);
NAll_RHSy_Compression = plot(N1_Cycle_MaxMin,NAV_RHSy_Min,'r','LineWidth',2);
%Formatting
title('AVERAGE COMPARISON: Vertical Motion of RHS Glenoid Edge');
ylabel('y (mm) ');
xlabel('Cycle');
ylim([-1 0]);
grid on;

figure(14);
shade(Cycle_shade_MaxMin,CSTD_RHSx_Max_PLUS,'b',Cycle_shade_MaxMin,CSTD_RHSx_Max_MINUS,'b','Li
newidth', 0.5 ,'FillType',[1 2]);
hold on
shade(Cycle_shade_MaxMin,NSTD_RHSx_Max_PLUS,'b',Cycle_shade_MaxMin,NSTD_RHSx_Max_MINUS,'b','Li
newidth', 0.5 ,'FillType',[1 2]);
shade(Cycle_shade_0,CSTD_RHSx_0_PLUS,'k',Cycle_shade_0,CSTD_RHSx_0_MINUS,'k','Linewidth',  0.5
,'FillType',[1 2]);
shade(Cycle_shade_0,NSTD_RHSx_0_PLUS,'k',Cycle_shade_0,NSTD_RHSx_0_MINUS,'k','Linewidth',  0.5
,'FillType',[1 2]);
shade(Cycle_shade_MaxMin,CSTD_RHSx_Min_PLUS,'r',Cycle_shade_MaxMin,CSTD_RHSx_Min_MINUS,'r','Li
newidth', 0.5 ,'FillType',[1 2]);
shade(Cycle_shade_MaxMin,NSTD_RHSx_Min_PLUS,'r',Cycle_shade_MaxMin,NSTD_RHSx_Min_MINUS,'r','Li
newidth', 0.5 ,'FillType',[1 2]);
%Tension
CAll_RHSx_Tension = plot(C1_Cycle_MaxMin,CAV_RHSx_Max,'--b','LineWidth',2);
NAll_RHSx_Tension = plot(N1_Cycle_MaxMin,NAV_RHSx_Max,'b','LineWidth',2);
%neutral
CAll_RHSx_neutral = plot(C1_Cycle_MaxMin,CAV_RHSx_0,'--k','LineWidth',2);
NAll_RHSx_neutral = plot(N1_Cycle_MaxMin,NAV_RHSx_0,'k','LineWidth',2);
%Compression
```

```
CAll_RHSx_Compression = plot(C1_Cycle_MaxMin,CAV_RHSx_Min,'--r','LineWidth',2);
NAll_RHSx_Compression = plot(N1_Cycle_MaxMin,NAV_RHSx_Min,'r','LineWidth',2);
%Formatting
title('AVERAGE COMPARISON: Horizontal Motion of RHS Glenoid Edge');
ylabel('x (mm) ');
xlabel('Cycle');
ylim([0 1]);
grid on;

figure(15);
shade(Cycle_shade_MaxMin,CSTD_RHSa_Max_PLUS,'b',Cycle_shade_MaxMin,CSTD_RHSa_Max_MINUS,'b','Li
newidth', 0.5 ,'FillType',[1 2]);
hold on
shade(Cycle_shade_MaxMin,NSTD_RHSa_Max_PLUS,'b',Cycle_shade_MaxMin,NSTD_RHSa_Max_MINUS,'b','Li
newidth', 0.5 ,'FillType',[1 2]);
shade(Cycle_shade_0,CSTD_RHSa_0_PLUS,'k',Cycle_shade_0,CSTD_RHSa_0_MINUS,'k','Linewidth',  0.5
,'FillType',[1 2]);
shade(Cycle_shade_0,NSTD_RHSa_0_PLUS,'k',Cycle_shade_0,NSTD_RHSa_0_MINUS,'k','Linewidth',  0.5
,'FillType',[1 2]);
shade(Cycle_shade_MaxMin,CSTD_RHSa_Min_PLUS,'r',Cycle_shade_MaxMin,CSTD_RHSa_Min_MINUS,'r','Li
newidth', 0.5 ,'FillType',[1 2]);
shade(Cycle_shade_MaxMin,NSTD_RHSa_Min_PLUS,'r',Cycle_shade_MaxMin,NSTD_RHSa_Min_MINUS,'r','Li
newidth', 0.5 ,'FillType',[1 2]);
%Tension
CAll_RHSa_Tension = plot(C1_Cycle_MaxMin,CAV_RHSa_Max,'--b','LineWidth',2);
NAll_RHSa_Tension = plot(N1_Cycle_MaxMin,NAV_RHSa_Max,'b','LineWidth',2);
%neutral
CAll_RHSa_neutral = plot(C1_Cycle_MaxMin,CAV_RHSa_0,'--k','LineWidth',2);
NAll_RHSa_neutral = plot(N1_Cycle_MaxMin,NAV_RHSa_0,'k','LineWidth',2);
%Compression
CAll_RHSa_Compression = plot(C1_Cycle_MaxMin,CAV_RHSa_Min,'--r','LineWidth',2);
NAll_RHSa_Compression = plot(N1_Cycle_MaxMin,NAV_RHSa_Min,'r','LineWidth',2);
%Formatting
title('AVERAGE COMPARISON: Tilt of RHS Glenoid Edge');
ylabel('\alpha (\circ) ');
xlabel('Cycle');
ylim([0 6]);
grid on;

figure(16);
shade(Cycle_shade_MaxMin,CSTD_LHSy_Max_PLUS,'r',Cycle_shade_MaxMin,CSTD_LHSy_Max_MINUS,'r','Li
newidth', 0.5 ,'FillType',[1 2]);
hold on
shade(Cycle_shade_MaxMin,NSTD_LHSy_Max_PLUS,'r',Cycle_shade_MaxMin,NSTD_LHSy_Max_MINUS,'r','Li
newidth', 0.5 ,'FillType',[1 2]);
shade(Cycle_shade_0,CSTD_LHSy_0_PLUS,'k',Cycle_shade_0,CSTD_LHSy_0_MINUS,'k','Linewidth',  0.5
,'FillType',[1 2]);
shade(Cycle_shade_0,NSTD_LHSy_0_PLUS,'k',Cycle_shade_0,NSTD_LHSy_0_MINUS,'k','Linewidth',  0.5
,'FillType',[1 2]);
shade(Cycle_shade_MaxMin,CSTD_LHSy_Min_PLUS,'b',Cycle_shade_MaxMin,CSTD_LHSy_Min_MINUS,'b','Li
newidth', 0.5 ,'FillType',[1 2]);
shade(Cycle_shade_MaxMin,NSTD_LHSy_Min_PLUS,'b',Cycle_shade_MaxMin,NSTD_LHSy_Min_MINUS,'b','Li
newidth', 0.5 ,'FillType',[1 2]);
%Tension
CAll_LHSy_Tension = plot(C1_Cycle_MaxMin,CAV_LHSy_Min,'--b','LineWidth',2);
NAll_LHSy_Tension = plot(N1_Cycle_MaxMin,NAV_LHSy_Min,'b','LineWidth',2);
%neutral
CAll_LHSy_neutral = plot(C1_Cycle_MaxMin,CAV_LHSy_0,'--k','LineWidth',2);
NAll_LHSy_neutral = plot(N1_Cycle_MaxMin,NAV_LHSy_0,'k','LineWidth',2);
%Compression
CAll_LHSy_Compression = plot(C1_Cycle_MaxMin,CAV_LHSy_Max,'--r','LineWidth',2);
NAll_LHSy_Compression = plot(N1_Cycle_MaxMin,NAV_LHSy_Max,'r','LineWidth',2);
%Formatting
title('AVERAGE COMPARISON: Vertical Motion of LHS Glenoid Edge');
ylabel('y (mm) ');
xlabel('Cycle');
ylim([-1 0]);
grid on;

figure(17);
shade(Cycle_shade_MaxMin,CSTD_LHSx_Max_PLUS,'r',Cycle_shade_MaxMin,CSTD_LHSx_Max_MINUS,'r','Li
newidth', 0.5 ,'FillType',[1 2]);
hold on
shade(Cycle_shade_MaxMin,NSTD_LHSx_Max_PLUS,'r'
,Cycle_shade_MaxMin,NSTD_LHSx_Max_MINUS,'r','Linewidth', 0.5 ,'FillType',[1 2]);
shade(Cycle_shade_0,CSTD_LHSx_0_PLUS,'k',Cycle_shade_0,CSTD_LHSx_0_MINUS,'k','Linewidth',  0.5
,'FillType',[1 2]);
```

```
shade(Cycle_shade_0,NSTD_LHSx_0_PLUS,'k',Cycle_shade_0,NSTD_LHSx_0_MINUS,'k','Linewidth',  0.5
,'FillType',[1 2]);
shade(Cycle_shade_MaxMin,CSTD_LHSx_Min_PLUS,'b',Cycle_shade_MaxMin,CSTD_LHSx_Min_MINUS,'b','Li
newidth', 0.5 ,'FillType',[1 2]);
shade(Cycle_shade_MaxMin,NSTD_LHSx_Min_PLUS,'b',Cycle_shade_MaxMin,NSTD_LHSx_Min_MINUS,'b','Li
newidth', 0.5 ,'FillType',[1 2]);
%Tension
CAll_LHSx_Tension = plot(C1_Cycle_MaxMin,CAV_LHSx_Min,'--b','LineWidth',2);
NAll_LHSx_Tension = plot(N1_Cycle_MaxMin,NAV_LHSx_Min,'b','LineWidth',2);
%neutral
CAll_LHSx_neutral = plot(C1_Cycle_MaxMin,CAV_LHSx_0,'--k','LineWidth',2);
NAll_LHSx_neutral = plot(N1_Cycle_MaxMin,NAV_LHSx_0,'k','LineWidth',2);
%Compression
CAll_LHSx_Compression = plot(C1_Cycle_MaxMin,CAV_LHSx_Max,'--r','LineWidth',2);
NAll_LHSx_Compression = plot(N1_Cycle_MaxMin,NAV_LHSx_Max,'r','LineWidth',2);
%Formatting
title('AVERAGE COMPARISON: Horizontal Motion of LHS Glenoid Edge');
ylabel('x (mm) ');
xlabel('Cycle');
ylim([-1 0]);
grid on;

figure(18);
shade(Cycle_shade_MaxMin,CSTD_LHSa_Max_PLUS,'r',Cycle_shade_MaxMin,CSTD_LHSa_Max_MINUS,'r','Li
newidth', 0.5 ,'FillType',[1 2]);
hold on
shade(Cycle_shade_MaxMin,NSTD_LHSa_Max_PLUS,'r',Cycle_shade_MaxMin,NSTD_LHSa_Max_MINUS,'r','Li
newidth', 0.5 ,'FillType',[1 2]);
shade(Cycle_shade_0,CSTD_LHSa_0_PLUS,'k',Cycle_shade_0,CSTD_LHSa_0_MINUS,'k','Linewidth',  0.5
,'FillType',[1 2]);
shade(Cycle_shade_0,NSTD_LHSa_0_PLUS,'k',Cycle_shade_0,NSTD_LHSa_0_MINUS,'k','Linewidth',  0.5
,'FillType',[1 2]);
shade(Cycle_shade_MaxMin,CSTD_LHSa_Min_PLUS,'b',Cycle_shade_MaxMin,CSTD_LHSa_Min_MINUS,'b','Li
newidth', 0.5 ,'FillType',[1 2]);
shade(Cycle_shade_MaxMin,NSTD_LHSa_Min_PLUS,'b',Cycle_shade_MaxMin,NSTD_LHSa_Min_MINUS,'b','Li
newidth', 0.5 ,'FillType',[1 2]);
%Tension
CAll_LHSa_Tension = plot(C1_Cycle_MaxMin,CAV_LHSa_Min,'--b','LineWidth',2);
NAll_LHSa_Tension = plot(N1_Cycle_MaxMin,NAV_LHSa_Min,'b','LineWidth',2);
%neutral
CAll_LHSa_neutral = plot(C1_Cycle_MaxMin,CAV_LHSa_0,'--k','LineWidth',2);
NAll_LHSa_neutral = plot(N1_Cycle_MaxMin,NAV_LHSa_0,'k','LineWidth',2);
%Compression
CAll_LHSa_Compression = plot(C1_Cycle_MaxMin,CAV_LHSa_Max,'--r','LineWidth',2);
NAll_LHSa_Compression = plot(N1_Cycle_MaxMin,NAV_LHSa_Max,'r','LineWidth',2);
%Formatting
title('AVERAGE COMPARISON: Tilt of LHS Glenoid Edge');
ylabel('\alpha (\circ) ');
xlabel('Cycle');
ylim([-6 0]);
grid on;

% %PLOT NEUTRAL DEFLECTION VALUES
figure(31);
shade(C1_Cycle_delta',CSTD_RHSy_deltaT_PLUS','b',C1_Cycle_delta',CSTD_RHSy_deltaT_MINUS','b','
Linewidth', 0.1,'FillType',[1 2]);
hold on
shade(C1_Cycle_delta',CSTD_RHSy_deltaC_PLUS','r',C1_Cycle_delta',CSTD_RHSy_deltaC_MINUS','r','
Linewidth', 0.1,'FillType',[1 2]);
shade(C1_Cycle_delta',NSTD_RHSy_deltaT_PLUS','b',C1_Cycle_delta',NSTD_RHSy_deltaT_MINUS','b','
Linewidth', 0.1,'FillType',[1 2]);
shade(C1_Cycle_delta',NSTD_RHSy_deltaC_PLUS','r',C1_Cycle_delta',NSTD_RHSy_deltaC_MINUS','r','
Linewidth', 0.1,'FillType',[1 2]);
%DTension
CAll_RHSy_DTension = plot(C1_Cycle_delta,CAV_RHSy_deltaT,'--b','LineWidth',1.5);
NAll_RHSy_DTension = plot(N1_Cycle_delta,NAV_RHSy_deltaT,'b','LineWidth',2);
%DCompression
CAll_RHSy_DCompression = plot(C1_Cycle_delta,CAV_RHSy_deltaC,'--r','LineWidth',2);
NAll_RHSy_DCompression = plot(N1_Cycle_delta,NAV_RHSy_deltaC,'r','LineWidth',2);
%Formatting
title('AVERAGE COMPARISON: Vertical Neutral Deflection of RHS Glenoid Edge');
ylabel('\Delta y (mm) ');
xlabel('Cycle');
ylim([-1 0]);
grid on;

figure(32);
```

```
%Control overall average plots
%Standard Deviations
shade(C1_Cycle_delta',CSTD_RHSx_deltaT_PLUS','b',C1_Cycle_delta',CSTD_RHSx_deltaT_MINUS','b','
Linewidth', 0.1,'FillType',[1 2]);
hold on
shade(C1_Cycle_delta',CSTD_RHSx_deltaC_PLUS','r',C1_Cycle_delta',CSTD_RHSx_deltaC_MINUS','r','
Linewidth', 0.1,'FillType',[1 2]);
shade(C1_Cycle_delta',NSTD_RHSx_deltaT_PLUS','b',C1_Cycle_delta',NSTD_RHSx_deltaT_MINUS','b','
Linewidth', 0.1,'FillType',[1 2]);
shade(C1_Cycle_delta',NSTD_RHSx_deltaC_PLUS','r',C1_Cycle_delta',NSTD_RHSx_deltaC_MINUS','r','
Linewidth', 0.1,'FillType',[1 2]);
%DTension
CAll_RHSx_DTension = plot(C1_Cycle_delta,CAV_RHSx_deltaT,'--b','LineWidth',2);
NAll_RHSx_DTension = plot(N1_Cycle_delta,NAV_RHSx_deltaT,'b','LineWidth',2);
%DCompression
CAll_RHSx_DCompression = plot(C1_Cycle_delta,CAV_RHSx_deltaC,'--r','LineWidth',2);
NAll_RHSx_DCompression = plot(N1_Cycle_delta,NAV_RHSx_deltaC,'r','LineWidth',2);
%Formatting
title('AVERAGE COMPARISON: Horizontal Neutral Deflection of RHS Glenoid Edge');
ylabel('\Delta x (mm) ');
xlabel('Cycle');
ylim([0 1]);
grid on;

figure(33);
%Control overall average plots
%Standard Deviations
shade(C1_Cycle_delta',CSTD_RHSa_deltaT_PLUS','b',C1_Cycle_delta',CSTD_RHSa_deltaT_MINUS','b','
Linewidth', 0.1,'FillType',[1 2]);
hold on
shade(C1_Cycle_delta',CSTD_RHSa_deltaC_PLUS','r',C1_Cycle_delta',CSTD_RHSa_deltaC_MINUS','r','
Linewidth', 0.1,'FillType',[1 2]);
shade(C1_Cycle_delta',NSTD_RHSa_deltaT_PLUS','b',C1_Cycle_delta',NSTD_RHSa_deltaT_MINUS','b','
Linewidth', 0.1,'FillType',[1 2]);
shade(C1_Cycle_delta',NSTD_RHSa_deltaC_PLUS','r',C1_Cycle_delta',NSTD_RHSa_deltaC_MINUS','r','
Linewidth', 0.1,'FillType',[1 2]);
%DTension
CAll_RHSa_DTension = plot(C1_Cycle_delta,CAV_RHSa_deltaT,'--b','LineWidth',2);
NAll_RHSa_DTension = plot(N1_Cycle_delta,NAV_RHSa_deltaT,'b','LineWidth',2);
%DCompression
CAll_RHSa_DCompression = plot(C1_Cycle_delta,CAV_RHSa_deltaC,'--r','LineWidth',2);
NAll_RHSa_DCompression = plot(N1_Cycle_delta,NAV_RHSa_deltaC,'r','LineWidth',2);
%Formatting
title('AVERAGE COMPARISON: Tilt Neutral Deflection of RHS Glenoid Edge');
ylabel('\Delta \alpha (\circ) ');
xlabel('Cycle');
ylim([0 6]);
grid on;

figure(34);
%Control overall average plots
%Standard Deviations
shade(C1_Cycle_delta',CSTD_LHSy_deltaT_PLUS','b',C1_Cycle_delta',CSTD_LHSy_deltaT_MINUS','b','
Linewidth', 0.1,'FillType',[1 2]);
hold on
shade(C1_Cycle_delta',CSTD_LHSy_deltaC_PLUS','r',C1_Cycle_delta',CSTD_LHSy_deltaC_MINUS','r','
Linewidth', 0.1,'FillType',[1 2]);
shade(C1_Cycle_delta',NSTD_LHSy_deltaT_PLUS','b',C1_Cycle_delta',NSTD_LHSy_deltaT_MINUS','b','
Linewidth', 0.1,'FillType',[1 2]);
shade(C1_Cycle_delta',NSTD_LHSy_deltaC_PLUS','r',C1_Cycle_delta',NSTD_LHSy_deltaC_MINUS','r','
Linewidth', 0.1,'FillType',[1 2]);
%DTension
CAll_LHSy_DTension = plot(C1_Cycle_delta,CAV_LHSy_deltaT,'--b','LineWidth',2);
NAll_LHSy_DTension = plot(N1_Cycle_delta,NAV_LHSy_deltaT,'b','LineWidth',2);
%DCompression
CAll_LHSy_DCompression = plot(C1_Cycle_delta,CAV_LHSy_deltaC,'--r','LineWidth',2);
NAll_LHSy_DCompression = plot(N1_Cycle_delta,NAV_LHSy_deltaC,'r','LineWidth',2);
%Formatting
title('AVERAGE COMPARISON: Vertical Neutral Deflection of LHS Glenoid Edge');
ylabel('y (mm) ');
xlabel('Cycle');
ylim([-1 0]);
grid on;

figure(35);
%Control overall average plots
%Standard Deviations
```

```
shade(C1_Cycle_delta',CSTD_LHSx_deltaT_PLUS','b',C1_Cycle_delta',CSTD_LHSx_deltaT_MINUS','b','
Linewidth', 0.1,'FillType',[1 2]);
hold on
shade(C1_Cycle_delta',CSTD_LHSx_deltaC_PLUS','r',C1_Cycle_delta',CSTD_LHSx_deltaC_MINUS','r','
Linewidth', 0.1,'FillType',[1 2]);
shade(C1_Cycle_delta',NSTD_LHSx_deltaT_PLUS','b',C1_Cycle_delta',NSTD_LHSx_deltaT_MINUS','b','
Linewidth', 0.1,'FillType',[1 2]);
shade(C1_Cycle_delta',NSTD_LHSx_deltaC_PLUS','r',C1_Cycle_delta',NSTD_LHSx_deltaC_MINUS','r','
Linewidth', 0.1,'FillType',[1 2]);
%DTension
CAll_LHSx_DTension = plot(C1_Cycle_delta,CAV_LHSx_deltaT,'--b','LineWidth',2);
NAll_LHSx_DTension = plot(N1_Cycle_delta,NAV_LHSx_deltaT,'b','LineWidth',2);
%DCompression
CAll_LHSx_DCompression = plot(C1_Cycle_delta,CAV_LHSx_deltaC,'--r','LineWidth',2);
NAll_LHSx_DCompression = plot(N1_Cycle_delta,NAV_LHSx_deltaC,'r','LineWidth',2);
%Formatting
title('AVERAGE COMPARISON: Horizontal Neutral Delfection of LHS Glenoid Edge');
ylabel('x (mm) ');
xlabel('Cycle');
ylim([-1 0]);
grid on;

figure(36);
%Control overall average plots
%Standard Deviations
shade(C1_Cycle_delta',CSTD_LHSa_deltaT_PLUS','b',C1_Cycle_delta',CSTD_LHSa_deltaT_MINUS','b','
Linewidth', 0.1,'FillType',[1 2]);
hold on
shade(C1_Cycle_delta',CSTD_LHSa_deltaC_PLUS','r',C1_Cycle_delta',CSTD_LHSa_deltaC_MINUS','r','
Linewidth', 0.1,'FillType',[1 2]);
shade(C1_Cycle_delta',NSTD_LHSa_deltaT_PLUS','b',C1_Cycle_delta',NSTD_LHSa_deltaT_MINUS','b','
Linewidth', 0.1,'FillType',[1 2]);
shade(C1_Cycle_delta',NSTD_LHSa_deltaC_PLUS','r',C1_Cycle_delta',NSTD_LHSa_deltaC_MINUS','r','
Linewidth', 0.1,'FillType',[1 2]);
%DTension
CAll_LHSa_DTension = plot(C1_Cycle_delta,CAV_LHSa_deltaT,'--b','LineWidth',2);
NAll_LHSa_DTension = plot(N1_Cycle_delta,NAV_LHSa_deltaT,'b','LineWidth',2);
%DCompression
CAll_LHSa_DCompression = plot(C1_Cycle_delta,CAV_LHSa_deltaC,'--r','LineWidth',2);
NAll_LHSa_DCompression = plot(N1_Cycle_delta,NAV_LHSa_deltaC,'r','LineWidth',2);
%Formatting
title('AVERAGE COMPARISON: Tilt Neutral Deflection of LHS Glenoid Edge');
ylabel('\alpha (\circ) ');
xlabel('Cycle');
ylim([-6 0]);
grid on;
```

C3 Glenoid Edge Motion Results and Statistical Analysis

The individual test runs for each of the variables presented as averaged values in Chapter 4 are given in this section. The individual variable motion vectors are listed in **Table C-2**.

Table C- 2 *Summary of all individual motion vectors variables.*

	Tension		Neutral		Compression	
Vertical (y)	LHSyT	RHSyT	LHSy0	RHSy0	LHSyC	RHSyC
	LHSyT_ND	RHSyT_ND			LHSyC-ND	RHSyC_ND
Horizontal (x)	LHSxT	RHSxT	LHSx0	RHSx0	LHSxC	RHSxC
	LHSxT_ND	RHSxT_ND			LHSxC-ND	RHSxC_ND
Tilt (α)	LHSαT	RHSαT	LHSα0	RHSα0	LHSαC	RHSαC
	LHSαT_ND	RHSαT_ND			LHSαC_ND	RHSαC_ND

In the data layouts that follow (**Figure C-1** to **Figure C-30**), sub-plots (a) to (e) should be read in conjunction with the Edge Motion Data Key provided.

Edge Motion Data Key:

Sub-plot (a) plots the individual test run data for all control and novel test runs (standard length runs only). The data is presented in both the unsmoothed state, as well as after smoothing by robust Loess (1%). The following legend is applicable to all data layout sub-plots (a):

(a) **Glenoid Edge Motion Vectors: All Test Runs (unsmoothed and smoothed with Robust Loess 1%)**

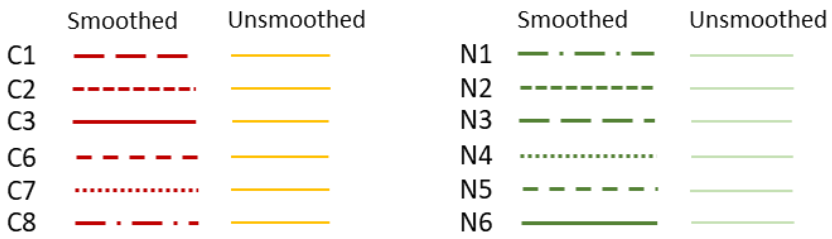

Sub-plot (b) and (c) plot the mean and standard deviation of the control and novel glenoid data for the given variable, where (b) is the unsmoothed and (c) is the smoothed data. The following legend is applicable to all data layout sub-plots (b) and (c):

(b) and (c) **Control and Novel Data Mean and Standard Deviation**

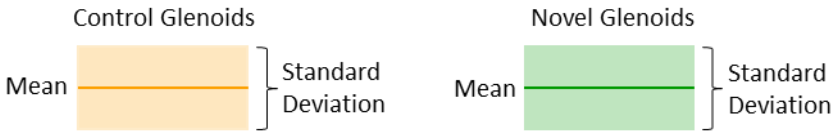

Sub-plots (d) and (e) provide the results of the statistical comparison of the control and novel glenoid data for the given motion variable using SPM1d. The plots show the significance level of the data for the length of the tests, as well as the threshold for significance at a probability cut-off for significance of $\alpha = 0.05$. Where data we found to be non- parametric (and analysed using the non-parametric t-test), this is indicated on the plot. Sub-plot (d) is the analysis for the unsmoothed data, and sub-plot (e) is the analysis for the smoothed data. The following legend is applicable to all data layout sub-plots (d) and (e):

(d) and (e) **Significance (Unsmoothed and Smoothed by Robust Loess 1%)**

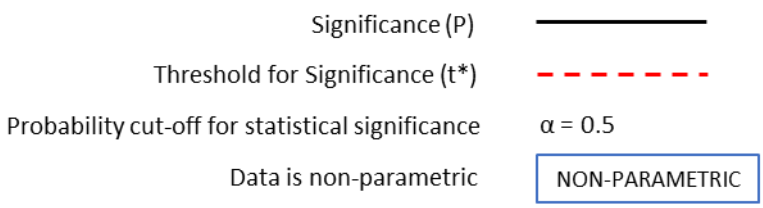

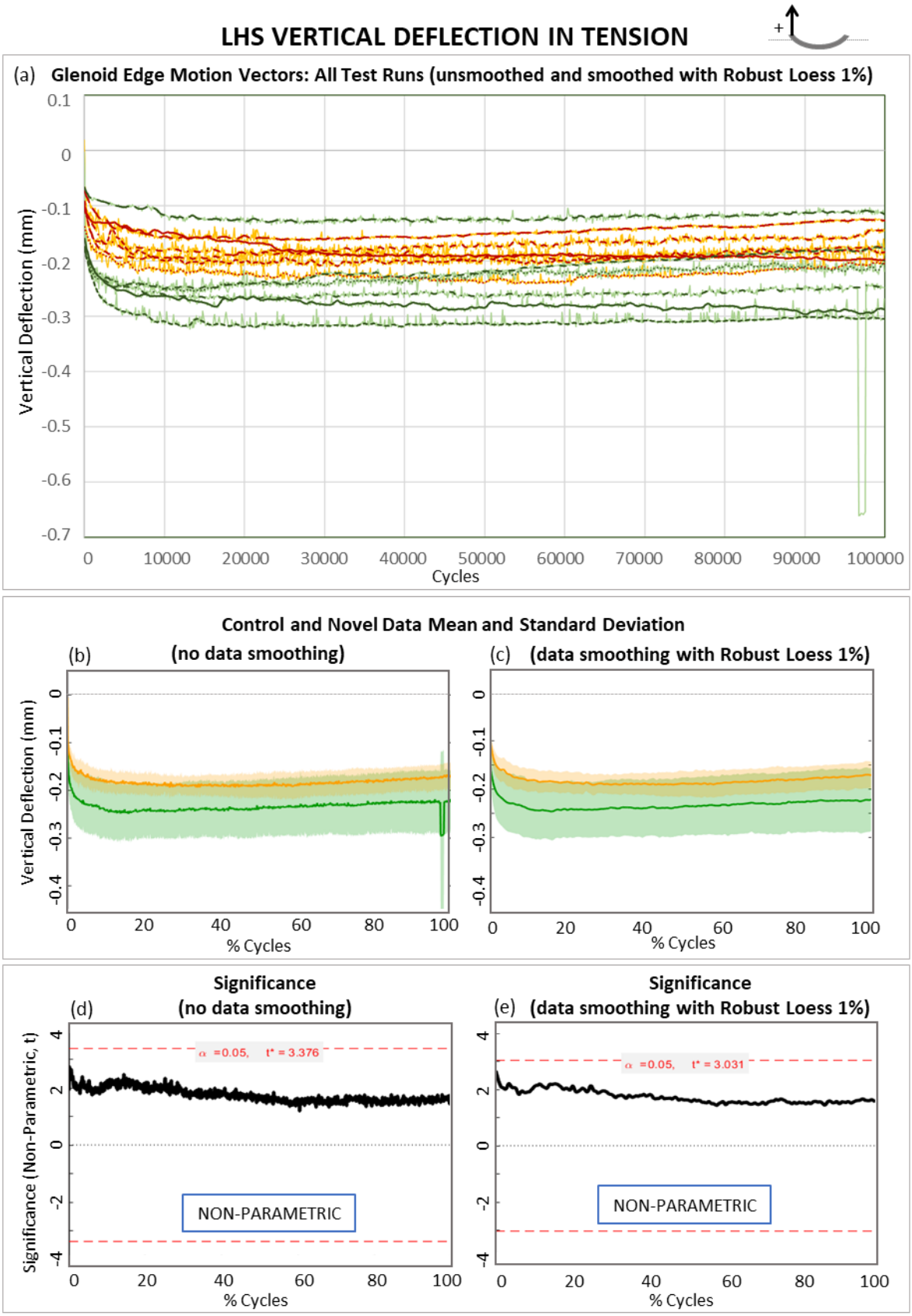

Figure C-1 *Vertical deflection of the LHS control (orange) and novel (green) glenoid edges in tension for all test runs. Unsmoothed data and the comparative data smoothed by 1% Robust Loess smothing are shown. Refer to* ***Edge Motion Data Key*** *for details of plots.*

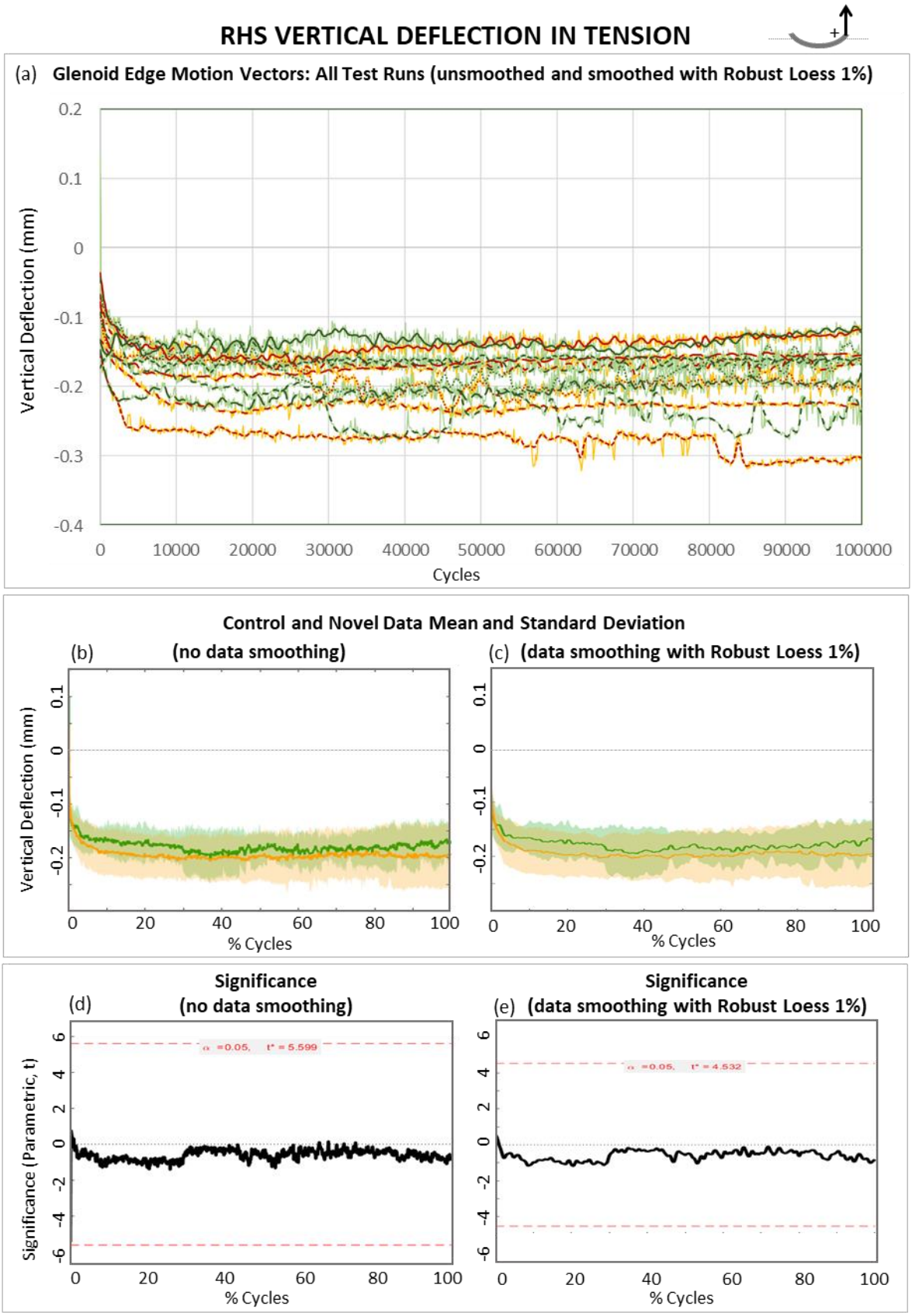

Figure C-2 *Vertical deflection of the RHS control (orange) and novel (green) glenoid edges in tension for all test runs. Unsmoothed data and the comparative data smoothed by 1% Robust Loess smothing are shown. Refer to* ***Edge Motion Data Key*** *for details of plots.*

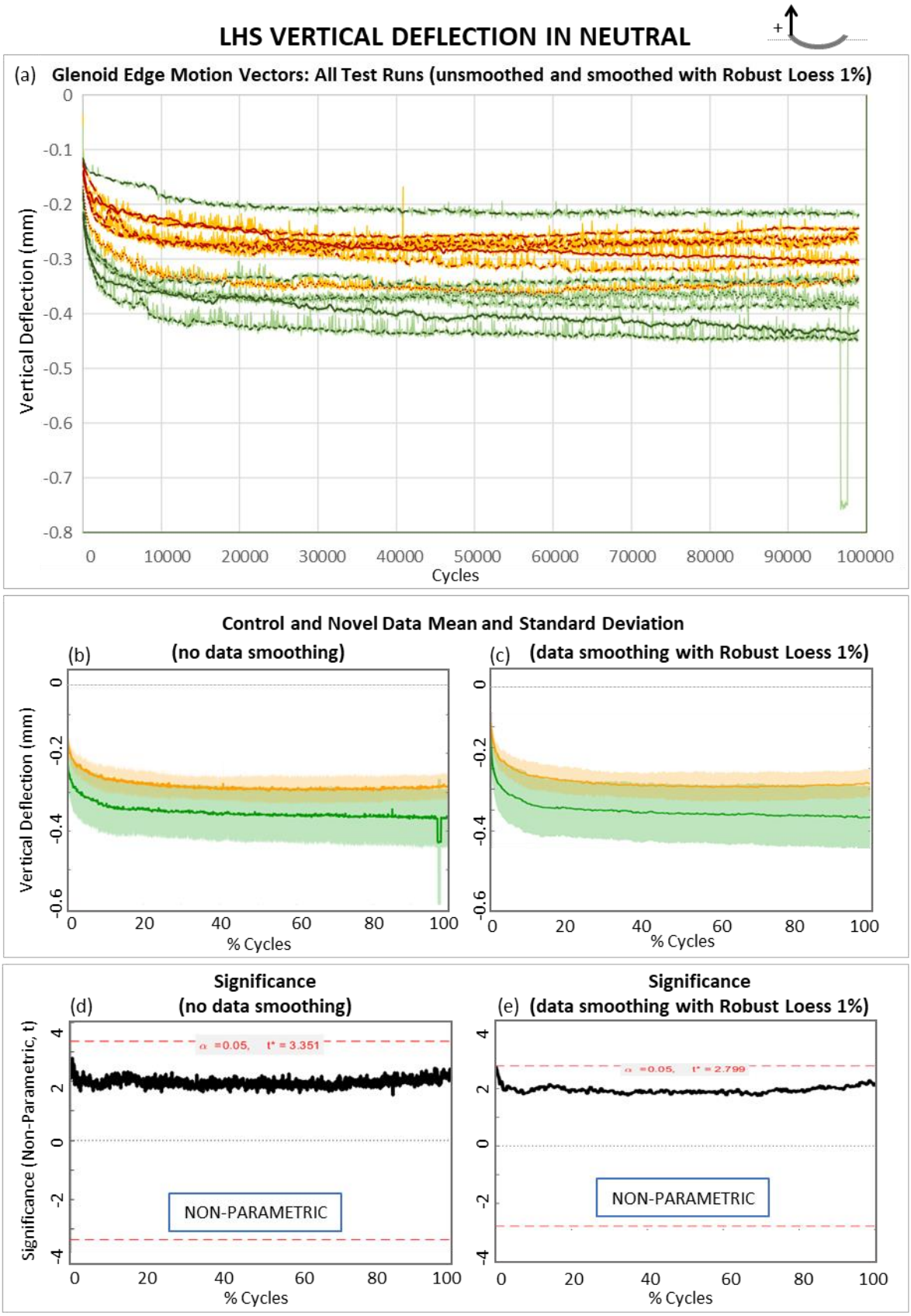

Figure C-3 *Vertical deflection of the LHS control (orange) and novel (green) glenoid edges in neutral for all test runs. Unsmoothed data and the comparative data smoothed by 1% Robust Loess smothing are shown. Refer to* ***Edge Motion Data Key*** *for details of plots.*

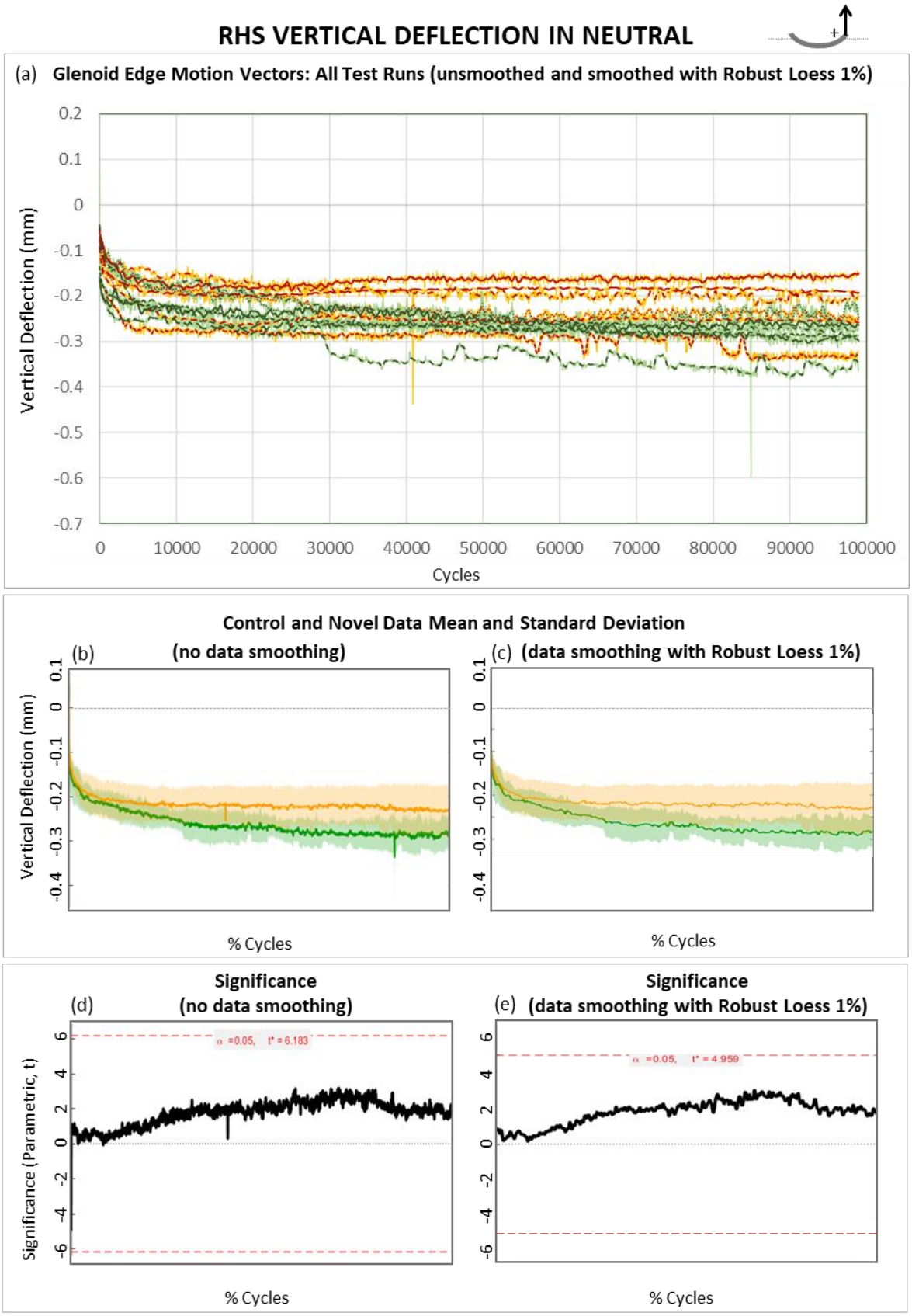

Figure C-4 *Vertical deflection of the RHS control (orange) and novel (green) glenoid edges in neutral for all test runs. Unsmoothed data and the comparative data smoothed by 1% Robust Loess smothing are shown. Refer to* ***Edge Motion Data Key*** *for details of plots.*

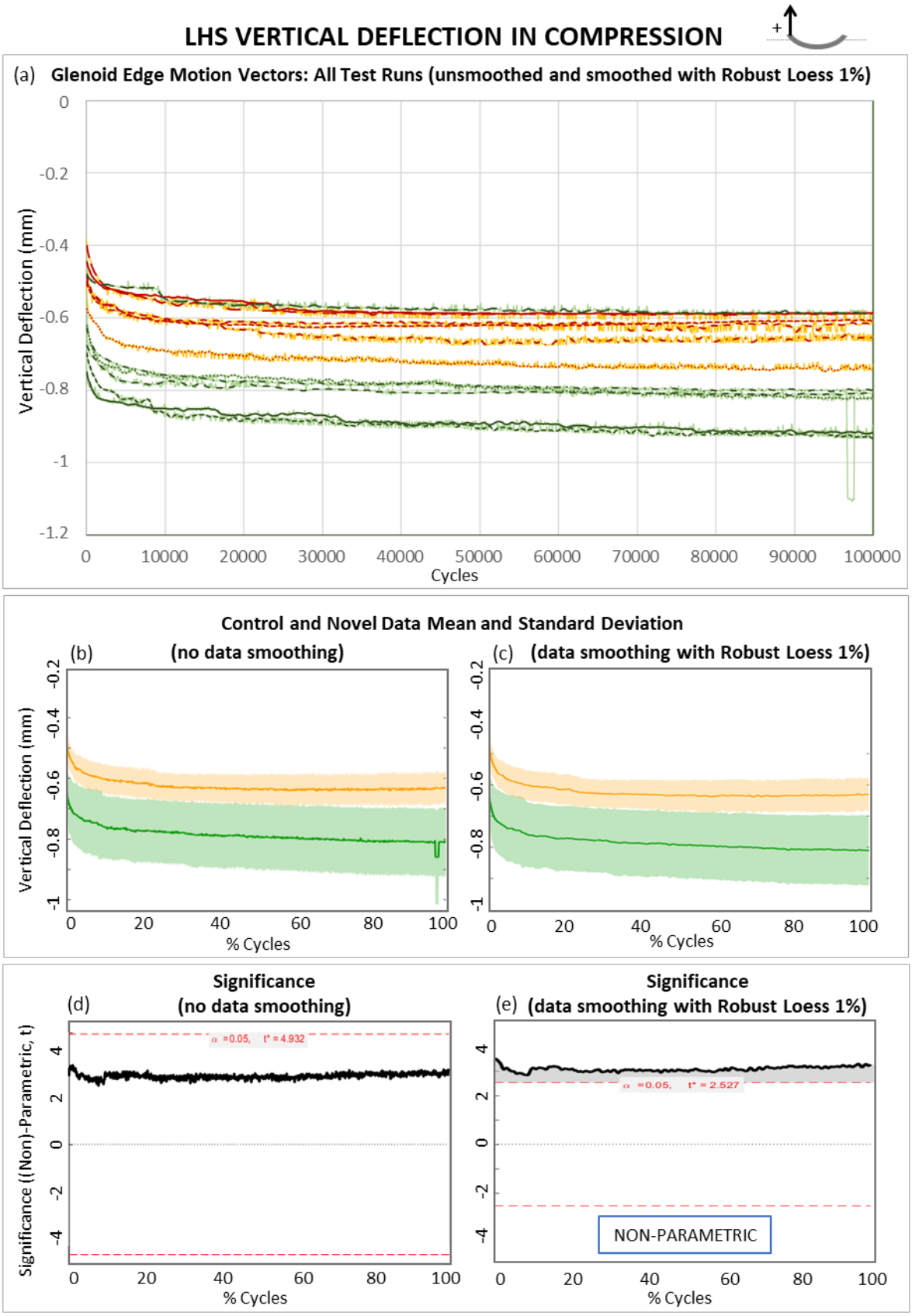

Figure C-5 *Vertical deflection of the LHS control (orange) and novel (green) glenoid edges in compression for all test runs. Unsmoothed data and the comparative data smoothed by 1% Robust Loess smothing are shown. Refer to* ***Edge Motion Data Key*** *for details of plots.*

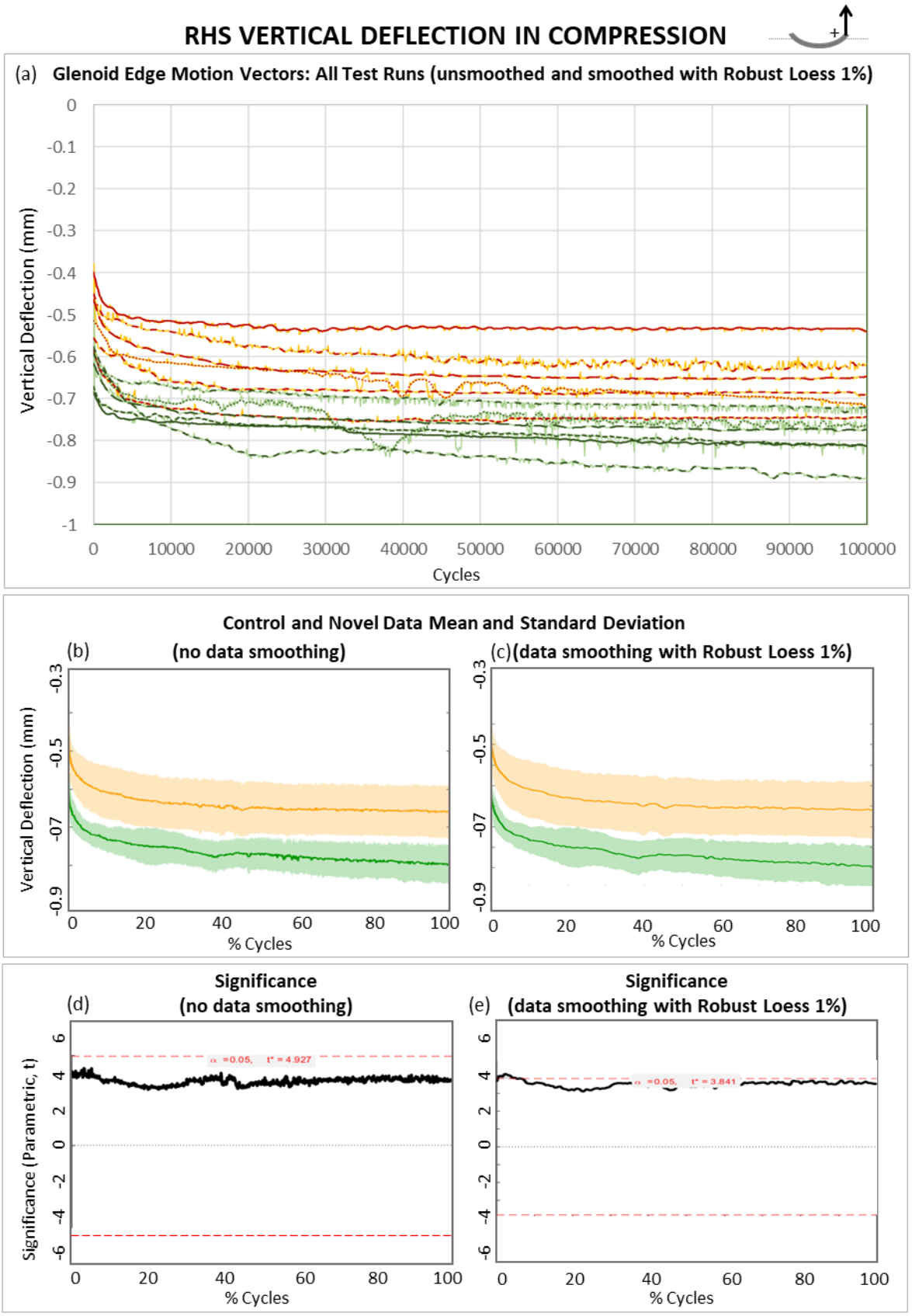

Figure C-6 *Vertical deflection of the RHS control (orange) and novel (green) glenoid edges in compression for all test runs. Unsmoothed data and the comparative data smoothed by 1% Robust Loess smothing are shown. Refer to* ***Edge Motion Data Key*** *for details of plots.*

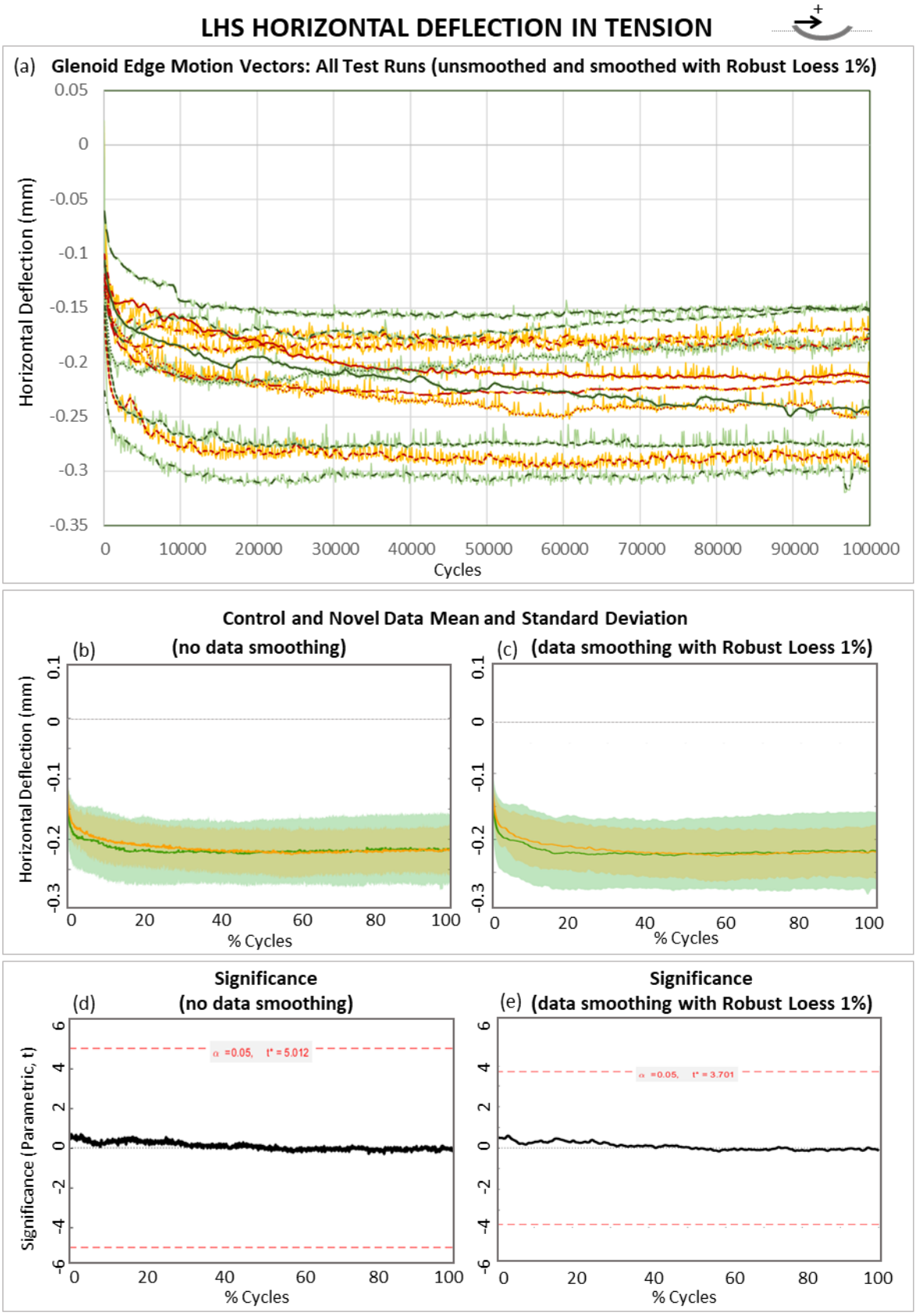

Figure C-7 *Horizontal deflection of the LHS control (orange) and novel (green) glenoid edges in tension for all test runs. Unsmoothed data and the comparative data smoothed by 1% Robust Loess smothing are shown. Refer to* ***Edge Motion Data Key*** *for details of plots.*

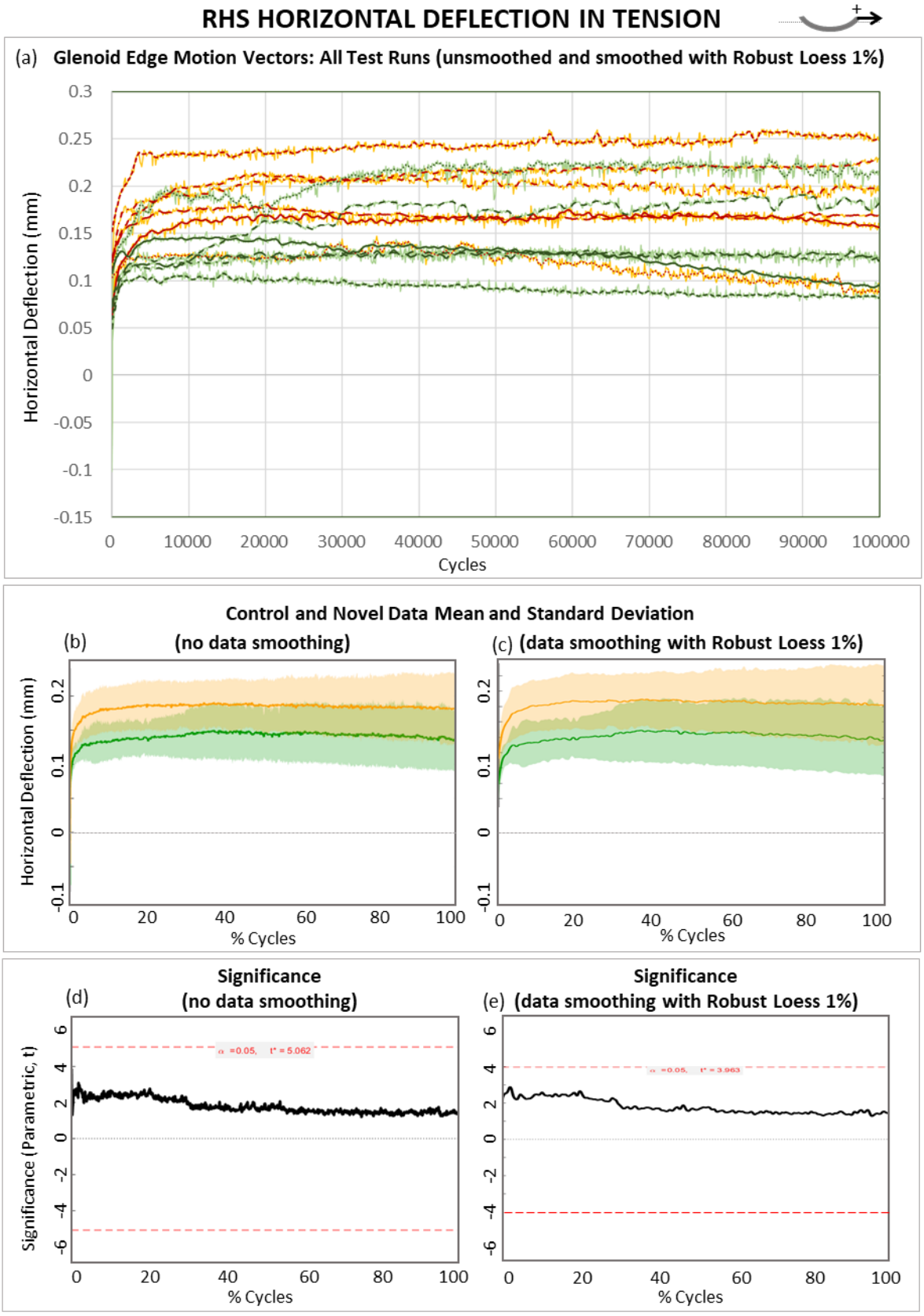

Figure C-8 *Horizontal deflection of the RHS control (orange) and novel (green) glenoid edges in tension for all test runs. Unsmoothed data and the comparative data smoothed by 1% Robust Loess smothing are shown. Refer to* ***Edge Motion Data Key*** *for details of plots.*

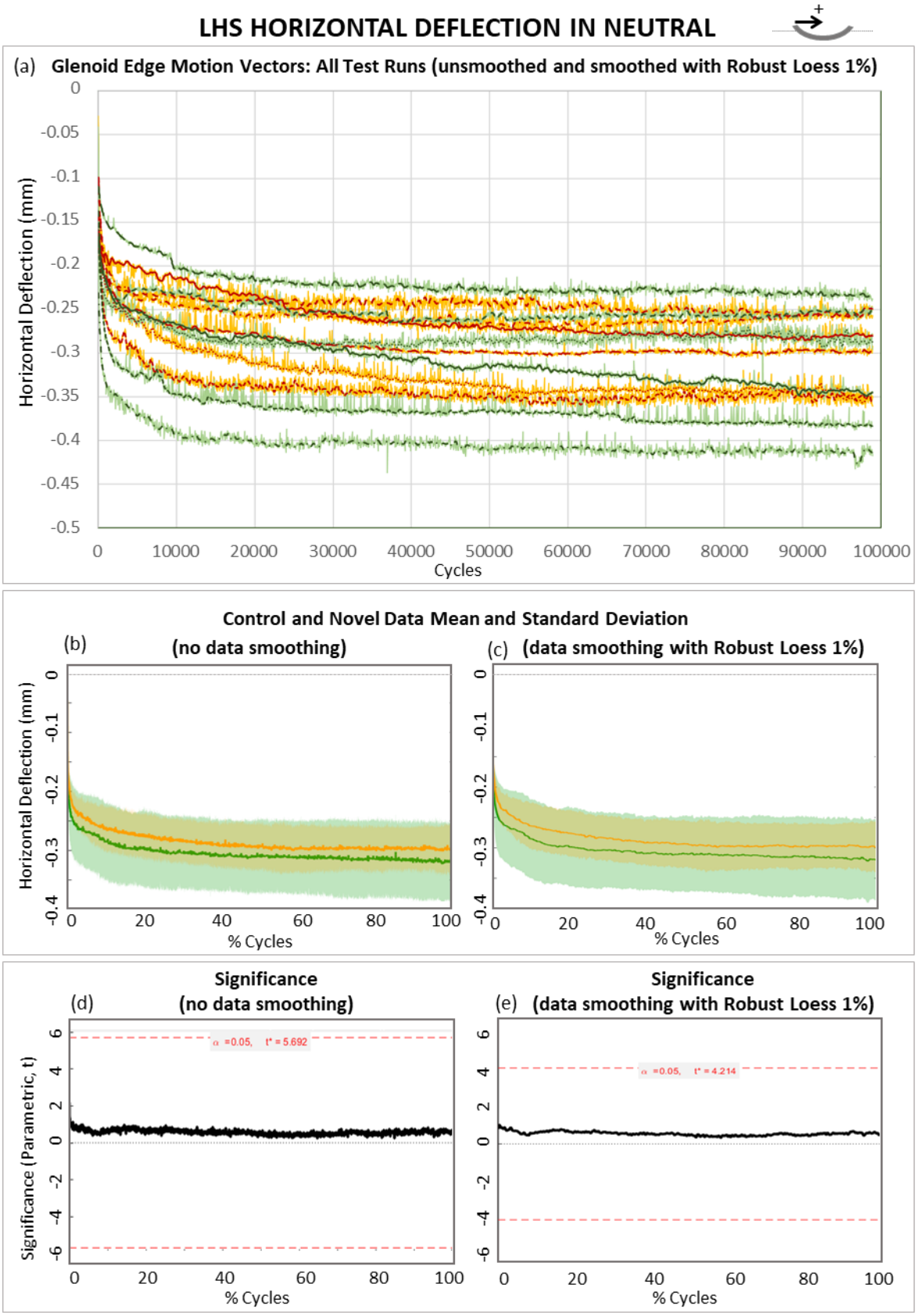

Figure C-9 *Horizontal deflection of the LHS control (orange) and novel (green) glenoid edges in neutral for all test runs. Unsmoothed data and the comparative data smoothed by 1% Robust Loess smothing are shown. Refer to* ***Edge Motion Data Key*** *for details of plots.*

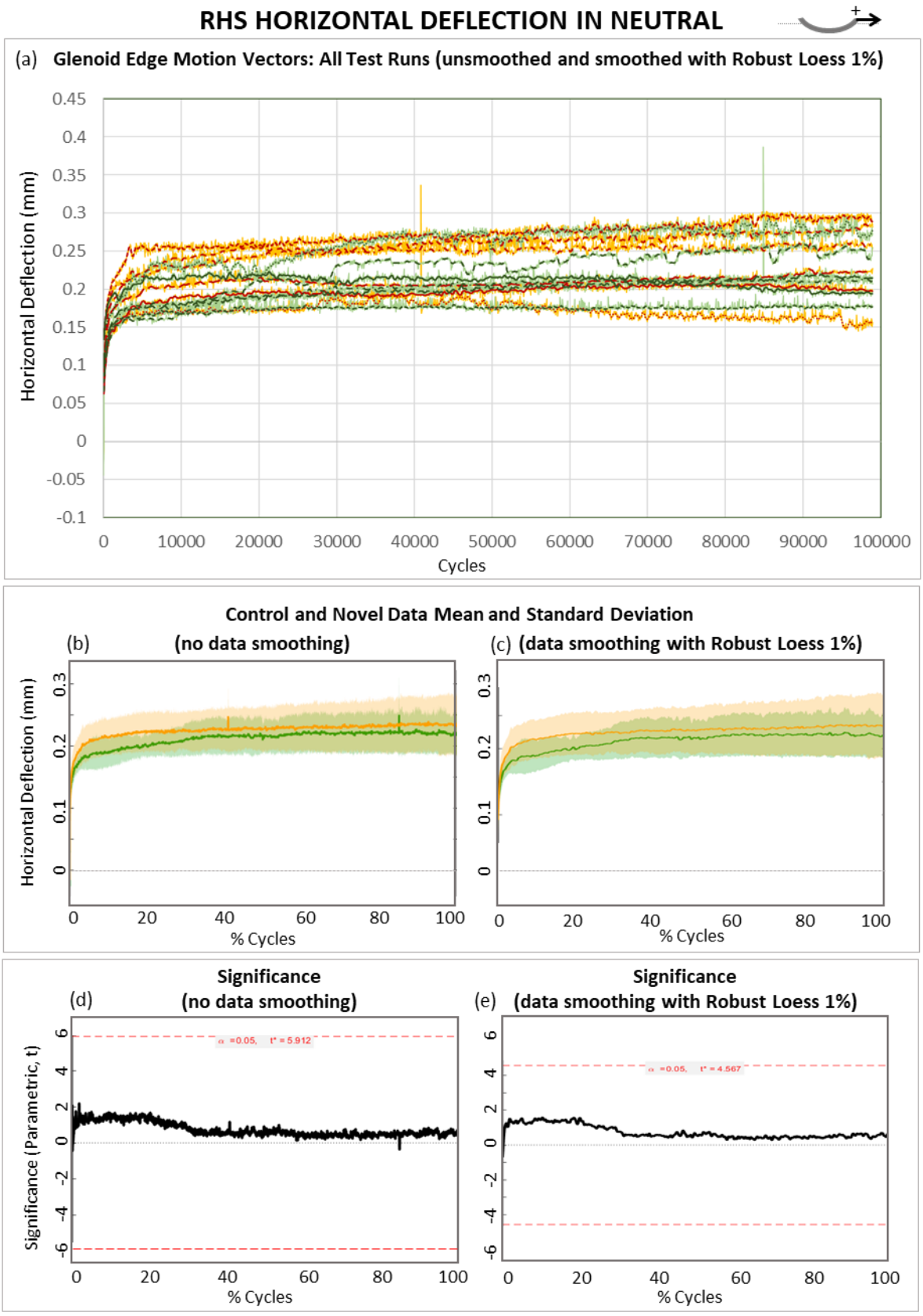

Figure C-10 *Horizontal deflection of the RHS control (orange) and novel (green) glenoid edges in neutral for all test runs. Unsmoothed data and the comparative data smoothed by 1% Robust Loess smothing are shown. Refer to* ***Edge Motion Data Key*** *for details of plots.*

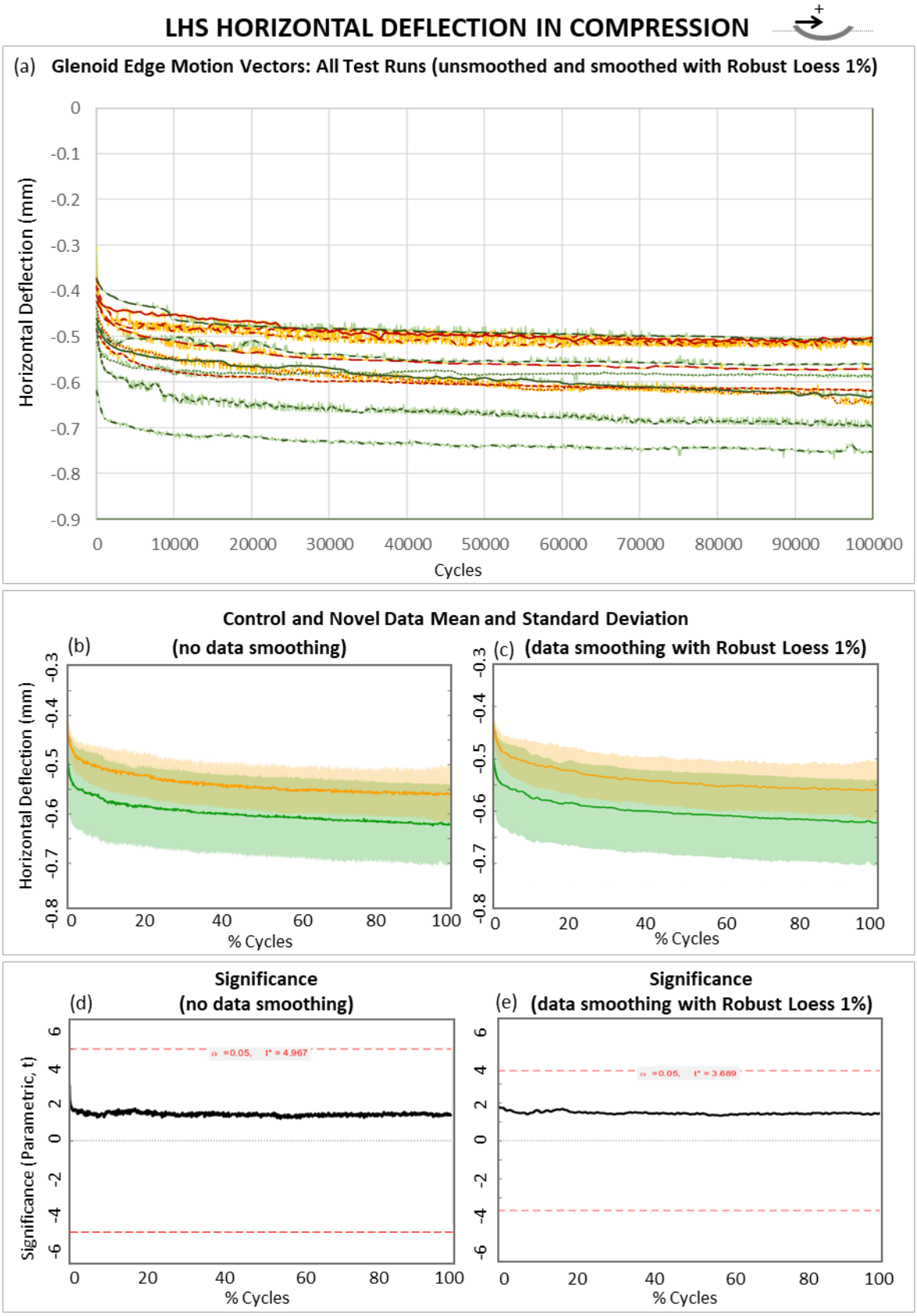

Figure C-11 *Horizontal deflection of the LHS control (orange) and novel (green) glenoid edges in compression for all test runs. Unsmoothed data and the comparative data smoothed by 1% Robust Loess smothing are shown. Refer to* ***Edge Motion Data Key*** *for details of plots.*

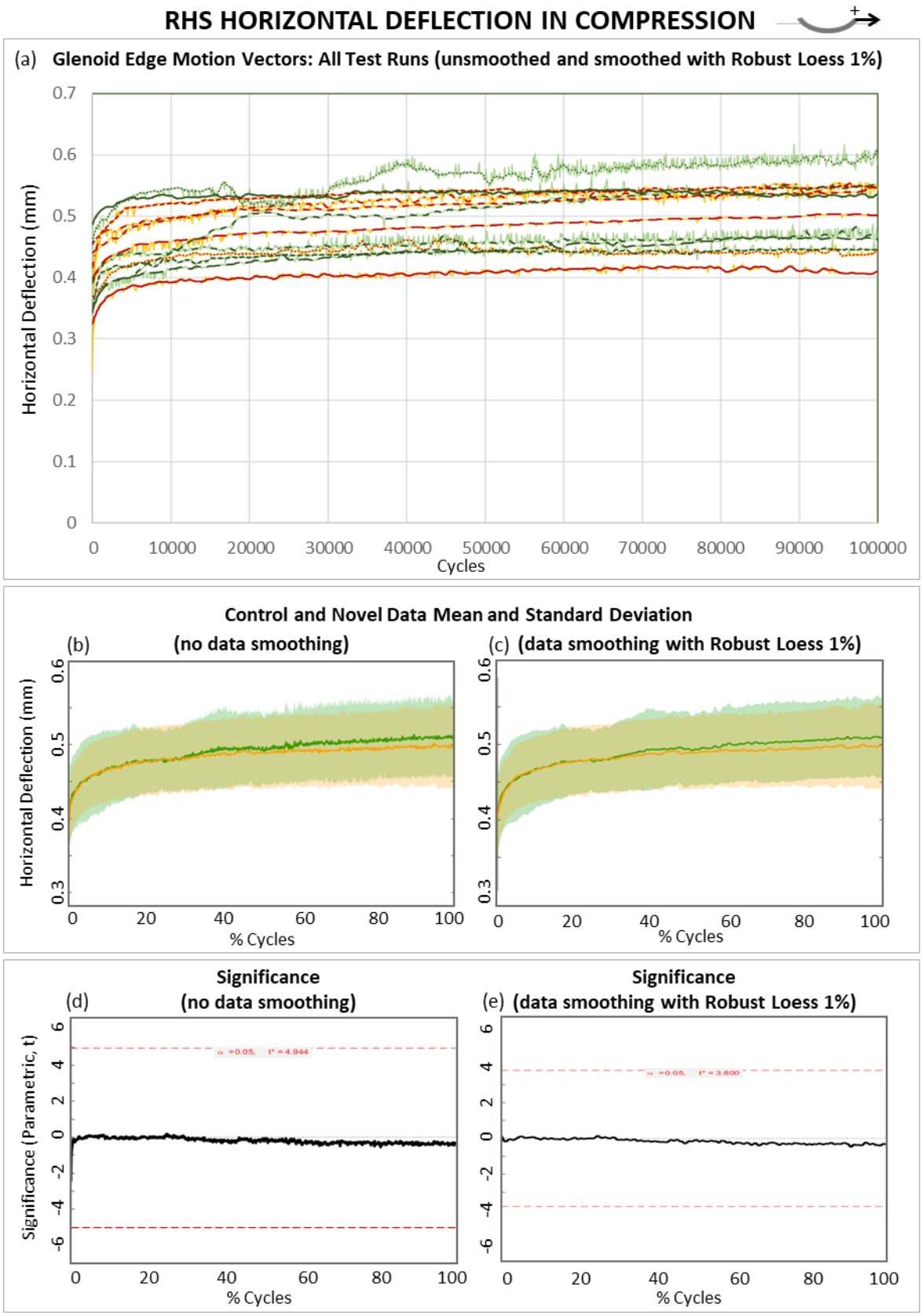

Figure C-12 *Horizontal deflection of the RHS control (orange) and novel (green) glenoid edges in compression for all test runs. Unsmoothed data and the comparative data smoothed by 1% Robust Loess smothing are shown. Refer to* ***Edge Motion Data Key*** *for details of plots.*

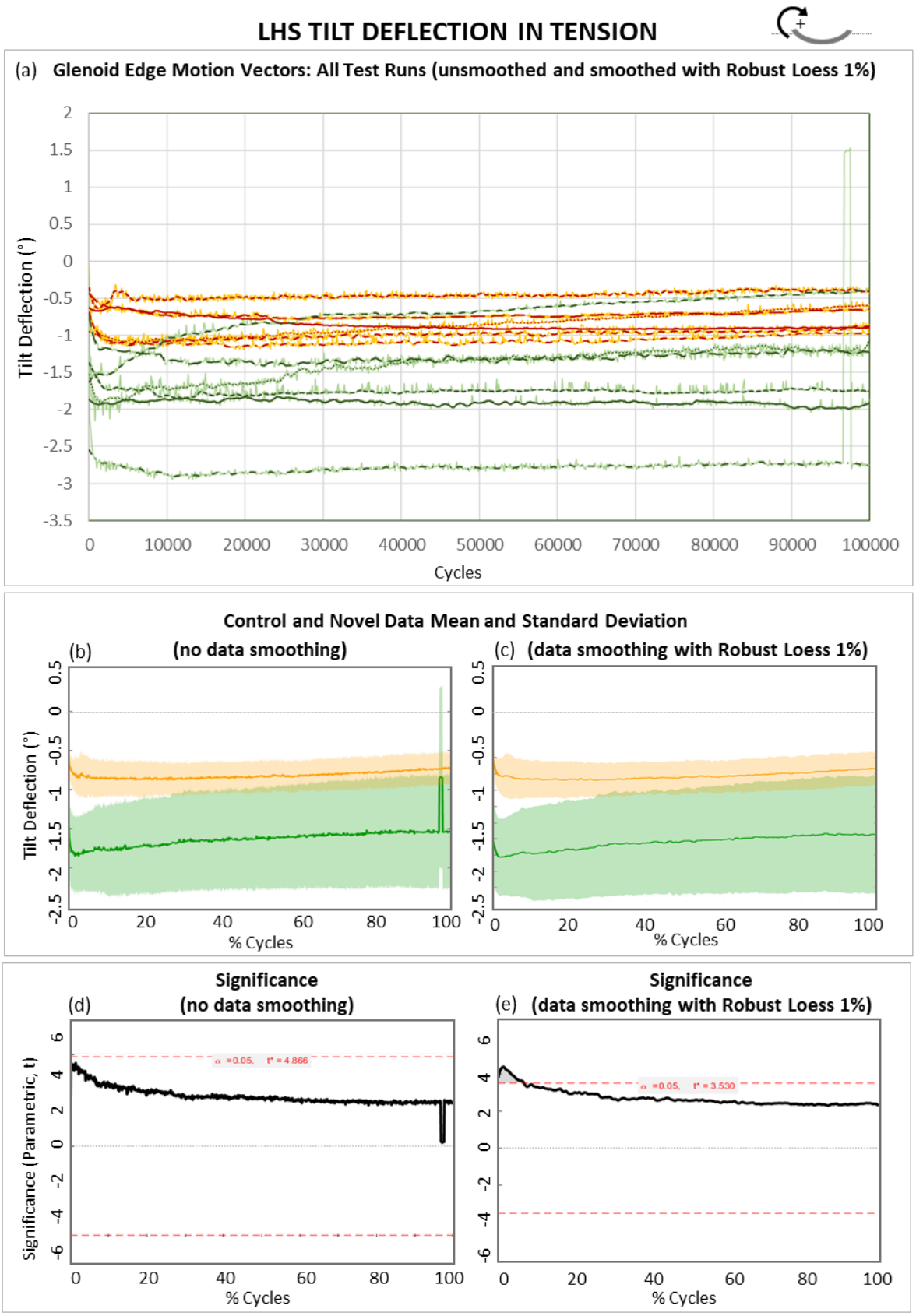

Figure C-13 *Tilt deflection of the LHS control (orange) and novel (green) glenoid edges in tension for all test runs. Unsmoothed data and the comparative data smoothed by 1% Robust Loess smothing are shown. Refer to* ***Edge Motion Data Key*** *for details of plots.*

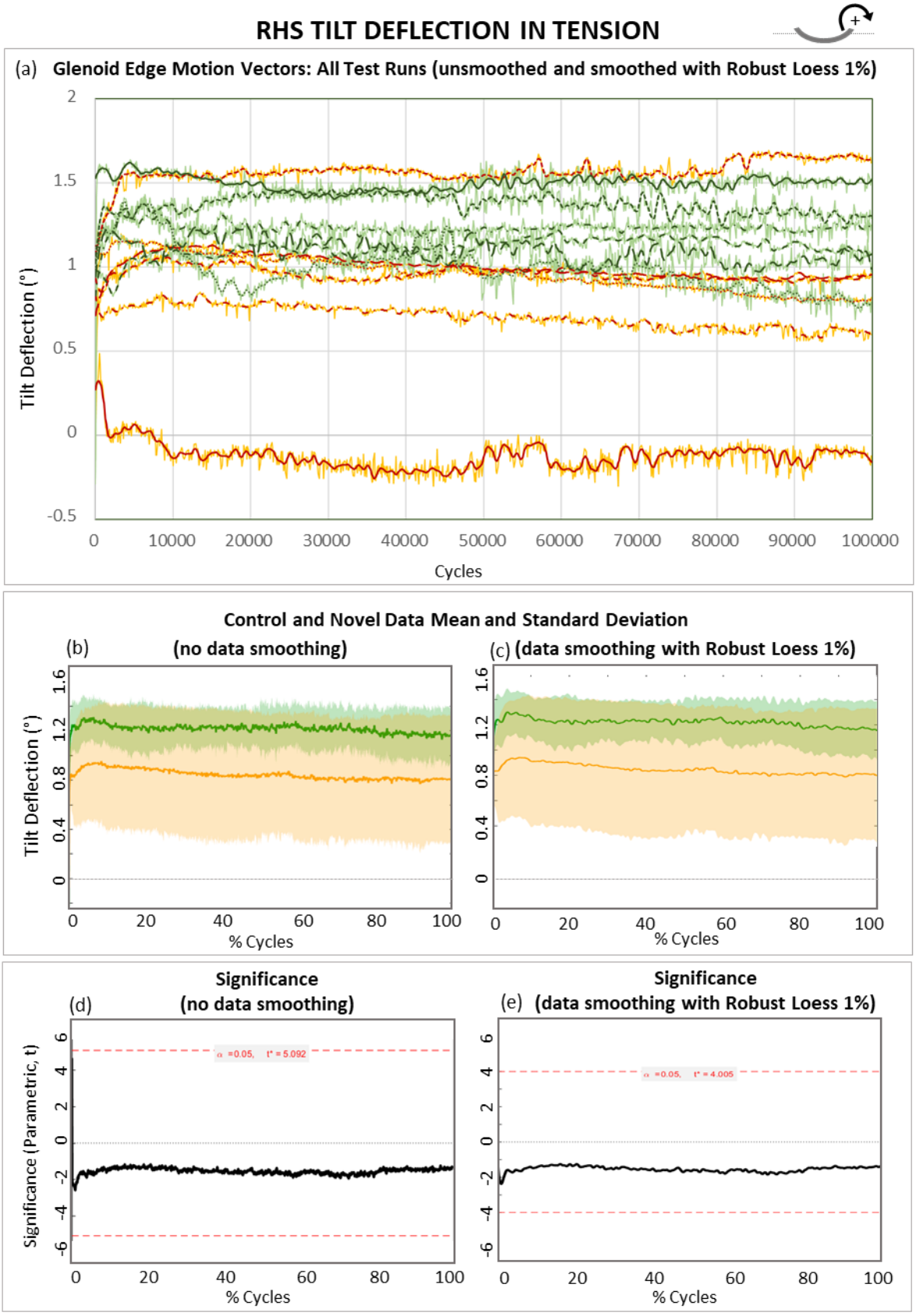

Figure C-14 *Tilt deflection of the RHS control (orange) and novel (green) glenoid edges in tension for all test runs. Unsmoothed data and the comparative data smoothed by 1% Robust Loess smothing are shown. Refer to* ***Edge Motion Data Key*** *for details of plots.*

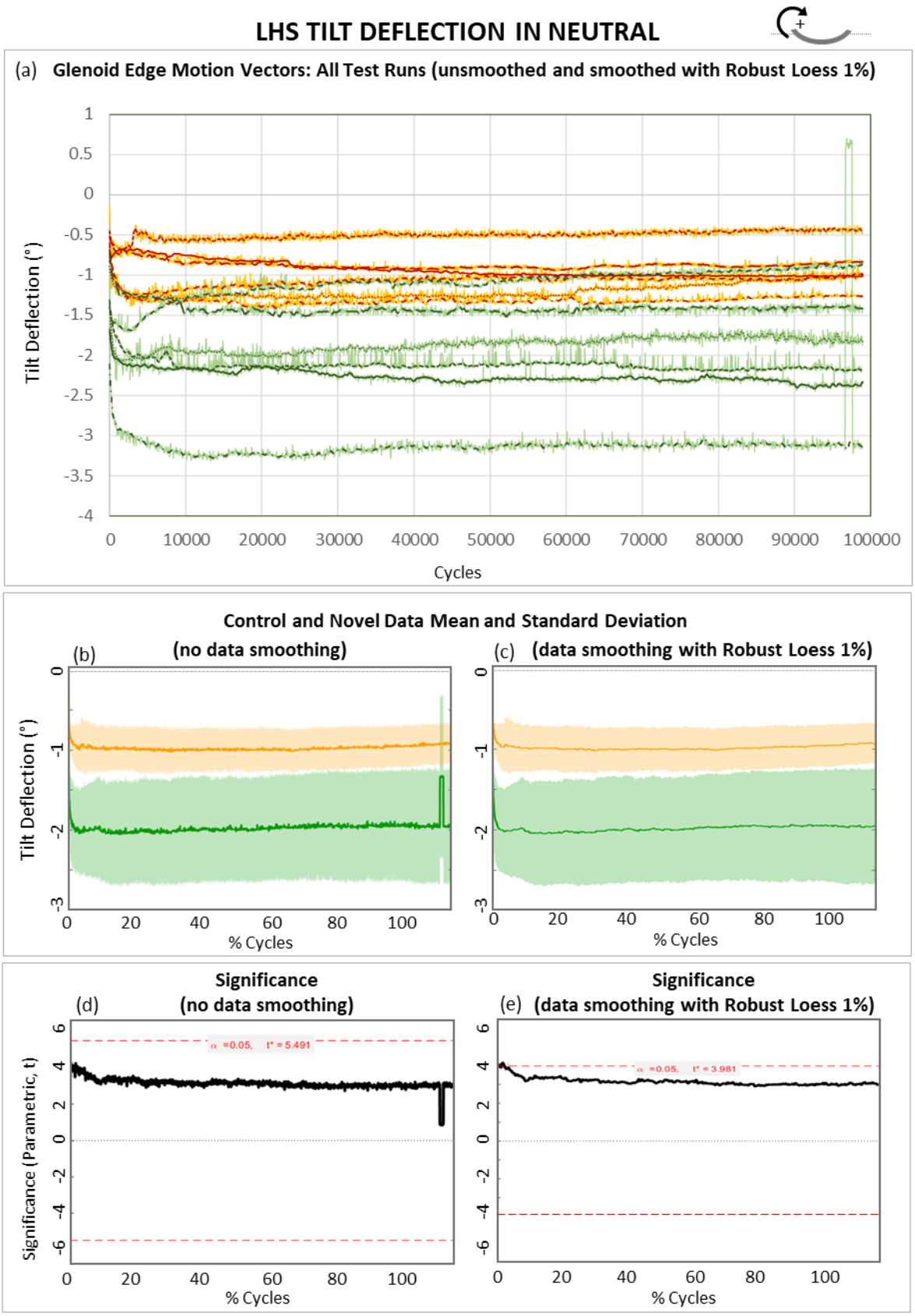

Figure C-15 *Tilt deflection of the LHS control (orange) and novel (green) glenoid edges in neutral for all test runs. Unsmoothed data and the comparative data smoothed by 1% Robust Loess smothing are shown. Refer to* ***Edge Motion Data Key*** *for details of plots.*

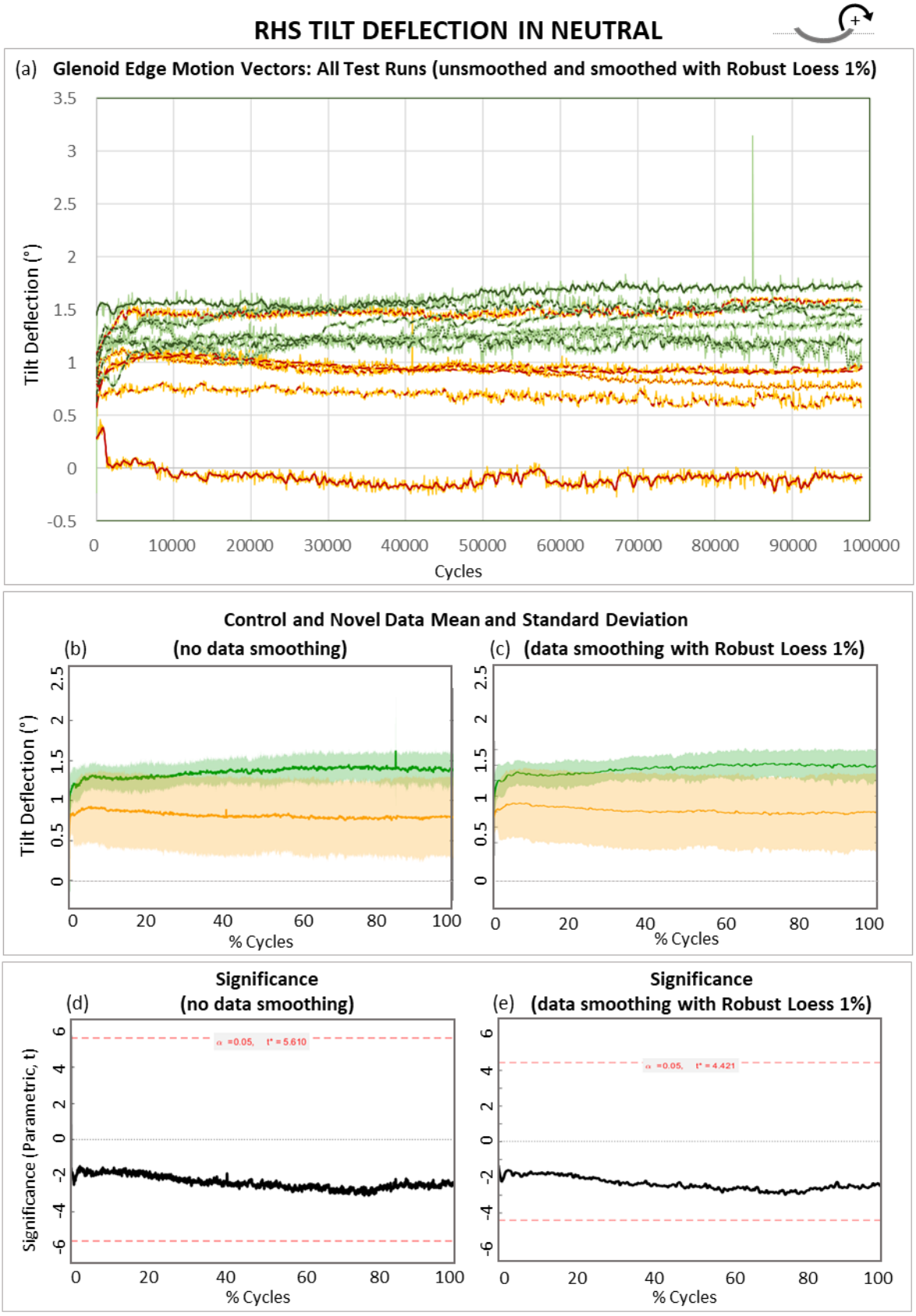

Figure C-16 *Tilt deflection of the RHS control (orange) and novel (green) glenoid edges in neutral for all test runs. Unsmoothed data and the comparative data smoothed by 1% Robust Loess smothing are shown. Refer to* ***Edge Motion Data Key*** *for details of plots.*

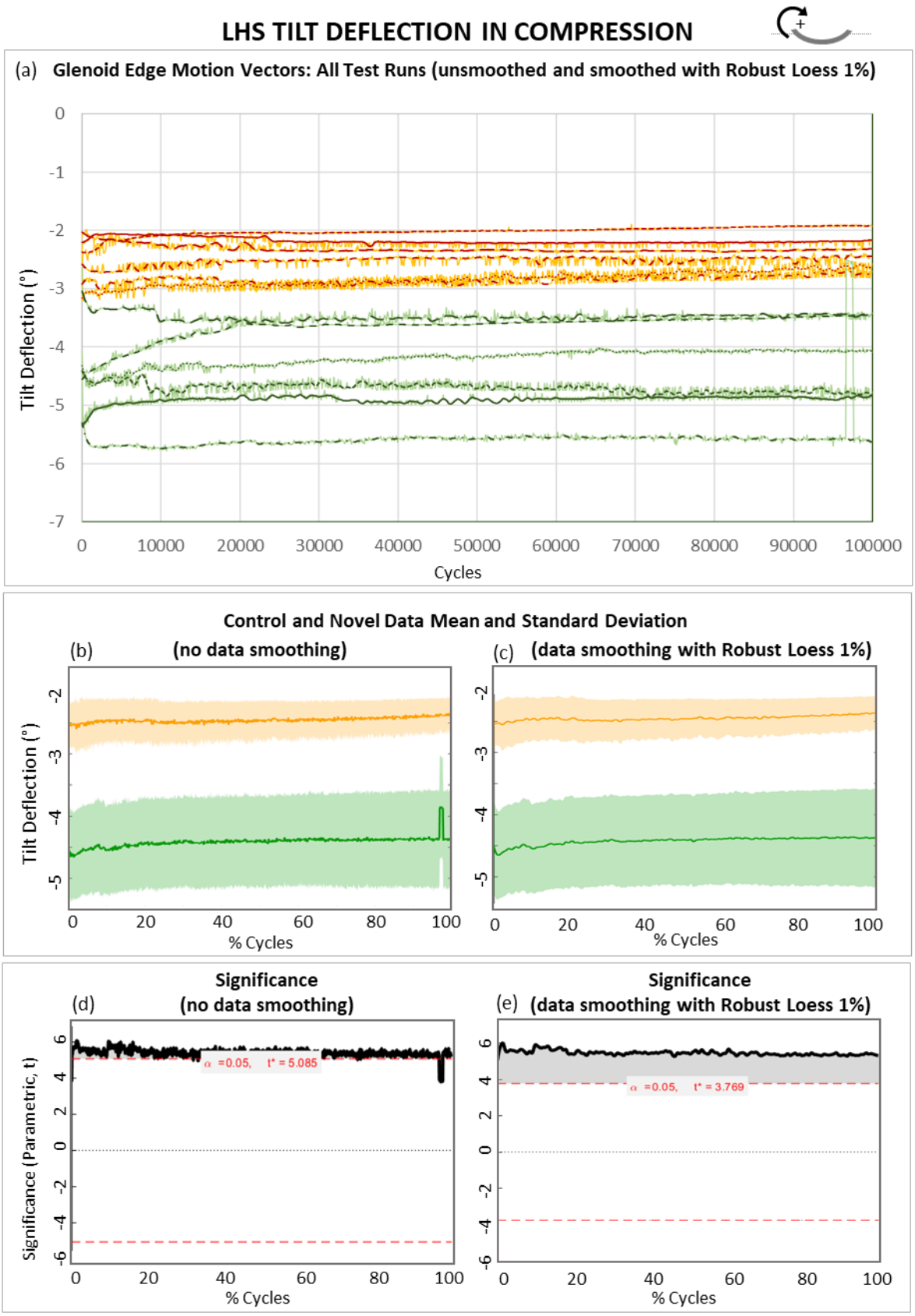

Figure C-17 *Tilt deflection of the LHS control (orange) and novel (green) glenoid edges in compression for all test runs. Unsmoothed data and the comparative data smoothed by 1% Robust Loess smothing are shown. Refer to* ***Edge Motion Data Key*** *for details of plots.*

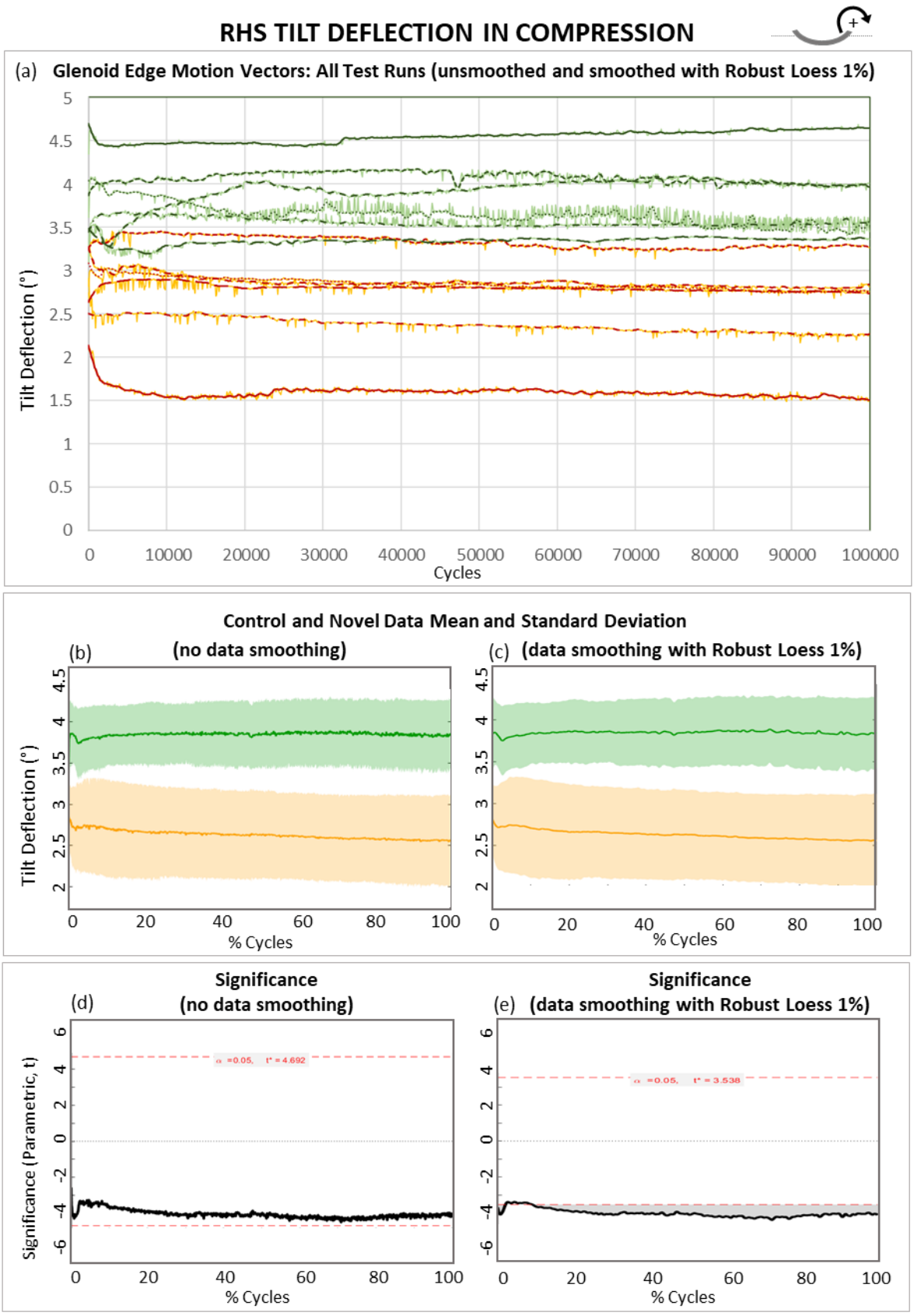

Figure C-18 *Tilt deflection of the RHS control (orange) and novel (green) glenoid edges in compression for all test runs. Unsmoothed data and the comparative data smoothed by 1% Robust Loess smothing are shown. Refer to* ***Edge Motion Data Key*** *for details of plots.*

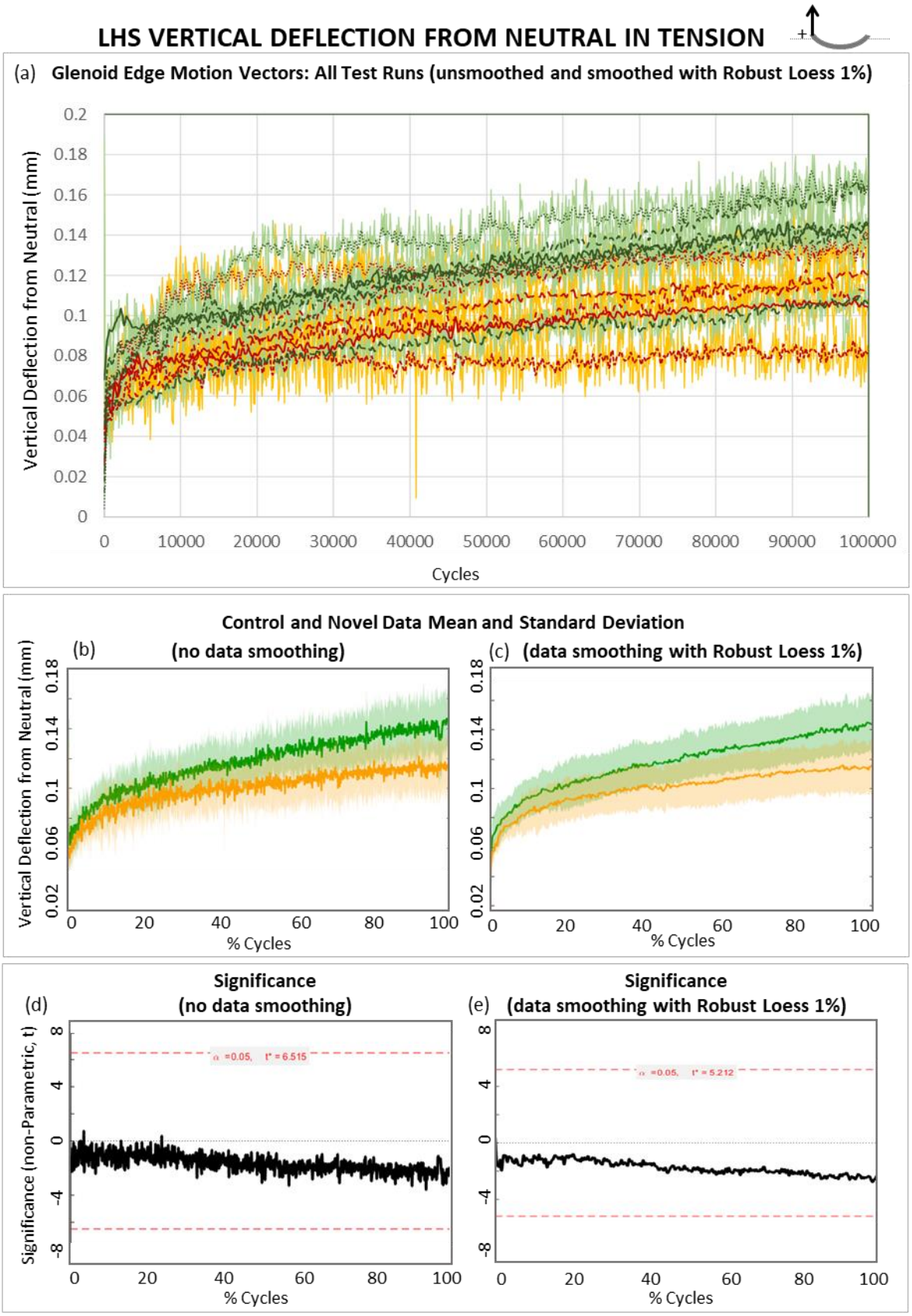

Figure C-19 *Vertical deflection from neutral of the LHS control (orange) and novel (green) glenoid edges in tension for all test runs. Unsmoothed data and the comparative data smoothed by 1% Robust Loess smothing are shown. Refer to* ***Edge Motion Data Key*** *for details of plots.*

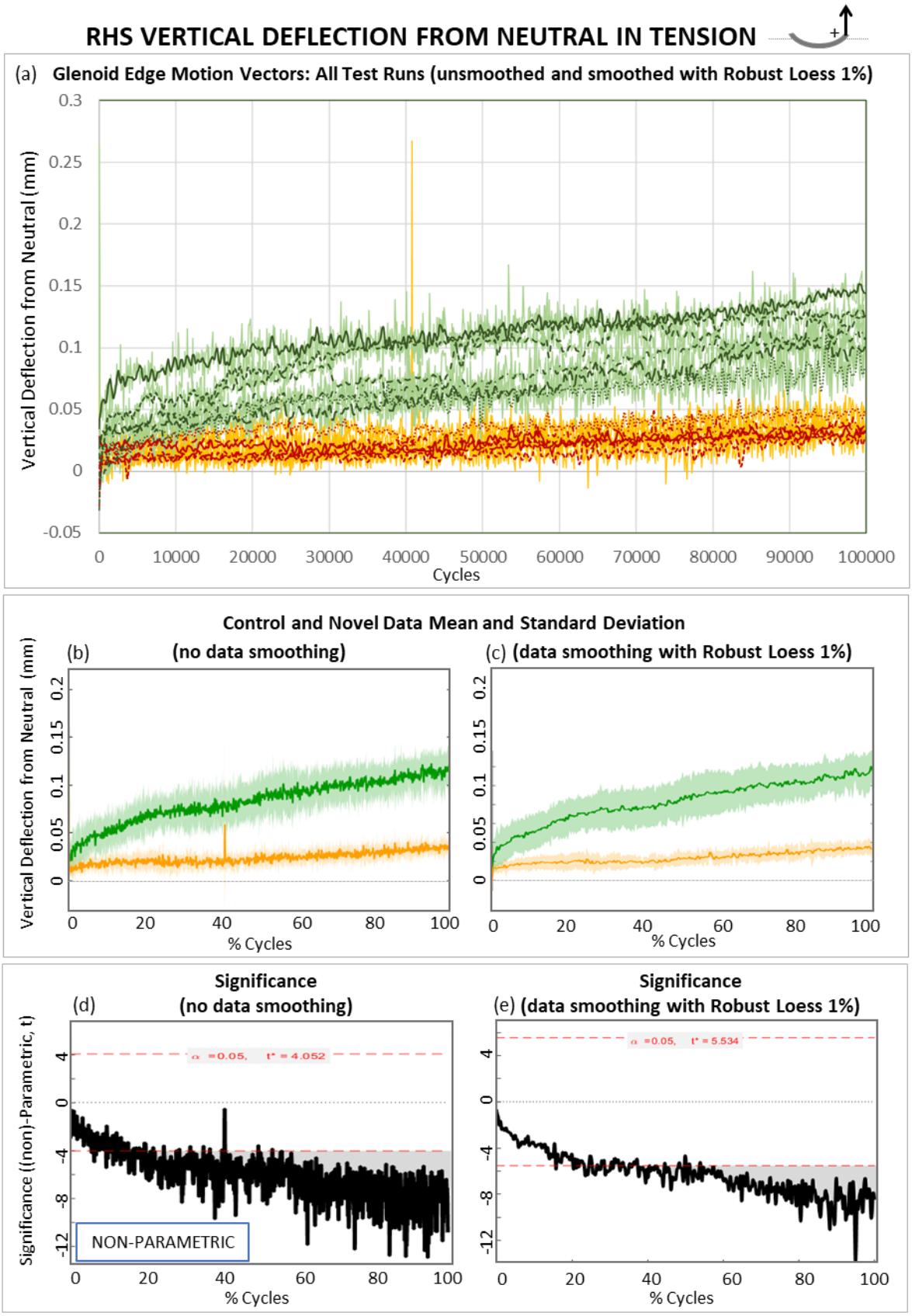

Figure C-20 *Vertical deflection from neutral of the RHS control (orange) and novel (green) glenoid edges in tension for all test runs. Unsmoothed data and the comparative data smoothed by 1% Robust Loess smothing are shown. Refer to* ***Edge Motion Data Key*** *for details of plots.*

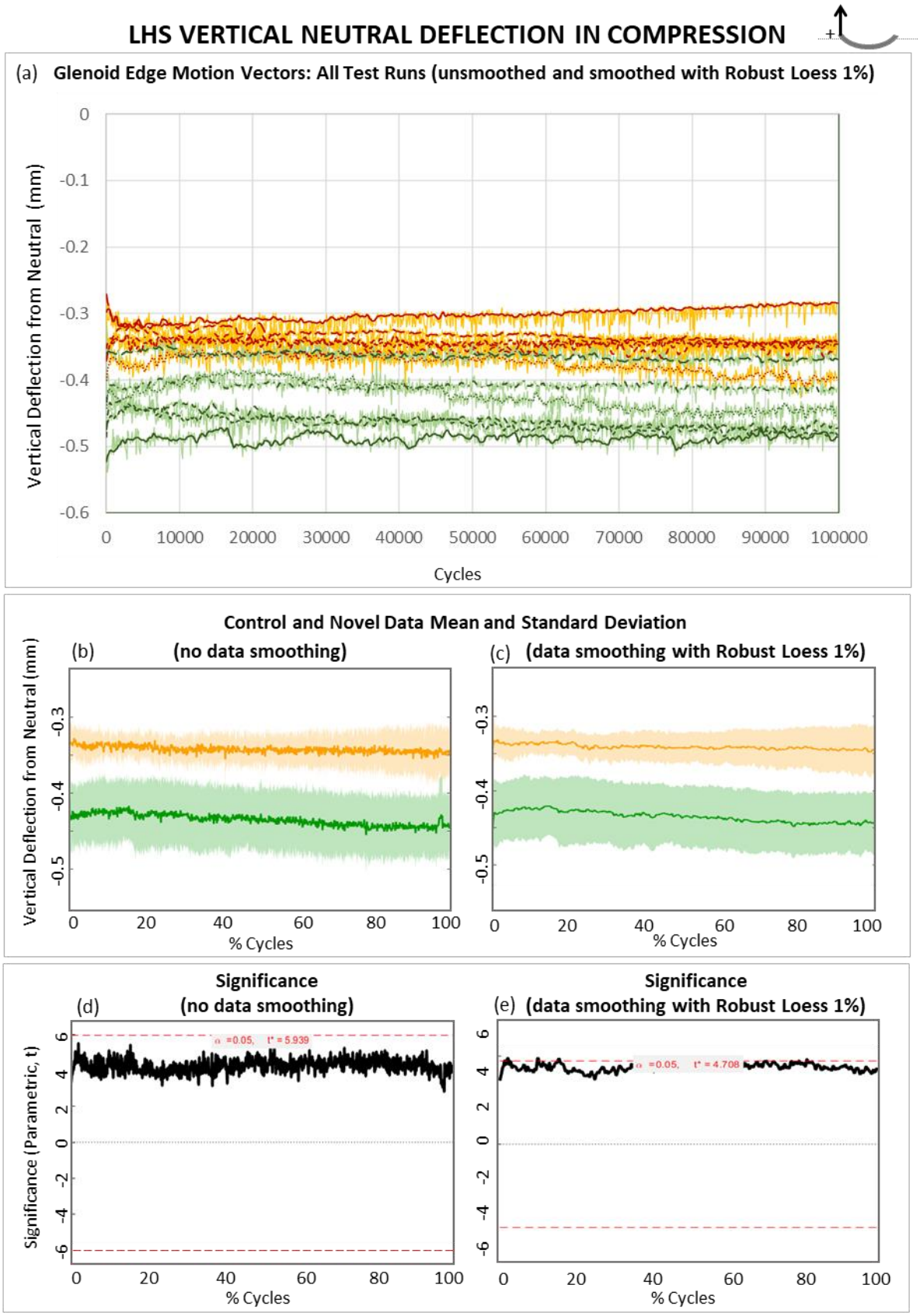

Figure C-21 *Vertical deflection from neutral of the LHS control (orange) and novel (green) glenoid edges in compression for all test runs. Unsmoothed data and the comparative data smoothed by 1% Robust Loess smothing are shown. Refer to* ***Edge Motion Data Key*** *for details of plots.*

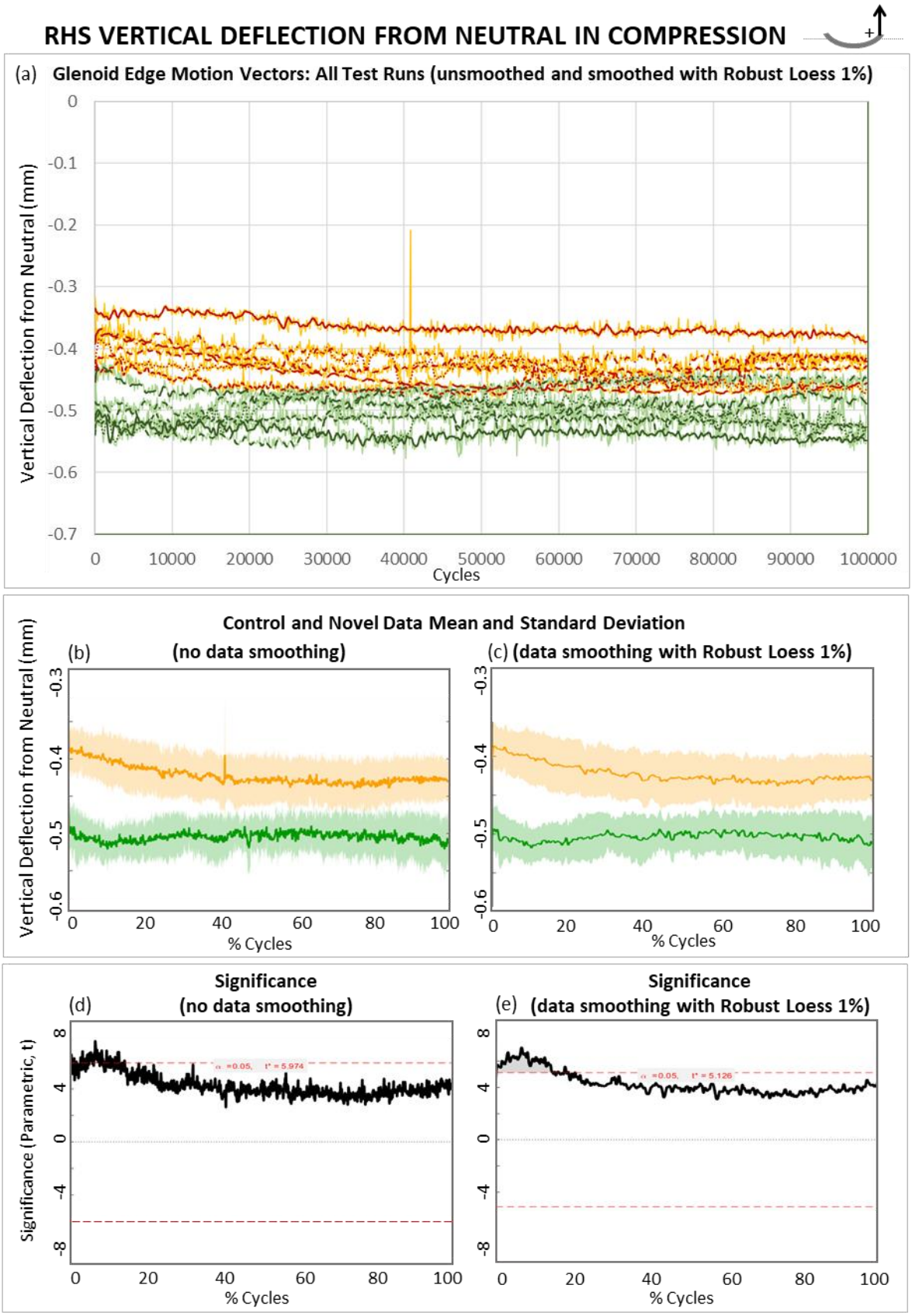

Figure C-22 *Vertical deflection from neutral of the RHS control (orange) and novel (green) glenoid edges in compression for all test runs. Unsmoothed data and the comparative data smoothed by 1% Robust Loess smothing are shown. Refer to* ***Edge Motion Data Key*** *for details of plots.*

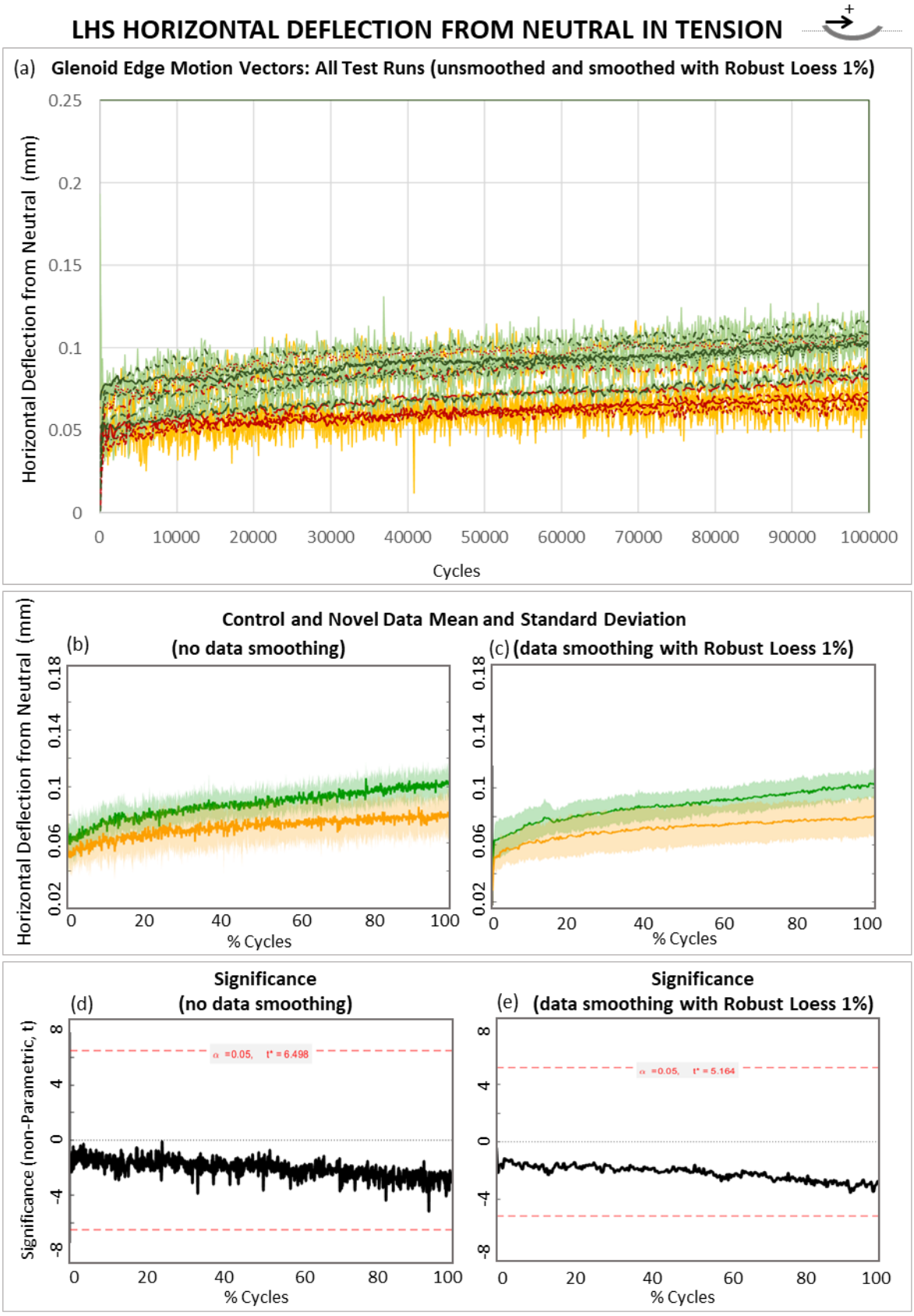

Figure C-23 *Horizontal deflection from neutral of the LHS control (orange) and novel (green) glenoid edges in tension for all test runs. Unsmoothed data and the comparative data smoothed by 1% Robust Loess smothing are shown. Refer to* ***Edge Motion Data Key*** *for details of plots.*

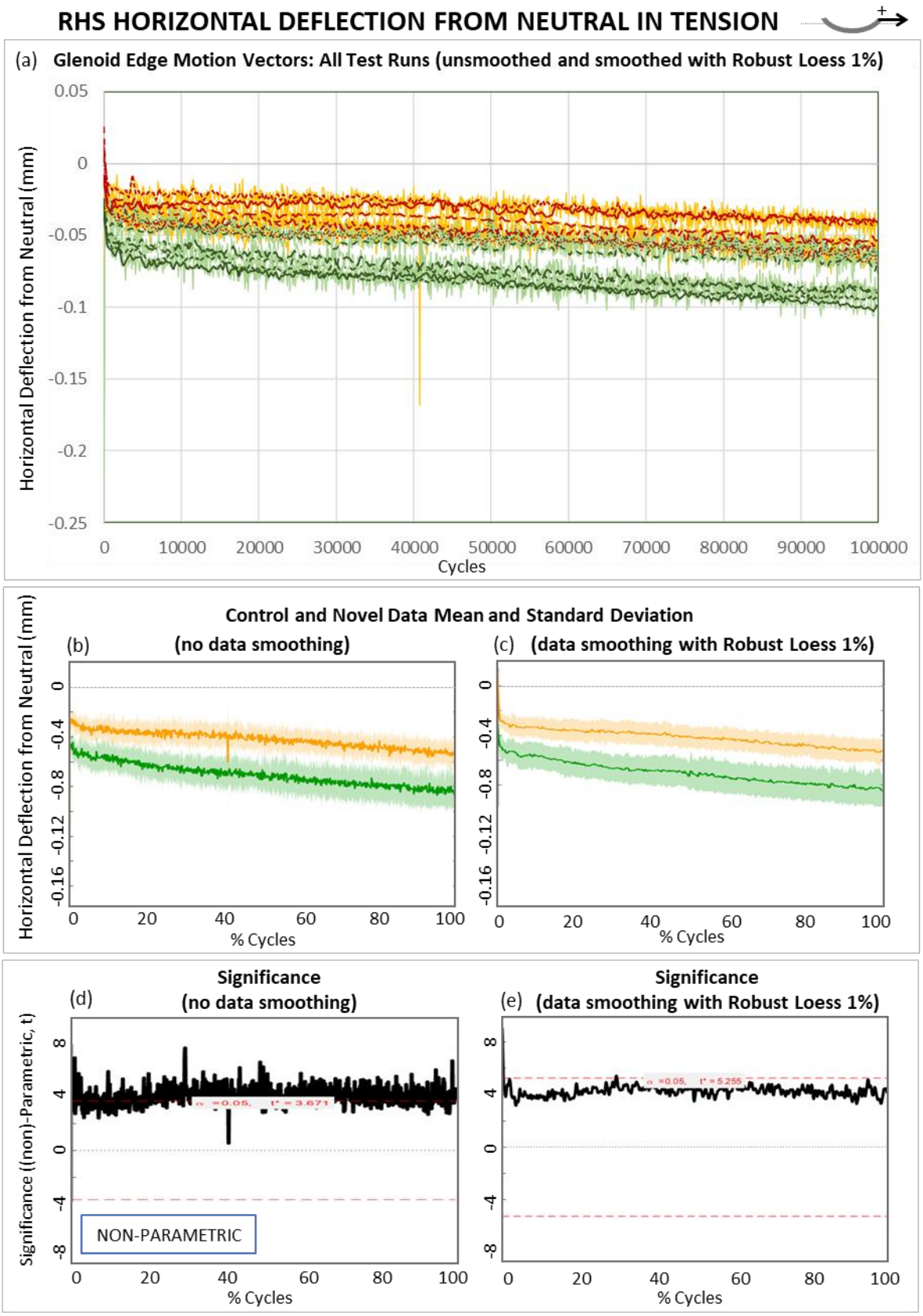

Figure C-24 *Horizontal deflection from neutral of the RHS control (orange) and novel (green) glenoid edges in tension for all test runs. Unsmoothed data and the comparative data smoothed by 1% Robust Loess smothing are shown. Refer to* ***Edge Motion Data Key*** *for details of plots.*

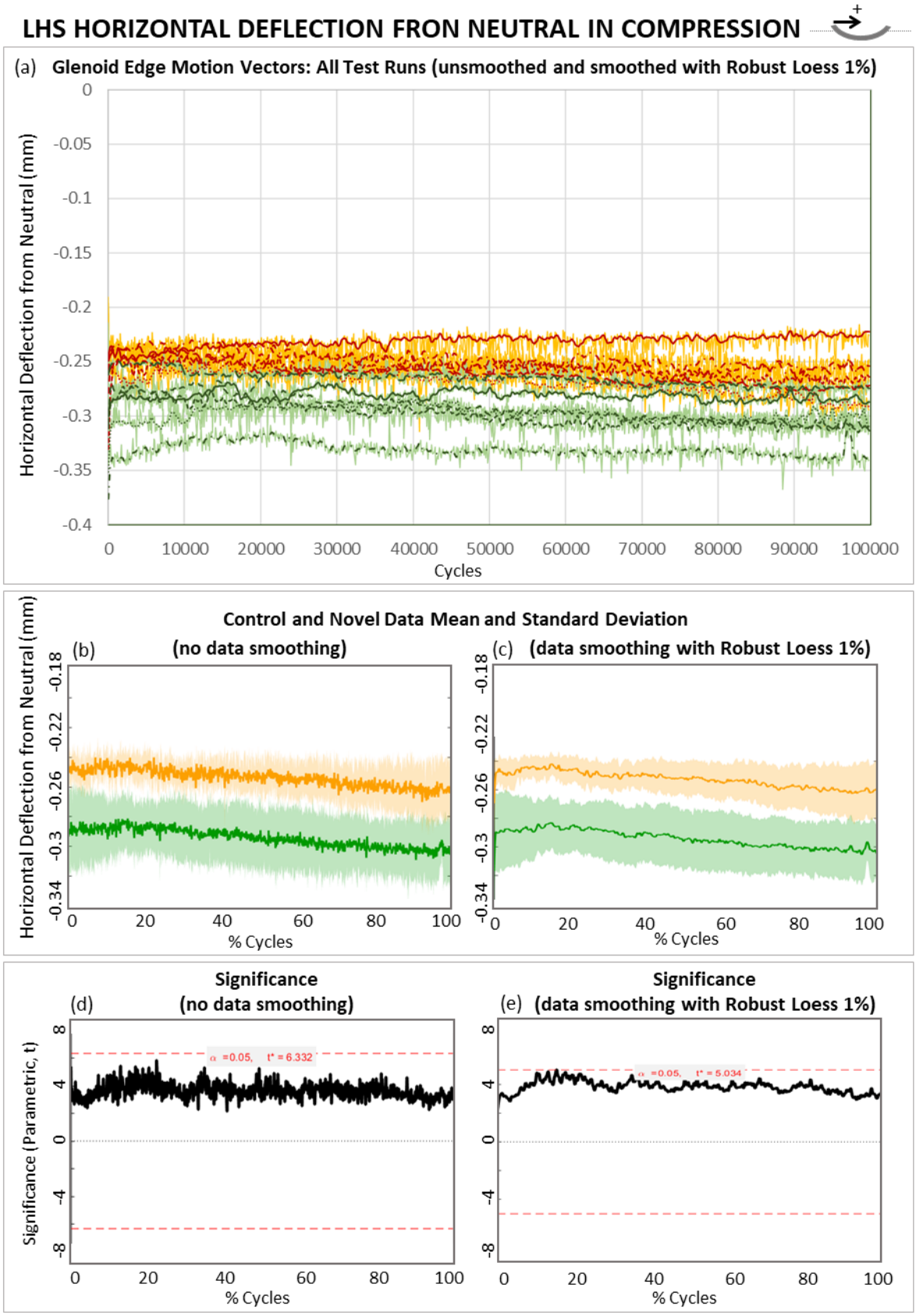

Figure C-25 *Horizontal deflection from neutral of the LHS control (orange) and novel (green) glenoid edges in compression for all test runs. Unsmoothed data and the comparative data smoothed by 1% Robust Loess smothing are shown. Refer to* ***Edge Motion Data Key*** *for details of plots.*

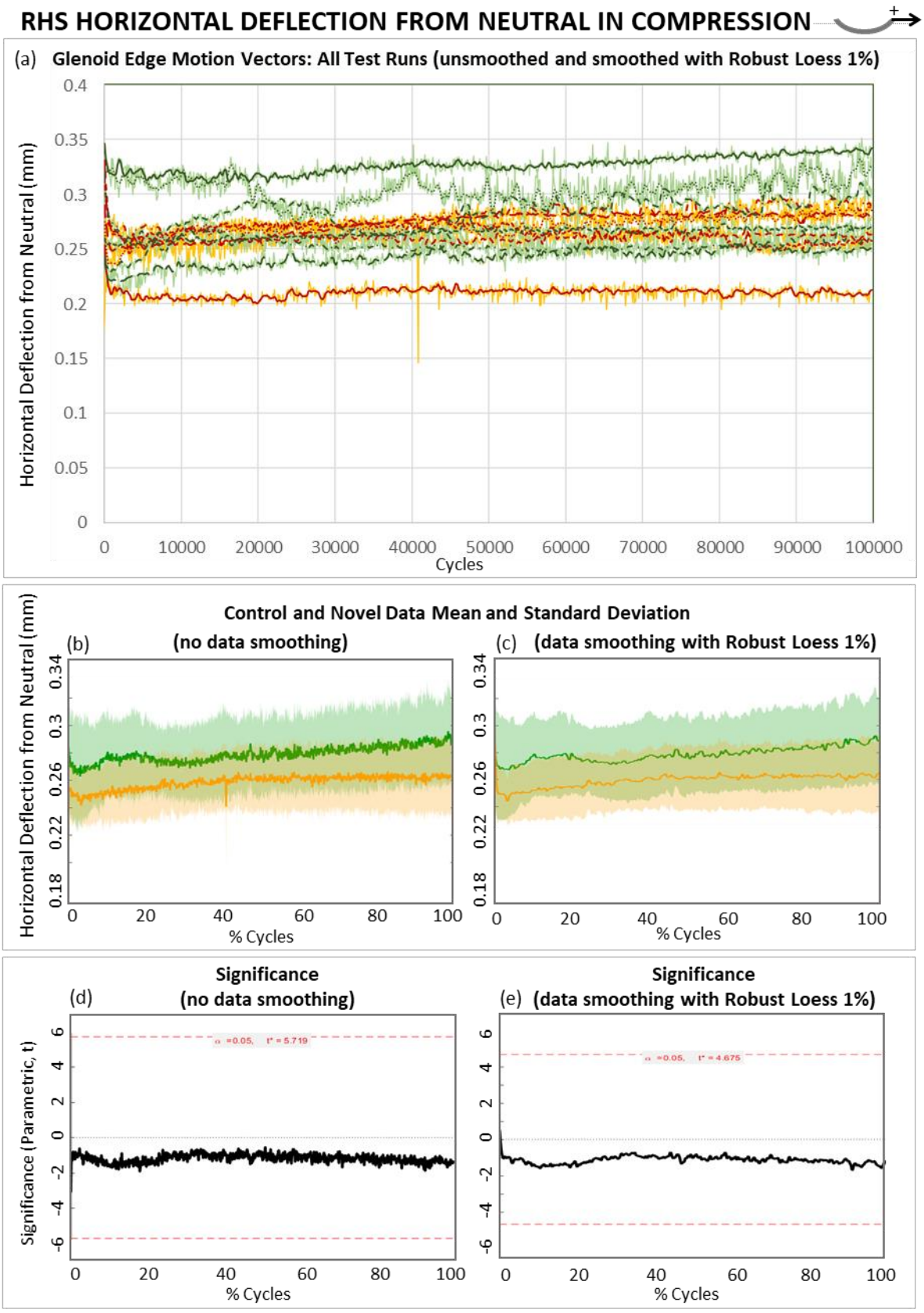

Figure C-26 *Horizontal deflection from neutral of the RHS control (orange) and novel (green) glenoid edges in compression for all test runs. Unsmoothed data and the comparative data smoothed by 1% Robust Loess smothing are shown. Refer to* ***Edge Motion Data Key*** *for details of plots.*

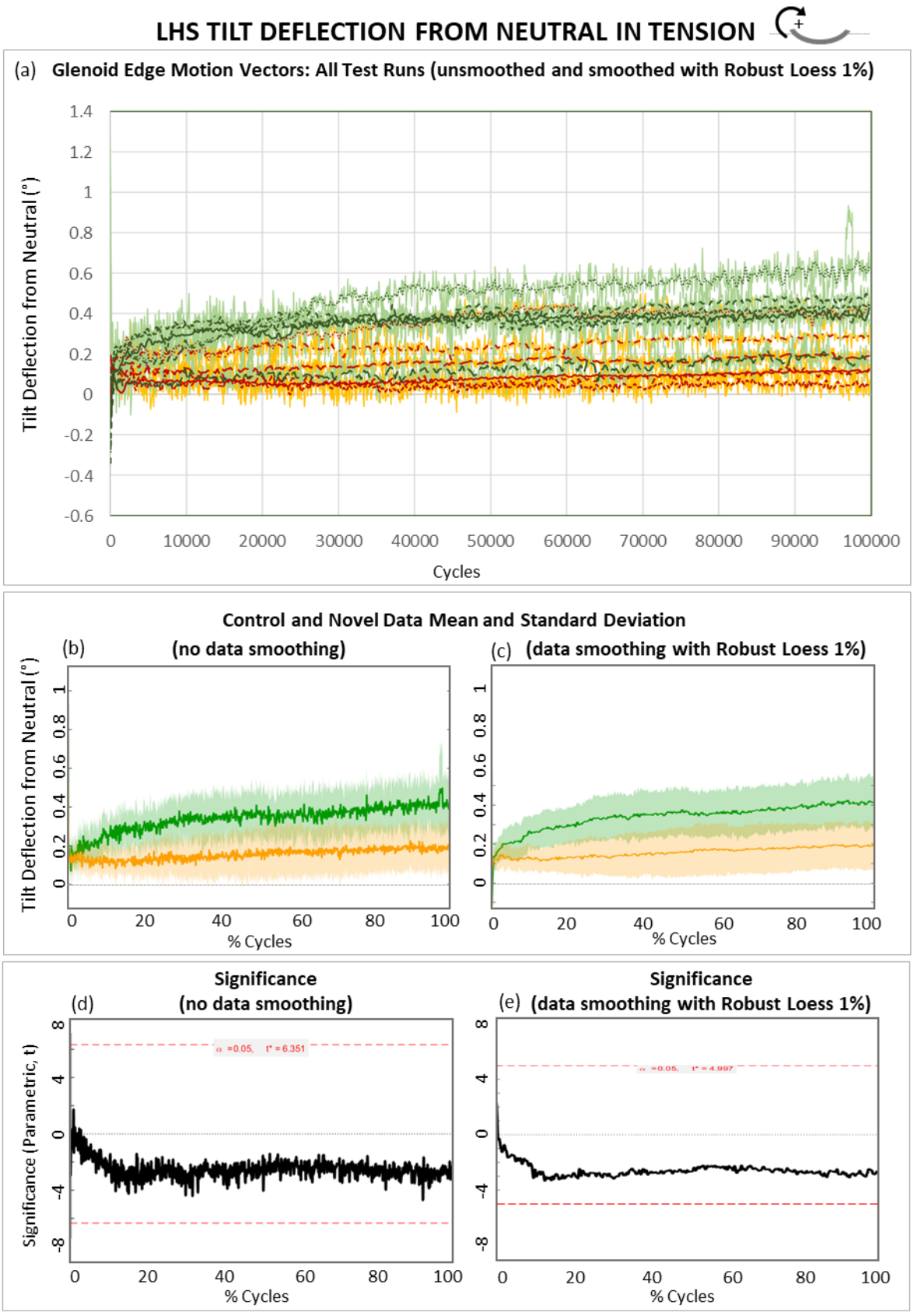

Figure C-27 *Tilt deflection from neutral of the LHS control (orange) and novel (green) glenoid edges in tension for all test runs. Unsmoothed data and the comparative data smoothed by 1% Robust Loess smothing are shown. Refer to* ***Edge Motion Data Key*** *for details of plots.*

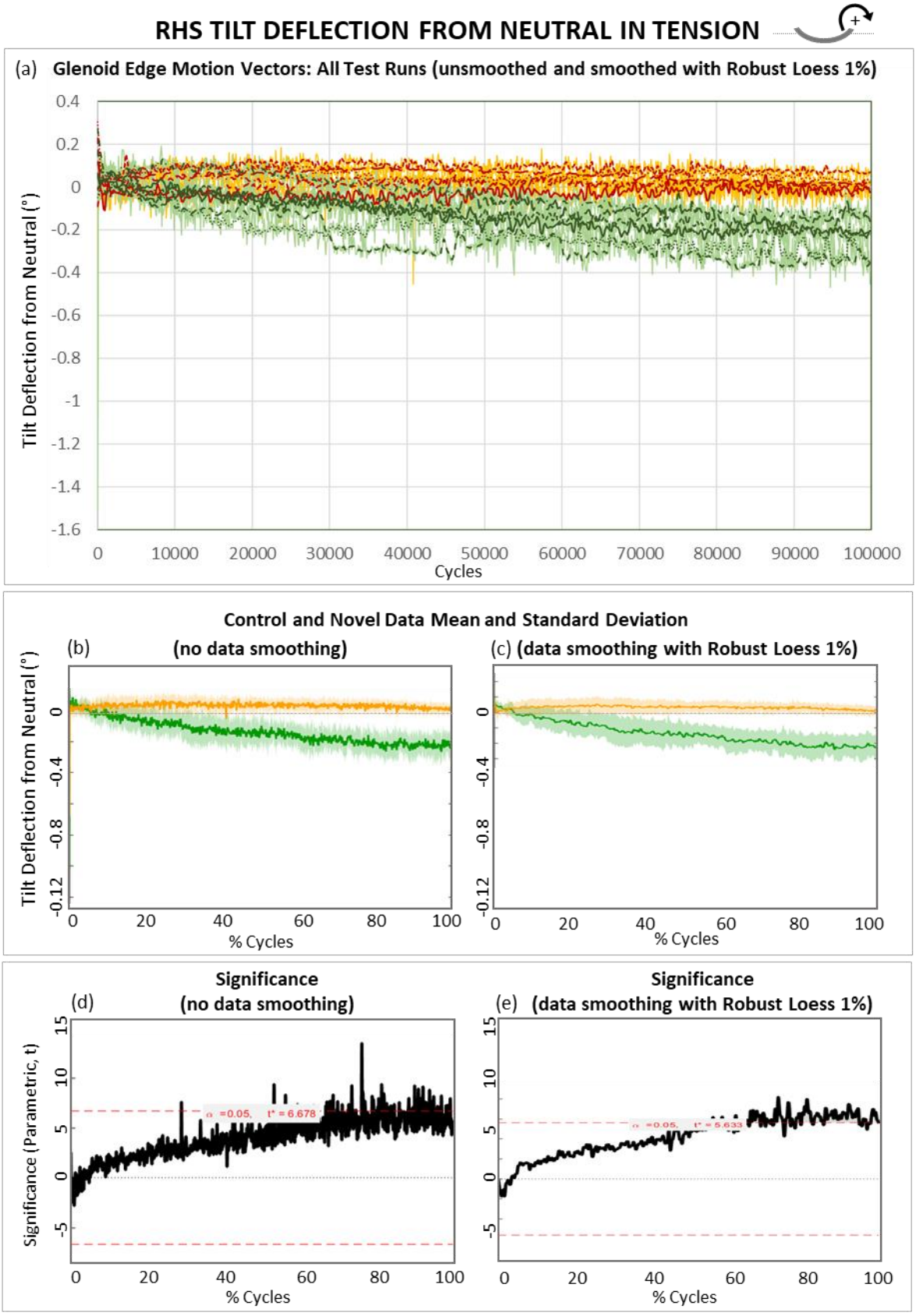

Figure C-28 *Tilt deflection from neutral of the RHS control (orange) and novel (green) glenoid edges in tension for all test runs. Unsmoothed data and the comparative data smoothed by 1% Robust Loess smothing are shown. Refer to* ***Edge Motion Data Key*** *for details of plots.*

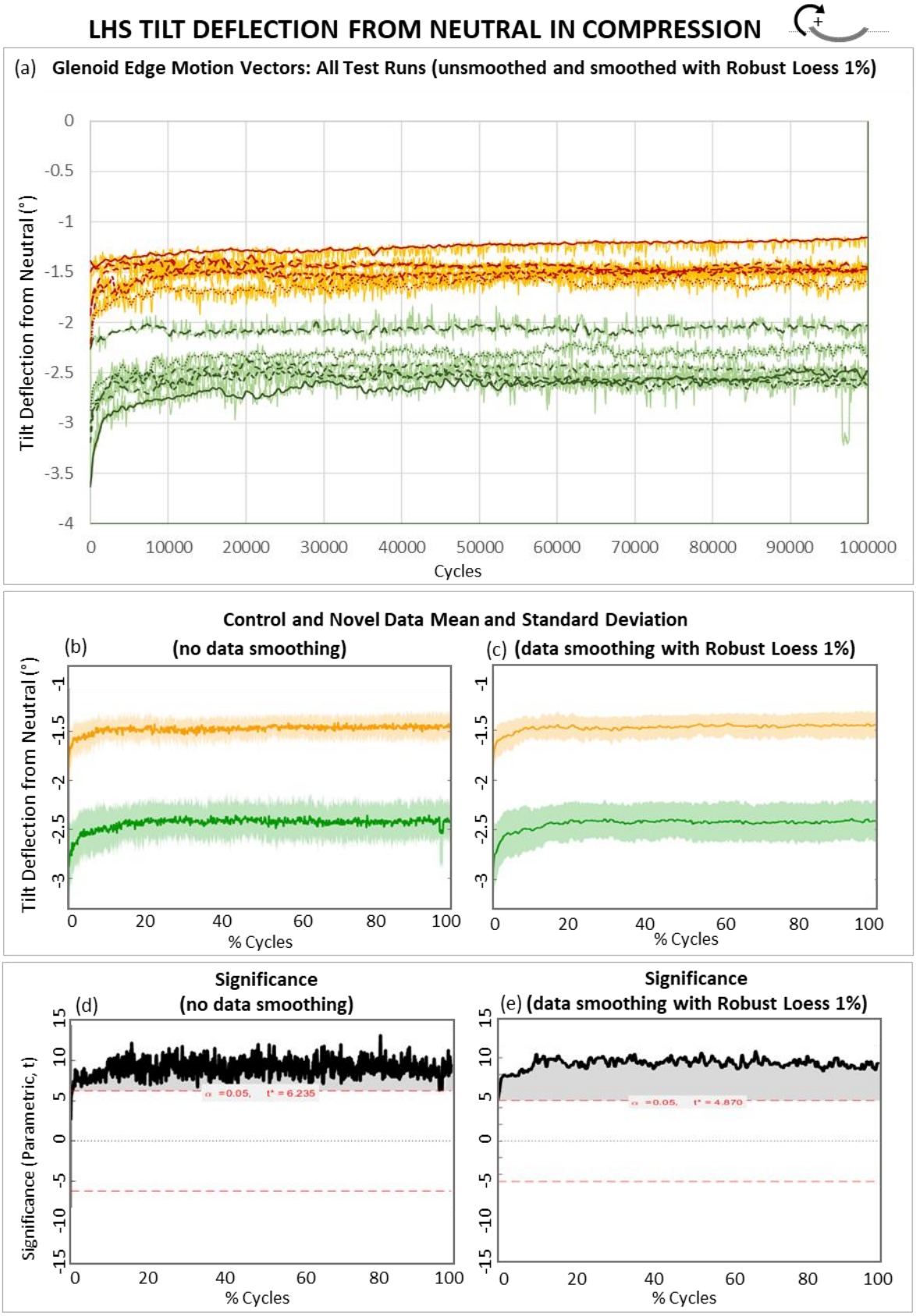

Figure C-29 *Tilt deflection from neutral of the LHS control (orange) and novel (green) glenoid edges in compression for all test runs. Unsmoothed data and the comparative data smoothed by 1% Robust Loess smothing are shown. Refer to* ***Edge Motion Data Key*** *for details of plots.*

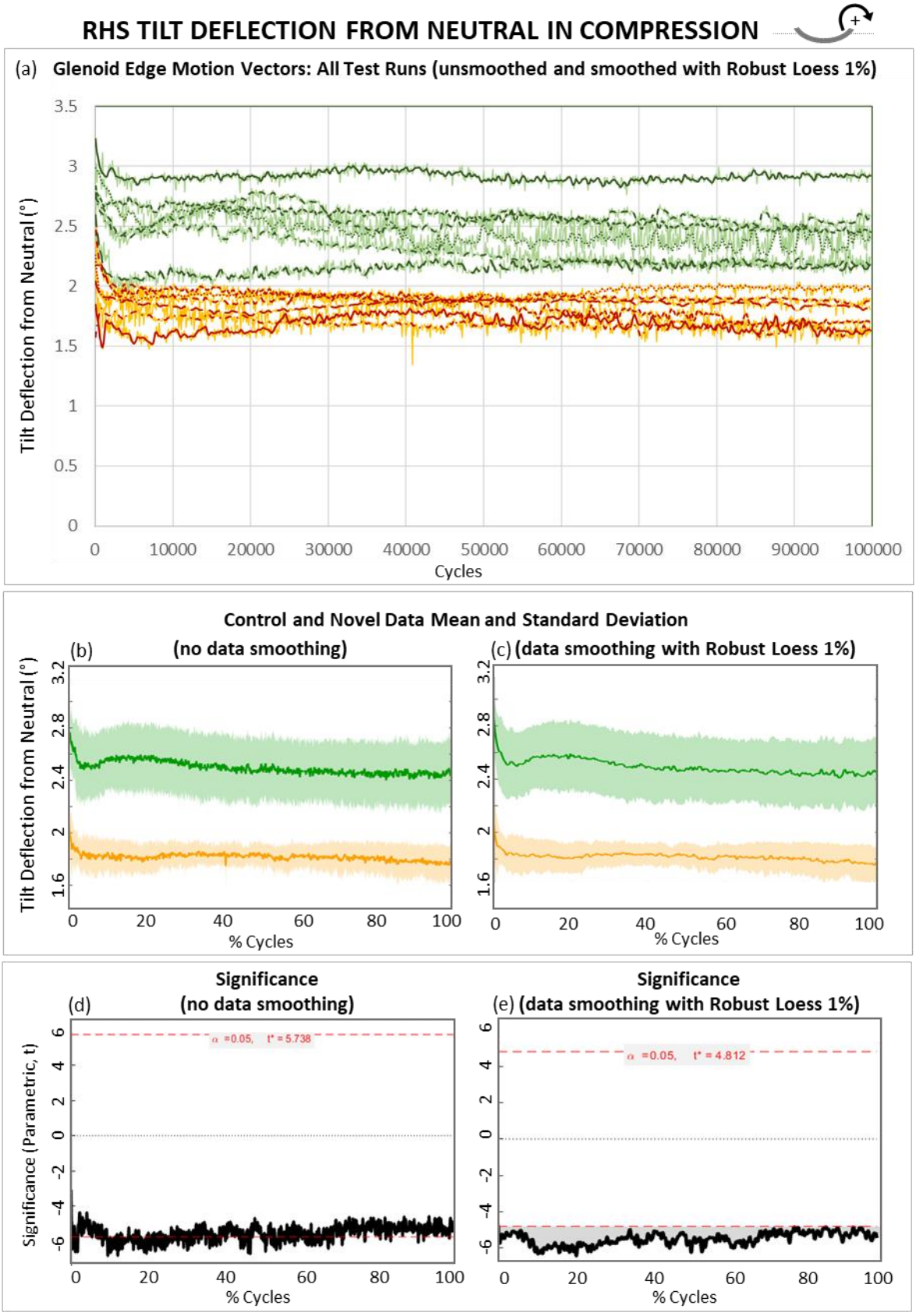

Figure C-30 *Tilt deflection from neutral of the RHS control (orange) and novel (green) glenoid edges in compression for all test runs. Unsmoothed data and the comparative data smoothed by 1% Robust Loess smothing are shown. Refer to* ***Edge Motion Data Key*** *for details of plots.*